Sensitizing triple negative breast cancer to approved therapies: Design, synthesis and biological activity of MNK inhibitors

Elisabeth Bou Petit

DOCTORAL THESIS

Title	**Sensitizing triple negative breast cancer to approved therapies: Design, synthesis and biological evaluation of MNK inhibitors**
Presented by	**Elisabeth Bou Petit**
Centre	**IQS School of Engineering**
Department	**Organic and Pharmaceutical Chemistry**
Directed by	**Dr. Jose I. Borrell Bilbao, Dr. Santiago Ramon y Cajal Agüeras and Dr. Roger Estrada Tejedor**

Als meus avis

i a la Nati

Education is the most powerful weapon which you can use to change the world

Nelson Mandela

This thesis was possible thanks to the predoctoral fellowship funded by the Secretaria d'Universitats i Recerca del Departament d'Empresa i Coneixement de la Generalitat de Catalunya and the European Social Funds.

Credentials:

2015 FI_B 00067

2016 FI_B1 00054

2017 FI_B2 00139

ACKOWLEDGMENTS

En primer lloc vull agrair als meus directors de tesi, Dr. Iñaki Borrell, Dr. Santiago Ramon y Cajal i Dr. Roger Estrada l'oportunitat de realitzar aquesta tesi doctoral. *Moltes gràcies per permetre'm realitzar una tesi tant multidisciplinària en que he pogut aprendre a combinar les eines computacionals, sintètiques i biològiques per aconseguir els millors resultats possibles. Gràcies pel suport i la confiança inclús quan les coses no sortien bé.*

També vull agrair a totes aquelles persones que amb el seu treball han estat part d'aquesta tesi: Helena, Nieves, Arnau, Andrea, Elsa, Alex, Aristarc, Matias, Carla i Leti. *Moltes gràcies per confiar en mi i voler participar en aquest projecte. Sense la vostra ajuda, no hagués estat possible. Moltes gràcies!*

A tots aquells que han fet aquest camí amb mi. Especialment als meus FotoQs (Uri, Bea, Joaquim i Roger). *Moltes gràcies per acollir-me als inicis de la tesi, quan no hi havia ningú més al laboratori de disseny molecular. Gràcies per anar sempre un pas endavant i ajudar-me a superar les diferents etapes de la tesi doctoral. Però sobretot, gràcies per la vostra amistat.*

Als sintètics i als Dismolers. Víctor, Carlos, Ángel, Dani, Gemma i Leti i a tots els que han passat per la secció durant aquests anys. *Gràcies per l'ajuda desinteressada en el moment en que més l'he necessitat*.

Al Rai i l'Ana, *gràcies pels consells i el suport. I gràcies per les hores compartides a les auxiliaries*.

Als que van començar amb mi des dels inicis. Raül, Gabi, Mire i Alba. *Després de 10 anys encara aconseguiu que m'oblidi dels problemes i recuperi l'alegria. Gràcies per estar-hi sempre*.

Als meus companys del VHIR, Pedro, Eva i Mº Jose, de qui he après tot el que se de cèl·lules. *Gràcies per les hores dedicades i la paciència per respondre a totes les meves preguntes.*
A mi técnico favorito, Pedro, a quien debo muchos experimentos. *Gracias por ayudarme a llegar a todo, por tu predisposición y por tu alegría constante. Tenías razón, al final, lo hemos conseguido!*
Al Stefan, *thanks for believing in me and in this project.*

Thanks to my supervisors in Montreal, Dr. Ivan Topisirovic and Dr. Sonia del Ricon for the opportunity to do a research stay.
To my friends in Canada. Justin, Sath, Alex and Hsiang. *Thanks for your help, your support and your friendship.*

Als que s'interessen per la tesi quan no entenen res. La Sonia, les meves nenes de Quart Creixent (Lau, Elena i Ali), la Laura C., les nenes de la Salle (Eira i Ona) i a l'Alex, el Frey i el Marc. A la Cris i l'Erik i la Bel i el Xim. *Gràcies per l'interès que sempre teniu. Gràcies per estar al meu costat.*

A la família Rosel Sola, *gracias por los ánimos y la comprensión*.

Als meus avis. Per l'interès i l'esforç per comprendre el que faig. Especialment a l'Àvia Consol amb qui més voldria compartir aquest moment.

Per últim, als que han fet possible que em trobi en aquest punt. Als meus pares. *Gràcies per tot el suport i recolzament. Gràcies per ajudar-me a perseguir els meus somnis. Gràcies per aixecar-me quan caic i donar-me sempre l'empenta per seguir endavant.*
Al Víctor (i la Claudia) i al Sergi (i la Maria). *Gràcies per la paciència i la comprensió, els ànims i els somriures.*

I al Toni. *Gràcies infinites. No ho hagués aconseguit sense tu*. *I love you three thousand.*

A tots els que heu fet aquest camí amb mi, moltes gràcies.

SUMMARY

Deregulation of protein synthesis is a common event in cancer. A key player in translational control is eIF4E whose function is modulated by the MAP kinase interacting kinases 1 and 2 (MNK1/2) through phosphorylation of a conserved serine (Ser209). In the recent years, eIF4E has been described as an independent prognostic factor associated with malignant progression and development of resistance. Moreover, eIF4E is found to be overexpressed in ovarian, breast, lung, colon, bladder and prostate cancer. eIF4E phosphorylation is necessary for oncogenic transformation while dispensable for normal development. Hence, pharmacologic MNK inhibitors may provide a non-toxic and effective anti-cancer strategy, especially in combination with approved treatments.

In this project, the pyrazolo[3,4-*b*]pyridinic systems have been proposed as potential candidates as MNK inhibitors due to their similarity with known effective inhibitors.
During this project, the synthetic possibilities offered by these scaffolds have been deeply studied defining general methodologies to achieve selective and controlled substitutions in 6 different points of the central core. Moreover, the reaction mechanisms have been described.

Up to 5 families of compounds based on the pyrazolo[3,4-*b*]pyridine scaffold were studied and one of the families showed interesting activity on the preliminary assays.
Three compounds (**EB1-3**), with IC_{50} values in the low μM range (0.7 to 4 μM), showed a complete and selective inhibition of MNKs (between 2.5 and 5 μM) and no significant cell toxicity in the triple negative breast cancer cell line MDA-MB-231. Moreover, co-treatment with **EB1** clearly increased the sensitivity of MDA-MB-231 cells to doxorubicin improving the efficacy of the drug in inhibiting cell growth.
A structure-based drug design strategy was applied to understand the mechanism of interaction of the different candidates. Models of the active/inactive forms of MNK1 were created and used to predict the binding mode of the hits. **EB1** seems to be a type II inhibitor which selectively binds to the inactive form of MNK1 and interacts with the DFD (Asp-Phe-Asp) motif, a unique feature of MNKs.

SUMARIO

La desregulación de la síntesis de proteínas es común en cáncer. Un factor clave en el control de la traducción de proteínas es el factor de inicio de la traducción 4E (eIF4E) cuya función está modulada por las quinasas MNK1/2 (*MAP kinase interacting kinases* 1 y 2) mediante fosforilación. En los últimos años, el eIF4E se ha descrito como un factor de pronóstico independiente asociado con la progresión maligna y el desarrollo de resistencia. Además, el eIF4E se encuentra sobreexpresado en cáncer de ovario, mama, pulmón, vejiga y próstata. La fosforilación del eIF4E es necesaria para la transformación tumoral pero es prescindible para el desarrollo normal. Por lo tanto, la inhibición farmacológica de las MNKs puede proporcionar una estrategia no tóxica y eficaz para el tratamiento del cáncer, especialmente en combinación con los tratamientos aprobados.

En este proyecto, se proponen los sistemas pirazolo[3,4-*b*]piridínicos como posibles candidatos a inhibidores de MNK debido a su similitud con inhibidores conocidos.
Se han estudiado las posibilidades sintéticas que ofrecen estas estructuras, definiendo metodologías generales para introducir sustituciones selectivas y controladas en 6 puntos diferentes de la molécula. Además, se han descrito los mecanismos de reacción.
Se han estudiado 5 familias de compuestos basados en los compuestos pirazolo[3,4-*b*]piridínicos y una de las familias ha mostrado una actividad interesante en los ensayos preliminares.
Se han identificado tres compuestos (**EB1-3**), con valores micromolares de IC_{50} (0.7 a 4 µM), que inhiben de forma completa y selectiva las MNKs (entre 2.5 y 5 µM) y sin presentar citotoxicidad en células de cáncer de mama triple negativo (MDA-MB-231). Además, el co-tratamiento con **EB1** aumenta la sensibilidad de las células MDA-MB-231 a la doxorrubicina, mejorando su eficacia de inhibir el crecimiento celular.

Se ha usado una estrategia de diseño basada en estructura para estudiar el mecanismo de interacción de los diferentes candidatos. Se han creado modelos de las formas activas e inactivas de MNK1 que se han usado para predecir el modo de unión de los hits. **EB1** se ha definido como un inhibidor de tipo II que se une selectivamente la forma inactiva de MNK1 e interacciona con el motivo DFD (Asp-Phe-Asp), característico de las MNKs.

SUMARI

La desregulació de la síntesi de proteïnes és comuna en càncer. Un factor clau en el control de la traducció de proteïnes és el factor d'inici de la traducció 4E (eIF4E) que es troba regulat per les cinases MNK1/2 (*MAP kinase interacting kinases* 1 i 2) mitjançant fosforilació. En els últims anys, l'eIF4E s'ha descrit com un factor de pronòstic independent associat amb la progressió maligna i el desenvolupament de resistència. A més, l'eIF4E es troba sobreexpressat en càncer d'ovari, mama, pulmó, bufeta i pròstata. La fosforilació de l'eIF4E és necessària per a la transformació tumoral però és prescindible per al desenvolupament normal. Per tant, la inhibició farmacològica de les MNKs pot proporcionar una estratègia no tòxica i eficaç per al tractament del càncer, especialment en combinació amb els tractaments aprovats.

En aquest projecte, es proposen els sistemes pirazolo[3,4-*b*]piridínics com a possibles candidats a inhibidors de MNK degut a la seva similitud amb inhibidors coneguts.
S'han estudiat les possibilitats sintètiques que ofereixen aquestes estructures, definint metodologies generals per introduir substitucions selectives i controlades en 6 punts diferents de la molècula. A més, s'han descrit els mecanismes de reacció.

S'han estudiat 5 famílies de compostos basades en les pirazolo[3,4-*b*]piridines i una de les famílies ha mostrat una activitat interessant en els assajos preliminars.
S'han identificat tres compostos (**EB1-3**), amb valors micromolars de IC_{50} (0.7-4 μM), que inhibeixen de forma completa i selectiva les MNKs (entre 2.5 i 5 μM) i sense presentar citotoxicitat en cèl·lules de càncer de mama triple negatiu (MDA-MB-231). A més, el co-tractament amb **EB1** augmenta la sensibilitat de les cèl·lules MDA-MB-231 a la doxorubicina, millorant la seva eficàcia d'inhibir el creixement cel·lular.

S'ha fet servir una estratègia de disseny basada en estructura per estudiar el mecanisme d'interacció dels diferents candidats. S'han creat models de les formes actives i inactives de MNK1 que s'han fet servir per predir la manera d'unió dels candidats. **EB1** s'ha definit com un inhibidor de tipus II que s'uneix selectivament la forma inactiva de MNK1 i interacciona amb el motiu DFD (Asp-Phe-Asp), característic de les MNKs.

LIST OF ABBREVIATIONS

ACN	Acetonitrile
AcOEt	Ethyl acetate
AcOH	Acetic acid
APCI	Atmospheric pressure chemical ionization
ATP	Adenosine triphosphate
$CDCl_3$	Deuterated chloroform
CDE	Dichloroethane
DCM	Dichloromethane
DIBAL-H	Diisobutylaluminum hydride
DMF	*N*,*N*'-dimethyl formamide
DMSO	Dimethyl sulfoxide
DMSO-d_6	Deuterated DMSO
EC_{50}	Half maximal effective concentration
EI	Electron ionization
eIF4E	Eukaryotic translation initiation factor 4E
Eq.	Equivalent
ESI	Electrospray ionization
Et	Ethyl
EtOH	Ethanol
eV	Electronvolt
HMBC	Heteronuclear Multiple Bond Correlation
HRMS	High resolution mass spectrometry
HSQC	Heteronuclear Single Quantum Correlation
IC_{50}	Half maximal inhibitory concentration
IR	Infrared spectroscopy
J	Coupling constant
Ki	Inhibition constant
m.p.	Melting point
Me	Methyl

MeO	Methoxy
MeOH	Methanol
MNK (MKNK)	MAP kinase-interacting kinase
MS	Mass spectrometry
MW	microwave irradiation
NOESY	Nuclear Overhauser Effect Spectroscopy
O/N	Overnight
Ph	Phenyl
p-TSA	p-toluensulfonic acid
QSAR	Quantitative structure-activity relationship
QSPR	Quantitative structure-property relationship
Rf	Retention factor
RT	Room temperature
SAR	Structure-activity relationship
TEA	Triethyl amine
THF	Tetrahydrofuran
TLC	Thin Layer Chromatography
TNBC	Triple negative breast cancer
WB	Western blot
^{1}H-NMR	Proton nuclear magnetic resonance
^{13}C-NMR	Carbon 13 nuclear magnetic resonance
4E-BP1	Eukaryotic translation initiation factor 4E (eIF4E)-binding protein 1

TABLE OF CONTENTS

CHAPTER 1

Introduction

1.1. Cancer

Cancer is one of the biggest health human issues due to its morbidity and mortality with 17 million new cases every year and 9.6 million cancer-related deaths (2018).[1,2] Moreover, the numbers increase every year and the World age-standardized (AS) incidence rate item shows that there are 204.7 new cancer cases for every 100,000 men in the world, and 175.6 for every 100,000 females.[1] The four most common types of cancer worldwide are lung, female breast, bowel (including anus) and prostate cancers and account for more than four in ten (43%) of all new cases.

The term "Cancer" includes a collection of diseases which share a common symptom: an uncontrolled cell growth and the capacity of cells to spread to the surrounding tissues leading to the formation of tumors. More than 100 cancer types have been identified. However, only five types (lung, colorectum, stomach liver and breast cancers) represent more than half of the annual cancer-related deaths.

Cancer is a multifactorial disease which arises from the transformation of normal cells into tumor cells in a multistage process. Several genetic mutations are accumulated on the cell genome, dysregulating the activity of genes that maintain genetic stability, control cell growth and regulate sensitivity to apoptosis.[3]

These mutations are the result of the interaction between internal and external drivers. Internal drivers include genetic factors as inherited mutations, hormones and immune conditions. External drivers include 3 categories of carcinogens: (1) Physical carcinogens, such as ultraviolet and ionizing radiation; (2) Chemical carcinogens, such as asbestos, components of tobacco smoke, aflatoxin (a food contaminant), or arsenic (a drinking water contaminant); and (3) Biological carcinogens, such as infections from certain viruses, bacteria or parasites.[4]

Tobacco, alcohol, unhealthy diet, and physical inactivity are major cancer risk factors worldwide. Cancer is highly dependent on age, gender, live style and even geographical situation. However, many types of cancer are considered a preventable disease as only 5-10% of all cases are attributed to heritable genetic defects.[4–6]

1.1.1. Carcinogenesis

Carcinogenesis is a multistep process where a successive accumulation of mutations, induced by chemical or physical agents, that dysregulate the activities of genes that control cell growth, regulate sensitivity to programmed cell death, and maintain genetic stability. Two classes of regulatory genes are directly involved in carcinogenesis: (1) oncogenes and (2) anti-oncogenes or tumor suppressor genes.[3,7,8] On one hand, oncogenes are genes related to cell proliferation, differentiation and cell death. Dysregulation of these genes induces an increase of their function. On the other hand, tumor suppressor genes control cell growth and promote genetic stability by checking cell cycle progression. Mutations on these genes implies a loss of function and promotes carcinogenesis.

Acquisition of a malignant phenotype occurs in three phases (1) initiation, (2) promotion and (3) progression (Figure 1.1). [3,8,9] Malignant cell transformation initiates with an irreversible genetic change caused by the exposure to a carcinogen (a genotoxic chemical or a reactive metabolite) leading to a DNA mutation on a key gene. Carcinogens are strong electrophiles that bind to DNA forming adducts which, if not repaired, lead to mutations. Mutations such as point mutations, deletions, insertions, chromosomal translocations and amplifications, can confer growth advantages, which allow affected cells to evolve and grow faster bypassing normal cellular growth controls and resulting on permanent alterations in the genome.

Promotion is a reversible process in which the population of transformed (initiated) cells is increased by the stimulation of chemical agents. Typically, promoting agents are non-genotoxic and are not capable to produce DNA damage however, they are able to stimulate cell proliferation. Therefore, tumor formation is dependent on repeated exposure to tumor promoting agents resulting in rapid growth of the initiated cells and the eventual formation of non-invasive tumors.

Finally, cells develop a malignant phenotype in the progression step. The capacity to invade surrounding tissues and metastasize is related to the acquisition of additional mutations. Such mutations are caused by the exposure to carcinogens or even by mutational evolution leading to subclonal diversification. Casasent *et al.* had recently described this process as multiclonal invasion. Using single cell sequencing the authors showed that genome evolution and acquisition of an invasive phenotype occurs at early stages of progression giving rise to multiple subclones capable to co-migrate to adjacent tissues and for an invasive tumor mass. [10,11]

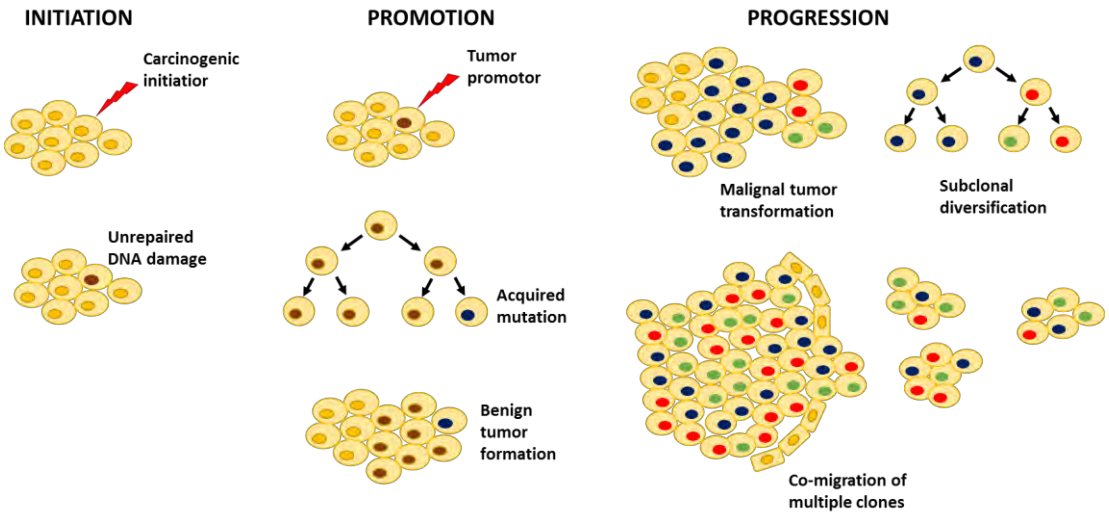

Figure 1.1. Malignant transformation of cells. The transformed (initiated) cell can remain harmless, unless and until it is stimulated to undergo further proliferation, upsetting the cellular balance. The subsequent changes of an initiated cell leading to neoplastic transformation may involve more than one step and requires repeated and prolonged exposures to promoting stimuli. During tumor progression the population of tumoral cells is diversified forming different clones that co-migrate and invade together [8,10,12,13]

The complexity of neoplastic disease is described by Hanahan *et al.*[14,15] when defining the hallmarks of cancer. The hallmarks describe the main common biological capabilities acquired by cells during the multistep development of human tumors (Figure 1.2). The first 6 hallmarks were described in year 2000 by Hanahan and Weinberg[14] as the six genetic alterations in cell physiology that collectively dictate malignant growth: (1) Limitless replicative potential (Immortality) caused by the up-regulation of telomerase activity which allows neoplastic cells to overcome telomere shortening. (2) Sustained proliferative signaling caused by the capacity of tumor cells to produce growth factors which induce proliferation of tumor cells even in the absence of external signals. (3) Insensitivity to antigrowth signals which allows tumor cells to avoid external signals that regulate cell proliferation. (4) Evasion of apoptosis being tumor cells resistant to cell death. (5) Inducing angiogenesis promoting the formation of new blood vessels to ensure oxygen and nutrient supply to allow tumor growth. (5) Activation of invasion and metastasis mechanisms that allow tumor cells to leave the primary tumor, survive in the absence of attachment and colonize foreign tissues.

In 2011[15], two additional hallmarks involved in the pathogenesis of cancer were included: (1) Deregulation of cellular energetics or reprogramming of the cellular metabolism to support neoplastic cell growth and proliferation. (2) Avoiding immune destruction from lymphocytes, macrophages and killer cells.

The authors also defined two enabling characteristics that allowed the acquisition of such hallmarks: (1) the genomic instability of tumor cells which causes a high rate of mutation due to an increased sensitivity to mutagenic agents or a breakdown in one or several components of the genomic maintenance machinery[16] and (2) the inflammation of malignant lesions that promotes tumor progression. The inflammatory state of malignant lesions driven by cells of the immune system is designed to fight infections and heal wounds. Paradoxically, it seems to enhance tumorigenesis and progression. Inflammation can contribute to the acquisition of hallmark capabilities by supplying bioactive molecules to the tumor microenvironment, such as growth factors that sustain proliferative signaling, survival factors that limit cell death, proangiogenic factors or extracellular matrix-modifying enzymes that facilitate angiogenesis, invasion and metastasis. In addition, inflammatory cells can release chemicals (reactive oxygen species), that are actively mutagenic for nearby cancer cells.

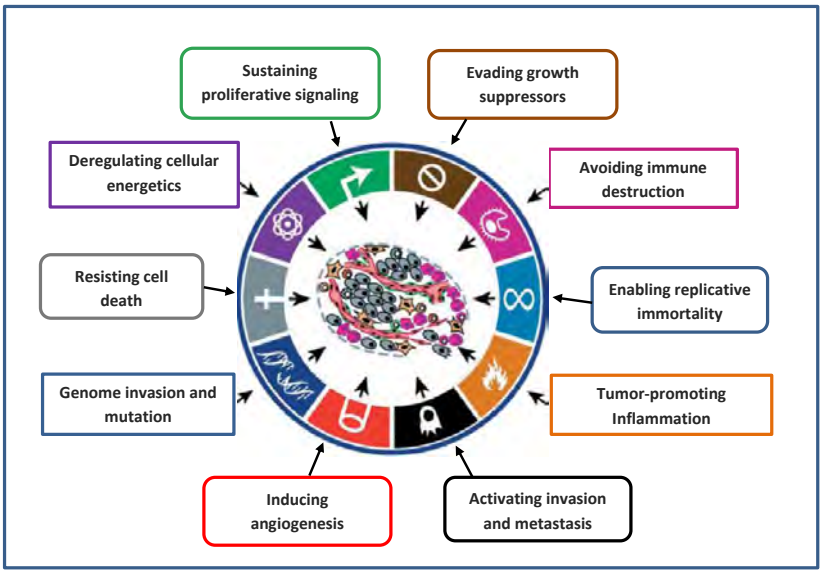

Figure 1.2. Hallmarks of cancer. Acquired characteristics of the neoplastic cells.[15]

In 2017, Fouad and Aanei[17] revisited the hallmarks of cancer providing them with a more evolutionary perspective. The authors consider carcinogenesis as a dynamic process that might initiate (and terminate) within cells' life-spans, with manifesting cancer hallmarks emerging throughout such a journey. They redefine the term hallmark as an acquired evolutionary-advantageous characteristic that complementarily promotes transformation of phenotypically normal cells into malignant ones and promote progression of malignant cells while sacrificing/exploiting host tissue.

They have reimagined the hallmarks of cancer into seven hallmarks: (1) selective growth and proliferative advantage, (2) altered stress response favoring overall survival, (3) vascularization, (4) invasion and metastasis, (5) metabolic rewiring, (6) an abetting microenvironment, and (7) immune modulation.

Human tumors are more than a mass of accumulating malignant cancer cells. Several cellular and non-cellular components forming the ‘‘tumor microenvironment’’ (TME) tightly interact with malignant cells and contribute to the acquisition of hallmark traits. Tumor cells recruit non-malignant cells (stromal cells, immune cells and vascular cells) by secreting stimulatory growth factors, chemokines and cytokines. These recruited cells release growth-promoting signals and intermediate metabolites as well as remodel tissue structure to build the microenvironment. Tumor cells and the supporting normal cells form an organ-like structure and make concerted efforts for rapid proliferation, local invasion and metastases. The TME consists of extracellular matrix (ECM), myofibroblasts, the blood and lymphatic vascular networks and non-transformed cells, such as fibroblasts, neuroendocrine cells, adipose cells or immunoinflammatory cells.[14,15,18–20]

At the same time, malignant cells forming a tumor present differences at both genomic and proteomic levels. Tumor heterogeneity describes the coexistence of genetic, epigenetic and phenotypically different clonal populations within the same lesion. The microenvironment appears to be important for the selection of the best-adapted clones and variations among tumor microenvironments such as hypoxic areas within a tumor, may be responsible for some of the phenotypic heterogeneity observed. The main global features of the tumor (tumor progression, metastatic potential or therapeutic resistance) seem to be a consequence of the cooperation between clones with different tumor-promoting features (Figure 1.3).[21]

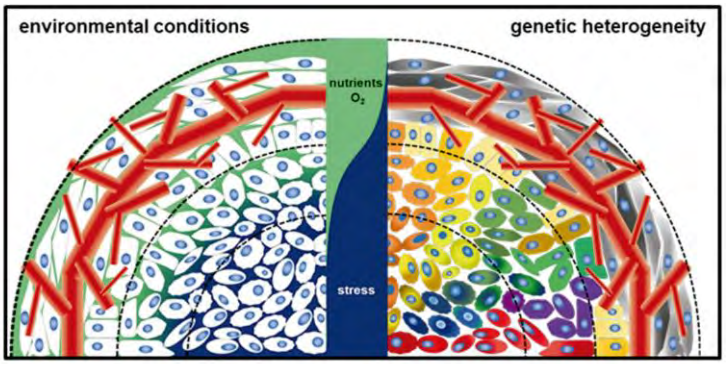

Figure 1.3. Schematic drawing of a tumor and the tumor microenvironment. Left: Cells within a tumor exposed to different microenvironmental cues. Nutrient and O_2 supply decreases from the periphery to the center of the tumor while stress conditions are elevated. Right: Genetic alterations of cells within a tumor are depicted by different colors. Importantly, genetic alterations are not strictly limited to the different environmental conditions. [21]

1.1.2. Breast cancer

Breast cancer is the most common cancer in women worldwide and the second leading cause of cancer related death. The high degree of heterogeneity of this disease leads to many subtypes of breast cancers with different treatments and prognosis.

Breast cancer is categorized into 3 major subtypes based on the presence or absence of molecular markers for hormone receptors (estrogen or progesterone) and human epidermal growth factor 2 (HER2): (1) hormone receptor positive/HER2 negative (70% of patients), (2) HER2 positive (15%-20%), and (3) triple-negative (tumors lacking all 3 standard molecular markers; 15%).[22,23]

Breast cancer treatment involves a complex interplay of three main treatment modalities: surgery, systemic therapy and radiation therapy. Traditionally, patients were treated with surgery and an adjuvant therapy, such as chemotherapy, hormonal therapy or radiotherapy. In the last years, the introduction of a first treatment, delivered before surgery, is being applied. Therefore, the treatment of nonmetastatic breast cancer has evolved to a three steps therapy where the patients are first treated with a neoadjuvant therapy followed by a surgical resection of the tumor and a final adjuvant treatment such as chemotherapy or radiation with the purpose of eradicating the tumor and preventing metastasis. This strategy has shown favorable outcomes especially for the triple-negative subtype. [24,25]

Systemic therapy may be preoperative (neoadjuvant) or postoperative (adjuvant) and is determined by subtype: (1) Patients with hormone receptor–positive tumors receive endocrine therapy to downregulate ER signaling (e.g. tamoxifen, letrozole) and a minority also receive chemotherapy. (2) Patients with HER2-positive tumors receive HER2-targeted antibody therapy (e.g. such as trastuzumab and pertuzumab) or small-molecule tyrosine kinase inhibitors (such as lapatinib and neratinib) combined with chemotherapy. (3) Patients with triple-negative tumors receive chemotherapy alone.[22] The most common chemotherapy drugs used for breast cancer include cytostatic drugs as taxanes (paclitaxel and docetaxel) and cytotoxic drugs as anthracycline antibiotics (doxorubicin and epirubicin).[26,27]

Metastatic breast cancer is also treated according to subtype. Unfortunately, therapeutic goals are prolonging life and palliating symptoms as metastatic breast cancer remains incurable in virtually all affected patients.[22]

1.2. Protein synthesis

Translation is the process where the nucleotide sequence encoded in a messenger RNA (mRNA) is converted into a protein product by applying the genetic code. This process is divided into three consecutive stages: initiation, elongation, and termination (Figure 1.4). [28]

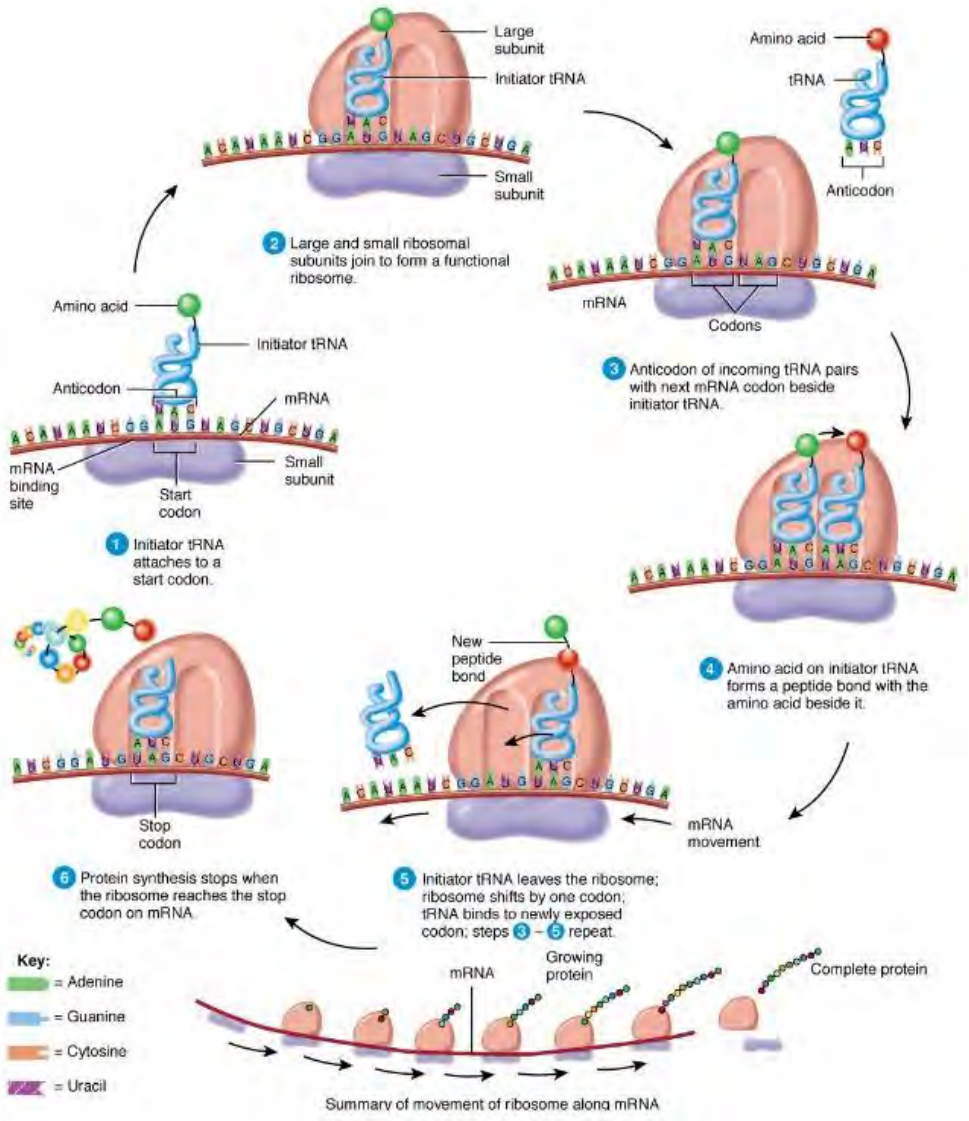

Figure 1.4. Protein synthesis process (1) Initiation: assembly of the translation complex formed by the two ribosomal units and the mRNA chain. (2) Elongation: following the relation defined by the genetic code, the corresponding amino acids, transported by the tRNAs, are bound to form the polypeptide sequence. (3) Termination: the detection of a stop codon (UAA, UGA or UAG) induces the release of the peptide.[29]

Initiation is the rate-limiting step and is highly regulated in eukaryotes. There are two main mechanisms of eukaryotic protein synthesis initiation: (1) cap-dependent and (2) cap-independent initiation of translation which differ in the requirement of a 7-methyl-guanosine cap at the 5'end of the mRNA chain (Figure 1.5).[28]

The capping process takes place co-transcriptionally in the nucleus as soon as the first 25–30 nucleotides are incorporated. The 7-methylguanosine cap is incorporated to the first transcribed nucleotide through a triphosphate linkage bound to the 5' hydroxyl group.[30,31]

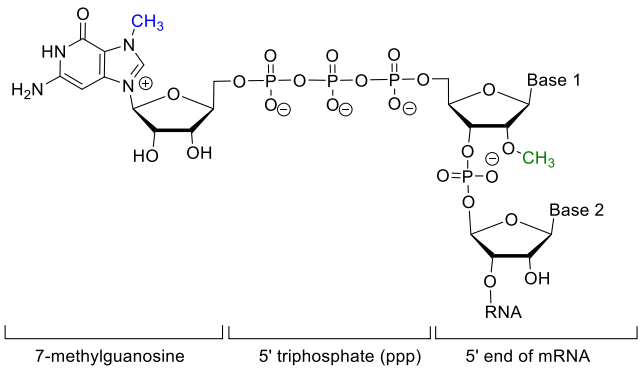

Figure 1.5. Structure of the 7-methyl-guanosine cap.

Cap-dependent translation is the most common mechanism to initiate translation. It requires the presence of a 5'-7-methylguanosine structure (known as m^7G-cap) located at the 5'end of the mRNAs (Figure 1.5). The mRNA is activated by the cap-binding complex eIF4F in a process which requires the involvement of several eukaryotic initiation factors (eIFs). First, the eukaryotic initiation factor 4E (eIF4E) binds the m^7G-cap structure and assists the formation of the cap-binding complex eIF4F. The complex, which consists on the cap-binding protein eIF4E, the "scaffold" protein eIF4G and the RNA helicase eIF4A, recruits the 43S pre-initiation complex (43S PIC) allowing its binding to the mRNA. The 43S PIC is formed by the 40S ribosomal subunit associated with eIF3 and the ternary complex which contains the methionine-charged initiator tRNA, the initiation factor eIF-2 and GTP. The 5' untranslated region (UTR) of mRNA is scanned until the start codon (AUG) is recognized. Following start codon recognition, the assembling of the 60S ribosomal subunit occurs forming the 80S complex and releasing the initiation factors from the ribosome (Figure 1.6 A).[32–35]

The cap-independent initiation mechanism does not require the m^7G-cap structure. These mRNAs present structural elements called internal ribosome entry sites (IRES) that mediate the direct ribosome recruitment independently of eIF4E and the cap structure. In this mechanism, the mRNA sequence itself presents the ability of binding and activating the translational machinery (Figure 1.6 B).[28,35]

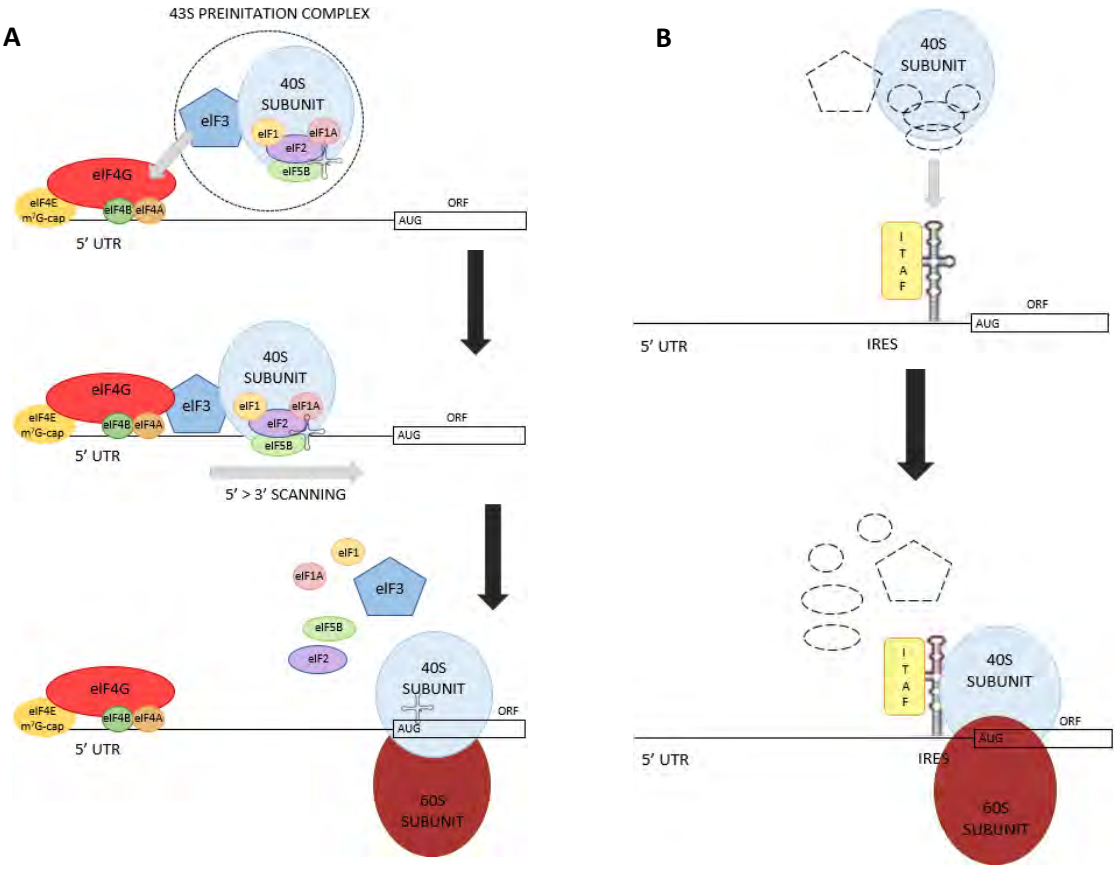

Figure 1.6. Protein translation: Initiation step. A) Cap- dependent translation. B) Cap-independent translation. Adapted from [20]

In cancer cells, hyperactivated signaling pathways influence translation rates to support the uncontrolled growth and survival. Consistently, several components of translation initiation system have been found to be mutated or differentially expressed, and some could act as oncogenes. In cancer, translational alterations can increase the overall rate of protein synthesis as well as activate the translation of specific mRNAs for the proteins that promote cancer progression and metastasis.

1.3. Eukaryotic initiation factor 4E (eIF4E)

eIF4E is a 25-kDa protein that plays an important role in protein translation as it is the limiting factor in the cap-dependent initiation. As described above, eIF4E binds the m^7G-cap structure of most eukaryotic mRNAs and, together with other initiation factors, mediates the recruitment of the ribosomal subunits to start the translation.[35,36]

The protein structure resembles a cupped hand and is characterized by eight antiparallel β-strands and three α-helices. Two major binding sites are present on the eIF4E structure: the cap-binding site and the dorsal surface.[35,37] The recognition of 5'-cap sequence occurs on the cap-binding pocket (at the concave face) through interaction with two tryptophan residues. The nucleobase is intercalated between the side chains of Trp102 and Trp56 forming a cation-π stacking. The interaction is further stabilized by the formation of hydrogen bonds between the N-1 and N-2 protons of 7-methyl-guanine and a conserved glutamate residue (Glu103). The phosphate tail also forms H-bonds with Arg157 and Lys162 residues. 4E-BPs and eIF4G compete for binding the dorsal surface through Trp73 and Trp43. [32,35,38,39] (Figure 1.7)

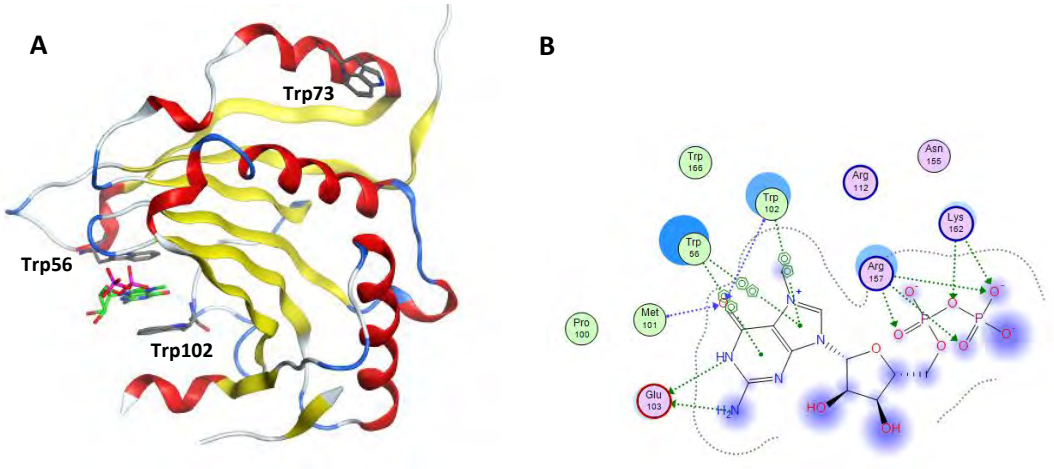

Figure 1.7. Structure of eIF4E. A) Three-dimensional structure of human eIF4E in complex with 5'-7-methylguanosine (green molecule) where interacting tryptophan residues are highlighted (from PDB 1EJH). B)Interaction between eIF4E and the m^7G-cap.

1.3.1. Biological functions of eIF4E

The eukaryotic translation initiation factor eIF4E plays important roles in controlling protein expression and its dysregulation has been associated with poor prognosis cancers.

The main role of eIF4E has been related to protein translation. The translation of most cellular mRNAs is mediated by a cap-dependent mechanism which is regulated by the limited availability of eIF4E. eIF4E binds the 5'-7-methylguanosine cap of mRNAs permitting the formation of the eIF4F complex and the subsequent binding of the ribosomal subunits to start protein translation.[32,40] Importantly, not all mRNAs are equally affected by cap-dependent translation.[35,41] "Strong" mRNAs with a short and unstructured 5'-UTRs (including housekeeping genes, such as β-actin) are efficiently translated even when the eIF4E levels are low. In contrast, "weak" mRNAs containing long and structured 5'-UTRs are more sensitive to eIF4E levels. These mRNAs, also known as "eIF4E-sensitive mRNAs" include mRNAs involved in cell growth, proliferation and immune responses.[42]

However, the function of eIF4E on mRNA life cycle is not limited to translation. eIF4E is found in cytoplasmic bodies such as processing bodies (P-bodies) and Stress Granules (SGs) where it is thought to balance repression and degradation of specific transcripts. eIF4E is thought to protect specific mRNAs from degradation by binding the m^7G cap and preventing association with the decapping enzymes.[43–45]

A significant fraction of eIF4E (up to 68%) is found in the nucleus where it regulates the export of specific mRNAs from the nucleus to the cytoplasm. These target RNAs typically contain a ~50-nucleotide eIF4E sensitivity element (4ESE) in the 3' UTR region and a 7-methylguanosine cap on the 5' end. To date, over 3000 transcripts, many encoding oncoproteins, were identified as potential nuclear eIF4E export targets. In this pathway, eIF4E overexpression leads to enhanced mRNA export for a subset of mRNAs that encode proteins involved in proliferation, survival, metastases and invasion. The nuclear import of eIF4E is driven by Importin 8, which binds to the cap-free eIF4E. [32,37,41,46,47]

Despite the advances on the elucidation of the functions of eIF4E, this protein is still under study and some possible extra functions have been suggested. On one hand, this protein could be involved in the translation of uncapped viral mRNAs. Caliciviruses present a viral protein (VPg) covalently linked to their viral mRNAs which mimics the cap structure allowing the use of the cap-dependent initiation mechanism for the translation of their RNAs.[32]

On the other hand, eIF4E has been suggested to be involved in the histone H4 mRNA translation. eIF4E interacts with the histone internal site without the need of a 5'cap end, promoting translation.[35,48]

The three main eIF4E functions (mRNA translation, export and stability/sequestration) share a common requirement of a m^7G cap structure on the involved mRNAs.[41] According to these functions, eIF4E governs cell cycle progression and cellular proliferation by coordinately orchestrating the expression of several genes at the post-transcriptional level.[49] Therefore, eIF4E functions as an RNA regulon[41,49] with an essential role in normal differentiation and development. Moreover, oncogenic activity of eIF4E can be related to the ability of to affect the expression of groups of cancer related mRNAs at multiple levels.[41]

1.3.2. Regulation of eIF4E

Despite the different functions described for eIF4E, the main regulation mechanisms described for this protein target its translational function. Regulation of eIF4E activity depends on the PI3K/Akt/mTOR and Ras/Raf/MAPK signaling pathways. The MNKs and 4E-BPs tightly regulate eIF4E by two different mechanisms that control eIF4E activation and availability.[35,50,51]

4E-binding proteins

4E-binding proteins (4E-BPs) are a family of 4E-interacting proteins that regulate the availability of eIF4E for the assembly of the eIF4F complex. The activity of 4E-BPs is regulated by phosphorylation *via* the PI3K/AKT/mTOR axis in response to different stimuli such as hormones (e.g., insulin), growth factors and amino acids.

Hypophosphorylated 4E-BPs sequester eIF4E preventing its binding to eIF4G and avoiding the formation of the eIF4F complex and therefore inhibiting protein translation. Sequential phosphorylation of 4E-BPs on four residues (Thr37, Thr46, Thr70 and Ser65) leads to the dissociation of the complex allowing the assembly of the eFI4F complex and the cap-dependent translation. [32,35,50,52]

However, in addition to the individual protein levels of the proteins and their phosphorylation status, the eIF4E/4E-BP ratio is considered of importance for controlling eIF4E function. [53,54] An increased eIF4E/4E-BP ratio has been observed in malignant cells and has been related to the acquisition of resistance to mTOR inhibition. [54]

As described by Alain *et al.*[53] a high eIF4E/4E-BP ratio leads to an incomplete and insufficient inhibition of translation of "eIF4E-sensitive" mRNAs permitting neoplastic growth. Therefore, the eIF4E/4E-BP ratio can be considered as a prognosis marker of the efficacy of dual mTOR1/2 inhibitors.

Phosphorylation *via* MNK1/2

The kinases MNK1 and MNK2 (Mitogen activated protein kinase interacting kinases 1 and 2) regulate eIF4E by phosphorylation on Ser209. eIF4E phosphorylation takes place when bound to the scaffold protein eIF4G. The interaction between eIF4G and MNKs brings them in close proximity to eIF4E allowing phosphorylation.[35,55] (Figure 1.8)

eIF4E is the only substrate validated *in vivo* for the MNKs, thus it is important to understand the physiological consequences of its phosphorylation. The initial interpretation by Marcotrigiano *et al*.[56] suggested that phosphorylation of Ser209 stabilized the association between p-eIF4E and capper mRNAs through the formation of a hydrogen bond between the phosphorylated Ser209 and Lys159. However, posterior studies using fluorescence spectroscopy and surface plasmon resonance techniques, indicate that phosphorylation of eIF4E reduces its affinity for capped RNA, due to an increased dissociation rate.[57] Later on, Slepenkov *et al.*[58] studied the binding of eIF4E and p-eIF4E to cap analogs and capped oligoribonucleotides by stopped-flow kinetic analysis and reported that the phosphorylation of eIF4E decreased k_{on} by 2 fold at 50–100 mM KCl but had no effect on the K_{off}. To date, there is not still a consensus and the question about the effect of eIF4E phosphorylation is still open.

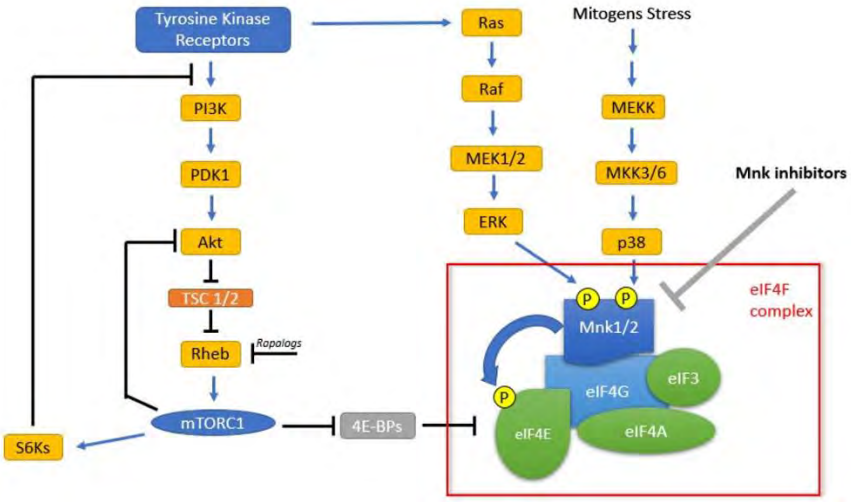

Figure 1.8. Regulation pathways of eIF4E phosphorylation[22]

1.4. MAP kinase-interacting kinase 1/2 (MNK1/2)

Mitogen-activated protein kinase (MAPK) interacting protein kinases 1 and 2 (MNK1/2) are serine/threonine kinases which regulate the activity of proteins involved in diverse cellular functions through phosphorylation. They play important roles in controlling mRNA translation and therefore are key mediators in oncogenic progression, development of drug resistance, cap-dependent translation and the production of inflammatory cytokines and cytokine signaling.

1.4.1. Structure of MNKs

MNKs comprise a subfamily of serine/threonine kinases and structurally belong to the group of Ca^{2+}/calmodulin-dependent kinases (CaMK), despite they are not regulated by Ca^{2+}/calmodulin.[59]

Humans possess two Mnk genes (*mnk1* and *mnk2*) which result in two different spliced forms each, leading to four different proteins MNK1*a*, MNK1*b*, MNK2*a* and MNK2*b*. The *a* isoforms are longer and contain a MAPK-binding domain which mediates the interaction with p-38 and ERK1/2 (Leu-Ala-Arg-Arg-Arg in MNK1 and Leu-Ala-Gln-Arg-Arg for MNK2). *b* isoforms are shorter and lack the C-terminal MAPK-binding motif being independent of MAPK regulation.[55,60]

Both MNK isoforms contain a polybasic sequence involved in the recognition of eIF4G that also acts as a nuclear localization sequence (NLS) that promotes MNK nuclear import. Although all MNKs contain this sequence, not all isoforms are nuclear as this is dependent on the presence of a nuclear exporting sequence (CRM1-type NES) in their C termini. The *b* isoforms are preferentially localized in the nucleus as they lack the C-terminal domain which contains the NES motive. MNK1*a* is found in both the nucleus and the cytoplasm while the MNK2*a* isoform is mostly cytoplasmatic.[60]

Sequence alignment revealed a perfectly conserved central kinase domain which is not affected by alternative splicing. [60]

The crystal structures of both proteins in their inactive form were published by Jauch *et al.*[61,62] The kinase domain of MNK1/2 presents the typical bilobed arrangement from protein kinases with the ATP binding cleft sandwiched between a N-terminal and a C-terminal lobe.[59] The N-terminal lobe is composed by a regulatory α-helix (αC) and a twisted sheet of five antiparallel β-strands (β1-β5). This region contains the essential elements for ATP binding: (1) a highly flexible glycine-rich loop (residues 51−62 in MNK1 and 86−97 in MNK2), (2) a conserved lysine (Lys78 in MNK1 and Lys113 in MNK2) and a conserved glutamic acid (Glu94 in MNK1 and Glu129 in MNK2) found in the strand β3 and in helix αC respectively, that form a salt bridge which is a key feature of the active conformations of the kinases. In the N-terminal regions it is also found the eIF4G binding site which allows the efficient phosphorylation of eIF4E.[59,62,63]

The C-terminal lobe mainly consists on hydrophobic α-helical bundles and contains the elements required for phosphate transfer and for peptide substrate binding: (1) the catalytic loop (C-loop, residues 169−175 in MNK1 and 204−210 in MNK2), (2) the magnesium-binding loop (Asn175 in MNK1 and Asn 210 in MNK2), and (3) the activation loop (A-loop, residues 191−225 in MNK1 and 226−260 in MNK2). The ATP binding pocket is a hydrophobic cleft found between the two lobes. Both MNK1/2 present an 78% identity of the active site despite the N-terminal lobe of MNK1 is inclined 10° leaving a slightly more closed binding site.[59,62,63] (Figure 1.9)

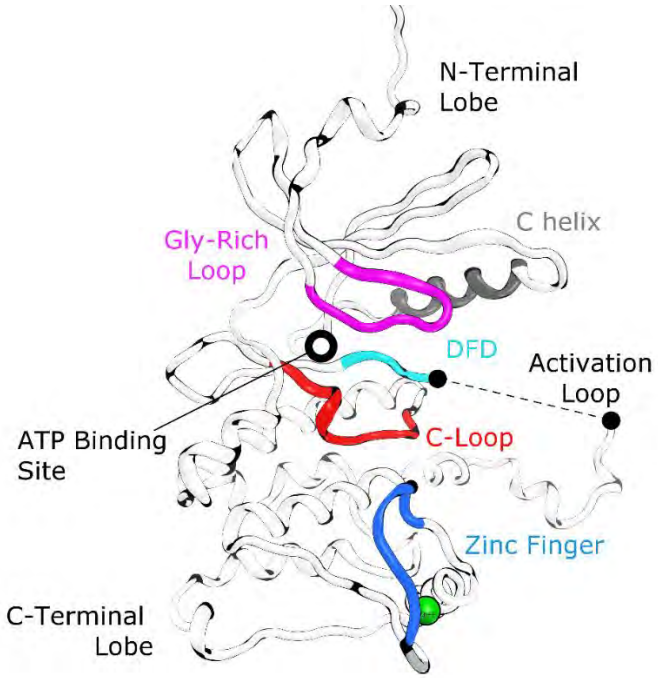

Figure 1.9. General structure of the MNK2 catalytic domain. The dotted line indicates that the activation loop has not been experimentally solved yet. Adapted from [61,64]

Moreover, MNKs present two unique features: [60,63,64]

- The catalytic domain presents three specific insertions (I1, I2 and I3) which are not found in other kinases and that are thought to serve for MNK activation or substrate recognition as they are conserved in MNK from other species.
- The kinase domain contains a DFD-motif (Asp191−Phe192−Asp193 in MNK1 and Asp226−Phe227−Asp228 in MNK2) which replaces the DFG-motif usually found in kinases. Due to the presence of this motif, MNKs present two possible conformations DFD-in (open/active) and DFD-out (closed/inactive) being the DFD-out the most stable form. The DFD fingerprint is unique within the human kinome.[63]

DFD-out/DFD-in MNK conformations

The MNK DFD-motif (Asp 191-Phe 192-Asp193 in MNK1 and Asp226-Phe227-Asp228 in MNK2) replaces the typical Asp-Phe-Gly motif (DFG motif) from kinases where the Asp residue coordinates a Mg^{2+} ion needed to activate the γ-phosphate of ATP. The DFD-motif can rotate 180° leading to a conformational change which allows autoinhibition of MNKs.

Due to the presence of the DFD-motif, MNKs can adopt two conformations: DFD-in (open/active) and DFD-out (closed/inactive). In the absence of ligands, the DFD-out conformation of the protein is stabilized. In the case of MNK2, Phe227 sticks into the ATP binding pocket and blocking the access to the binding site.[62,63] This conformation is stabilized by (1) a hydrogen bonding interaction between the carbonyl of Phe227 and the side chain amino group of Lys113 and (2) by positioning Phe227 in a hydrophobic pocket formed by Leu143 and the non-conserved Phe159 (also called gatekeeper as it acts as a selective filter for ATP-competitive drugs).[61] The initial studies performed by Jauch *et al.*[61] seem to indicate that Asp228 had no direct role in the stabilization of the DFD-out conformation (PDB ID 2AC3). However, crystallographic studies of a the D228G mutant presenting a DFG-motif (PDB ID code: 2HW7 and 2AC5) showed a conformation change to an apparent DFG-in conformation[61,62] demonstrating an effect of Asp228 in the stabilization of the DFD-out conformation. Computational studies performed by Hou *et al.*[63] support this hypothesis as the wild type MNK2 adopted an inactive DFD-out conformation while the DFG mutant was able to adopt both DFG-in and DFG-out conformations.

Therefore, the flip of the DFD-motif between the DFD-out conformation to DFD-in conformation would be essential for the protein activation. During the DFD-out to DFD-in transition, Phe227 flips clockwise about 180°. During this process, the salt bridge between Asp226 and Lys234 present in the DFD-out conformation is broken and a new salt bridge between Asp226 and Lys113 is formed which is characteristic of the active kinase conformation (DFD-in conformation). The existent salt bridge between Asp228 and Arg128 is broken and then restored during this transition. The formation of the salt bridge allows the stabilization of the unusual DFD-out inactive conformation by controlling the flexibility of the activation loop. The mutation of Asp 228 in the DFG-mutant would cause Asp226 to take this role and allow the formation of the salt bridge with Lys113 and Arg125 leading to the active and inactive forms. MD simulation studies suggested that DFD flip is associated with a conformational change (open/close) of the A-loop due to the balance of the electrostatic and hydrophobic interactions.[63]

The effect of the DFG/D-out/in conformations on ATP binding was studied by Jauch *et al.*[61]. ATP binding assays with non-phosphorylated and phosphorylated forms of MNK2 and MNK2(D228G) showed that both proteins were able to bind ATP independently of the phosphorylation-dependent activation of the proteins. However, only the phosphorylated forms of MNK2 and MNK2(D228G) exerted kinase activity. These results establish that phosphorylation of MNK2 is a prerequisite for catalytic activity, but not for ATP binding. Thus, the DFD-out/DFD-in shift is ligand-dependent.

1.4.2. Biological function of MNKs

eIF4E is the major and most characterized target of MNKs. MNKs associate to the eIF4F complex by directly binding to eIF4G scaffold protein and phosphorylating eIF4E at Ser209. Phosphorylation eIF4E has been related to increased protein synthesis, cellular proliferation, survival and malignant transformation of cells.[65,66]

In addition to eIF4E phosphorylation, MNKs have been reported to phosphorylate other proteins with different functions on the cell cycle (Figure 1.10). Like eIF4E, several of these proteins are either components of the translational machinery (e.g. eIF4G) or proteins that bind mRNA (e.g., heterogeneous nuclear RNA-binding protein A1 (hnRNP A1) and the polypyrimidine-tract binding protein-associated splicing factor (PSF)). Additional substrates are cytoplasmic proteins: On one hand, cytoplasmic phospholipase A2 ($cPLA_2$) which plays a key role in the production of eicosanoids (with important roles in immunity and inflammation). On the other hand, Sprouty2 which acts as a regulator of multiple receptor tyrosine kinase pathways by negatively controlling the ERK pathway.[65,66]

There is extensive and definitive evidence that MNK kinases regulate the phosphorylation and/or activity of proteins involved in diverse cellular functions. As a result of such effects, MNKs play important roles in cancer biology, development of drug resistance to anti-oncogenic therapies, cap-dependent and cap-independent translation, as well in mediating pro-inflammatory cytokine production and cytokine signalling.[65]

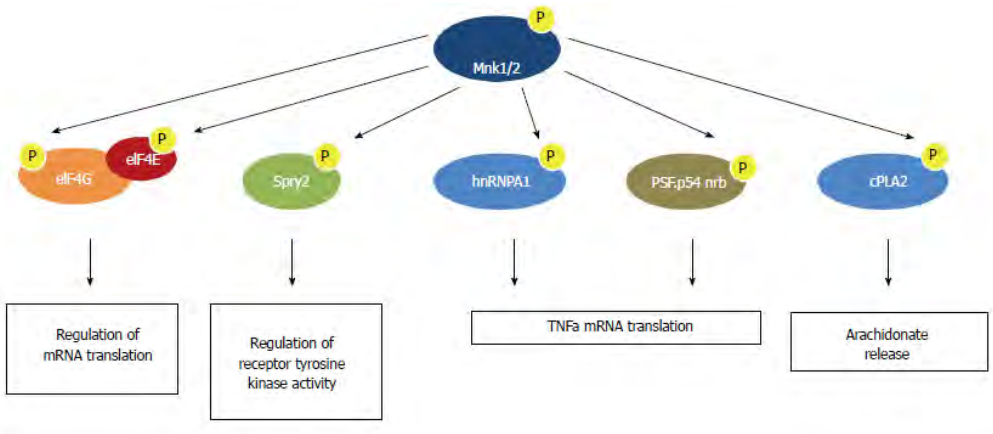

Figure 1.10. Effectors of the MNK kinases. MNKs can regulate multiple biological processes by phosphorylating multiple substrates. MNK mediated phosphorylation of eIF4E and eIF4G can play an important role in mediating cap dependent translation. The MNK substrates hnRNPA1 and PSF play an important role in mediating the translation of AU rich elements containing mRNAs such as the TNF-α mRNA (Tumor necrosis factor-α). The MNK kinases also phosphorylate cPLA2 which plays an important role in eicosanoid production.[65,66]

1.4.3. Regulation of MNKs

MNK kinase activity is regulated through phosphorylation (Thr 209/214 in MNK1 and Thr244/249 in MNK2) by extracellular regulated kinase 1/2 (ERK1/2) and p38 mitogen-activated protein kinases (MAPKs) in response to multiple extracellular stimuli. Activated MNKs bind to eIF4G, bringing the kinase and substrate into proximity, thus facilitating the phosphorylation of eIF4E.[64,67]

The basal activity and regulation of MNKs by MAPK agonists vary depending on the isoform. As phosphorylation sites are localized in the C-terminus, MNK1*b* and MNK2*b* respond poorly to external activation. The basal activity of MNK1*b* was found to be higher than that of MNK2*b*.[68] MNK2*a* presents a high basal activity and is only slightly affected by ERK activation while MNK1*a* is an inducible form with a low basal activity that can be phosphorylated by both ERK and p38α/β in response to external growth factors, UV radiation, mitogens and stress inducing agents.[55,60] (Table 1.1)

Table 1.1 Regulation of the four isoforms of MNK [65,66]

Isoform	Basal activity	Regulation	Localization	Special features
MNK1*a*	low	ERK1/2 and p-38	Nuclear, Cytoplasmatic	Long C-terminus contains NES and MAP kinase-binding site
MNK1*b*	high	-	Nuclear	Very short C-terminus lacks MAP kinase binding site
MNK2*a*	high	ERK1/2	Cytoplasmatic	C-terminus contains the MAP kinase binding site, but lacks functional NES
MNK2*b*	low	-	Nuclear	C-terminus lacks NES and MAP kinase binding site

1.5. Protein translation and cancer: The role of eIF4E phosphorylation *via* MNK in cancer

Overexpression of the components of the translation initiation machinery has been correlated to malignant transformation and the regulation of the initiation step of protein translation is a possible cancer treatment. For this reason, cap-dependent proteins can be considered as anticancer targets. In addition, these treatments would not equally affect the translation of all mRNAs only avoiding translation of mRNAs dependent on the activity of the eIF4F complex. Moreover, inhibition would be selective by having a minimal effect on cap-independent translation.[39]

Deregulation of protein synthesis is a common event in cancer and elevated levels of eIF4E have been described many types of tumors such as ovarian, breast, lung, colon, bladder and prostate cancer.[69] Aberrant posttranslational phosphorylation of eIF4E by MNK1 and MNK2 has been associated with cell transformation and tumorigenesis. Moreover, eIF4E has been described as an independent prognostic factor which correlates with disease severity, poor survival and metastasis.[70] For example, upregulation of p-eIF4E and the distinct isoforms of MNKs has been linked to poor prognosis and decreased survival in head, neck, ovarian, breast, pancreas, prostate and lung cancer.[55]

Overexpression of eIF4E does not lead to a global increase of protein synthesis but an upregulation on the export and translation of 4E-sensitive mRNAs which encode proteins involved in cell proliferation and tumourigenesis.[32] This effect on malignancy occurs because eIF4E-regulated mRNAs encode proteins involved in cell cycle progression (cyclin D1, c-myc), promoters of cell growth and angiogenesis, growth factors (VEGF, FGF-2), invasion (MMP-9, heparanase), anti-apoptotic proteins (Mcl-1) and survival (surviving, BCL-2). Through up-regulation of those malignancy-related mRNAs, eIF4E overexpression transforms cells leading to tumor formation and metastasis.[71,72]

Phosphorylation of eIF4E is a critical event in tumorigenesis[73] but seems to be dispensable for normal cell growth and development. Ueda *et al.*[74] engineered MNK1/2 knockout (KO) mice showed a normal phenotype (mice were viable, fertile and developed normally) proving that phosphorylation of Ser209 is not necessary for normal cell development. Moreover, MNK1/2 knockout cells presented undetectable levels of eIF4E phosphorylation indicating that MNK1 and MNK2 are exclusive kinases that regulate inducible and constitutive eIF4E phosphorylation, respectively.

The correlation between eIF4E phosphorylation and the oncogenic transformation was demonstrated in 2010 by Furic *et al.*[73] and Ueda *et al.*[75] Knock-in mice expressing a non-phosphorylatable mutant of eIF4E (eIF4E S209A) are resistant to tumorigenesis[73] and MNK1/2-double knock-out tPTEN−/− mice showed attenuated tumor growth compared to the parental tPTEN−/−mice.[75]

All these studies suggest that the expression of MNK1 and/or MNK2 and the phosphorylation of eIF4E is critical for tumor development but not necessary for cell survival. Therefore, the inhibition of MNK1/2 could provide an effective and non-toxic alternative cancer treatment.[51]

MNK inhibitors in combined therapy with chemotherapeutics

Alteration of protein synthesis has been related to adaptation to chemotherapies. While the overall protein synthesis levels are reduced upon cellular stress, the translation of mRNAs required for the adaptation to a stress-resistant phenotype is favored. eIF4E is a key player in the cell response to stress signals from the tumor environment. The function of eIF4E is regulated by MNK1/2, which in turn are regulated by the ERK and p38 MAPK stress pathways.

Resistance to different types of therapies (e.g. DNA damaging agents or hormone treatments) has been linked to increased p-eIF4E levels in tumors like breast and prostate.[76] In addition, alteration in the phosphorylation status of eIF4E has been described to promote tumor progression and confer resistance to chemotherapeutic treatments.[77,78]

Moreover, in the last years, tumor heterogeneity has emerged as a key factor on the response to therapeutic agents. During the course of the disease, tumors become more heterogeneous presenting a diverse collection of cells harboring distinct molecular signatures and with differential levels of sensitivity to treatment. This heterogeneity underlies resistance and site-specific responses and complicates the selection of globally effective therapeutic agents.[78,79] Contrary to other targets showing intra-tumor heterogeneity, eIF4E expression is homogeneous throughout the tumor opening the possibility to treat with therapies that combine targeting of eIF4E.[21]

For all these reasons, co-treating with MNK1/2 inhibitors appears to be an attractive strategy to overcome resistance to approved therapies for the treatment of different types of cancers.[80–82]

1.6. MNK inhibitors

Inhibition of MNKs is considered an interesting clinical strategy for cancer treatment. However, despite the progress on defining the function of these proteins and their role in tumor development, mono- and/or dual-specific MNK inhibitors with satisfactory levels of selectivity are still lacking.[55]

However, the studies from the last years provide a solid base for the development of new selective and potent inhibitors in the near future. The development of specific inhibitors will open the doors to a new therapy while at the same time permit further functional studies of the MNK-eIF4E axis.

While the overall structural architecture of MNKs resembles other protein kinases, they contain several unusual elements. These differences enable the development of highly selective inhibitors, and structural studies during recent years have proposed different types of interactions between ligands and active sites of kinases.

As other kinase inhibitors, MNK inhibitors can be categorized according to the interaction modes between ligands and active sites of kinases.[55,83–85] This classification divides MNK inhibitors in 5 different categories: (1) Type I inhibitors are small molecules that bind to the ATP pocket of an active conformation (DFG/D-in) of the kinase. (2) Type II inhibitors bind to an inactive conformation of the kinase (DFG/D-out). (3) Allosteric ligands are non-ATP competitive inhibitors bind to a site distinct from the active site. Gavrin and Saiah[86] divided allosteric inhibitors depending on the position of the binding site. Type III are allosteric inhibitors that bind close to the ATP-site while Type IV bind far from to the ATP-site. (4) Type VI or covalent inhibitors bind to the ATP site forming a covalent bond usually irreversible.

For the development of clinically useful MNK inhibitors, understanding the mode of action of these inhibitors is crucial for two reasons: (1) Selectivity and (2) treatment efficacy.
On one hand, the mode of action will define the chances to present off-target effects. For example, ATP competitive inhibitors are more likely to present off-target effect by also affecting other kinases due to the similarity of the ATP-binding pocket among the kinase family. The use of allosteric inhibitors would decrease the probability to develop a pan-inhibitor by targeting specific characteristics of each kinase of interest.

On the other hand, the efficacy of these inhibitors might critically depend on the applied treatment schemes (previous, simultaneous or post chemotherapy). For example, while Type I inhibitors require the activation of the kinase, Type II inhibitors might exceed their highest efficacy before the kinase gets activated. Thus, the mode of interaction is a key point on the development of new inhibitors and the accessibility to inhibitors with different modes of action will be relevant for the clinics as some inhibitor types might be more suitable for a certain clinical setting than others.

In this work, the published MNK inhibitors are classified according to their modes of interactions and then divided depending on their core scaffold as suggested by Dreas *et al.*[55]

1.6.1. Type I inhibitors

Type I inhibitors are the most represented group of MNK inhibitors. These compounds are ATP-competitors that bind to the active conformation (DFG/D-in) of kinases and mimic the interactions of the adenine moiety of ATP forming at least one hydrogen bond with the hinge region.

Achieving high selectivity is the biggest challenge of these compounds due to the high homology between ATP binding pockets across the entire kinome. Structural similarity enforces low diversity of chemical scaffolds and as a result narrows a freedom to operate. Small differences around the ATP pocket can be used to gain selectivity such as the variations in the size, shape, and polarity of the gatekeeper residue or the hydrophilic region of the enzyme normally occupied by the ribose moiety of ATP.[55,83,84]

Staurosporine like MNK Inhibitors

Staurosporine (**1**) is an alkaloid obtained from *Streptomyces staurosporesa* described as a potent, non-specific inhibitor of protein kinases with nanomolar to low micromolar dissociation constants. **CGP052088** (**2**), a close derivative of staurosporine, was the first described inhibitor for MNK1 kinase (data for MNK2 are not available) with an IC_{50} value of 70 nM and a high cytotoxicity (GI_{50} value of 4.5 µM).[51,55] (Figure 1.11)

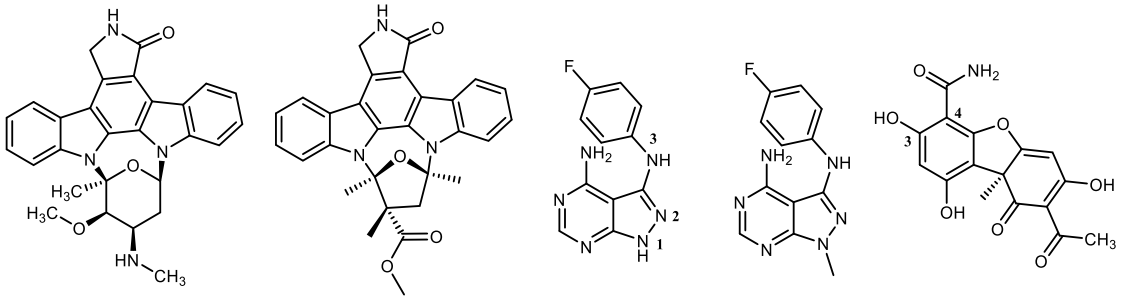

Figure 1.11. First described MNK1/2 inhibitors

CGP57380 and related MNK Inhibitors

4-amino-3-(p-fluorophenylamino)-pyrazolo[3,4-*d*]pyrimidine (**CGP57380**, **3**, Figure 1.11) is a low molecular weight compound from Novartis that inhibits MNK1 and MNK2 with *in vitro* IC_{50} values of 0.87 µM and 1.6 µM respectively.[87] **CGP57380** is not selective for MNK1/2 as it also targets other kinases as CK1, Aurora B, DYRK, SGK, BRSK2, and Lck within a low micromolar IC_{50} range. The compound blocks eIF4E phosphorylation at Ser209 by occupying the ATP pocket found between the two lobes of MNK subunit. The pyrazolo[3,4-*d*]-pyrimidine moiety occupies the adenine subsite of the pocket where the backbone residues of Glu160, Lys161, and Met162 form hydrogen-bonds with the 1-NH, 2-N and 3-NH groups. In addition, the 4-fluoroaniline portion projects into the hydrophobic region of the pocket. In addition, it inhibits proliferation by inducing G1 phase cell cycle and suppresses colony formation in leukemia, glioblastoma, breast and colorectal cancer cell lines.[55]

Recently, novel scaffolds (Table 1.2) have been designed by Diab *et al.*[88] based on the close inspection of the **CGP57380** binding mode. In addition, the pyrrolopyrimidine scaffold has been also explored in the series of MNK1 and/or MNK2 inhibitors developed by Bayer Pharma AG[89] Despite displaying the low micromolar and nanomolar and good selectivity for MNKs further results have not been disclosed.[55,89]

Table 1.2. New MNK inhibitors based on **CGP57380**. Ki values calculated by the authors by using IC_{50} values and the appropriate Km (ATP) values for each kinase. Adapted from [55]

Chemical name	General structure	Example	Ki (µM)
N-(pyridinyl)-1*H*-pyrazolo[3,4-*d*]pyridin-3-amines[88]	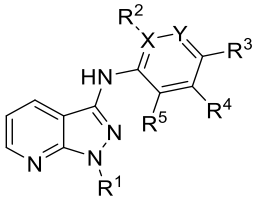 **6**	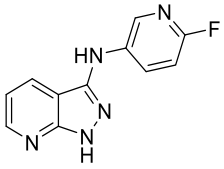 **6a**	MNK1 = 3.76 MNK2 > 10
N-(pyridinyl)-1*H*-pyrrolo[2,3-*b*]pyridin-4-amines[88]	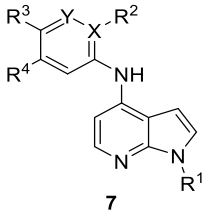 **7**	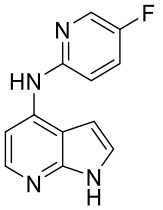 **7a**	MNK1 = 3.2 MNK2 = 0.77
N-(pyridinyl)-7*H*-pyrrolo[2,3-*d*]pyrimidin-4-amines[88]	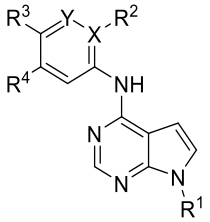 **8**	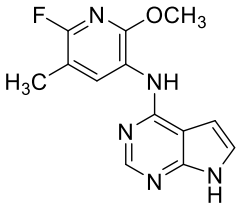 **8a**	MNK1 = 0.74 MNK2 = 1.32
1-(7*H*-pyrrolo[2,3-*d*]pyrimidin-4-yl)-1*H*-indazol-4-amine[88]	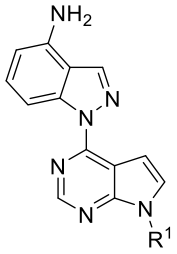 **9**	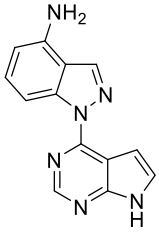 **9a**	MNK1 = 0.15 MNK2 = 0.04
N-(1*H*-indazol-5-yl) - 7*H*-pyrrolo[2,3-*d*]pyrimidin-4-amine (Bayer Pharma AG[89])	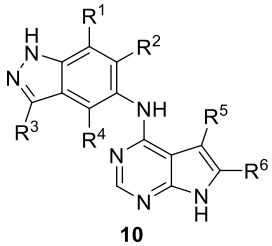 **10**	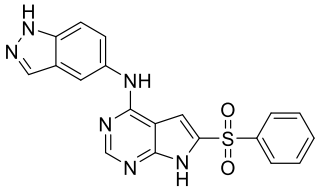 **10a**	MNK1 = 10^{-3}

Cercosporamide and related MNK inhibitors

Cercosporamide (**5,** Figure 1.11) is a broad-spectrum antifungal agent isolated from *Cercosporidium henningsii*. In 2011, a high-throughput screening (HTS) identified it as a potent MNK inhibitor, with IC_{50} values of 43 nM for MNK1 and 38 nM for MNK2.[90] Cercosporamide blocks eIF4E phosphorylation in a number of leukemia and colorectal cancer cell lines.[91,92] Moreover, it has been shown to induce apoptosis, suppress proliferation and anchorage-independent growth *in vitro*. *In vivo* experiments in xenografted human tumors showed that cercosporamide reduces tumor growth and metastasis. This compound binds to the ATP-pocket with similar binding than **CGP57380**: the amide NH and carbonyl groups of residues Glu160, Lys161 and Met162 form hydrogen bonds with the 3-OH and 4-carboxamide of the phenyl portion of the ligand.[51] The selectivity of cercosporamide was evaluated in a panel of 141 kinases and revealed inhibition of additional kinases with similar or greater potency than MNK kinases, i.e. PRK2, MARK2, MARK3, BRSK1, BRSK2, IKKε and MAP4K3.[90]
Recently, cercosporamide derivatives have been designed using a fragment-based approach. Wang *et al.*[93] have described a family of benzofuran derivatives that inhibited MNK2 with a low micromolar *in vitro* IC_{50}. As described for cercosporamide, the compounds also showed anti-proliferative activity in leukemia (THP-1, MOLM-13) and colon cancer (HCT-116) cell lines.

Pyrimidine-based MNK inhibitors

Structure-driven approach has resulted in the development of pyrimidine-thiazolone derivatives[94] as a potent MNK2 inhibitors (data for MNK1 are not published). Starting from a series of 2-anilino-4-(2-aminothiazol-5-yl)pyrimidines, previously described as CDK2 and CDK9 inhibitors, Diab *et al.* applied a SAR analysis to optimize the compounds. (Figure 1.12)

The best selectivity and potency are observed for compound **11a** (R^1, R^3 = $-OCH_3$, R^2 = -H) and compound **11b** (R^1=$OCHF_2$, R^2, R^3 = -H) (MNK2 Ki = 0.37 μM and 0.12 μM respectively). Both compounds were tested in a small panel of six tumor cell lines (AML, breast, colon, ovarian, prostatic and pancreatic carcinoma) showing cell-type-specific effects. Despite a potent antiproliferative activity was observed only in MV4-11 AML cells (GI_{50} = 0.78 μM and 0.88 μM), phosphorylation of eIF4E at Ser209 is blocked at 20 μM.

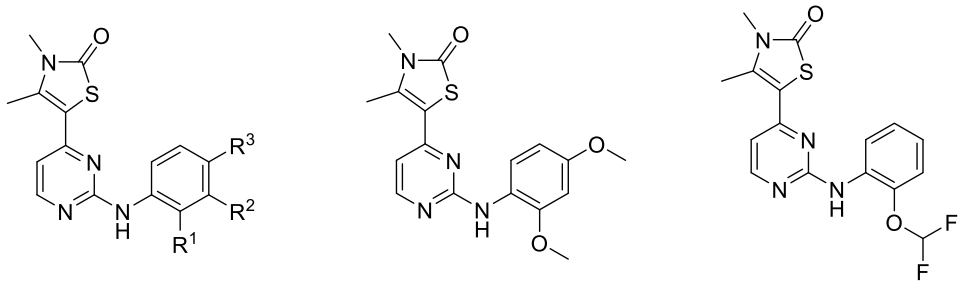

Figure 1.12. Pyrimidine-based MNK inhibitors Diab *et al.*[94]

Thieno[2,3-*d*]pyrimidine-based Inhibitors

Teo *et al*.[95,96] identified a series of thieno[2,3-*d*]pyrimidine derivatives as potent MNK inhibitors by virtual screening of a commercial database (ChemBridge) combining docking and ligand alignment based strategies. Three compounds were selected based on their drug-like properties, commercial availabilities and selectivity against MNK2, while at the same time ensuring the following criteria on their interaction pattern: possession of (1) at least one hydrogen bond with the hinge residues (i.e. Glu160, Lys161 and Met162), (2) a central aromatic moiety that forms π-π stacking interactions with the gatekeeper Phe159 within a distance of 4 Å or less, and (3) one hydrophobic group pointing towards the hydrophobic regions of the pocket. Two of these compounds contained the thieno[2,3-*d*]pyrimidine core (**HIT1** and **HIT3**) while **HIT2** had a pyrazolo[3,4-*d*]pyrimidine scaffold (Figure 1.13).

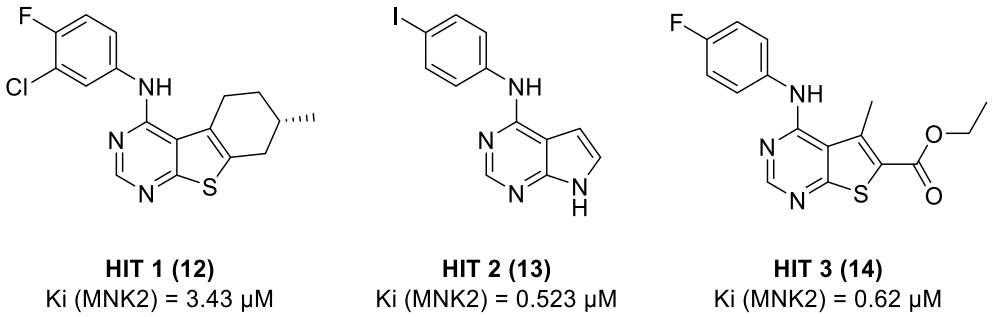

Figure 1.13. Thieno[2,3-*d*]-pyrimidine-based Inhibitors described by Teo *et al.*[95,96]

The best candidate (**HIT3**) was selected for further development. Docking studies were used to optimize the structure by including additional substituents on the aniline moiety and modifying the ester group (Table 1.3).[95]

Compounds **15b** (**MNKI-19**) and **15d** (**MNKI-85**) were respectively developed as a dual-specific MNK1/ inhibitor and a potent and selective MNK2 inhibitor with substantial anti-leukemic properties.[97] Compounds **15b** and **15d** were tested in a panel of AML and CML cell lines. Interestingly, these compounds inhibit phosphorylation of eIF4E at Ser209 *via* MNK inhibition (there is no interference with upstream activating kinases) and show anti-proliferative activity for MV4-11 and MOLM-13 mutated FLT3 cell lines (GI_{50} 5.7 µM and 7.2 µM respectively).[97]

Such structures were also studied by Boehringer Ingelheim.[98] Compound **15e** with an *in vitro* IC_{50} of 7 nM was further studied by Beggs *et al.*[90] to demonstrate the effect of MNKs on cell migration. The compound was shown to inhibit eIF4E phosphorylation in different cell lines at low micromolar concentrations with no effect on cell viability. Recently, Jin *et al.*[99] prepared a series of derivatives based on compound **15e** with low micromolar activity using SAR methods. Among all the studies structures, compound **15f** was selected by the authors as a hit for future studies. (Figure 1.14)

Table 1.3. Compound optimization performed by Teo *et al.*[95,97]

General structure	Example compound	Substituents		Ki(µM)	
		R^1	R^2	MNK1	MNK2
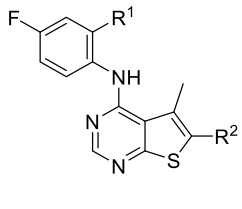 15	**15a**		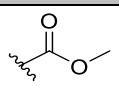	> 10	> 10
	15b (**MNKI-19**)		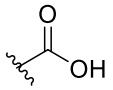	0.068	0.186
	15c		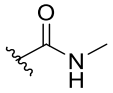	0.018	0.106
	15d (**MNKI-85**)		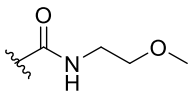	0.031	> 10

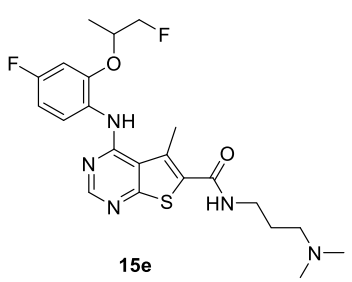
15e

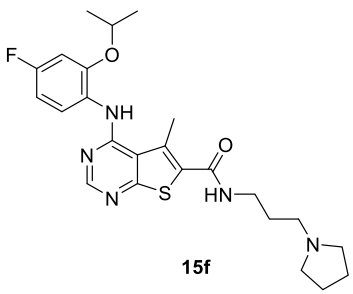
15f

Figure 1.14. Examples of the thienopyrimidine compounds studied by described by Beggs *et al.* and Jin *et al.*[90,99]

Further exploration of thienopyrimidine scaffold was described by Yu *et al*.[100] modifying the aniline group to different dihydropyridinone moieties. Two groups of compounds (Series I and Series II) based on (dihydropyridinonyl)amino-5-methylthieno[2,3-*d*]-pyrimidine framework were characterized as low micromolar to sub-micromolar MNK inhibitors with a moderate or weak cytotoxicity (GI_{50} values between 5.7 µM and 90 µM) in MV4-11 cell line. Compounds **16a**, **16c** and **16d** block phosphorylation of eIF4E at Ser209 at 20 µM, arrest proliferation of cells at G1 phase and induce apoptosis in MV4-11 cells. (Table 1.4) Moreover, compounds **16a**, **16b** and **16c** show selectivity against a panel of 9 kinases (CDK2/A, CDK9/T1, MAPK1, mTOR, PKBα, SAPK2a, PI3K, FLT3 and PIM-1).[55,100]

Table 1.4. Exploration of thienopyrimidine scaffold described by Yu *et al*.[100]

Structure	Compound	Substituents		Ki	
		R1	R2	MNK1 (µM)	MNK2 (µM)
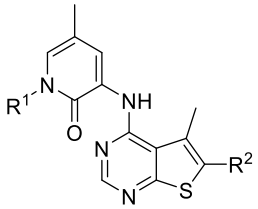 **16** (Series I)	**16a**		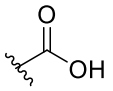	4.82	0.35
	16b	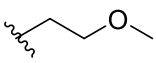	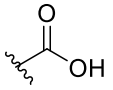	2.06	0.24
	16c		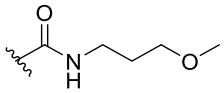	5.00	2.63
	16d	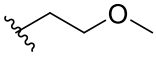	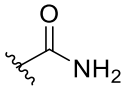	2.33	0.34
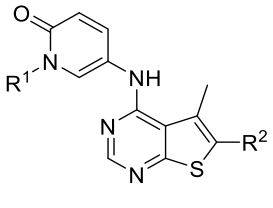 **17** (Series II)	**17a**		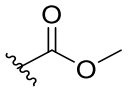	>10	>10
	17b		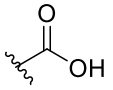	2.15	0.90
	17c		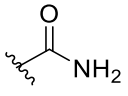	4.51	1.60

Novel series of compounds with the thienopyrimidine moiety were studied by Bayer as MNK1 inhibitors (data for MNK2 are not published). The compounds were active in a nanomolar and sub-nanomolar range and presented promising selectivity in a small panel of 20 kinases (Table 1.5).

Table 1.5. Thienopyrimidine derivatives studied by Bayer as MNK1 inhibitors

General structure	Example	Ki MNK1	PATENT
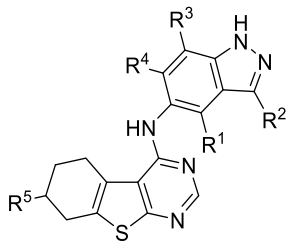 **18**	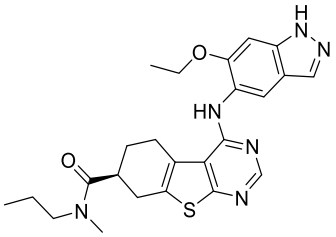 **18a**	0.1 nM	WO 2015/074986 A1[101] WO 2013/174744 A1[102]
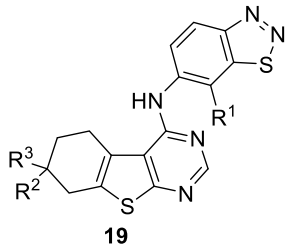 **19**	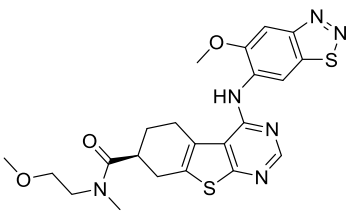 **19a**	0.6 nM	WO 2015/181104 A1[103]
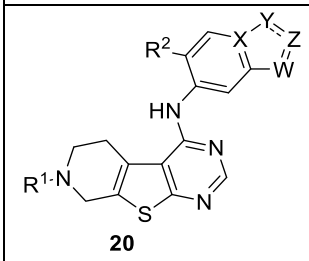 **20**	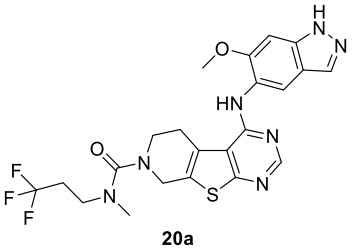 **20a**	1 nM	WO 2015/181063 A1[104]

BAY 11433296, whose chemical structure has not been revealed, entered into clinical trials in 2015 (NCT02439346) alone and as a combinational therapy with docetaxel in NSCLC. There are no further studies and the compounds seems to be discontinued due to portfolio reprioritization. **BAY 11433296**, described as an ATP-competitive inhibitor, has a moderate biochemical activity (IC_{50} values of 40 nM for MNK1 and 904 nM for MNK2) and inhibits eIF4E at Ser209 in a range from 0.5 µM to 2.6 µM in cancer cells. The compound shows anti-cancer activity in cell lines and patient-derived NSCLC xenograft models in mice after oral administrations. Moreover, combinational therapy with docetaxel significantly improves anti-tumor activity when compared with monotherapy *in vivo*.[55,105]

Aminopyrazine-based inhibitors

Novartis researchers developed series of potent and selective inhibitors for *in vitro* target validation of MNK1/2 based on the 3-(1,3-Benzodiazol-2-yl)pyridin-2-amine scaffold.[106] Compound **21**, with a submicromolar activity (0.7 µM for MNK1 and 0.9 µM for MNK2) was discovered by high throughput screening (HTS). The structure was optimized with a SAR strategy. Using docking analysis, Han *et al.*[106] developed a more potent structure (**22**) for MNK1/2 (0.004 and 0.002 µM, respectively). The compound was further modified to improve cell permeability and solubility resulting in compound **23** a potent MNK1/2 inhibitor (IC_{50} of 3 nM for both proteins) with excellent selectivity against 53 other kinases and an interesting cellular activity (**23** inhibits phosphorylation of eIF4E with EC_{50} = 0.6 nM and shows moderate antiproliferative activity in KMS11-luc human multiple myeloma tumor cell line (EC_{50} =1.7 µM)). Despite the good properties, up to now, there are no reports regarding pharmacokinetic and pharmacodynamic parameters *in vivo*.[55,106] (Figure 1.15)

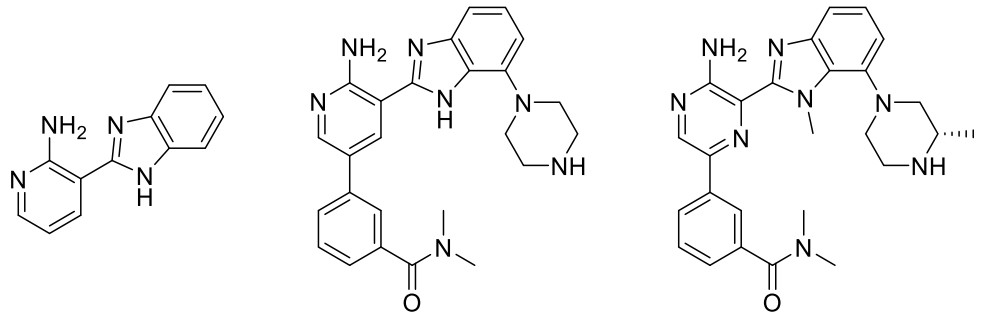

Figure 1.15. Aminopyrazine-based inhibitors described by Han *et al.*[106]

Indazole-based inhibitors

Screening of a library of small molecules performed by Selvita resulted in the discovery of novel indazole compound (1-benzyl-5-(1*H*-indazol-6-yl)-1,2-dihydropyridin-2-one, **24**) which inhibited MNK1 and MNK2 with IC_{50} values of 315 nM and 480 nM, respectively and presented selectivity in a panel of 414 kinases (Figure 1.16).

Further optimization of this compound by a structure-driven approach led to the development of amino-1*H*-indazol-1,2-dihydropyridin-2-one derivatives with improved biochemical potency against MNK1 and MNK2. These compounds inhibited phosphorylation of eIF4E at Ser209 at IC_{50} below 100 nM with no cytotoxicity on a panel of various cell lines of leukemia, breast and prostate.[55]

Compound **25** (**Sel201**) is a potent ATP-competitive inhibitor with an IC_{50} of 10.8 nM and 5.4 nM for MNK1 and MNK2, respectively and few off-targets. **25** suppresses MNK1/2 activity of mutant KIT-melanoma lines and reduces clonogenicity and migration. Moreover, *in vivo* experiments showed that **Sel201** significantly decreased both the number and the size of metastases in the lung.[107]

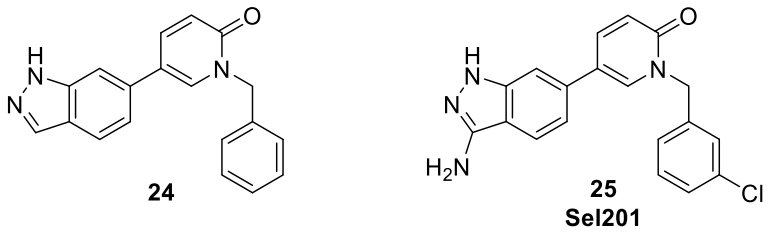

Figure 1.16. Indazole based inhibitors identified by Selvita.[55,107]

Pyridone amine -based inhibitors

Reich *et al.*[108], from Effector Therapeutics, used a structure-based strategy to design a potent MNK1/2 inhibitor with a 6-amino-2,3-dihydroimidazo[1,5-*a*]-pyridine-1,5-dione scaffold. (Figure 1.17)

An initial reference scaffold (**26**) was selected from the analysis of the crystal structures of 6 possible scaffolds in complex with MNK2 (DFG-mutant). Compound optimization included the formation of the lactam and the deconstruction of the purine to pyrimidine (**27**). The introduction of the pyridone ring increased compound selectivity (**28**).

Using molecular modelling, potential substituents were studied. 6-member ring spirocyclic compounds were preferred together with the present of a substituent (F, Cl or Me) at position 5. An amino group in the pyrimidine ring forms a hydrogen bond with the Met162 backbone carbonyl while at the same time reducing metabolic issues. Compound **29** (**eFT508**) presented the best overall profile when considering cellular p-eIF4E potency, *in vivo* efficacy, metabolic stability and kinome selectivity.[109] (Figure 1.17)

Compound **29** blocks eIF4E phosphorylation *via* selective MNK inhibition on a panel of cell lines including lymphoma, breast, lung and colon with IC_{50} values ranging from 1.4 to 22 nM and no toxicity or anti-proliferative effects up to 30 µM. *In vivo* studies demonstrate potent antitumor activity in multiple cancer models (breast, lung and DLBCL).[109]

Compound **29** (**eFT508**) entered clinical trials on November 2015 (NCT02605083) to define dose and response rate and at the same time evaluate safety, drug distribution and effects (plasma concentration, eIF4E phosphorylation in blood cells). Results have not been published yet. **eFT508** (now tomivosertib) is now in Phase II clinical trials in combination with immunotherapy (checkpoint inhibitors PD-1 and PD-L1) or as a monotherapy for the treatment Advanced Castrate-resistant Prostate Cancer (NCT03616834, NCT03690141)

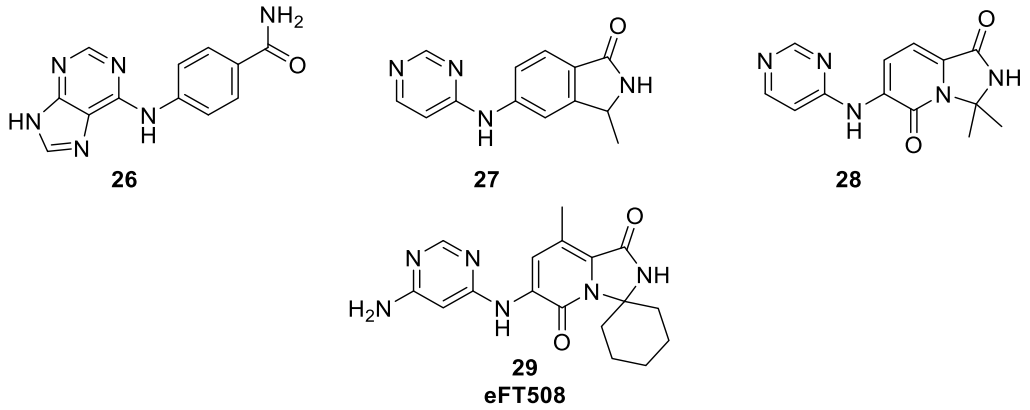

Figure 1.17. Examples of compound optimization performed by Reich *et al.*

Other bicyclic heteroaryl compounds

Bicyclic heteroaryl compounds have been reported as potential MNK1/2 inhibitors on different patent applications. (Table 1.6)

Boehringer Ingelheim has described compounds with pyrrolotriazines and sulfoximine substituted quinazoline scaffolds with activities in a low nanomolar range for both MNK1 and MNK2. Detailed data regarding selectivity and efficacy are not published.[110–112] Imidazopyridazine has been published by Bayer as a new scaffold for low nanomolar MNK1 inhibitors (data for MNK2 are not published).[113–116] Finally, several various bicyclic cores containing nitrogen atoms have been patented by the A*STAR (Agency for Science, Technology and Research) with submicromolar and nanomolar activities.[117] The binding mode of this compounds was studied in depth by Kannan *et al.*[59] providing detailed information of the interaction of the inhibitors and the DFD-in forms of the kinases.

Table 1.6. Bicyclic heteroaryl compounds reported on patent applications

Company	General structure	Example	Patents
Boehringer Ingelheim	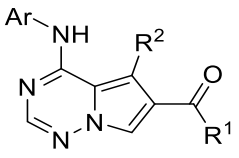 **30**	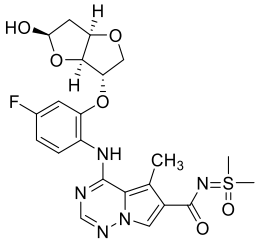 **30a** IC_{50} (MNK1) = 1 nM IC_{50} (MNK2) = 14 nM	WO 2015/091156 A1 [118]
Boehringer Ingelheim	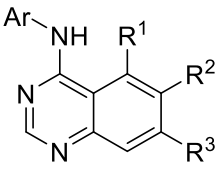 **31**	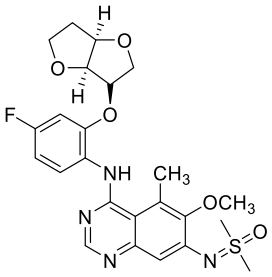 **31a** IC_{50} (MNK1) = 18 nM IC_{50} (MNK2) = 0.8 nM	WO 2015/169677 A1[112] WO 2014/206922 A1 [111] WO 2014/072244 A1 [110]
Bayer Pharma	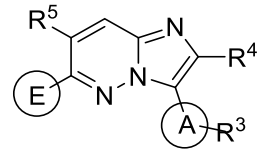 E = 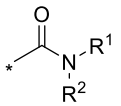 **32**  **33** 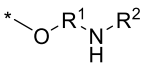 **34**	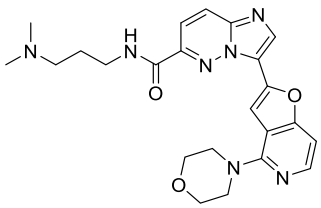 **32a** IC_{50} (MNK1) = 1.5 nM	WO 2015/104254 A1[113] WO 2014/076162 A1 [114] WO 2013/149909 A1 [115] WO 2012/156367 A1 [116]
A*STAR	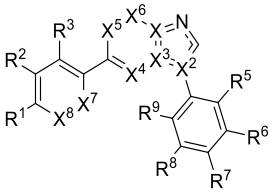 **35**	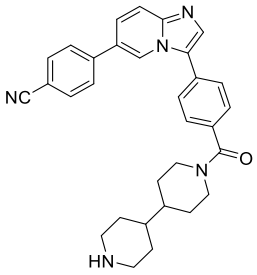 **35a** IC_{50} (MNK1) = 23 nM IC_{50} (MNK2) = 18 nM	WO 2013/147711 A1 [117]

1.6.2. Type II inhibitors

Type II inhibitors reversibly bind to the inactive form of protein kinases (DFG/D-out). The inhibitor reversibly interacts with the kinase forming one, two or three hydrogen bonds with the protein in the 'hinge region'. Moreover, the inactive conformation exposes an additional hydrophobic pocket adjacent to the active site that can be used by Type II inhibitors to form extra interactions and lock the kinase in the inactive conformation.

Type II inhibitors present a higher selectivity in comparison to those of Type I due to their ability to recognize structurally distinctive regions of the active cleft outside the highly conserved ATP binding site that can only be reached in the inactive form of the kinase. Combinations of different conformational states of helix C, the A-loop, and/or P-loop can generate various inactive conformations of the kinase domain and each individual kinase has a preferred inactive conformation. This provides higher selectivity of these molecules towards other kinases.[55,83,84]

Dual MNK1/2 and BCR-ABL1 type II inhibitors

Cherian *et al*.[119,120] proposed a new series of compounds based on a known Type II inhibitor AST-487 (**36**). This molecule was previously described as a FLT3 and KIT inhibitor and inhibits MNK1 and MNK2 with IC_{50} values of 1.76 µM and 20 nM, respectively.[121] By applying a SAR analysis and molecular docking, the compound was optimized to increase selectivity and potency. Compound **37** showed an increased selectivity and displayed IC_{50} values of 577 nM and 14 nM for MNK1 and MNK2 but was not effective against ABL1. (Figure 1.18)

The structure was further modified to achieve dual ABL1-MNK1/2 inhibition resulting in compounds **38a** and **38b**. Both compounds inhibit phosphorylation of eIF4E (substrate of MNK1/2) and CRKL (substrate of ABL1) in K562 cells and showed anti-proliferative activity at low nanomolar ranges in a panel of CML cell lines. These compounds were tested against a panel of 104 kinases showing additional targets. Both compounds were shown to display oral bioavailability and cause tumor regression in *in vivo* xenograft models of K562 cells overexpressing eIF4E in NOD-SCID mice (Figure 1.18). Further modifications on the pyridine moiety (compound **39**) led to an increased activity against MNKs.

Docking combined with molecular dynamic studies with both MNK1 and MNK2 inactive structures (PDB ID 2HW6 and 2AC3) showed characteristic features for Type II inhibitors (In MNK2, interactions with a backbone nitrogen of Glu129 and the hydrophobic pocket and a phenyl ring sandwiched between the gatekeeper Phe159 and Phe227).[120,122]

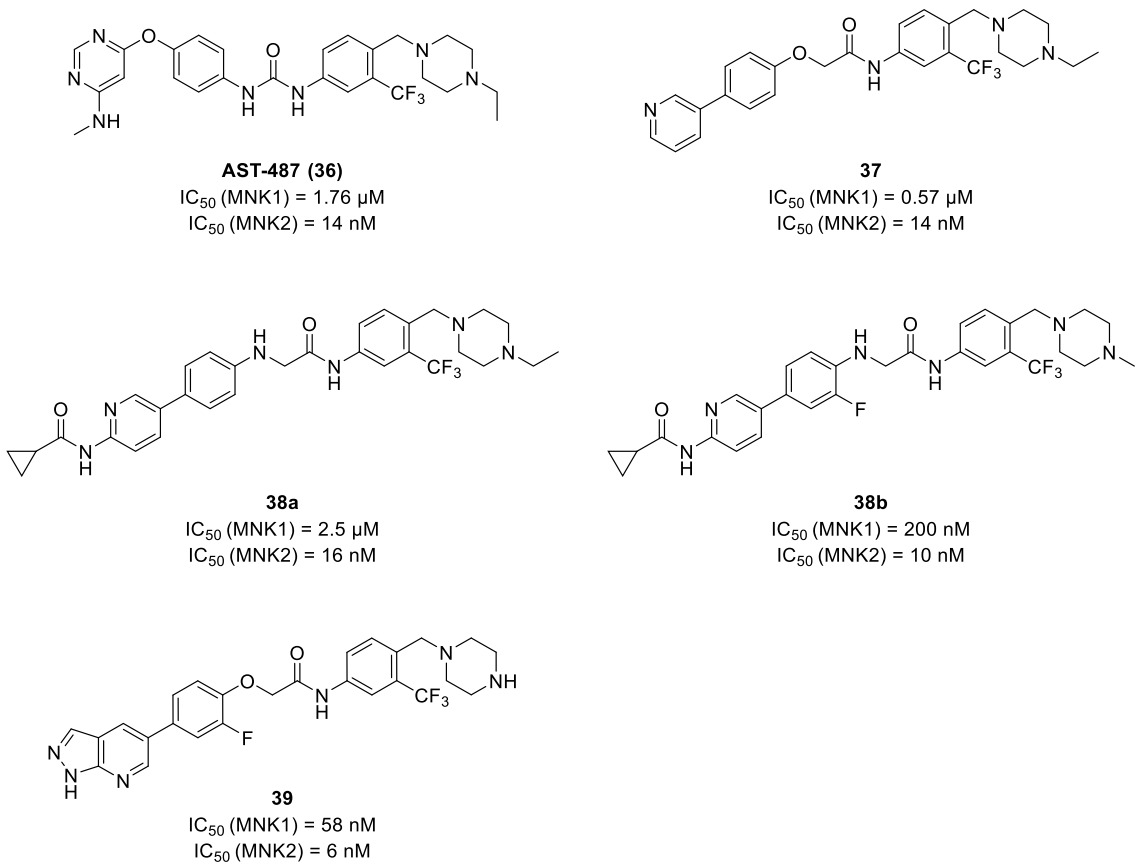

Figure 1.18. Development of dual MNK1/2 and BCR-ABL1 inhibitors by Cherian *et al.*[119,120]

A novel series of derivatives including al alkyne linker were reported in 2015.[123] All synthesized compounds were tested against MNK1/2 kinases and ABL with activities in the submicromolar range. (Figure 1.19)

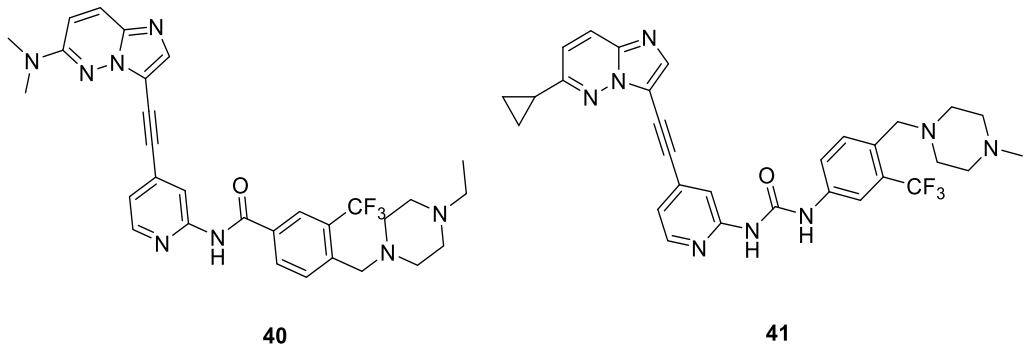

Figure 1.19. Examples of new heteroaryl alkyne derivatives described as dual MNK-ABL inhibitors.[123]

1.6.3. Allosteric inhibitors

These inhibitors are non-ATP-competitive molecules which target an allosteric binding site. These molecules bind outside the ATP binding site, in regions that are involved in the regulatory catalytic domain modulating the activity of the kinase in an allosteric manner.[83] These inhibitors can be classified into two groups depending on the localization of the allosteric site. (1) Type III inhibitors occupy a site next to the ATP-binding pocket, normally a hydrophobic cleft next to the ATP site also known as the "back pocket". The hydrophobic pocket exhibits high level of variability among protein kinases, and as a result these compounds show improved selectivity. (2) Type IV allosteric inhibitors bind to sites distant from the ATP binding pocket. These inhibitors bind to a distinct allosteric site on the kinase and induce conformational changes that make the protein inactive. The exact location of the site is not specifically defined and may be anywhere on the kinase except for the pocket adjacent to the ATP site.[83–86]

Type III and IV inhibitors are believed to allow higher specificity due to the fact that the strongly conserved ATP binding pocket is not involved in the binding and the explored binding sites and regulatory mechanism are unique for each target. Unfortunately, the lack of structural information regarding allosteric sites of many protein kinases limits possibilities for rational design of such compounds.[55,83]

Allosteric Inhibitors Based on Thienopyrimidine Scaffold

Pyrimidine based compounds have been previously described as Type I inhibitors.[95,96,100] However, Basnet *et al.*[97] demonstrated that small changes in the structure can cause changes on the binding mode. The binding mode of 20 selected from thienopyrimidine[95,96,100] anilinopyrimidine[94] and pyrazolo[3,4-*d*]pyrimidine series was studied with an ADP-Glo Kinase Assay. Nine compounds from the first series (with a thienopyrimidine core) displayed non-ATP- and non-substrate-competitive (-/-) binding mode what corresponds to Type III inhibitors. Moreover, the mode of action was proven to be susceptible to minor changes as half of the molecules were found to be type III inhibitors and half type I. As an example, compound **15b** (**MNK1-19**) presents Type III inhibition while compound **15d** (**MNK1-85**) is a Type I inhibitior (Figure 1.20).

Despite the versatility and interesting activity shown by these compounds, it is essential to carefully analyze the binding mode of any thienopyrimidine based molecule when used in a SAR strategy for the development of new inhibitors.

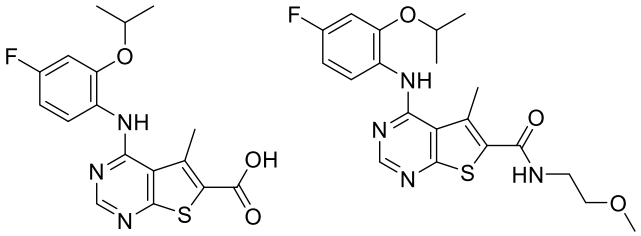

Figure 1.20. Examples of Type III and Type I thienopyrimidine-based compounds

1.6.4. Type VI inhibitors: Covalent inhibitors

These kinase inhibitors directly target a nucleophile from the active site and form an irreversible covalent bond. These compounds contain an electrophilic group that reacts with an exposed cysteine residue in or around the active site, preventing the binding of ATP to the protein kinase. The cysteine residue can undergo a SN2 reaction (when the molecule contains a good leaving group) or react with a Michael acceptor incorporated within the inhibitor.[83,84]

A major challenge with these compounds is to find the right balance between benefits related to the high efficacy and the risks related to unspecific reactivity.[55]

Analogs of Hypothemycin as Covalent Inhibitors (Type VI)

The concept of irreversible MNK1/2 kinase inhibitors has been validated on a group of macrocyclic products (resorcylic acid lactones) based on the naturally occurring cytotoxic compound Hypothemycin (**42**). The cis-enone system of this compound forms an irreversible, covalent bond with a cysteine residue in the ATP binding site (Cys225 in MNK2) through a Michael addition reaction.[124]

Xu *et al*.[124] proposed analogs of Hypothemycin with a simplified structure as potential covalent inhibitors of MNK1/2 kinases. Nine compounds were studied with variation on the stereochemistry of the enone moiety (cis/trans), the protection of the amide group and the protection of alcohol groups (MOMO, MeO, OH). (Figure 1.21)

Compound **43** (trans-enone and with *N*-acetylamide and both unprotected -OH groups) displays the best potency towards MNK1/2 kinases: IC_{50} values of 9 µM and 1.3 µM, respectively and 90% inhibition of eIF4E phosphorylation in HeLa cells (10 µM) with no aparent cytotoxicity (>50 µM). Moderate cytotoxicity is observed in other cell lines: MD-MB-435s (18.5 µM) and K562 (19.5 µM). The covalent inhibition was demonstrated by mass spectrometry proving the formation of the Michael adduct of the ligands with both kinases.[55,124]

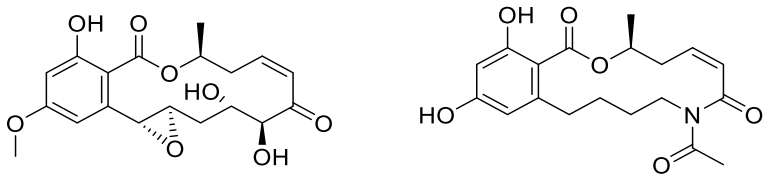

42
Hypothemycin

43

Figure 1.21. Structure of hypothemycin and a derivative as covalent MNK inhibitors.[124]

1.7. Design of new MNK inhibitors

The development of novel MNK inhibitors has experienced a significant progress in the last years. Starting from unselective products of natural origin (**staurosporine** or **cercosporamide**) and a first synthetic micromolar inhibitor (**CGP57380**), several chemical scaffolds have been studied and optimized using computer aided strategies (SAR analysis, docking, molecular dynamics, …) obtaining selective compounds with activities in the nanomolar range. These new molecules are potent candidates as investigational drugs specially for cancer treatment and as molecular probes for further mechanistic studies.[55]

Moreover, in the last 4 years, the two first MNK1/2 inhibitors have entered clinical trials. For years, the development of new inhibitors was motivated by the results from *in vitro* and *in vivo* experiments demonstrating that inhibition of eIF4E phosphorylation *via* MNK could regulate tumor growth with minimal effects on normal cell development. With **BAY 1143269** and **eFT508** from Bayer AG and Effector Therapeutics respectively, the hypothesis of treating cancer by inhibiting MNKs becomes a real fact. For the first time, we will be able to know the effectiveness of such treatment and the benefits of the expected low side effects.

However, despite the important advances from the last years, many questions remain unresolved. Further research is necessary to give light to the biological function of eIF4E phosphorylation and its role in tumorigenesis.

Moreover, there is still room for the development of new inhibitors when considering the activity differences between the biochemical assays and the *in vitro* cellular assays. Therefore, it is of interest to study in depth the different possible binding modes to develop different types of inhibitors.

Most of the currently described molecules are Type I (ATP-competitive) inhibitors. Some efforts have been made to develop non-ATP-competitive inhibitors providing new exciting information such as the identification of alternative pockets different from the ATP-binding site.[97,122] However, this field remains unexplored providing an interesting way to develop alternative candidates. The availability of molecules with different binding modes but equivalent functions will allow to define the most suitable treatment for each patient.

There is still controversy on the *in vitro* effects of these inhibitors. Initial studies considered cytotoxicity and anti-proliferative effects as a positive consequence of MNK inhibition. However, most recent studies demonstrate that MNK inhibition does not induce apoptosis and cells with no expression of the proteins present a normal phenotype. *In vivo* studies also support this hypothesis as KO mice present a normal growth.

The expected cytotoxic effects of MNK inhibitors are questioned in the most recent publications where the authors relate the cell death caused by initial MNK inhibitors with their off-target effects.[109] This fact is of great importance on the development and characterization of new inhibitors.

Finally, some compounds seem to be cell line dependent. Despite providing treatments for specific cancer types it is of interest to develop new compounds with activity in different cell lines. Current studies suggest that combining MNK inhibitors with other specific treatments lead to synergic effects.[80–82,125–127] The availability of non-selective co-treatment agents will provide new opportunities on the treatment of resistant types of tumors while improving the treatment for those already resolved.

Computer aided strategies

In order to reduce time and cost, the traditional trial and error method of drug development has been progressively substituted by high throughput screening methods and computer-aided drug design.

Drug development is a long multistep cyclic process. The information available in literature is used to design new candidates that are synthetized and tested. The information regarding the studied molecules is then used to improve compound design of the next generation of candidates.

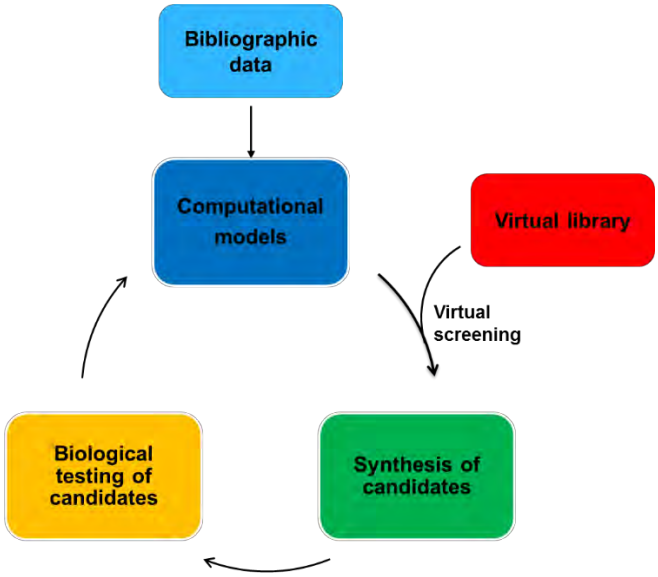

Figure 1.22. Drug development is a cyclic process where the available data is used to create computational models that allow the selection of candidates from a virtual database. The candidates are then synthesized and their activity is tested. The new data are included to the models to improve their predictive capacity.

Computational chemistry applies computer aided techniques to understand the structure and properties of molecules and predict the behavior of molecular systems with the purpose of increasing the number of hits and the information about the interaction between systems.

Computational methods are classified depending on the information used: (1) Structure-based methods depend on the availability of a target structure. Structure-based approaches include ligand docking, pharmacophore and *De novo* ligand design methods. Despite ligand information is not essential, the availability of active ligands allows validation and consequently the obtention of more accurate results. (2) Ligand-based methods such as ligand-based pharmacophores and quantitative structure-activity relationships (QSAR) need information about active and non-active molecules for the target of interest.[128,129]

In the case of MNK1/2 inhibitors structure-based strategies have been used. Despite the limited structural information, many authors[88,95,99,100,106,120] have based their studies on Structure-Activity Relationship (SAR) which allows the derivatization of hit compounds based on the structural motives of the target with the purpose of creating new interactions that increase target-ligand affinity. This strategy permits the development compounds with specific binding modes or with dual activity.

Several crystal structures of MNKs have been published in the Protein Data Bank (PDB) (Table 1.7). However, the structural information is still limited as the available structures only include information of the inactive forms (DFD-out) of MNK1 (apo form and in complex with a ligand), the apo form of inactive MNK2 (DFD-out) and the active form of MNK2 D228G (DFG-in), this structure is crystalized with different ligands (Figure 1.23), but it contains an important mutation in the activation loop. Unfortunately, the activation loop is not resolved for any of the available forms.

On this work, the available structures are used to perform studies in the effect of the DFD-out/DFD-in conformational change and the study of biding modes.

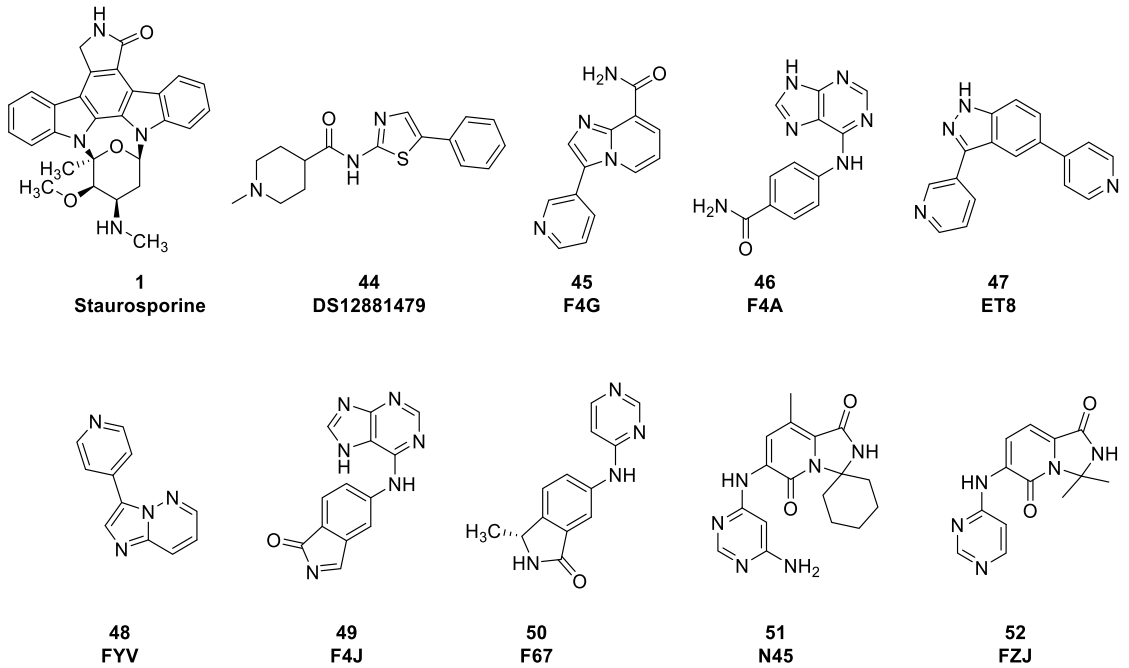

Figure 1.23. Inhibitors contained in crystal structures for MNK2

Table 1.7. MNK1/2 crystal structures published in the PDB

Kinase	PDB ID	Ligand	DFG/D in/out	Sequence coverage	Res (Å)	Year
MNK1 wild	2HW6 [62]	apo	out	37-196, 223-260, 290-335	2.5	2006
MNK1 wild	5WVD [130]	DS12881479 (**44**)	out	41-197, 221-260, 290-334	3	2018
MNK2 wild	2AC3 [61]	apo	out	70-231, 251-369	2.1	2005
MNK2 D228G	2AC5 [61]	apo	in	70-228, 250-369	3.2	2005
MNK2 D228G	2HW7 [62]	Staurosporine (**1**)	in	70-228, 252-299, 303-304, 310-371	2.7	2006
MNK2 D228G	6CJ5 [109]	F4G (**45**)	in	70-228, 252-299, 303-304, 310-371	2.8	2018
MNK2 D228G	6CJE [109]	F4A (**46**)	in	71-228, 250-299, 303-304, 310-371	3.36	2018
MNK2 D228G	6CJH [109]	ET8 (**47**)	in	70-228, 252-299, 303-304, 310-371	3.6	2018
MNK2 D228G	6CJW [109]	FYV (**48**)	in	71-228, 252-299, 303-304, 310-371	3.38	2018
MNK2 D228G	6CJY [109]	F4J (**49**)	in	70-228, 252-299, 303-304, 310-371	3.05	2018
MNK2 D228G	6CK3 [109]	F67 (**50**)	in	70-228, 252-299, 303-304, 310-371	2.9	2018
MNK2 D228G	6CK6 [109]	N45 (**51**)	in	70-228, 252-299, 303-304, 310-371	3.32	2018
MNK2 D228G	6CKI [109]	FZJ (**52**)	in	70-228, 252-299, 303-304, 310-371	2.95	2018

1.8. Pirazolopyridines as MNK inhibitors

Pharmacological inhibition of MNKs has emerged as a new therapy for cancer treatment. In the last years, many efforts have been made in the development of new selective and potent MNK inhibitors. However, further research is needed for the development of new molecules which inhibit eIF4E phosphorylation with no anti-proliferative effects caused by the presence of off-targets and with no cell line dependent activity. These molecules will be extremely useful as molecular probes allowing to obtain of new information of the biology of the eIF4E-MNK axis while at the same time serve as drug candidates for the treatment of disease related with this pathway.

Deep analysis of the actual MNK inhibitors reveals a high structural complexity of the molecules with natural origins what has centered the actual studies in the development of new synthetic structures. Bicyclic nitrogenated compounds seem to be a privileged scaffold for the inhibition of these proteins. Moreover, the presence of a planar aromatic core permits the formation of π-π interaction with essential residues of both the ATP-binding site and the allosteric site. The substitution of the molecules should allow the formation of several hydrogen bond, providing the molecule with both H-bond donors and acceptors. The main interactions formed in each binding mode have been described and can be used for the design of new molecules while at the same time suggesting a possible mode of action.

Pyrazolo[3,4-*b*]pyridinic systems were proposed as an scaffold of interest due to its similarity with **CGP57380** and **SHN-093** core structure, the available synthetic structures at the beginning of the project (Figure 1.24).

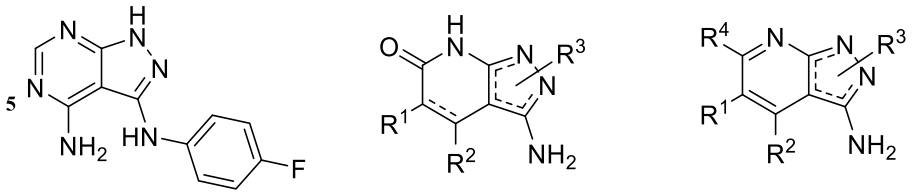

Figure 1.24. Structures of CGP57380 and the pyrazolo[3,4-*b*]pyridinc systems under study in this project

In the last years, the suitability of the scaffold has been confirmed as several new structures with similar cores have been described as potent inhibitors. In 2016, Diab *et al.*[94] reported that the 5-N of **CGP57380** is not involved in the interaction pattern of the molecule in the MNK2 ATP binding site, indicating that the pyridine and pyridone-based scaffolds under study could serve as an alternative to the widely reported pyrimidine structures. Moreover, Yu *et al.*[100] suggested that the 3-amino group would form an additional interaction with Phe227 in the MNK ATP binding pocket indicating the importance of this functional group.

1.8.1. Uses and preparation of pyrazolopyridones and pyrazolopyridines

Heterocyclic compounds represent a very important family of molecules in drug development as these scaffolds are present in both natural and synthetic bioactive substances.[131] Pyrazolo derivatives such as pyrazolo[3,4-*b*]pyridin-6-ones and pyrazolo[3,4-*b*]pyridines are part of this family and many display biological activity. These compounds are described as antimicrobial agents[132,133] and antiviral agents[134] or even photographic materials[135] and hair dyes.[136] The molecules are also under study as drugs for atherosclerosis and high cholesterol treatment[137], as immunosuppressants and antidepressants[138], for cardiovascular diseases[139–141] or as kinase inhibitors for the treatment of diseases such as diabetes, inflammation, hypertension[142,143], neurogenerative diseases[144] and cancer (angiogenic and hyperproliferative diseases)[142–148]. Some molecules have been described as JNK inhibitors[149], BTK inhibitors[150] and EphA4 receptor tyrosine kinase inhibitors[151].

The versatility of pyrazolo[3,4-*b*]pyridines and pyrazolo[3,4-*b*]pyridones makes of special interest the development of synthetic methodologies to prepare this type of compounds. Synthetic routes to these bicyclic molecules can be achieved in different ways depending on the order where the two rings are formed.

The classical method of synthesizing 3-aminopyrazoles is the reaction of closing the pyrazole ring through a reaction with hydrazine. The same approach can be used in the synthesis of pyrazolo[3,4-*b*]pyridin-6-ones using the reaction of an 3-cyano-6-pyridin-6-one intermediate with hydrazine.[131,152–154] This strategy is also useful for the preparation of pyrazolo[3,4-*b*]pyridines[155,156] (Figure 1.25 A)

A second strategy for the formation of pyrazolo[3,4-*b*]pyridones and pyrazolo[3,4-*b*]pyridines is based on the annelation of the pyridone/pyridine ring to the already formed pyrazole moiety. Most strategies start from 5-amino-pyrazole-4-carbonitriles or 5-amino-pyrazole-4-carbaldehydes which are cyclized with diethylmalonate or similar products.[131,156] Unfortunately, this strategy does not allow to directly obtain the 3-amino substituted product. (Figure 1.25 B)

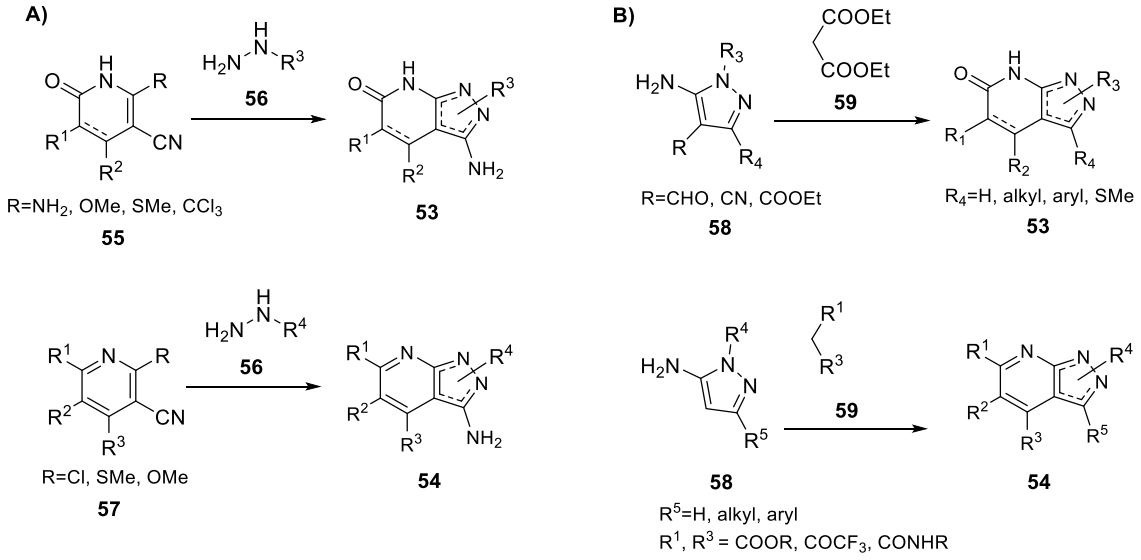

Figure 1.25. A) Synthesis of pyrazolopyridones and pyrazolopyridines *via* the annelation of the pyrazole ring onto the pyridone/pyridine. B) Synthesis of pyrazolo[3,4-*b*]pyridones and pyrazolo[3,4-*b*]pyridines is based on the annelation of the pyridone/pyridine ring to the already formed pyrazole

1.8.2. Synthesis of pyrazolo[3,4-*b*]pyridones in the GQF

The Grup de Química Farmacèutica (GQF) from IQS has an excellent experience on the synthesis of two privileged bicyclic scaffolds: pyrido[2,3-*d*]pyrimidin-7(8*H*)-ones[157–160] and pyrazolo[3,4-*b*]pyridin-6-ones[153,161]. These structures have been modified to act as kinase inhibitors such as BCR kinase inhibitors for B-cell non-Hodgkin lymphoma [160,162] or EGFR inhibitors [163], as HCV (Hepatitis C) inhibitors[159] or hypnotic drugs[153].

The group uses the first strategy to synthetize the candidates. The synthesis starts with a Michael reaction between a α,β-unsaturated ester and malononitrile in NaOMe/MeOH to form the intermediate compound 2-methoxy-6-oxo-1,4,5,6-tetrahydropyridine-3-carbonitrile (**62**). Substituents in position C4 (R^2) and C5 (R^1) correspond to the α and β substituents of the ester molecule. Cyclization of **62** with hydrazine or substituted (alkyl or aryl) hydrazines renders the corresponding pyrazolo[3,4-*b*]pyridin-6-ones (**63** and **64**).

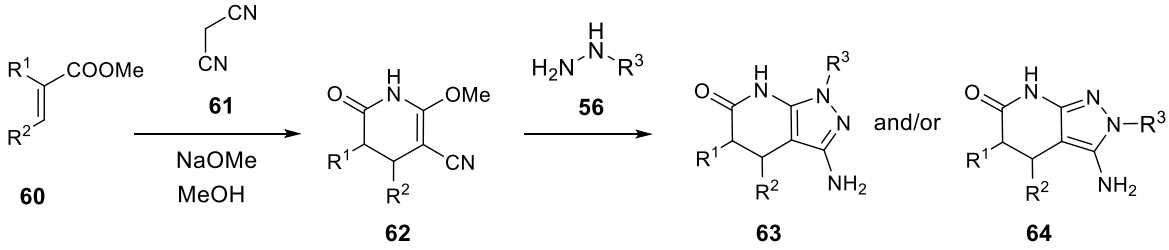

Figure 1.26. Synthesis of pyrazolo[3,4-*b*]pyridonic systems used by the GQF

1.9. Development of new pyrazolo[3,4-*b*]pyridine scaffolds as MNK inhibitors as a collaborative project

This project combines the expertise of two research groups to develop new MNK inhibitors based on a pyrazolo[3,4-*b*]pyridine scaffold.

On one side, the Grup de Química Farmacèutica (GQF) from IQS, headed by Dr. Jose I. Borrell, has a wide experience on the design and the synthesis of potential kinase inhibitors. The research performed by the group combines computational design and synthetic approaches to create new pharmaceutical candidates. Moreover, the GQF has demonstrated to have a deep knowledge of the synthesis of pyrazolo[3,4-*b*]pyridine-6-one derivatives.[153,161]

On the other hand, the Translational Molecular Biology Group from the VHIR (Vall d'Hebron Institut de Recerca), headed by Dr. Santiago Ramón y Cajal, is focused on translational research with the central aim of identifying druggable cell signaling factors with a central role in cancer progression. The main goal of their research is to identify factors, which are overexpressed in malignant cells regardless specific genetic alterations. Data from the group could demonstrate that p-eIF4E overexpression decreases cell apoptosis and confers resistance to oxidative stress, starvation and treatment with DNA damaging agents in the triple negative breast cancer cell line MDA-MB-231.[76] The research conducted in the group for the last years has identified phosphorylated eIF4E (p-eIF4E) as independent prognostic factor with poor prognosis in different types of human tumors.[21,164,165]

The tight collaboration of both groups is essential for the development of the project. The development of a translational project needs the combination of a series of expertise areas from chemistry to biology, which cannot be achieved by a single group. On one side, the GQF from IQS, focused in computational and synthetic chemistry has no capabilities to carry out advanced biological testing of the candidates and, on the other hand, Translational Molecular Biology Group from the VHIR with a large expertise on translational biology, has no means for the design and development of potential drug candidates. By developing the project between the two groups, we ensure to take advantage of the expertise of each group and achieve better and faster results while at the same time starting a collaboration that covers all the stages for drug design and should be capable to prepare drug candidates ready to be tested *in vivo*.

1.10. Hypothesis

Combination of MNK inhibitors with the current chemotherapies is considered an interesting new strategy for cancer treatment. Increased levels of p-eIF4E has been related to cellular stress causing resistance to different therapies such as chemotherapeutic treatments.[77,78] Thus, the combination with MNK inhibitors can be used to sensitize tumors to the current treatments and overcome such resistance problems.[80–82] Moreover, eIF4E expression seems to be unaffected by tumor heterogeneity, the main cause of resistance, suggesting a higher rate of success of therapies that combine targeting of eIF4E.[21]

Furthermore, eIF4E phosphorylation seems to be essential for tumor development but dispensable for normal cell development suggesting that the pharmacological inhibition of MNK1/2 would be an effective and non-toxic treatment.[51]

Therefore, the development of new potent and selective MNK1/2 inhibitors is of special interest. Despite the important advances in the recent years and the promising *in vitro* and *in vivo* results, the clinical effects of this inhibitors are still unknown. Thus, it is essential to develop new candidates, preferable with different modes of action, which can be studied as potent drugs for cancer treatment specially in combination with chemotherapy.

1.11. Objectives

The main goal of this thesis is to develop new MNK inhibitors based on the pyrazolo[3,4-*b*]pyridine scaffold. With this purpose, the following specific objectives are defined:

1. Preparation of a family of pyrazolo[3,4-*b*]pyridin-6-ones (**53**) as potential MNK inhibitors. Development of general methodologies to selectively modify the different points susceptible to modification and including the selective preparation of the N1 and N2 isomers.

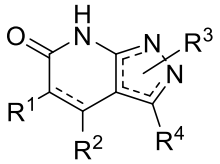

53

2. Preparation of a family of pyrazolo[3,4-*b*]pyridin-3-amines (**54**) as potential MNK inhibitors. Development of general methodologies to obtain the desired combination of substituents.

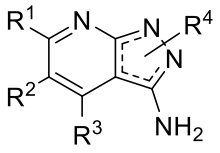

54

3. Study of the *in vitro* activity of the different candidates as MNK inhibitors and characterization of the identified hits.

4. Design of computational strategies to support the development of MNK inhibitors using both ligand-based and structure-based approaches. Development of both QSAR models to guide candidate selection and structural models to identify binding modes and facilitate hit to lead optimization.

1.12. References

1. Cancer Research UK. Worldwide cancer incidence statistics. Available at: https://www.cancerresearchuk.org/health-professional/cancer-statistics/worldwide-cancer/incidence. (Accessed: 20th April 2019)
2. International Agency for Research on Cancer (World Health Organization). Estimated number of deaths in 2018. Available at: http://gco.iarc.fr/today/home. (Accessed: 20th April 2019)
3. Abraham, D. in *Burger's Medicinal chemistry and drug discovery* (Wiley Interscience, 2003).
4. World Health Organization. Cancer. (2018). Available at: https://www.who.int/en/news-room/fact-sheets/detail/cancer. (Accessed: 20th April 2019)
5. Anand, P. *et al.* Cancer is a preventable disease that requires major lifestyle changes. *Pharm. Res.* **25,** 2097–2116 (2008).
6. National Cancer Institute. Risk Factors for Cancer. (2015). Available at: https://www.cancer.gov/about-cancer/causes-prevention/risk. (Accessed: 20th April 2019)
7. Ashkenazi, R., Gentry, S. N. & Jackson, T. L. Pathways to Tumorigenesis—Modeling Mutation Acquisition in Stem Cells and Their Progeny. *Neoplasia* **10,** 170–1182 (2008).
8. Devi, U. P. Basics of carcinogenesis. *Heal. Adm* **XVII,** 16–24 (2004).
9. Basu, A. K. DNA damage, mutagenesis and cancer. *Int. J. Mol. Sci.* **19,** (2018).
10. Casasent, A. K. *et al.* Multiclonal Invasion in Breast Tumors Identified by Topographic Single Cell Sequencing. *Cell* **172,** 205–217 (2018).
11. Shee, K. *et al.* Ductal Carcinoma in Situ Biomarkers in a Precision Medicine Era. *Am. J. Pathol.* **189,** 956–965 (2019).
12. Cooper, G. M. Cancer: The development and causes of cancer. *Cell A Mol. Approach.* (2000).
13. Caligur, V. Carcinogenesis and Epigenetics. *BioFiles* **3,** 18–23 (2008).
14. Hanahan, D. & Weinber, R. A. Hallmarks of cancer. *Cell* **100,** 57–70 (2000).
15. Hanahan, D. & Weinberg, R. a. Hallmarks of cancer: the next generation. *Cell* **144,** 646–74 (2011).
16. Negrini, S., Gorgoulis, V. G. & Halazonetis, T. D. Genomic instability an evolving hallmark of cancer. *Nat. Rev. Mol. Cell Biol.* **11,** 220–228 (2010).
17. Fouad, Y. A. & Aanei, C. Revisiting the hallmarks of cancer. *Am. J. Cancer Res.* **7,** 1016–1036 (2017).
18. Wang, M. *et al.* Role of tumor microenvironment in tumorigenesis. *J. Cancer* **8,** 761–773 (2017).

19. Yuan, Y., Jiang, Y. C., Sun, C. K. & Chen, Q. M. Role of the tumor microenvironment in tumor progression and the clinical applications (Review). *Oncol. Rep.* **35,** 2499–2515 (2016).

20. Balkwill, F. R., Capasso, M. & Hagemann, T. The tumor microenvironment at a glance. *J. Cell Sci.* **125,** 5591–5596 (2012).

21. Ramon Cajal, S. Y. *et al.* Beyond molecular tumor heterogeneity: Protein synthesis takes control. *Oncogene* **37,** 2490–2501 (2018).

22. Waks, A. G. & Winer, E. P. Breast Cancer Treatment: A Review. *J. Am. Med. Assoc.* **321,** 288–300 (2019).

23. Breast Cancer Organization. Molecular Subtypes of Breast Cancer. (2019). Available at: https://www.breastcancer.org/symptoms/types/molecular-subtypes. (Accessed: 21st April 2019)

24. Arnaout, A. *et al.* Neoadjuvant therapy for breast cancer: updates and proceedings from the Seventh Annual Meeting of the Canadian Consortium for Locally Advanced Breast Cancer. *Curr. Oncol.* **25,** 490–498 (2018).

25. Miller, E. *et al.* Current treatment of early breast cancer: adjuvant and neoadjuvant therapy. *F1000Research* **3,** 198 (2014).

26. von Minckwitz, G. Docetaxel/anthracycline combinations for breast cancer treatment. *Expert Opin. Pharmacother.* **8,** 485–495 (2007).

27. Andreopoulou, E. & Sparano, J. A. Chemotherapy in Patients with Anthracycline and Taxane-Pretreated Metastatic Breast Cancer: An Overview. *Curr. Breast Cancer Rep.* **5,** 42–50 (2013).

28. Ozretic, P., Bisio, A., Inga, A. & Levanat, S. The growing relevance of cap-independent translation initiation in cancer-related genes. *Period. Biol.* **114,** 471–478 (2012).

29. Clancy, S. & Brown, W. Translation: DNA to mRNA to Protein. *Nat. Educ.* **1,** 101 (2008).

30. Ramanathan, A., Robb, G. B. & Chan, S.-H. mRNA capping: biological functions and applications. *Nucleic Acids Res.* **44,** 7511–7526 (2016).

31. Cowling, V. H. & Cole, M. D. Myc Regulation of mRNA Cap Methylation. *Genes Cancer* **1,** 576–579 (2010).

32. Goodfellow, I. G. & Roberts, L. O. Molecules in Focus Eukaryotic initiation factor 4E. *Eur. PMC Funders Gr.* **40,** 2675–2680 (2011).

33. Gray, N. K. & Wickens, M. Control of Translation. *Annu. Rev. Cell Dev. Biol.* **14,** 399–458 (1998).

34. Hashem, Y. *et al.* Structure of the Mammalian Ribosomal 43S Preinitiation Complex Bound to the Scanning Factor DHX29. *Cell* **153,** 1108–1119 (2013).

35. Piserà, A., Campo, A. & Campo, S. Structure and functions of the translation initiation factor eIF4E and its role in cancer development and treatment. *J. Genet. Genomics* **45,** 13–24 (2018).

36. Rhoads, R. E. EIF4E: New family members, new binding partners, new roles. *J. Biol. Chem.* **284,** 16711–16715 (2009).

37. Volpon, L. *et al.* Importin 8 mediates m 7 G cap-sensitive nuclear import of the eukaryotic translation initiation factor eIF4E . *Proc. Natl. Acad. Sci.* **113,** 5263–5268 (2016).

38. Fan, W. *et al.* Elevated levels of p-Mnk1, p-eIF4E and p-p70S6K proteins are associated with tumor recurrence and poor prognosis in astrocytomas. *J. Neurooncol.* **131,** 485–493 (2017).

39. Muller, M. Anthraquinones as pharamacological tools and drugs. *Med. Res. Rev.* **36,** 705–748 (2016).

40. Graff, J. R., Konicek, B. W., Carter, J. H. & Marcusson, E. G. Targeting the Eukaryotic Translation Initiation Factor 4E for Cancer Therapy. *Cancer Res.* **68,** 631–634 (2008).

41. Borden, K. L. B. The eukaryotic translation initiation factor eIF4E wears a 'cap' for many occasions. *Translation* **4,** e1220899 (2016).

42. Uttam, S., Wong, C., Price, T. J. & Khoutorsky, A. eIF4E-Dependent Translational Control: A Central Mechanism for Regulation of Pain Plasticity. *Front. Genet.* **9,** 1–10 (2018).

43. Parker, R. & Sheth, U. P Bodies and the Control of mRNA Translation and Degradation. *Mol. Cell* **25,** 635–646 (2007).

44. Decker, C. J. & Parker, R. P-Bodies and Stress Granules: Possible Roles in the Control of Translation and mRNA Degradation. *Cold Spring Harb. Perspect. Biol.* **4,** (2012).

45. Luo, Y., Na, Z. & Slavoff, S. A. P-Bodies: Composition, Properties, and Functions. *Biochemistry* **57,** 2424–2431 (2018).

46. Culjkovic-Kraljacic, B. & Borden, K. L. B. Aiding and abetting cancer: MRNA export and the nuclear pore. *Trends Cell Biol.* **23,** 328–335 (2013).

47. Volpon, L. *et al.* A biochemical framework for eIF4E-dependent mRNA export and nuclear recycling of the export machinery. *Rna* **23,** 927–937 (2017).

48. Martin, F. *et al.* Cap-Assisted Internal Initiation of Translation of Histone H4. *Mol. Cell* **41,** 197–209 (2011).

49. Culjkovic, B., Topisirovic, I. & Borden, K. L. B. Controlling gene expression through RNA regulons: The role of the eukaryotic translation initiation factor eIF4E. *Cell Cycle* **6,** 65–69 (2007).

50. Müller, D. *et al.* 4E-BP restrains eIF4E phosphorylation. *Translation* **1,** (2013).

51. Hou, J., Kam, F., Proud, C. G. & Wang, S. Targeting Mnks for Cancer Therapy. *Oncotarget* **3,** 118–131 (2012).

52. Qin, X., Jiang, B. & Zhang, Y. 4E-BP1, a multifactor regulated multifunctional protein. *Cell Cycle* **15,** 781–786 (2016).

53. Alain, T., Sonenberg, N. & Topisirovic, I. mTOR inhibitor efficacy is determined by the eIF4E/4E-BP ratio. *Oncotarget* **3,** 1491–1492 (2012).

54. Alain, T. *et al.* eIF4E/4E-BP Ratio Predicts the Efficacy of mTOR Targeted Therapies. *Cancer Res.* **72,** 6468–6476 (2012).

55. Dreas, A. *et al.* Mitogen-activated Protein Kinase (MAPK) Interacting Kinases 1 and 2 (MNK1 and MNK2) as Targets for Cancer Therapy: Recent Progress in the Development of MNK Inhibitors. *Curr. Med. Chem.* **24,** 3025–3053 (2017).

56. Marcotrigiano, J., Gingras, A. C., Sonenberg, N. & Burley, S. K. X-ray studies iof the messenger RNA 5' cap-binding protein (eIF4E) bound to 7-methyl-GDP. *Nucleic Acids Symp Ser* **36,** 8–11 (1997).

57. Scheper, G. C. & Proud, C. G. Does phosphorylation of the cap-binding protein eIF4E play a role in translation initiation? *Eur. J. Biochem.* **269,** 5350–5359 (2002).

58. Slepenkov, S. V., Darzynkiewicz, E. & Rhoads, R. E. Stopped-flow kinetic analysis of eIF4E and phosphorylated eIF4E binding to cap analogs and capped oligoribonucleotides: Evidence for a one-step binding mechanism. *J. Biol. Chem.* **281,** 14927–14938 (2006).

59. Kannan, S. *et al.* Probing the binding mechanism of Mnk inhibitors by docking and molecular dynamics simulations. *Biochemistry* **54,** 32–46 (2015).

60. Cargnello, M. & Roux, P. P. Activation and Function of the MAPKs and Their Substrates, the MAPK-Activated Protein Kinases. *Microbiol. Mol. Biol. Rev.* **75,** 50–83 (2011).

61. Jauch, R. *et al.* Crystal Structures of the Mnk2 Kinase Domain Reveal an Inhibitory Conformation and a Zinc Binding Site. *Structure* **13,** 1559–1568 (2005).

62. Jauch, R. *et al.* Mitogen-activated protein kinases interacting kinases are autoinhibited by a reprogrammed activation segment. *EMBO J.* **25,** 4020–4032 (2006).

63. Hou, J., Teo, T., Sykes, M. J. & Wang, S. Insights into the Importance of DFD-Motif and Insertion I1 in Stabilizing the DFD-Out Conformation of Mnk2 Kinase. *ACS Med. Chem. Lett.* **4,** 736–41 (2013).

64. Diab, S. *et al.* MAP Kinase-Interacting Kinases—Emerging Targets against Cancer. *Chem. Biol.* **21,** 441–452 (2014).

65. Joshi, S. Mnk kinase pathway: Cellular functions and biological outcomes. *World J. Biol. Chem.* **5,** 321 (2014).

66. Buxade, M. The Mnks: MAP kinase-interacting kinases (MAP kinase signal-integrating kinases). *Front. Biosci.* **13,** 5359 (2008).

67. Shveygert, M., Kaiser, C., Bradrick, S. S. & Gromeier, M. Regulation of Eukaryotic Initiation Factor 4E (eIF4E) Phosphorylation by Mitogen-Activated Protein Kinase Occurs through Modulation of Mnk1-eIF4G Interaction. *Mol. Cell. Biol.* **30,** 5160–5167 (2010).

68. Diab, S. *et al.* MAP kinase-interacting kinases - Emerging targets against cancer. *Chem. Biol.* **21,** 441–452 (2014).

69. Konicek, B. W. *et al.* Therapeutic Inhibition of MAP Kinase Interacting Kinase Blocks Eukaryotic Initiation Factor 4E Phosphorylation and Suppresses Outgrowth of Experimental Lung Metastases. *Cancer Res.* **71,** 1849–1857 (2011).

70. Xie, J., Merrett, J. E., Jensen, K. B. & Proud, C. G. The MAP kinase-interacting kinases (MNKs) as targets in oncology. *Expert Opin. Ther. Targets* **23,** 187–199 (2019).

71. Altman, J. K. *et al.* Inhibition of Mnk kinase activity by cercosporamide and suppressive effects on acute myeloid leukemia precursors. *Blood* **121,** 3675–3681 (2013).

72. Nasr, Z., Robert, F., Porco, J. A., Muller, W. J. & Pelletier, J. eIF4F suppression in breast cancer affects maintenance and progression. *Oncogene* **32,** 861–871 (2013).

73. Furic, L. *et al.* eIF4E phosphorylation promotes tumorigenesis and is associated with prostate cancer progression. *Proc. Natl. Acad. Sci.* **107,** 14134–14139 (2010).

74. Ueda, T., Watanabe-Fukunaga, R., Fukuyama, H., Nagata, S. & Fukunaga, R. Mnk2 and Mnk1 Are Essential for Constitutive and Inducible Phosphorylation of Eukaryotic Initiation Factor 4E but Not for Cell Growth or Development. *Mol. Cell. Biol.* **24,** 6539–6549 (2004).

75. Ueda, T. *et al.* Combined deficiency for MAP kinase-interacting kinase 1 and 2 (Mnk1 and Mnk2) delays tumor development. *Proc. Natl. Acad. Sci.* **107,** 13984–13990 (2010).

76. Martínez, A. *et al.* Phosphorylation of eIF4E Confers Resistance to Cellular Stress and DNA-Damaging Agents through an Interaction with 4E-T: A Rationale for Novel Therapeutic Approaches. *PLoS One* **10,** (2015).

77. Adesso, L. *et al.* Gemcitabine triggers a pro-survival response in pancreatic cancer cells through activation of the MNK2/eIF4E pathway. *Oncogene* **32,** 2848–2857 (2013).

78. Duncan, R. F., Peterson, H. & Sevanian, A. Signal transduction pathways leading to increased eIF4E phosphorylation caused by oxidative stress. *Free Radic. Biol. Med.* **38,** 631–643 (2005).

79. Dagogo-Jack, I. & Shaw, A. T. Tumour heterogeneity and resistance to cancer therapies. *Nat. Rev. Clin. Oncol.* **15,** 81–94 (2017).

80. Grzmil, M. *et al.* Inhibition of MNK pathways enhances cancer cell response to chemotherapy with temozolomide and targeted radionuclide therapy. *Cell. Signal.* **28,** 1412–1421 (2016).

81. Hu, K., Zhang, J., Yu, M. & Xiong, C. Inhibition of Mnk-eIF4E pathway sensitizes the efficacy to chemotherapy in anaplastic thyroid cancer. *Futur. Oncol.* **13,** 489–498 (2017).

82. Li, P. *et al.* Inhibition of Mnk enhances apoptotic activity of cytarabine in acute myeloid leukemia cells. *Oncotarget* **7,** (2016).

83. Blanc, J., Geney, R. & Menet, C. Type II Kinase Inhibitors: An Opportunity in Cancer for Rational Design. *Anticancer. Agents Med. Chem.* **13,** 731–747 (2013).

84. Fabbro, D. 25 Years of Small Molecular Weight Kinase Inhibitors: Potentials and Limitations. *Mol. Pharmacol.* **87,** 766–775 (2014).

85. Roskoski, R. Classification of small molecule protein kinase inhibitors based upon the structures of their drug-enzyme complexes. *Pharmacol. Res.* **103,** 26–48 (2016).

86. Gavrin, L. K. & Saiah, E. Approaches to discover non-ATP site kinase inhibitors. *Med. Chem. Commun.* **4,** 41–51 (2013).

87. Bain, J. *et al.* The selectivity of protein kinase inhibitors : a further update. **315,** 297–315 (2007).

88. Diab, S. *et al.* Unveiling new chemical scaffolds as Mnk inhibitors. *Future Med. Chem.* **8,** 271–285 (2016).

89. Klar, U. *et al.* Substituted indazol-pyrrolopyrimidines useful in the treatment of hyperproliferative diseases. WO 2014048869A1 (2014).

90. Beggs, J. E. *et al.* The MAP kinase-interacting kinases regulate cell migration, vimentin expression and eIF4E/CYFIP1 binding. *Biochem. J.* **467,** 63–76 (2015).

91. Konicek, B. W. *et al.* Therapeutic Inhibition of MAP Kinase Interacting Kinase Blocks Eukaryotic Initiation Factor 4E Phosphorylation and Suppresses Outgrowth of Experimental Lung Metastases. *Cancer Res.*1849–1858 (2011).

92. Altman, J. K. *et al.* Inhibition of Mnk kinase activity by cercosporamide and suppressive effects on acute myeloid leukemia precursors. **121,** 3675–3682 (2016).

93. Wang, S. *et al.* Design and synthesis of novel 6-hydroxy-4-methoxy-3-methylbenzofuran-7-carboxamide derivatives as potent Mnks inhibitors by fragment-based drug design. *Bioorg. Med. Chem.* **26,** 4602–4614 (2018).

94. Diab, S. *et al.* Discovery of 5-(2-(phenylamino)pyrimidin-4-yl)thiazol-2(3H)-one derivatives as potent Mnk2 inhibitors: synthesis, SAR analysis and biological evaluation. *ChemMedChem* **9,** 962–972 (2014).

95. Teo, T. *et al.* An integrated approach for discovery of highly potent and selective Mnk inhibitors: Screening, synthesis and SAR analysis. *Eur. J. Med. Chem.* **103,** 539–550 (2015).

96. Teo, T. *et al.* Pharmacologic Inhibition of MNKs in Acute Myeloid Leukemia. *Mol. Pharmacol.* **88,** 380–389 (2015).

97. Basnet, S. K. C. *et al.* Identification of a Highly Conserved Allosteric Binding Site on Mnk1 and Mnk2. *Mol. Pharmacol.* **88,** 935–948 (2015).

98. Heckel, A. *et al.* Thienopyrimidines containing a substituted alkyl group for pharmaceutical compositions. WO 2011104340A1 (2011).

99. Jin, X. *et al.* Design, synthesis and activity of Mnk1 and Mnk2 selective inhibitors containing thieno[2,3-d]pyrimidine scaffold. *Eur. J. Med. Chem.* 735–751 (2019).

100. Yu, M. *et al.* Discovery of 4-(dihydropyridinon-3-yl)amino-5-methylthieno[2,3-d]pyrimidine derivatives as potent Mnk inhibitors: synthesis, structure–activity relationship analysis and biological evaluation. *Eur. J. Med. Chem.* **95,** 116–126 (2015).

101. Klar, U. *et al.* Thienopyrimidines as mknk1 and mknk2 inhibitors. WO 2015/074986 Al (2015).

102. Kettschau, G. *et al.* Thienopyrimidines. WO 2013/174744 A1 (2013).

103. Richter, A. *et al.* Benzothiadiazolamines. WO 2015/181104 A190 (2015).

104. Klar, U. *et al.* Substituted tetrahydropyridothienopyrimidines. WO 2015/181063 A1 (2015).

105. Santag, S. *et al.* BAY 1143269, a novel MNK1 inhibitor, targets oncogenic protein expression and shows potent anti-tumor activity. *Cancer Lett.* **390,** 21–29 (2017).

106. Han, W. *et al.* Discovery of a Selective and Potent Inhibitor of Mitogen-Activated Protein Kinase-Interacting Kinases 1 and 2 (MNK1/2) Utilizing Structure-Based Drug Design. *J. Med. Chem.* **59,** 3034–3045 (2016).

107. Zhan, Y. *et al.* MNK1/2 inhibition limits oncogenicity and metastasis of KIT-mutant melanoma. *J. Clin. Invest.* **127,** 4179–4192 (2017).

108. Reich, S., Sprengeler, P. A. ., Webber, S. E. ., Xiang, A. X. & Ernst, J. T. Mnk inhibitors and methods related thereto. WO 2015200481 A1 (2015).

109. Reich, S. H. *et al.* Structure-based Design of Pyridone-Aminal eFT508 Targeting Dysregulated Translation by Selective Mitogen-activated Protein Kinase Interacting Kinases 1 and 2 (MNK1/2) Inhibition. *J. Med. Chem.* **61,** 3516–3540 (2018).

110. Blum, M. *et al.* Sulfoximine substituted quinazolines for pharmaceutical compositions. WO 2014/072244 A1 (2014).

111. Blum, A. *et al.* Sulfoximine substituted quinazolines and their use as mnk1 and/or mnk2 kinase inhibitors. WO 2014/206922 A1 (2014).

112. Blum, A. Sulfoximine substituted quinazolines for pharmaceutical compositions. WO 2015/169677 A1 (2015).

113. Schulze, V. *et al.* Amido-substituted imidazopyridazines useful in the treatment of hyper-proliferative and/or angiogenesis disorders. WO 2015/104254 A1 (2015).

114. Zorn, L. *et al.* Aminoimidazopyridazines. WO 2014/076162 A1 (2014).

115. Eis, K. *et al.* Amino-substituted imidazopyridazines. WO 2013/149909 A1 (2013).

116. Eis, K. *et al.* Amino-substituted imidazopyridazines as mknk1 kinase inhibitors. WO 2012/156367 A1 (2012).

117. Nacro, K., Duraiswamy, J. A. & Chennamaneni, L. R. Bicyclic heterocyclic derivatives as mnk1 and mnk2 modulators and uses thereof. WO 2013/147711 A1 (2013).

118. Wiedenmayer, D., Blum, A., Gottschling, D. & Heckel Armin, H. J. P. Sulfoximine substituted pyrrolotriazines for pharmaceutical compositions. WO 2015/091156 A1 (2015).

119. Cherian, J., Duraiswamy, A. & Nacro, K. Compounds including map kinase interacting kinases 1 and 2 (mnk1 and mnk2) modulators and abl and abl (t315i) inhibitors, and uses thereof. WO 2014088519A1 (2014).

120. Cherian, J. *et al.* Structure-Activity Relationship Studies of Mitogen Activated Protein Kinase Interacting Kinase (MNK) 1 and 2 and BCR-ABL1 Inhibitors Targeting Chronic Myeloid Leukemic Cells. *J. Med. Chem.* **59,** 3063–3078 (2016).

121. Karaman, M. W. *et al.* A quantitative analysis of kinase inhibitor selectivity. *Nat. Biotechnol.* **26,** 127–132 (2008).

122. Kannan, S. *et al.* Small Molecules Targeting the Inactive Form of the Mnk1/2 Kinases. *ACS Omega* **2,** 7881–7891 (2017).

123. Nacro, K., Chennamaneni, L. R., Cherian, J. & Poulsen, A. Heteroaryl alkyne derivatives and uses thereof. WO 2015108490A2 (2015).

124. Xu, J. *et al.* Rational design of resorcylic acid lactone analogues as covalent MNK1/2 kinase inhibitors by tuning the reactivity of an enamide Michael acceptor. *ChemMedChem* **8,** 1483–1494 (2013).

125. Kwegyir-Afful, A. K. *et al.* Galeterone and its analogs inhibit Mnk-eIF4E axis, synergize with gemcitabine, impede pancreatic cancer cell migration, invasion and proliferation and inhibit tumor growth in mice. *Oncotarget* **8,** 52381–52402 (2016).

126. Li, Z. *et al.* Inhibiting the MNK-eIF4E-beta-catenin axis increases the responsiveness of aggressive breast cancer cells to chemotherapy. *Oncotarget* **8,** 2906–2915 (2017).

127. Liu, S., Zha, J. & Lei, M. Inhibiting ERK/Mnk/eIF4E broadly sensitizes ovarian cancer response to chemotherapy. *Clin. Transl. Oncol.* **20,** 374–381 (2018).

128. Palermo, G. & Diego, S. Encyclopedia of nanotechnology. *Choice Rev. Online* **50,** 50-3014-50–3014 (2013).

129. Sliwoski, G., Kothiwale, S., Meiler, J. & Lowe, E. W. Computational Methods in Drug Discovery. *Pharmacol. Rev.* **66,** 334–395 (2013).

130. Matsui, Y. *et al.* A novel inhibitor stabilizes the inactive conformation of MAPK-interacting kinase 1. *Acta Crystallogr. Sect. F Struct. Biol. Commun.* **74,** 156–160 (2018).

131. Komarova, E. S., Makarov, V. A., Granik, V. G. & Párkányi, C. Synthesis of Pyrazolo[3,4- b]pyridin-6-ones. *J. Heterocycl. Chem.* **49,** 969–998 (2012).

132. Attaby, F., Elneairy, M. A. & Elsayed, M. S. in *Phosphorus, Sulfur and Silicon and the Related Elements* 49–64 (1999).

133. Goda, F. E., Abdel-Aziz, A. A. M. & Attef, O. A. Synthesis, antimicrobial activity and conformational analysis of novel substituted pyridines: BF3-promoted reaction of hydrazine with 2-alkoxy pyridines. *Bioorganic Med. Chem.* **12,** 1845–1852 (2004).

134. Mertens, A., König, B. & Leser, U. Indazole derivatives and antiviral drugs that contain them. WO 1994024109A1 (1994).

135. Mayer, K.-H., Sasse, K. & Koenig, A. Fotografisches material mit einem stabilisierungsmittel, verfahren zu dessen herstellung, ein entwicklungsverfahren, neue pyrazole, ein verfahren zu deren herstellung sowie zwischenprodukte. DE 3001498A1 (1980).

136. Fadli, A., Vidal, L. & Sabelle, S. Dye composition useful for keratinous fibers i.e. as hair dye, comprises an oxidation dye such as amino pyrazolo-pyridine derivative. FR 2892924A1

137. Kathawala, F. Pyrazolopyridine analogs of mevalonolactone and derivatives thereof useful for inhibiting cholesterol biosynthesis in mammals. US 4822799 (1994).

138. Chen, Y. Pyrazolo and pyrrolopyridines. WO 1995034563A1 (1995).

139. Straub, A. *et al.* 3-(4-amino-5-ethylpyrimidin-2-yl)-1-(2-fluorbenzyl)-1h-pyrazolo[3,4-b]pyridin. WO 2000006567A1 (1999).

140. Hartung, I. *et al.* Substituted aminopyrazolopyridines and salts thereof, pharmaceutical compositions comprising same, methods of preparing same and uses of same. US 7825114 B2 (2010).

141. Briem, Hans; Thierauch, Karl-Heinz; Kettschau, Georg; Schaefer, Martina; Schwere, Wolfganf; Husermann, Manfred; Ter Laak, Antonius; Luenzer, H. Pyrazolopyridines, their preparation and their medical use. WO 2006077168 A1 (2006).

142. Cusack, K. *et al.* Kinase Inhibitors as therapeutic agents. WO 2005110410A2 (2005).

143. Dai, Y., Hartandi, K. & Michaelides, M. M. Novel Kinase Inhibitors. WO 2006050109A2 (2006).

144. Schwere, W. *et al.* 3-amino-pyrazolo(3,4b)pyridines used as inhibitors of protein tyrosine kinases for treating angiogenic, hyperproliferative or neirodegenerative diseases. WO 2006/063805A1 (2006).

145. Ronan, B. *et al.* Substituted pyrazolo-pyridines, compositions containing them, method for the production thereof, and their use. WO 2006/077319A1 (2006).

146. Klar, U. *et al.* Substituted pyrazolo-pyridinamines. WO 2015/004024 A1 (2015).

147. Klar, U. *et al.* Substituted pyrazolopyridines. US 2016/0159789 A1 (2016).

148. Dow, R. L., Koch, K. & Schulte, G. R. 4-aminopyrazolo(3-,4-D)pyrimidine and 4-aminopyrazolo-(3,4-D)pyridine tyrosine kinase inhibitors. US 5593997A (1995).

149. Ford, R., Leroux, F., Stocks, M. & Swahn, B.-M. Indazole/pyrazolo(4,3-c)pyridine derivatives as JNK inhibitors, compositions and methods related thereto as well as intermediates thereof. WO 2004/113303A1 (2004).

150. Duan, J., Jiang, B. & Lu, Z. Azaindazoles as BTK kinase modulators and use thereof. WO 2011/019780 A1 (2011).

151. Rajapakse, H. A. *et al.* EphA4 RTK inhibitors for treatment of nerological and neurodegenerative disrorders and cancer. US 2010/0113415 A1 (2010).

152. Ammar, Y. A. *et al.* Novel Pirfenidone Analogues: Synthesis of Pyridin-2-ones for the Treatment of Pulmonary Fibrosis. *Arch. Pharm. (Weinheim).* **339,** 429–436 (2006).

153. Falcó, J. L. *et al.* Design, synthesis and biological activity of acyl substituted 3-amino-5-methyl-1,4,5,7-tetrahydropyrazolo[3,4-b]pyridin-6-ones as potential hypnotic drugs. *Eur. J. Med. Chem.* **40,** 1179–1187 (2005).

154. Faty, R. & Youssef, A. Oxothioxopyridinecarbonitriles as Precursors for Thiazolopyridines, Pyrazolopyridotriazines and Pyridothiazolopyrimidines. *Curr. Org. Chem.* **13,** 1577–1584 (2009).

155. Lynch, B. M., Khan, M. A., Teo, H. C. & Pedrotti, F. Pyrazolo[3,4- b]pyridines: Syntheses, reactions, and nuclear magnetic resonance spectra. *Can. J. Chem.* **66,** 420–428 (1988).

156. K. Dodiya, D., R. Trivedi, A., B. Kataria, V. & H. Shah, V. Advances in the Synthesis of Pyrazolo[3,4-b]Pyridines. *Curr. Org. Chem.* **16,** 400–417 (2012).

157. Galve, I. *et al.* Synthesis of 2-arylamino substituted 5,6-dihydropyrido[2,3-d]pyrimidine-7(8H)-ones from arylguanidines. *Mol. Divers.* **16,** 639–649 (2012).

158. Camarasa, M., Barnils, C., Puig de la Bellacasa, R., Teixidó, J. & Borrell, J. I. A new and practical method for the synthesis of 6-aryl-5,6-dihydropyrido[2,3-d]pyrimidine-4,7(3H,8H)-diones. *Mol. Divers.* **17,** 525–536 (2013).

159. Camarasa, M. *et al.* Design, synthesis and biological evaluation of pyrido[2,3-d]pyrimidin-7-(8H)-ones as HCV inhibitors. *Eur. J. Med. Chem.* **115,** 463–483 (2016).

160. Puig de la Bellacasa, R. *et al.* 4-Amino-2-arylamino-6-(2,6-dichlorophenyl)-pyrido[2,3-d]pyrimidin-7-(8H)-ones as BCR kinase inhibitors for B lymphoid malignancies. *Eur. J. Med. Chem.* **86,** 664–675 (2014).

161. Bou-Petit, E. *et al.* An Unequivocal Synthesis of 2-Aryl Substituted 3-Amino-2,4,5,7-tetrahydro-6 H -pyrazolo[3,4- b]pyridin-6-ones. *ChemistrySelect* **2,** 3668–3672 (2017).

162. Balsas, P. *et al.* Activity of the novel BCR kinase inhibitor IQS019 in preclinical models of B-cell non-Hodgkin lymphoma. *J. Hematol. Oncol.* **10,** 80 (2017).

163. Lavecchia, M. J., Puig de la Bellacasa, R., Borrell, J. I. & Cavasotto, C. N. Investigating molecular dynamics-guided lead optimization of EGFR inhibitors. *Bioorg. Med. Chem.* **24,** 768–778 (2016).

164. Martínez-Sáez, E. *et al.* peIF4E as an independent prognostic factor and a potential therapeutic target in diffuse infiltrating astrocytomas. *Cancer Med.* **5,** 2501–2512 (2016).

165. Pons, B. *et al.* The effect of p-4E-BP1 and p-eIF4E on cell proliferation in a breast cancer model. *Int. J. Oncol.* **39,** 1337–45 (2011).

CHAPTER 2

N-alkyl and *N*-aryl substituted 3-amino-pyrazolo[3,4-*b*]pyridin-6-ones as MNK inhibitors

---

2.1. Study of the chemistry of the pyrazolo[3,4-*b*]pyridin-6-ones

2.1.1. Introduction

As stated above, pyrazolo[3,4-*b*]pyridin-6-ones are very versatile compounds that have been used for many different applications. The distribution of the different possible substitution points around the scaffold provides an interesting 3D structure that can be modulated to act in many different types of receptors and have different and specific functions. Moreover, the small size of the central core permits an increase in size of the molecules allowing the development of candidates with druggable properties.

The synthesis of these compounds can be achieved by different methodologies[1,2] leading to different substituents placed in strategic points of the molecule. The Grup de Química Farmacèutica (GQF) of the IQS has been working for years in this type of scaffolds and has described an interesting synthetic pathway for preparing such compounds[3–5].

This project started with the study of compounds based on scaffold (**53**) as possible new MNK inhibitors. The four different points of derivatization together with the possible oxidation of the pyridone ring provide a huge range of synthetic possibilities that can provide potency and selectivity to a new drug candidate.

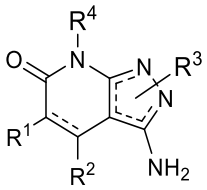

53

Figure 2.1. General structure of pyrazolo[3,4-*b*]-pyridin-6-ones

By adapting the methodologies described by our group [3–5], an initial study was performed with the purpose of obtaining the maximum number of derivatives of this central core by mainly changing the substituents placed in R^1, R^2 and R^3. These compounds could then be slightly changed by means of two last step modifications. On one side, R^4 could be modified from H to methyl by methylation of the NH of the lactam. On the other hand, the pyridone ring could be further oxidized to obtain a more planar structure.

Here the synthetic possibilities, including the selective obtention of two possible isomers, have been studied and methodologies for each reaction have been optimized to have the most general procedures for the synthesis of any derivative of interest.

2.1.2. Synthesis of 2-methoxy-6-oxo-1,4,5,6-tetrahydropyridin-3-carbonitriles (62)

2-methoxy-6-oxo-1,4,5,6-tetrahydropyridin-3-carbonitriles (**62**) needed for the preparation of the compounds of interest can be synthetized from the corresponding α,β-unsaturated esters (**60**). The α,β-unsaturated esters (**60**) react with 1.2 eq. of malononitrile (**61**) in NaOMe/MeOH to form the pyridine ring (Figure 2.2). The reaction time for this step is highly dependent on the R^1 and R^2 substitution.

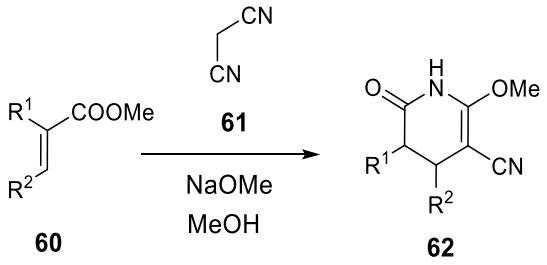

Figure 2.2. Preparation of 2-methoxy-6-oxo-1,4,5,6-tetrahydropyridin-3-carbonitriles (**62**)

The non-commercial 2-arylacrylates (**60**{*x*,*1*}) were prepared with the methodology described by Grosjean *et al*.[6] from the corresponding aryl acetates (**67**) by condensation with paraformaldehyde in the presence of K_2CO_3 in DMF. Compounds **67** were obtained, when necessary, by Fischer esterification of the corresponding aryl acetic acids (**66**). (Figure 2.3). Table 2.1 summarizes the compounds **62** used in this project.

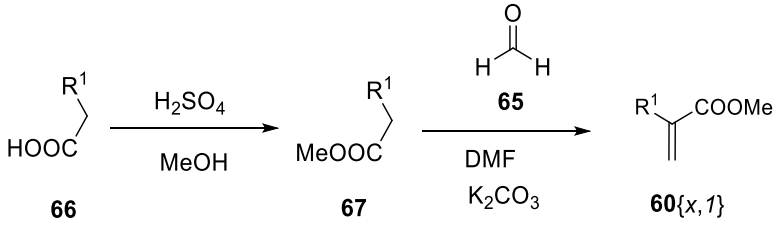

Figure 2.3. Preparation of 2-arylacrylates (**60**{*x*,*1*})

Table 2.1. 2-methoxy-6-oxo-1,4,5,6-tetrahydropyridin-3-carbonitriles (**62**) prepared in this project and the reaction conditions optimized for each compound. Yield (**62**) corresponds to the yield of the cyclization of **62**. Yield (**60**) refers to the yield of the reaction to form the corresponding acrylate (**60**)

Structure	Name	Reaction conditions	Yield (62)	Yield (60)
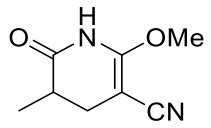	**62**{*2*,*1*}	5h Reflux (100 °C)	41%	commercial
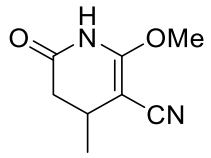	**62**{*1*,*2*}	5h Reflux (100 °C)	34%	commercial
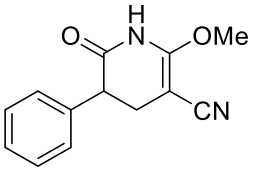	**62**{*3*,*1*}	3h Reflux (100 °C)	67%	62%
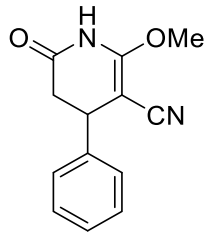	**62**{*1*,*3*}	5h Reflux (100 °C)	78%	commercial
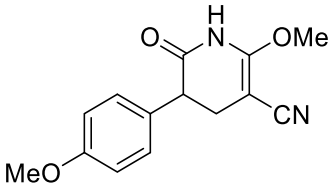	**62**{*4*,*1*}	36h 40 °C	70%	33%
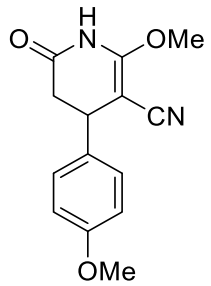	**62**{*1*,*4*}	4.5h Reflux (100 °C)	77%	commercial

Structure	Name	Reaction conditions	Yield (62)	Yield (60)
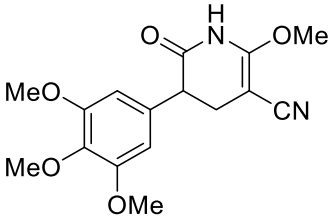	**62**{*5*,*1*}	MW, 30min, 85 °C	49%	47% (72h, 40 °C)
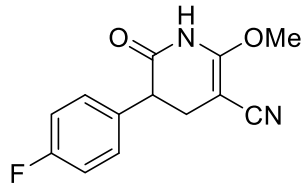	**62**{*6*,*1*}	MW, 30min, 85 °C	42%	84%
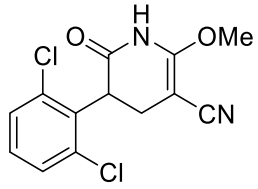	**62**{*7*,*1*}	5h Reflux (100 °C)	83%	91%
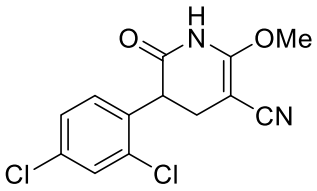	**62**{*8*,*1*}	4.5h Reflux (100 °C)	84%	44%

There are two possible mechanisms that explain the formation of such product[7]. In both cases, the malononitrile (**61**) molecule is ionized by the base (MeO^-) and attacks the β position of the ester forming the Michael adduct (**70**).

The Michael adduct (**70**) can suffer two different cyclization mechanisms. If the alkoxide group attacks one of the nitrile groups (path B), an iminoether structure (**71**) is formed which can then cyclize with the ester group. Tautomerization of **72** yields the pyridone **62**. Alternatively, if compound **70** is ionized renders the cetenimine intermediate (**74**) which can suffer the addition of the alkoxide group (**75**) and cyclize to render **62**. (Figure 2.4)

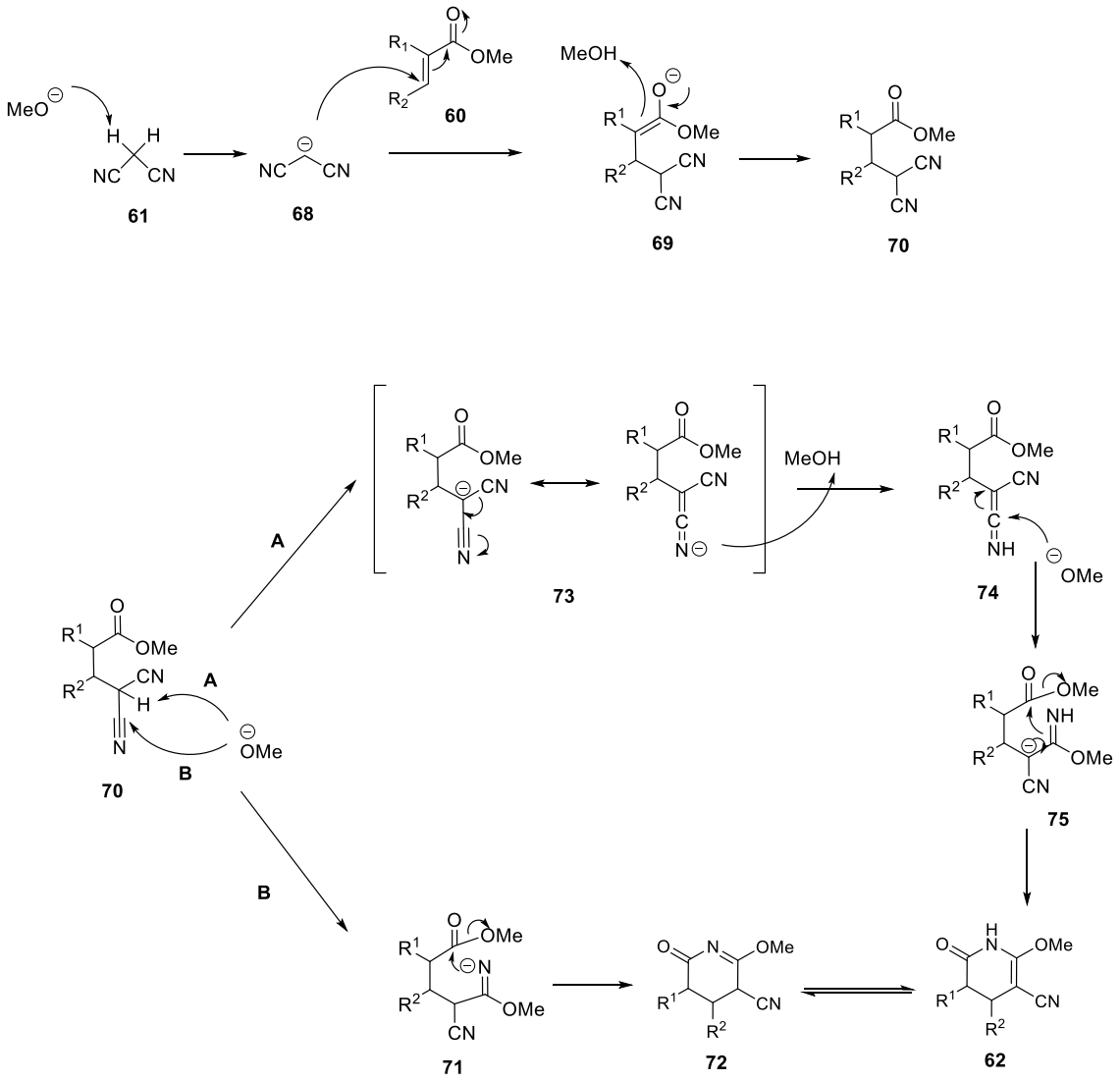

Figure 2.4. Reaction mechanism of the formation of 2-methoxy-6-oxo-1,4,5,6-tetrahydropyridin-3-carbonitriles (**62**)[7]

2.1.3. Study of the regiochemistry of the cyclization reaction

According to the general methodologies described by the Grup de Química Farmacèutica (GQF)[4,8], *N*-alkyl and *N*-aryl substituted pyrazolo[3,4-*b*]pyridone systems (**63** and **64**) can be obtained under microwave irradiation by cyclization of 2-methoxy-6-oxo-1,4,5,6-tetrahydropyridin-3-carbonitriles (**62**), with alkyl or aryl hydrazines (**56**). A deep study of this cyclization reaction has been performed to define the regiochemistry of the obtained products.

Cyclization of **62** with substituted hydrazines (**56**) could afford two different positional isomers (**63** or **64**) depending on the reaction mechanism. The nucleophilic attack on the methoxy group of the pyridone ring could occur from both nitrogen atoms of the hydrazine molecule leading to two different molecules: If the substitution takes place by the attack of the NH_2 group of the substituted hydrazine (NH_2-NH-R^3), the subsequent cyclization onto the cyano group would afford the N2 substituted compound (**64**). On the other hand, if the nucleophile is the NH group of the hydrazine the reaction would yield the N1 substituted isomer (**63**) (Figure 2.5).

As an initial hypothesis, we considered that the initial substitution should be governed by the relative nucleophilicity of both nitrogen atoms of the hydrazine which should be highly dependent on the substituent present in the hydrazine molecule.

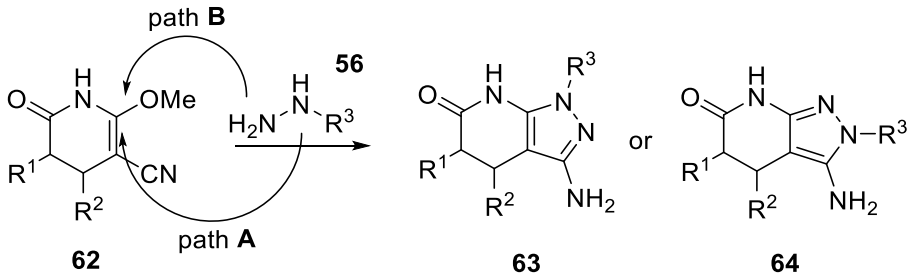

Figure 2.5. Possible reaction pathways in the synthesis of pyrazolo[3,4-*b*]pyridin-6-ones.

In order to prove our hypothesis, the reaction was analyzed using phenylhydrazine and methylhydrazine. These two hydrazines present substituents that will modify the nucleophilicity of the nitrogen atoms allowing the study of the reaction in two very different conditions.

2.1.3.1. Cyclization with phenylhydrazine (56{*3*})

The study was focused initially on the reaction with phenylhydrazine. The difference between the pKa values of the nitrogen atoms (as a measure of the nucleophilicity) should be a determining factor of the reaction path and an excellent prove of concept for our study. According to the hypothesis, due to the higher pKa of the NH_2 group (pKa=27.8) the reaction should follow the path B obtaining isomer **64** as a major product. However, this hypothesis does not agree with the results published by C. E. Rodrigues-Santos *et al.*[9] that claim that this reaction affords only isomer **63**.

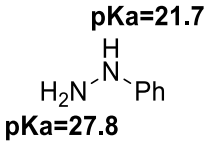

Figure 2.6. Calculated pKa values of phenylhydrazine (**56**{*3*}).

The cyclization of these compounds with phenylhydrazine (**56**{*3*}) was deeply studied to elucidate the mechanism of this reaction. The correct characterization of this family of compounds together with the possibility to selectively control the preparation of the different isomers required a careful study of this reaction and the generated products. With this purpose, different synthetic strategies were performed and the products were analyzed and characterized by means of spectroscopic tools: NMR, IR, AEO and MS. As a first example, the reaction was carried out with pyridone **62**{*1,3*} with R^1=H and R^2 = Ph.

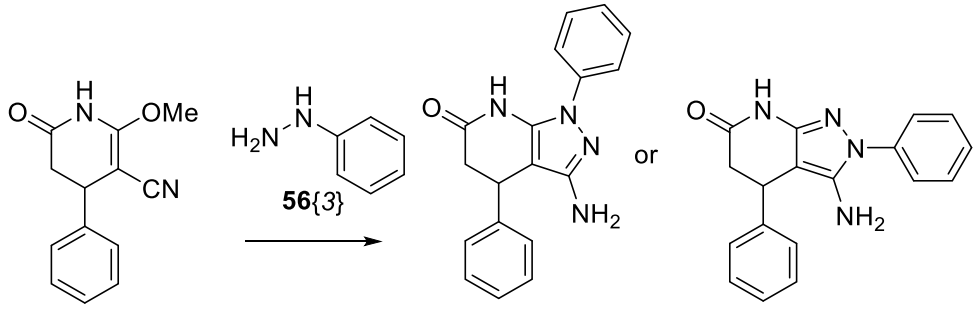

62{*1,3*} **63**{*1,3,3*} **64**{*1,3,3*}

Figure 2.7. Possible product obtained in the cyclization of **62**{*1,3*} with phenyl hydrazine.

Two different methodologies were compared to identify possible mechanistic issues that could allow the selective formation of the different isomers. The main difference between both methodologies was the heating of the reaction: Rodriguez-Santos *et al.*[9] used conventional heating while our group[8,10] uses microwave irradiation to perform the reaction.

Surprisingly, when the cyclization was carried out using the conventional heating methodology (at reflux for 24h using MeOH as solvent), a product different from **63**{*1*,*3*,*3*} or **64**{*1*,*3*,*3*} was isolated in a 74 % yield. The IR spectrum (Figure 2.9) was specially revealing, as a band at 2256 cm^{-1} corresponding to a stretching of the C≡N group indicated that the cyclization had not been achieved.

In the ^{1}H-NMR spectrum (Figure 2.10), the absence of the singlet corresponding to the methoxy group together with the presence of two labile and exchangeable with D_2O signals indicated that the reagent was transformed. Moreover, the integral value (1H) and the chemical shift of the second exchangeable signal (9.11 ppm) suggested that the isolated solid was not the expected product (the NH_2 group of the product was expected around 6 ppm and with a 2H integral).
Finally, a signal corresponding to a CH group with doublet multiplicity was detected at 4.69 ppm. With the available data, the isolated product was assigned as an open intermediate **76**{*1*,*3*,*3*} where only the first substitution step onto the methoxy group had taken place.
The structure was confirmed by NOESY spectroscopy (Figure 2.11) where the coupling between H_{12} of the phenyl group and the N_2-H was observed together with the coupling between the two exchangeable signals (N_1-H/N_2-H) demonstrating its proximity.

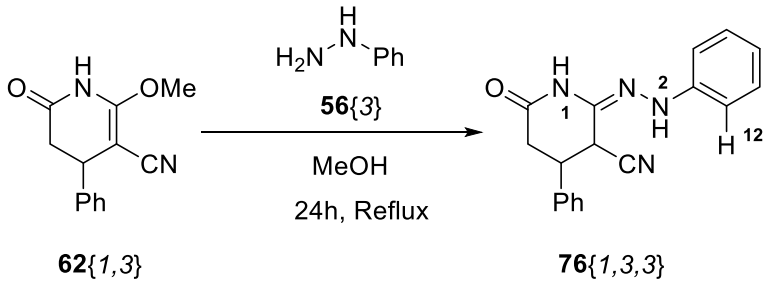

Figure 2.8. Obtention of the open intermediate **76**{*1*,*3*,*3*} when using conventional heating.

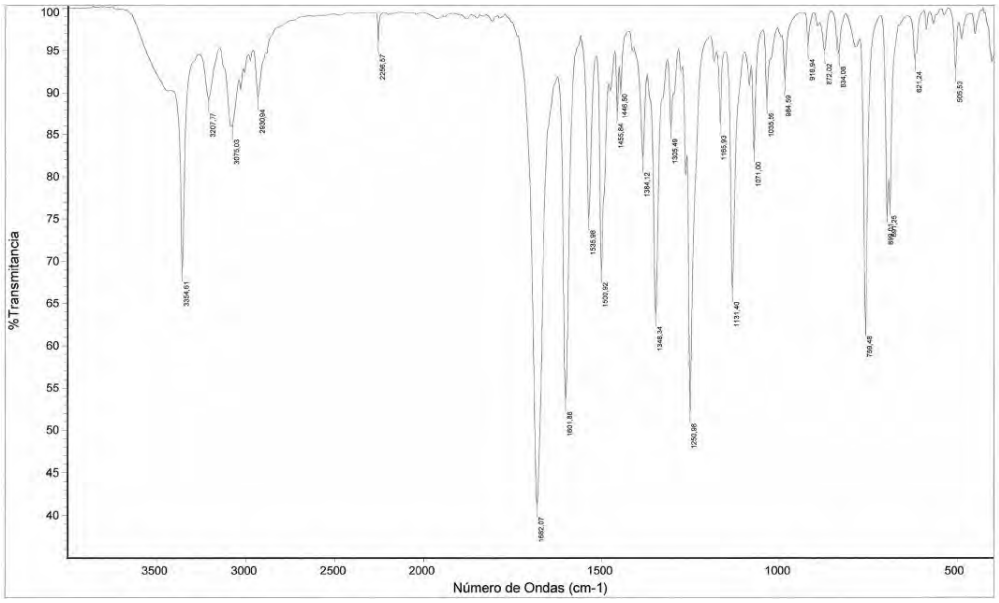

Figure 2.9. IR spectrum of intermediate **76**{*1,3,3*}. The band at 2256 cm^{-1} corresponds to the C≡N stretching and demonstrates that cyclization did not complete.

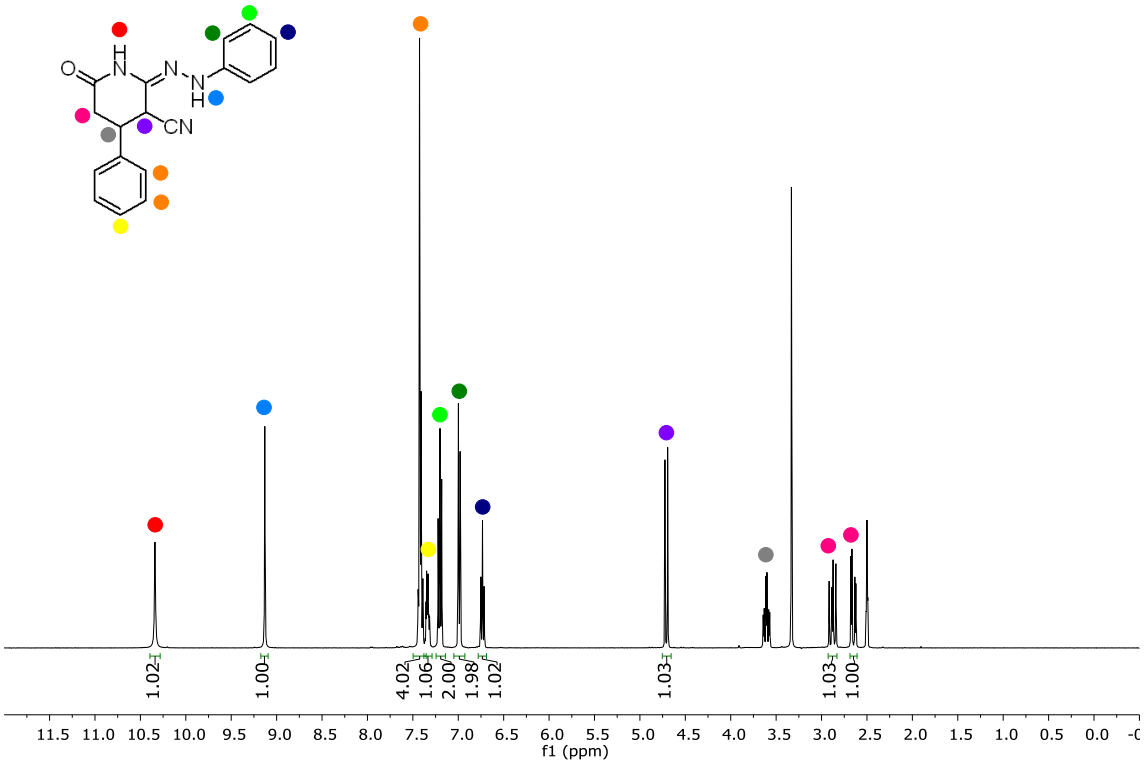

Figure 2.10. ^{1}H-NMR of intermediate **76**{*1,3,3*}.

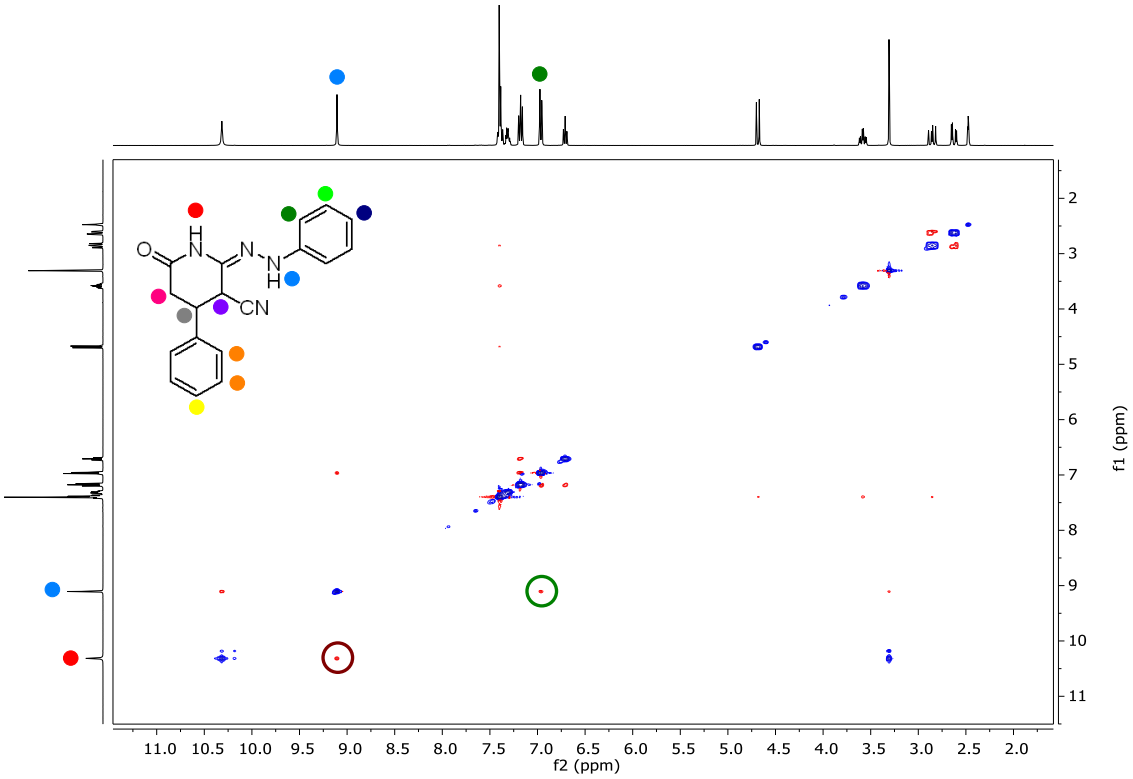

Figure 2.11. NOESY spectrum of intermediate **76**{*1*,*3*,*3*}. The correlation between both NH groups (red circle) and between the NH and the phenyl protons (green circle) confirms the structure.

When the reaction was carried out under microwave irradiation at 140 °C, the cyclization of the pyrazole ring did take place and the compound obtained in a 50% yield was identified as the 3-amino-2,4-diphenyl-4,5-dihydro-2*H*-pyrazolo[3,4,*b*]pyridin-6(7*H*)-one **64**{*1*,*3*,*3*}. In this case, the IR spectrum did not present any C≡N stretching (Figure 2.12). Moreover, the ^{1}H-NMR presented a signal exchangeable with D_2O at 5.28 ppm of integral 2H corresponding to the new NH_2 formed after the cyclization (Figure 2.13).

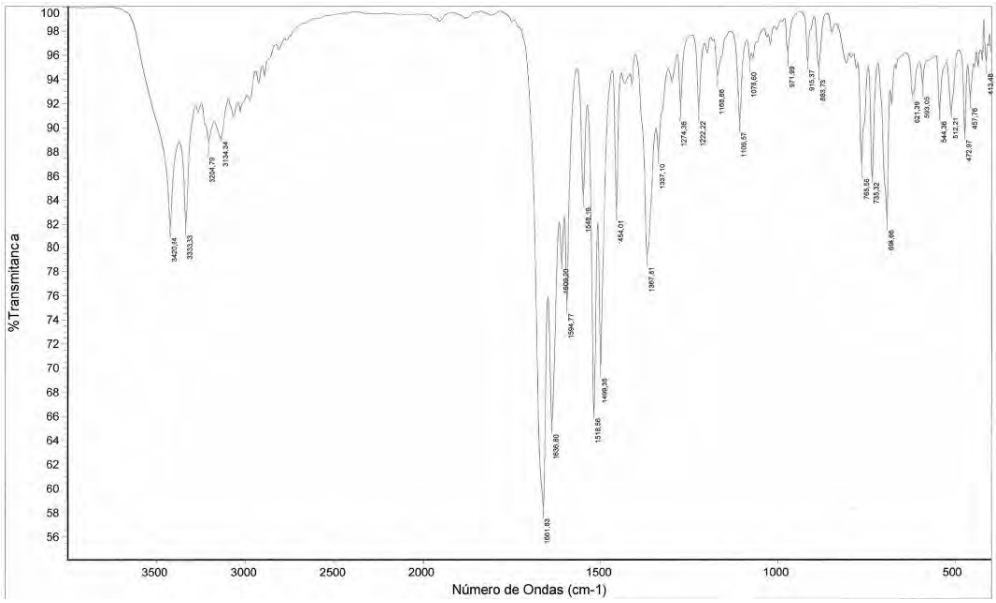

Figure 2.12. IR spectrum corresponding to **64**{*1*,*3*,*3*} with no bands indicating the absence of the CN group.

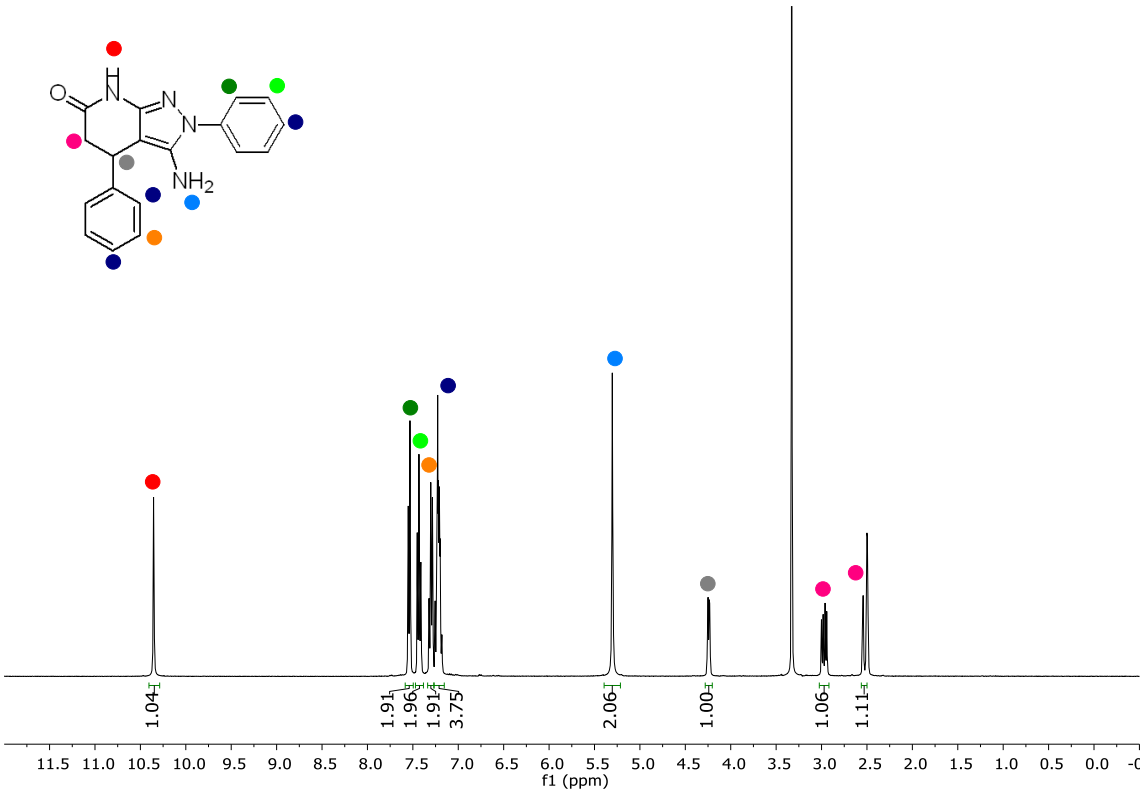

Figure 2.13. ^{1}H-NMR spectrum of **64**{*1*,*3*,*3*}. A new signal at 5.28 ppm of integral 2H and exchangeable with D_2O confirms the cyclization of the product.

The 2D-NOESY spectroscopy was necessary to confirm the obtention of isomer **64**{*1*,*3*,*3*}. The spectrum shows a correlation of the amine group (NH_2) with the aromatic protons confirming the N2-substitution. This correlation is not possible for isomer **63**{*1*,*3*,*3*} where a correlation between the aromatic protons and the NH of the lactam should appear.

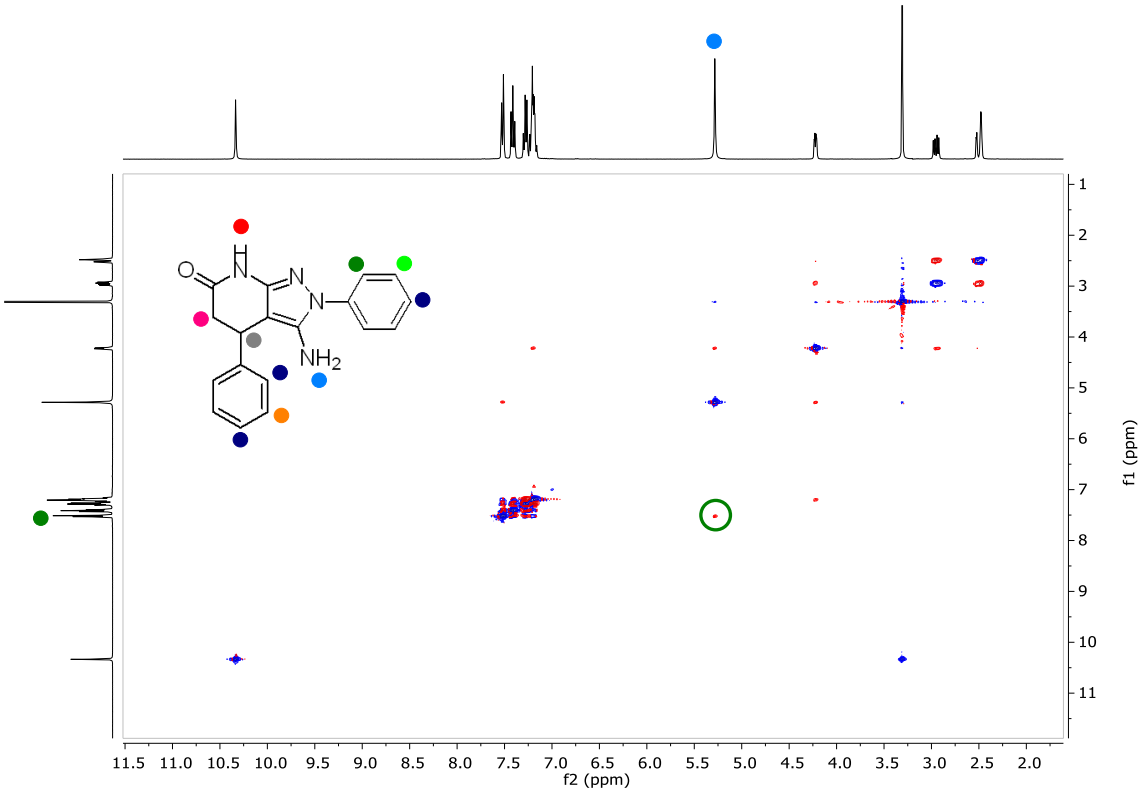

Figure 2.14. NOESY spectrum of 3-amino-2,4-diphenyl-4,5-dihydro-2*H*-pyrazolo[3,4-*b*]pyridin-6(7*H*)-one (**64**{*1*,*3*,*3*}).

Before suggesting a possible mechanism for the reaction, the effects of different reaction factors (hydrazine equivalents, solvent, temperature and time) were studied. Moreover, two different work-up methods were compared (i.e. filtration and CH_2Cl_2 extraction) to isolate the final product. (Table 2.2)

Table 2.2. Experimental conditions tested for the treatment of **62**{*1*,*3*} with phenylhydrazine (**56**{*3*}). [a] Heating method is indicated (microwave irradiation or reflux). [b] Work-up: (1) filtration, (2) CH_2Cl_2 extraction. [c] isolated compound, ^{1}H-NMR spectra of mother liquors presented only signals corresponding to **76**{*1*,*3*,*3*} or **64**{*1*,*3*,*3*}, depending on the experiment and excess of phenylhydrazine (**56**{*3*}).

Solvent	Equiv. of 56{*3*}	Temp. (°C) [a]	Time (h)	Work-up[b]	Product obtained (Yield)[c]
MeOH	2	140 mw	0.5	1	**64**{*1*,*3*,*3*} (50%)
	2	140 mw	0.5	2	**64**{*1*,*3*,*3*} (47%)
	2	reflux	24	1	**76{***1*,*3*,*3*} (70%)
	1	140 mw	0.5	2	**76**{*1*,*3*,*3*} + **64**{*1*,*3*,*3*}
	1	140 mw	0.5	1	**76**{*1*,*3*,*3*} + **64**{*1*,*3*,*3*}
	2	reflux	24	2	**76**{*1*,*3*,*3*} (74%)
	2	60 mw	0.5	1	**76**{*1*,*3*,*3*} (23%)
Solvent free	1	140 mw	0.25	2	**64**{*1*,*3*,*3*} (39%)
	1	60 mw	0.25	2	**76**{*1*,*3*,*3*} (27%)
THF	1	60 mw	0.25	1	**76**{*1*,*3*,*3*} (7%)
	1	140 mw	0.25	1	**76**{*1*,*3*,*3*} impure
	1	140 mw	0.5	1	**76**{*1*,*3*,*3*} (9%)
	2	140 mw	0.25	1	**76**{*1*,*3*,*3*} (3%)
	2	reflux	24	1	**76**{*1*,*3*,*3*} (25%)
CH_2Cl_2	2	140 mw	0.5	1	**76**{*1*,*3*,*3*} (15%)

The results show that both steps require different conditions. The formation of the open intermediate **76**{*1*,*3*,*3*} occurred at low temperatures and was not affected by solvent polarity or hydrazine equivalents. On the other hand, the cyclization step requires higher temperatures and polar solvents (MeOH). Moreover, to achieve a complete transformation, 2 equivalents of phenylhydrazine are needed demonstrating a contribution of the hydrazine excess to the cyclization reaction in MeOH. Importantly, isomer **63**{*1*,*3*,*3*} was not observed in any case. No differences were observed when comparing both purification methods.

Finally, the cyclization of the isolated intermediate **76**{*1*,*3*,*3*} to isomer **64**{*1*,*3*,*3*} was achieved when heated in methanol at 140 °C for 30 minutes under microwave irradiation in quantitative yield. This fact demonstrates that the formation of **64**{*1*,*3*,*3*} undergoes a two-step cyclization pathway where **76**{*1*,*3*,*3*} is the reaction intermediate.

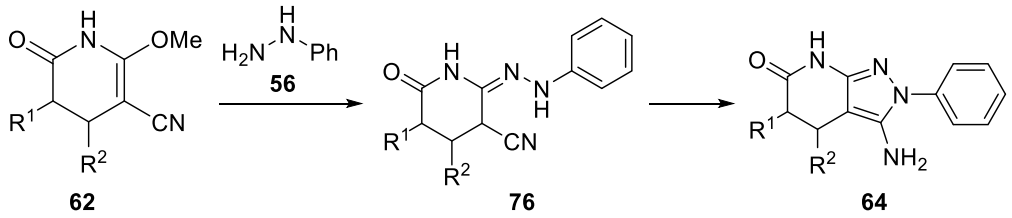

Figure 2.15. Two step reaction for the formation of **64**{*1*,*3*,*3*}.

General applicability of the synthesis

To establish the general applicability of this synthetic methodology, we extended the reaction to three other pyridones: **62**{*3*,*1*} (R^1 = Ph, R^2 = H), **62**{*2*,*1*} (R^1 = Me, R^2 = H) and **62**{*1*,*4*} (R^1 = H, R^2 = *p*-MeO-Ph). Some of the experiences previously studied for pyridone **62**{*1*,*3*} were repeated observing the same behavior previously described (Table 2.3).

When the reactions with 2 equivalents of phenylhydrazine (**56**{*3*}) were carried out at room temperature or under reflux in MeOH for 24h the corresponding open intermediates **76**{*3*,*1*,*3*}, **76**{*2*,*1*,*3*} and **76**{*1*,*4*,*3*} were obtained in 81%, 60% and 70% yield, respectively. The same reactions carried out at 140 °C under microwave irradiation afforded the cyclized products **64**{*3*,*1*,*3*} (48%), **64**{*2*,*1*,*3*} (58%) and **64**{*1*,*4*,*3*} (85%) respectively. In all cases, the structures were confirmed by NMR spectroscopy observing the expected signals in the ^{1}H-NMR and the NOESY spectra. Also, IR spectroscopy was used to identify the presence or absence of the CN group.

Cyclization of intermediates **76** was achieved upon heating in MeOH at 140 °C under microwave irradiation and the cyclized compounds **64** were obtained with yields higher than 95%.

The spectroscopic data confirmed the formation of isomer **64** as the only cyclized product, with no signs of isomer **63**. Despite the available information confirming our hypothesis, the results were still contradictory to some published works.[9]

Table 2.3. Experimental conditions tested for the reaction of **62**{*3,1*}, **62**{*2,1*} and **62**{*1,4*} with phenylhydrazine (**56**{*3*}).

Pyridone	Equiv. of 56{*3*}	Time (h)	Temp. (°C)	Product obtained (Yield)
62{*3,1*} R^1= Ph, R^2=H	2	0.5	140	**64**{*3,1,3*} (48%)
	1	0.25	140	**64**{*3,1,3*} + **76**{*3,1,3*}
	1	0.25	60	**76**{*3,1,3*} (11%)
	2	24h	rt	**76**{*3,1,3*} (81%)
	2	0.25	60	**76**{*3,1,3*} (26%)
62{*2,1*} R^1=Me, R^2=H	1	0.5	140	**64**{*2,1,3*} (16%)
	1	0.5	60	**76**{*2,1,3*} (13%)
	2	0.5	140	**64**{*2,1,3*} (58%)
	2	24	rt	**76**{*2,1,3*} (60%)
62{*1,4*} R^1=H, R^2=*p*-MeO-Ph	1	0.5	140	**76**{*1,4,3*} (17%)
	2	0.5	140	**64**{*1,4,3*} (85%)
	2	24h	60	**76**{*1,4,3*} (70%)

The final confirmation of the correct assignment of the structure of the obtained isomer was achieved by X-ray crystallography.

The crystal structure of compound **64**{*1,4,3*} was resolved by single crystal X-ray diffraction by the group of Dr. Cristina Puigjaner of the Unitat de Difracció de RX. Centres Científics i Tecnològics de la Universitat de Barcelona (CCiTUB) proving the structure of isomer **64** with the substitution of the pyrazole ring in the N2 position (Figure 2.16). Single crystals were grown by vapor diffusion of water into a solution of 5 mg of **64**{*1,4,3*} in 3mL of MeOH. Crystallographic data are summarized in Annex 2.

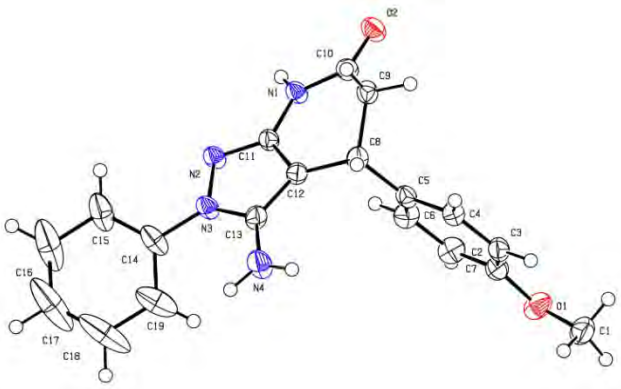

Figure 2.16. Crystal structure of **64**{*1,4,3*}.

Reaction mechanism

The results seem to be equivalent for the cyclization of any pyridone **62**{*x*,*y*} with phenylhydrazine (**56**{*3*}) and can be summarized as follows: a) when the reaction between pyridones **62** and phenylhydrazine (**56**{*3*}) is carried out in MeOH (or other solvents) at temperatures below 140 °C, intermediates **76** are formed in 60-80% yield; b) such intermediates can be converted in the corresponding 2-aryl substituted 3-amino-2,4,5,7-tetrahydro-6*H*-pyrazolo[3,4-*b*]pyridin-6-ones **64** by heating in MeOH under microwave irradiation at 140 °C in quantitative yields (90%); and c) pyrazolopyridones **64** can be directly obtained by heating pyridones **62** and phenylhydrazine (**56**{*3*}) in MeOH under microwave irradiation at 140 °C in 40-60% yield. Isomer **63** has not been observed in any case.

From these results, the reaction mechanism for the cyclization of 2-methoxy-6-oxo-1,4,5,6-tetrahydropyridin-3-carbonitriles **62** with phenylhydrazine **56**{*3*} is proposed. The reaction follows a two-step mechanism: First an open intermediate is formed from the nucleophilic substitution of the NH_2 of the phenylhydrazine onto the methoxy group of the pyridone. Then, the intermediate cyclizes at higher temperatures to only yield compound **64**. This reaction only occurring at high temperatures suggests that the cyclization of intermediate **76** has a very high activation energy (Figure 2.17).

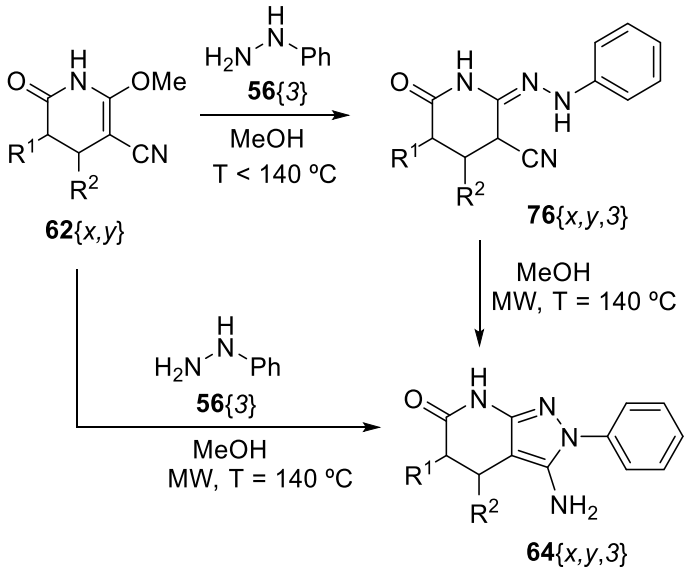

Figure 2.17. General mechanism. Conversion of pyridones **62** in open intermediates **76** or pyrazolopyridones **64** depending on the reaction temperature.

Study of the activation energies

In order to understand the high thermal level needed for the cyclization of intermediates **76**, the activation energies of the two steps involved in the formation of pyrazolopyridones **64** were determined.

Preliminary *ab-initio* calculations using Gaussian 09[11] indicated that the second barrier is higher than the first one, but the values obtained were both too high.

Consequently, the energetic barriers were experimentally determined using differential scanning calorimetry (DSC) techniques. A 1:2 mixture of **62**{*2*,*1*} and phenylhydrazine **56**{*3*} in MeOH was introduced in a medium pressure stainless steel crucible and heated from 40 °C to 160 °C at different heating rates (2, 5, 10, 20 °C/min) under a nitrogen stream (Figure 2.18). The activation energy was then determined using the kinetic methods of Ozawa[12] and Kissinger[13] to afford 15.6±1.6 kcal·mol^{-1} and 14.3±1.6 kcal·mol^{-1}, respectively. (Annex 2)

Despite heating at temperatures higher than 140 °C, the measures only provided the values corresponding to the first step. The measures at high temperatures were not conclusive as the crucible did not held the methanol pressure altering the results at these temperatures.

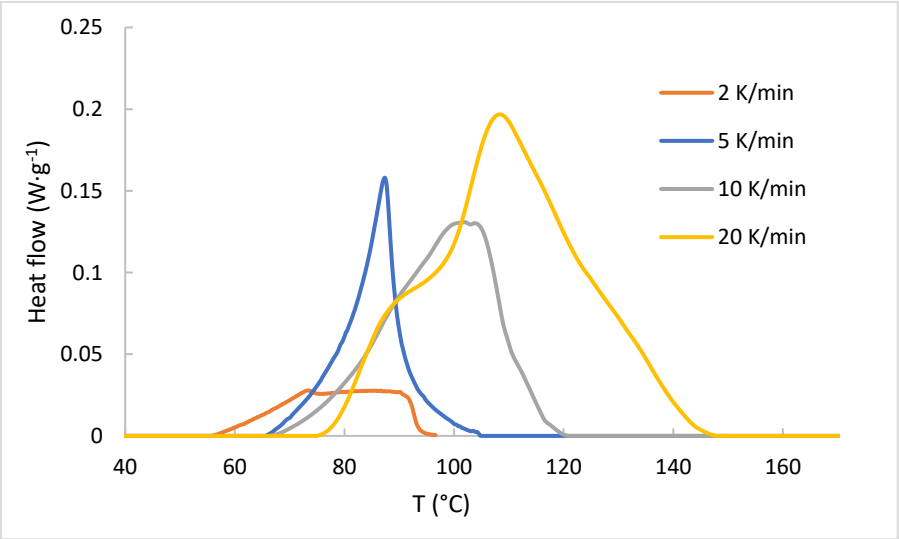

Figure 2.18. DSC curves for the first step (formation of **76**{*2*,*1*,*3*}). 10 mg of **62**{*2*,*1*} and 14 mg of hydrazine **56**{*3*} are dissolved in 0.5 mL de MeOH. 40 µL are placed in a stainless-steel crucible. Temperature = 40-160 °C. Heating rates: 2, 5, 10, 20 °C/min.

In order to measure the energetic barrier of the second step, the process is repeated with **76**{*2*,*1*,*3*} in MeOH. However, the crucibles did not bear such a high pressure and the measures were not possible. For this reason, the measures were performed in solid state: 5 mg of intermediate **76**{*2*,*1*,*3*} were heated in absence of solvent in a standard aluminium crucible with a pierced lid from 120 °C to 220 °C at different heating rates (1, 3, 5, 10 °C/min) under a nitrogen stream (Figure 2.19). The activation energy was determined using the kinetic methods of Ozawa[12], Kissinger[13] and Kissinger-Akahira-Sunose[14]. The results obtained were 42.4±2.3, 42.8±2.4 and 40.6±0.2 kcal·mol^{-1}, respectively. (Annex 2)

The ^{1}H-NMR spectrum of the contents of the standard aluminum crucible showed the complete transformation of intermediate **76**{*2*,*1*,*3*} to pyrazolopyridine **64**{*2*,*1*,*3*} (Figure 2.20)

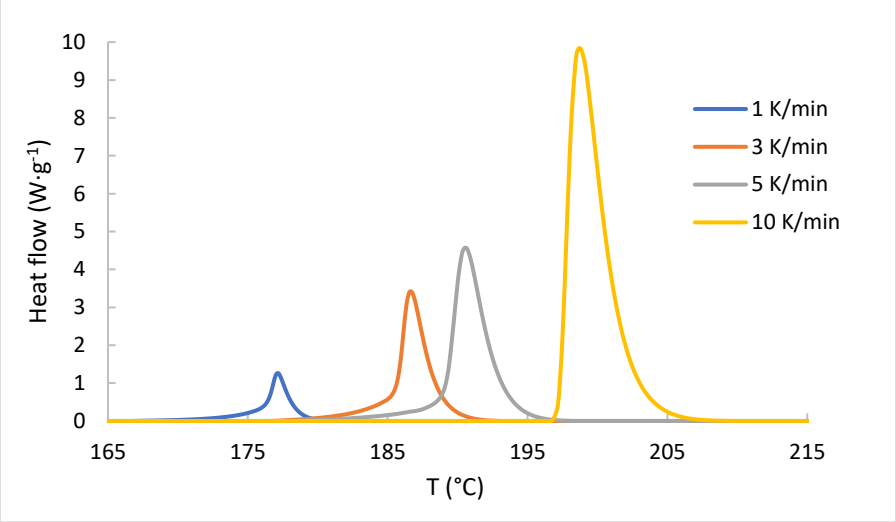

Figure 2.19. DSC curves for the second step (cyclization of **76**{*2*,*1*,*3*}). 5 mg of **76**{*2*,*1*,*3*} are placed in a stainless-steel crucible. Temperature = 120-220 °C. Heating rates: 1, 3, 5, 10 °C/min.

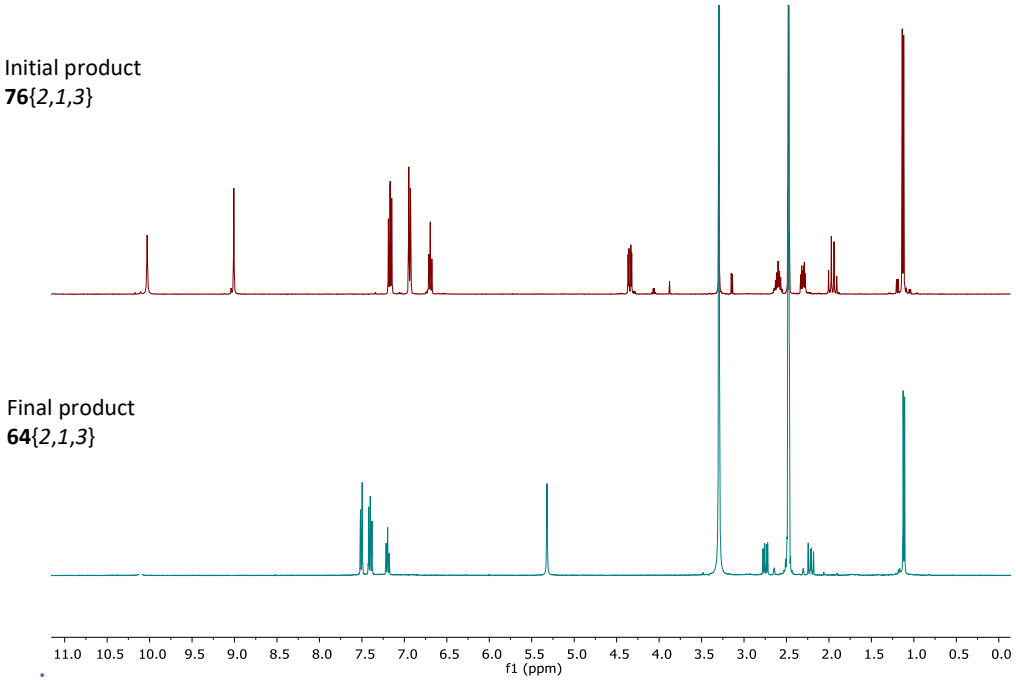

Figure 2.20. ^{1}H-NMR spectrum of the contents of the standard aluminum crucible heated from 120 °C to 220 °C showing the complete transformation of intermediate **76**{*2*,*1*,*3*} to pyrazolopyridone **64**{*2*,*1*,*3*}.

These results are clearly compatible with the temperatures observed experimentally and demonstrate the different thermal levels needed for each step. In fact, the relation between the experimental conditions needed and the measured activation energies obtained agrees with the observations of Rodríguez *et al.*[15] who established that reactions with activation energies below 20 kcal·mol^{-1} occur easily by conventional heating, while reactions with activation energies above 30 kcal·mol^{-1} need highly polar solvents under microwave irradiation.

2.1.3.2. Cyclization with methylhydrazine

The results obtained from the cyclization of **62** with phenylhydrazine **56**{*3*} are in agreement with our hypothesis that the initial substitution is governed by the relative nucleophilicity of the two nitrogen atoms present in NH_2-NH-R^3. The difference in pKa values of the phenylhydrazine nitrogen atoms caused by the electron withdrawing capacity of the phenyl group which enhances the nucleophilicity of the NH_2 induces that the initial substitution proceeds through the NH_2 nitrogen, thus leading to isomer **64**.

According with the hypothesis, the smaller difference between the nitrogen atoms of methylhydrazine (**56**{*2*}) should allow the formation of both isomers (**63**{*x*,*y*,*2*} and **64**{*x*,*y*,*2*}). In this case, the methyl group is an electron donating group which participates in the equilibration of the pKa values of both nitrogen atoms making them both capable to initiate the reaction.

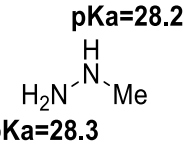

Figure 2.21. Calculated pKa values of methylhydrazine.

The reaction was studied with the previously described 2-methoxy-6-oxo-1,4,5,6-tetrahydropyridin-3-carbonitriles **62**{*x,y*} at the same stablished conditions. (Table 2.4).

Table 2.4. Summarized results for 2-methoxy-6-oxo-1,4,5,6-tetrahydropyridin-3-carbonitriles **62** and methylhydrazine **56**{*2*}. Percentages determined by ^{1}H-NMR integrating the methyl signals of both isomers

Temp. (°C)	Pyridone	Isomer 63 (%)	Isomer 64 (%)
140	**62**{*1,3*}	24	76
	62{*3,1*}	28	72
	62{*2,1*}	28	72
	62{*1,4*}	35	65
60	**62**{*1,3*}	33	67
	62{*3,1*}	18	82
	62{*2,1*}	26	74
	62{*1,4*}	26	74

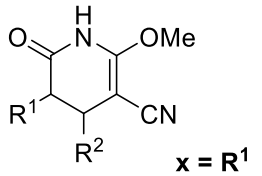

62{*x*,*y*}

x = R^1
y = R^2

x/y	R^1/R^2
1	H
2	Me
3	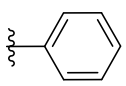
4	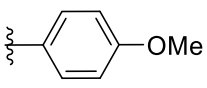

In agreement with our initial hypothesis, both isomers were obtained. Surprisingly, the mixtures presented similar proportions of both isomers independently of the reaction temperature. Probably, the rate of isomers obtained for this reaction is more affected by the steric hindrance that by the difference in nucleophilicity. The methyl group hampers the attack of the NH group favoring the obtention of isomer **64**.

In addition, the reaction with methylhydrazine, requires lower thermal levels as for both temperatures the cyclized product was obtained, and it was not possible to isolate the open intermediate. Several attempts to capture such intermediate were performed with compound **62**{*1*,*3*} by modifying the reaction temperature with no positive results. In addition to the already described trials using microwave irradiation, the reaction was performed under conventional heating at 60 °C, at room temperature, at 0 °C and at -20 °C. For the three first conditions, the reaction lead to a mixture of both isomers with the same ratio as in previous experiments. The reaction at -20 °C did not take place and the starting material was detected. However, the reaction evolved to the same mixture of the isomers when the cooling bath was removed and the crude was allowed to reach room temperature. Probably, the similar reactivity of both nitrogen atoms enables a fast cyclization once the initial substitution has occurred impeding the isolation of the reaction intermediate.

For each mixture, both isomers were separated by flash chromatography (Al_2O_3 column, with a gradient of $CHCl_3$/MeOH from 0 to 3% in 30 minutes) and analyzed by NMR spectroscopy to assign the corresponding structure to each product. Using the NOESY spectra the pyrazole substitution was unequivocally assigned by observing the correlation between the methyl group with the NH of the lactam (isomer **63**) or the NH_2 (isomer **64**). Figure 2.22 shows the spectroscopy of the mixture of **63**{*1*,*3*,*2*} and **64**{*1*,*3*,*2*} as an example of the characterization process. The 2D NOESY was essential to unequivocally determine the structure of both isomers (Figure 2.23).

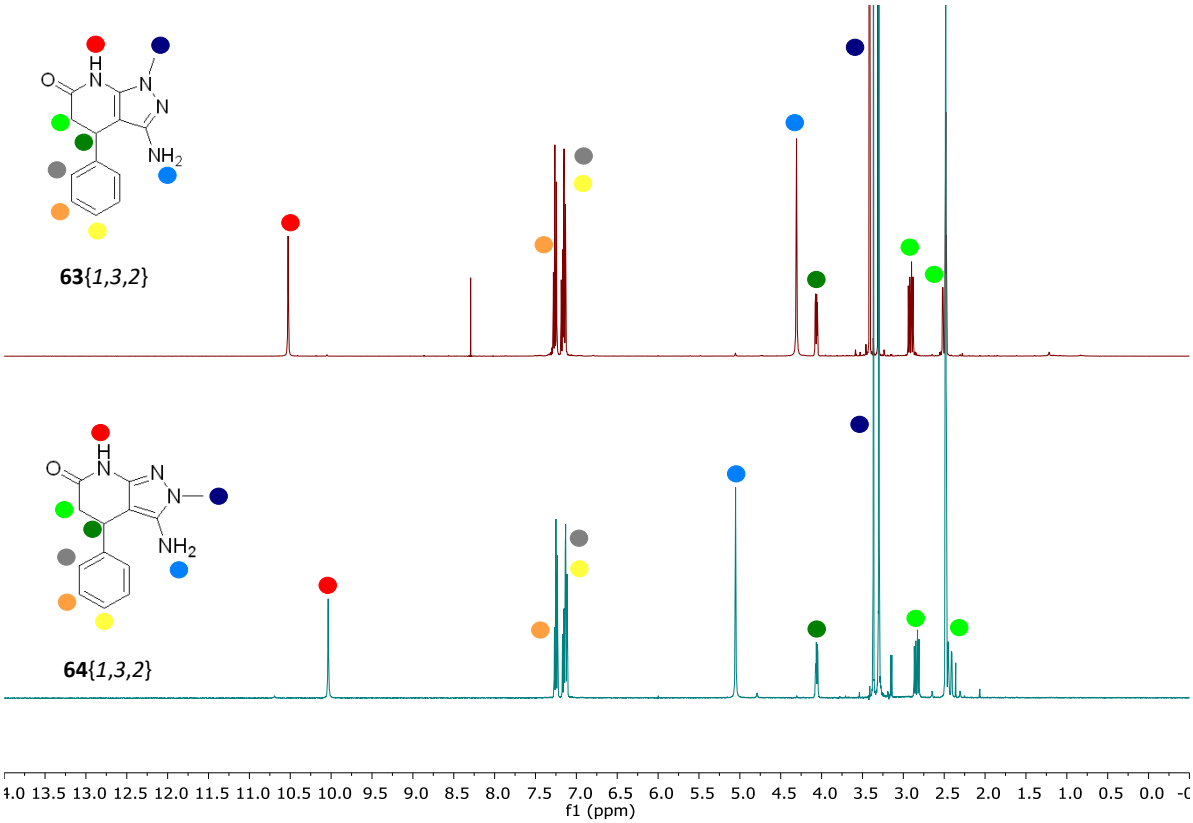

Figure 2.22. Comparison for the ^{1}H-NMR spectra of both isomers.

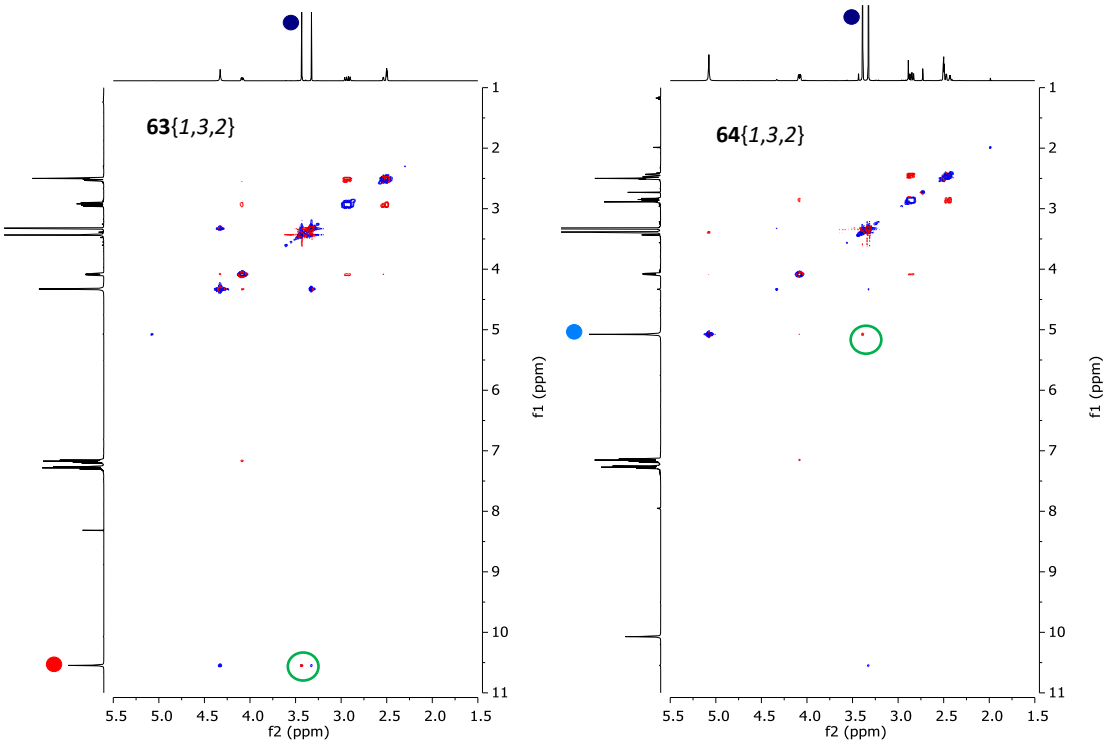

Figure 2.23. NOESY spectrum of **63**{*1,3,2*} and **64**{*1,3,2*}. The correlation between the methyl group and NH or the NH_2 group confirms the structure of the compounds.

Again, our hypothesis is confirmed by the results which prove that in the case of methylhydrazine **56**{*2*} the reaction is not regiospecific. However, the major formation of isomer **64** cannot be explained based on nucleophilicity differences proving that other factors such as the steric hindrance of the substituent also have an effect on the result of the reaction. However, the reaction mechanism should be equivalent to the one observed with phenylhydrazine. In this case, both nitrogen atoms of the methylhydrazine can perform the nucleophilic attack onto the methoxy group leading to two different intermediates. Despite the equivalent nucleophilicity of both groups, intermediate **76**{*x,y,2*} is the major product of this first step due to the steric hindrance of the methyl group which hampers the attack of the NH group.

Once the corresponding intermediate is formed, the cyclization onto the CN group immediately takes place. The reaction does not require high thermal levels due to high reactivity of the free nitrogen group. (Figure 2.24)

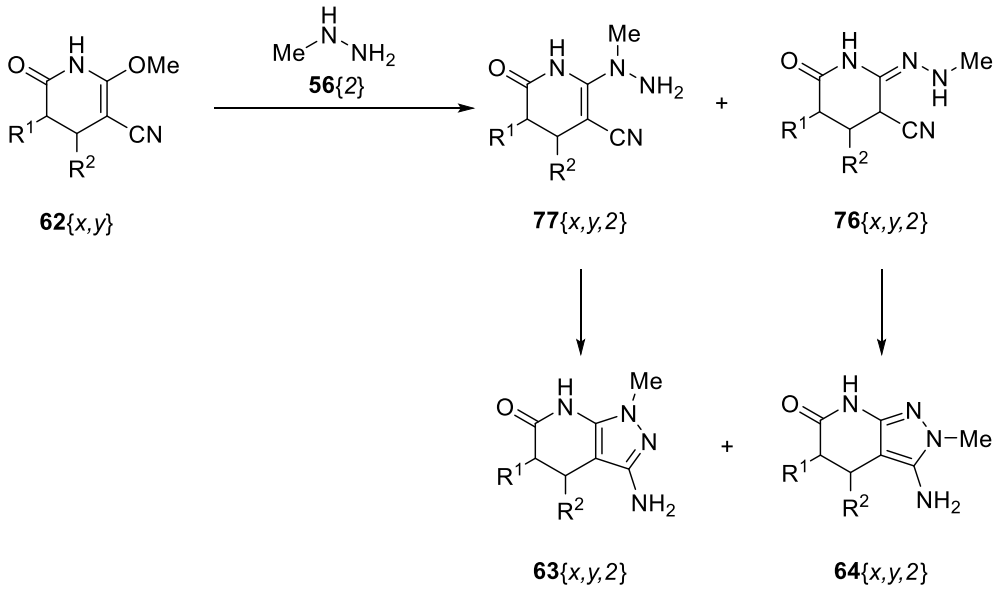

Figure 2.24. Suggested reaction pathway for the formation of isomers **63**{*x,y,2*} and **64**{*x,y,2*}

2.1.3.3. Conclusion

The cyclization reaction between pyridones **62** and substituted hydrazines (methyl **56**{*2*} and phenyl **56**{*3*}) has been studied and the regiochemistry of the formed products together with a reaction mechanism have been elucidated.

The reaction has two different steps: a) the substitution of the methoxy group present in pyridones **62** with hydrazine **56** to afford an open intermediate **76**/**77**; and b) the cyclization of intermediates **76**/**77** to yield pyrazolopyridones **63/64** (Figure 2.25). The regiochemistry of the products is highly dependent on the hydrazine used. When both N atoms present equivalent nucleophilicities, the reaction renders two different open intermediates which easy cyclize leading to two different isomers N1 and N2 substituted. The ratio of the isomers is affected by the steric hindrance of the hydrazine substituents. On the other hand, when the hydrazine moiety presents electron withdrawing groups (e.g., aryl groups) that unbalance the nucleophilicity of the N atoms, a single open intermediate is formed coming from the attack of the free NH_2 group. Depending on the substituent, elevated thermal levels are needed to achieve cyclization of the open intermediate and, in this case, only the N2 substituted isomer is obtained.

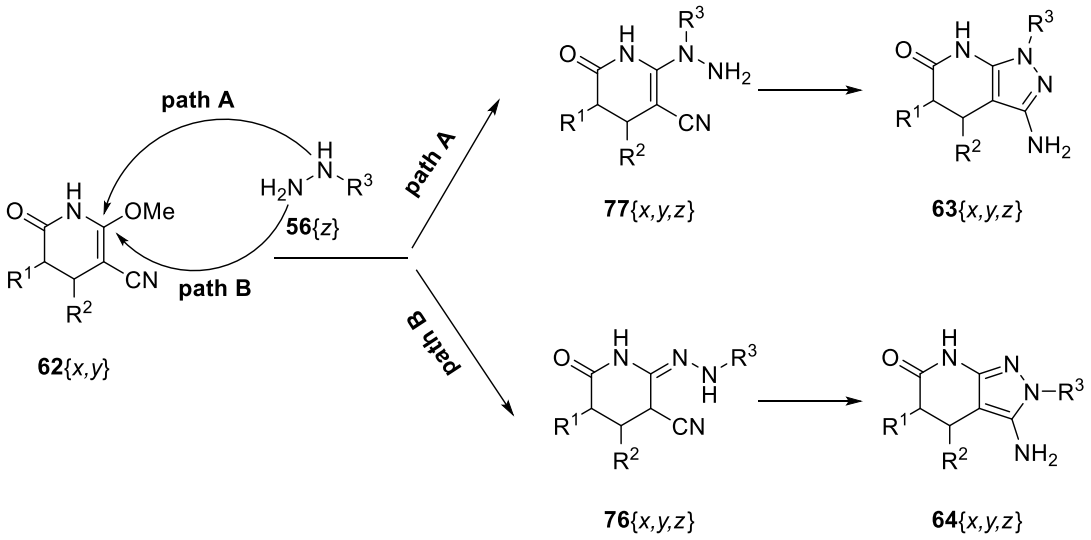

Figure 2.25. General reaction pathway for the formation of isomers **63** and **64**

2.1.4. Selective synthesis of N1 and N2 substituted pyrazolo[3,4-*b*]pyridin-6-ones

In order to explore the biological activities of N1 and N2 substituted pyrazolo[3,4-*b*]pyridin-6-ones, it is interesting to define methodologies to selectively obtain both isomers, especially in the case of aryl substituted molecules for which isomer **63** was not detected. For this reason, alternative methodologies to obtain these compounds were studied.

2.1.4.1. Synthesis of isomer 63 *via* an 6-oxo-2-(1-phenylhydrazinyl)-1,4,5,6-tetrahydropyridine-3-carbonitrile intermediate (77)

After discarding the obtention of the isomer **63** by direct cyclization, a new methodology is proposed based on the formation of a 6-oxo-2-(1-phenylhydrazinyl)-1,4,5,6-tetrahydropyridine-3-carbonitrile (**77**{*x*,*y*,*3*}) intermediate. This methodology involves the substitution of the methoxy group of **62** with aniline, followed by the nitrosation of the secondary amine and the following reduction to form the hydrazinyl intermediate and allow the cyclization of the pyrazole ring. (Figure 2.26)

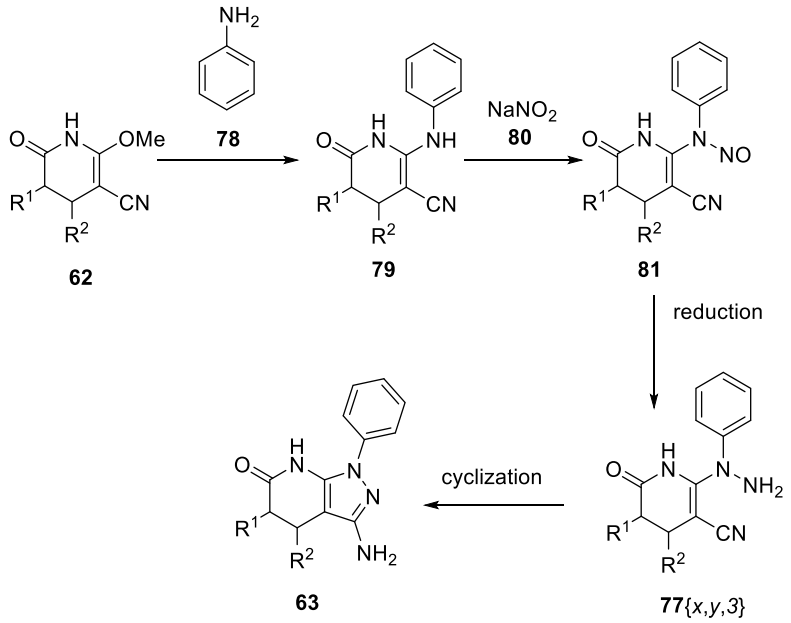

Figure 2.26. Alternative synthesis of isomer 63 *via* an 6-oxo-2-(1-phenylhydrazinyl)-1,4,5,6-tetrahydropyridine-3-carbonitrile intermediate (**77**)

The first substitution reaction of **62** with aniline (10 equivalents excess) in MeOH was studied with conventional heating and microwave irradiation. The temperature was progressively increased up to 140 °C when decomposition of the product was observed, without achieving a complete conversion. However, when the reaction was performed using an excess of aniline as solvent, a complete conversion was achieved in a 69% yield after 24h at 65 °C. (Table 2.5)

Table 2.5. Studied conditions for the nucleophilic substitution of pyridone **62**{*2*,*1*} with aniline (**78**) (10 eq.). When solvent is used, dilution is (5 mL/100 mg).

Solvent	Temp. (ºC)	Time (h)	Result
MeOH	100 (mw)	3	Mixture reagent (**62**{*2*,*1*}):product (**79**{*2*,*1*,*3*}) (1:0,4)
MeOH	120 (mw)	1	Mixture reagent (**62**{*2*,*1*}):product (**79**{*2*,*1*,*3*}) (1:0,6)
MeOH	140 (mw)	1	Product decomposition
MeOH	65 (reflux)	20	Mixture reagent (**62**{*2*,*1*}):product (**79**{*2*,*1*,*3*}) (1:1,1)
Solvent free	65	20	Complete conversion

For the nitrosation step, two different methodologies were tested and $NaNO_2$ (**80**) was used as a nitrosating agent for both. In the first experience, the typical reaction in AcOH was explored[16-19] while in the second procedure, the conditions described by Borikar *et al.*[20] (using p-TSA (p-toluensulfonic acid) in DCM (dichloromethane)) were applied. Surprisingly, the two methods yield diastereotopic mixtures of different products with different localizations of the NO group.

In the first methodology, nitrosation of **62**{*2*,*1*} was performed using $NaNO_2$/AcOH (1.6 eq.), 1h at room temperature, yielding a mixture of two diastereoisomers that was assigned as compound **82**{*2*,*1*,*3*}. The assignment of this structure was possible when a correlation between the diasterotopic protons with the NO was observed in a ^{15}N-HMBC spectrum. (Annex 2)

The second methodology **62**{*2*,*1*} was treated with sodium nitrite (1.05 eq.) and p-TSA (1.05 eq.) in DCM at room temperature for 1h. The authors describe this method as a selective nitrosation process for secondary amines under mild and heterogeneous conditions.[20] Again, a mixture of two diastereoisomers was obtained which was assigned as the desired compound **81**{*2*,*1*,*3*}. (Figure 2.27)

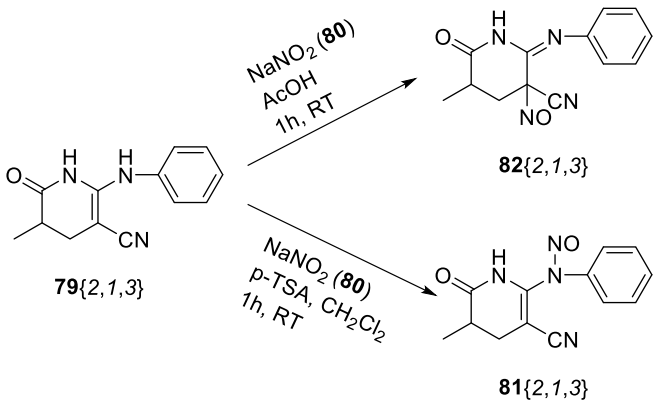

Figure 2.27. Summary results obtained from the nitrosation studies.

The reduction of compound **81**{*2*,*1*,*3*} was tested using different reductive conditions. As the first option, Zn was used as a reducing agent[21] in H_2O/EtOH stirred in the presence of $(NH_4)_2CO_3$ and NH_3 for 3h at room temperature but no product was obtained. As a second option, compound **81**{*2*,*1*,*3*} was stirred at room temperature for 1h with $LiAlH_4$ (2 eq.) in THF. However, a complete decomposition of the product occurred. As a third method, a recently described reduction method for N-nitrosamines based on the use of thiourea dioxide (TDO) as reducing agent was used.[22] The TDO was prepared from thiourea and hydrogen peroxide as described by Chaudhary *et al.*[22] Compound **81**{*2*,*1*,*3*} was then heated at 40 °C with TDO and NaOH in EtOH for 5h but degradation of the product occurred. The reaction was carried out at room temperature for 3h and 1h respectively with exact results. Finally, a catalytic hydrogenation was tried with H_2 and Pd/C (10%) in MeOH observing the immediate decomposition of the product (after 5 minutes).

To sum up, the reduction of the nitrosamine group is essential for the synthesis of the final N1 substituted pyrazolopyridone. However, any of the tested reducing agents ($LiAlH_4$, $Zn/(NH_4)_2CO_3$, TDO and H_2/Pd) yielded the compound of interest leading to a complete decomposition of the starting material in all cases. Due to the impossibility to reduce the nitroso group, this strategy was discarded for the synthesis of **63**.

2.1.4.2. Synthesis of isomer 63 *via* an Ullman reaction

The cyclization of 2-methoxy-6-oxo-1,4,5,6-tetrahydropyridin-3-carbonitriles (**3**) with substituted arylhydrazines yields a single N2-aryl substituted isomer **64**. The formation of the N1-aryl substituted isomer **63** is still needed to provide a complete and selective synthetic route for all the possible positional isomers of the pyrazolopyridin-6-one scaffold.

The synthesis of **63**{*x*,*y*,*3*} by direct cyclization was not possible by using the different reaction conditions assayed, which always yielded isomer **64**{*x*,*y*,*3*} *via* the open intermediate **76**{*x*,*y*,*3*}. The formation of intermediate **77**{*x*,*y*,*3*} (6-oxo-2-(1-phenylhydrazinyl)-1,4,5,6-tetrahydropyridine-3-carbonitrile intermediate) *via* an alternative method consisting on a substitution with aniline, followed by a nitrosation of the secondary amine and the subsequent reduction, did not yield the desired compound. With this in mind, a new strategy is proposed which consists on a metal catalyzed substitution on the preformed pyrazolopyridin-6-one **64/63**{*x*,*y*,*1*} molecule, result of the cyclization of the corresponding pyridone **62** with hydrazine **56**{*1*}. (Figure 2.28)

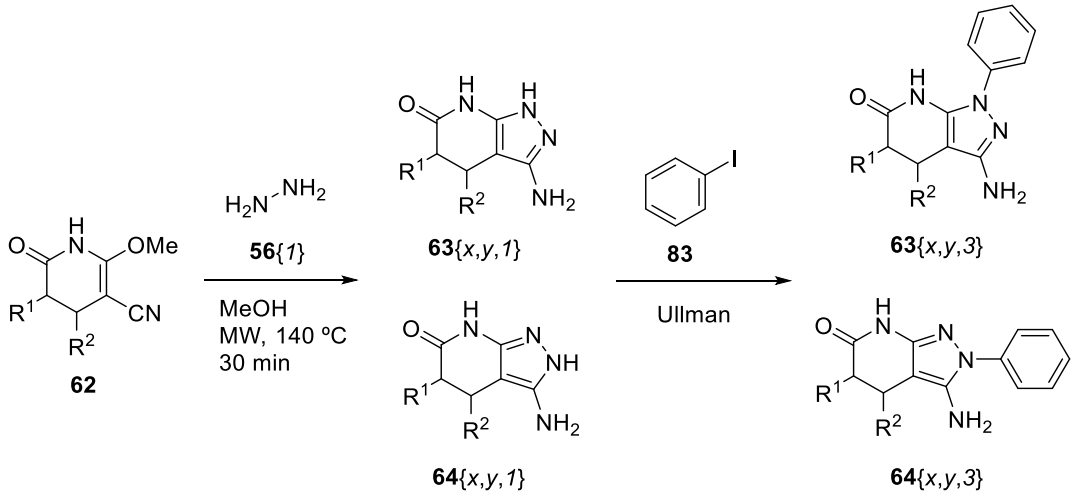

Figure 2.28. Scheme of the alternative synthesis of compound **63**{*x*,*y*,*3*}, by Ullman reaction.

However, the reaction between **62** and **56**{*1*} can afford the two isomers (in fact tautomers) **63**{*x*,*y*,*1*} and **64**{*x*,*y*,*1*}. The relative stability of both isomers will be crucial to obtain the desired compound **63**{*x*,*y*,*3*}. In order to predict the result of the reaction, quantum mechanics calculations were performed using Gaussian 09.[11] The studies were performed with both, the starting materials **63**{*x*,*y*,*1*} and **64**{*x*,*y*,*1*} (R^3 = H) and the expected products **63**{*x*,*y*,*3*} and **64**{*x*,*y*,*3*} (R^3 = Ph) bearing a phenyl ring in the R^1 position of the pyridone ring. (Table 2.6)

The results previously described in this chapter have shown a clear preference for the formation of the N2-aryl substituted isomer **64**{*x*,*y*,*3*}. A literature search carried out with SciFinder seems to indicate that the formation of N2-substituted isomers **53A** is quite general in fused pyrazolopyridines when the 6-member ring is not aromatic while, on the contrary, the N1 substituted isomers **54** are only depicted when the 6-member ring is an aromatic pyridine. (Figure 2.29)

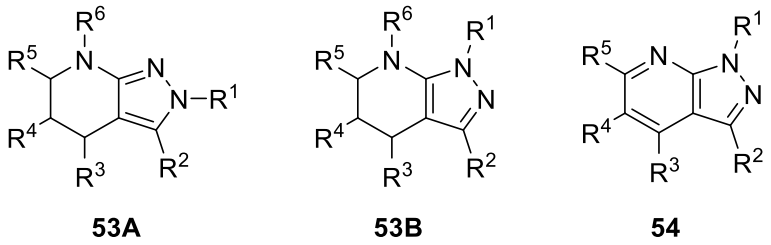

Figure 2.29. Most common substitution of the published structures similar to 3-aminopyrazolo[3,4-*b*]pyridin-6-ones

This observation seems to indicate that the pyrazole ring fused to a non-aromatic ring is more stable with the two double bonds exocyclic to the six membered ring (**53A**) than sharing a double bond in the fusion of both rings (**53B**). If this is true, the unsubstituted pyrazolopyridone **64**{*x*,*y*,*1*} should be more stable than the corresponding tautomer **63**{*x*,*y*,*1*} thus favoring that the Ullman arylation affords the N2-aryl substituted isomer **64**{*x*,*y*,*3*}. Having this in mind, we propose that the introduction of double bond in C4-C5 of the lactam ring of the intermediate previous to the Ullman arylation (see below **84**{*3*,*1*,*1*} and **85**{*3*,*1*,*1*} *vs* **63**{*3*,*1*,*1*} and **64**{*3*,*1*,*1*}) could influence the electron distribution of the pyrazole ring allowing the formation of the N1-aryl substituted compound **84**{*3*,*1*,*3*}. For this reason, all the corresponding dehydrogenated compounds were also included in the calculations (Table 2.6).

Table 2.6. Energy values of the different isomers calculated with DFT B3LYP 6-311++G(d,p).

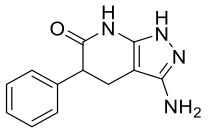

63{*3*,*1*,*1*}

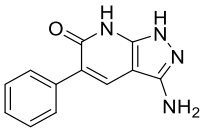

84{*3*,*1*,*1*}

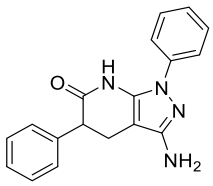

63{*3*,*1*,*3*}

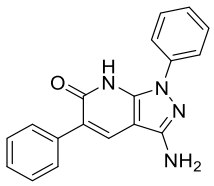

84{*3*,*1*,*3*}

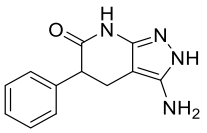

64{*3*,*1*,*1*}

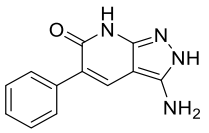

85{*3*,*1*,*1*}

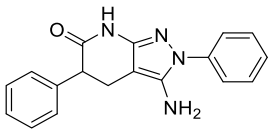

64{*3*,*1*,*3*}

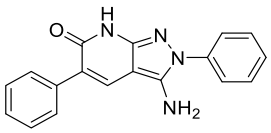

85{*3*,*1*,*3*}

REAGENTS	
	ENERGY (kcal/mol)
64{*3*,*1*,*1*}	-476098.3
63{*3*,*1*,*1*}	-476096.4
85{*3*,*1*,*1*}	-475355.9
84{*3*,*1*,*1*}	-475356.2

PRODUCTS	
	ENERGY (kcal/mol)
64{*3*,*1*,3}	-621069.3
63{*3*,*1*,3}	-621067.8
85{*3*,*1*,3}	-620327.1
84{*3*,*1*,3}	-620327.6

	Δ ENERGY (kcal/mol)
64-63	-1.9
85-84	0.3

	Δ ENERGY (kcal/mol)
64-63	-1.5
85-84	0.5

In the case of the non-dehydrogenated compounds, the energy differences between each pair of isomers (**64**{*3*,*1*,*1*}/**63**{*3*,*1*,*1*} and **64**{*3*,*1*,*3*}/**63**{*3*,*1*,*3*}) was high (around 1.5 kcal/mol) being the N2 substituted isomer (**64**{*3*,*1*,*1*} and **64**{*3*,*1*,*3*}) the more stable. Such result agrees with the tendency observed in the literature search pointing out that the pyrazole ring fused to a non-aromatic 6-member ring is more stable with an exocyclic position of the double bonds independently of the substituents in R^1, R^2 or R^3. The stability difference between isomers, both in the case of the staring material of the Ullman arylation and the arylated product, will certainly not favor the obtention of the N1-arylated isomer **63**{*3*,*1*,*3*}.

On the contrary, when the lactam ring presents a double between C4-C5, although not being a totally aromatic pyridine ring, the difference of energies between the pairs of isomers (**85**{*3*,*1*,*1*}/**84**{*3*,*1*,*1*} and **85**{*3*,*1*,*3*}/**84**{*3*,*1*,*3*}) not only decreases in value but also inverts the sign pointing out to greater stability of the N1 substituted isomer both for the starting material **84**{*3*,*1*,*1*} and the final arylated compound **84**{*3*,*1*,*3*}. This result seems to indicate that, in the case of the C4-C5 unsaturated compound, the presence in solution of the H-N1 tautomer

84{*3*,*1*,*1*} is more likely allowing the arylation in N1 of the pyrazole ring and subsequently the formation of **84**{*3*,*1*,*3*}.

The computational predictions were then experimentally validated by preparing the unsubstituted pyrazolopyridone intermediate, oxidizing the lactam ring when necessary and performing an Ullman-type Cu-catalyzed substitution reaction to form a new C-N bond introducing a phenyl group in the pyrazole ring.

Thus, **62**{*3*,*1*} was cyclized with hydrazine to obtain the unsubstituted pyrazolopyridone (**64**{*3*,*1*,*1*}/**63**{*3*,*1*,*1*}) (despite theoretically both isomers are possible, the N2 substituted isomer seems to be more stable). The NMR spectra in d_6-DMSO of the possible mixture of isomers only shows the signals corresponding to one structure. However, the structure was not possible to be unequivocally assigned.

Using the Ullman reaction conditions described by Beyer *et al.*[23] compound **64**{*3*,*1*,*1*}/**63**{*3*,*1*,*1*} was treated with iodobenzene (**83**) for 24h using CuI as catalyst, Cs_2CO_3 as base and *N*-methylpyrrolidine (NMP) as solvent. After the corresponding work up, the crude material was analyzed to determine the compound or compounds present in it.

The arylation of **64**{*3*,*1*,*1*}/**63**{*3*,*1*,*1*} yields a single compound which corresponds to the N2-aryl substituted molecule 3-amino-2,5-diphenyl-2,4,5,7-tetrahydro-6*H*-pyrazolo[3,4-*b*]pyridin-6-one (**64**{*3*,*1*,*3*}). The structure assignment was carried out by means of NMR spectroscopy and by direct comparison with the pure product previously obtained by cyclization of **62**{*3*,*1*} with phenylhydrazine (**56**{*3*}) (Figure 2.31).

This result is in accordance with the computational calculations that predicted a ~2 kcal/mol energy difference in favor of the H-N2 isomer **64**{*3*,*1*,*1*}. Because of that, the reaction yielded **64**{*3*,*1*,*3*} as a single product. (Figure 2.30). Moreover, the regionspecificity of the reaction seems to indicate the cyclization product of the starting pyridone **62**{*3*} with hydrazine is in fact the H-N2 tautomer **64**{*3*,*1*,*1*}.

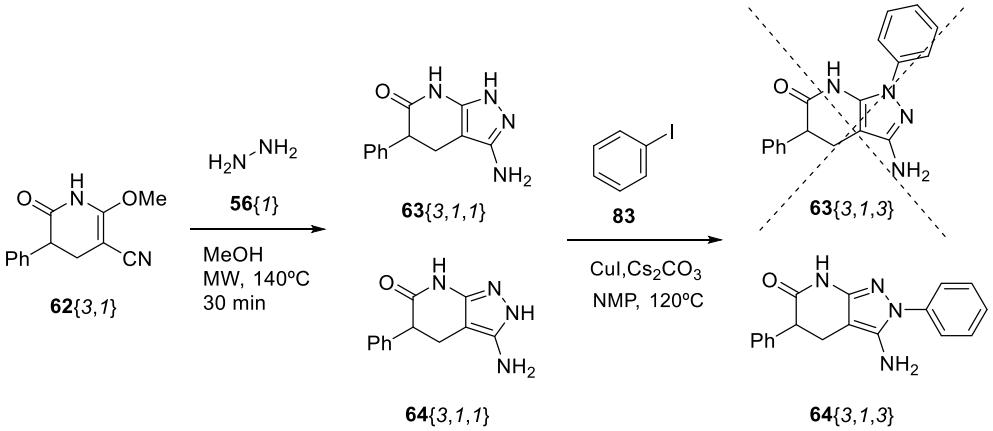

Figure 2.30. Results of the Ullman reaction on the unoxidized pyrazolopyridone.

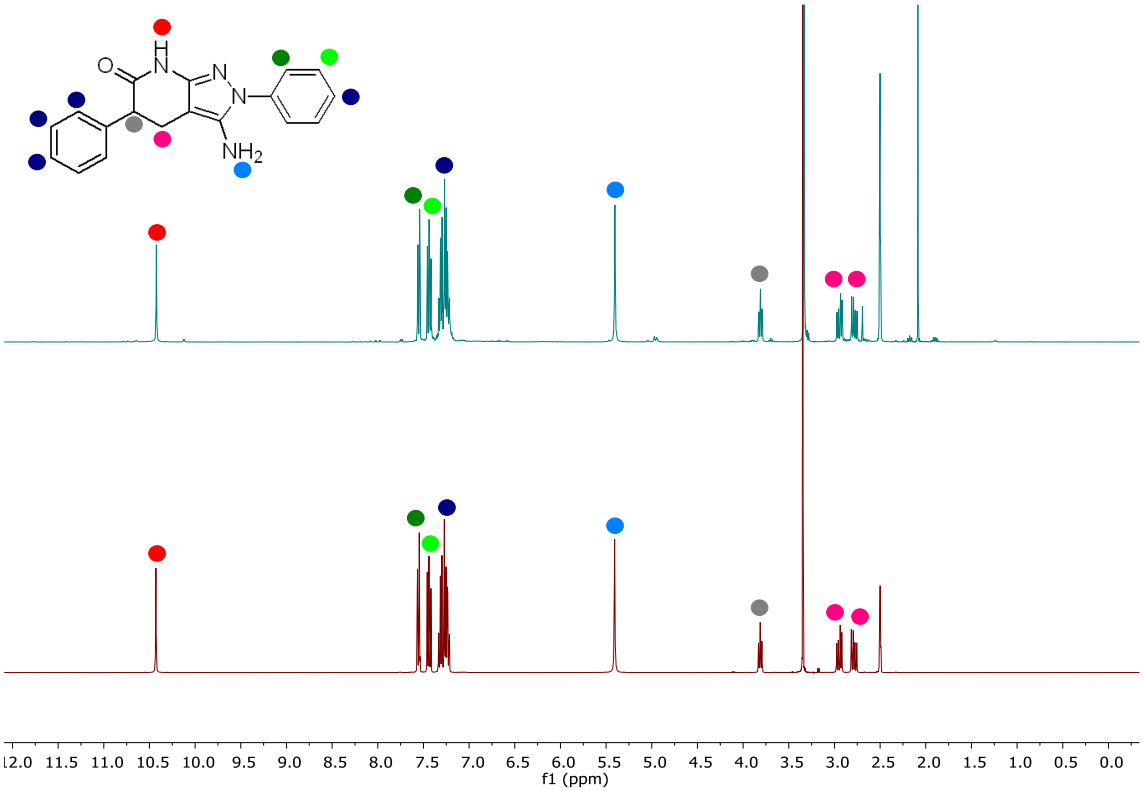

Figure 2.31. Comparison of the ^{1}H-NMR spectra of compound **64**{*3,1,3*} obtained by Ullman reaction (blue) and by direct cyclization of pyridone **62**{*3,1*} with phenylhydrazine (red).

Such result, in agreement with our computational predictions, seems to indicate that the Ullman reaction on the C4-C5 unsaturated molecule should allow the obtention of the N1-arylated isomer, probably in a mixture with the N2-arylated isomer.

Oxidation of compound **64**{*3*,*1*,*1*} was achieved by heating the compound with 1.5 eq. of DDQ (2,3-dichloro-5,6-dicyano-1,4-benzoquinone) in MeOH at reflux for 3h. Higher times lead to the decomposition of the product while other solvents such as dioxane did not yield a complete transformation. Again, the NMR spectrum in d_6-DMSO presented the signals of a single compound that was not possible to be unequivocally identified as **85**{*3*,*1*,*1*} or **84**{*3*,*1*,*1*}.

The same transition-metal-catalyzed arylation was then carried out. Compound **85**{*3*,*1*,*1*}/**84**{*3*,*1*,*1*} was treated with Iodobenzene (**83**), CuI and Cs_2CO_3 in NMP. (Figure 2.32)

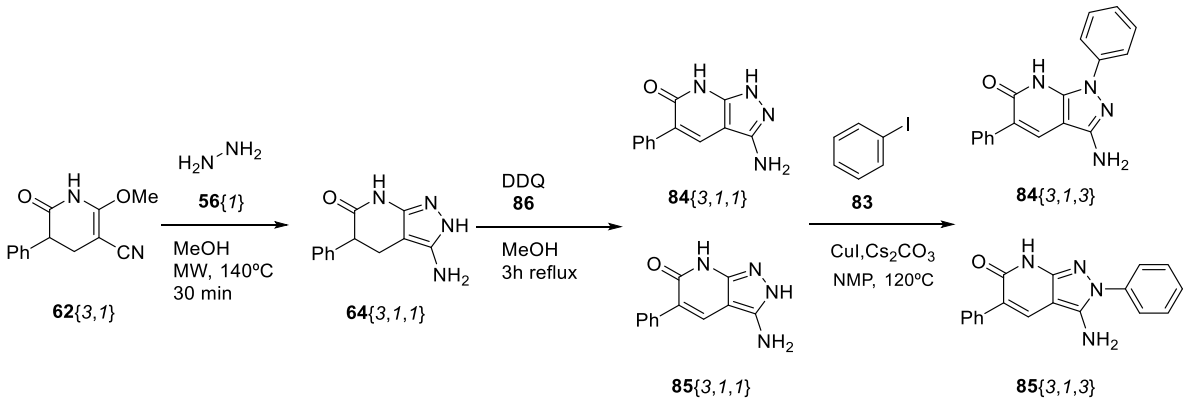

Figure 2.32. Results of the Ullman reaction on the C4-C5 unsaturated pyrazolopyridone.

The analysis of the reaction crude by TLC showed a complete conversion of the starting material into two different compounds. ^{1}H-NMR spectrum of the reaction crude confirmed the presence of two different compounds in unequal proportions. The purification method was a critical point. If the product was precipitated in MeOH only the major compound (80%) was obtained which corresponded to the N2-aryl substituted isomer **85**{*3*,*1*,*3*}. This molecule presented a lower solubility begin the only product isolable by precipitation. Identification of the product was carried out by direct comparison with the pure compound obtained by oxidation of **64**{*3*,*1*,*3*} with DDQ. (Figure 2.33 and Figure 2.34)

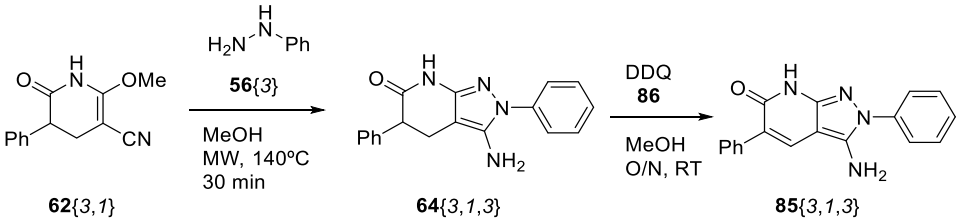

Figure 2.33. Oxidation of **64**{*3*,*1*,*3*} with DDQ.

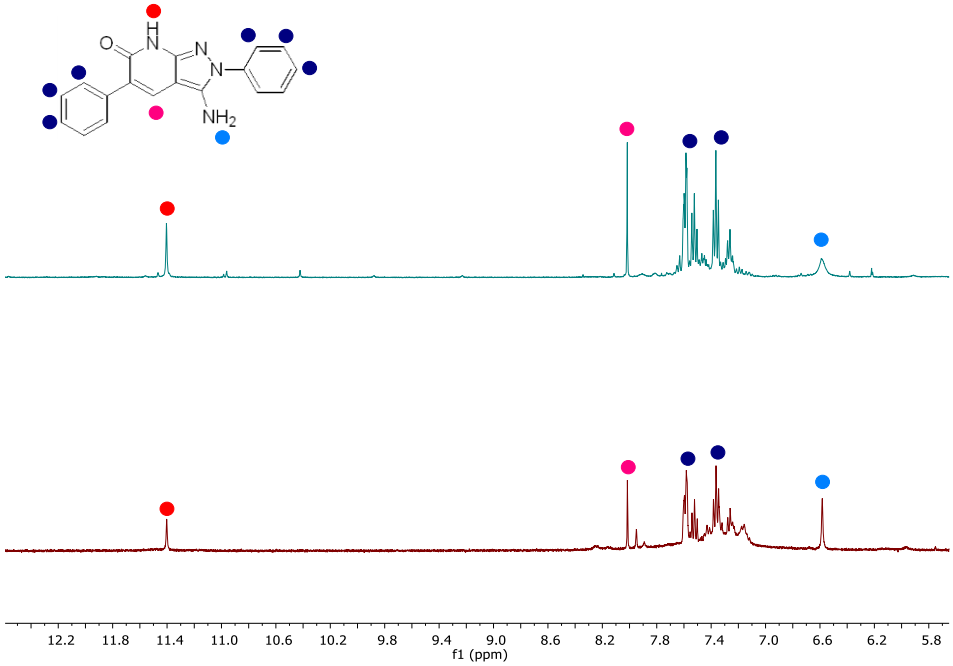

Figure 2.34. Comparison of the ^{1}H-NMR spectra of compound **85**{*3,1,3*} obtained by Ullman reaction (red) and by oxidation of compound **64**{*3,1,3*} with DDQ (blue).

When the crude was purified by column chromatography (silica column with ethyl acetate as eluent) a second product was isolated. This compound was found in a minor proportion in the reaction crude (~20% by NMR integration). The new product presented the same signal profile as **85**{*3,1,3*} but different chemical shifts. The ^{1}H-NMR signal pattern together with the results of the computational simulations supported the idea of having obtained isomer **84**{*3,1,3*}.

84{*3,1,3*}

85{*3,1,3*}

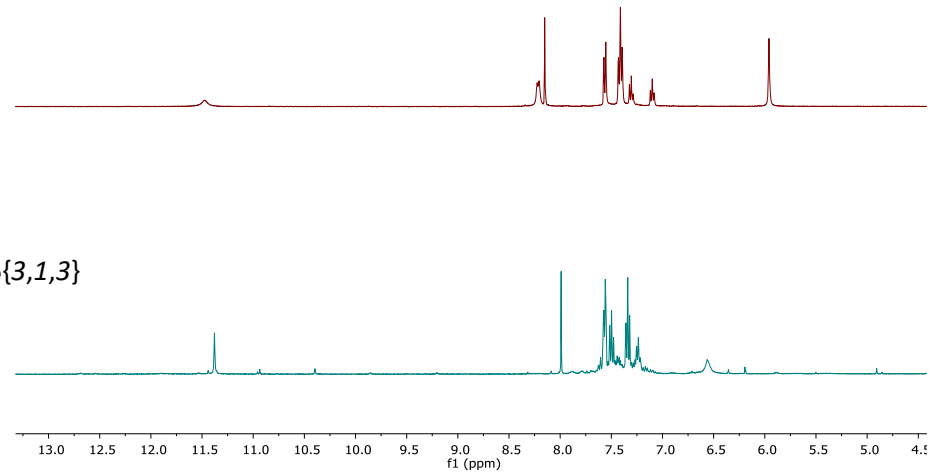

Figure 2.35. Comparison of the ^{1}H-NMR spectra of compounds **84**{*3,1,3*} and **85**{*3,1,3*}.

The confirmation of the structure was not possible by NMR spectroscopy as the NOESY spectra did not show any confirming correlation (a correlation between the NH of the lactam and the phenyl of the pyrazole ring was expected). In order to increase the possibilities to observe a correlation, the labile protons of the amines were methylated. Compound **84**{*3*,*1*,*3*} was ionized with 3 equivalents of NaH in DMSO and then methylated with 3 equivalents of MeI (**87**). (Figure 2.36)

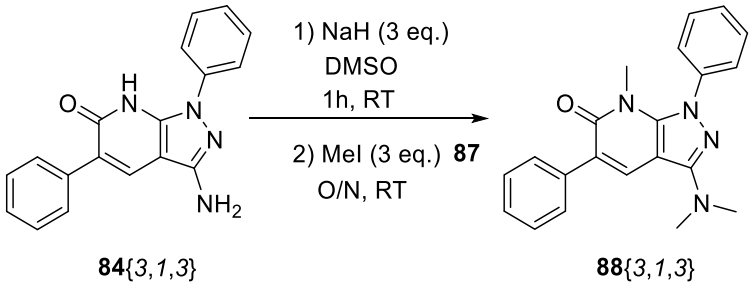

Figure 2.36. Synthesis of 3-(dimethylamino)-7-methyl-1,5-diphenyl-1,7-dihydro-6*H*-pyrazolo[3,4-*b*]pyridin-6-one (**88**{*3*,*1*,*3*}).

This time, the 1D NOESY spectrum where the phenyl protons were irradiated showed a clear correlation with the methyl group of the lactam confirming the substitution point and the obtention of the N1-aryl substituted compound **84**{*3*,*1*,*3*}. (Figure 2.37)

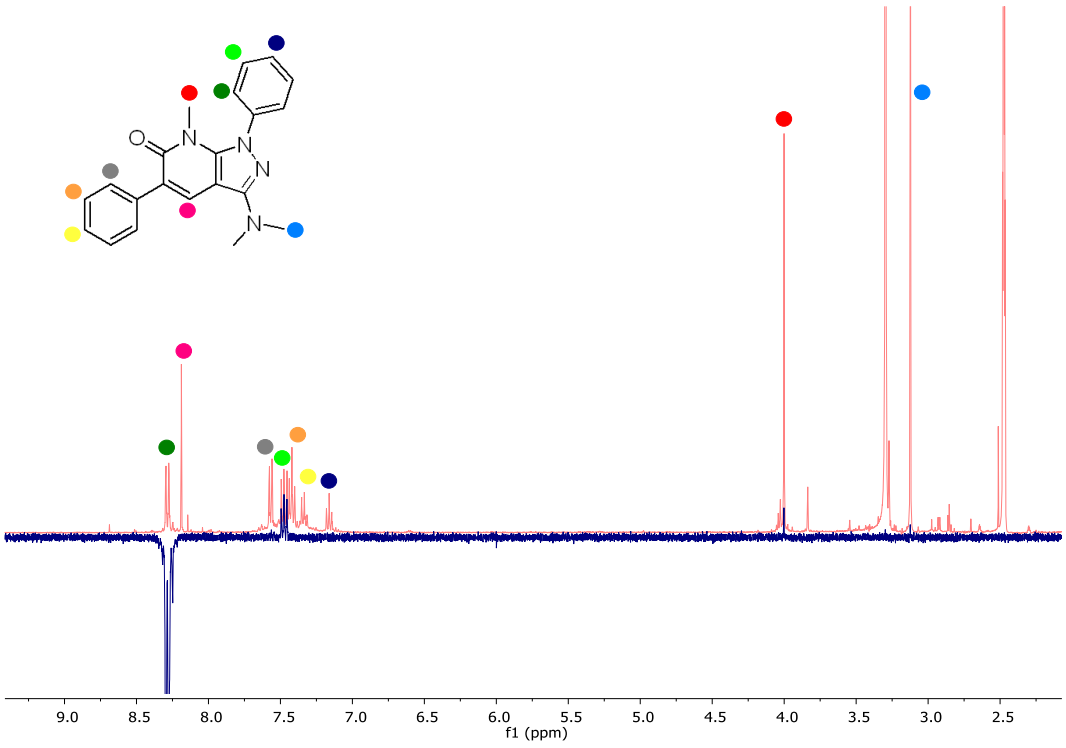

Figure 2.37. 1D NOESY spectrum showing the correlation of the aromatic protons (purple) with the lactam methyl group (green) demonstrating the structure of compound **84**{*3*,*1*,*3*}.

Finally, it was possible to obtain a monocrystal of compound **84**{*3*,*1*,*3*} and the crystal structure was resolved by single crystal X-ray diffraction by the group of Dr. Cristina Puigjaner of the Unitat de Difracció de RX. Centres Científics i Tecnològics de la Universitat de Barcelona (CCiTUB). Single crystals were grown by vapor diffusion of water into 1mL of a MeOH solution of 2mg of **84**{*3*,*1*,*3*}.

The results confim that the minor compound obtained with the Ullman reaction and isolated by column chromatography was compound **84**{*3*,*1*,*3*} with the phenyl substitution in the N1 position of the pyrazole ring. Crystallographic data are summarized in Annex 2. (Figure 2.38)

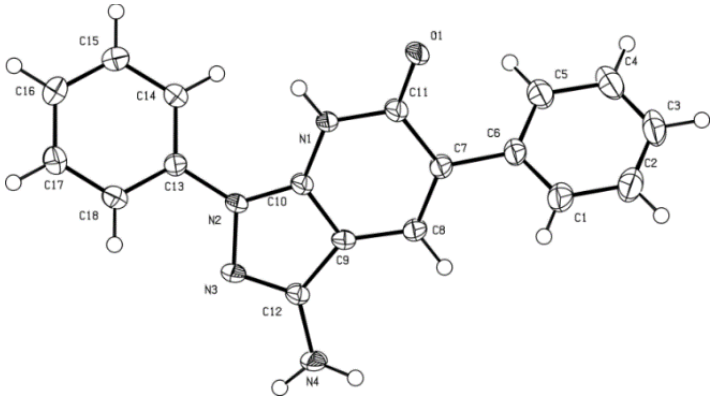

Figure 2.38. X-ray diffraction structure corresponding to isomer **84**{*3*,*1*,*3*}

These results were again in accordance with the computational calculations and confirmed the initial hypothesis. The similar stability of the dehydrogenated tautomers (**84**{*3*,*1*,*1*} and **85**{*3*,*1*,*1*}) allows the synthesis of both aryl substituted isomers (**84**{*3*,*1*,*3*} and **85**{*3*,*1*,*3*}).

For the first time, it was possible to obtain the N1-aryl substituted compound (3-amino-1,5-diphenyl-2,7-dihydro-6*H*-pyrazolo[3,4-*b*]pyridin-6-one (**84**{*3*,*1*,*3*})). However, the proportions between both isomers were not equivalent (20 to 80 respectively), being isomer **84**{*3*,*1*,*3*} the minor product with an isolated yield of only 20%.

2.1.4.3. Alternative synthesis of 1-aryl-3-amino-2,7-dihydro-6*H*-pyrazolo[3,4-*b*]pyridin-6-ones (84).

Up to this point, the synthesis of 1-aryl-3-amino -2,7-dihydro-6*H*-pyrazolo[3,4-*b*]pyridin-6-ones has been deeply studied. However, only an Ullman based methodology has allowed its preparation but with very low yields and always as a minor product from an unequal mixture of both positional isomers.

Here an alternative synthesis for the preparation of this product is proposed and studied. It consists on a "inversed synthesis" adapted from Pettus *et al.*[24] in which the pyrazole ring with the phenyl in the N1 position is first formed (compound **90**) and then cyclized to form the lactam ring (compound **94**) . The ester group present at position C5 of intermediate **94** will be changed by any aryl group of interest by the subsequent transformation into a bromine atom (compound **96**) susceptible to suffer Suzuky reactions with different boronic acids. A last step would imply adding the primary amine in the pyrazole ring of compound **98** *via* the corresponding iodo derivative **99** to afford the desired N1-aryl substituted derivative **84**{*3*,*1*,*3*}. (Figure 2.39)

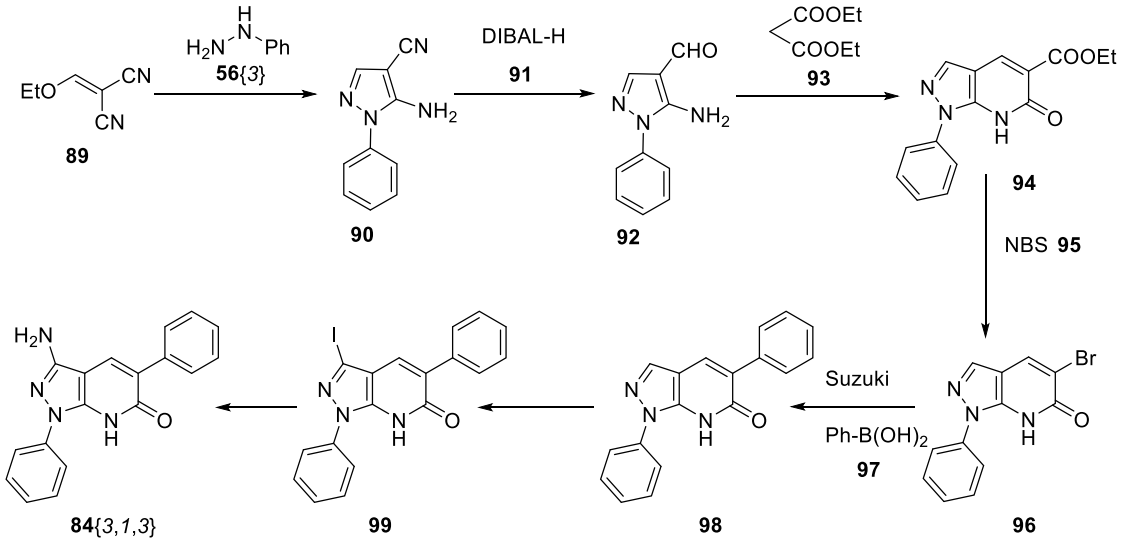

Figure 2.39. Scheme of the alternative synthesis of 3-amino-2,5-diphenyl-2,7-dihydro-6*H*-pyrazolo[3,4-*b*]pyridin-6-one (**84**{*3*,*1*,*3*}).

The formation of the pyrazole ring is achieved by the reaction between phenyl hydrazine (**56**{*3*}) and 2-(ethoxymethylene)-malononitrile (**89**) in EtOH in presence of triethylamine to afford the aromatic heterocycle 5-amino-1-phenyl-1*H*-pyrazole-4-carbonitrile (**90**).

In order to achieve the cyclization to the desired pyrazolopyridone heterocycle, the nitrile group present in the pyrazole ring of **90** needs to be reduced to an aldehyde. The original methodology described by Pettus *et al.*[24] was modified by changing the reducing agent from H_2/Raney nickel to DIBAL-H selective for the CN to aldehyde reduction.

The reaction was optimized by adjusting the reaction time, temperature and equivalents of DIBAL-H (Annex 2). At the optimal conditions, compound **90** was treated with 2 equivalents of DIBAL-H (**91**) in toluene for 1 hour. Then 2 extra equivalents were added, and the mixture was stirred for 24h at room temperature. The reaction was quenched by adding water and the reduced product **92** was purified by column chromatography (silica column with a Cy:AcOEt (1:1) mixture as eluent). Despite the uncomplete conversion, a yield of 77% was obtained and the reaction could be scalable up to 600 mg of reagent.

Finally, the cyclocondensation of 5-amino-1-phenyl-1*H*-pyrazolo-4-carbaldehyde (**92**) with diethylmalonate (**93**), in the presence of piperidine in ethanol afforded the bicyclic ester **94** after 24h at reflux.

At this point, it was considered of importance to confirm the position of the phenyl ring. As the common spectroscopic experiments do not provide this information and the NOESY spectrum did not show any clear correlations, the molecule was methylated to improve the signal of possible spatial correlations. The product was dissolved in DMSO and treated with 3 equivalents of NaH for 1 h under Ar atmosphere. 3 equivalents of MeI were added and the reaction was stirred overnight at room temperature. The product was then precipitated by the addition of water and filtered. (Figure 2.40)

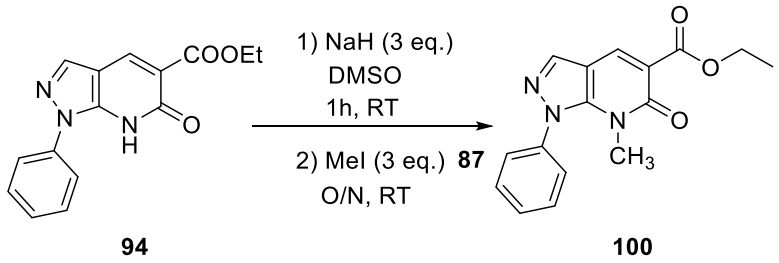

Figure 2.40. Methylation of ethyl 6-oxo-1-phenyl-6,7-dihydro-1*H*-pyrazolo[3,4-*b*]pyridine-5-carboxylate (**94**)

The 1D-NOESY spectrum of compound **100** confirmed the position of the phenyl group by showing a correlation between the aromatic protons and the methyl when directly irradiating the first.

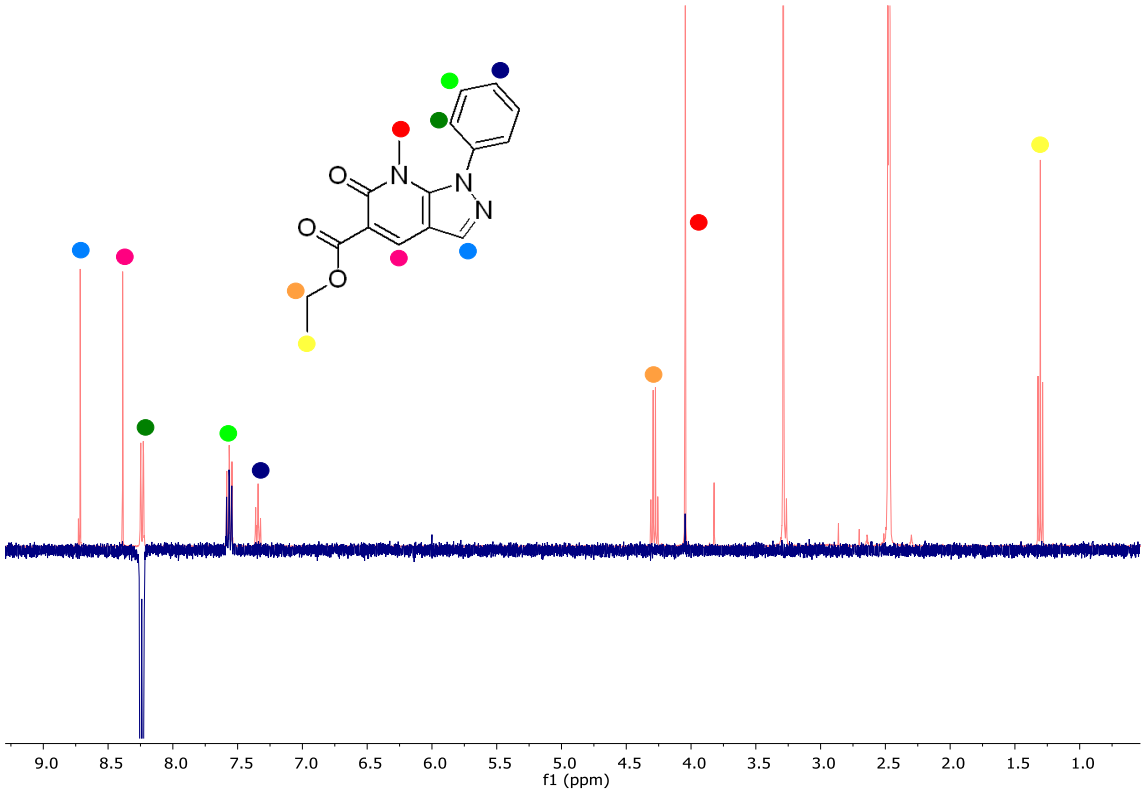

Figure 2.41. 1D NOESY spectrum showing the correlation of the aromatic protons (light blue) with the lactam methyl group (dark blue) demonstrating the structure of compound **100**.

In order to obtain a general structure susceptible to derivatization at position C5, the ester moiety was substituted by a bromine atom that could be later modified by metal-catalyzed reactions to many other groups. 5-bromo-1-phenyl-1,7-dihydro-6*H*-pyrazolo[3,4-*b*]pyridin-6-one (**96**) was obtained treating **94** with *N*-bromosuccinimide (2 x 1eq.) and lithium hydroxide monohydrate (2.5 eq.) in aqueous acetonitrile.

The substitution of the bromine group was performed by finding the best conditions for its reaction with phenylboronic acid under Suzuki reaction conditions. 5-bromo-1-phenyl-1,7-dihydro-6*H*-pyrazolo[3,4-*b*]pyridin-6-one (**96**) was dissolved in THF:H_2O (4:1). Phenyl boronic acid (**97**) (1.4 eq.), K_2CO_3 (3.5 eq.) and $Pd(PPh_3)_4$ (0.17 eq.) were added and the mixture was stirred at 80°C for 19 h. The reaction crude was analyzed by ^{1}H-NMR but the reaction result was not clear as it was not possible to clearly identify the desired product but neither the reagent was present.

Then, a Suzuky-Miyaura coupling was carried out (Figure 2.42). The reagents, together with the palladium (II) acetate ($Pd(OAc)_2$) and triphenylphosphine (PPh_3) were heated in glyme under microwave irradiation at 180 °C for 15 minutes. The product was purified by column chromatography (Silica column with a $CHCl_3$/MeOH gradient from 0% to 5% in 40 minutes).

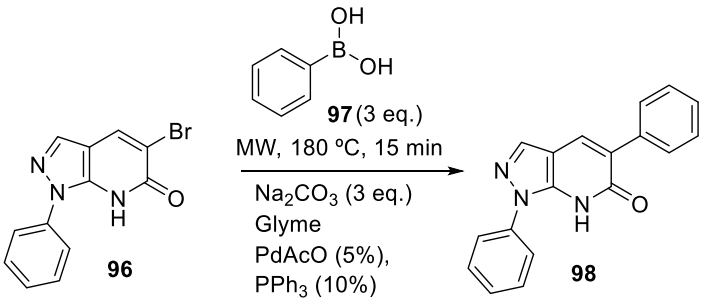

Figure 2.42. Synthesis of 1,5-diphenyl-1,7-dihydro-6*H*-pyrazolo[3,4-*b*]pyridin-6-one (**98**) by a Suzuky-Miyaura coupling

The ^{1}H-NMR (Figure 2.43) confirmed that the substitution was achieved successfully, as the aromatic signals of the new phenyl group were observed. However, the NOESY spectrum did not show clear correlations to confirm the substitution. For this reason, compound **98** was methylated (Figure 2.44) to easily confirm the position of the phenyl group in the pyrazole group by 1D NOESY. (Figure 2.45)

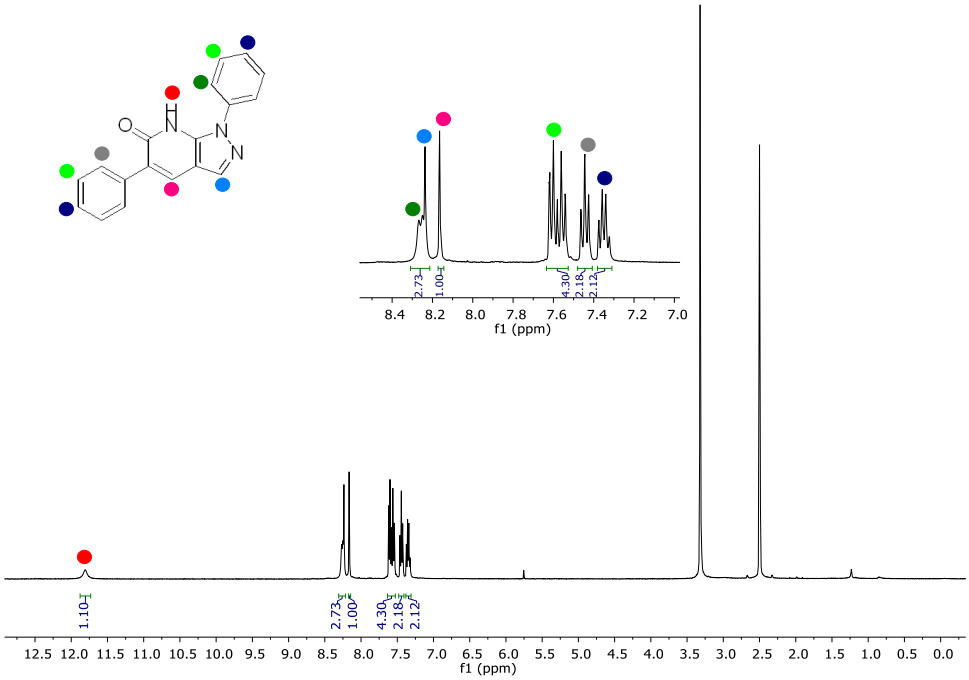

Figure 2.43. ^{1}H-NMR of 1,5-diphenyl-1,7-dihydro-6*H*-pyrazolo[3,4-*b*]pyridin-6-one (**98**).

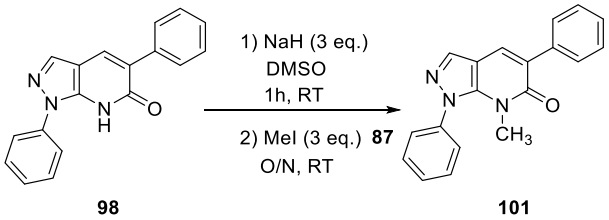

Figure 2.44. Methylation of compound **98**

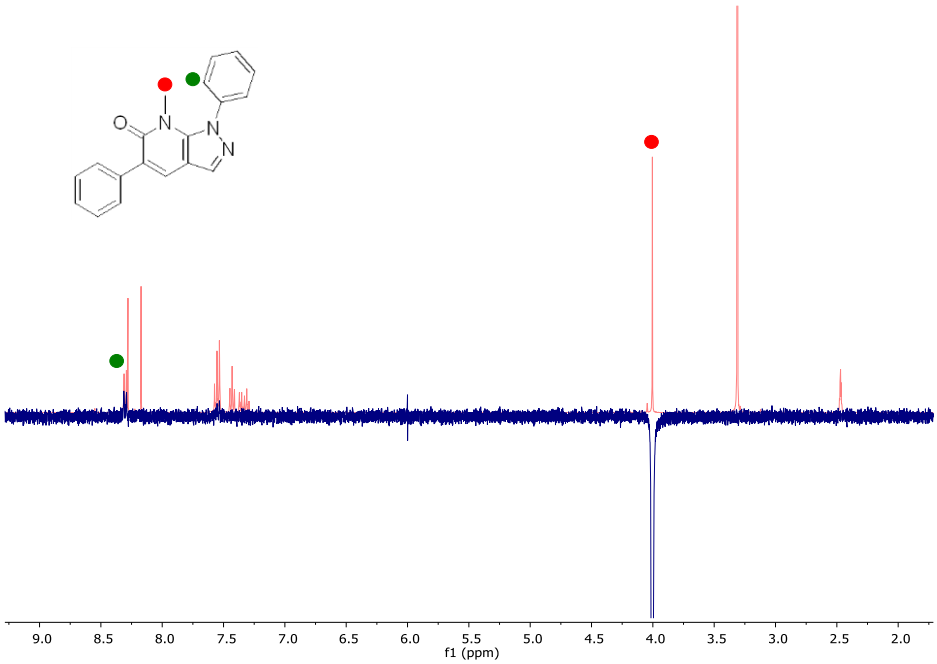

Figure 2.45. 1D-NOESY of compound **101** irradiating the methyl group. A correlation with the protons of the phenyl ring is observed confirming the position of the aromatic ring.

At this point, the only difference between **101** and **84**{*3*,*1*,*3*} was the presence of the primary amine in the pyrazole ring. The introduction of a iodine atom at position C3 of **101** should favor the introduction of the amine group. However, several attempts to introduce the iodine atom to achieve compound **99** were carried out (Table 2.8) with unsuccessful results.

Table 2.7. Attempts for the iodination of compound **98**

Reagent	Halogen source	Conditions	Result
98	NIS, ACN	MW, 10 min, 100°C	Reagent
98	NIS. ACN	MW, 3h, 110°C	Reagent
98	NIS, DCE	Reflux, 8h. Quenched with NaS_2O_3[25]	Reagent
98	NIS, DCE	Reflux, 24h. Quenched with NaS_2O_3	Iodination on Phenyl ring
98	NIS, DCE	MW, 10 min, 100°C	Product decomposition
98	BuLi, NBS	THF, -78°C (45min), RT (2hours)	Reagent

2.1.4.4. Conclusion

Alternative synthesis for the obtention of the *N*1-aryl substituted pyrazlo[3,4-*b*]pyridin-6-ones has been studied.

A first strategy *via* an 6-oxo-2-(1-phenylhydrazinyl)-1,4,5,6-tetrahydropyridine-3-carbonitrile intermediate (**77**) was not successful as such intermediate was not possible to be obtained *via* the reduction of the nitroso intermediate (*N*-(3-cyano-5-methyl-6-oxo-1,4,5,6-tetrahydropyridin-2-yl)-*N*-phenylnitrous amide (**81**)).

In a second attempt, using a Ullman reaction on the unsubstituted pyrazolopyridone, it was possible to obtain the 3-amino-1,5-diphenyl-2,7-dihydro-6*H*-pyrazolo[3,4-*b*]pyridin-6-one (**84**{*3*,*1*,*3*}) isomer despite in low yields (20%).

Finally, a "reverse synthesis" was studied but unfortunately. the alternative synthesis was not possible to be completed as the final product obtained **101** lacked the NH_2 group at position C3, an essential part of the desired N1-aryl substituted derivative **84**{*3*,*1*,*3*}. Further investigation on this field should consider the introduction of the amine group (or a precursor of it) in earlier steps of the synthetic route providing a more general scaffold for N1-aryl substituted pyrazolo[3,4-*b*]pyridine-6-ones.

2.2. Synthesis of a library of pyrazolo[3,4-*b*]pyridin-6-ones as MNK inhibitors

During the studies performed around the pyrazolopyridone scaffold several methodologies were developed with the aim of creating a chemical library to test the biological activity of such compounds. Figure 2.47 summarizes all the methodologies developed during this project and that will be used to create the library of compounds.

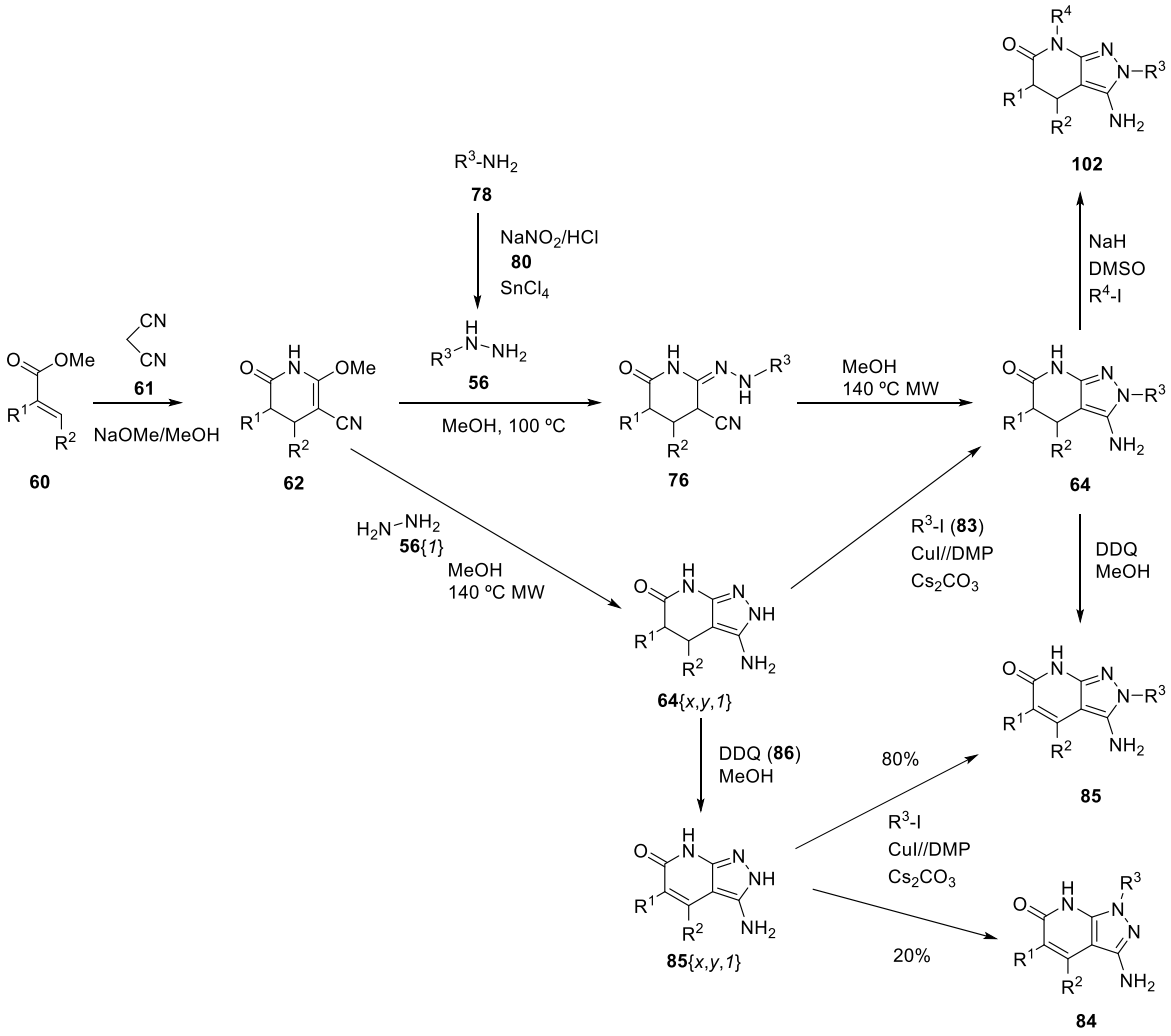

Figure 2.46. Synthetic strategies to modify the pyrazolopyridone scaffold.

The initial bicyclic pyrazolo[3,4-*b*]pyridone structures (**64**) were prepared upon treatment of 2-methoxi-6-oxo-1,4,5,6-tetrahidropyridin-3-carbonitrile intermediates (**62**) with hydrazine or aryl and alkyl substituted hydrazines (**56**) in MeOH. As stated before, this reaction needs a high thermal level that could only be achieved using microwave irradiation in a sealed vial. A general procedure to obtain these compounds included a 30 minutes microwave irradiation at 140 °C using two equivalents of hydrazine for each equivalent of **62**. This methodology was scaled up to 600 mg.

If the thermal level was lower than 140 °C (MeOH reflux) an open intermediate (**76**) was obtained. This intermediate could be converted in the cyclized product by heating it up at 140 °C using microwave irradiation. In some cases, this two-step strategy provided products with a higher purity than the direct cyclization.

In this project the 2-methoxy-6-oxo-1,4,5,6-tetrahydropyridine-3-carbonitriles (**62**) included in Figure 2.47 were used. These compounds were obtained from α,β-unsaturated esters **60** treated with malononitrile (**61**) in NaOMe/MeOH.

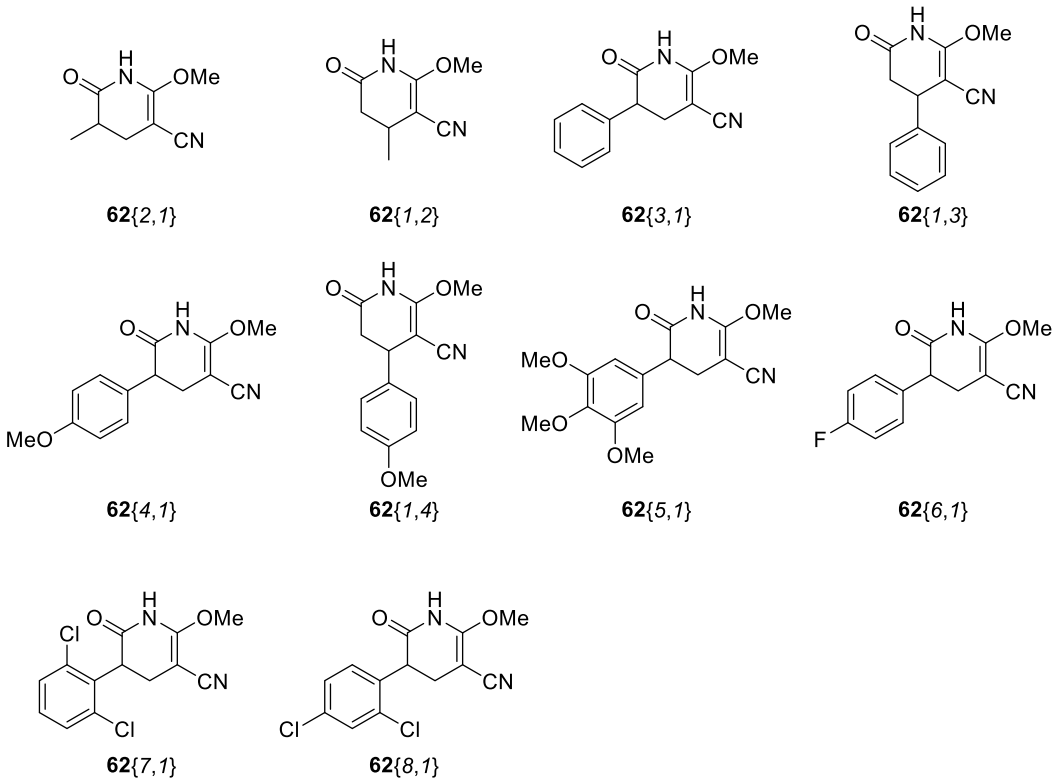

Figure 2.47. 2-methoxy-6-oxo-1,4,5,6-tetrahydropyridine-3-carbonitriles (**62**) synthetized in this project.

For the mechanistic studies, commercial methyl and phenyl hydrazines were used. However, for the preparation of the chemical library of pyrazolopyridones several substituted arylhydrazines (**56)** were required. These arylhydrazines were synthesized from the corresponding anilines using a two-steps process. First, the corresponding aniline (**78**) was treated with 1.2 equivalents of sodium nitrite ($NaNO_2$) in 6M HCl 30 minutes at -10 °C to afford the corresponding diazonium salt **103**. Then, a solution of $SnCl_2 \cdot 2H_2O$ (3 equivalents) in concentrated HCl was added dropwise to precipitate the hydrazine hydrochloride **104**. The salt formed is the best way to store the arylhydrazines (**56**) until needed.[26,27]

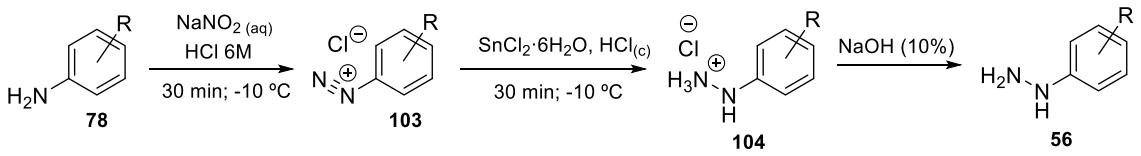

Figure 2.48. Synthesis of arylhydrazines (**56**).

When used to cyclize with the corresponding pyridone **62**, the hydrazine hydrochloride was treated with a basic aqueous solution (10% NaOH or K_2CO_3) and extracted with diethyl ether to obtain the free hydrazine (**56**). In some cases, when the final pyrazolopyridone **64** was not soluble in MeOH, the reaction could be performed *via* a two-steps one-pot methodology stirring the salt with 1 equivalent of a base in MeOH (K_2CO_3 or TEA), filtering the precipitated salts and adding the pyridone (**62**) to the solution for the microwave irradiation. Figure 2.49 includes the hydrazines used in this project.

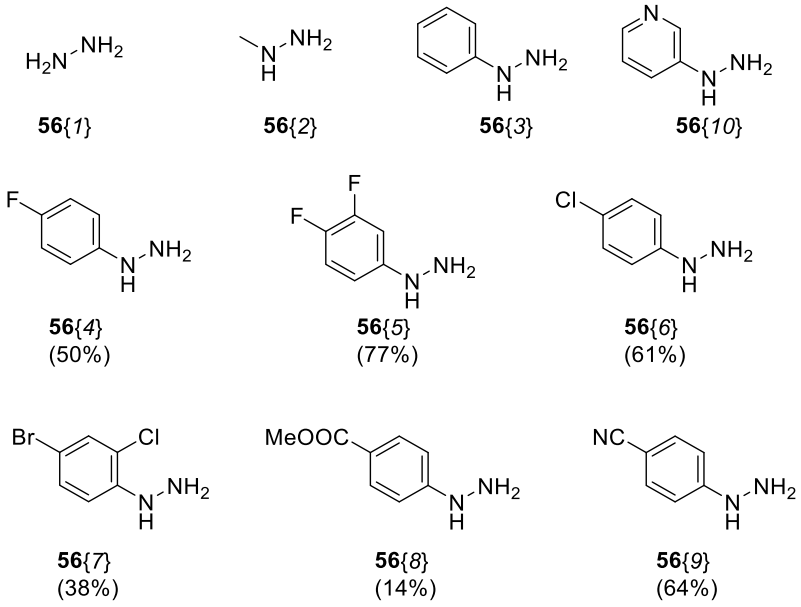

Figure 2.49. Hydrazines used in this project. Values under each molecule indicate the yield from the obtention of the free hydrazine. Molecules with no yield are commercial.

The 2-methoxy-6-oxo-1,4,5,6-tetrahydropyridine-3-carbonitriles (**62**) were cyclized with the different hydrazines (**56**) in MeOH under microwave irradiation (140 °C, 30 min) to obtain a family of pyrazolopyridones. In some cases, the synthesis of the product was performed in two steps to obtain a higher purity, consequently the open intermediate **76** was first isolated (Figure 2.50) after an overnight reaction in MeOH (reflux) and then cyclized at 140 °C using microwave irradiation.

Moreover, the synthesis of the open intermediates **76,** with a wide range of substituents around the central core, confirms the general applicability of the previously described synthetic methodology and demonstrates the proposed reaction mechanism.

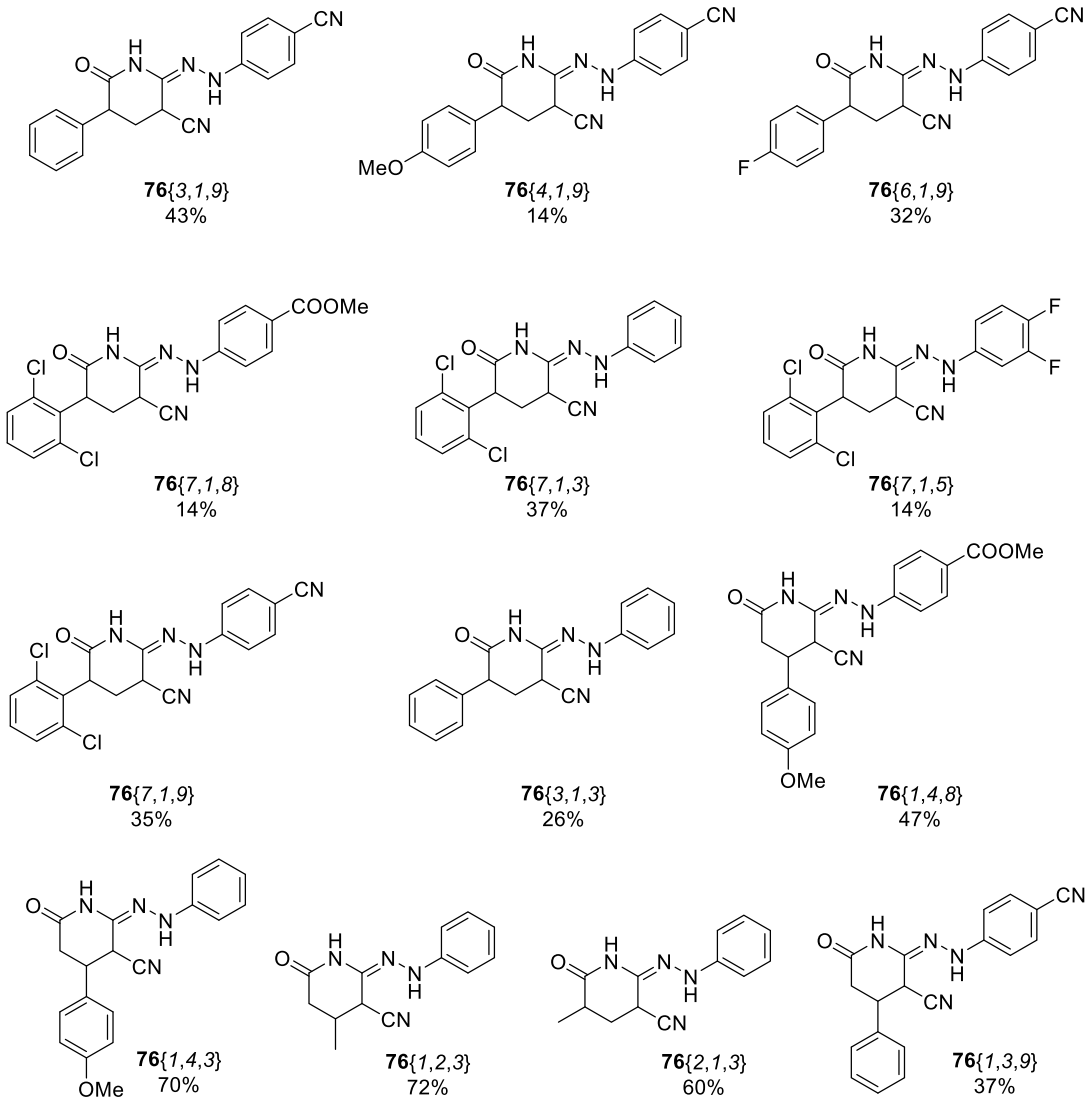

Figure 2.50. Open intermediates (**76**) prepared in this project and the corresponding isolated yields.

Compounds with no substituent in the pyrazole ring increase the number of H-bond donating and accepting groups with the extra NH group and the exposure of the polar front with any steric hindrance. Moreover, with these molecules, the effect of the substituents in the lactam ring can be analysed.

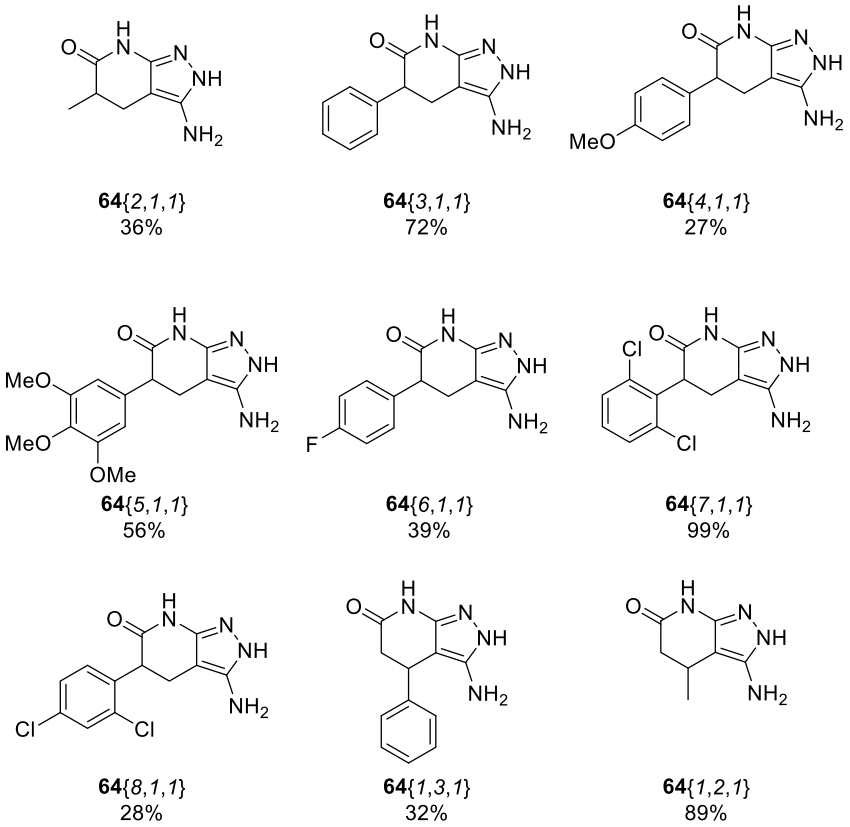

Figure 2.51. Pyrazolo[3,4-*b*]pyridin-6-ones with unsubstituted pyrazole prepared in this project and the corresponding isolated yields.

*N*1 and *N*2-methyl substituted 3-amino-pyrazolo[3,4-*b*]pyridin-6-ones present a more hydrophobic area on the pyrazole moiety with the smallest possible steric hindrance. This extra hydrophobic front points towards different directions in the two different positional isomers.

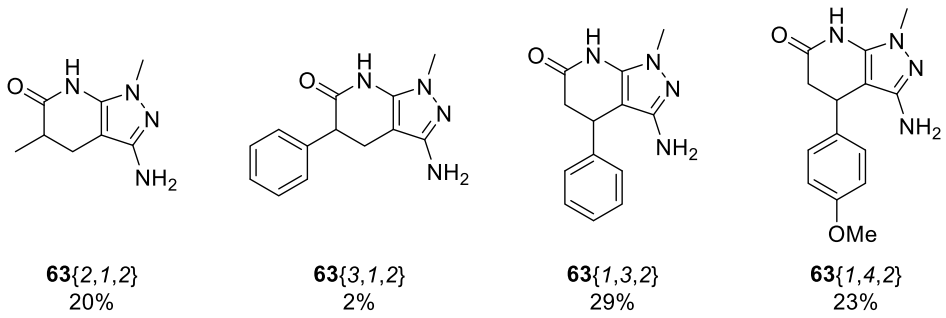

Figure 2.52. *N*1-methyl pyrazolo[3,4-*b*]pyridin-6-ones prepared in this project and the corresponding isolated yields.

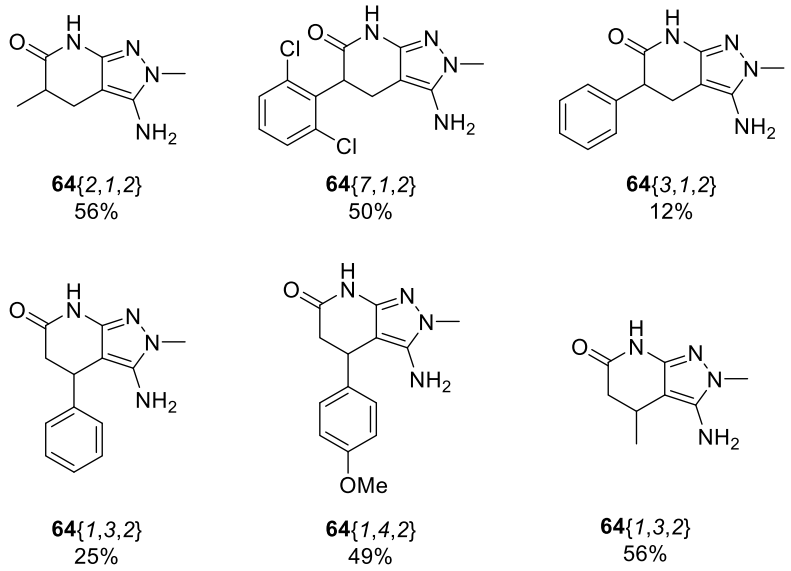

Figure 2.53. *N*2-methyl pyrazolo[3,4-*b*]pyridin-6-ones prepared in this project and the corresponding isolated yields.

*N*2-aryl substituted 3-amino-pyrazolo[3,4-*b*]pyridin-6-ones present two easily modifiable areas that could provide compound selectivity when placing the correct substituents in the correct positions. On one hand, N2-phenyl substituted compounds provide a bulky but planar substituent that can interact with aromatic and aliphatic residues by π-π stacking and can fit in a hydrophobic cleft increasing compound potency and selectivity by guiding the orientation of the drug in the binding site. On the other hand, substituents in the lactam ring could affect compound binding by forming new interactions with the adequate residues. Finally, further substitution of the N2-phenyl ring should allow the formation of specific interaction with residues in the hydrophobic cleft. The correct substitution will provide extra potency and selectivity.

The amount of different possibilities added by these modifications should help us to identify the best combination of substituents and allow and easy and versatile *hit to lead* optimization of the candidates. (Figure 2.54 and Figure 2.55)

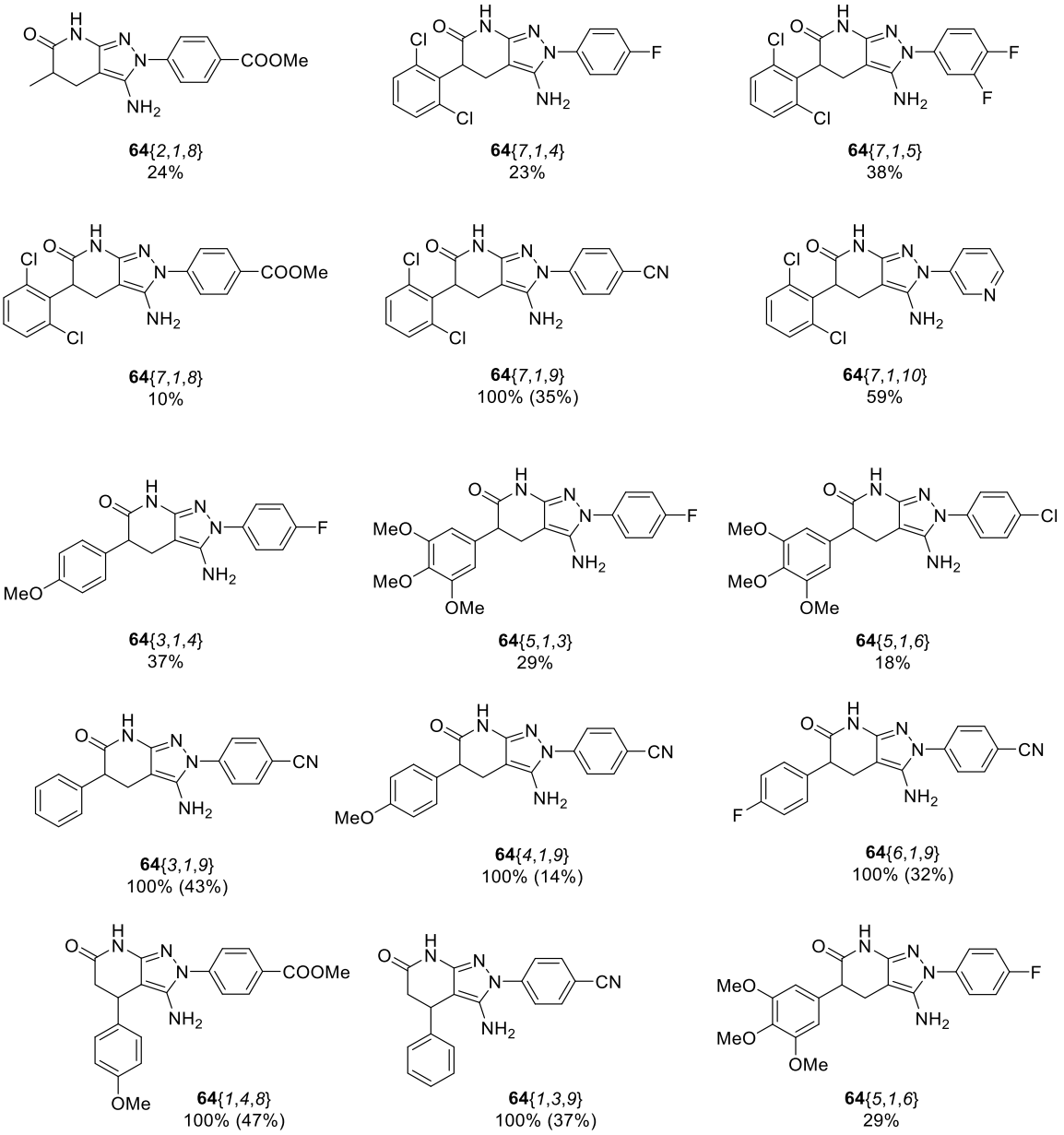

Figure 2.54. *N*2-aryl pyrazolo[3,4-*b*]pyridin-6-ones prepared in this project and the corresponding isolated yields. When two yields are included, the reaction was performed *via* the corresponding open intermediate (**76**) and the first yield corresponds to the cyclization step while the second yield is the global yield for both steps.

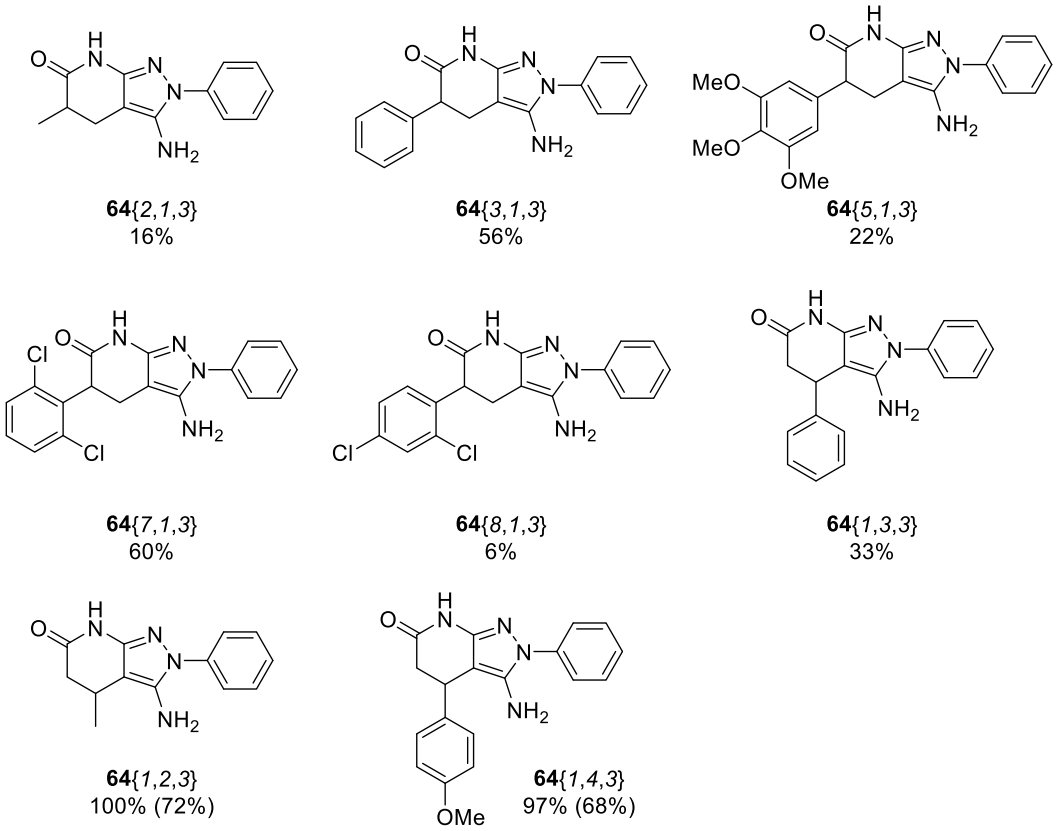

Figure 2.55. *N*2-phenyl pyrazolo[3,4-*b*]pyridin-6-ones prepared in this project and the corresponding isolated yields. When two yields are included, the reaction was performed *via* the corresponding open intermediate (**76**) and the first yield corresponds to the cyclization step while the second yield is the global yield for both steps.

Finally, compounds **64** can be further derivatized by oxidation and methylation.

The methylation of the NH group of the lactam is interesting as it modifies the polar front that the compounds present with a H-bond donor and a H-bond acceptor in the same ring. This front allows the dimerization of the compounds and helps the stacking of the molecules causing the low solubility of these products. For this reason, the methylation increases the solubility of the compounds. (Figure 2.56)

The best procedure to obtain the methylated compounds (**102**) consisted on treating (**64**) with NaH (3 eq) in anhydrous DMSO for 1 hour followed by the addition of MeI (1.1 eq) and stirring overnight at room temperature under Ar atmosphere. The product was then precipitated by the addition of water and filtered.

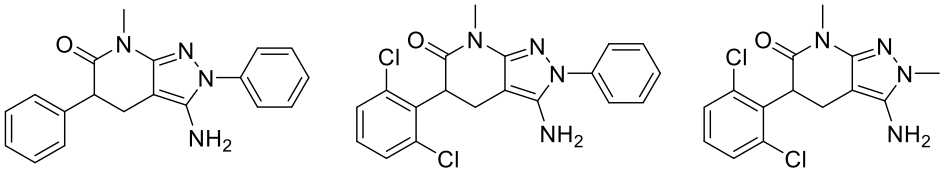

102{*3*,*1*,*3*}
83%

102{*7*,*1*,*3*}
55%

102{*7*,*1*,*2*}
12%

Figure 2.56. Methylated pyrazolo[3,4-*b*]pyridin-6-ones prepared in this project and the corresponding isolated yields.

The oxidation of **64** also modifies the three-dimensional structure of the molecule as it eliminates the chiral centre created by the presence of R^1 and R^2 substituents. This is of importance specially for drug development as it avoids the need of extra considerations about the chirality of the molecule. Moreover, this modification gives a higher planarity to the molecule which can be of interest for the development of ATP competitive drugs. The oxidation of the lactam ring was achieved by treatment of **64** with 1.5 eq. DDQ in MeOH. The reaction conditions are very dependent on the solubility of **64**. For R^3=Ph the reaction is carried out overnight at RT and the final product was filtered and washed with MeOH. However, for R^3=H the reaction needs heating at 100 °C for 3h. The solvent was removed under reduced pressure and the solid was suspended in AcOEt and filtered. With these methodologies, we avoid the use of other solvents described in bibliography (DMF, dioxane, toluene, ...) that yielded uncomplete conversions and presented purification problems. With these solvents, some DDQ remained in the product after filtration and it was necessary to do several washes with 0.5 M NaOH (aq).

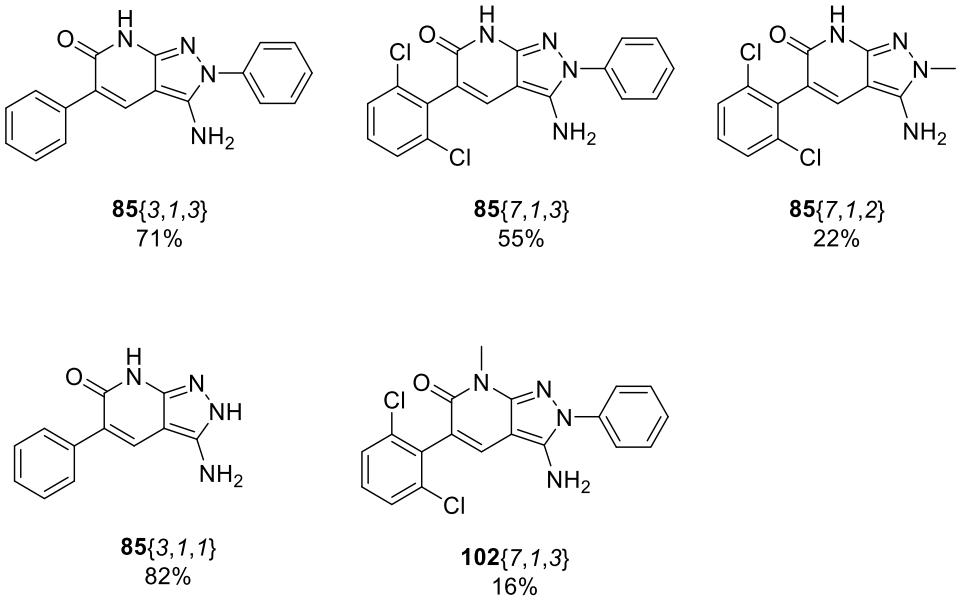

85{*3*,*1*,*3*}
71%

85{*7*,*1*,*3*}
55%

85{*7*,*1*,*2*}
22%

85{*3*,*1*,*1*}
82%

102{*7*,*1*,*3*}
16%

Figure 2.57. Oxidized pyrazolo[3,4-*b*]pyridin-6-ones prepared in this project and the corresponding isolated yields.

2.3. Biological Activity

The family of molecules based on the pyrazolopyridone scaffold is considered of interest due to its similarity with some already described MNK inhibitors such as **CGP57380** (**CGP** from now on) and the thieno[2,3-*d*]pyrimidines described by Teo *et al.*[28]. The different derivatization points of this scaffold provide many opportunities to identify new MNK inhibitors. Moreover, the huge structural diversity that can be obtained from the initial scaffold would allow an easy hit to lead optimization process in the case of a hit identification.

The *in vitro* study of this family of compounds as MNK inhibitors was done at enzymatic and cellular level. On one side, an external company tested the compounds for their ability to inhibit the activity of recombinant MNK kinases *in vitro* (^{33}PanQinase® Activity Assay from Proqinase® (www.proqinase.com)). The assay is based on the measurement of phosphorylation of a model substrate using radiolabeled phosphate (^{33}P) (see Chapter 6). The kinase activity can be determined radiometric and the residual activity after the treatment with the compounds reflects their inhibitory effect.

On the other side, the candidate compounds were tested for their biological activity in different cell lines. To measure their activity towards MNKs, the phosphorylation status of eIF4E (p-eIF4E), a direct target of the kinases, was determined by western blot analysis. Comparison of the levels of phosphorylated eIF4E in cells treated with either the vehicle (DMSO) or the compounds was used to identify those molecules capable of inhibiting the kinase activity of MNKs.

The study of pyrazolopyridones as MNK inhibitors started by testing a first generation of 14 compounds obtained with commercial hydrazines (with a hydrogen, methyl or phenyl group in the pyrazole ring) (Table 2.8)

Table 2.8. Results from the enzymatic radiometric assay performed by Proqinase®. Values indicate the residual activity (%) of kinases MNK1 and MNK2 after treatment with the indicated compounds. Cercosporamide and CGP are known MNK inhibitors used as positive controls

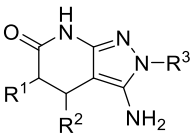

64{*x*,*y*,*z*}

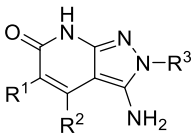

85{*x*,*y*,*z*}

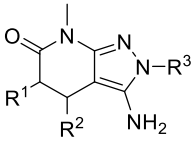

102{*x*,*y*,*z*}

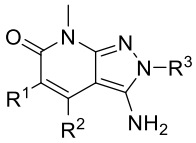

105{*x*,*y*,*z*}

x	R^1
2	Me
3	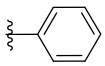
7	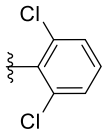

y	R^2
1	H

z	R^3
1	H
2	Me
3	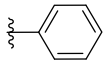

Compound	MNK1	MNK2
Cercosporamide	0	1
CGP	25	59
64{*2*,*1*,*3*}	145	112
64{*3*,*1*,*1*}	133	134
102{*7*,*1*,*3*}	142	99
85{*7*,*1*,*3*}	12	7
105{*7*,*1*,*3*}	8	108
102{*7*,*1*,*2*}	133	27

Compound	MNK1	MNK2
85{*7*,*1*,*2*}	150	112
102{*3*,*1*,*3*}	136	131
85{*3*,*1*,*3*}	145	97
64{*2*,*1*,*1*}	113	123
64{*2*,*1*,*2*}	150	125
64{*7*,*1*,*3*}	8	4
64{*7*,*1*,*2*}	135	110
64{*3*,*1*,*3*}	133	74

The results from the first set of compounds appeared promising, since four of the compounds clearly reduced the activity of at least one of the tested kinases. The family with a dichlorophenyl substitution in R^1 and a phenyl in R^3 seemed to induce a reduction of the kinase activity in both the oxidized and unoxidized forms.

However, when testing these inhibitors in cell-based assays, we could not observe a clear inhibition of MNK1/2 kinases. While the positive control **CGP** clearly reduced the phosphorylation levels of eIF4E, this was not the case for the tested compounds.

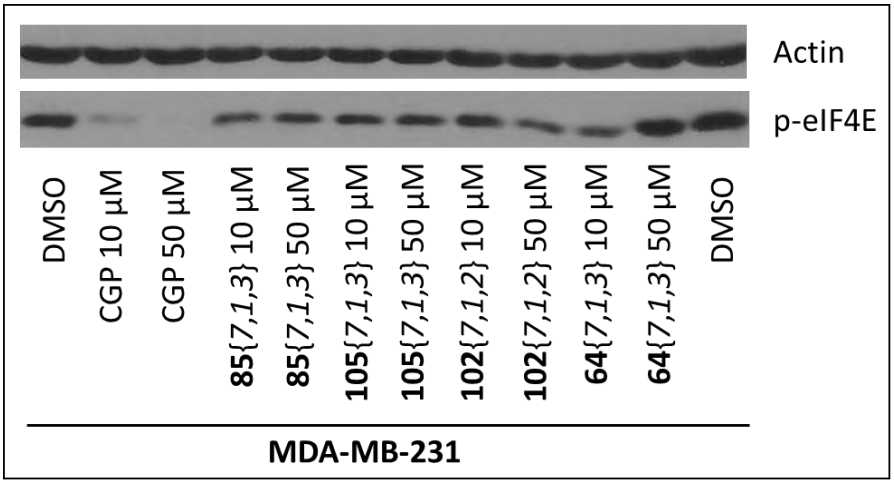

Figure 2.58. Example of the results obtained on the western blots from the first generation of compounds. WB was performed after 24h of treatment at two different concentrations. Final DMSO concentration 0.1%. CGP is a known inhibitor used as a positive control.

In order to explain the failure of these compounds in cell-based assays, different hypotheses were tested.

Product crystallization

Since pyrazolopyridones present an extremely low solubility in water, we first hypothesized that the failure of these compounds might be due to crystallization of the product in the cell culture media.

As a first and fast approach, the corresponding salts (sulfate and maleate) of the compounds were prepared. However, the solubility in water was not significantly increased and no effect was observed in the in the biological activity when p-eIF4E was analyzed by western blot. As there was no clear improvement, the analysis was continued with the parent compounds.

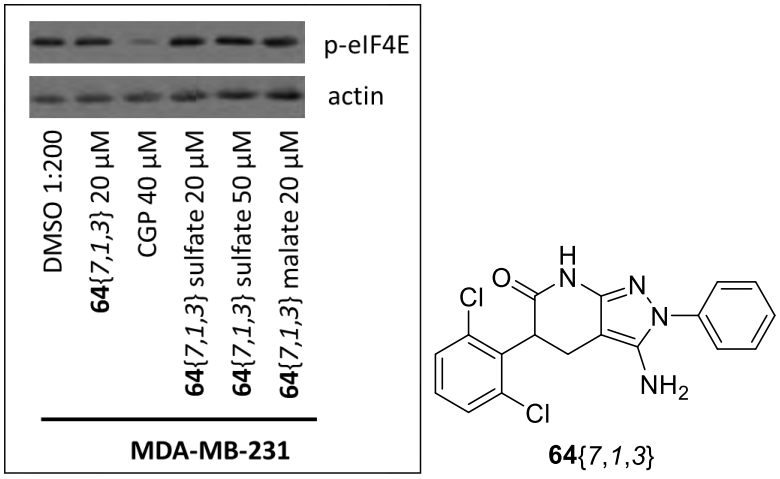

Figure 2.59. Example of the analysis of the salts by western blot. WB was performed after 24h of treatment. Final DMSO concentration 0.1%. CGP is a known inhibitor used as a positive control.

Compounds **85**{*7*,*1*,*3*}, **102**{*7*,*1*,*3*} and **105**{*7*,*1*,*3*} were fluorescent and could be observed under a fluorescence microscope. The presence of 0.1% DMSO (1000x stock) was not enough to ensure the solubility of the compound at the working concentrations (20 µM and 50 µM) and, in some cases, crystals of the compounds could be observed on top of the cells (Figure 2.60). When increasing the amount of DMSO to 0.5% (200x stock), no crystals were observed, and all compounds were completely dissolved in cell culture medium. Therefore, 0.5% DMSO was defined as the optimal concentration, since it ensures compounds solubility without adverse effects on cell viability in most of the tested cell lines. Even though the compounds were completely soluble at the defined DMSO concentration, no inhibitory effect on the MNK kinases could be detected in the western blot analysis.

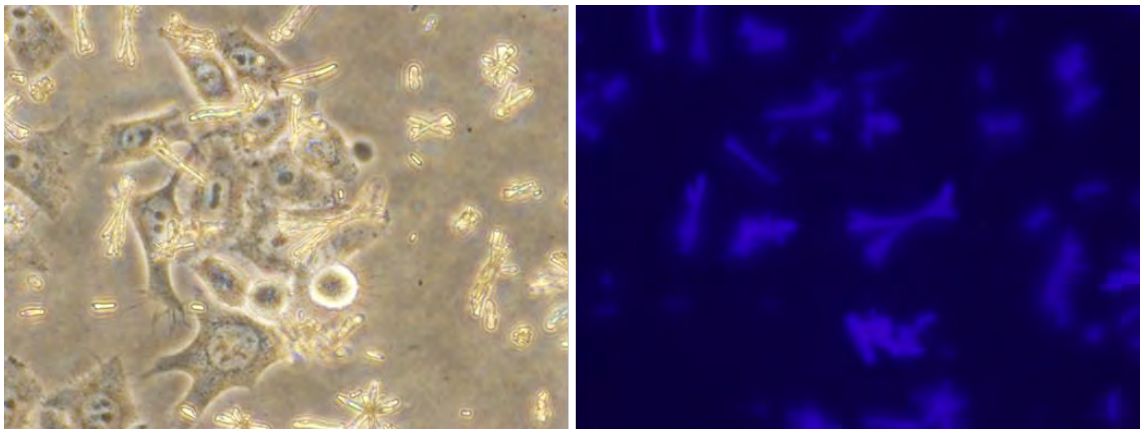

Figure 2.60. Crystals of compound **105**{*7*,*1*,*3*} formed on top of HeLa cells after a 24h 50 µM treatment with 0.1% DMSO.

Kinase reactivation

Despite having ensured that the compounds were soluble in cell culture medium, they still did not display biological activity. We next considered the possibility of a short lifetime of the compound and reactivation of the kinase. To test it, we performed short treatments with the compound in a time course manner (1h, 3h, 6h, 12h, 24h and 48h) in two breast cancer cell lines (MDA-MB-231, MCF7) and a non-tumoral breast line (MCF10). However, in none of the tested conditions, phosphorylation of eIF4E was significantly affected (Figure 2.61).

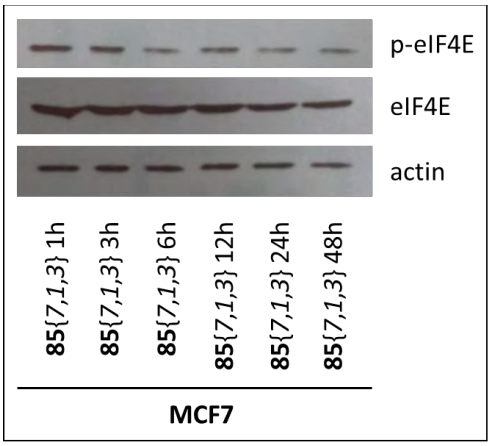

Figure 2.61. Example of the time course analysis of compound **85**{*7,1,3*} by western blots. WB was performed at 20 μM. Final DMSO concentration 0.5%.

Low membrane permeability

An alternative explanation for the inactivity of the compounds in cell- based experiments would be their inability to cross the cell membrane. In order to overcome this putative limitation, we employed two strategies: (1) mild detergent treatment to increase the permeability of the cell membrane and (2) encapsulating the compound in nanoparticles.

To increase membrane permeability, cells were co-treated with the compound and various concentrations (0.1% to 0.01%) of triton-X100.[29] This detergent should increase permeability of the cell membrane to permit entry of compound in the cytosol. However, no improvement could be observed in the cases of co-treatment. (Figure 2.62)

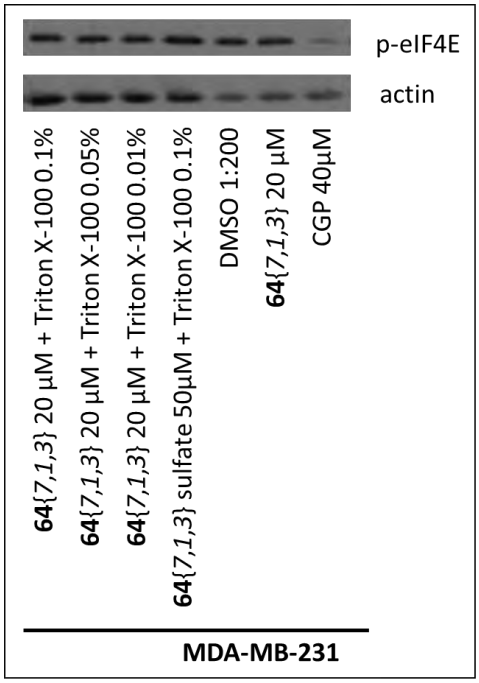

Figure 2.62. Example of the treatment of MDA-MB-231 cells with compound **64**{*7,1,3*} and triton X-100 to permeabilize the membrane. WB performed after 24h of treatment. Final DMSO concentration 0.5%. Triton X-100 was shown to be non-toxic at 0.5% (data not shown). CGP is a known inhibitor used as a positive control.

Following this idea, compound **64**{*7,1,3*} was encapsulated in PLGA nanoparticles and niosomes to facilitate cell permeability (Annex 2). Compound encapsulation was performed at the group of Dr. Manuel Arruebo (Department of Chemical Engineering, Aragon Nanoscience Institute, Zaragoza (Spain)) using their optimized encapsulation methods[30–32]. Besides the successful encapsulation of the compounds in nanoparticles, no effect on the activity of MNK1/2 kinase activity could be observed when tested in the four breast cancer cell lines MDA-MB-231, MCF7, MDA-MB-468 and BT-549 (Annex 2).

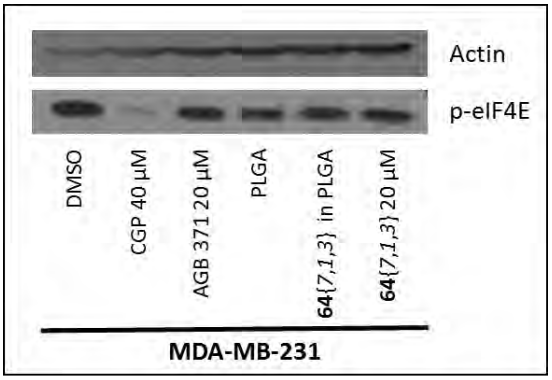

Figure 2.63. Example of the treatment of MDA-MB-231 cells with compound **64**{*7,1,3*} encapsulated in PLGA. AGB371 corresponds to a compound from a different project. WB performed after 24h of treatment. Final DMSO concentration 0.5%. CGP is a known inhibitor used as a positive control.

Cell line selectivity

Lastly we considered cell line specific effects of MNK inhibitors as described by others.[33–35] As some leukemia cell lines were reported to be more sensitive to the inhibition of MNK1/2, the compounds were tested in MV4-11 cells, derived from a case of acute myeloid leukemia. Compound **106**, described to be active towards MNK1/2 in this cell line, was synthetized as described by Diab *et al.*[33] and included as an additional positive control in the cell culture based assays. Both controls (**CGP57380** and **106**) showed activity in the MV4-11 cells but no effect from **64**{*7*,*1*,*3*} was observed. As expected, compound **106** was not effective on other tested cell lines such as MDA-MB-231, MFC7, MDA-MB-468, BT-549, HeLa or A549 (Annex 2).

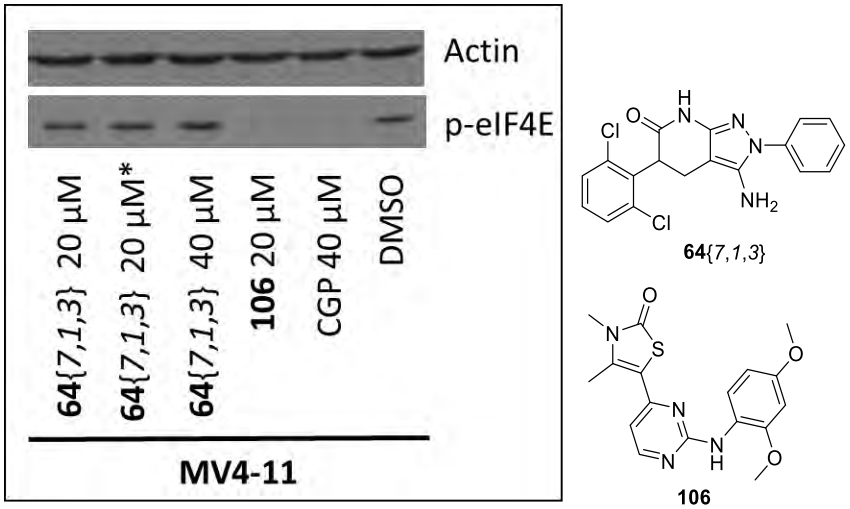

Figure 2.64. Treatment of MV4-11 cells with compounds **64**{*7*,*1*,*3*} and **106**. WB performed after 24h of treatment. Final DMSO concentration 0.5% except for * with a final concentration of 0.1%.

Being unable to achieve any biological activity of this compounds, a second set of pyrazolo[3,4-*b*]pyridone derivatives was synthesized and tested first in the kinase assay of Proqinase®. Surprisingly, compound **64**{*7*,*1*,*3*}, the most active product according to the initial test, did not show any activity. When comparing the test conditions of the first and the second set of assays at Proqinase®, we realized that some methodological changes had been introduced. While the effect of these changes remains unclear, the results of the second kinase assay are in line with the data obtained in cell-based experiments. It can therefore be concluded that the results obtained during the second testing at Proqinase® are correct and the first results were a false positive.

Table 2.9. Results from the second enzymatic radiometric assay performed by Proqinase ®. Values indicated as residual activity (%) of kinases MNK1 and MNK2 after treatment with the indicated compounds (10µM).

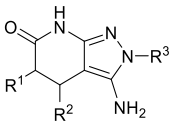

64{*x*,*y*,*z*}

x	R^1		y	R^2		z	R^3	
1	H	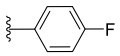	1	H	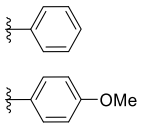	1	H	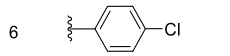
2	Me		2	Me		2	Me	
3		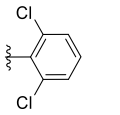	3			3		
4	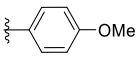		4			4	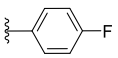	
5	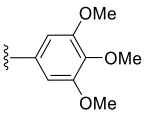					5	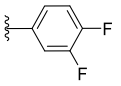	

Compound	MNK1	MNK2
106	55	42
64{*7*,*1*,*4*}	131	109
64{*7*,*1*,*10*}	103	70
64{*8*,*1*,*3*}	144	102
64{*7*,*1*,*8*}	84	68
64{*7*,*1*,*9*}	45	48
64{*6*,*1*,*1*}	88	103
64{*4*,*1*,*1*}	105	107
64{*5*,*1*,*1*}	88	97
64{*1*,*3*,*2*}	90	92

Compound	MNK1	MNK2
64{*1*,*3*,*3*}	89	98
64{*2*,*1*,*8*}	88	85
64{*5*,*1*,*5*}	111	73
64{*8*,*1*,*1*}	88	95
64{*5*,*1*,*3*}	105	108
64{*7*,*1*,3}	92	97
64{*5*,*1*,*6*}	90	107
64{*7*,*1*,*5*}	117	64
64{*4*,*1*,*4*}	86	98
64{*1*,*4*,*3*}	86	94

In the second round of testing at Proqinase®, two compounds displayed a mild inhibition of MNKs being one of them the positive control **106**. Four compounds reduced the residual activity of MNK2 by 30%. However, taken into consideration, that the tests were performed at concentrations of 10 µM, the potency of this inhibitors appears rather low. In line with this, even the most active compound in the *in vitro* kinase assay (**64**{*7*,*1*,*9*}), did not show inhibitory effect on MNK activity in any of the tested cell lines (MDA-MB-231, MCF7, MDA-MB-468, BT-549 and MV4-11).

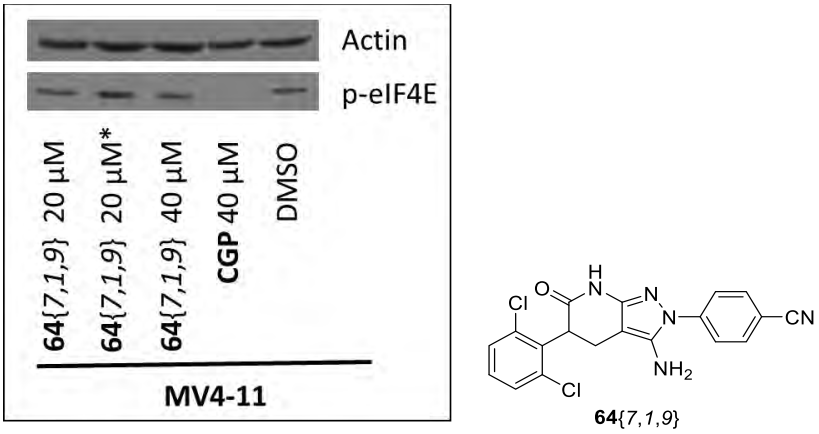

Figure 2.65. Treatment of MV4-11 cells with compound **64**{*7*,*1*,*9*}. WB performed after 24h of treatment. Final DMSO concentration 0.5% except for * with a final concentration of 0.1%. CGP is used as a positive control.

In order to improve the biological activity of the compound **64**{*7*,*1*,*9*}, several derivatives were synthesized as a third set of compounds and tested kinase assays at Proqinase®. As a result of this study, none of the tested compounds showed significant activity as MNK inhibitors (Table 2.10) and even the previously observed activity for **64**{*7*,*1*,*9*} was reduced. Parallel testing of some of those compounds in cell-based experiments did not reveal any significant inhibitory effect towards MNK1/2 confirming the obtained results (Figure 2.66).

Table 2.10. Results from the third enzymatic radiometric assay performed by Proqinase ®. Values indicated as residual activity (%) of kinases MNK1 and MNK2 after treatment with the indicated compounds (10 µM). CGP and cercosporamide are used as a positive controls.

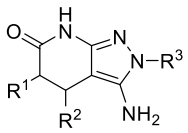

64{*x*,*y*,*z*}

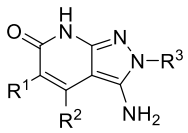

85{*x*,*y*,*z*}

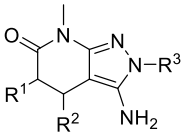

102{*x*,*y*,*z*}

x	R^1		y	R^2		z	R^3	
1	H	6	1	H	1	3		3
3		7	3		3	8		8
4			4		4	9		9

Compound	MNK1	MNK2
64{*7*,*1*,3}	106	104
85{*7*,*1*,3}	115	103
64{*1*,*4*,9}	99	101
64{*6*,*1*,9}	106	95
64{*4*,*1*,9}	101	98
64{*1*,3,9}	114	104
64{*1*,4,8}	96	99

Compound	MNK1	MNK2
64{*3*,*1*,9}	117	99
64{*7*,*1*,9}	79	85
85{*1*,3,3}	81	126
102{*7*,*1*,3}	95	106
106	60	38
cercosporamide	6	1
CGP	21	39

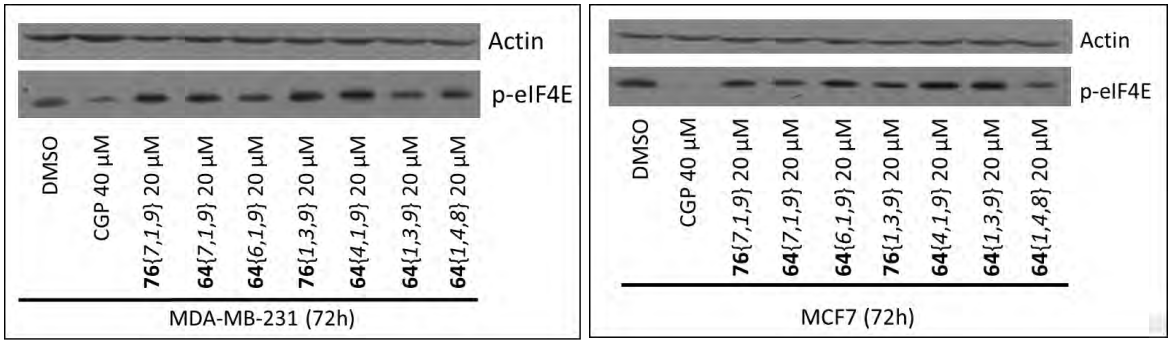

Figure 2.66. Treatment of MDA-MB-231 and MCF7 cells with some compounds from the last set. WB performed after 72h of treatment. Final DMSO concentration 0.5%. CGP is a known inhibitor used as a positive control.

Finally, we aimed at determining the IC_{50} values of some of those compounds to be able to compare them to the described MNK inhibitors **CGP57380** and **106**. We choose the compounds **85**{*7*,*1*,*3*}, **102**{*7*,*1*,*3*}, **64**{*7*,*1*,*3*} and **64**{*7*,*1*,*9*} which have shown inhibition of MNK1 or MNK2 in at least one of the measurements at Proqinase®. As describe above, the inhibitors only displayed a mild activity at 10 µM and further increase of the concentration was not possible due to solubility issues. As at this concentration not even 50% of inhibition could be observed for most of the compounds, the IC_{50} values were determined based on mathematical approximations (Table 2.11).

The combination between the water solubility problems presented by these compounds and the IC_{50} values, close to the maximum possible concentration, could be an explanation for the variability in the obtained results, especially for **64**{*7*,*1*,*9*}. Particularly, the crystallization/precipitation problem might cause major changes in the final concentrations applied and since working close to the solubility border, any small changes in the concentration (caused for example by weighting errors, solvent evaporation, etc.) might result in major changes in the outcome of the results.

Table 2.11. IC_{50} values measured by Proqinase®

Compound	MNK1	MNK2
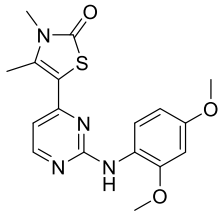 **106**	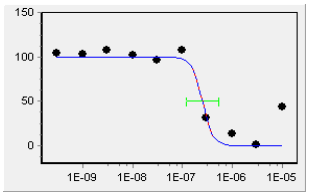 $IC_{50} = 2.5 \cdot 10^{-7}$M	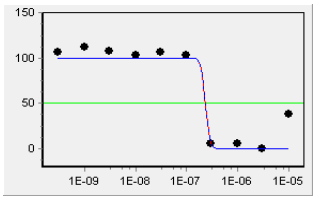 $IC_{50} = 2.32 \cdot 10^{-7}$ M
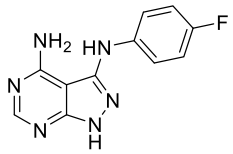 **CGP**	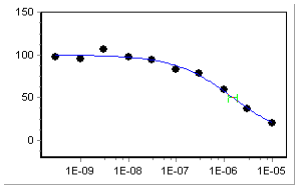 $IC_{50} = 1.52 \cdot 10^{-6}$ M	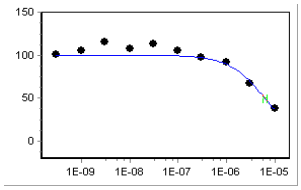 $IC_{50} = 6.27 \cdot 10^{-6}$ M
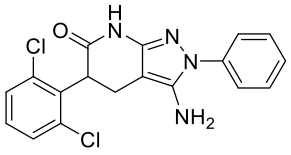 **64**{*7,1,3*}	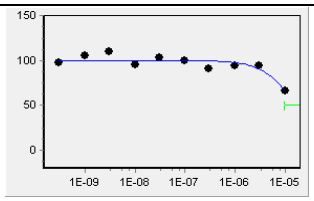 $IC_{50} = 1.71 \cdot 10^{-5}$ M	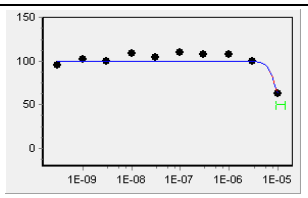 $IC_{50} = 1.13 \cdot 10^{-5}$ M
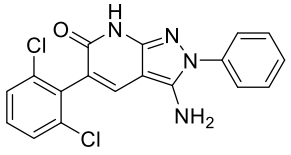 **85**{*7,1,3*}	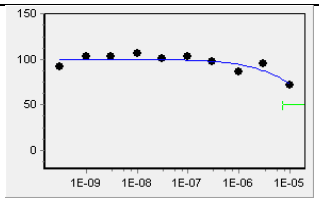 $IC_{50} = 3.73 \cdot 10^{-5}$ M	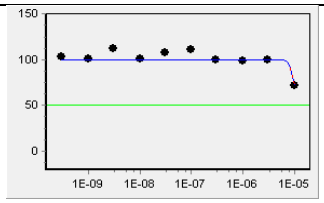 $IC_{50} = 1.11 \cdot 10^{-5}$ M
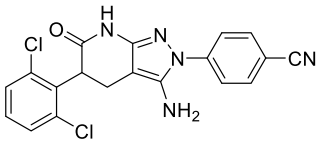 **64**{*7,1,9*}	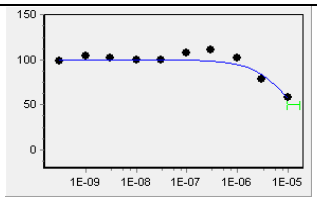 $IC_{50} = 1.32 \cdot 10^{-5}$ M	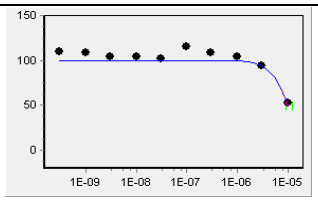 $IC_{50} = 1.05 \cdot 10^{-5}$ M

Finally, the family of *N*1-aryl substituted pyrazolo[3,4-*b*]pyridin-6-ones was also tested to evaluate whether the lack of the NH_2 group or the different position of the substituent on the pyrazole ring had an effect on the activity. The results from both, the enzymatic assay (Table 2.12) and the cell-based *in vitro* assay (Figure 2.67) did not indicate any interesting activity.

Table 2.12. Radiometric assay performed by Proqinase ® on the N1-aryl substituted compounds (10 µM). Values indicated as residual activity (%) of kinases MNK1 and MNK2 after treatment with the indicated compounds.

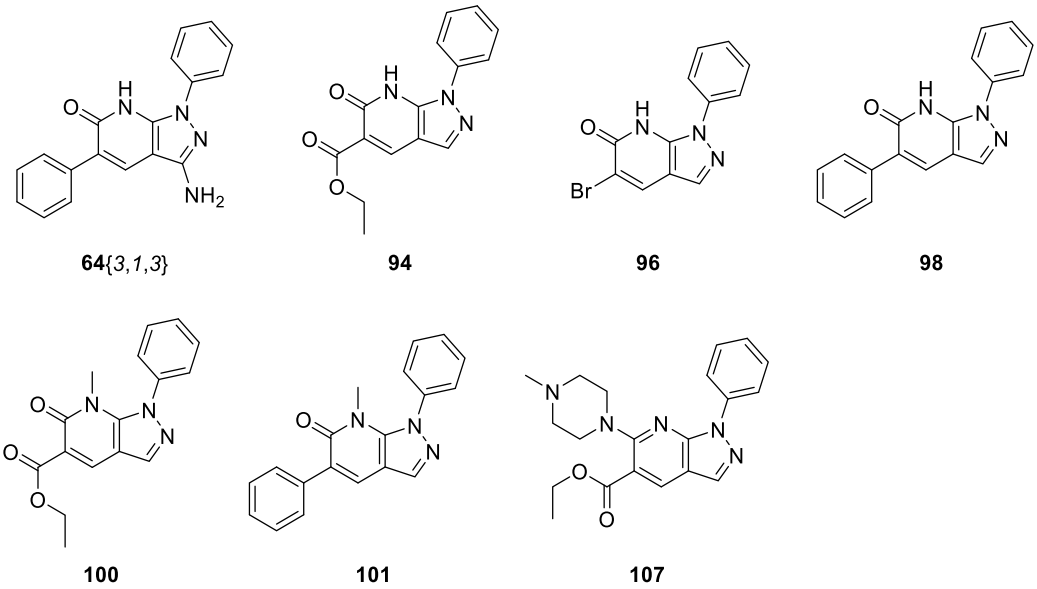

Compound	MNK1	MNK2
94	89	96
100	95	102
96	109	94
98	99	105
101	91	111
64{*3*,*1*,*3*}	95	108

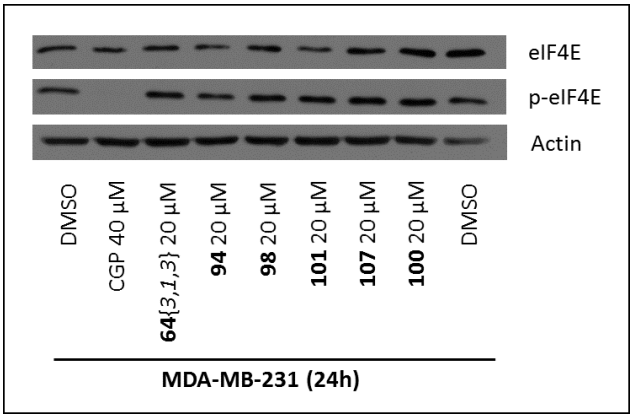

Figure 2.67. Treatment of MDA-MB-231 cells the N1-aryl substituted compounds. WB performed after 24h of treatment. Final DMSO concentration 0.5%. CGP is used as a positive control.

2.4. Conclusion

The study of the family of pyrazolopyridones as MNK inhibitors was hampered by several technical problems during the study. Most variable within these results was the inhibitory effect determined by the kinase assays. To verify these results independently, the assays were finally repeated at a second company. As a result, no significant inhibition of MNKs could be detected for the tested compounds (Annex 2). Some compounds showed variable activity values in the different assays that seem to be caused by the low solubility of the products. However, as the compounds did not present activity in cell-based assays, they were considered as inactive.

During the development of this family of compounds, it appeared in several instances, that results obtained in the *in vitro* kinase assays did not correlate with the activity of the compound in cell-based assays. As this is not a unique problem to the inhibitors tested in the project, it is in general recommended to analyze small molecule inhibitors by both techniques in parallel if possible. As presented here, the results of the kinase assays were complemented by *in vitro* analysis of the inhibition of eIF4E phosphorylation by western blot in different cell lines.

Unfortunately, despite all the work and precautionary measures taken during this study, it was not possible to identify a molecule presenting *in vitro* activity in any of the tested cell lines. For this reason, this family of compounds was discarded.

2.5. References

1. Komarova, E. S., Makarov, V. A., Granik, V. G. & Párkányi, C. Synthesis of Pyrazolo[3,4-b]pyridin-6-ones. *J. Heterocycl. Chem.* **49,** 969–998 (2012).
2. K. Dodiya, D., R. Trivedi, A., B. Kataria, V. & H. Shah, V. Advances in the Synthesis of Pyrazolo[3,4-b]Pyridines. *Curr. Org. Chem.* **16,** 400–417 (2012).
3. Falcó, J. L. *et al.* Design, synthesis and biological activity of acyl substituted 3-amino-5-methyl-1,4,5,7-tetrahydropyrazolo[3,4-b]pyridin-6-ones as potential hypnotic drugs. *Eur. J. Med. Chem.* **40,** 1179–1187 (2005).
4. Martínez-Teipel, B. *et al.* 2-Methoxy-6-oxo-1,4,5,6-tetrahydropyridine-3-carbonitriles: Versatile Starting Materials for the Synthesis of Libraries with Diverse Heterocyclic Scaffolds. *J. Comb. Chem.* **7,** 436–448 (2005).
5. Bou-Petit, E. *et al.* An Unequivocal Synthesis of 2-Aryl Substituted 3-Amino-2,4,5,7-tetrahydro-6 H -pyrazolo[3,4- b]pyridin-6-ones. *ChemistrySelect* **2,** 3668–3672 (2017).
6. Grosjean, C. *et al.* Product identification and distribution from the oscillatory versus non-oscillatory palladium(II) iodide-catalysed oxidative carbonylation of phenylacetylene. *J. Mol. Catal. A Chem.* **284,** 33–39 (2008).
7. Cazorla, R. P. de la B. Disseny, síntesi i avaluació biològica d'inhibidors potencials de les etapes inicials del cicle de replicació del VIH. (IQS, Universitat Ramon Llull, 2010).
8. Galve, I. *et al.* Synthesis of 2-arylamino substituted 5,6-dihydropyrido[2,3-d]pyrimidine-7(8H)-ones from arylguanidines. *Mol. Divers.* **16,** 639–649 (2012).
9. Rodrigues-Santos, C. E. & Echevarria, A. Convenient syntheses of pyrazolo[3,4-b]pyridin-6-ones using either microwave or ultrasound irradiation. *Tetrahedron Lett.* **52,** 336–340 (2011).
10. Camarasa, M., Barnils, C., Puig de la Bellacasa, R., Teixidó, J. & Borrell, J. I. A new and practical method for the synthesis of 6-aryl-5,6-dihydropyrido[2,3-d]pyrimidine-4,7(3H,8H)-diones. *Mol. Divers.* **17,** 525–536 (2013).
11. Frisch, M. J. *et al.* Gaussian (G09). Wallingford CT (2009).
12. Ozawa, T. A New Method of Analyzing Thermogravimetric Data. *Bull. Chem. Soc. Jpn.* **38,** 1881–1886 (1965).
13. Kissinger, H. E. Reaction Kinetics in Differential Thermal Analysis. *Anal. Chem.* **29,** 1702–1706 (1957).
14. T. Akahira & T. Sunose. *Trans. Joint Convention of Four Electrical Institutes*. **246,** (1969).
15. Rodríguez, A. M. *et al.* Influence of Polarity and Activation Energy in Microwave-Assisted Organic Synthesis (MAOS). *ChemistryOpen* **4,** 308–317 (2015).
16. Li, P. *et al.* Discovery of a Tetracyclic Quinoxaline Derivative as a Potent and Orally Active Multifunctional Drug Candidate for the Treatment of Neuropsychiatric and Neurological Disorders. *J. Med. Chem.* **57,** 2670–2682 (2014).

17. Zhou, B. *et al.* Rh(III)-Catalyzed Intramolecular Redox-Neutral or Oxidative Cyclization of Alkynes: Short, Efficient Synthesis of 3,4-Fused Indole Skeletons. *Org. Lett.* **16,** 3900–3903 (2014).

18. Patil, M., Hunoor, R. & Gudasi, K. Transition metal complexes of a new hexadentate macroacyclic N2O4-donor Schiff base: Inhibitory activity against bacteria and fungi. *Eur. J. Med. Chem.* **45,** 2981–2986 (2010).

19. Banert, K., Hagedorn, M. & Schlott, J. Synthesis and Reactions of the First Allenyl Azo Compounds. *Chem. Lett.* **32,** 360–361 (2003).

20. Borikar, S. P. & Paul, V. N -Nitrosation of Secondary Amines Using p -TSA-$NaNO_2$ as a Novel Nitrosating Agent Under Mild Conditions. *Synth. Commun.* **40,** 654–660 (2010).

21. Hayes, B. T. & Stevens, T. S. Reduction of Nitrosamines to Hydrazines. *J. Chem. Soc.* 1088–1089 (1970).

22. Chaudhary, P., Gupta, S., Sureshbabu, P., Sabiah, S. & Kandasamy, J. A metal free reduction of aryl-N-nitrosamines to the corresponding hydrazines using a sustainable reductant thiourea dioxide. *Green Chem.* **18,** 6215–6221 (2016).

23. Beyer, A., Castanheiro, T., Busca, P. & Prestat, G. Copper(I)/Copper(II)-Assisted Tandem Catalysis: The Case Study of Ullmann/Chan-Evans-Lam N 1 ,N 3 -Diarylation of 3-Aminopyrazole. *ChemCatChem* **7,** 2433–2436 (2015).

24. Pettus, L. H. *et al.* Discovery and Evaluation of 7-Alkyl-1,5-bis-aryl-pyrazolopyridinones as Highly Potent, Selective, and Orally Efficacious Inhibitors of p38α Mitogen-Activated Protein Kinase. *J. Med. Chem.* **53,** 2973–2985 (2010).

25. Cross, J. B. *et al.* Discovery of Pyrazolopyridones as a Novel Class of Gyrase B Inhibitors Using Structure Guided Design. *ACS Med. Chem. Lett.* **7,** 374–378 (2016).

26. Yang, W. *et al.* Discovery of 4-Aryl-7-Hydroxyindoline-Based P2Y 1 Antagonists as Novel Antiplatelet Agents. *J. Med. Chem.* **57,** 6150–6164 (2014).

27. Minkkilä, A. *et al.* Screening of Various Hormone-Sensitive Lipase Inhibitors as Endocannabinoid-Hydrolyzing Enzyme Inhibitors. *ChemMedChem* **4,** 1253–1259 (2009).

28. Teo, T. *et al.* An integrated approach for discovery of highly potent and selective Mnk inhibitors: Screening, synthesis and SAR analysis. *Eur. J. Med. Chem.* **103,** 539–550 (2015).

29. Jamur, M. C. & Oliver, C. Permeabilization of Cell Membranes in *Clinical Endocrinology* **51,** 63–66 (2010).

30. Garcia-Salinas, S., Himawan, E., Mendoza, G., Arruebo, M. & Sebastian, V. Rapid on-Chip Assembly of Niosomes: Batch versus Continuous Flow Reactors. *ACS Appl. Mater. Interfaces* **10,** 19197–19207 (2018).

31. Mendoza, G. *et al.* Near infrared dye-labelled polymeric micro- and nanomaterials: in vivo imaging and evaluation of their local persistence. *Nanoscale* **10,** 2970–2982 (2018).

32. Arruebo, M. *et al.* Continuous synthesis of drug-loaded nanoparticles using microchannel emulsification and numerical modeling: effect of passive mixing. *Int. J. Nanomedicine* **11,** 3397–3416 (2016).

33. Diab, S. *et al.* Discovery of 5-(2-(phenylamino)pyrimidin-4-yl)thiazol-2(3H)-one derivatives as potent Mnk2 inhibitors: synthesis, SAR analysis and biological evaluation. *ChemMedChem* **9,** 962–972 (2014).

34. Teo, T. *et al.* An integrated approach for discovery of highly potent and selective Mnk inhibitors: Screening, synthesis and SAR analysis. *Eur. J. Med. Chem.* **103,** 539–550 (2015).

35. Teo, T. *et al.* Pharmacologic Inhibition of MNKs in Acute Myeloid Leukemia. *Mol. Pharmacol.* **88,** 380–389 (2015).

CHAPTER 3

N-acetyl and *N*-benzoyl substituted 3-amino-pyrazolo[3,4-*b*]pyridin-6-ones as MNK inhibitors

---

3.1 Benzoylation of the pyrazole ring. Kinetic *vs*. thermodynamic control

3.1.1 Introduction

Pyrazolo[3,4-*b*]pyridin-6-ones with no substitution on the pyrazole ring can be further derivatized by different nucleophilic substitutions. As mentioned in the previous chapter, reactions catalyzed by metals, as the Ullman reaction, can be used to introduce new substituents on the pyrazole ring at the end of the synthesis.

A second option to derivatize these molecules would be acylation, such as the benzoylation and acetylation. In principle, these molecules have 3 points of possible acylation: the lactam NH, the 3-NH_2 group and the pyrazole NH group. The NH group on the pyrazole ring is expected to be the most reactive point and, therefore, to be the easiest substitution point. Previous studies performed in the group by Falco *et al.*[1] support this hypothesis. However, as discussed in Chapter 2, the acylation of the pyrazole ring can also lead to two different isomers: N1 and *N*2-acyl substituted 3-amino-pyrazolo[3,4-*b*]pyridin-6-ones (**109** and **110**).

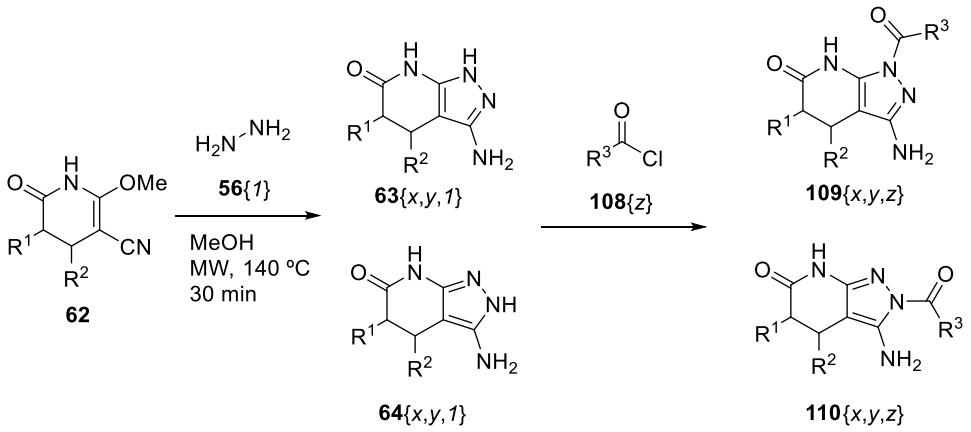

Figure 3.1. Possible structures from the acylation of 3-amino-pyrazolo[3,4-*b*]pyridin-6-ones

3.1.2 Study of the benzoylation of 3-amino-pyrazolo[3,4-*b*]pyridin-6-ones

For the initial study, compound **63**/**64**{*1*,*2*,*1*} (R^1=H, R^2=Me) was selected to react with benzoyl chloride (**108**{*3*}). By using the general procedure described by Falco *et al.*[1], where the starting material was stirred with 1 equivalent of benzoyl chloride and 1.5 eq. of TEA at room temperature for 24h in THF, a major compound was obtained. However, the reaction crude showed a small amount of a second product with equivalent signals. (Figure 3.2) Due to the tautomeric nature of the starting pyrazolepyridone, it was possible that both isomers (N1 and N2 substituted) had been obtained. The fact that a second isomer was observed, although in low amount, was of interest as this behavior had not been seen in the previous reactions carried out with 3-amino-pyrazolo[3,4-*b*]pyridin-6-ones **63**/**64**.

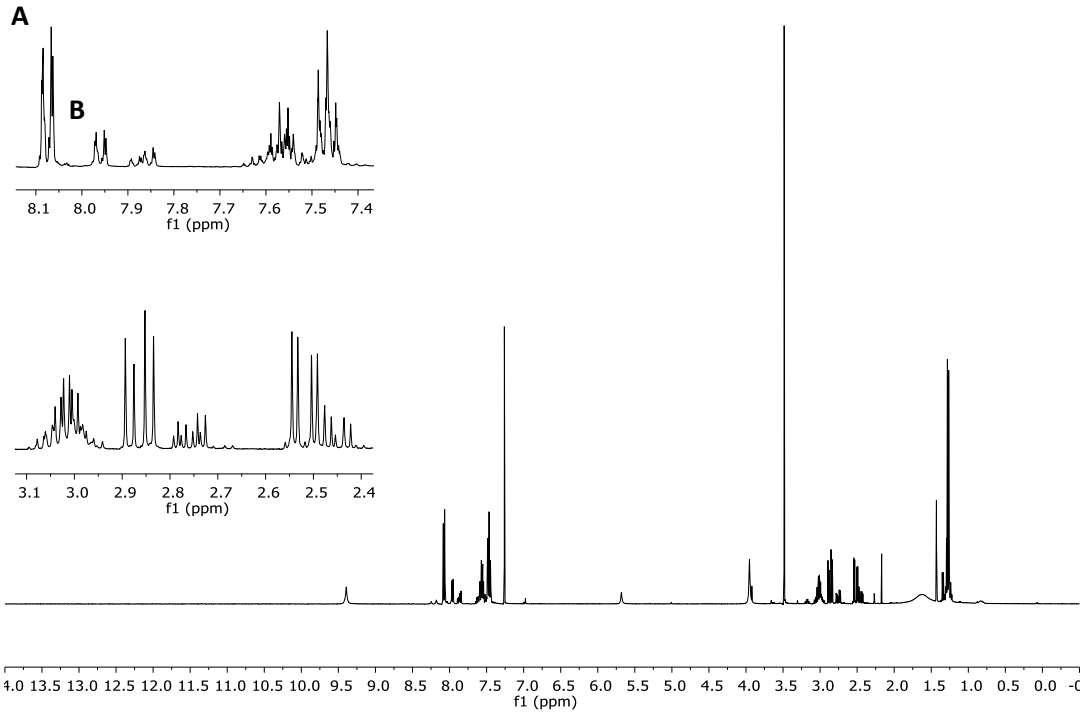

Figure 3.2. ^{1}H-NMR spectra of the reaction crude showing the presence of two compounds. Ampliations show the duplication of signals observed in the both aromatic (benzoyl protons) and the aliphatic (lactam protons) parts. A and B indicate the multiplets used for the random assignment of isomers.

In order to understand if, in this case, the temperature of the reaction could control the formation of the two compounds, the reaction was repeated at different temperatures ranging from 25 °C to 200 °C. The reaction crude was analyzed after heating at each temperature showing the formation of two different products with varying proportions depending on the reaction temperature.

Two different heating methods were studied: microwave irradiation and conventional heating. For temperatures lower than 100 °C both methods were tested obtaining similar proportions of each product independently of the heating method. Temperatures of 120 °C or higher were only reached by using microwave irradiation and working in a sealed vial. Moreover, for the 25 °C, 40 °C and 60 °C experiments, using THF or dioxane as solvent showed equivalent results.

When the reaction crudes were analyzed, two sets of equivalent signals were identified. Both compounds presented the expected signals: a doublet corresponding to the methyl group, the three aliphatic protons of the lactam ring and the aromatic protons confirming that the benzoylation did take place. At this point, it was not possible to assign the structure of each isomer. For this reason, letters **A** and **B** were assigned to the isomers according to the aromatic multiplet signal corresponding to the benzoyl group and the ratio of both isomers was calculated using the integrals of those signals. Thus, isomer **A** corresponds to the compound with the aromatic protons at a lower chemical shift (8.07 ppm in $CDCl_3$ and 7.95 ppm in d_6-DMSO) and isomer **B** to the one with the proton signals at a higher chemical shift (7.96 ppm in $CDCl_3$ and 7.82 ppm in d_6-DMSO). (Figure 3.2)

A clear correlation between temperature and the proportion of the isomers was observed. The proportion of isomer **A**, obtained as a major product in the initial reaction at room temperature, decreased with the increase of temperature down to 15%. On the other hand, isomer **B** was obtained in higher proportions when temperature was increased. It was not possible to obtain each isomer alone upon heating. For both isomers **A** and **B**, in the best case, the reaction crudes contained around 15% of the other isomer (Figure 3.3, Annex 3).

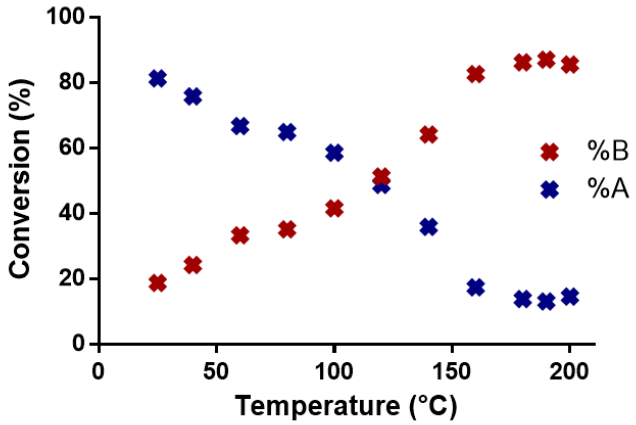

Figure 3.3. Correlation between the isomers A and B and the reaction temperature.

The treatment of **63**/**64**{*1*,*2*,*1*} with benzoyl chloride (**108**{*3*}) can lead to two different compounds **109**{*1*,*2*,*3*} and **110**{*1*,*2*,*3*} (Figure 3.4).The experiments carried out showed that two compounds were formed in different proportions depending on the thermal level employed. When the reaction was carried out at room temperature, a first benzoyl derivative was formed as the major product (assigned as **A**) but, on the contrary, when the reaction was performed under microwave irradiation at 180 °C a second benzoyl derivative (**B**) was the major product. Conventional spectroscopic techniques did not provide the necessary information to unequivocally assign the structures of **A** and **B** to each compound (**109**{*1*,*2*,*3*} and **110**{*1*,*2*,*3*}).

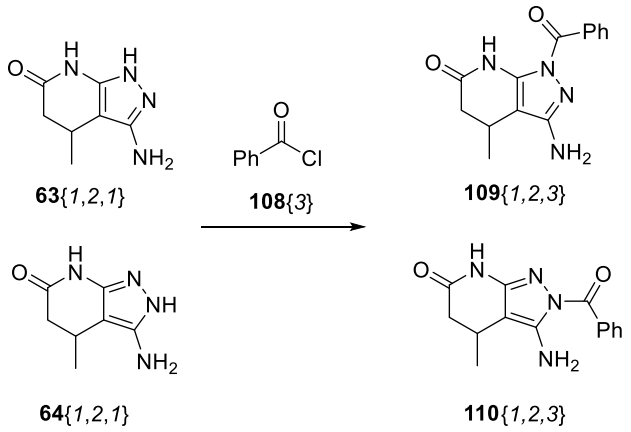

Figure 3.4. Structure of the possible products obtained in the reaction of **63**/**64**{*1*,*2*,*1*} with benzoyl chloride (**108**{*3*})

Surprisingly, isomer **A** was transformed to isomer **B** when heated at high temperatures (180 °C). Thus, a mixture of **A** and **B** containing mainly the first isomer (**A**) was heated in dioxane at 180 °C under microwave irradiation for 30 minutes with no extra reagents. The final mixture contained a mixture composed majorly by isomer **B**.

The results suggest that the behavior of the reaction may correspond to a kinetic *vs* thermodynamic control[2] where isomer **A** corresponds to the kinetic isomer and isomer **B** to the thermodynamic isomer. This types of reactions have been described with similar examples in the literature[3]. If this is the case, the kinetic isomer **A** should be the one with the lower activation energy barrier while the thermodynamic isomer **B** should be the one with the higher activation energy barrier but the most thermodynamically stable one.

3.1.2.1 Assignment

In order to assign the different products **A** and **B** with their correct structures different approaches were used, including a computational study of the relative stabilities of the compounds and several synthetic strategies such as structure modification, alternative synthesis and isotopic labelling with ^{13}C.

Computational studies

The relative stability of the different isomers was determined by DFT calculations using Gaussian.09[4] (6-311++G(d,p)). As said before, if the reaction responds to a kinetic *vs*. thermodynamic control, the most stable isomer should be obtained at higher temperatures and correspond to the thermodynamic isomer. Therefore, the less stable isomer could be related to the kinetic isomer obtained at lower temperatures. The calculations were performed for the starting material (3-amino-pyrazolo[3,4-*b*]pyridin-6-ones, **63** and **64**) and the benzoylated products (**109**{*1*,*y*,*3*} and **110**{*1*,*y*,*3*}) each with two different substituents in the lactam ring (R^2 = Me and R^2 = Ph) to analyze the potential effect of the substitution. (Table 3.1)

Table 3.1. Energy values for the different isomers calculated with DFT 6-311++G(d,p)

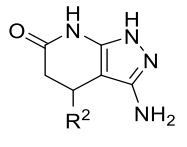

63{*1*,*2*,*1*}: R^2 = Me
63{*1*,*3*,*1*}: R^2 = Ph

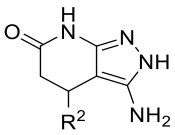

64{*1*,*2*,*1*}: R^2 = Me
64{*1*,*3*,*1*}: R^2 = Ph

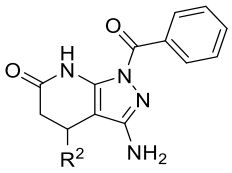

109{*1*,*2*,*3*}: R^2 = Me
109{*1*,*3*,*3*}: R^2 = Ph

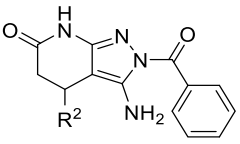

110{*1*,*2*,*3*}: R^2 = Me
110{*1*,*3*,*3*}: R^2 = Ph

ENERGY (kcal/mol)	
64{*1*,3,*1*}	-476101.2
63{*1*,3,*1*}	-476098.6
64{*1*,*2*,*1*}	-355788.4
63{*1*,*2*,*1*}	-355786.4

ENERGY (kcal/mol)	
110{*1*,3,*3*}	-692211.7
109{*1*,3,*3*}	-692209.7
110{*1*,*2*,*3*}	-571898.9
109{*1*,*2*,*3*}	-571897.1

Δ ENERGY (kcal/mol)	
64-63{*1*,*3*,*1*}	-2.6
64-63{*1*,*2*,*1*}	-2.0

Δ ENERGY (kcal/mol)	
110-109{*1*,*3*,*1*}	-2.0
110-109{*1*,*2*,*1*}	-1.8

For the benzoylated products, isomer **110** was always the most stable product with an energy difference of ~2 Kcal/mol. Isomer **110** should therefore correspond to the thermodynamic isomer which should be obtained at higher temperatures. Thus, isomer **110** was assigned as isomer **B** being compound **109** assigned as **A**, the kinetic isomer obtained at lower temperatures. The same results were observed for the starting material of the reaction as compound **64** was also the most stable compound in both cases. The substituent of the lactam ring had no effect on the stability of the different isomers as in all cases the N2 substituted isomer was the more stable.

Synthetic studies

Despite an initial assignment of the compounds was performed using the energetic calculations, it was interesting to obtain experimental data that could confirm and validate the computational results. For this reason, several synthetic studies were performed to unequivocally assign the structures of the isomers **A** and **B**.

Spectroscopic studies

For the initial study, both compounds were obtained separately by working at different temperatures and purifying the samples by column chromatography. In both cases, the starting material **64** was stirred with 1 equivalent of benzoyl chloride and 1.5 equivalents of TEA in dry THF or dioxane. On one hand, a mixture containing isomer **A** as the major compound was prepared heating at 40 °C overnight. On the other hand, a second mixture were isomer **B** was the major product was obtained by heating 30 minutes under microwave irradiation at 180 °C. The mixtures were purified by column chromatography DCM:MeOH (98.5:1.5) to obtain the pure desired isomers (Figure 3.5).

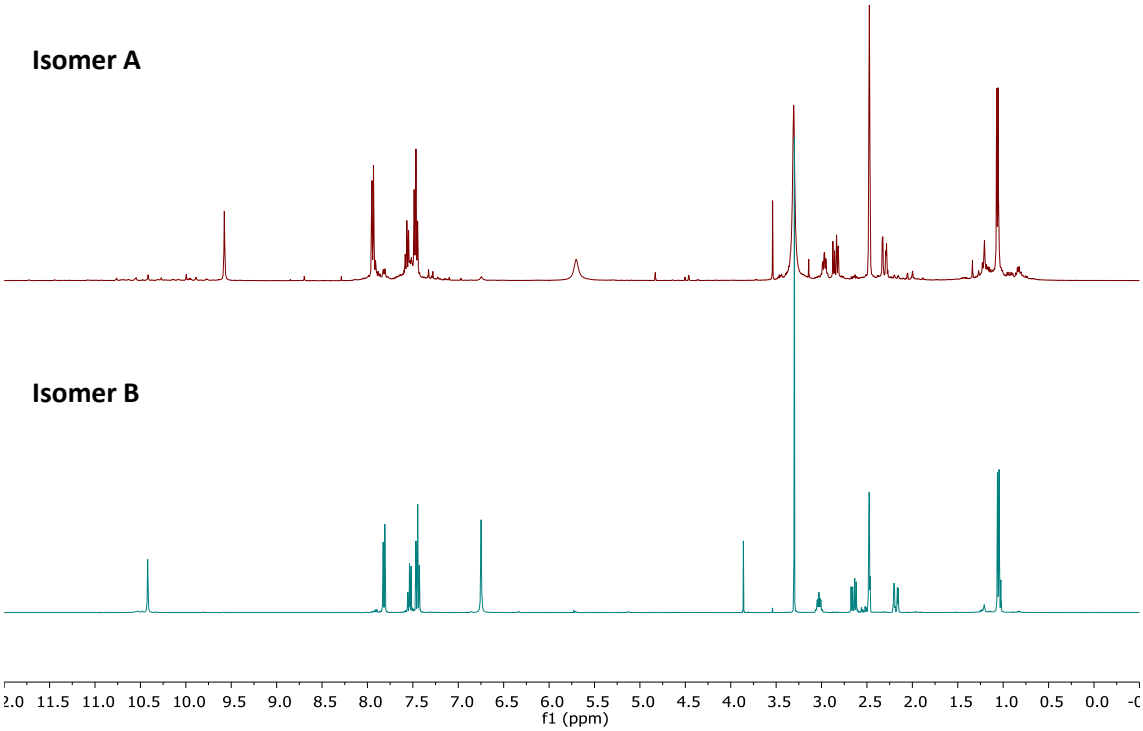

Figure 3.5. Comparison of the ^{1}H-NMR spectra of isomer **A** and **B.**

Conventional NMR spectroscopy allowed to identify all the fragments of the isomers. However, it was not possible to differentiate the point of substitution. Spatial NMR spectroscopy like NOESY 1D and 2D was performed with the hope to observe proximity correlations between the lactam NH or the NH_2 with the phenyl protons. Unfortunately, these spectra did not provide the expected information as the labile protons of the NH and NH_2 did not show any useful correlations. Maybe, the geometry of the molecules under study precludes the observation of such correlations.

Synthetic modification studies

In order to increase the chances to see a correlation by common spectroscopic methods and identify each isomer **A** and **B**, the molecules were modified to include new fragments capable of providing better correlations.

As a first try, methylation of the amines and amides of the molecules was tried. Despite several trials with different methylating agents (MeI, DMS), bases (NaH, KOH, t-BuOK) and solvents (DMSO, THF, Dioxane) it was not possible to obtain compound **111**. In all cases, the benzoyl group was easily eliminated reverting to compound **64**. Any of the tested methodologies was effective to provide a methylated product that may have increased the chances to see a spatial correlation in the NOESY spectrum.

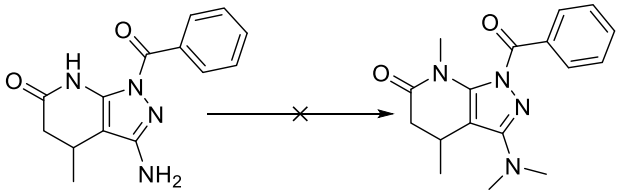

109{*1*,*2*,*3*} **111**

Figure 3.6. Methylation of compound **109**{*1*,*2*,*3*}.

A second strategy consisted on the formation of an imine of the NH_2 group to create a new spatial correlation between the new group and the benzoyl group. The presence of the imine would also allow the identification of the carbons of the pyrazole (using the HMBC and HSQC spectra) which are not distinguishable by the traditional methods.

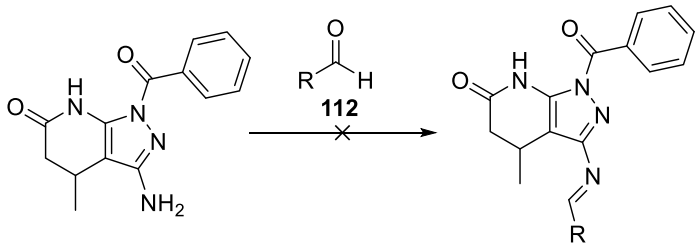

109{*1*,*2*,*3*}

124{*1*,*2*,*1*}: R = Me
124{*1*,*2*,*2*}: R = Et
124{*1*,*2*,*3*}: R = Ph
124{*1*,*2*,*4*}: R = 4-Br-Ph

Figure 3.7. Assays of formation of an imine of **109**.

Several aldehydes were used at different conditions of time and temperature (Table 3.2) with no positive results. The desired product was not obtained in any case as the reaction only yielded the reagent **109**{*1,2,3*} (at milder conditions like less reactive aldehydes and short times) or the loss of the benzoyl group (with more reactive aldehydes) reverting to **64**.

Table 3.2. Assays for the formation of compounds **124**.

Aldehyde	Solvent	Temp.(°C)	Time	Result
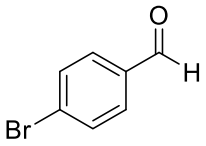 **112**{*4*}	EtOH (MW)	140	15 min	**109**{*1,2,3*}
	EtOH Conventional heating	80	3h	**109**{*1,2,3*}
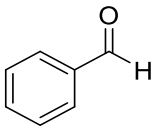 **112**{*3*}	EtOH (MW)	140	30 min	**109**{*1,2,3*}
	EtOH + AcOH (3 drops) Conventional heating	80	3h	**109**{*1,2,3*}
 **112**{*1*}	MeOH Conventional heating with a sealed vial	60	o/w	**64**{*1,2,1*}
	MeOH Conventional heating with a sealed vial	90	o/w	**64**{*1,2,1*}
	MeOH (MW)	140	30 min	**64**{*1,2,1*}
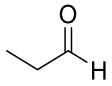 **112**{*2*}	MeOH Conventional heating	65	30h	**64**{*1,2,1*}

The reactivity problem was identified as a stearic hindrance problem as the same reaction on compound **64**{*1,2,1*} did easily take place (Figure 3.8).

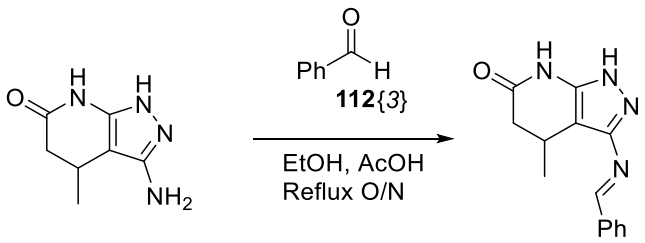

64{*1,2,1*} **125**

Figure 3.8. Imine formation on **64** with benzaldehyde

Alternative synthesis studies

An alternative synthesis to obtain one of the isomers was proposed based on the previous knowledge of the group. As described in Chapter 2, the cyclization of 2-methoxy-6-oxo-1,4,5,6-tetrahydropyridin-3-carbonitriles (**62**) with phenylhydrazine leads to the formation of *N*2-aryl substituted pyrazolo[3,4-*b*]pyridin-6-ones as a single isomer due to the different nucleophilicity of the two nitrogen atoms of the hydrazine. With this in mind, we propose the use of benzhydrazide (**113**) to obtain the N2 substituted product **110**.

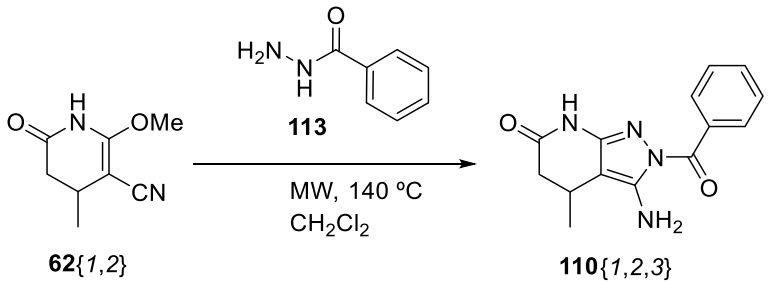

Figure 3.9. Alternative synthesis for compound **110**{*1,2,3*}.

62{*1,2*} was reacted with 3 equivalents of benzhydrazide (**113**) in CH_2Cl_2 using microwave irradiation for 2h at 140 °C to achieve complete transformation. After the reaction, the solution was washed with water to remove the excess of benzhydrazide (**113**). In this case, CH_2Cl_2 allowed the direct obtention of the cyclized product and was preferred instead of methanol to facilitate the purification and avoid the formation of an impurity from the decomposition of benzhydrazide in this solvent.

The product obtained **110**{*1,2,3*} corresponds to isomer **B** (Figure 3.10). This result would confirm the initial hypothesis extracted from the computational calculations according to which the N2 substituted isomer (**110**{*1,2,3*}) should be the most stable isomer obtained at high temperatures and corresponds to the thermodynamic isomer.

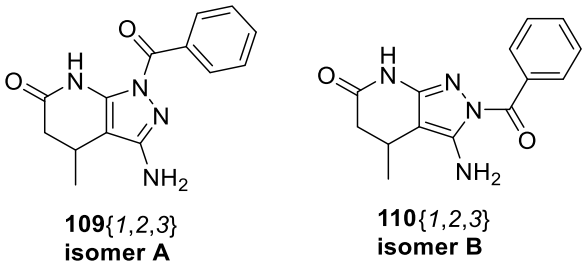

Figure 3.10. Assignment of the structures of isomers **A** and **B** according to the alternative reaction with benzhydrazide.

Labelling with ^{13}C

The computational and the mechanistic studies have allowed a first assignment of the two isomers where the thermodynamic isomer **B** should correspond to isomer **110**{*1*,*2*,*3*} while isomer **109**{*1*,*2*,*3*} would be the kinetic isomer. A final strategy to unequivocally confirm the structures of the isomers was to include a ^{13}C atom in the molecule to facilitate the identification of NMR correlations and allow a spectroscopic assignment.

Benzhydrazide labelled with ^{13}C was prepared from the corresponding ^{13}C benzoic acid. The reaction conditions were first optimized with the unlabeled benzoic acid (**114**). Two different methodologies were studied to obtain **113** both with the formation of an ethyl ester as intermediate (Table 3.3). In the first strategy, the corresponding ester intermediate (**115**) was obtained by Fisher esterification in EtOH using acid catalysis (H_2SO_4). Then, hydrazine was added to form the corresponding benzhydrazide. In a second strategy, the ester was formed *via* the benzoyl chloride using microwave irradiation. The formation of benzhydrazide was achieved with a 10 minutes microwave reaction.

Table 3.3. Optimized reaction conditions for the obtention of benzhydrazide (**113**).

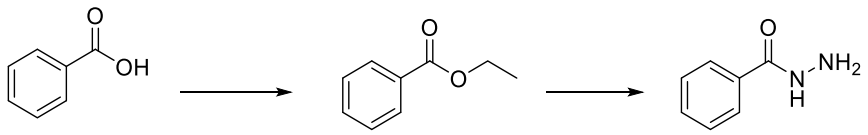

114 **115** **113**

Conditions	Result (yield)
(1) H_2SO_4, EtOH (4h, 90 °C) (2) NH_2-NH_2·H_2O (1h, 90 °C)	**113** (56%)
(1) $SOCl_2$, EtOH (MW, 30min, 100 °C) (2) NH_2-NH_2·H_2O (MW, 10min, 100 °C)	**113** (57%)

Benzhydrazide labelled with ^{13}C (**117**) was prepared as stated above from benzoic acid-α-^{13}C (**116**). However, the reactivity of the labelled product was slightly different of that of the unlabelled product. Using the first strategy, the reaction did not yield the final product and only the ester was recovered. With the second strategy, the conversion of the second step was not complete and an impurity was formed. Pure ^{13}C-bezhydrazide (**117**) was obtained through a crystallization in ether.

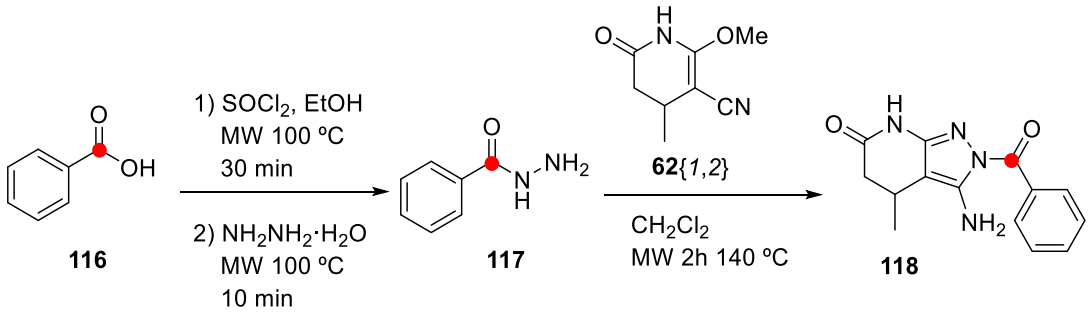

Figure 3.11. Obtention of ^{13}C labelled compound **118**.

The cyclization of **62** with ^{13}C-bezhydrazide (**117**) also presented a slightly different reactivity than the cyclization with the unlabelled product and again the cyclization reaction was not complete. For this reason, in order to obtain the pure final labelled product, a column chromatography purification was needed.

The ^{1}H-NMR spectrum presented all the expected signals previously observed in the unlabeled product. The presence of an exchangeable signal of integral 2H at 6.77 ppm confirmed the cyclization while the aromatic signals indicated the incorporation of the benzoyl group. The ^{13}C-NMR spectrum showed the coupling of the aromatic carbons with the ^{13}C-labelled carbonyl moiety (Figure 3.12).

The HMBC spectrum of product **118** showed a correlation between the NH_2 and the ^{13}C of the carbonyl group of the benzoyl moiety which was not visible with the unlabelled molecule. This correlation at 4 bond distance proves that the product obtained by the cyclization with benzhydrazide (compound **118** labelled and compound **110** unlabelled) is isomer **B**, corresponding to the N2 substituted molecule and the thermodynamic isomer. This correlation would not be possible for isomer **109** as the NH_2 group is found at 5 bonds of distance from the carbonyl group.(Figure 3.13).

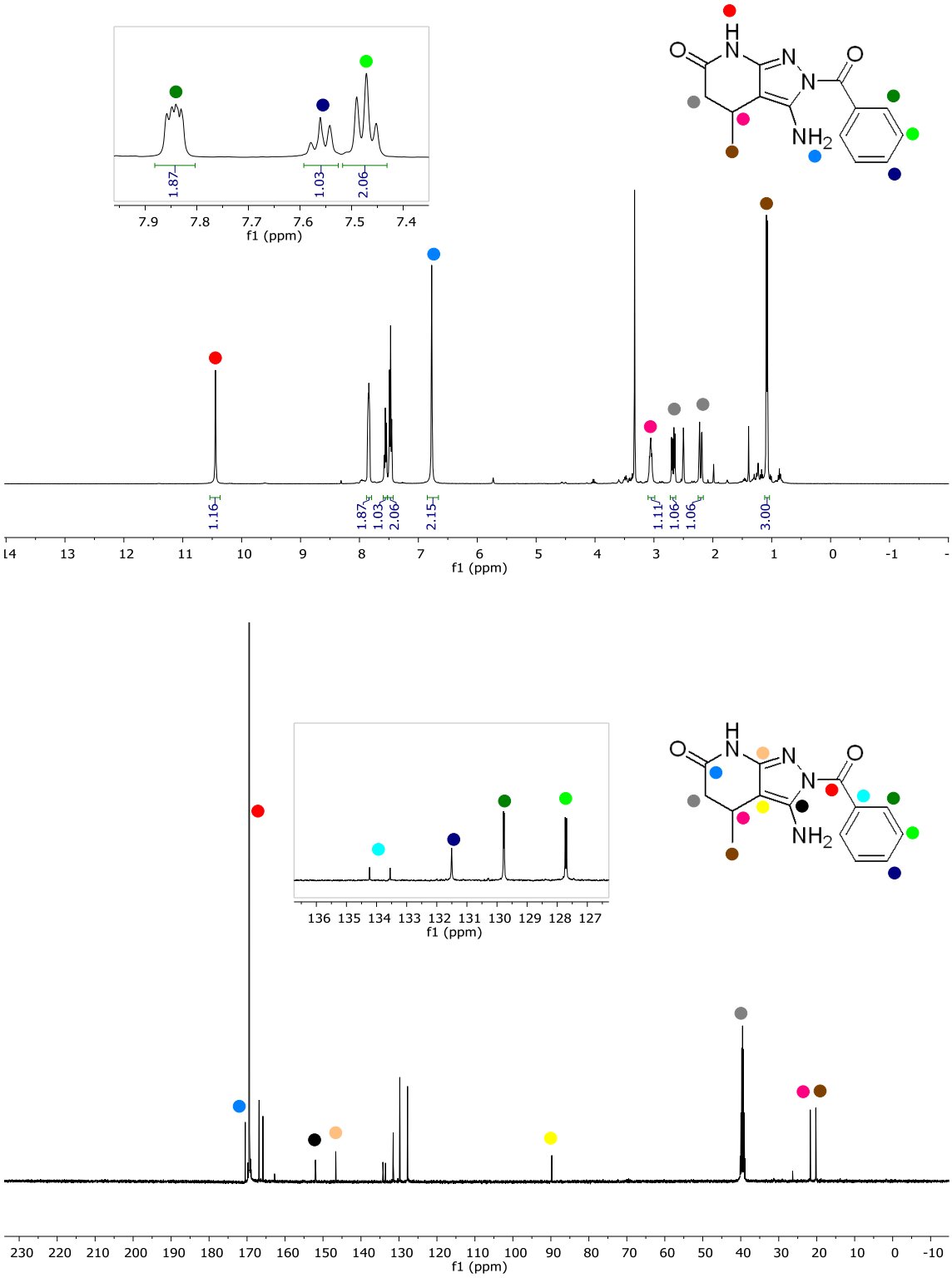

Figure 3.12. ^{1}H-NMR and ^{13}C-NMR spectra of compound **118**.

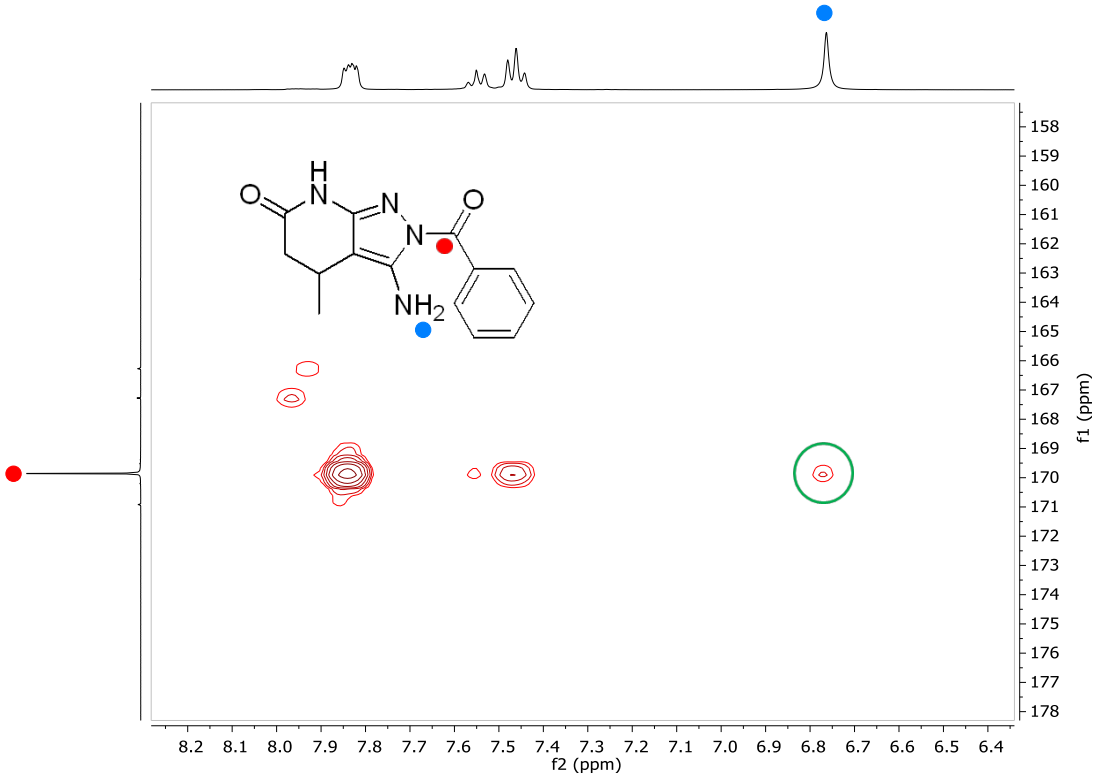

Figure 3.13. HMBC of compound **118** demonstrating the N2 substitution.

3.1.2.2 Conclusion

The benzoylation of 3-amino-pyrazolo[3,4-*b*]pyridin-6-ones was studied in depth to determine the structure of the resulting products. The reaction can lead to two different isomers following a kinetic *vs*. thermodynamic control. The synthetic studies, together with the calculations and the NMR experiments carried out indicate that the 2-benzoyl substituted isomer **110,** which is obtained at higher temperatures and has a higher stability, is the thermodynamic isomer. Moreover, this isomer can also be obtained by the cyclization of **62** with benzyhydrazide (**113**) and, according to the different nucleophilicity of the amine groups of the hydrazide, this cyclization should only lead to the N2-benzoyl substituted compound. Isomer **109** corresponds to the kinetic isomer obtained at lower temperatures. When exposed to high temperatures, compound **109** evolves to **110**.

A rationalization of the formation of both isomers is included in (Figure 3.14) The treatment of the initial pyridone **62** with hydrazine **56**{*1*} could afford a mixture of the two tautomers **63** and **64**. The energy calculations have shown that **64** is more stable than **63** and, convergently, only one compound was detected in solution in the NMR experiment. Then, it is more likely that **64** is the only tautomer present at room temperature (or at least detectable). Consequently, the subsequent treatment with benzoyl chloride **108**{*3*} affords the N1-benzoyl substituted derivative **109** *via* the nucleophile attack of the lone pair of the non-protonated N1 nitrogen to the benzoyl chloride affording the kinetic isomer.

When the reaction is carried out at higher temperatures, probably the tautomeric equilibrium from **64** to **63** is favored (although we have never detected tautomer **63**) and the nucleophilic attack of the lone pair of the non-protonated N2 nitrogen atom of **63** affords the N2-benzoyl substituted pyrazolo[3,4-*b*]pyridin-6-one **110**, that is to say the thermodynamic isomer.

However, taking into account the direct transformation of the kinetic isomer **109** into the thermodynamic isomer **110** upon heating at high temperature, similar to other reactions described in the literature such as the isomerization of naphthalene-1-sulfonic acid to naftalene2-sulfonic acid[5] or the isomerization of the 4-acylphenol to 2-acylphenol in the Fries rearrangement[6], we cannot exclude that in the reactions at high temperature, after the initial formation of **109**, such isomerization to **110** can take place.

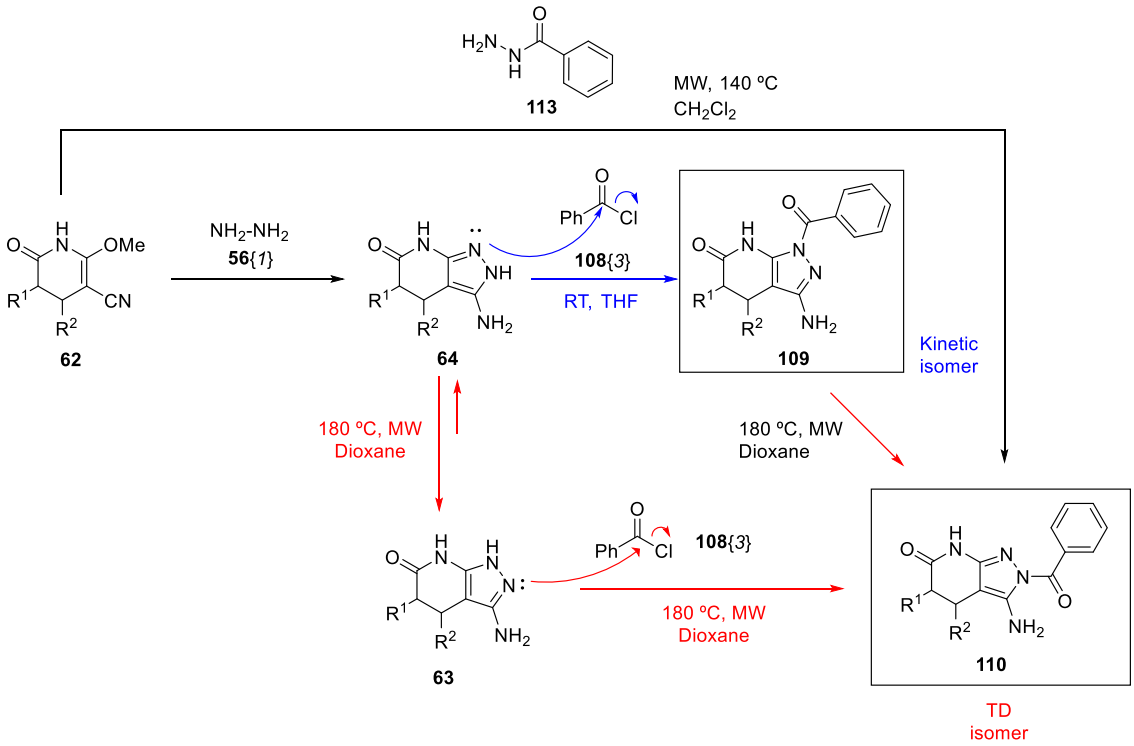

Figure 3.14. General scheme of the formation of isomers **109** and **110** at different temperatures.

3.2 Synthesis of a family of *N*-acetyl and *N*-benzoyl pyrazolo[3,4-*b*]pyridin-6-ones

A general methodology to prepare isomers **109** and **110** was stablished from the results obtained in the study of the benzoylation of **64**{*1*,*2*,*1*}. In order to demonstrate the general applicability of such methodology, a family of *N*-acyl 3-amino-pyrazolo[3,4-*b*]pyridin-6-ones was prepared.

1-acyl substituted isomers (**109**) were prepared from the direct substitution of the corresponding unsubstituted pyrazolo[3,4-*b*]pyridin-6-one **64**. (Figure 3.14) Two compounds were prepared with substituents on the R^2 position of the lactam ring (**109**{*1*,*2*,*3*} and **109**{*1*,*3*,*3*}) which were purified from the corresponding crude materials containing **109** as the major product by column chromatography (DCM:MeOH, 98.5:1.5). Surprisingly, the preparation of compounds substituted at the R^1 position **109**{*3*,*1*,*3*} and **109**{*2*,*1*,*3*} yielded two other extra compounds substituted on the NH_2 groups: the disubstituted compounds **119** and **121** and the monosubstituted compounds **120** and **122** with the benzoyl group attached to the NH_2 group. All these compounds were separated using column chromatography (DCM:MeOH, 99:1). Finally, compound **109**{*2*,*1*,*4*} was obtained from the reaction with picolinoyl chloride, previously prepared upon treatment of the corresponding picolinic acid with 5 eq. of $SOCl_2$ in toluene (O/N reflux) (Figure 3.15).

N2 substituted 3-amino-pyrazolo[3,4-*b*]pyridin-6-ones (**110**) were prepared by the direct cyclization reaction with the corresponding hydrazide (**113**) as previously described. Two commercial hydrazides were used: benzhydrazide **113**{*3*} and acethydrazide **113**{*2*} to yield a total of 6 products (Figure 3.16).

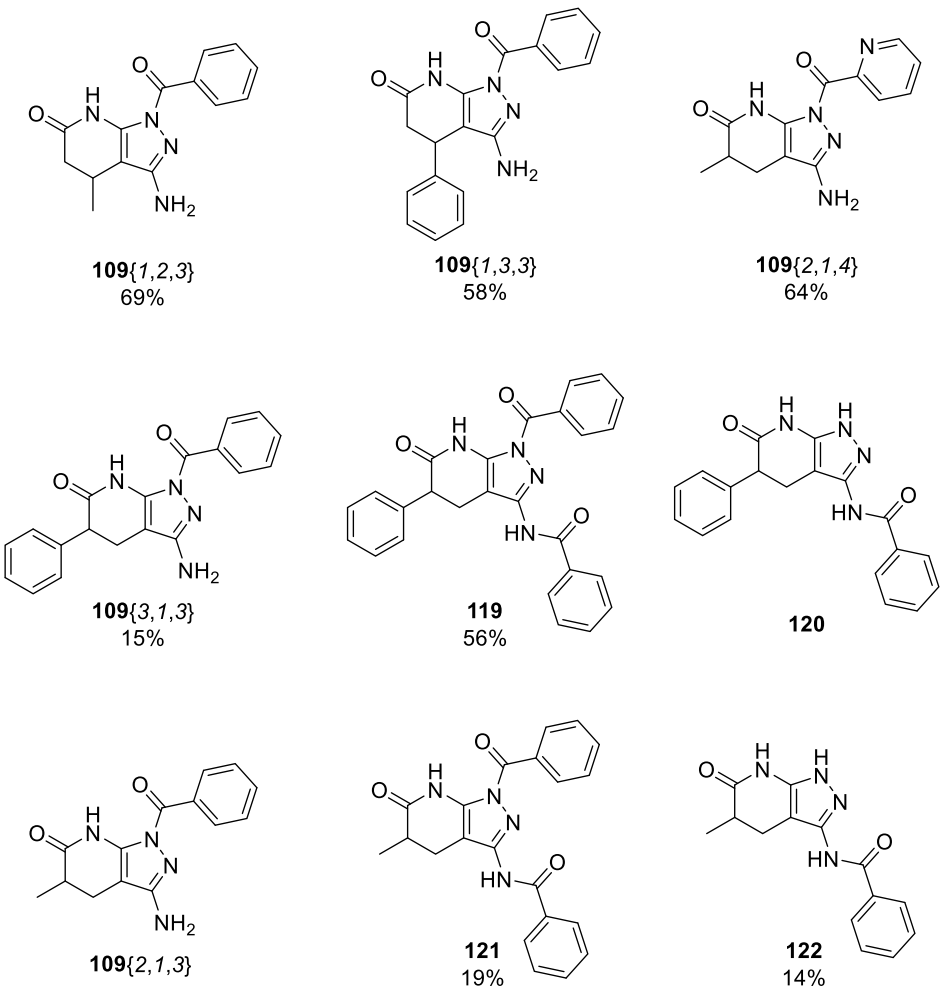

Figure 3.15. *N*1-substituted 3-amino-pyrazolo[3,4-*b*]pyridin-6-ones. Yield corresponds to the isolated product obtained on the benzoylation step from the corresponding reactants **64**. Compounds with no yield were not possible to isolate as pure products.

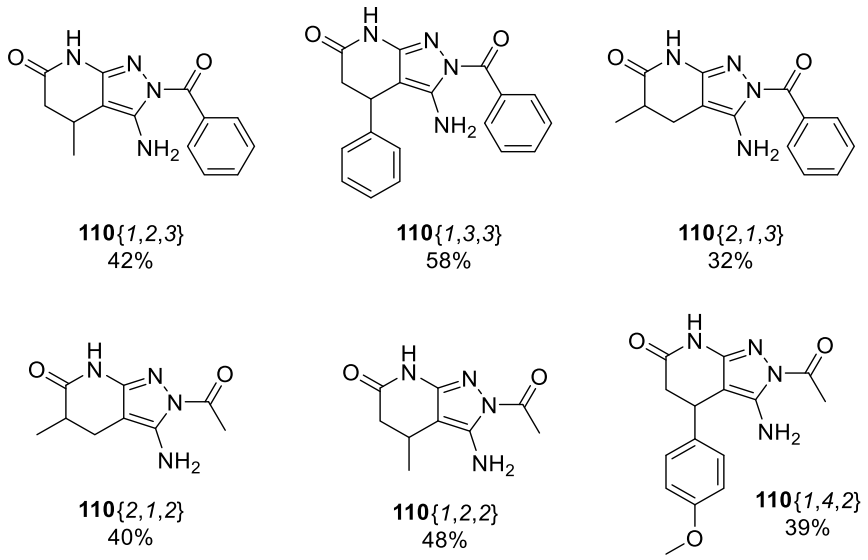

Figure 3.16. *N*2-substituted 3-amino-pyrazolo[3,4-*b*]pyridin-6-ones. Yield corresponds to the isolated product obtained on the cyclization step of the corresponding reagents **62** with hydrazides.

3.3 Biological activity

Following the synthesis of this family of compounds, we next aimed at assessing the impact of this modifications on the inhibition of MNKs. Based on the chemical modifications introduced, different biological effects could be expected because the carbonyl moiety changes the 3D structure of the compounds and incorporates a new H-bond acceptor to the scaffold. Moreover, the benzoyl group could act as a protecting group for the pyrazole ring what could be considered a step towards a prodrug of the inhibitor.

To test the effect of this modifications on the inhibition of MNK1/2 kinase activity, we used the protein-based assays (Proqinase®) and experiments in cell culture as described before (Chapter2).

As shown in Table 3.4, none of the newly developed molecules was able to inhibit MNK1/2 kinase activity in the radiometric protein kinase assay (^{33}PanQinase® Activity Assay from Proqinase®). In addition, the compounds also did not reveal measurable effects on MNK1/2 kinase activity in cells, as judged by the phosphorylation status of eIF4E by Western Blot (Figure 3.17).

In conclusion, any of the compounds developed in this part of the project showed the expected activity as MNK inhibitors and this family of inhibitors was therefore discontinued.

Table 3.4. Results from the enzymatic radiometric assay performed by Proqinase ®. Values indicated as residual activity of kinases MNK1 and MNK2 after treatment with the indicated compounds at 10 µM. Cercosporamide and CGP are used as positive controls.

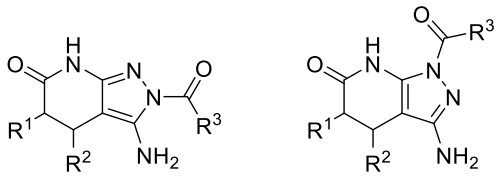

110{*x*,*y*,*z*}

109{*x*,*y*,*z*}

x	R^1
1	H
2	Me

y	R^2
1	H
2	Me
3	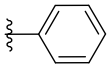
4	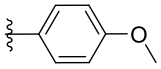

z	R^3
2	Me
3	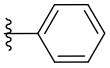

Compound	MNK1	MNK2
cercosporamide	6	1
110{*1*,*3*,*3*}	108	104
109{*1*,*3*,*3*}	113	101
110{*1*,*2*,*2*}	102	94
109{*1*,*2*,*3*}	98	102

Compound	MNK1	MNK2
CGP	34	39
110{*1*,*4*,*2*}	104	101
110{*2*,*1*,*2*}	102	99
110{*2*,*1*,*3*}	105	95
110{*1*,*2*,*3*}	103	101

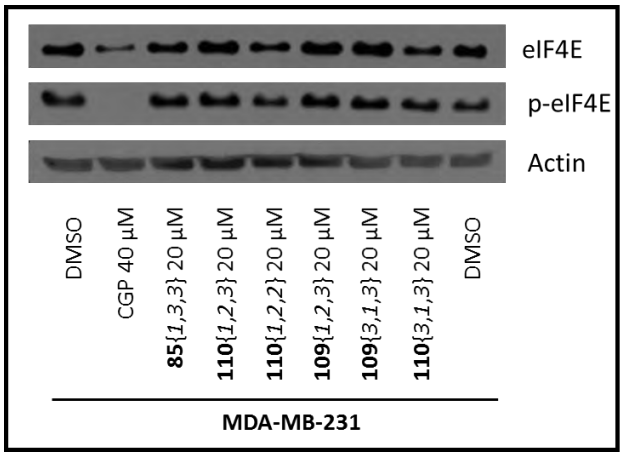

Figure 3.17 Example of the results obtained from the analysis of the compounds by western blot. WB was performed after 24h of treatment. Final DMSO concentration 0.5%. CGP is used as positive control.

3.4 References

1. Falcó, J. L. *et al.* Design, synthesis and biological activity of acyl substituted 3-amino-5-methyl-1,4,5,7-tetrahydropyrazolo[3,4-b]pyridin-6-ones as potential hypnotic drugs. *Eur. J. Med. Chem.* **40,** 1179–1187 (2005).
2. Lin, K. Understanding product optimization: Kinetic versus thermodynamic control. *J. Chem. Educ.* **65,** 857 (1988).
3. Fandrick, D. R. *et al.* A Michael Equilibration Model To Control Site Selectivity in the Condensation toward Aminopyrazoles. *Org. Lett.* **17,** 2964–2967 (2015).
4. Frisch, M. J. *et al.* Gaussian (G09). Wallingford CT (2009).
5. Lantz, R. Mechanism of the monosulfonation of naphthalene. *Comptes Rendus Chim.* **201,** 149–152 (1935).
6. Effenberger, F. & Gutmann, R. Die Fries-Umlagerung als Gleichgewichtsreaktion. *Chem. Ber.* **115,** 1089–1102 (1982).

CHAPTER 4

Pyrazolo[3,4-*b*]pyridin-3-amines as MNK inhibitors

4.1. Derivatization of pyrazolo[3,4-*b*]pyridin-6-ones to pyrazolo[3,4-*b*]pyridines

4.1.1. Introduction

The chemistry of 3-amino-pyrazolo[3,4-*b*]pyridin-6-ones have been widely studied in the previous chapters providing methodologies to obtain compounds with different substituents in R^1, R^2, R^3 and R^4. The scaffold of all these products is the bicyclic pyrazolo[3,4-*b*]pyridine-6-one formed by the aminopyrazole ring and the lactam ring. The lactam is a main feature of these molecules which, in one side, affects the planarity of the molecule in structures presenting sp^3 carbons at C4 and C5 of the pyridone ring and, on the other side, modulates the solubility as it permits the presence of a polar front which contains several H-bond donors and acceptors.

We expected that the presence of such group would allow a higher potency and selectivity of the candidates as observed in other similar compounds with very interesting activities.[1–4] Unfortunately, none of the studied compounds showed activity to inhibit the MNKs and subsequently reduce the phosphorylation levels of eIF4E.

For this reason, at this point of the work we considered of interest to evaluate the modification of the lactam ring. Particularly, the elimination or substitution of the amide group were studied and new candidates were proposed.

4.1.2. Direct modification of the amide moiety

As a first strategy, the modification of the amide group was considered as a last step modification of the corresponding 3-amino-pyrazolo[3,4-*b*]pyridin-6-one prepared according the previously described methodologies that allow the derivatization of the scaffold at R^1, R^2 and R^3 positions (Figure 4.1).

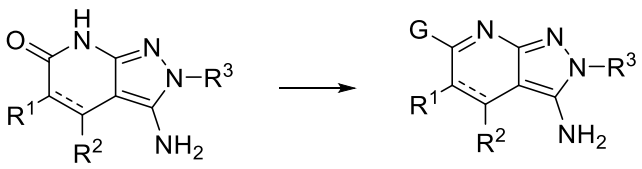

Figure 4.1. General scheme of the last step modification of the amide group of the lactam ring.

4.1.2.1. Carbonyl reduction

We first focused on the direct reduction of the carbonyl group to a methylene group. As shown in Table 4.1, several reducing agents and reaction conditions were tested. However, it was not possible to obtain the desired product and, in all cases, the starting material was recovered.

Conventional reducing agents were not effective probably due to the low reactivity of the carbonyl group. More drastic conditions would be necessary to force the reduction of this group; however, they will probably affect other functional groups present in the molecule impeding the development of a general methodology and, consequently, we decided to stop the study of such reduction.

Table 4.1. Studied conditions for the direct reduction of the lactam carbonyl group.

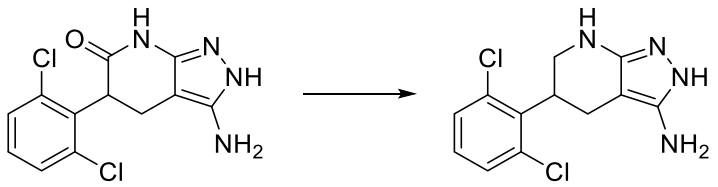

64{*7*,*1*,*1*} **128**

Reducing agent	Conditions	Purification method
H_2; Pd/C (10%); MeOH	20 h; RT	Filter through Celite® and remove solvent under reduced pressure
H_2; Pd/C (10%); MeOH	72h; RT	Filter through Celite® and remove solvent under reduced pressure
$LiAlH_4$·(3.8 eq.); THF	14 h; 90 °C + 3h RT	Filter
BH_3·SMe_2 (0.8 eq.); THF	6 h; 90 °C	Remove solvent under reduced pressure and purify by column chromatography
BH_3·SMe_2 (0.8 eq.); THF	8h; 90 °C	Remove solvent under reduced pressure. Add water, neutralize with NaOH 6M and filter

4.1.2.2. 6-chloro-pyrazolo[3,4-*b*]pyridin-3-amines

As a second option, the conversion of the amide group into a chloroimino group was assayed using different halogenating agents ($POCl_3$, $POCl_3/PCl_5$, $SOCl_2$) and conditions on four different scaffolds (Figure 4.2).

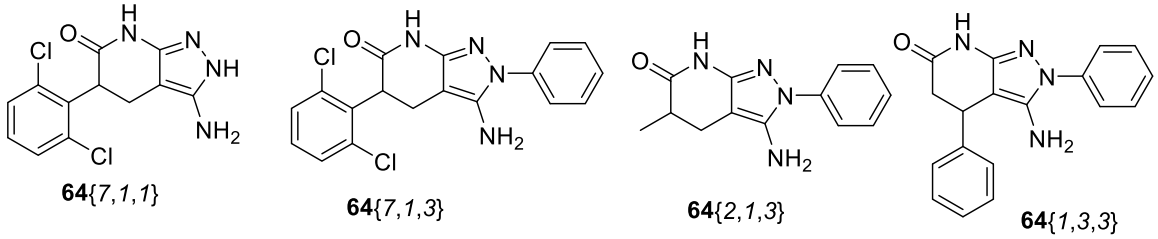

Figure 4.2. Scaffolds used in the study of the conversion of the amide group into a chloroimino group

The studies were started with compound **64**{*7,1,3*}. This compound showed variable results in the activity tests that could be related to the proximity between the IC_{50} values and its maximum solubility. For this reason, it was considered a good starting point for this transformation as changes on the lactam group were expected to increase the solubility of the compound.

Initially, the conditions described by Burikhanov *et al.*[5] were tested. **64**{*7,1,3*} was suspended in phosphoryl chloride ($POCl_3$) and refluxed for 3 h. The mixture was quenched with water and neutralized with 10% aqueous sodium carbonate solution. A precipitate was collected by filtration and dried *in vacuo.* The analysis of the filtered solid by TLC showed the presence of two products. The reaction crude was purified by column chromatography (alumina column with a Cy:AcOEt gradient: 0-30% AcOEt in 30 min) but unfortunately only one product (**123**) was recovered in a very low yield (14%). It was not possible to isolate and identify the second product.

Surprisingly, the ^{1}H-NMR spectrum of the isolated product did not show any aliphatic signals and a new singlet appeared at 8.16 ppm which correlated with a sp^2 carbon in the HSQC spectrum. Moreover, the IR spectrum did not show the band corresponding to the carbonyl C=O stretching (Figure 4.4). These observations together indicated that the lactam ring had been oxidized to a pyridine ring and the product obtained was the 6-chloro-5-(2,6-dichlorophenyl)-2-phenyl-2*H*-pyrazolo[3,4-*b*]pyridin-3-amine (**123**) (Figure 4.3).

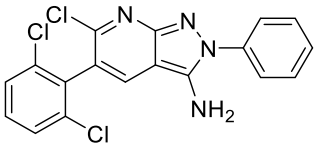

123

Figure 4.3. Structure obtained in the treatment of compound **64**{*7,1,3*} with $POCl_3$.

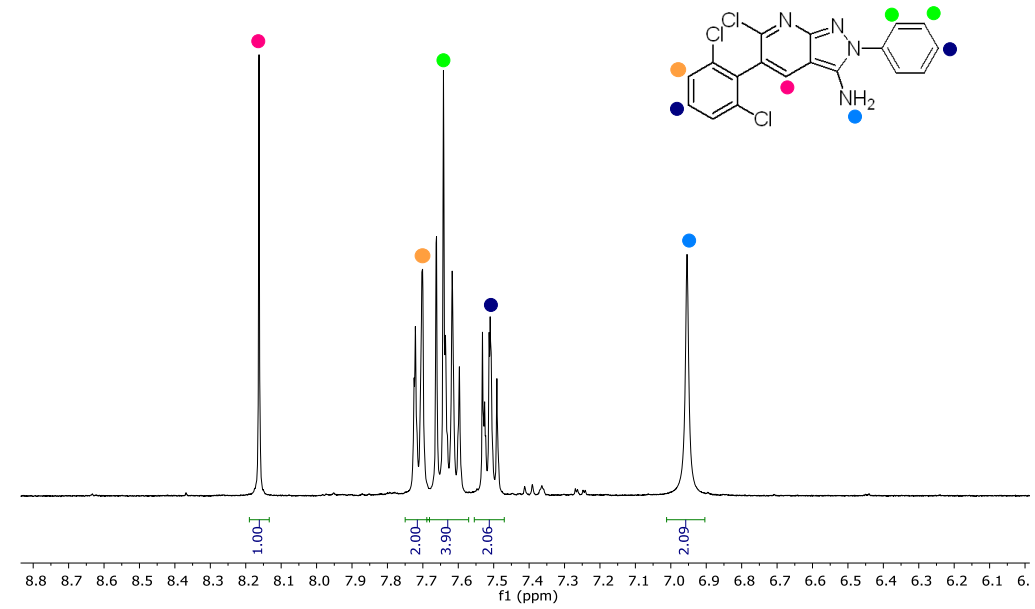

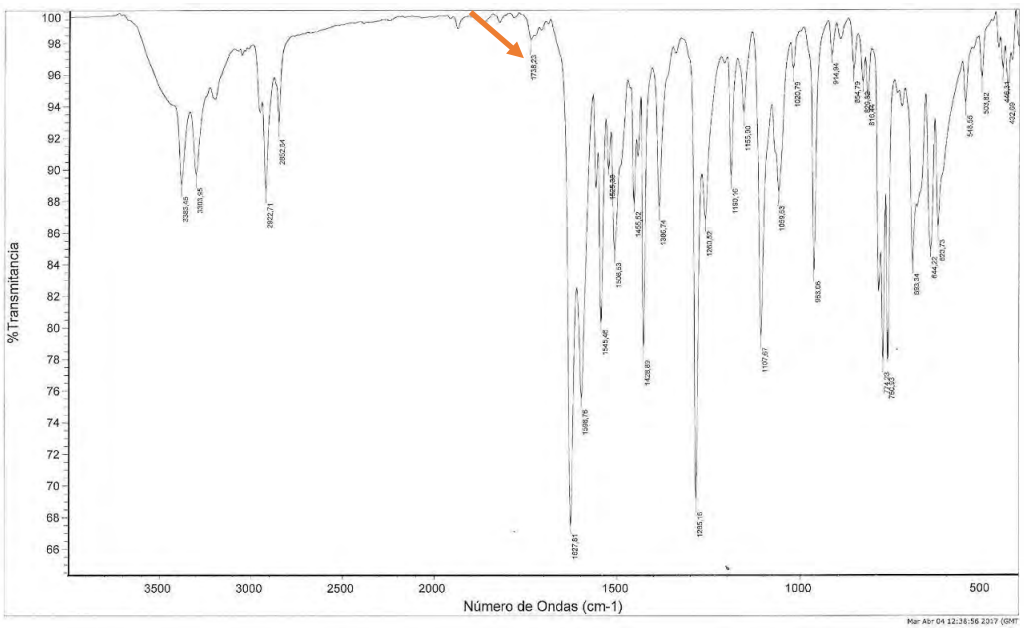

Figure 4.4. ^{1}H-NMR and IR spectra of compound **123**.

The treatment of **64**{*7*,*1*,*3*} with $POCl_3$ yielded the corresponding halogenated product **123** in very low yields. In order to increase the purity of the crude and the loss of mass during the purification by column chromatography, the reaction conditions were studied and optimized. In the first place, the reaction time was extended to 6h and 12h but the proportion between the products in the crude (compound **123** and the impurity) was maintained. Also, the workup was changed to extractions with $CHCl_3$ with no positive results either. In all cases, column purification was needed and yielded the same single product with equivalent yields. Changing the heating method to microwave irradiation yielded a reaction intermediate (**125**) which was not possible to isolate by column chromatography or characterize.

Finally, the addition of TEA (0.3 eq.) to the reaction avoided the column purification as the impurity was not isolated with the product. After a 6h reflux, the product was extracted with AcOEt to yield a product that could be used without further purification in the next reaction steps. Unfortunately, the yields were still low.

In order to cast light on the reaction mechanism for the formation of **123**, the reaction was tested on compounds **85**{*7*,*1*,*3*} and **101**{*7*,*1*,*3*} (Figure 4.5). If the molecule was already dehydrogenated (**85**{*7*,*1*,*3*}) or methylated (**101**{*7*,*1*,*3*}) the reaction led to the decomposition of the starting material. These results seem to indicate that the mechanism of formation of **123** is complex, including halogenation in several points of the pyridone ring that finally induce the dehydrogenation of the ring to afford an aromatic pyridine. Moreover, the fact that **85**{*7*,*1*,*3*} is not converted indicates that the dehydrogenation is not the first step of the mechanism. Convergently, the methylated pyridone **101**{*7*,*1*,*3*}, which cannot be converted in the chloroimino derivative, is also not dehydrogenated.

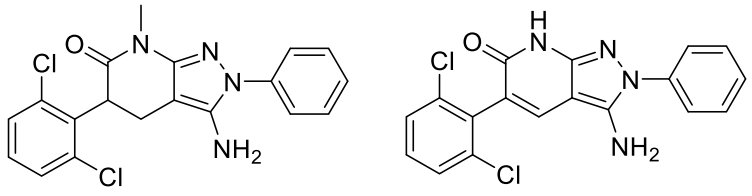

101{*7*,*1*,*3*} **85**{*7*,*1*,*3*}

Figure 4.5. Treatment of compounds **85**{*7*,*1*,*3*} and **101**{*7*,*1*,*3*} with $POCl_3$ did not yield any product.

Hino *et al.*[6] described two alternative methodologies for the obtention of 6-chloropyridines using PCl_5 or $SOCl_2$ as halogenating agents. First, compound **64**{*7*,*1*,*3*} was treated with $POCl_3$ and PCl_5 (5 eq.) at reflux for 18h. The reaction was quenched in ice and the resulting solid was filtered and purified by column chromatography (Alumina column with DCM:MeOH (99.5:0.5) as solvent). The analysis of the solid revealed that the compound obtained corresponded to the oxidized product **85**{*7*,*1*,*3*} and that no alteration of the carbonyl group had occurred.

On the other hand, compound **64**{*7*,*1*,*3*} was stirred overnight in $CHCl_3$ in the presence of $SOCl_2$ and DMF. Then, the solvent was removed under reduced pressure and the crude was neutralized with $NaHCO_3$. The filtered solid, which contained a single compound with small traces of impurities, was purified by column chromatography (Alumina column with an AcOEt:Cy gradient 0-75% of AcOEt in 35 minutes).

The ^{1}H-NMR spectroscopy presented a signal exchangeable by D_2O at 10.65 ppm and three aliphatic signals indicating that the lactam ring was unaltered. The lack of the NH_2 group and the presence of 3 new signals with a profile similar to DMF suggested the insertion of the DMF molecule in the compound (Figure 4.6 and Figure 4.7). This hypothesis was confirmed by observing a correlation between the new CH group (blue) and the C3 carbon (orange) of the pyrazole ring in the HMBC spectrum.

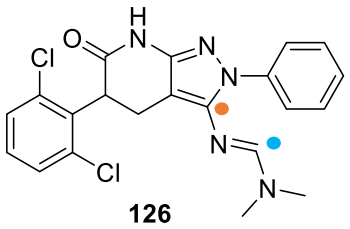

126

Figure 4.6. Possible structure of compound **126** resulting from the treatment of **64**{*7*,*1*,*3*} with $SOCl_2$ and DMF.

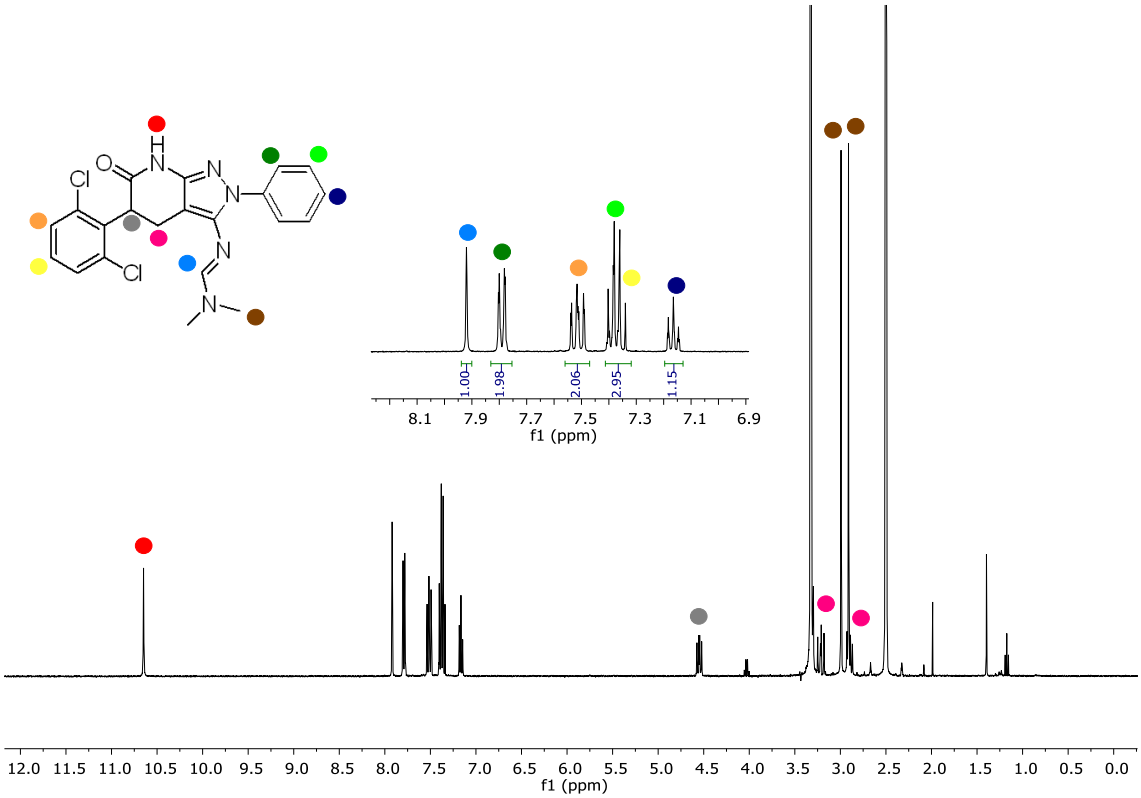

Figure 4.7. 1H-NMR spectrum of compound **126**.

The reactions were also studied with compounds **64**{*7*,*1*,*1*}, **64**{*2*,*1*,*3*} and **64**{*1*,*3*,*3*} (Figure 4.2). Compound **64**{*7*,*1*,*1*} was treated with $POCl_3$ (3h at reflux), but despite of using different work-up procedures, the expected product was not obtained as the starting material decomposed in all cases.

Equivalent studies were performed with **64**{*2*,*1*,*3*}. On one hand, treatment with $POCl_3$ lead to the decomposition of the reactant even after 1h. On the other hand, when using $SOCl_2$ in $CHCl_3$, the compound did not react, and the starting material was recovered at both room temperature and reflux conditions.

Compound **64**{*1*,*3*,*3*} decomposed when treated in $POCl_3$. However, the reaction of **64**{*1*,*3*,*3*} with $POCl_3$/PCl_5 yielded an isolable product (Figure 4.8). Compound **64**{*1*,*3*,*3*} was treated with $POCl_3$ and PCl_5 (5 eq.) and refluxed for 18h. The reaction was quenched in ice, neutralized and a solid was filtered. (72% yield). The absence of aliphatic signals and the NH of the lactam in the ^{1}H-NMR suggested the transformation of the lactam ring onto a pyridine ring. Moreover, the lack of the singlet corresponding to CH of the pyridine indicated a complete substitution of the ring by chlorine atoms (Figure 4.9). The product was assigned as compound **127** and the structure composition was confirmed by HRMS.

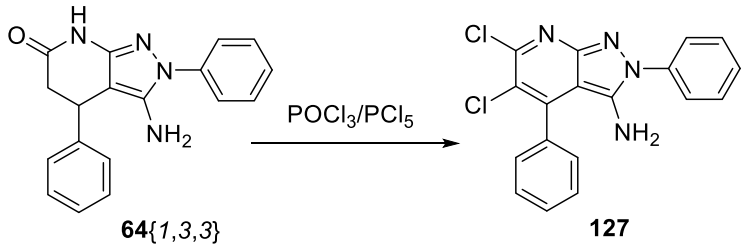

Figure 4.8. Possible structure of compound **127** resulting from the treatment of **64**{*1,2,3*} with $POCl_3/PCl_5$.

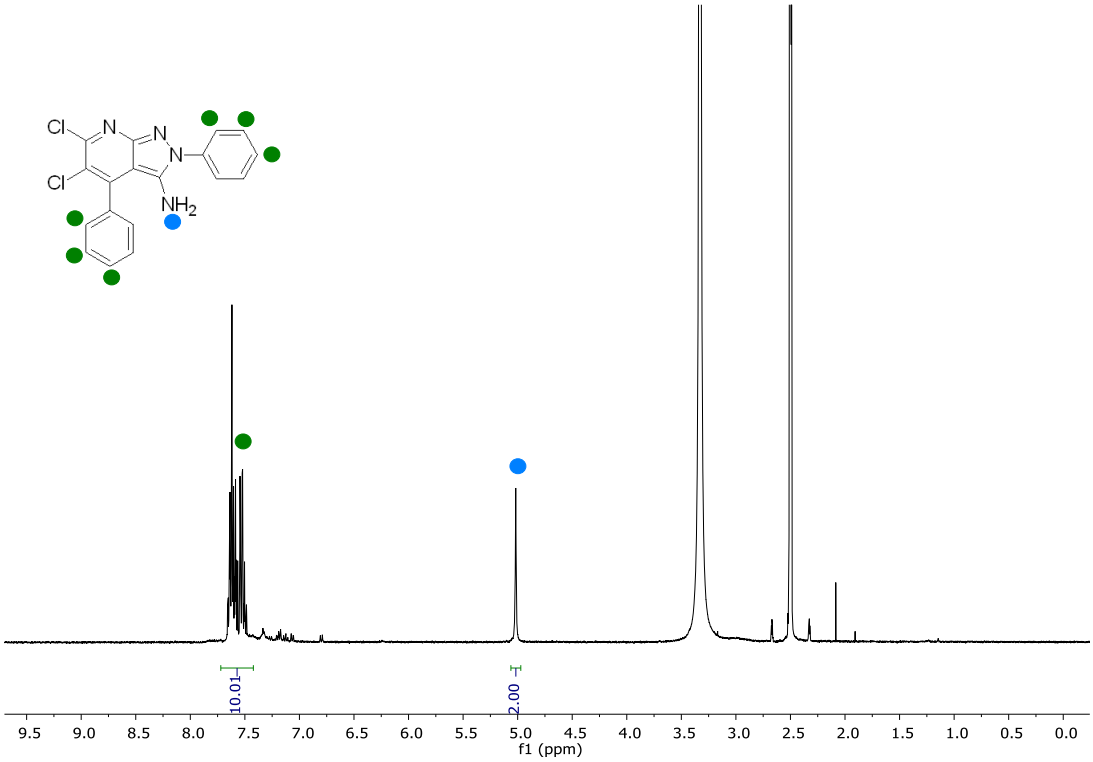

Figure 4.9. ^{1}H-NMR spectra of compound **127**.

The reduction of the chlorine atom of compound **123** was studied with two different reducing agents (H_2 Pd/C and CH_3COOH/ Zn) with no alteration of the compound. This reaction path may not be the most useful for further studies as the reaction would need drastic conditions to achieve the elimination of the chlorine atoms. The required conditions would affect other functional groups in case the methodology needs to be used in other scaffolds.

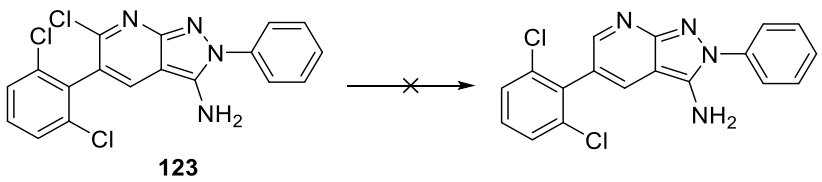

Figure 4.10. The elimination of the chlorin atom did not yield any product.

4.1.2.3. 3-amino-pyrazolo[3,4-*b*]pyridin-6-yl trifluoromethanesulfonates

A third option to transform the carbonyl of the pyrazolo[3,4-*b*]pyridin-6-ones is to capture the enolic form with a triflate group that could be further substituted by many other functional groups. Triflates are excellent leaving groups and can be substituted by many different functional groups such as boronic acids (Suzuky reaction), amines, thiols, alcohols or nitriles[7–11] and being compatible with a huge variety of other functional groups like esters, ethers, halogens or tertiary amines. [7–11] For this reason, introducing a triflate group into the molecule would allow to have a general scaffold easily amenable to substitution at position C6 of the pyridine ring.

With this purpose, to transform the carbonyl group into a triflate group two different strategies were tested. In both cases, the source of triflate was triflic anhydride (Tf_2O).[12–14]

Both methodologies were applied on scaffolds with different R^1 and R^2 substituents (H, Me, Ph), dehydrogenated and non-dehydrogenated pyridone rings and different R^3 substituents (H, Me, Ph) in the pyrazole ring. Despite several efforts, it was not possible to obtain the products of interest.

As shown in Table 4.2, it was not possible to capture the enolic form of the pyridone ring of the 3-amino-pyrazolo[3,4-*b*]pyridin-6-ones. Apparently, these molecules easily formed a triflic salt with the NH_2 group which later did not react to form the corresponding 3-amino-pyrazolo[3,4-b]pyridin-6-yl trifluoromethanesulfonate. Only in the case of **64**{*1*,*2*,*1*} a different product was obtained but it corresponded to the introduction of the triflate group on the pyrazole ring.

Table 4.2. Studied conditions for the introduction of a triflate group in the carbonyl group of the lactam ring.

Starting material	Conditions	Product
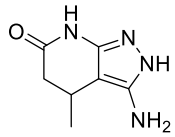 **64**{*1,2,1*}	OTf_2 (1.5 eq.), Py (1.5 eq.), CH_2Cl_2 20 min, 0°C	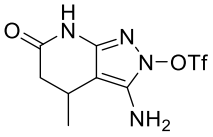 **128** + **129**: salt of **64**{*1,2,1*}
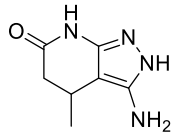 **64**{*1,2,1*}	OTf_2 (2 eq.), Py 30 min at RT	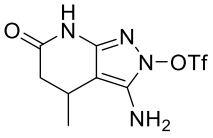 **128** + **129**: salt of **64**{*1,2,1*}
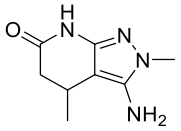 **64**{*1,2,2*}	OTf_2 (1.5 eq.), Py (1.5 eq.), CH_2Cl_2 30 min at RT	**130**: salt of **64**{*1,2,2*}
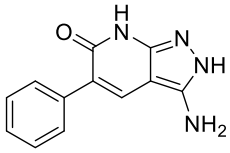 **85**{*3,1,1*}	OTf_2 (1.5 eq.), Py (1.5 eq.), CH_2Cl_2 30 min, 0°C	Decomposition
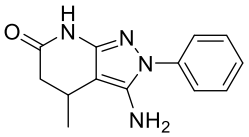 **64**{*1,2,3*}	OTf_2 (1.5 eq.), Py (1.5 eq.), CH_2Cl_2 30 min, 0°C	**131**: salt of **64**{*1,2,3*}
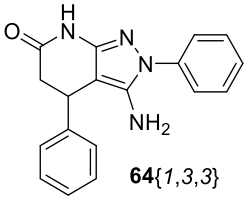 **64**{*1,3,3*}	OTf_2 (1.5 eq.), Py (1.5 eq.), CH_2Cl_2 O/N at RT	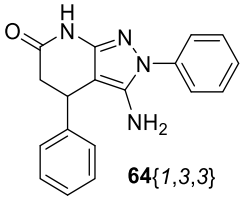 **64**{*1,3,3*}

Surprisingly, in the case of molecule **94** (see Chapter 2) which does not contain a NH_2 group and presents a substituted pyrazole group, the introduction of the triflate group occurred under mild conditions and the group was later easily substituted by *N*-methylpiperazine (**133**). (Figure 4.11). Figure 4.12 and Figure 4.13 show the NMR spectra of these molecules confirming the introduction of the triflate group and its substitution. These results indicate that, for 3-amino-pyrazolo[3,4-*b*]pyridin-6-ones, the presence of a basic nitrogen (NH, NH_2) is not compatible with the introduction of a triflate group at position C6.

Consequently, further studies should be performed, including the protection of such nitrogen atoms, to use this methodology which shows a promising versatility and should allow the preparation of an interesting scaffolds.

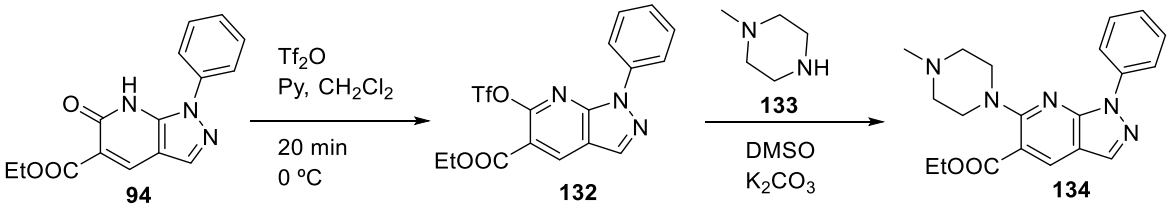

Figure 4.11. Introduction of the triflate group in compound **94** and subsequent substitution by 1-methylpiperazine (**133**).

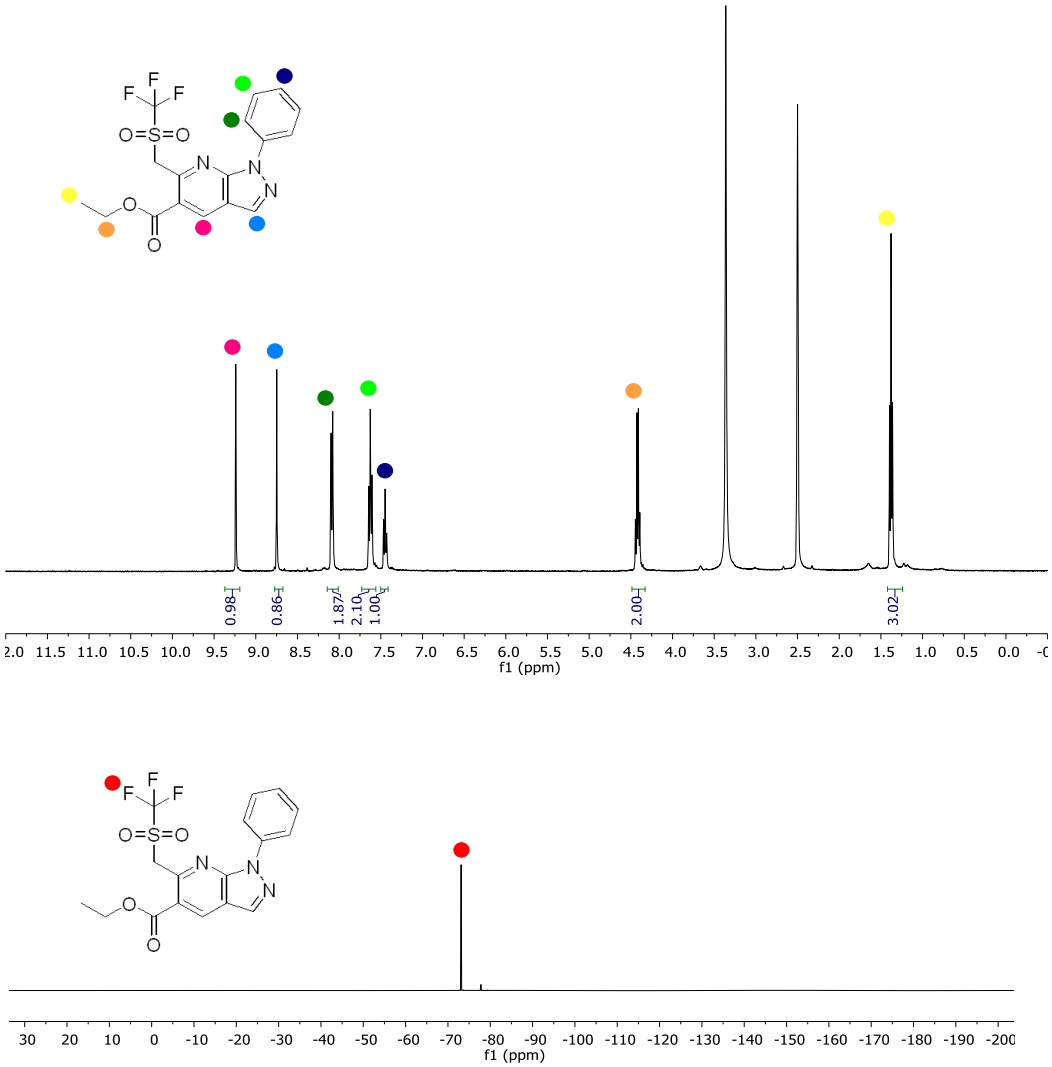

Figure 4.12. ^{1}H and ^{19}F-NMR spectra of compound **132** showing the introduction of the triflate group in the molecule.

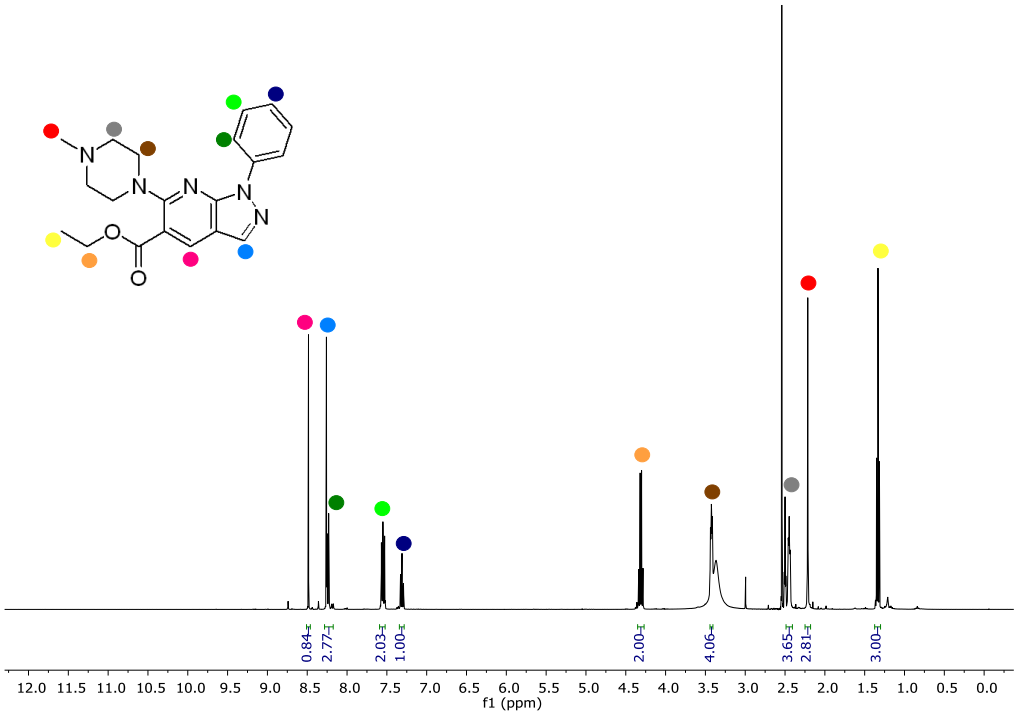

Figure 4.13. ^{1}H-NMR spectrum of the substituted compound **134**. The new aliphatic signals indicate the successful substitution of the triflate by the 1-metyhlpiperazine.

4.1.3. Biological activity

The first set of compounds with the carbonyl group substituted by a chlorine atom were tested for their biological activity in the cell lines MDA-MB-231 (breast cancer) and MV4-11(leukemia). Cells were treated for 24h with the compounds and MNK1/2 activity was monitored by the phosphorylation status of eIF4E. While there was no inhibitory effect of the compounds observed in MDA-MB-231 cells, compound **127** was able to reduce MNK activity significantly in the more sensitive MV4-11 leukemia cell line (Figure 4.15).

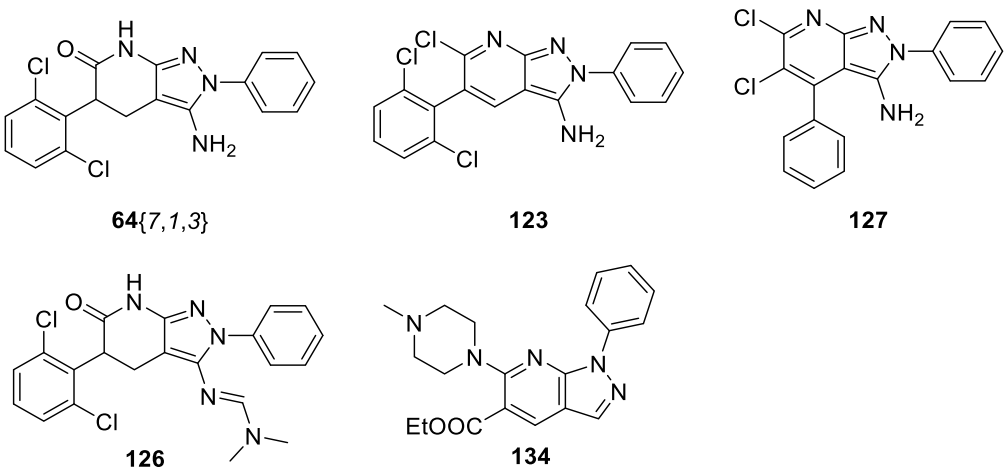

Figure 4.14. Structure of the compounds prepared during the study of the substitution of the carbonyl moiety.

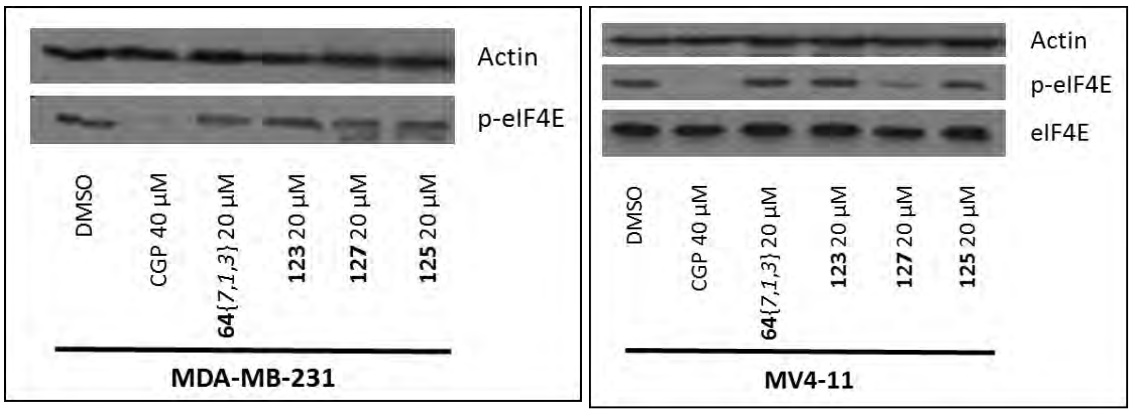

Figure 4.15. Study of the *in vitro* activity of the compounds on MDA-MB-231 and MV4-11 cells. WB was performed after 24h of treatment with the compounds. Final DMSO concentration 0.5%. CGP is a MNK inhibitor used as positive control.

In order to determine the potency of the compound **127**, we performed titration curves in the MV4-11 cell line at different time points. When judging the results by western blot analysis, we could observe a clear inhibition of MNK1/2 activity at concentrations higher than 20 µM. The activity of the compound at a concentration of 20 µM appears to be moreover time dependent and while after 6h of treatment only a mild effect could be observed, a clear inhibition can be detected after 24h. However, at the concentrations that effectively inhibit MNK activity, the compound was cytotoxic. As MNK1/2 kinases are reported to be non-essential for life, such effect was not expected and may indicate potential off-target effects.

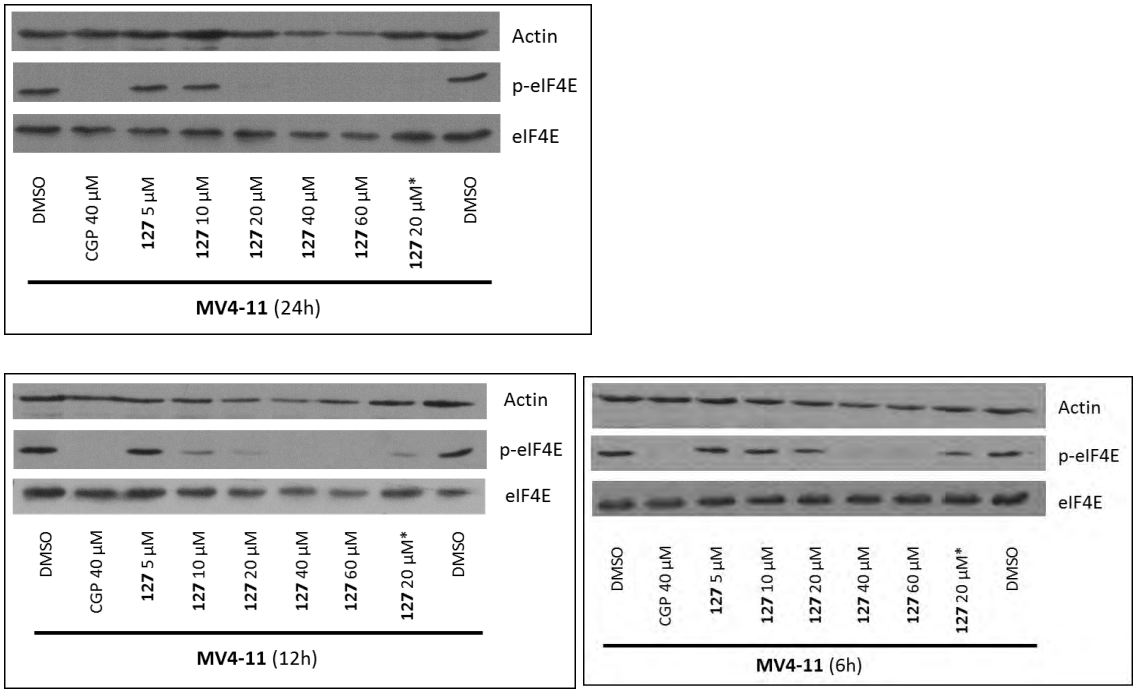

Figure 4.16. Titration curves of compound **127** on MV4-11 cells at different treating times. Final DMSO concentration: 0.5%. CGP is used as a positive control * indicates a stock of the compound, prepared separately one a week before the experiment.

Compound **127** was further studied during a pre-doctoral research stay at the Lady Davis Institute, McGill University in Montreal (Canada) under the supervision of Dr. Sonia del Rincon and Dr. Ivan Topisirovic. To extend the previous study, three additional cell lines were included to test the biological activity of **127**: two melanoma cell lines (A375M and MeWo) and an ovarian cell line (A2780). In contrast to the results obtained in MV4-11 cells, **127** was not able to reduce the phosphorylation of eIF4E. Nonetheless, altered cell growth induced by the compound **127** was observed in all the tested cell lines accompanied by alterations in the protein levels of p-AKT, 4EBP1 and MNK1. (Annex 4)

MV4-11 cells have been described to be more sensitive to MNK inhibitors due to the presence of a mutation (FLT3-ITD).[15,16] In order to test, if the increased sensitivity is linked to this mutation, we used a the AML (Acute Myeloid Leukemia) cell lines MOLM-14, heterozygous for FLT3-ITD mutation and HL-60 as wild-type control. In these cell lines, inhibition of eIF4E phosphorylation could only be observed at the highest concentration used (40 µM) and this reduction was furthermore accompanied with reduced levels of other proteins in the same signaling cascade such as 4E-BP1, MNK1 and ERK. Thus, the reduction of eIF4E phosphorylation appears to be rather an off-target effect than readout for selective inhibition of MNK kinases.

This potential off target effect of the compound **127** was supported by the kinase assays at Proqinase®, since no direct inhibition of the MNKs could be detected (Table 4.3). We finally concluded, that compound **127** was not directly inhibiting MNKs but altering related signaling pathways, which in the case of MV4-11 cells, result in an indirect reduction of eIF4E phosphorylation.

Table 4.3. Results from the enzymatic radiometric assay performed by Proqinase ®. Values indicated as residual activity of kinases MNK1 and MNK2 after treatment with the indicated compounds (10 µM). CGP and cercosporamide are used as positive controls.

Compound	MNK1	MNK2
cercosporamide	6	1
CGP	34	39
127	103	102

Compound	MNK1	MNK2
123	97	99
126	111	106
134	94	95

4.1.4. Conclusion

The carbonyl moiety of the lactam ring may be negatively affecting the activity of the pyrazolo[3,4-*b*]pyridin-6-one scaffold and its elimination or substitution is considered an interesting alternative to study this problem. Unfortunately, direct substitution was not possible to be achieved.

As an alternative, halogenation was studied on different compounds. Despite the substitution was achieved for two of the scaffolds it was not possible to obtain a general methodology. For example, the treatment of **64**{*7*,*1*,*3*} with $POCl_3$ lead to the obtention of compound **123** while the reaction with $POCl_3$ / PCl_5 only yields the dehydrogenated product **85**{*7*,*1*,*3*} and the reaction with $SOCl_2$ in the presence of DMF and $CHCl_3$ yields as a major product the imine **126**. On the other hand, the treatment of **64**{*1*,*3*,*3*} in the same conditions only lead to the disubstituted product **127** in the case of the treatment with $POCl_3$/PCl_5. For the other compounds, it was not possible to isolate any new product.

The halogenation reaction was highly dependent on the substitution of the molecule and the conditions should be optimized for each scaffold of interest. This would only be useful if the final objective of the reaction is to have a halogen atom in the molecule. However, when the objective of the halogenation is to introduce a new good leaving group susceptible to be eliminated or substituted later, it is interesting to look for a more general methodology.

A final strategy to prepare a general structure to substitute position C6 of the pyridine was to introduce a triflate group. Unfortunately, the nature of the scaffold hampered the synthesis of such products.

The prepared compounds were tested as MNK inhibitors. Only compound **127** reduced eIF4E phosphorylation in the more sensitive cell line MV4-11 apparently with no direct inhibition of MNKs.

4.2. Synthesis of aromatic pyrazolo[3,4-*b*]pyridin-3-amines

4.2.1. Introduction

The development of a general methodology for the elimination/substitution of the carbonyl moiety and the oxidation of the pyridone ring of pyrazolo[3,4-*b*]pyridin-6-ones (**64**) did not provide the expected results as the tested methods were not compatible with the key elements of the scaffold or did not allow the development of a general methodology.

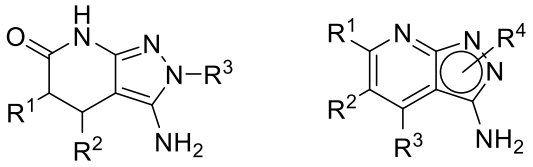

64 **138**

Figure 4.17. General structures of pyrazolo[3,4-*b*]pyridin-6-ones (**64**) and pyrazolo[3,4-*b*]pyridin-3-amines (**138**)

An alternative approach for the preparation of products not containing the carbonyl group of **64** and being aromatic was considered. 3-amino-pyrazolo[3,4-*b*]pyridines (**138**) were selected for this purpose because the transformations that we wanted to carry out on compounds **64** would have produced final products equivalent to **138**. The synthesis of 3-amino-pyrazolo[3,4-*b*]pyridines (**138**) would consist on the cyclization of the already substituted pyridines with different hydrazines (**56**).

In the case of compounds **64** the cyclization reaction to form the pyrazole ring starting from 2-methoxy-6-oxo-1,4,5,6-tetrahydropyridine-3-carbonitriles (**62**) proceeds *via* direct substitution of the methoxy group by the most nucleophilic N of the hydrazine and the subsequent cyclization onto the nitrile moiety. However, in the case of 3-methoxynicotinonitriles (**135**), the reactivity of the methoxy group is lower due to the aromaticity of the pyridine, being necessary to convert the methoxy group in a bromine atom to achieve a nucleophilic displacement[17] (Figure 4.18).

As a prove of concept, such approach to aromatic 3-amino-pyrazolo[3,4-*b*]pyridines (**138**) was tested with two different 3-methoxynicotinonitriles (**135**): the unsubstituted product **135**{*1*,*1*} (R^1, R^3 = H) and the 4,6-diphenyl substituted product **135**{*3*,*3*} (R^1, R^3 = Ph). 4,6-diphenyl-2-methoxynicotinonitrile (**135**{*3*,*3*}) was previously synthesized in our group[17] *via* a condensation of malononitrile with (*E*)-chalcone using a one-step synthesis. The second compound, 2-methoxynicotinonitrile (**135**{*1*,*1*}), is commercially available from Fluka.

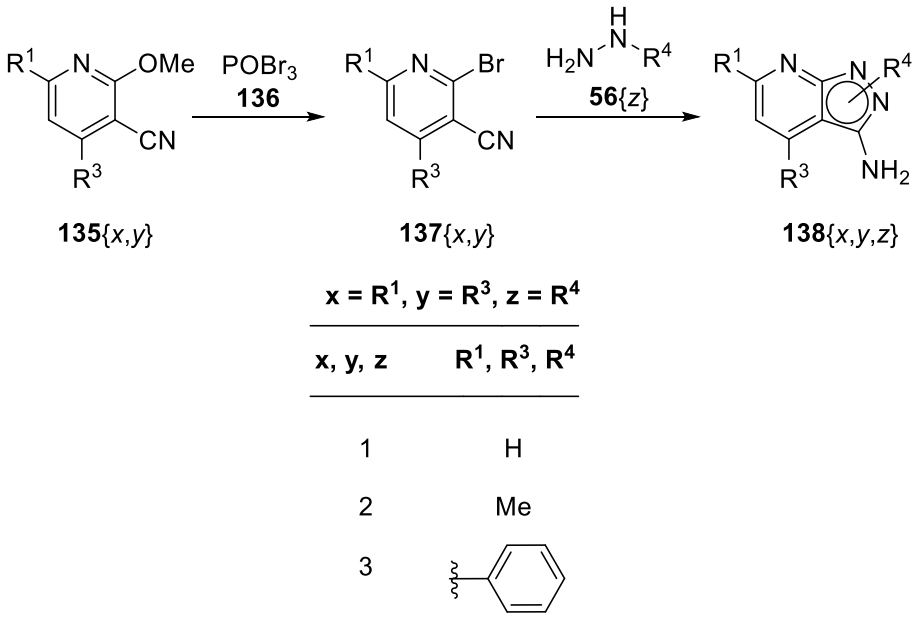

Figure 4.18. Proposed synthetic strategy for the preparation of 3-amino-pyrazolo[3,4-*b*]pyridines (**138**).

4.2.2. Preparation of 2-bromonicotinonitriles

As expected, direct cyclization of compound **135**{*1*,*1*} with hydrazine was not achieved under the previously described conditions (MW irradiation for 30 min at 140 °C). Therefore, in order to favor the formation of the pyrazole ring, the methoxy group of **135**{*1*,*1*} was substituted by a bromine group.

The optimization of the bromination protocol was carried out using compound **135**{*3*,*3*}. The methodology of Liu *et al.*[18] was used as a starting point: compound **135**{*3*,*3*} was treated with $POBr_3$ (2.2 eq.), pyridinium-HBr (0.014 eq.) and H_3PO_4 (0.014 eq.) in dioxane. When the mixture was refluxed for 1h or 3h, conversion was not complete (50% and 80% respectively), and purification by flash column chromatography was needed. Moreover, heating at reflux for times greater than 3 hours caused decomposition of reaction crude. Temperature was then reduced to 60 °C and the mixture was heated for 18h obtaining complete conversion to the bromine substituted compound **137**{*3*,*3*} in 84% yield. The work up described in literature[18,19], which consisted on extractions of the product with an organic solvent, was replaced by a quenching with ice, neutralization with NaOH (6M) and filtration of the product.

These reaction conditions were also used to prepare compound **137**{*1*,*1*} which was obtained in a 50% yield.

4.2.3. Preparation of aromatic pyrazolo[3,4-*b*]pyridin-3-amines

Compounds **137**{*1*,*1*} and **137**{*3*,*3*} were cyclized with three different hydrazines: phenylhydrazine (**56**{*3*}), methylhydrazine (**56**{*2*}) and hydrazine (**56**{*1*}).

Due to the lower reactivity of this scaffolds in comparison to the 2-methoxy-6-oxo-1,4,5,6-tetrahydropyridine-3-carbonitriles, it was necessary to readjust the cyclization conditions. Heating under reflux again did not provide enough energy to achieve the final cyclized product. However, this time no open intermediate was obtained (as in the case of 2-methoxy-6-oxo-1,4,5,6-tetrahydropyridine-3-carbonitriles **62**) and only the starting material was recovered. All cyclizations were carried out using microwave irradiation which allowed to overcome higher energy barriers by working at higher thermal levels and higher pressures. However, for each example, the reaction conditions had to be slightly modified in terms of time and temperature.

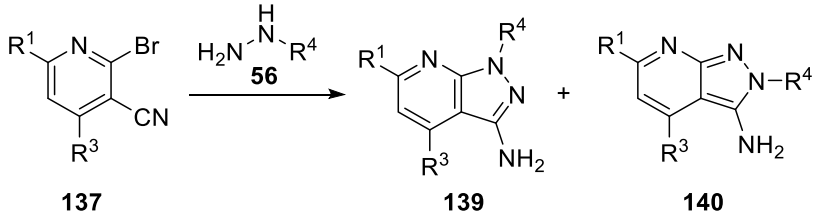

Figure 4.19. General scheme of the cyclization reaction of 2-bromonicotinonitriles (**137**) with hydrazines (**56**).

The cyclization of 2-bromonicotinonitriles **137** with substituted hydrazines can lead to two possible regioisomers (**139** and **140**). In the preceding chapters, we have already demonstrated that the reaction path is dependent on the different nucleophilicities of the N atoms of the hydrazine. Moreover, the reaction of 2-methoxy-6-oxo-1,4,5,6-tetrahydropyridin-3-carbonitriles (**62**) with phenylhydrazine (**56**{*2*}) only yields the N2 substituted isomer while the reaction with methylhydrazine (**56**{*1*}) yields a mixture of both isomers. Computational calculations performed on both isomers also support the formation of a major N2 substituted compounds as it has a higher stability.

However, in the case of 2-bromonicotinonitriles **137**, the formation of the N2 substituted isomer **140** would totally change the aromatic conjugation of the system. As it can be seen in Figure 4.20, the N1 substituted structures **139** present aromatic circulation in both rings thanks to the double bond that can be drawn in the fusion of both rings (Figure 4.20).

On the contrary, in the case of the N2 substituted structures **140** (Figure 4.20) is only possible a peripheric aromatic circulation and the double circulation is impossible due to the forced positions of the insaturations in the pyrazole ring. This fact, together with the nucleophilicities of the nitrogen atoms of the substituted hydrazine, can lead to completely different results with respect to those obtained with pyrazolo[3,4-*b*]pyridin-6-ones (**63/64**).

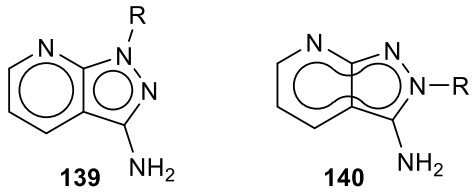

Figure 4.20. Aromatic conjugation of pyrazolo[3,4-*b*]pyridines depending on the position of the substituents of the pyrazole ring.

A prediction of the relative stability of both isomers using quantum mechanics calculations performed with Gaussian.09[20] (Table 4.4) suggested that, for aromatic pyrazolo[3,4-*b*]pyridin-3-amines, the N1 substituted isomer would be the most stable isomer and, therefore, the most suitable compound to be obtained. In other words, it seems clear that the double aromatic circulation is better than the peripheric circulation.

Table 4.4. Energy values of the different isomers calculated with DFT B3LYP 6-311++G(d,p). For * DFT B3LYP 6-311G(d,p) was used.

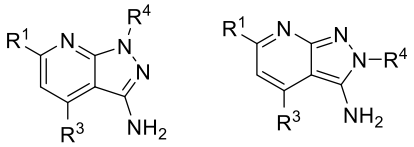

x = R1, y = R3, z = R4

x,y,z	R
1	H
2	Me
3	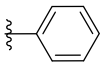

ENERGY (kcal/mol)	
140{*1,1,3*}	-428120.0
139{*1,1,3*}	-428131.8
140{*1,1,2*}	-307808.2
139{*1,1,2*}	-307818.8
140{*1,1,1*}	-283149.8
139{*1,1,1*}	-283160.9

ENERGY (kcal/mol)	
140{*3,3,3*}	-718061.5*
139{*3,3,3*}	-718073.3*
140{*3,3,2*}	-597759.4
139{*3,3,2*}	-597769.2
140{*3,3,1*}	-573101.1
139{*3,3,1*}	-573111.4

Δ ENERGY (kcal/mol)	
140{*1,1,3*} - **139**{*1,1,3*}	11.8
140{*1,1,2*} - **139**{*1,1,2*}	10.5
140{*1,1,1*} - **139**{*1,1,1*}	11.1

Δ ENERGY (kcal/mol)	
140{*3,3,3*} - **139**{*3,3,3*}	11.8
140{*3,3,2*} - **139**{*3,3,2*}	9.8
140{*3,3,1*} - **139**{*3,3,1*}	10.3

4.2.3.1. Cyclization with hydrazine

Firstly, 2-bromonicotinonitriles **137**{*1*,*1*} and **137**{*3*,*3*} were cyclized with unsubstituted hydrazine (**56**{*1*}). A mixture of the corresponding **137** and 2 eq. of hydrazine monohydrate in MeOH was heated under microwave irradiation at 140 °C for 1 hour. The expected products were obtained after resuspending the reaction crude in MeOH.

This reaction can, of course, lead to **139**{*x*,*y*,*1*} and **140**{*x*,*y*,*1*} which are interconvertible tautomers. According to the calculations, isomer **139**{*x*,*y*,*1*} is the more stable tautomer and is considered to be the main product of the reaction.

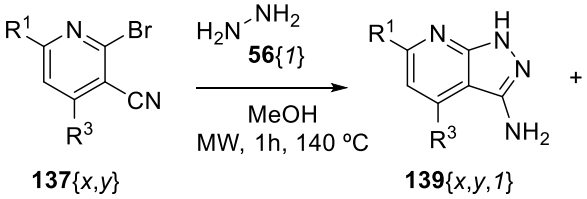

x = R¹, y = R³	
x,y,z	**R**
1	H
2	Me
3	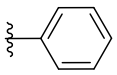

Figure 4.21. Cyclization of 2-bromonicotinonitriles (**137**) with hydrazine (**56**{*1*}).

Using the aforementioned protocol, compound **139**{*3*,*3*,*1*} was obtained in 54% yield. This is therefore the first time that **139**{*3*,*3*,*1*} is obtained from **137**{*3*,*3*} by microwave irradiation. Deeb *et al.*[21] described a two-step synthesis to obtain **139**{*3*,*3*,*1*} from 3-cyano-4,6-diphenylpyridine-2-sulfonyl chloride using anhydrous hydrazine due to the high reactivity of the reagent. A more similar procedure was described by Abdel-Hafez *et al.*[22] using 2-chloro-4,6-diphenylpyridine-3-carbonitrile at reflux for 4 hours in EtOH with hydrazine hydrate.

Similarly, **139**{*1*,*1*,*1*}, the simplest molecule of the aromatic pyrazolo[3,4-*b*]pyridin-3-amine family, was formed in a 68% yield. Despite the synthesis of this compound is well reported [23–28], only Sharma *et al.*[28] describe a microwave assisted methodology to obtain **139**{*1*,*1*,*1*} and all the published protocols use 2-chloro-pyridine-3-carbonitrile as reactant.

Although these aromatic pyrazolo[3,4-*b*]pyridin-3-amines are not new, we have demonstrated that the cyclization can take place with the 2-bromonicotinonitriles in similar conditions to those used for the formation of pyrazolopyridin-6-ones and we have increased the number of molecules of this study.

4.2.3.2. Cyclization with methylhydrazine

As mentioned before, the cyclization of **137** with methylhydrazine could lead to two different isomers **139**{*x*,*y*,*2*} and **140**{*x*,*y*,*2*} (Figure 4.22). In contrast to the results obtained with the pyridone scaffold, the cyclization of 2-bromonicotinonitriles **137**{*1*,*1*,*1*} and **137**{*3*,*1*,*3*} with methyl hydrazine **56**{*2*} using microwave irradiation at 140 °C for 1 hour only yielded one compound in both cases: the corresponding *N*1-methyl substituted pyrazolo[3,4-*b*]pyridin-3-amines **139**{*1*,*1*,*2*} and **139**{*3*,*3*,*2*} (in isolated yields of 43% and 57%, respectively)**.** The HMBC spectrum of **139**{*1*,*1*,*2*} confirmed the substitution point with a correlation between the methyl group and the bridge carbon of the pyrazole ring (Figure 4.23). The reaction crude was consciously analyzed to discard the presence of a second isomer.

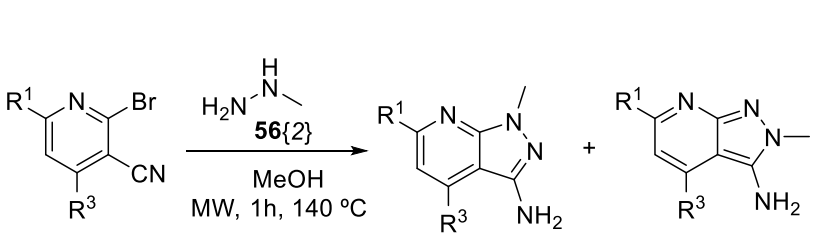

x = R^1, y = R^3	
x,y,z	**R**
1	H
2	Me
3	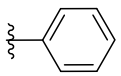

Figure 4.22. Possible products of the cyclization of 2-bromonicotinonitriles (**137**) with methylhydrazine (**56**{*2*}).

The nucleophilicity of the two nitrogen atoms of the methylhydrazine molecule is similar and, as described before, the cyclization with pyridones (**62**) led to the formation of two different isomers (**63** and **64**). However, in this case, the formation of the isomer **140** is less favorable due to the high energetic difference (around 10 kcal/mol) caused by the different aromatic conjugation of **139** and **140** previously discussed. The stability of the final product seems to be more important than the steric hindrance of the methyl hydrazine which regulated the ratio between the two isomers in the case of pyridones (**62**).

Compound **139**{*1*,*1*,*2*} has been previously synthesized by B. Lynch *et al.* using long refluxes, however there are no reports of a synthesis of compound **139**{*3*,*3*,*2*}.

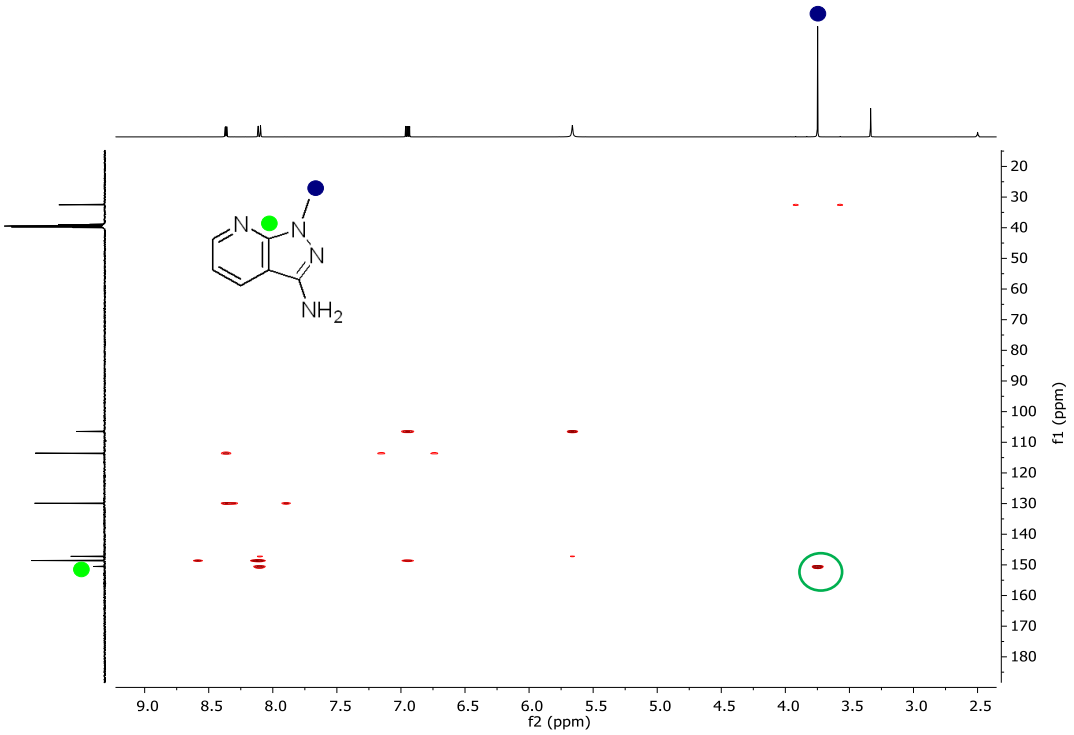

Figure 4.23. HMBC spectrum of **139**{*1,1,2*}. The correlation between the protons of methyl group (blue) and the bridge carbon (green) confirms the substitution point of the pyrazole.

4.2.3.3. Cyclization with phenylhydrazine

As in the preceding case, the reaction with phenylhydrazine can lead to two possible regioisomers **139**{*x,y,3*} and **140**{*x,y,3*} (Figure 4.24). We have previously shown that in the case of piridones **62** the reaction with phenylhydrazine **56**{*3*} only yields the N2 substituted isomer due to the different nucleophilicity of the N atoms of the phenylhydrazine. However, in this case, the formation of the N2-phenyl substituted isomer **140**, according to the nucleophilicity of the phenylhydrazine, would imply the formation of a by far less stable compound.

Convergently, the cyclization of 2-bromonicotinonitriles with methylhydrazine only afforded the corresponding N1-methyl substituted pyrazolo[3,4-*b*]pyridines.

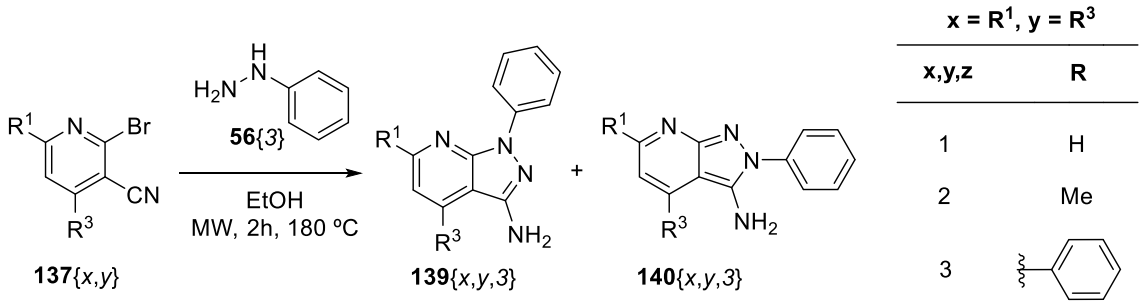

x = R¹, y = R³	
x,y,z	**R**
1	H
2	Me
3	

Figure 4.24. Cyclization of 2-bromonicotinonitriles (**137**) with phenylhydrazine (**56**{*3*})

Firstly, **137**{*1,1*} was treated with phenylhydrazine **56**{*3*}. When using the previously optimized conditions (2 eq. of phenylhydrazine in MeOH heated using microwave irradiation at 140 °C for 1h) no product was formed. The temperature and time were increased (2h at 180°C in EtOH) to observe the formation of a mixture of products. The resulting crude was purified by automated flash column chromatography (Alumina column with a Cy:AcOEt gradient 0-20% for 15 min and isocratic at 20% for 10 min) to afford two main products with equivalent signals in the ^{1}H-NMR spectra which, surprisingly, seemed to correspond to the two isomers **139**{*1,1,3*} and **140**{*1,1,3*} (isolated yields 3% and 9%). Despite it was not possible to unequivocally stablish the structure of both compounds, the structure of each isomer was assigned according to the chemical shifts of the NH_2 groups. As observed previously in this work, the NH_2 signal of the N2 substituted isomers is found more downfield than the corresponding group in the N1 substituted compounds. (Figure 4.25)

A close inspection of the reaction crude in comparison with the isolated products indicated that the reaction mixture contained approximately one third of each isomer and one third of the unreacted starting material. Some extra impurities were also present in minimal quantities.

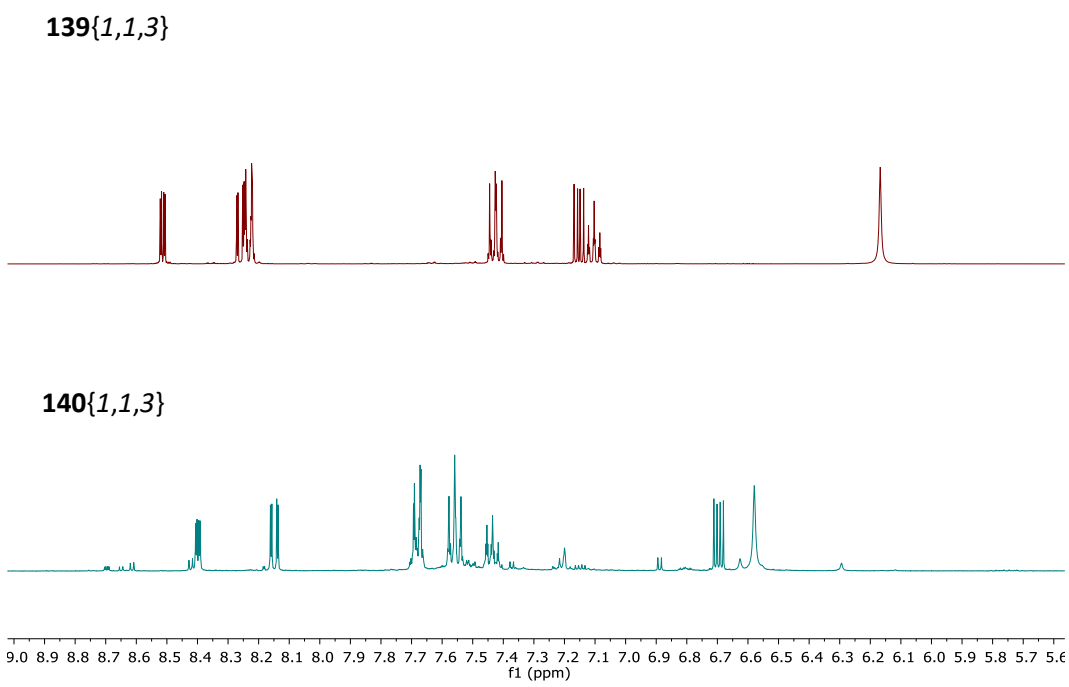

Figure 4.25. ^{1}H-NMR spectra of the isomers **139**{*1,1,3*} and **140**{*1,1,3*}. The structure of each compound was assigned according to the chemical shift of the NH_2 group.

Similar results were obtained in the cyclization of compound **137**{*3*,*3*}. Again, it was necessary to adjust the reaction conditions and compound **137**{*3*,*3*} and 2 eq. of **56**{*3*} were heated using microwave irradiation at 180°C for 2h in EtOH. Inspection of the reaction crude by ^{1}H-NMR indicated that the reaction mixture contained 3 products: unreacted compound **137**{*3*,*3*} and two compounds with equivalent signals. The compounds were successfully isolated by automated flash-column chromatography (Alumina column with a Cy:AcOEt gradient 0-20% for 40 min) and analyzed by NMR spectroscopy confirming that both isomers (**139**{*3*,*3*,*3*} and **140**{*3*,*3*,*3*}) had been obtained. Close inspection of the reaction crude comparing with the isolated products indicated that the mixture was approximately 50% of the starting product, and 25% of each isomer. Isolated yields for both isomers were similar: 17% for **139**{*3*,*3*,*3*} and 19% for isomer **140**{*3*,*3*,*3*}.

Bidimensional NMR spectroscopy, including NOESY spectroscopy, did not provide any useful information for the assignment of the structure of each isomer. Therefore, the structure of the isomers was again assigned based on the chemical shift of the NH_2 group and on the theoretical chemical shift of the N1/N2 phenyl group which in this case is significantly different (Figure 4.26).

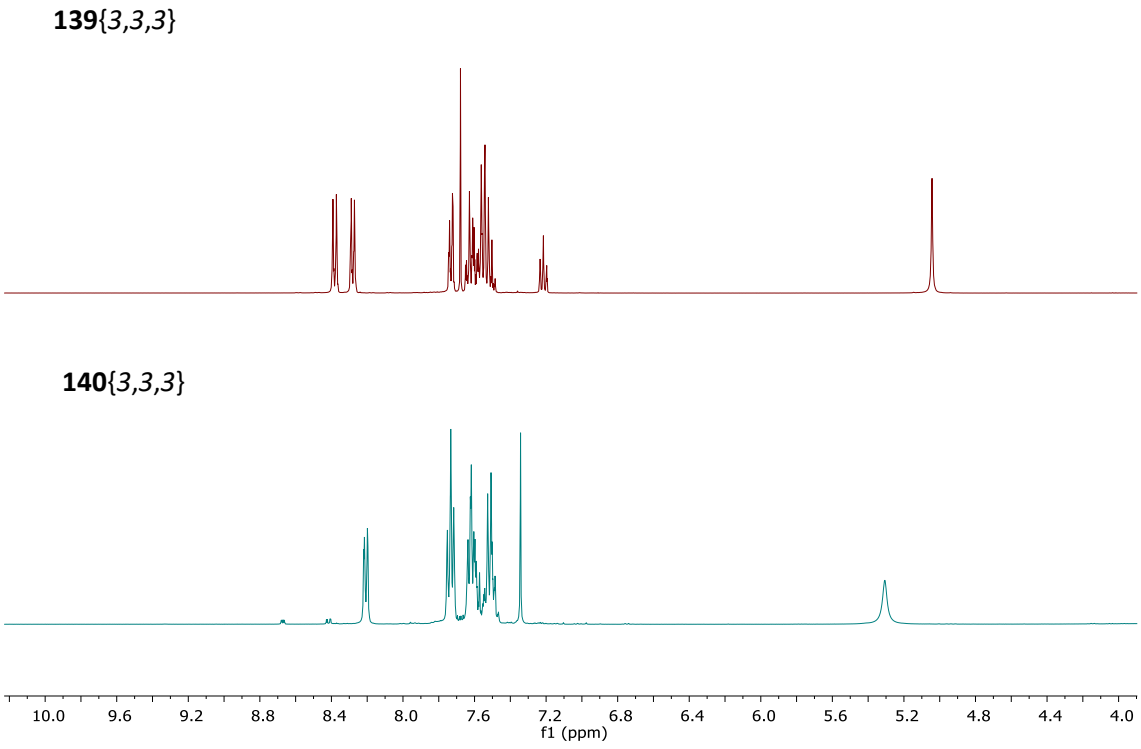

Figure 4.26. ^{1}H-NMR spectra of the isomers **139**{*3*,*3*,*3*} and **140**{*3*,*3*,*3*}. The structure of each compound was assigned according to the chemical shift of the NH_2 group and the pyrazole phenyl group.

Surprisingly, in both cases, the reaction of 2-bromonicotinonitriles with phenylhydrazine yielded two isomers although the energetic barriers were even higher than the ones previously observed on the cyclization of 2-methoxy-6-oxo-1,4,5,6-tetrahydropyridin-3-carbonitriles (**62**) with phenylhydrazine. Consequently, microwave irradiation in sealed vials was needed in this case (EtOH at 180°C) for reaching the energetic levels required to allow the cyclization step. Such high energetic barriers are caused by the competition between the generation of the most stable product through a reaction mechanism in which the less nucleophilic nitrogen atom of the phenylhydrazine must attack first (isomer **139**) and the formation of the less stable product obtained by the attack of the most nucleophilic nitrogen atom (isomer **140**).

The formation of isomer **139** would be extremely disfavored due to the low reactivity of the NH group in the phenylhydrazine molecule but, if the thermal level is enough to allow such attack, the final product presents a higher stability as the aromaticity of the pyridine ring is conserved. On the other hand, the formation of isomer **140** is expected also to be disfavored as the final product is less stable due to the peripheral aromaticity of the final product as previously discussed.

The thermal levels required to carry out the reaction with a certain conversion renders both pathways possible and the reaction yields both isomers (**139** and **140**) in low yield but similar proportions.

4.2.4. Biological activity

As described for previous compounds, we tested the activity of the pyrazolo[3,4-*b*]pyridin-3-amine family of compounds for the inhibition of MNKs in parallel at enzymatic and cellular levels with the radiometric kinase assay and by western blot analysis of MDA-MB-231 cells respectively (Table 4.5 and Figure 4.27).

Among the tested compounds, **139**{*3*,*3*,*1*} reduced significantly the activity of both kinases at 10 µM but being more effective in inhibiting MNK1 than MNK2.

Table 4.5. Results from the enzymatic radiometric assay performed by Proqinase ®. Values indicated as residual activity of kinases MNK1 and MNK2 after treatment with the indicated compounds at 10 µM.

Compound	MNK1	MNK2
139{*3*,*3*,*2*}	80	117
139{*3*,*3*,*1*}	14	52
139{*1*,*1*,*1*}	95	102
139{*1*,*1*,*2*}	106	95

Moreover, 20 µM of **139**{*3*,*3*,*1*} significantly inhibited eIF4E phosphorylation in the triple negative breast cancer cell line MDA-MB-231.

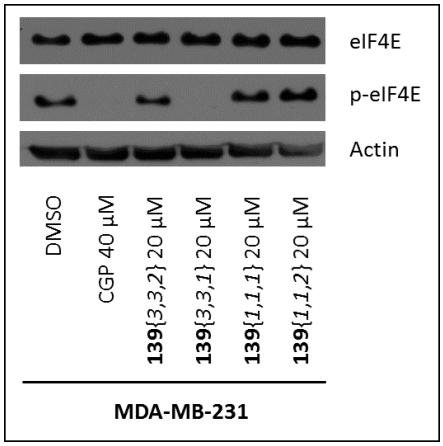

Figure 4.27. Treatment of MDA-MB-231 cells the 3-amino-pyrazolo[3,4-*b*]pyridinic compounds. WB performed after 24h of treatment. Final DMSO concentration 0.5%. CGP is used as a positive control.

As **139**{*3*,*3*,*1*} was the first striking hit in this group of compounds, we compared its structure to the inactive compounds and could conclude that the presence of the two phenyl rings at the C4 and C6 positions of the pyrazolo[3,4-*b*]pyridine appears to be essential for the activity of the compound. Moreover, the pyrazole ring should also be unsubstitued as the presence of a methyl group completely renders the molecule inactive.

4.2.5. Conclusion

The cyclization of 2-bromonicotinonitriles with hydrazines provides an versatile synthesis for the preparation of aromatic pyrazolo[3,4-*b*]pyridin-3-amines. The cyclization can afford two possible isomers, with substitution at N1 or N2. The formation of either isomer is governed by the stability of the final product and the relative nucleophilicity of the hydrazine nitrogen atoms. Cyclization with methylhydrazine leads to a single isomer (**139**, N1 substituted) while in the reaction with phenylhydrazine both isomers are obtained.

The compounds of this new family were tested as MNK inhibitors. Compound **139**{*3*,*3*,*1*} was identified as a first hit with a significant activity on the kinase activity in *in vitro* assay and a clear reduction of the phosphorylation of the MNK target protein eIF4E in MDA-MB-231 cells.

4.3. Derivatization of pyrazolo[3,4-*b*]pyridin-3-amines

4.3.1. Introduction

Compound **139**{*3*,*3*,*1*} was identified as a potential hit with the capacity to reduce the kinase activity of MNK1 and MNK2 and to avoid eIF4E phosphorylation in MDA-MB-231 cells. However, this compound was the only one among the tested molecules to show such properties. For this reason, it is interesting to study in depth this structure and elucidate if the activity detected is an individual case or if we have identified a new family of compounds with potential activity as MNK inhibitors.

In the previous section, we have shown that the presence of two phenyl rings at positions C4 and C6 is essential for the activity as the compounds lacking such substituents did not present any activity and the pyrazolo[3,4-*b*]pyridine core is not enough to inhibit these proteins. Furthermore, the preliminary kinase assay seems to indicate that an unsubstituted pyrazole ring is also necessary for the activity of the compounds and the presence of a methyl group attached completely drops the activity. Therefore, in order to investigate this family of compounds as MNK inhibitors and to prove the effect of the substituents on the biological activity, a new family of 4,6-diphenyl-1*H*-pyrazolo[3,4-*b*]pyridin-3-amines was designed and synthesized.

4.3.2. Synthesis of substituted 4,6-diphenyl-pyrazolo[3,4-*b*]pyridin-3-amines

Several derivatives of compound **139**{*3*,*3*,*1*} were prepared including different substituents in both phenyl rings. The synthetic possibilities of this ring substitution will allow to modulate the activity of the different compounds by affecting the interaction with the receptor.

The previously optimized synthetic protocol was also applied for the synthesis of the new compounds. However, as the initial 2-methoxynicotinonitriles (**135**) were not commercial an extra step was included to the synthetic route (Figure 4.28).

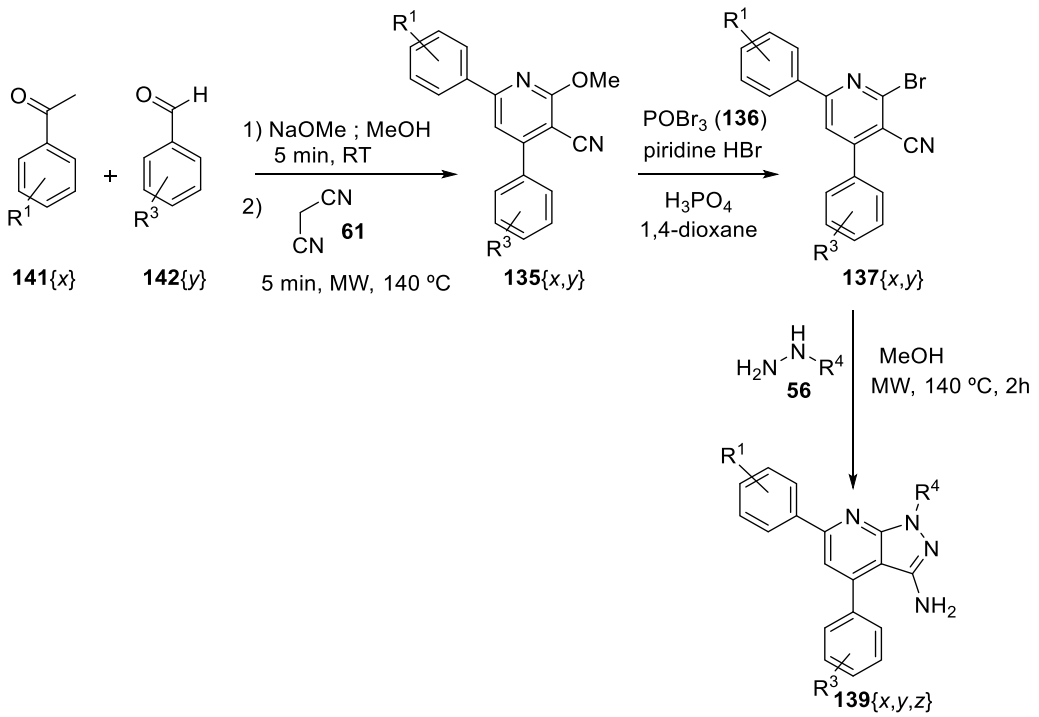

Figure 4.28. Synthesis of substituted 4,6-diphenyl-pyrazolo[3,4-*b*]pyridin-3-amines (**139**).

The final products were therefore obtained by a three-step synthesis. The first step was adapted from the methodology described by Amer *et al.*[29] which consisted on a One-Pot Two-Steps cyclization reaction to form the pyridine ring. The corresponding aldehyde and ketone were treated under basic conditions (1.1 eq. of NaOMe in MeOH) to form the chalcone intermediate that was later cyclized with malononitrile using microwave irradiation (5 minutes at 140 °C) to obtain the corresponding 2-methoxynicotinonitriles (**135**). In order to avoid the purification by column chromatography, the solvent of the reaction crude was eliminated under reduced pressure and the crude solid was suspended in MeOH to obtain the pure product **135**.

As previously described, the low reactivity of these methoxy substituted pyridines makes necessary a bromination step to obtain the corresponding 2-bromonicotinonitriles (**137**), that can be later cyclized with hydrazine. Compounds **135** were refluxed for 18h in 1,4-dioxane with $POBr_3$ (2.2 eq.) in presence of pyridinium-HBr and H_3PO_4. The reaction was neutralized with NaOH to filter the corresponding 2-bromonicotinonitrile (**137**).

Finally, compounds **137** were suspended in MeOH with 2 eq. of hydrazine monohydrate and heated using microwave irradiation for 2h at 140 °C. The solvent was removed under reduced pressure and the solid was suspended in MeOH to yield the corresponding pure 4,6-diphenyl-pyrazolo[3,4-*b*]pyridin-3-amine (**139**).

Unfortunately, the general method described in Figure 4.28 did not allow the synthesis of monosubstituted pyridines. Also, it was not possible to obtain products with dimethylamine substituents as the conditions for the bromination step seem to be not compatible with the presence of such functional group.

In order to clarify the importance of the unsubstituted pyrazole ring, compounds **137**{*4*,*4*} and **137**{*3*,*4*} were also cyclized with methylhydrazine to obtain the corresponding products **139**{*4*,*4*,*2*} and **139**{*3*,*4*,*2*}.

With this general methodology a set of 12 compounds were prepared with different substitutions on the phenyl rings on positions C4 and C6 of the pyrazolo[3,4-*b*]pyridine ring. 10 compounds contained an unsubstituted pyrazole ring and 2 were N1-methyl substituted. The final products and their yields are included in Figure 4.29 and Figure 4.30. Table 4.6 summarizes the yields of the formation of intermediates **135** and **137**.

Table 4.6. Yields of the preparation of compounds **135** and **137** according to the methodology described in Figure 4.28.

R_1 = x	R_2 = y	Yield 135{*x*,*y*} (%)		Yield 137{*x*,*y*} (%)	
p-OMe	*p*-OMe	**135**{*4*,*4*}	25	**137**{*4*,*4*}	92
Ph	*p*-OMe	**135**{*3*,*4*}	33	**137**{*3*,*4*}	82
p-OMe	*p*-$N(CH_3)_2$	**135**{*4*,*7*}	20	**137**{*4*,*7*}	-
p-OMe	*p*-Me	**135**{*4*,*5*}	33	**137**{*4*,*5*}	83
m-OMe	*p*-$N(CH_3)_2$	**135**{*5*,*7*}	18	**137**{*5*,*7*}	-
m-OMe	*p*-F	**135**{*5*,*6*}	25	**137**{*5*,*6*}	67
m-OMe	Ph	**135**{*5*,*3*}	20	**137**{*5*,*3*}	68
m-OMe	*p*-OMe	**135**{*5*,*4*}	20	**137**{*5*,*4*}	90
p-$N(CH_3)_2$	*p*-$N(CH_3)_2$	**135**{*7*,*7*}	26	**137**{*7*,*7*}	-
o-OMe	*p*-$N(CH_3)_2$	**135**{*6*,*7*}	10	**137**{*6*,*7*}	-
o-OMe	*p*-OMe	**135**{*6*,*4*}	65	**137**{*6*,*4*}	75
o-OMe	*p*-Me	**135**{*6*,*5*}	88	**137**{*6*,*5*}	65
Ph	*p*-F	**135**{*3*,*6*}	62	**137**{*3*,*6*}	85

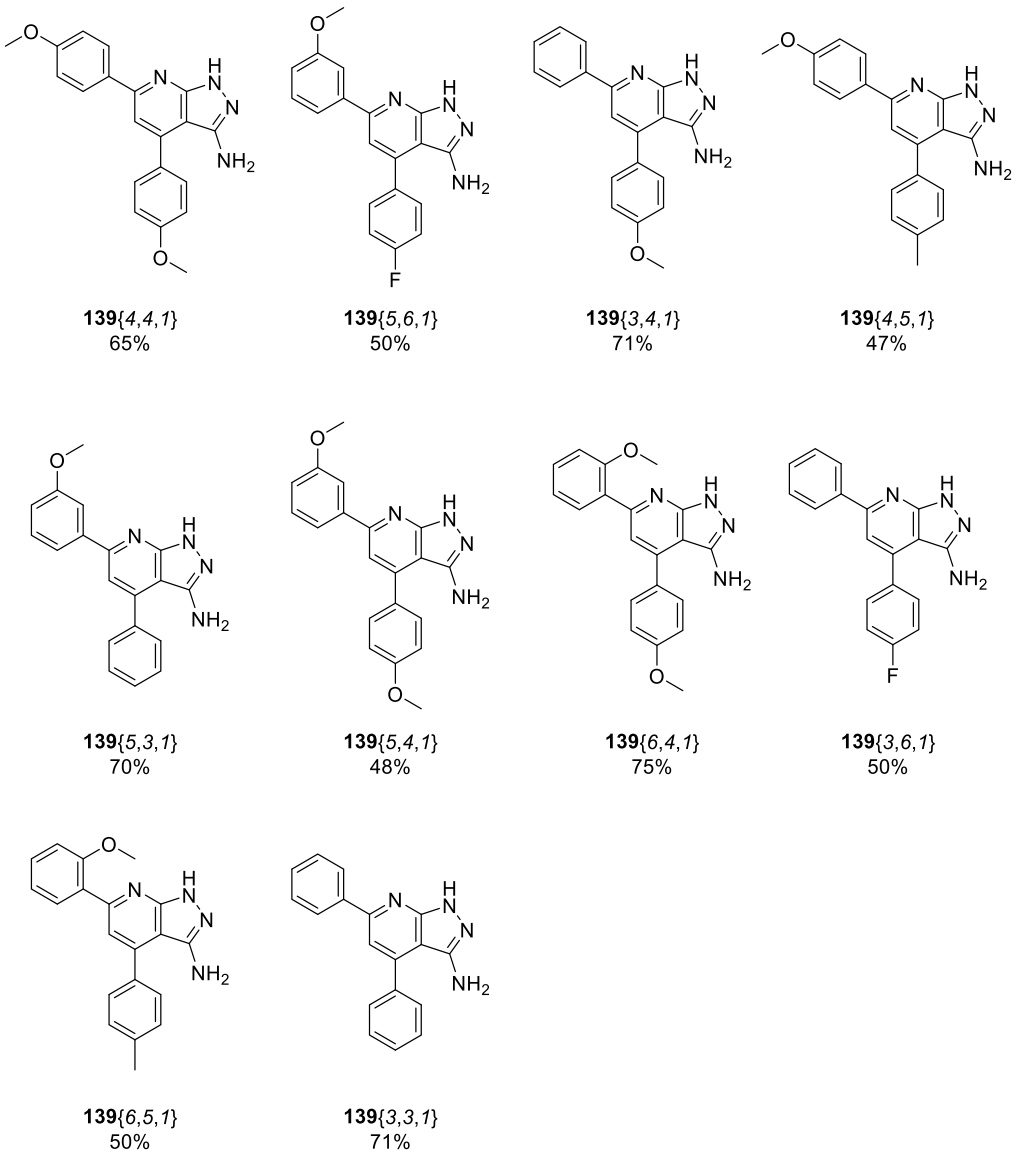

Figure 4.29. Unsubstituted 4,6-diphenyl-pyrazolo[3,4-*b*]pyridin-3-amines **139** synthetized in this project. The yield of the last step is described under each compound.

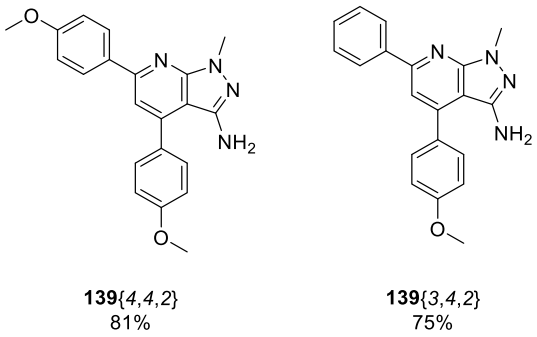

Figure 4.30. *N*1-methyl substituted 4,6-diphenyl-pyrazolo[3,4-*b*]pyridin-3-amines synthetized in this project. The yield of the last step is described under each compound.

4.3.3. Biological activity

In order to identify a new family of MNK inhibitors based on the structure of the initial hit (compound **139**{*3,3,1*}) several derivatives were synthesized using the methodology described above. Following synthesis, we first characterized the activity of this compounds towards MNKs in protein kinase assay (Table 4.7).

Table 4.7. Results from the enzymatic radiometric assay performed by Proqinase®. Values indicated as residual activity of kinases MNK1 and MNK2 after treatment with the indicated compounds at 10 µM. Cercosporamide is used as a positive control.

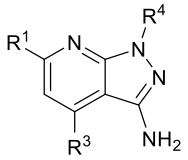

139{*x,y,z*}

x	R^1
3	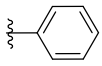
4	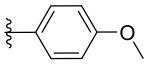
5	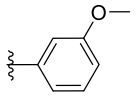
6	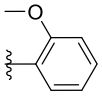

y	R^3
3	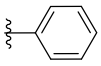
4	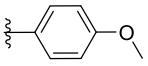
5	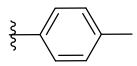
6	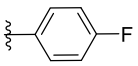

z	R^4
1	H
2	Me

Compound	MNK1	MNK2
Cercosporamide	-1	0
139{*3,3,1*}	22	58
139{*4,5,1*}	45	82
139{*3,4,1*}	25	74
139{*5,3,1*}	38	74
139{*5,4,1*}	41	92
139{*4,4,2*}	94	154

Compound	MNK1	MNK2
139{*3,4,2*}	102	145
139{*6,4,1*}	63	109
139{*3,6,1*}	31	62
139{*4,4,1*}	60	101
139{*5,6,1*}	51	82
139{*3,3,1*}	19	56
139{*6,5,1*}	61	123

The results could firstly confirm the initial data obtained for the compound **139**{*3*,*3*,*1*} and revealed furthermore, that several derivatives of this compound are able to inhibit the kinase activity of MNKs. SAR analysis revealed that the aromatic and planar structure of the pyrazolo[3,4-*b*]pyridine system is essential for the biological activity. This is in particular exemplified by the compounds of the group 3-amino-4,5-dihydropyrazolo[3,4-*b*]pyridin-6-ones (**64**), which did not reveal inhibition of MNKs in the kinase assay. The presence of a carbonyl group in the pyridine ring of such compounds seems to exert a clear unfavorable effect.

Moreover, the results confirm as a structural requirement the presence of an unsubstituted pyrazole moiety as the activity of the methyl substituted compounds **139**{*4*,*4*,*2*} and **139**{*3*,*4*,*2*} drops in comparison with the corresponding unsubstituted compounds **139**{*4*,*4*,*1*} and **139**{*3*,*4*,*1*}. The presence of a H-bond donor in such ring is therefore essential for the activity of these scaffolds. All the compounds presenting the unsubstituted pyrazole ring showed activity in at least one of the MNK proteins, being all of them more active for MNK1. Five of the compounds were apparently selective for MNK1 while compounds **139**{*3*,*4*,*1*}, **139**{*5*,*3*,*1*} and **139**{*3*,*6*,*1*} showed a dual activity for both proteins. Close inspection of the results seemed to indicate that the presence of a methoxy group in the phenyl ring at position C6 (R^1) favors the selectivity of MNK1 while the unsubstituted phenyl in such position promotes a dual activity.

In order to support the results from the kinase assay, the compounds were tested in MDA-MB-231 cells and the effect on the activity of MNKs was determined by the western blot analysis of p-eIF4E (Figure 4.31).

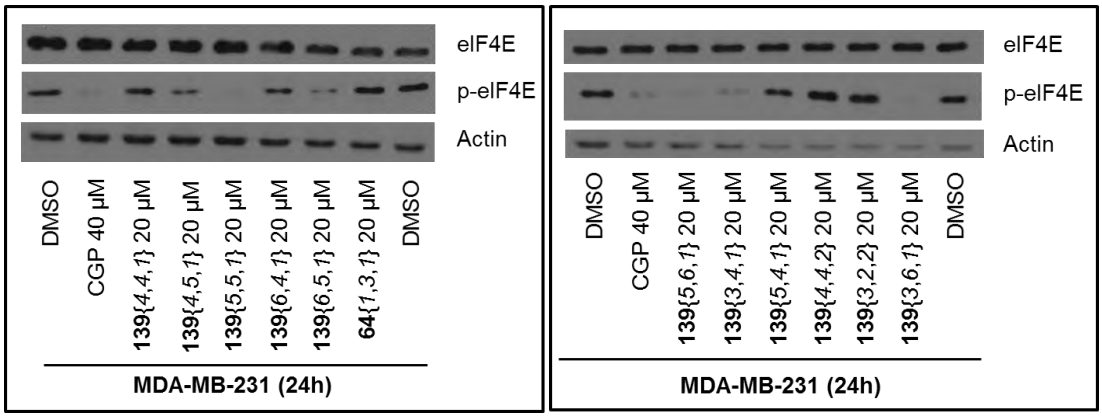

Figure 4.31. Results obtained by the western blots of the pyrazolo[3,4-*b*]pyridine derivatives. WB was performed after 24h of treatment. Final DMSO concentration 0.5%. CGP was used as a positive control. Compounds **139**{*3*,*4*,*1*}, **139**{*6*,*4*,*1*} and **139**{*6*,*5*,*1*} presented a relative cytotoxicity

The analysis by western blot correlates with the results observed in the enzymatic assay. The strongest effect was observed with the compounds **139**{*5*,*3*,*1*} and **139**{*3*,*6*,*1*} which exhibited a dual activity. The third compound with dual activity (**139**{*3*,*4*,*1*}) was discarded due to strong cytotoxic effects. Apart from the dual MNK inhibitors, the MNK1 selective compound **139**{*5*,*6*,*1*} was also able to strongly reduce phosphorylation level of eIF4E.

According to the data presented above, the compounds **139**{*5*,*3*,*1*}, **139**{*3*,*6*,*1*} and **139**{*5*,*6*,*1*} were selected for future studies in addition to the initial hit **139**{*3*,*3*,*1*}.

4.3.4. Characterization of compound 139{*3*,*3*,*1*} and its derivatives

Preliminary biological studies performed with the new family of pyrazolo[3,4-*b*]pyridin-3-amines revealed that compound **139**{*3*,*3*,*1*} (**EB1** from now on) reduces the kinase activity of MNK1/2 and inhibits eIF4E phosphorylation in MDA-MB-231 cells.

A family of derivatives of **EB1** was synthesized and 3 new candidates were selected according to their inhibitory effect on the kinase activity of MNKs in *in vitro* kinase assays and the inhibition of MNKs in MDA-MB-231 cells as judged by the western blot analysis of the phosphorylation status of eIF4E.

Compounds **139**{*5*,*3*,*1*}, **139**{*3*,*6*,*1*} and **139**{*5*,*6*,*1*} will be characterized together with **EB1** to understand their activity, selectivity and mode of action and to elucidate, if those compounds could ultimately be converted into a drug for future clinical studies. In order to facilitate the nomenclature, the compounds will be renamed as **EB2**, **EB3** and **EB4** respectively (Figure 4.32). Compounds **139**{*5*,*3*,*1*} and **139**{*3*,*6*,*1*} were found to be dual inhibitors which completely inhibit eIF4E phosphorylation at 20 µM. Compound **139**{*5*,*6*,*1*} is a more selective inhibitor for MNK1 and has a lower potency in inhibiting of eIF4E phosphorylation.

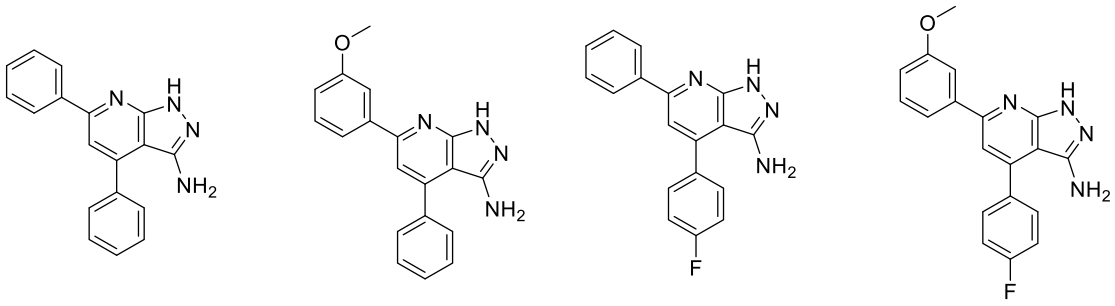

Figure 4.32. Substituted 4,6-diphenyl-pyrazolo[3,4-*b*]pyridin-3-amines under study.

4.3.4.1. Primary analysis of the inhibition of MNK1/2

In order to compare the different inhibitors with each other, the respective IC_{50} values were determined (Table 4.8). Calculation of the IC_{50} values revealed, that **EB1** was the more potent inhibitor in the kinase assay with an IC_{50} of 0.69 µM and 9.4 µM for MNK1 and MNK2 respectively.

Table 4.8. IC_{50} values measured for the compounds under study. Cercosporamide and CGP are used as positive controls.

	Residual activity		**IC_{50} (M)**	
	MNK1	**MNK2**	**MNK1**	**MNK2**
Cercosporamide	-1	0		
CGP57380	21	39	1.52E-06	6.27E-06
EB1	19	56	6.90E-07	9.40E-06
EB2	38	74	4.20E-06	2.20E-05
EB3	31	62	1.30E-06	4.10E-05

The selectivity towards MNK1 might favor the use of these compounds in putative future applications as sensitizing agent for approved therapies. This is based on the fact, that while MNK2 has a rather constant basal activity, MNK1 is particularly activated under cellular stress conditions. As it is believed, that activation of MNK1 might be one of the mechanisms used by cancer cells to resist stress conditions like chemotherapy, combinatorial treatments with MNK1 inhibitors may help to overcome the induction of resistance to chemotherapeutic agents.

4.3.4.2. *In vitro* inhibition of MNK1/2

The biological effect of these compounds was further studied cell-based experiments *in vitro*. The activity of the hits was measured by western blot analysis of p-eIF4E at different concentrations of the compounds to determine the effective concentrations in cells. In parallel, the activity state of different members of the signaling cascade, merging into the activation of MNKs and the phosphorylation of eIF4E was analyzed. These studies will help to exclude potential off-target effects, that may equally account for a reduction of eIF4E phosphorylation. The effect of the compounds on cell growth was determined by the crystal violet assay in a time and dose dependent manner. Furthermore, the characterization of the compounds was completed by analysis of cell migration, invasion and colony formation.

As shown in Figure 4.33, **EB1** inhibited eIF4E phosphorylation with an *in vitro* EC_{50} of ~1.5 µM having a nearly complete inhibition at concentrations higher than 2.5 µM.

The effect was fast and maintained for at least 72h. Moreover, at the tested times there was no difference between the compound being refreshed every 24h, 48h or 72h demonstrating that the inhibition was maintained stable after a single treatment for at least 72h.

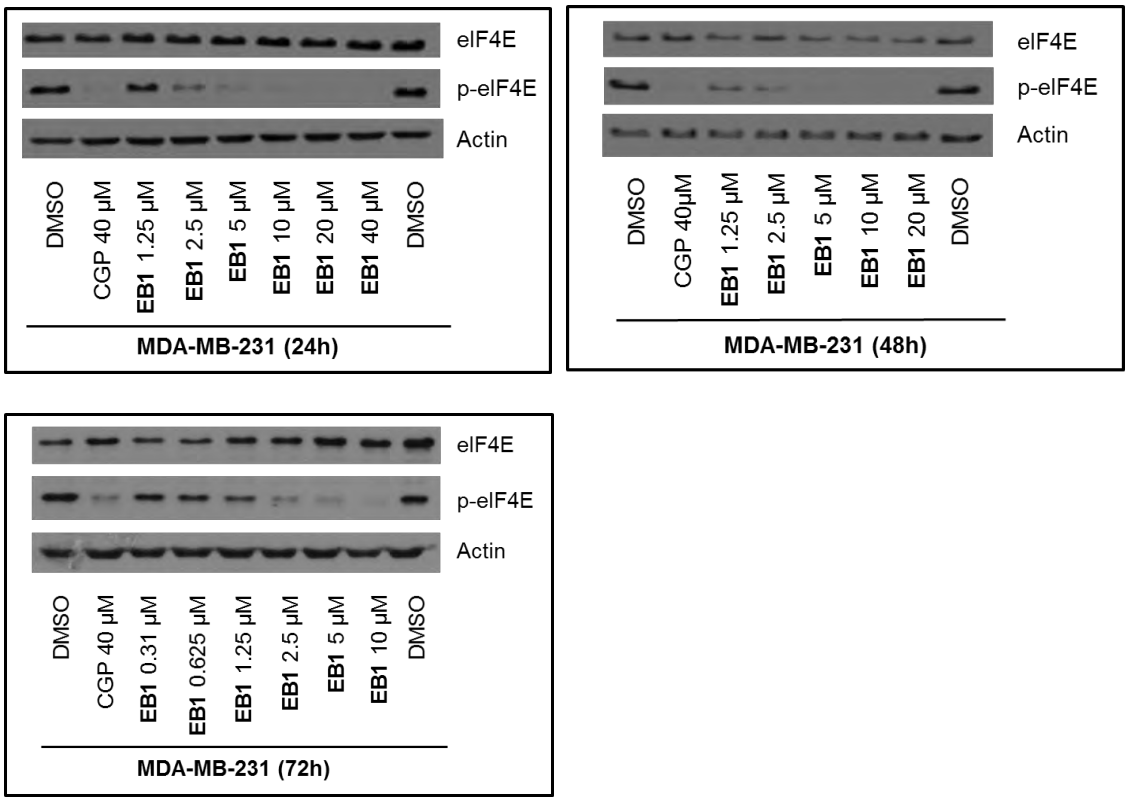

Figure 4.33. Titration curves of **EB1** in MDA-MB-231 cells. Final DMSO concentration 0.5%. CGP is used as a positive control.

EB1 significantly reduced eIF4E phosphorylation at concentrations higher than 2.5 µM. This reduction is not caused by a decrease in the amount of total eIF4E as judged by the analysis of total eIF4E. This effect appears to be caused by direct inhibition of MNKs, since none of the tested upstream components of this signaling pathway is affected by the treatment (Figure 4.34). In particular, ERK and p38 regulate the activity of MNKs by phosphorylation. **EB1** did not alter the phosphorylation state of MNKs, pointing towards a selective mode of action of **EB1** in cells. In addition, the downstream kinase of the MAP-kinase signaling pathway ERK is equally phosphorylated in control and **EB1** treated cells, indicating similar activity of the pathway. Due to the low abundance of p-38 in MDA-MB-231 cells, the analysis of its phosphorylation and activation state could not be carried out.

Finally, the phosphorylation of the eIF4E binding protein 4E-BP1 was not altered either (Figure 4.34). In summary the data indicate, that the diminished phosphorylation of eIF4E in **EB1** treated cells is most likely due to direct inhibition of the MNK kinases.

The effect of **EB1** was also tested on immortalized non-tumor breast cancer cells (MCF10) with similar results (EC_{50} = 0.7 µM) (Figure 4.35).

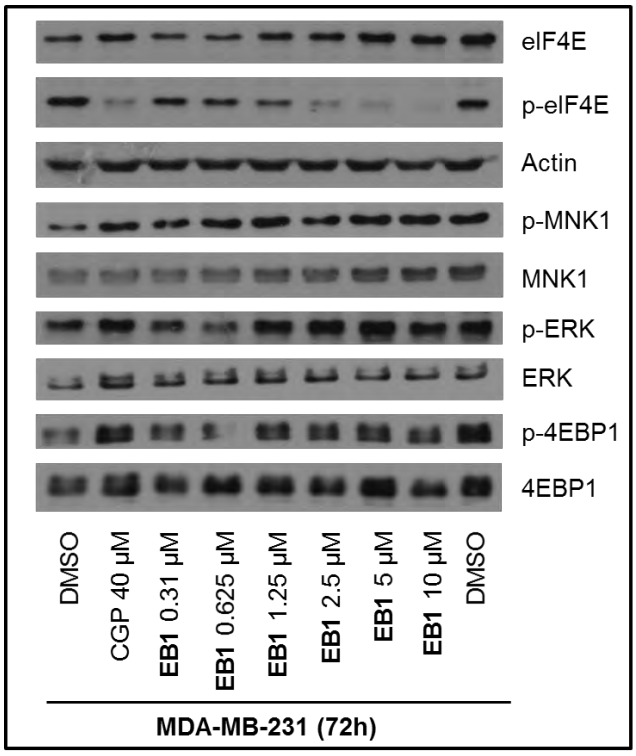

Figure 4.34. Example of the titration curves of **EB1** in MDA-MB-231 cells showing no effects on up-stream proteins and proving selective MNK1/2 inhibition. Results were equivalent at 24h and 48h (Annex 4). DMSO final concentration: 0.5%. CGP is used as positive control.

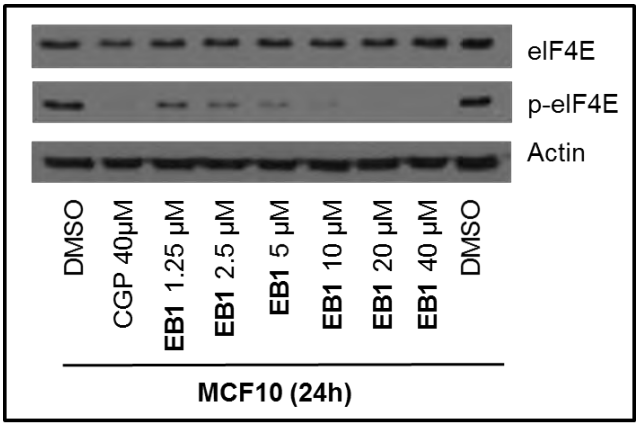

Figure 4.35. Titration curve of **EB1** in MCF10 cells. Final DMSO concentration 0.5%. CGP is used as positive control.

Similar results in terms of activity and selectivity were obtained for the compounds **EB2** and **EB3** (Figure 4.36). Both compounds reduced p-eIF4E levels at low micromolar concentrations with no significant alteration of other pathway related proteins indicating a selective inhibition of MNKs.

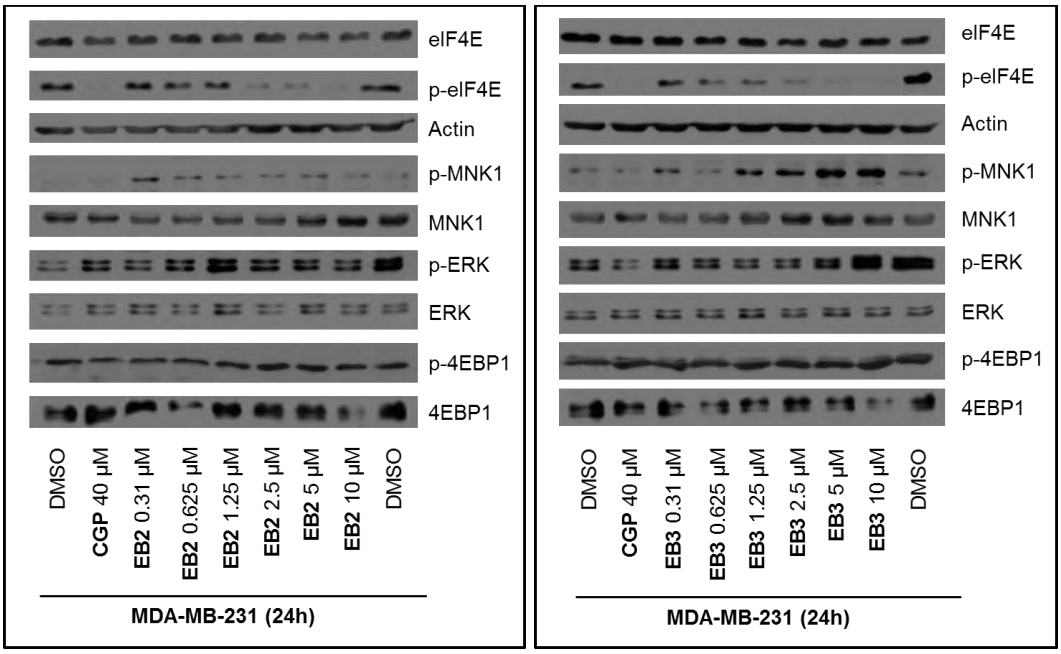

Figure 4.36. Example of the titration curves of **EB2** and **EB3** in MDA-MB-231 cells showing no effects on up-stream proteins and proving selective MNK1/2 inhibition. DMSO final concentration: 0.5%. CGP is used as positive control.

In line with the data obtained in the kinase assays, the compound **EB4** was less potent in inhibiting eIF4E phosphorylation in MDA-MB-231 cells compared to the other derivatives of **EB1** tested (EC_{50} = 5.2 µM). Like in the case of the other derivatives, no alterations in upstream signaling factors could be observed, indicating that the direct inhibition of MNKs is the cause of the reduced phosphorylation levels of eIF4E. (Figure 4.37)

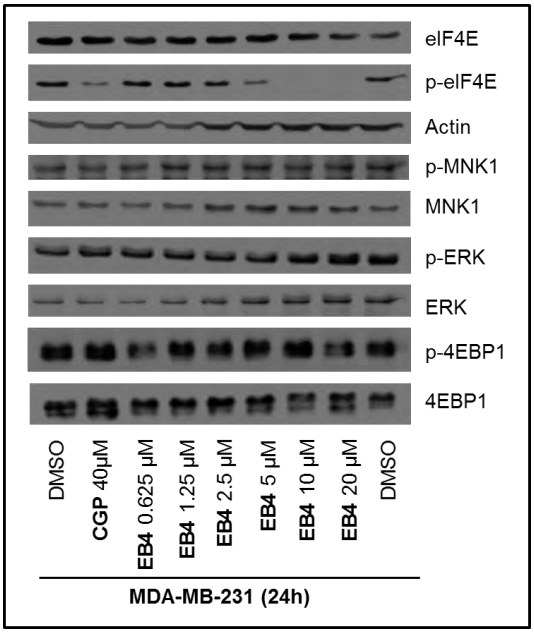

Figure 4.37. Example of the titration curves of **EB4** in MDA-MB-231 cells showing no effects on up-stream proteins and proving selective MNK1/2 inhibition. DMSO final concentration: 0.5%. CGP is used as positive control.

4.3.4.3. Study of cell growth

Based on the fact that MNK1/2 knock-out mice are viable, both proteins are proposed to not be essential for basic cellular functions that would impede cell growth. This is also supported by the fact that shRNA mediated knockdown of both proteins does not alter cell viability and growth. Based on this data, we predict that MNK inhibitors are not expected to reduce cell growth. Therefore, we tested if the compounds impede cell growth at concentrations, which are sufficient to inhibit eIF4E phosphorylation.[30,31]

The growth curves of MDA-MB-231 cells performed at different concentrations of **EB1** showed no toxicity at 24h and only a significant reduction of the number of cells after 48h of treatment at the higher tested concentration (40 µM). After 72h of treatment, the number of cells was significantly reduced at 10 µM and higher (Figure 4.38). These results were obtained from an experimental setup, in which the compound was refreshed after 48h. Experiments recently carried out in the lab further indicate, that with a single dose of inhibitor, eIF4E phosphorylation remains low until 72h after treatment and significant reduction in the cell growth can only be observed if concentrations higher than 20µM are used.

Besides breast cancer cell lines, we also tested the effect of **EB1** on immortalized non-tumor breast cancer cells (MCF10). As shown in Figure 4.39 similar results compared to MDA-MB-231 were obtained.

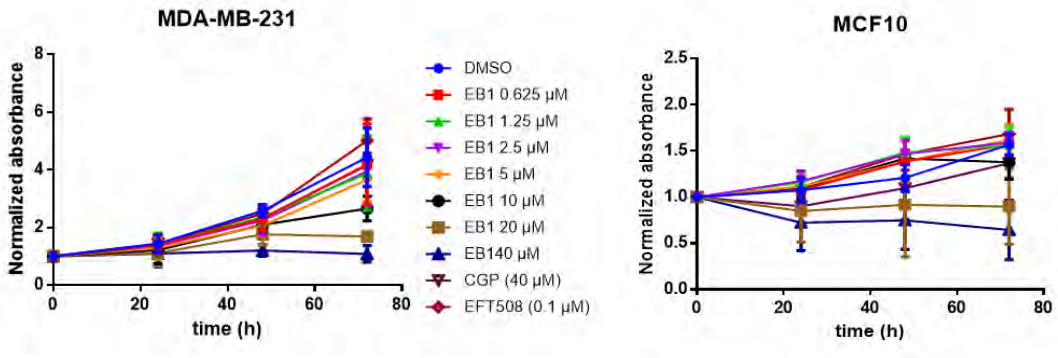

2-way ANOVA			
Tukey's test (multiple comparisons)			
	24h	48h	72h
DMSO vs. 5 µM	ns	ns	ns
DMSO vs. 10 µM	ns	ns	**
DMSO vs. 20 µM	ns	ns	****
DMSO vs. 40 µM	ns	*	****

2-way ANOVA			
Tukey's test (multiple comparisons)			
	24h	48h	72h
DMSO vs. 5 µM	ns	ns	ns
DMSO vs. 10 µM	ns	ns	ns
DMSO vs. 20 µM	ns	ns	**
DMSO vs. 40 µM	ns	ns	****

Figure 4.38. Proliferation curves for **EB1** in MDA-MB-231 and MCF10 cells Compound was refreshed after 48h of treatment. DMSO concentration was 0.5%. CGP and EFT508 were used as positive control.

To determine, how cell growth is affected at higher concentrations of **EB1**, we performed FACS analysis to monitor the cell cycle state and the percentage of cells in subG1 as indicator of cell death. As positive control for cell death, cells were treated with 100 nM of doxorubicin which resulted in a strong increase of cells in the subG1 phase. In contrast to doxorubicin, concentrations of up to 40 µM **EB1** did not result in increased cell death. Instead, a dose dependent increase of cells in G1-phase of the cell cycle could be observed. These results, therefore indicate, that the reduced cell growth at higher concentrations of **EB1** is caused by a delay in cell cycle progression rather than the induction of cell death. Notably, the same results have been described for the MNK1/2 inhibitor **BAY 11433296**.[32] (Figure 4.39)

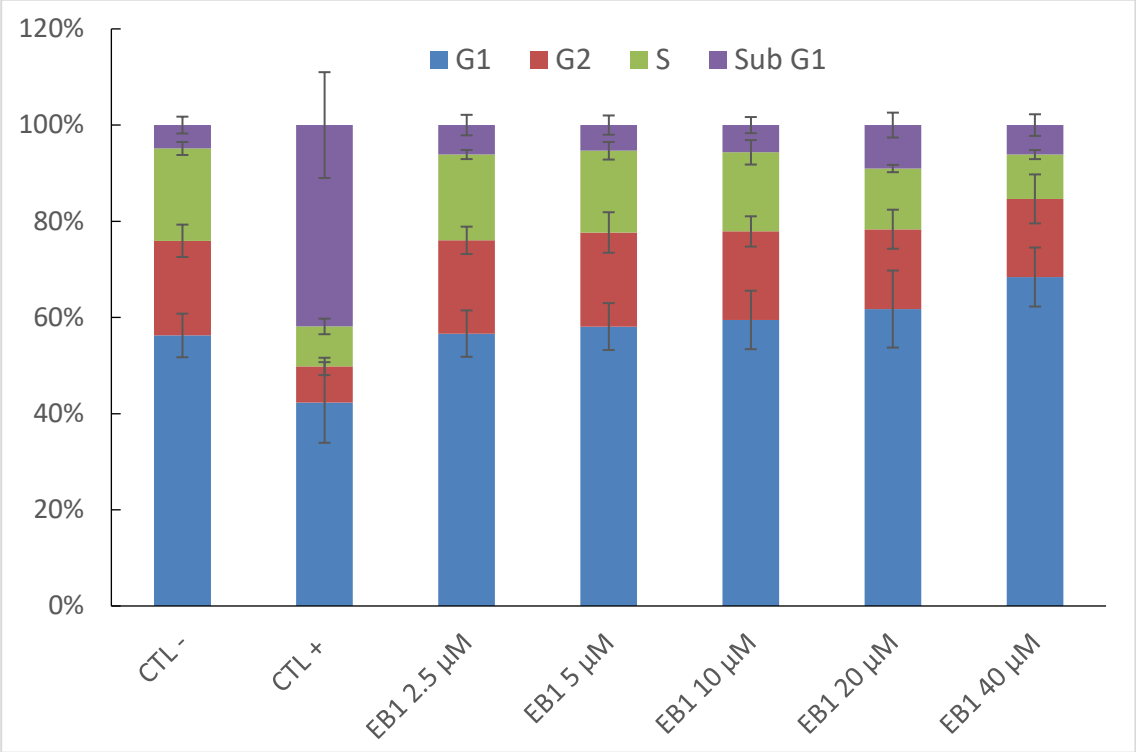

Figure 4.39. Cell cycle of MDA-MB-231 treated with **EB1** for 72h. DMSO 0.5% is used as the negative control while doxorubicin 100 nM is used as a positive control of cell death

In summary, **EB1** did not affect cell growth of tumor and non-tumor cells at concentrations sufficient to inhibit MNK activity, which supports the selective mode of action towards MNKs and a provides a first indication for a safe mode of action in future clinical studies.

Finally, we also tested the derivatives of **EB1** (**EB2**, **EB3**, **EB4**) in the cell growth assay. As in the case of **EB1**, the compounds **EB2** and **EB3** showed reduced cell growth at concentrations higher than 20 µM after at least 48h of treatment while compound **EB4** reduced cell growth at 10 µM after 72h. (Figure 4.40)

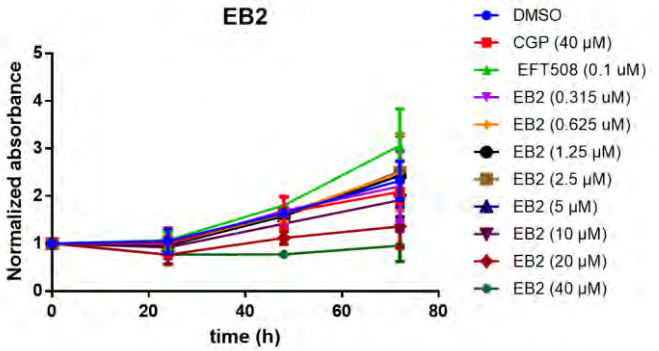

2-way ANOVA			
Tukey's test (multiple comparisons)			
	24h	48h	72h
DMSO vs. 5 uM	ns	ns	ns
DMSO vs. 10 uM	ns	ns	ns
DMSO vs. 20 uM	ns	ns	*
DMSO vs. 40 uM	ns	*	***

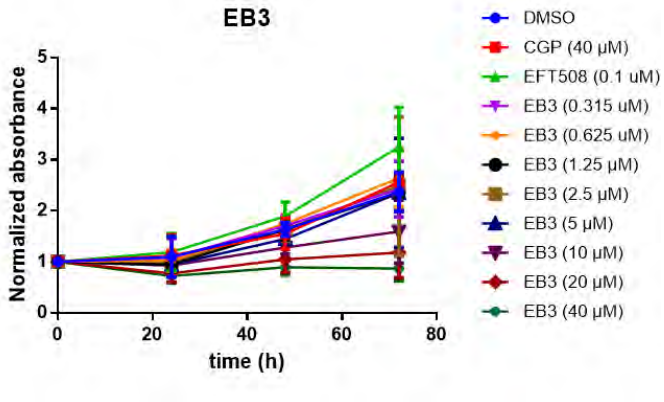

2-way ANOVA			
Tukey's test (multiple comparisons)			
	24h	48h	72h
DMSO vs. 5 uM	ns	ns	ns
DMSO vs. 10 uM	ns	ns	ns
DMSO vs. 20 uM	ns	ns	**
DMSO vs. 40 uM	ns	ns	****

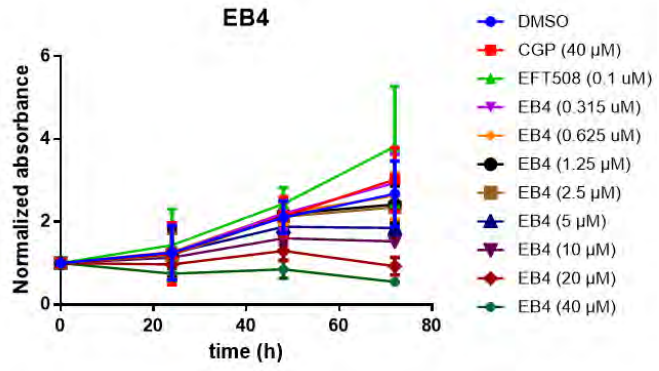

2-way ANOVA			
Tukey's test (multiple comparisons)			
	24h	48h	72h
DMSO vs. 5 uM	ns	ns	ns
DMSO vs. 10 uM	ns	ns	*
DMSO vs. 20 uM	ns	ns	***
DMSO vs. 40 uM	ns	*	****

Figure 4.40. Proliferation curves for **EB2**, **EB3** and **EB4** in MDA-MB-231 cells. Compound was refreshed after 48h of treatment. DMSO concentration was 0.5%. CGP and EFT508 were used as positive control.

4.3.4.4. Study of the effect of the compounds on cell migration, invasion and colony formation

Treatment of MNK inhibitors was shown to reduce the migration and invasive capability of tumoral cells[31]. MDA-MB-231 cells present a high migration and invasion potential. In these experiments the ability of these cells to migrate and invade when treated with the compounds is evaluated. For the study of the migration, a wound healing assay is used. A wound is performed in a confluent layer of cells and its closure is measured after 8h and 24h. The size of the wound was compared between the compounds under study and the controls: the DMSO as a negative control and CGP57380 and EFT508 as an example of known MNK inhibitors.

In the case of the invasion assay, the cells are seeded inside an insert coated with Matrigel. The invasion capacity is quantified by counting the number of cells capable of degrading the Matrigel and passing through the pores of the membrane of the insert.

Compound **EB1** reduced the migration of MDA-MB-231 cells by 40% after 8h of treatment in the concentration range where we see a reduction of eIF4E phosphorylation. The effect on migration of **EB1** was higher than on the controls used at concentrations where p-eIF4E was not detected (Figure 4.41).

The effect on migration of MDA-MB-231 cells of the two derivatives (**EB2** and **EB3**) was smaller than for **EB1** and after 8h of treatment the reduction in the migration potential was only significant at 10 μM. (Figure 4.42)

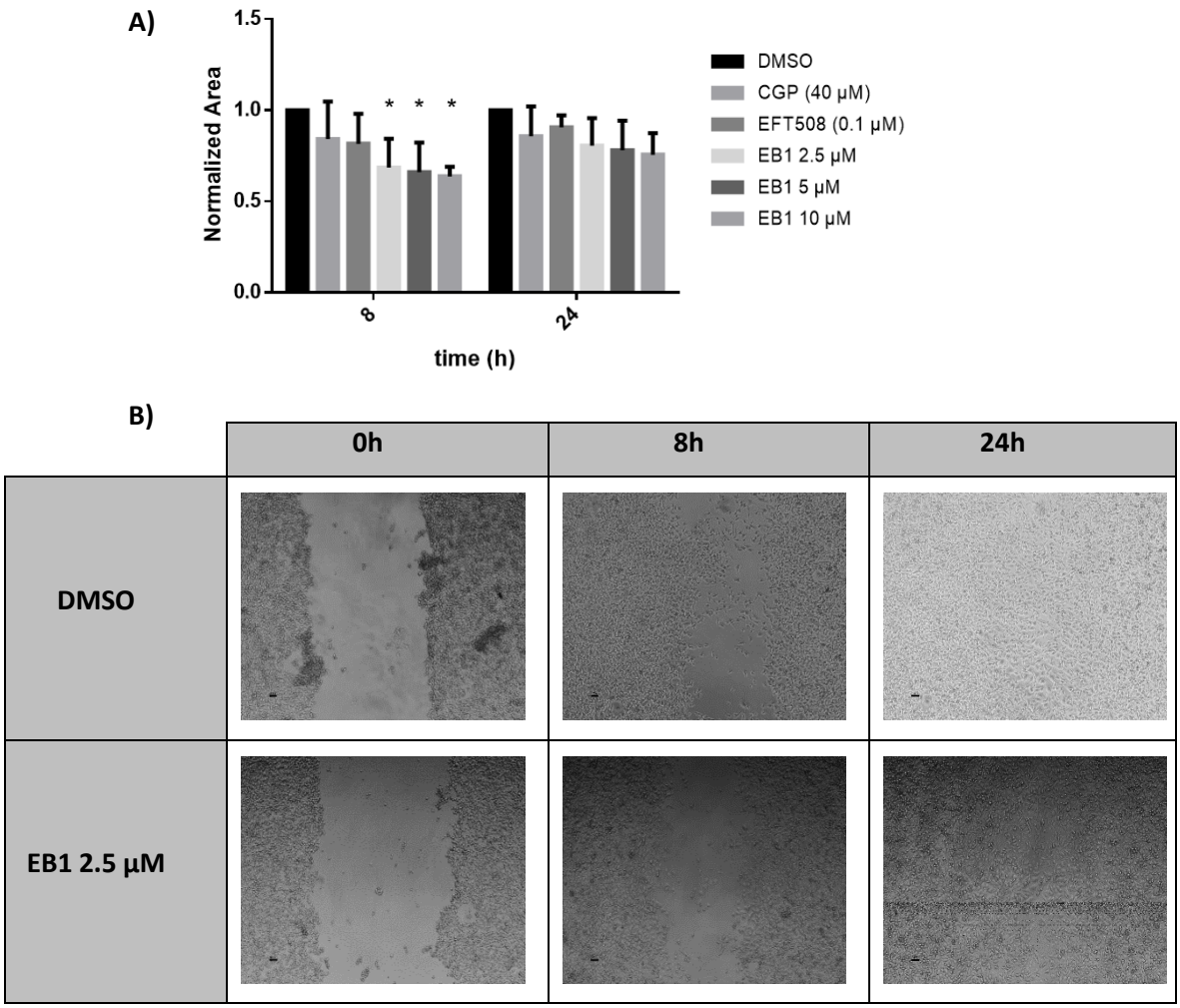

Figure 4.41. Effect of **EB1** on the migration capacity of MDA-MB-231 cells. A) Summary of 4 experiments. B) Example of the wound healing images obtained in each experiment

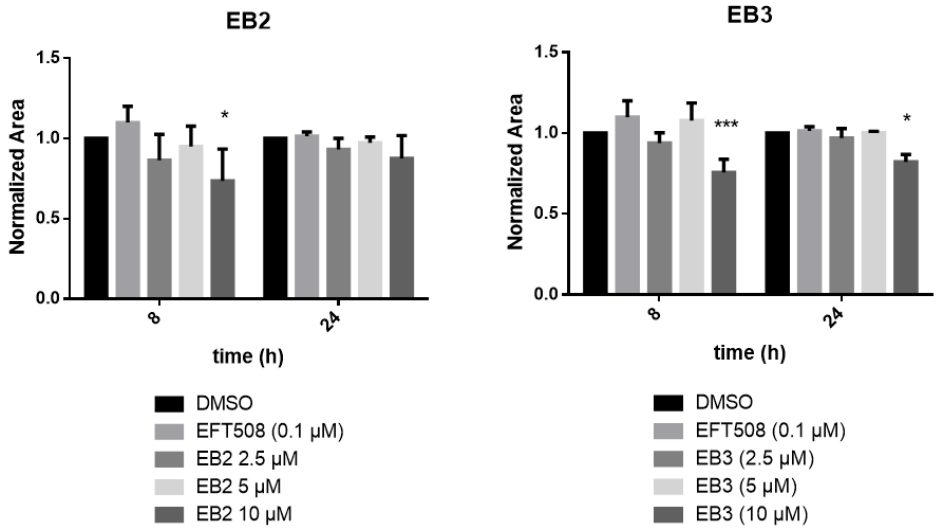

Figure 4.42. Effect of **EB2** and **EB3** on the migration capacity of MDA-MB-231 cells.

Preliminary results indicate that compound **EB1** also has an effect on cell invasion reducing the invasive capacity of MDA-MB-231 cells by around 40%. However, despite the clear tendency observed, the huge variation of the replicates prevents the obtention of significant differences. (Figure 4.43) No effect on the invasive capacity of the MDA-MB-231 cells was observed for any of the two derivatives (**EB2** and **EB3**).

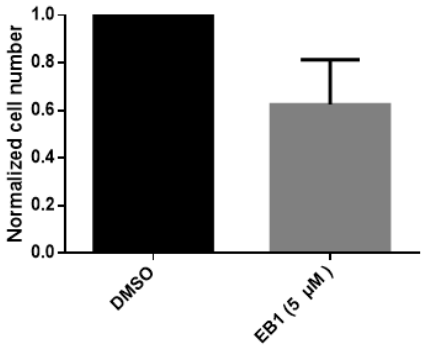

Figure 4.43. Effect of **EB1** on the invasion capacity of MDA-MB-231 cells after 24h.

Despite tested, it was not possible to see any effect on the colony formation assay. For such a long assay, it was necessary to change the treatments every few days to ensure the effect of the drug. Because of this, the colonies were slightly altered, and it was not possible to obtain clear results.

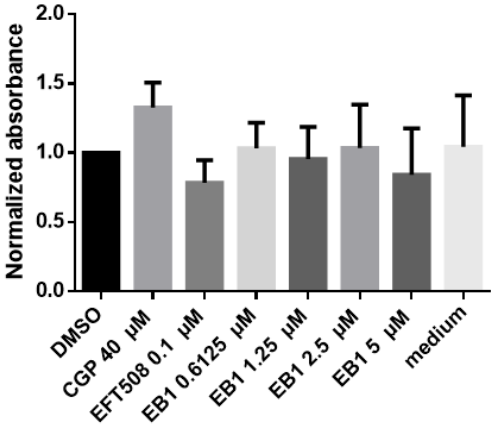

Figure 4.44. Effect of **EB1** on the colony formation capacity of MDA-MB-231 cells.

4.3.4.5. Study of the compound selectivity

The study of the compounds by western blot indicated that no other proteins related to the eIF4E pathway were affected indicating a selective activity of the compounds for MNK1/2. However, as the inhibition of MNKs was proven to be non-cytotoxic, the effects observed at the highest concentrations on the proliferation curves could be cause by an off-target.

To further support the selective mode of action, we next tested the activity of **EB1** against a panel of different kinases (Proqinase®) (Figure 4.45). **EB1** showed excellent selectivity at 1 µM in a panel of 320 kinases. Only 16 other kinases were affected equally or better by the **EB1** (Annex 4). A literature survey of those affected kinases did not reveal any significant implication of the pathways affecting phosphorylation of eIF4E. As for many of those candidates affected in the kinase assay, structural data are available. We will use this information to identify putative common binding elements of **EB1**, which in turn will enable us to generate a new series of derivatives, with improved selectivity profiles. Thus, even though the kinome wide study indicated that selectivity and potency of the compound can be further improved, the results are very promising for a first hit.

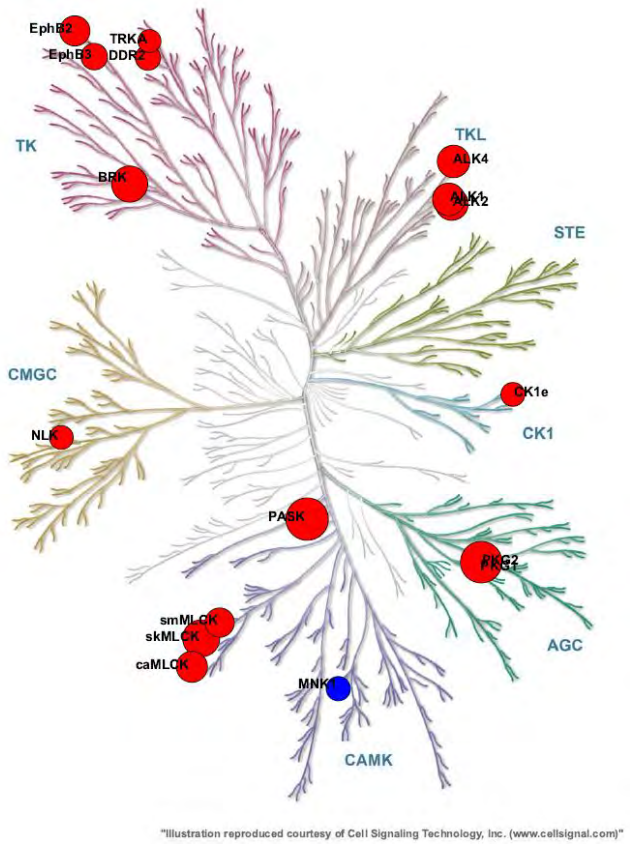

Figure 4.45. Kinome profile for **EB1**. The compound was profiled at 1 µM against 320 kinases showing promising selectivity. The size of the dots represents the measured activity. MNK1/2 are marked in blue.

4.3.4.6. Study of the cell line dependency

Reports on previously identified MNK inhibitors often describe cell line specific effects. In order to test if this is also the case for the compounds (**EB1-3**), the titration curves were performed on cell lines originating from different tumor types, such as leukemia cells (MV4-11), melanoma cells (A375M) and breast cancer (MDA-MB-468).

The three compounds were active on all the tested cell lines proving that the activity of this family of compounds as MNK inhibitors is not cell line dependent. (Figure 4.46, Figure 4.47 and Figure 4.48). In difference to previous reports where MV4-11 cells were described as more susceptible to MNK inhibitors, these cells displayed similar EC_{50} values to the other tested cell line. These results might indicate that the mode of action of the compounds is different to the previously described inhibitors, enabling them to act in cell lines which are not affected by previously reported compounds.

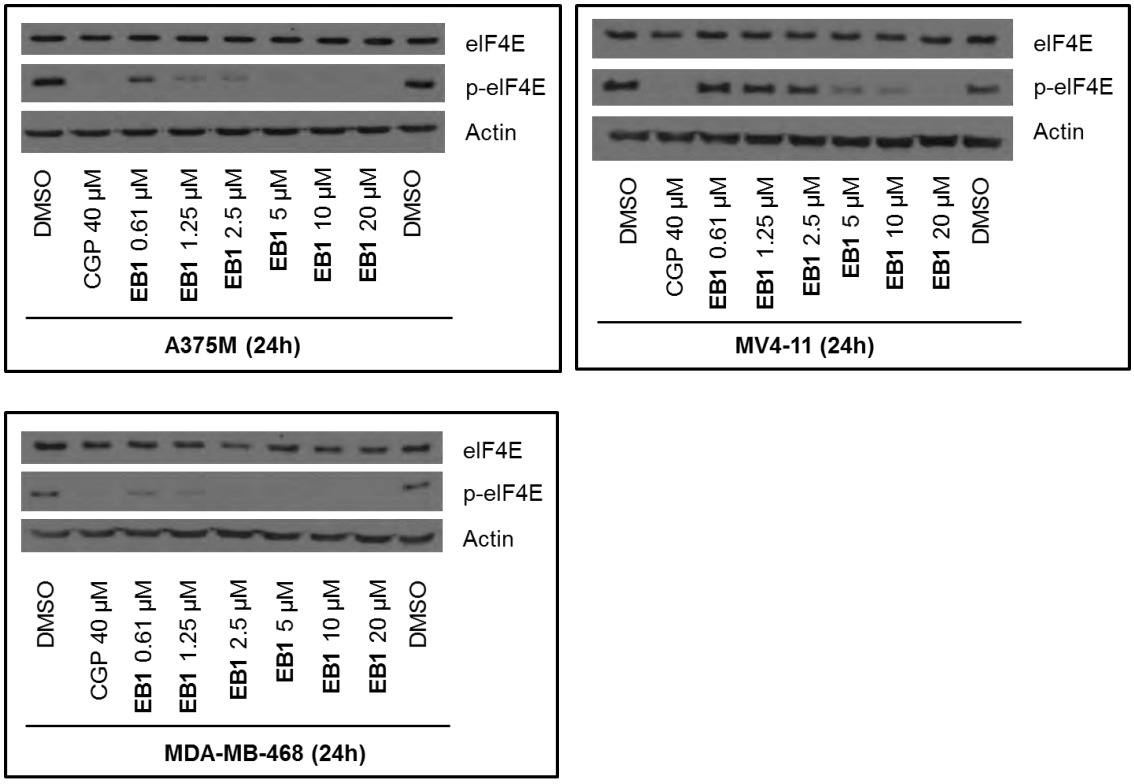

Figure 4.46. Titration curve of **EB1** on A375M, MV4-11 and MDA-MB-468 cells. Final DMSO concentration 0.5%. CGP is used as a positive control.

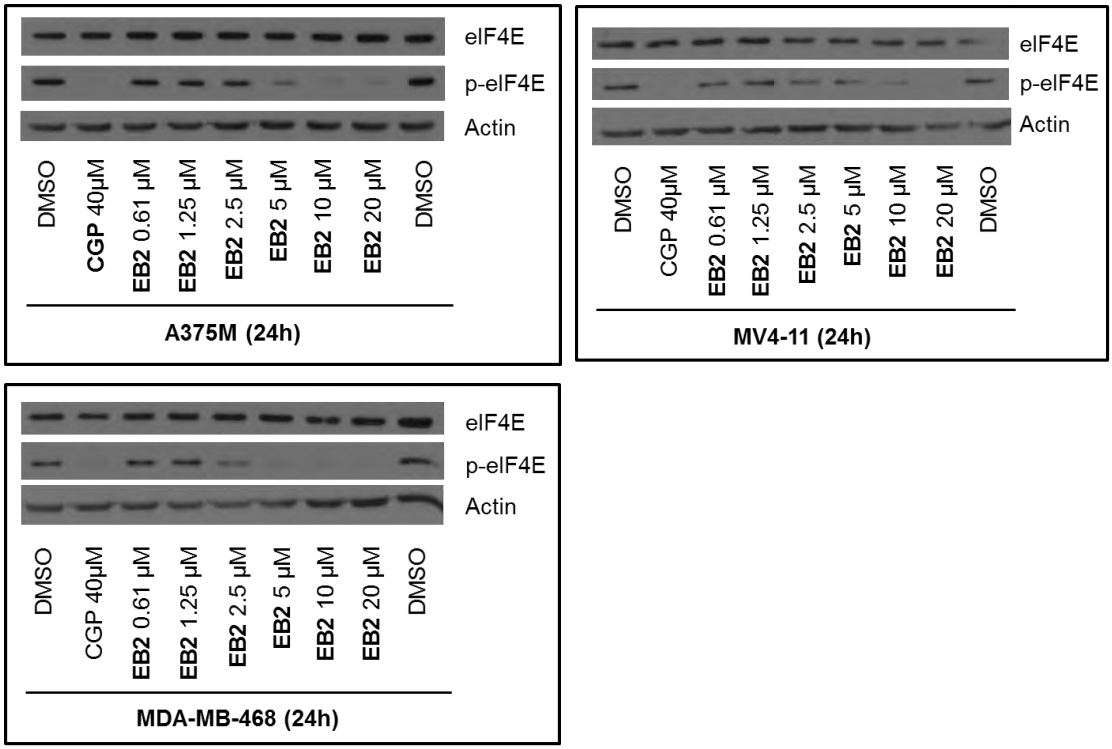

Figure 4.47. Titration curve of **EB2** on A375M, MV4-11 and MDA-MB-468 cells. Final DMSO concentration 0.5%. CGP is used as a positive control

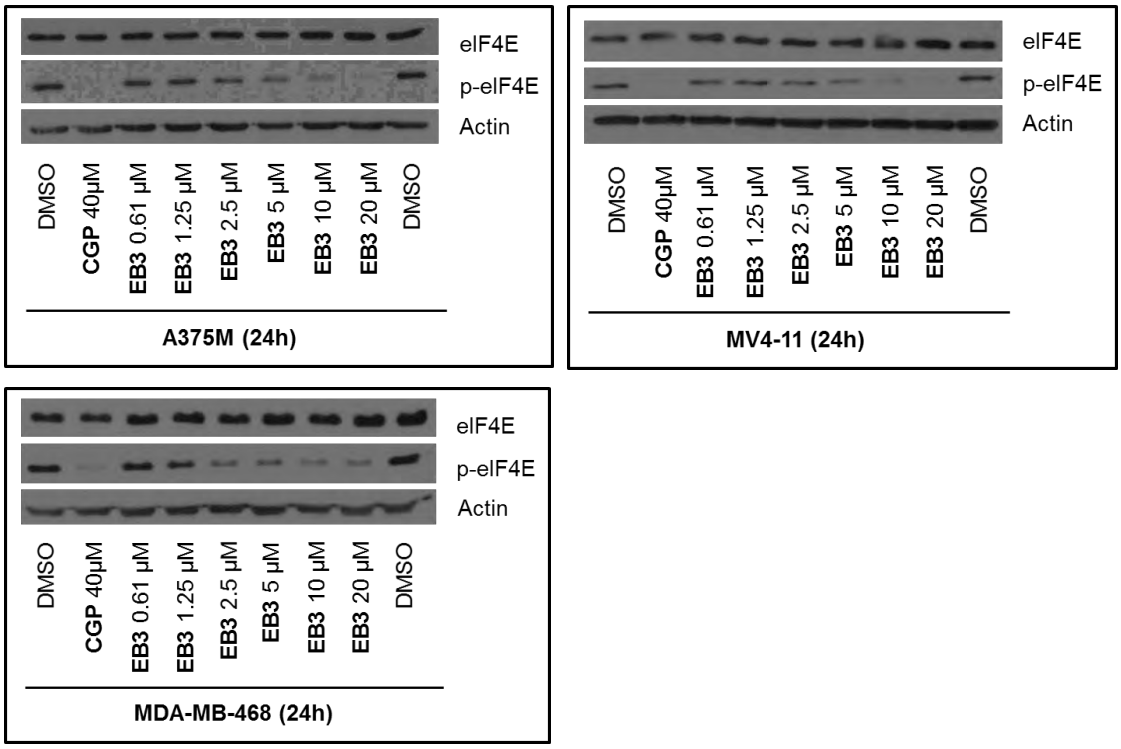

Figure 4.48. Titration curves of **EB3** on A375M, MV4-11 and MDA-MB-468 cells. Final DMSO concentration 0.5%. CGP is used as a positive control.

4.3.4.7. Sensitizing tumoral cells to approved therapies

Inhibition of eIF4E phosphorylation *via* MNKs has emerged as a new anti-cancer strategy in combination with other approved therapies. The treatment with MNK inhibitors has been described to sensitize tumoral cells[33–38] to common therapies. This therapy schemes are particularly important for cancer types, in which targeted therapies are not available such as triple negative breast cancer. However, up to today no examples for the use of MNK inhibitors to sensitize triple negative breast cancer to approved chemotherapies have been reported.

Combination of **EB1** with doxorubicin on MDA-MB-231 cells showed promising results. The increase of eIF4E phosphorylation due to the cellular stress caused by doxorubicin was confirmed and could be reversed by 5 µM **EB1** (Figure 4.49A).

Moreover, the co-treatment with **EB1** increased the efficacy of Doxorubicin to inhibit cell growth. The IC_{50} of doxorubicin was reduced in combination with **EB1** from 350 nM to 225 nM (Figure 4.49B).

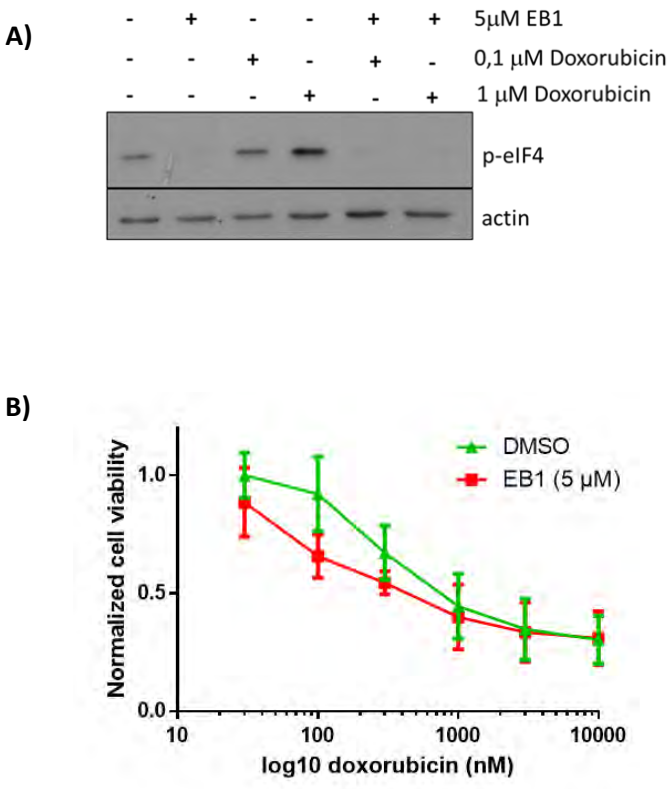

Figure 4.49. Combination of doxorubicin with **EB1** increases the efficacy of the chemotherapeutic drug (B) and reverses the increment of p-eIF4E caused by cellular stress related to the treatment with doxorubicin (A).

4.3.5. Conclusion

The compounds of this new family were tested as MNK inhibitors.

EB1 was identified as a selective MNK inhibitor with an enzymatic IC_{50} of 0.7 µM and an *in vitro* EC_{50} of around 1.5 µM in MDA-MB-231 cells. Complete inhibition of eIF4E phosphorylation was achieved at concentrations higher than 2.5 µM. Moreover, the results were not cell line dependent and the compound was shown to be active on leukemia cells (MV4-11), melanoma cells (A375M) and breast cancer (MDA-MB-468). Finally, the compound seems to reduce cell migration and invasion even presenting a low cytotoxicity. The selectivity of the compound for MNK was studied on a panel of 320 kinases and showing an excelled initial selectivity for a hit as only 16 other proteins were affected.

Several derivatives of this compounds were prepared and tested proving that 4,6-diphenyl substituted pyrazolo[3,4-*b*]pyridines are useful as MNK inhibitors. Out of the primary screening performed by measuring the residual activity of MNK1 and MNK2 after the treatment with the inhibitors, the three compounds (**EB2**, **EB3** and **EB4**) were selected and further studied. **EB2** and **EB3** showed similar results as **EB1** regarding inhibition of eIF4E phosphorylation and cytotoxicity but presented smaller effects on cell migration and invasion. Compound **EB4** was the worst candidate as higher concentrations of the compound are needed to achieve the expected effect.

Therefore, compound **EB1** is still the most interesting compound with good inhibitory activity and an interesting selectivity. Moreover, **EB1** was shown to increase the sensitivity of MDA-MB-231 tumoral cells to chemotherapy when combined with doxorubicin.

4.4. References

1. Camarasa, M. *et al.* Design, synthesis and biological evaluation of pyrido[2,3-d]pyrimidin-7-(8H)-ones as HCV inhibitors. *Eur. J. Med. Chem.* **115,** 463–483 (2016).
2. Falcó, J. L. *et al.* Design, synthesis and biological activity of acyl substituted 3-amino-5-methyl-1,4,5,7-tetrahydropyrazolo[3,4-b]pyridin-6-ones as potential hypnotic drugs. *Eur. J. Med. Chem.* **40,** 1179–1187 (2005).
3. Balsas, P. *et al.* Activity of the novel BCR kinase inhibitor IQS019 in preclinical models of B-cell non-Hodgkin lymphoma. *J. Hematol. Oncol.* **10,** 80 (2017).
4. Lavecchia, M. J., Puig de la Bellacasa, R., Borrell, J. I. & Cavasotto, C. N. Investigating molecular dynamics-guided lead optimization of EGFR inhibitors. *Bioorg. Med. Chem.* **24,** 768–778 (2016).
5. Burikhanov, R. *et al.* Arylquins target vimentin to trigger Par-4 secretion for tumor cell apoptosis. *Nat. Chem. Biol.* **10,** 924–926 (2014).
6. Hino, K., Nagai, Y. & Uno, H. Synthesis and pharmacological activities of 3-phenyl-2-(1-piperazinyl)quinolines and related compounds. *Chem. Pharm. Bull. (Tokyo).* **35,** 2819–2824 (1987).
7. Arcadi, A., Cacchi, S., Fabrizi, G., Manna, F. & Pace, P. Ethyl N-(o -Ethynyl)malonanilide as a Useful Building Block for the Preparation of 3,4-Disubstituted-2(1 H)-quinolones, 3,4-Disubstituted- and 2,3,4-Trisubstituted Quinolines. *Synlett* **1998,** 446–448 (1998).
8. Cacchi, S., Carangio, A., Fabrizi, G., Moro, L. & Pace, P. A Convenient Synthesis of Nitrogen-Containing Heterocycles Bearing Amino Substituents from Heteroaryl Triflates. *Synlett* **1997,** 1400–1402 (1997).
9. Dyck, B. *et al.* Potent, Orally Active Corticotropin-Releasing Factor Receptor-1 Antagonists Containing a Tricyclic Pyrrolopyridine or Pyrazolopyridine Core. *J. Med. Chem.* **48,** 4100–4110 (2005).
10. Giordanetto, F. *et al.* Optimization of ketone-based P2Y12 receptor antagonists as antithrombotic agents: Pharmacodynamics and receptor kinetics considerations. *Bioorg. Med. Chem. Lett.* **24,** 2963–2968 (2014).
11. Green, N. J. *et al.* Structure–activity studies of a series of dipyrazolo[3,4-b:3’,4’-d]pyridin-3-ones binding to the immune regulatory protein B7.1. *Bioorg. Med. Chem.* **11,** 2991–3013 (2003).
12. Ishida, N., Nakanishi, Y., Moriya, T. & Murakami, M. Synthesis of Phenanthridinones and Phenanthridine Derivatives through Palladium-catalyzed Oxidative C–H Coupling of Benzanilides. *Chem. Lett.* **40,** 1047–1049 (2011).
13. Semakul, N., Jackson, K. E., Paton, R. S. & Rovis, T. Heptamethylindenyl (Ind*) enables diastereoselective benzamidation of cyclopropenes via Rh(III)-catalyzed C–H activation. *Chem. Sci.* **8,** 1015–1020 (2017).
14. Figueroa Perez, S. *et al.* Aryl-or heteroaryl-substituted pyrido[2,3-d]pyrimidines and pharmaceutical compositions of the same. US 8399471 B2 (2013).

15. Diab, S. *et al.* Unveiling new chemical scaffolds as Mnk inhibitors. *Future Med. Chem.* **8,** 271–285 (2016).

16. Nogami, A. *et al.* FLT3-ITD confers resistance to the PI3K/Akt pathway inhibitors by protecting the mTOR/4EBP1/Mcl-1 pathway through STAT5 activation in acute myeloid leukemia. *Oncotarget* **6,** (2015).

17. Victory, P., Borrell, J. I. & Vidal-Ferran, A. A simple synthesis of 2-methoxypyridine-3-carbonitriles. *Heterocycles* **36,** 769–776 (1993).

18. Liu, G. *et al.* Inhibitors of c-Jun N-terminal kinases. US 20060173050 A1 (2006).

19. Victory, P., Borrell, J. I., Cirujeda, J. & Vidal-ferran, A. Synthesis of 2-cyanamino-4,6-diphenyl-pyridine-3-carbonitrile. *Heterocycles* **36,** 777–783 (1993).

20. Frisch, M. J. *et al.* Gaussian (G09). Wallingford CT (2009).

21. Deeb, A., Essawy, A. & Shaban, A. Heterocyclic Synthesis with 3-Cyano-2(1H)pyridinethione: Synthesis of 3-Oxo-2,3-dihydroisothiazolo[5,4-b]pyridine and Related Compounds. *Monatshefte für Chemie* **121,** 281–287 (1990).

22. Abdel Hafez, A. A., Awad, I. M. A. & Ahmed, R. A. New heterocyclo-substituted pyrazolo[3,4-b]pyridine derivatives. *Collect. Czechoslov. Chem. Commun.* **58,** 1198–1202 (1993).

23. Goda, F. E., Abdel-Aziz, A. A. M. & Attef, O. A. Synthesis, antimicrobial activity and conformational analysis of novel substituted pyridines: BF3-promoted reaction of hydrazine with 2-alkoxy pyridines. *Bioorganic Med. Chem.* **12,** 1845–1852 (2004).

24. Lavecchia, G., Berteina-Raboin, S. & Guillaumet, G. Synthesis and functionalisation of 1H-pyrazolo[3,4-b]pyridines involving copper and palladium-promoted coupling reactions. *Tetrahedron Lett.* **45,** 2389–2392 (2004).

25. Ye, Q. *et al.* Synthesis and evaluation of novel 7-azaindazolyl-indolyl-maleimide derivatives as antitumor agents and protein kinase C inhibitors. *Bioorg. Med. Chem.* **17,** 4763–4772 (2009).

26. Dolzhenko, A. V., Bai, S., Dolzhenko, A. V. & Chui, W. K. Synthesis and Structure of 3,4-Dihydropyrido[2',3':3,4]pyrazolo[1,5- a][1,3,5]triazin-2-amines. *J. Heterocycl. Chem.* **49,** 763–767 (2012).

27. Nageswar Rao, D., Rasheed, S., Vishwakarma, R. A. & Das, P. Copper-catalyzed sequential N-arylation of C-amino-NH-azoles. *Chem. Commun.* **50,** 12911–12914 (2014).

28. Sharma, L. K. *et al.* A High-Throughput Screen Reveals New Small-Molecule Activators and Inhibitors of Pantothenate Kinases. *J. Med. Chem.* **58,** 1563–1568 (2015).

29. Amer, A. A. & Abdelhamid, A. A. Microwave-Assisted, One-Pot Multicomponent Synthesis of Some New Cyanopyridines. *J. Heterocycl. Chem.* **54,** 3126–3132 (2017).

30. Reich, S. H. *et al.* Structure-based Design of Pyridone-Aminal eFT508 Targeting Dysregulated Translation by Selective Mitogen-activated Protein Kinase Interacting Kinases 1 and 2 (MNK1/2) Inhibition. *J. Med. Chem.* **61,** 3516–3540 (2018).

31. Zhan, Y. *et al.* MNK1/2 inhibition limits oncogenicity and metastasis of KIT-mutant melanoma. *J. Clin. Invest.* **127,** 4179–4192 (2017).

32. Santag, S. *et al.* BAY 1143269, a novel MNK1 inhibitor, targets oncogenic protein expression and shows potent anti-tumor activity. *Cancer Lett.* **390,** 21–29 (2017).

33. Grzmil, M. *et al.* Inhibition of MNK pathways enhances cancer cell response to chemotherapy with temozolomide and targeted radionuclide therapy. *Cell. Signal.* **28,** 1412–1421 (2016).

34. Hu, K., Zhang, J., Yu, M. & Xiong, C. Inhibition of Mnk-eIF4E pathway sensitizes the efficacy to chemotherapy in anaplastic thyroid cancer. *Futur. Oncol.* **13,** 489–498 (2017).

35. Kwegyir-Afful, A. K. *et al.* Galeterone and its analogs inhibit Mnk-eIF4E axis, synergize with gemcitabine, impede pancreatic cancer cell migration, invasion and proliferation and inhibit tumor growth in mice. *Oncotarget* **8,** 52381–52402 (2016).

36. Li, Z. *et al.* Inhibiting the MNK-eIF4E-beta-catenin axis increases the responsiveness of aggressive breast cancer cells to chemotherapy. *Oncotarget* **8,** 2906–2915 (2017).

37. Li, P. *et al.* Inhibition of Mnk enhances apoptotic activity of cytarabine in acute myeloid leukemia cells. *Oncotarget* **7,** (2016).

38. Liu, S., Zha, J. & Lei, M. Inhibiting ERK/Mnk/eIF4E broadly sensitizes ovarian cancer response to chemotherapy. *Clin. Transl. Oncol.* **20,** 374–381 (2018).

CHAPTER 5

Computational studies supporting the development of new MNK inhibitors

5.1. Computational strategies on Drug Design

Drug development is an expensive and time-consuming process. For this reason, computer-aided drug design has emerged as a basic strategy for the systematic design of new drugs replacing the old trial and error approaches.[1]

Depending on the available information, drug design strategies can be classified into two major categories: (1) structure-based when information about the structure of the protein is accessible and (2) ligand-based when the biological and physicochemical properties of bound ligands are used.[2]

Structure-based drug-design methods are routinely applied in the drug development process when sufficient structural information of the receptor is available as for example the crystal structure of the target protein. These strategies simulate the interactions between a ligand and a protein with different techniques such as molecular dynamics and docking.

Ligand-based drug-design strategies are often used when little or no information about the structure of the target protein is available. These methods classify the new candidates based on the analysis of the biological and chemical properties of a set of ligands.

5.2. Ligand based drug design strategies

As previously mentioned, ligand-based drug-design (LBDD) strategies use the biological and physicochemical properties of the ligands to create mathematical models to predict an unknown property of the new candidates. An example of ligand-based drug design is the Quantitative Structure–Property Relationship (QSPR) modeling, widely used for prediction of properties, activities and/or toxicities of new chemicals.

QSPR modeling represents applications of chemometric tools to explore quantitative relationships between a given property (including biological activity and toxicity) and descriptors (a set of properties quantifying information encoded in the molecular structure). In a broad sense, QSPR includes Quantitative Structure–Activity Relationship (QSAR) and Quantitative Structure–Toxicity Relationship (QSTR) studies.[3]

QSAR is a method that correlates chemical and structural information of a molecule to a biological or chemical activity using mathematical models. The process of constructing a QSAR model can be summarized as follows: (1) The information about the ligands and their activities is collected on a database. (2) A set of properties, known as molecular descriptors, are calculated and selected. (3) A mathematical model is created by using structural descriptors as independent variables and the activity as the dependent variable. (4) The predicting ability of the models is tested by internal and/or external validation procedures. (5) Finally, the QSAR model can be used to predict the activity of a novel compound and screen a database of potential molecules.[1]

5.2.1. Initial qualitative QSPR and quantitative QSAR models

The application of a ligand-based strategy for the selection of dual MNK inhibitors was designed as a combination of a qualitative QSPR and a quantitative QSAR models using a tree decision approach. The new candidates will be first classified as active (1) or inactive (0) by filtering them through MNK1 and MNK2 binary classification models (QSPR). Then, the activity values of the molecules predicted as active (1) are predicted using a QSAR model.

On one hand, the available information from published articles and from the ChEMBL database [4–6] was used to create the classificatory models for both proteins (classificatory QSPR). On the other hand, the published active molecules were used to create the corresponding QSAR models to predict the activity of new candidates.

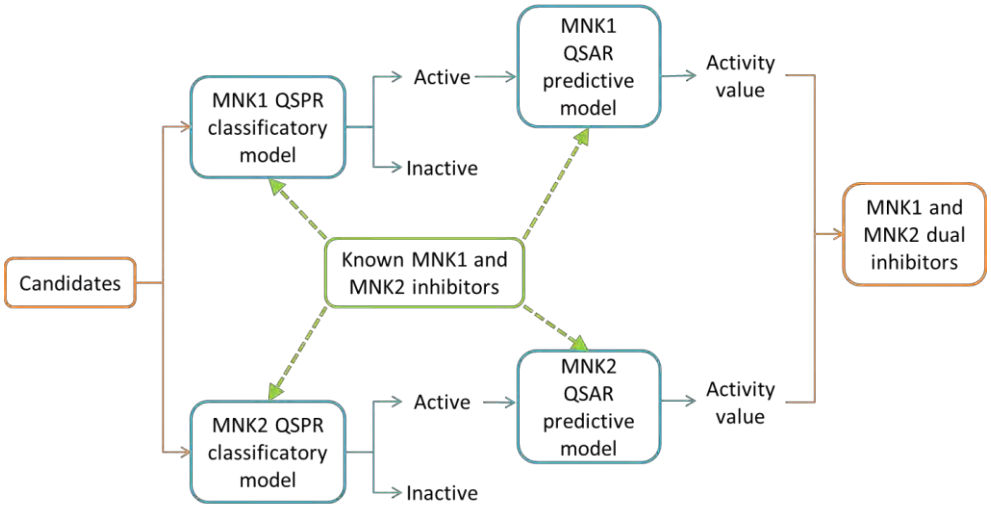

Figure 5.1 Workflow of the selection of candidates by LBDD strategies. Based on published data, classificatory and predictive models will be prepared. New active candidates will be first sorted using the classificatory models and their activity will be predicted with the predictive models to identify dual inhibitors. [7]

5.2.1.1. Preparation of the data set: Study of known MNK1 and MNK2 inhibitors

The general data set used for both QSPR and QSAR models was prepared using the information available in literature and in the ChEMBL database[4–6]. The molecules published by Oyzarzabal *et al.*[8], Diab *et al.*[9], Kannan *et al.*[10], Teo *et al.*[11,12], Yu *et al.*[13] and Cherian *et al.*[14] were used to create the databases of MNK1 and MNK2 inhibitors.

The inhibitors found in different articles were drawn and added to a database together with their activity value using Molecular Operating Environment (MOE) software.[15] The vast majority of the activities were described either as IC_{50} or Ki values, although a few inhibition activities were described as residual activity or inhibition percentage. The MNK1 database (*database_papers_mnk1*) consisted of a set of 123 compounds, and the activity data was given as IC_{50} (76 entries), Ki (29 entries), inhibition percentage (1 entry) and residual activity (22 entries). The MNK2 database (*database_papers_mnk2*) consisted of a set of 119 compounds, with activities given as IC_{50} (51 entries), Ki (51 entries), inhibition percentage (1 entry) and residual activity (22 entries).

In order to increase the information to be used for the creation of the models, the information about molecules tested on MNK1/2 available in the online database ChEMBL [4–6] (reference code for MNK1: Q9BUB5 and reference code for MNK2: Q9HBH9) was also considered. Three databases were created using the information of the website, importing the molecules from ChEMBL to MOE2014.09.[15] The first one included MNK1 inhibitors, with 611 entries and the activity given as inhibition percentage (*database_chembl_mnk1*). The other two databases included MNK2 inhibitors: *database_chembl_mnk2_resact* was formed by 314 entries with their corresponding residual activity percentage and *database_chembl_mnk2* was a balanced database which consisted on 60 entries, 50% of which were active and 50% inactive.

Due to the huge variability of the compounds from ChEMBL, the complete databases could not be used for the creation of the classificatory and predictive models. For this reason, these databases were used only as a source of decoys (molecules with no MNK inhibitory activity). The criterion used for the selection of inactive molecules was their similarity to those inhibitors described in the articles.

5.2.1.2. QSPR classificatory models

MNK1 and MNK2 QSPR classificatory models, with the ability to classify the candidates as active and inactive, were created using the information of both active and inactive published molecules.

Database creation

In order to create the QSPR model for MNK1, a database with both active and inactive known inhibitors was created. This database contained the information from the articles (*database_papers_mnk1*) and from ChEMBL (*database_chembl_mnk1*. Only those entries with a percentage of inhibition between 0-50% tested at 1 μM).

For the MNK2 QSPR classificatory model, a second database with both active and inactive known inhibitors was created containing the information from the articles (*database_papers_mnk2*) and from ChEMBL (*database_chembl_mnk2*. Entries with a percentage of inhibition between 0-50% and a residual activity > 50% when tested at 1 μM).

The different molecules were classified as active (1) or inactive (0) according to the criteria described in Table 5.1. The final MNK1 database contained a total of 218 entries, 92 active and 125 inactive molecules while the MNK2 database contained 229 entries, 90 active and 139 inactive molecules.

Table 5.1: Criteria to classify the molecules as active or inactive inhibitors depending on their activity values and tests.

	IC_{50} (μM)	Ki	Residual Activity %	Inhibition %
ACTIVE (1)	<10	<10	<50	>50
INACTIVE (0)	≥10	≥10	≥50	≤50

Descriptors selection

The database was prepared by eliminating the ions and energy minimizing the molecules with MOE2014.09. Then, all 2D and i3D descriptors (344 descriptors) available in MOE were calculated.

The selection of descriptors was performed using RapidMiner Studio.[16] First, the correlation between the activity and each descriptor was calculated to select those descriptors with the higher correlation (13 descriptors for the MNK1 model and 19 descriptors for the MNK2 model). Then, the correlation between the selected descriptors was avoided by calculating the correlation between each pair of descriptors and discarding one out of the two correlated parameters. Finally, the useless descriptors (those descriptors with the same value in most of the compounds) were eliminated. The number of selected descriptors for the MNK1 model was reduced to 7: a_base, b_double, PEOE_VSA_FPOS, SlogP_VSA3, SlogP_VSA4, PM3_dipole, vsurf_HB1. For the MNK2 model also 7 descriptors were selected: PC-, PEOE_VSA_POS, ASA_P, FCASA+, PM3_dipole, vsurf_HB1, vsurf_W3.

Model building

RapidMiner Studio was used to create the classificatory models. The data set was divided into two groups, the training set (80%) and the test set (20%) with stratified sampling (dividing the data in random subsets ensuring that the class distribution in the subsets is the same as in the whole training set). The models were generated by artificial neural networks using supervised learning with the training set. The model was applied on the test set and the results were analyzed to calculate the accuracy of the model. The different parameters were optimized to obtain the best model to describe the available data (Annex 5).

In order to choose the best parameters, the minimum acceptable accuracy of the model for both the training and the test were defined as 80%. Also, despite it is important to minimize both the false positives and the false negatives, we prioritized the minimization of false positives as the selected candidates will be later classified with the QSAR predictive model (which will be only capable of predicting the activity of active molecules). Moreover, the reduction of the false positives will increase the rate of success to synthetize active molecules in the laboratory to be used as starting hits.

The best MNK1 model was obtained using a 7-6-4-2 artificial neural network with 0.05 learning rate and 15000 training cycles (QSPR_MNK1_11 model, annex 5). The model shows accuracy percentages above 80% in both the training and the test sets and high percentages of class recall and class precision with a low number of false positives. The results obtained are summarized in Table 5.2.

For MNK2, the best model was obtained using a 7-7-4-2 artificial neural network with 0.04 learning rate and 15000 training cycles (QSPR_MNK2_6 model, annex 5). Accuracy percentages were higher than 85% in both the training and the test sets. The class recall and class precision percentages were also higher than 85% and the model presented a low number of false positives. The results obtained are summarized in Table 5.3.

Table 5.2: Results obtained for the best MNK1 classification method.

TRAINING	**True 1**	**True 0**	**Class precision**
Pred. 1	66	4	94.3%
Pred. 0	6	107	94.7%
Class recall	91.7%	96.4%	***Accuracy: 94.5%***
TEST	**True 1**	**True 0**	**Class precision**
Pred. 1	13	2	86.7%
Pred. 0	5	26	83.9%
Class recall	72.2%	92.9%	***Accuracy: 84.8%***

Table 5.3: Results obtained for the best MNK2 classification method.

TRAINING	**True 1**	**True 0**	**Class precision**
Pred. 1	72	1	98.6%
Pred. 0	2	99	98.0%
Class recall	97.3%	99.0%	***Accuracy: 98.3%***
TEST	**True 1**	**True 0**	**Class precision**
Pred. 1	16	3	84.2%
Pred. 0	2	22	91.7%
Class recall	88.9%	88.0%	***Accuracy: 88.4%***

5.2.1.3. QSAR predictive models

In order to predict the activity of potential MNK1 and MNK2 inhibitors, two QSAR prediction models were created. The purpose of these models was to predict the activity values of those molecules previously classified as active with the QSPR classificatory models to rank them according to their predicted activity.

Database creation and descriptors selection

For these models, only the active molecules described in literature were used. The MNK1 and MNK2 databases were prepared with the active molecules with activities measured as IC_{50} and contained a total of 67 and 47 molecules respectively.

Using MOE2014.09, all 2D and i3D descriptors were calculated after energy minimizing the molecules. The selection of descriptors was performed with RapidMiner Studio. Descriptors with a correlation with the activity lower than 0.3 were removed together with the useless and one of each correlated pair of descriptors. A total of 7 descriptors were selected for the MNK1 QSAR model: BCUT_PEOE_1, b_1rotR, KierA3, Q_RPC+, SlogP_VSA6, E_tor, vsurf_IW8. 5 descriptors were chosen for the MNK2 QSAR model: a_acc, GCUT_PEOE_1, PEOE_VSA-1, E_strain, PM3_IP.

Model building

The QSAR models were created using the in house developed software ArIS.[17] The models were built with the selected descriptors and the activity values as pIC_{50}. A split-validation was used as the external validation method, thus the training set used to create the model contained 80% of the entries and the test used the validation of the model 20%. The parameters were optimized to obtain the best model. (Annex 5)

On the MNK1 model, an experimental design was used to study the effect of the learning rate and iterations applying a 3^2 full factorial design (two variables with three different levels each). The results (Annex 5) show that the main contribution of the R^2 value comes from the learning rate. This variable should be maintained at high values in order to increase the response. Moreover, despite its low contribution, the iteration number should be maintained in the highest level.

The best MNK1 model was obtained using a 7-6-4-1 artificial neural network with 0.0001 learning rate and 30000 iterations (QSAR_MNK1_6_2 model, annex 5) while of MNK2 a 5-5-3-1 artificial neural network with 0.001 learning rate and 30000 iterations (QSAR_MNK2_18_1) was chosen as the best option. The results were plotted in a graph representing the predicted pIC_{50} *vs* the real pIC_{50} (Figure 5.2 and Figure 5.3).

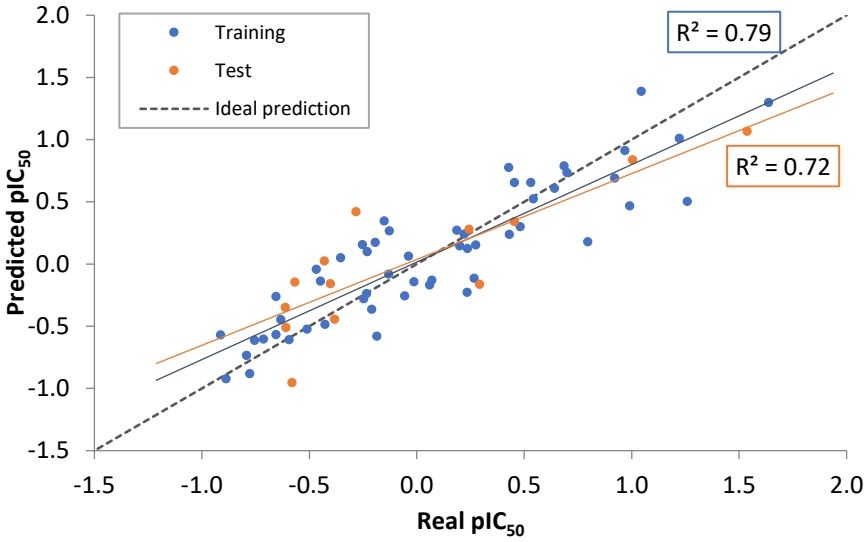

Figure 5.2: Results of the QSAR_MNK1_6_2. After the creation of the model using the training set, the activity of the training molecules was predicted to ensure a good correlation between the predicted and the real values. Then, the test molecules which had not been used for the creation of the model are predicted to know the capacity of the model to predict the activity of new molecules. The RMSE values (0.00 for the training and 0.18 for the test) indicate that the model has a good ability to predict the activity values while the Spearman coefficients (1.00 for the training and 0.99 test) indicate a good correlation between the predicted and the real values.

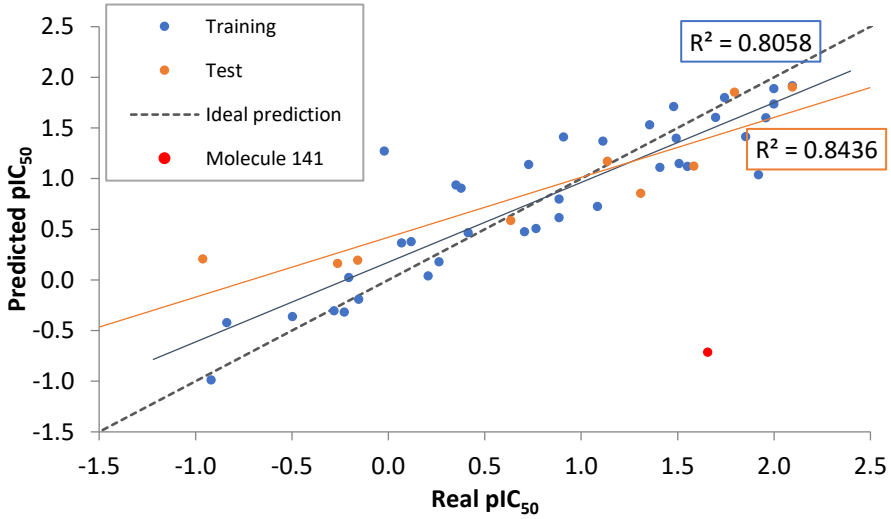

Figure 5.3. Results of the QSAR_MNK2_18. After the model was created, the activity of both the training molecules used for the creation of the model and the test molecules was predicted. Molecule 141 from the test set was identified as an outlier and was discarded for the calculation of the suitability of the model (see Annex 5). The RMSE values (0.02 for the training and 0.27 for the test) and the Spearman coefficients (1.00 for the training and 0.99 test) indicate a good prediction capacity of the model and a good correlation with the real values.

Both models were validated with the same database used to build the model (*database_papers_mnk1* and *database_papers_mnk2*). The ROCS curve for both the training and the test sets were represented (Annex 5) indicating a great capacity of the models to correctly classify molecules with low IC_{50} values.

5.2.1.4. Virtual screening of a chemical library of synthetically accessible compounds

The first models were used to select a set of compounds presenting a pyrazolo[3,4-*b*]pyridin-6-one scaffold to be synthetized and tested as MNK1/2 inhibitors. These systems had not been studied before as MNK inhibitors and there was no available information about their possible activity. Therefore, the models did not contain any similar molecules and their capacity to predict the activity of this type of scaffold was unknown. The experimental results would provide a validation of the models and the biological results will be used to improve the model and allow more accurate predictions for future iterations.

With this purpose, a combinational library was created with all the synthetic possibilities and the best candidates were selected by applying the models (QSPR classificatory and QSAR predictive models).

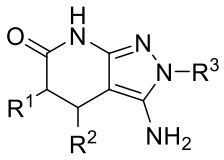

Figure 5.4. General scaffold of the 3-aminopyrazolo[3,4-*b*]pyridin-6-ones studied as MNK inhibitors and selected with the models.

Database creation

A database (*database_candidates*) with 108 compounds was created by combining 9 different scaffolds (Figure 5.5) and 12 hydrazine substituents (Figure 5.6). The scaffolds include the different substituents for R^1 and R^2 while the hydrazine substituents will occupy the R^3 position.

The combination of the scaffolds and the hydrazine substituents was performed with MOE2014.09. The molecules were energy minimized and the descriptors needed for the different models were calculated.

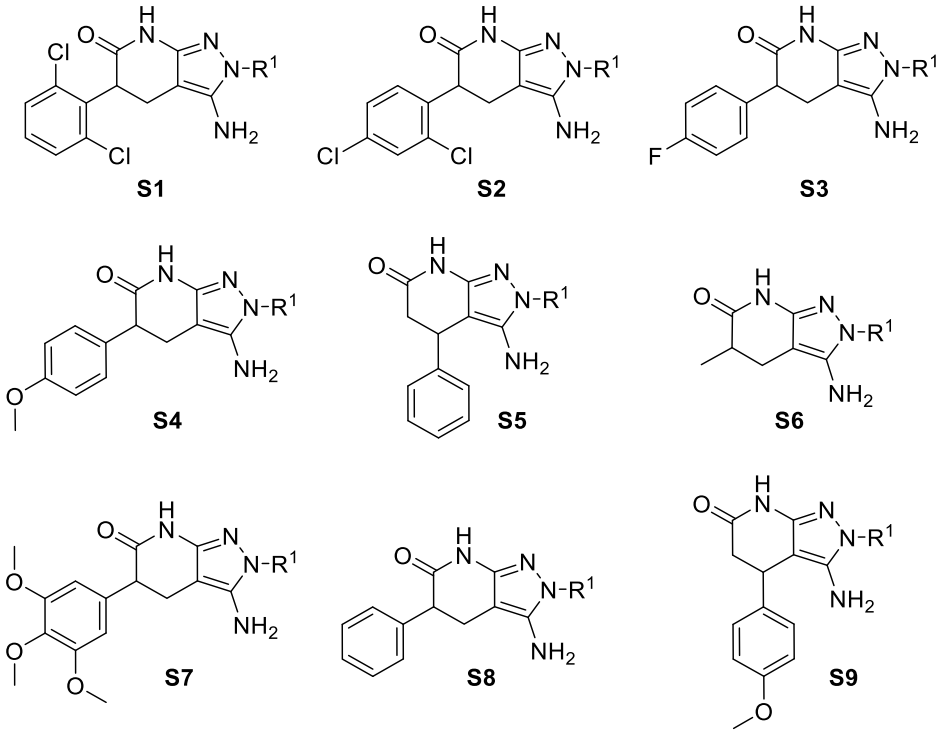

Figure 5.5. Scaffolds studied for the candidate selection with the models.

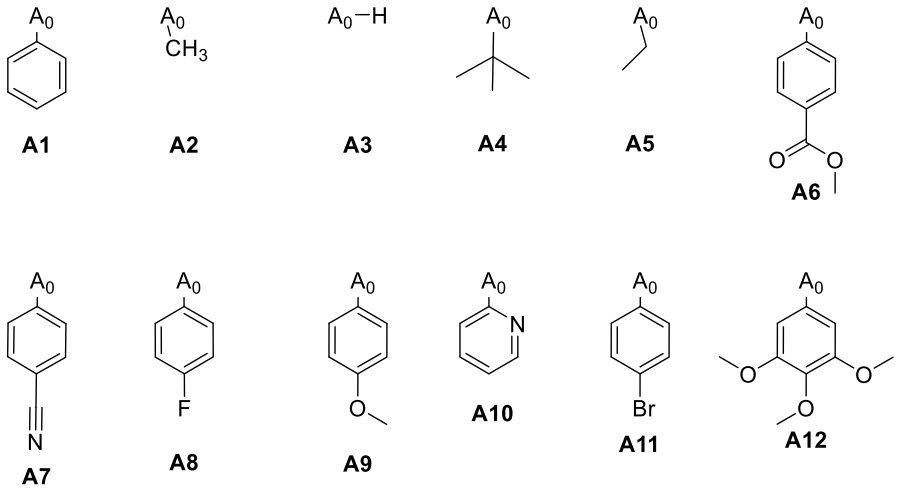

Figure 5.6. Substituents studied for the candidate selection with the models.

Application of QSPR classificatory and QSAR predictive models

Using RapidMiner, the database was filtered through both QSPR classificatory models (QSPR_MNK1_11 and QSPR_MNK2_6). Out of the 108, 21 molecules were predicted to be active for MNK1 and 20 molecules were predicted as active for MNK2.

Then, the QSAR models (QSAR_MNK1_6_2 and QSAR_MNK2_18_1) were applied to the selected molecules to predict their activity values.

Table 5.4: Results of the prediction of the QSPR and QSAR models on the candidates. Molecules marked in green are selected as dual inhibitors. Molecules in bold meet the selection criteria with a predicted activity lower than 6 μM in both proteins. The C* indicates the code for the molecule in the database (Annex 5) while the (S*, A*) represents the molecule as the combination of the two fragments found in Figure 5.5 and Figure **5.6**.

MNK1		MNK2	
QSPR active predicted molecules	**QSAR IC_{50} prediction**	**QSPR active predicted molecules**	**QSAR IC_{50} prediction**
C7 (S1, A7)	1.10	C12 (S1, A12)	0.19
C19 (S2, A7)	1.00	C24 (S2, A12)	0.04
C31 (S3, A7)	**4.86**	**C31 (S3, A7)**	**2.31**
C36 (S3, A12)	9.76	C36 (S3, A12)	0.08
C43 (S4, A7)	**3.64**	C42 (S4, A6)	1.59
C48 (S4, A12)	8.55	**C43 (S4, A7)**	**2.71**
C55 (S5, A7)	**4.76**	C50 (S5, A1)	0.13
C60 (S5, A12)	10.64	C51 (S5 A2)	0.67
C67 (S6, A7)	3.95	C54 (S5, A3)	0.57
C72 (S6, A12)	9.51	**C55 (S5, A7)**	**1.52**
C74 (S7, A1)	10.86	C60 (S5, A12)	0.06
C78 (S7, A6)	1.23	C66 (S6, A6)	0.66
C80 (S7, A8)	8.98	C80 (S7, A8)	0.03
C81 (S7, A9)	9.14	C82 (S7, A10)	0.35
C82 (S7, A10)	10.37	**C91 (S8, A7)**	**1.65**
C84 (S7, A12)	0.65	C98 (S9, A2)	54.94
C91 (S8, A7)	**5.37**	**C102(S9, A6)**	**1.59**
C98 (S9, A2)	6.34	C103 (S9, A7)	2.79
C102 (S9, A6)	**2.01**	C105 (S9, A8)	1.48
C106 (S9, A10)	**3.15**	**C106(S9, A10)**	**2.38**
C108 (S9, A12)	3.74		

The main objective of this study was to identify possible dual MNK1 and MNK2 inhibitors. For this reason, only the molecules that were selected as active for both models were considered of interest. Only 11 molecules achieved this requirement. The predicted activity values for MNK2 were higher than those predicted for MNK1. Therefore, an activity threshold of 6 μM was defined. A total of 6 molecules were selected as possible candidates. (Table 5.4)

The selected molecules were prepared and included in the third set of compounds tested with the enzymatic assay (Chapter 2). Unfortunately, the molecules did not show any activity, demonstrating the models were not capable to predict the activity of this type of structures and that it is necessary to include similar molecules in the database to correctly predict this family of molecules.

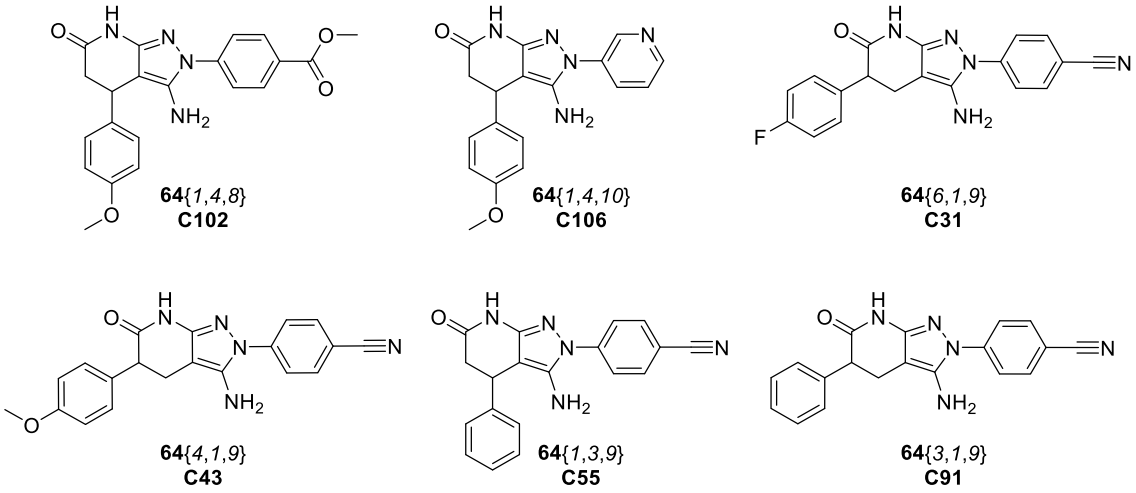

Figure 5.7. Pyrazolo[3,4-*b*]pyridines selected with the classification and prediction models. C* indicates the number of the molecule in the combinatorial library.

5.2.2. The iterative drug design process: Modification of the models

5.2.2.1. Usefulness of the initial models

During the course of the project, new MNK1/2 inhibitors were developed. It is considered of importance to make sure that the best possible models for the selection of new candidates are available and, if necessary, to periodically optimize them to include all the available information.

For this reason, the suitability of the models was studied by trying to predict the activity of the new published molecules. In this case, a new database containing the information of new publications was used.

A new database with the compounds described by Diab *et al.*[18], Reich *et al.*[19], Han *et al.*[20] and Zhan *et al.*[21] was created. The inhibitors were constructed in MOE2014.09[15] and added to a database together with their activity value. The molecules were considered as active (1) or inactive (0) according to the same previously described criteria (Table 5.1).

The molecules were classified by applying the QSPR model using RapidMiner. Surprisingly, the prediction of the new molecules was not acceptable as the MNK1 QSPR model had only predicted correctly the 38% of the molecules while the MNK2 QSPR model had a 53% of success. However, it was interesting that the number of false positives was very low in comparison with the number of false negative results (Annex 5). The models were therefore considered of limited use due to the important information loss during the screening (as false negatives). Therefore, it was necessary to modify the models including all the new available information.

5.2.2.2. Modification of the models

Database creation

The database of new compounds was joined to the old database containing the molecules from the previously used publications and the decoys from ChEMBL. Finally, the information regarding the activity of the first and second set of 3-aminopyrazolo[3,4-*b*]pyridin-6-ones (see chapter 2) was also included into the database (*2018_mnk1_proq.mdb* and *2018_mnk2_proq.mdb*).

Descriptors selection

The database was prepared by eliminating the ions, calculating partial charges and energy minimizing the molecules with MOE2014.09. Then, all 2D and i3D descriptors (344 descriptors) available in MOE were calculated.

Again, the selection of descriptors was performed using RapidMiner Studio. The descriptors with a higher correlation with the activity were selected. After removing the useless and correlated descriptors, 13 descriptors were selected to create the modified MNK1 QSPR model: b_double, h_pKb, GCUT_PEOE_0, logP(o/w), PEOE_VSA_FNEG, PEOE_VSA_POS, Q_VSA_FNEG, SlogP_VSA3, SMR_VSA2, vsurf_A, vsurf_CW2, vsurf_HB1, vsurf_IW6. For the MNK2 model, 6 descriptors were selected: a_nN, h_ema, PEOE_VSA_POS, Q_RPC-, vsurf_HB1, vsurf_HB5

Model building

The model was generated using RapidMiner Studio. The dataset was divided into training set (80%) and test set (20%) using a stratified sampling. The model was performed with the training set and validated with the test set. We considered of importance to study the dependence of the prediction with the selected training set. For this reason, the models (obtained with an artificial neural network (13-7-4-1 for MNK1 and 6-7-4-1 for MNK2) with 0.04 learning rate and 15000 training cycles) were validated using a cross-validation with 5 validations (the model was created and validated with 5 different combinations of training and test sets).

Different results were observed for the 5 different combinations. Such variations could be caused by a dependency of the model with the selected training and test sets and therefore it was not possible to define which combination of training and test would be the best for the selection of new candidates. In order to overcome the variability and consider all the different models, a “voting” strategy was applied. 5 equivalent models were generated using different combination of training and test sets. The new molecules were classified with the 5 models and the best candidates were selected according to the results of the 5 different predictions. Table 5.5 and Table 5.6 summarize the results of the “voting” methods as the mean results of the 5 separated methods that will be used for the selection.

Table 5.5. Results from the cross-validation of the new MNK1 QSPR model.

MNK1	True 1	True 0	Class precision
Pred. 1	102	41	**71.3%**
Pred. 0	37	194	**84.0%**
Class recall	**73.4%**	**82.6%**	

Accuracy: 79.1% ±3.9%
Mean recall: 77.9% ±4.5%
Mean precision: 78.0% ±4.1%

Table 5.6. Results from the cross-validation of the new MNK2 QSPR model.

MNK2	True 1	True 0	Class precision
Pred. 1	101	36	**73.7%**
Pred. 0	33	180	**84.5%**
Class recall	**75.4%**	**83.3%**	

Accuracy: 80.3% ±3.4%
Mean recall: 79.2% ±4.0%
Mean precision: 78.1% ±4.2%

5.2.3. Final model. Prediction of the activity of pyrazolopyrin-6-ones and pyrazolo[3,4-*b*]pyridin-3-amine

The new model was validated by predicting the activity of all the compounds that have been prepared and analyzed with the enzymatic assay during this project.

Before filtering the molecules, we ensured that we were not extrapolating and that the area covered by the selected descriptors included the properties of the new molecules. With this purpose, the molecules were represented using a Principal Component Analysis (PCA) of their 13 descriptors of the MNK1 models or the 6 descriptors of the MNK2 model. The first 3 PCAs were represented in a 3D chart to observe that the synthetized molecules (red) were included in the area covered by the molecules used for the models (blue). Therefore, in this case, the predictions of the model would not be an extrapolation (Figure 5.8 and Figure 5.9).

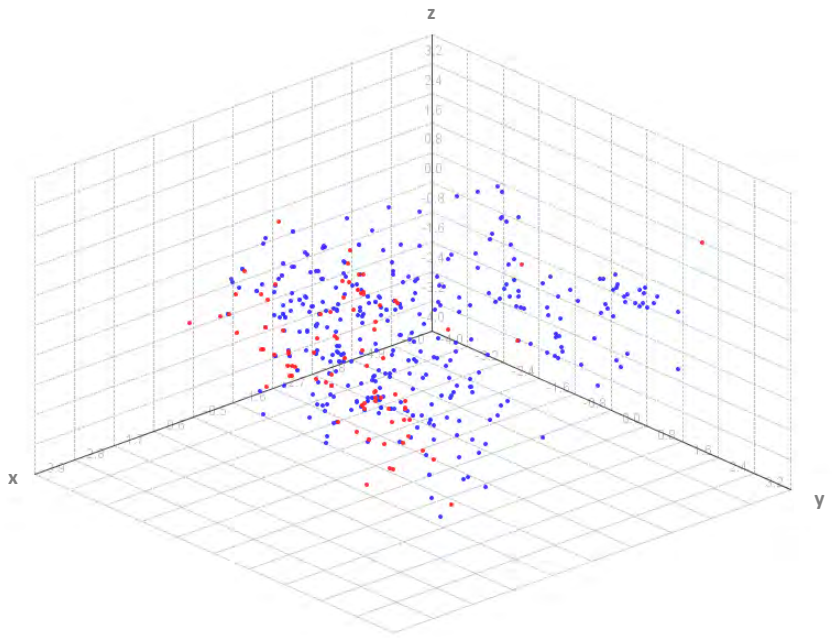

Figure 5.8. PCA analysis of the MNK1 model. PCA representation of the molecules used in the model (blue) and the new molecules that will be predicted (red) indicating that the new molecules can be represented by the information contained in the model.

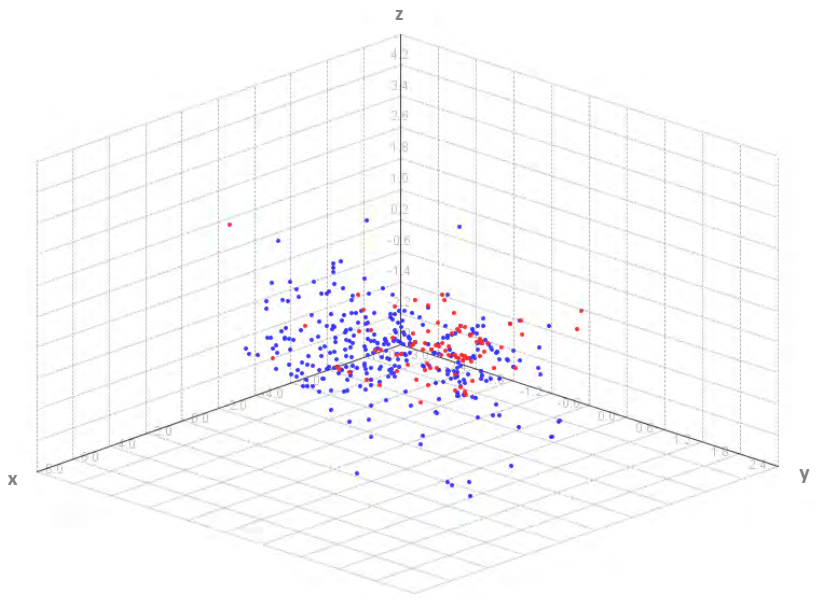

Figure 5.9. PCA analysis of the MNK2 model. PCA representation of the molecules used in the model (blue) and the new molecules that will be predicted (red) indicating that the new molecules can be represented by the information contained in the model.

This time, the model was able to correctly predict the 89% of the activities for MNK1 and 82% for MNK2. Moreover, the prediction avoids the generation of false positives, a fact that has been considered as essential in the creation of the models for the screening and selection of new molecules (Annex 5).

Table 5.7. Validation of the models with the compounds developed in this project.

MNK1	True 1	True 0	Class precision
Pred. 1	7	2	**77.8%**
Pred. 0	8	72	**90.0%**
Class recall	**46.7%**	**97.3%**	

MNK2	True 1	True 0	Class precision
Pred. 1	3	11	**21.43%**
Pred. 0	5	70	**93.33%**
Class recall	**37.5%**	**86.4%**	

However, a high number of false negatives was detected. The results indicate that, for more accurate results, molecules similar to the 4,6-diphenylpyrazolo[3,4-*b*]pyridin-3-amine family need to be included in the model. For MNK1, 4 out of 5 molecules predicted by the model as active are correct. However, 5 active molecules are incorrectly discarded. On the other hand, the MNK2 model classified all the molecules of this family as inactive and did not select any of the dual inhibitors.

5.2.4. Conclusion

A ligand-based drug design strategy has been applied in the study of the scaffolds 3-aminopyrazolo[3,4-*b*]pyridin-6-ones and pyrazolo[3,4-*b*]pyridin-3-amines. The initial models created for the selection of 3-aminopyrazolo[3,4-*b*]pyridin-6-ones did not provide the expected results as they were not capable to correctly predict the activity of this scaffold provably due to the lack of equivalent molecules in the model.

However, in this project the process of drug design was approached as a cyclic process where the information generated during the study was used to improve the initial models and provide more accurate and useful results on the future selections of compounds.

Applying this strategy, a second set of models was created using the information obtained from the preliminary test of the 3-aminopyrazolo[3,4-*b*]pyridin-6-one molecules. The new methods were able to correctly predict the activity of the last set of molecules based on this scaffold and to correctly identify 4 molecules of the pyrazolo[3,4-*b*]pyridin-3-amine family as MNK1 inhibitors.

In the future, the models will be again modified and improved by including the information of the biological activity of the family of pyrazolo[3,4-*b*]pyridin-3-amines together with other possible molecules published in literature.

5.3. Structure based drug design strategies

Design of new inhibitors to target MNK proteins has become an interesting starting point for searching novel cancer therapies. In this regard, computational aided techniques have risen as an effective strategy to guide the drug design process reducing time and cost. Despite the increasing number of publications related to new molecules with activity as MNK inhibitors, ligand-based strategies are limited to the available information and have been poorly used in the last years.

In view of the lack of ligand-based information, structural information about the receptor becomes mandatory to allow the application of structure-based drug design. SBDD strategies have been widely used in pharmaceutical research and have been applied for the development of MNK inhibitors in the optimization of hit candidates[11,13,19,20] and the elucidation of binding mechanisms[10,22,23]. Unfortunately, the available information is limited to the inactive conformation of the proteins (DFD-out)[24–26] and the active DFG-mutants (DFG-in)[19,24].

Moreover, in the case of MNKs, this process has been mainly focussed on MNK2 inhibitors due to the higher amount of information available for this protein. Having reliable models of both proteins is essential for the correct application of SBDD strategies and therefore it is necessary to design strategies to overcome the limitations caused by the lack of information.

5.3.1. Study of MNK2. Importance of the modelling of the activation loop for SBDD

MNK2 is the most used protein for SBDD studies specially in the development of ATP competitive (Type I) inhibitors. However, some studies directly apply the crystal structures available in the PDB without taking in consideration the limitations caused by the presence of some mutations or the missing fragments in the crystals. Here, we analyze the importance of including these fragments into the simulations. The results were published by Bou-Petit *et al.*[27]

As described in Chapter 1, the molecular structure of MNK proteins has a strong resemblance to other protein kinases[25,28] but presents two unique features [29,30]: (1) an specific insert in the catalytic domain (corresponding to the EAFSE sequence in MNK2) and (2) the replacement of the conserved DFG-motif by a particular DFD-motif. Due to the presence of the DFD motif, MNKs can adopt an active (DFD-in) conformation where the ATP binding pocket is exposed and an inactive (DFD-out) where the pocked is blocked by the Phe227 residue.[28]

To the best of our knowledge, the crystal structure of the wild-type (wt) MNK2 protein presenting the DFD-in active conformation has not been described yet, and the wildtype protein is only available for the DFD-out conformation (PDB ID: 2AC3[25]). Most of the studies reported in literature are based on crystallographic structures of D228G MNK2 mutants[8,11,13,31] (PDBID: 2HW7[24], 2AC5[25]), considering that this mutation does not affect the ATP binding and its kinase activity. Moreover, none of the available crystallographic structures includes information about the activation loop and, consequently, this part of the protein is usually neglected. This would lead to an over-simplistic model, particularly when molecular dynamics simulations suggested that the flip of the DFD motif is directly associated with conformational changes in the activation loop.[28,32]

5.3.1.1. Effect of the activation loop in the design of new inhibitors

We have studied the importance of the activation loop in the binding of ligands and therefore the importance of its presence in structure-based drug design strategies. The effect of the activation loop was evaluated by predicting the interaction mechanism of well-known MNK2 inhibitors (i.e. staurosporine, cercosporamide and CGP57380, Figure 5.10) by means of molecular docking.

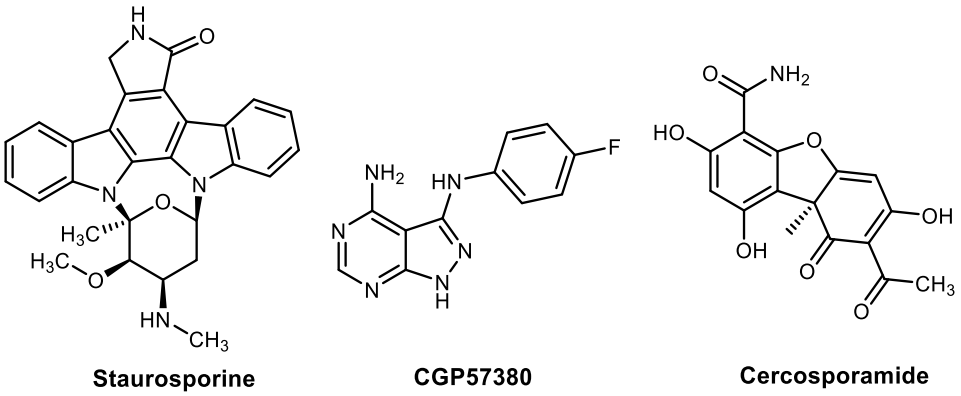

Figure 5.10. Molecular structure of known MNK1/2 inhibitors taken as reference in this study.

Three models were considered for the evaluation of the activation loop effect: (1) the reported PDB structure (2HW7), which contains the resolved structure for only few atoms of the activation loop and presents the DFG mutation, (2) the wildtype MNK2 protein with the modelled loop and (3) 2HW7 without loop (the PDB structure where the residues of the loop had been removed). (Figure 5.11)

Figure 5.11. Models used in this study.[27]

Two docking methods (rigid and induced fit docking) were compared in order to discuss the relevance of the D228G mutation and the presence of the activation loop when studying the binding mechanism of drug candidates to MNK2. In both cases, molecular docking protocols were validated (RMSD < 0.25 Å) by predicting the binding mechanism of staurosporine and comparing the result to the crystal structure of staurosporine complexed to the MNK2 D228G mutant structure available in the PDB (2HW7).

Rigid docking

The reference compounds were docked on the three MNK2 models with a blind rigid docking using AutoDock4.[33]

Cluster analysis of the docked conformations showed that staurosporine was able to mostly recognize the active site in all models, suggesting that the presence of the loop did not induce a remarkable effect on the location of the ligand.

On the contrary, the presence of the activation loop hindered the access to the active site of cercosporamide and CGP57380. The combined effect of activation loop and the DFD motif conformations blocked the active site abutting the C-helix, moving their preferred binding site from the ATP binding site to the helix region at the C-terminal lobe (Figure 5.12).

However, despite an appreciable percentage of conformations were located in the ATP binding site, conformations located into the active site did not correspond to the best ranked conformations in terms of the scoring function and leading to confusing results.

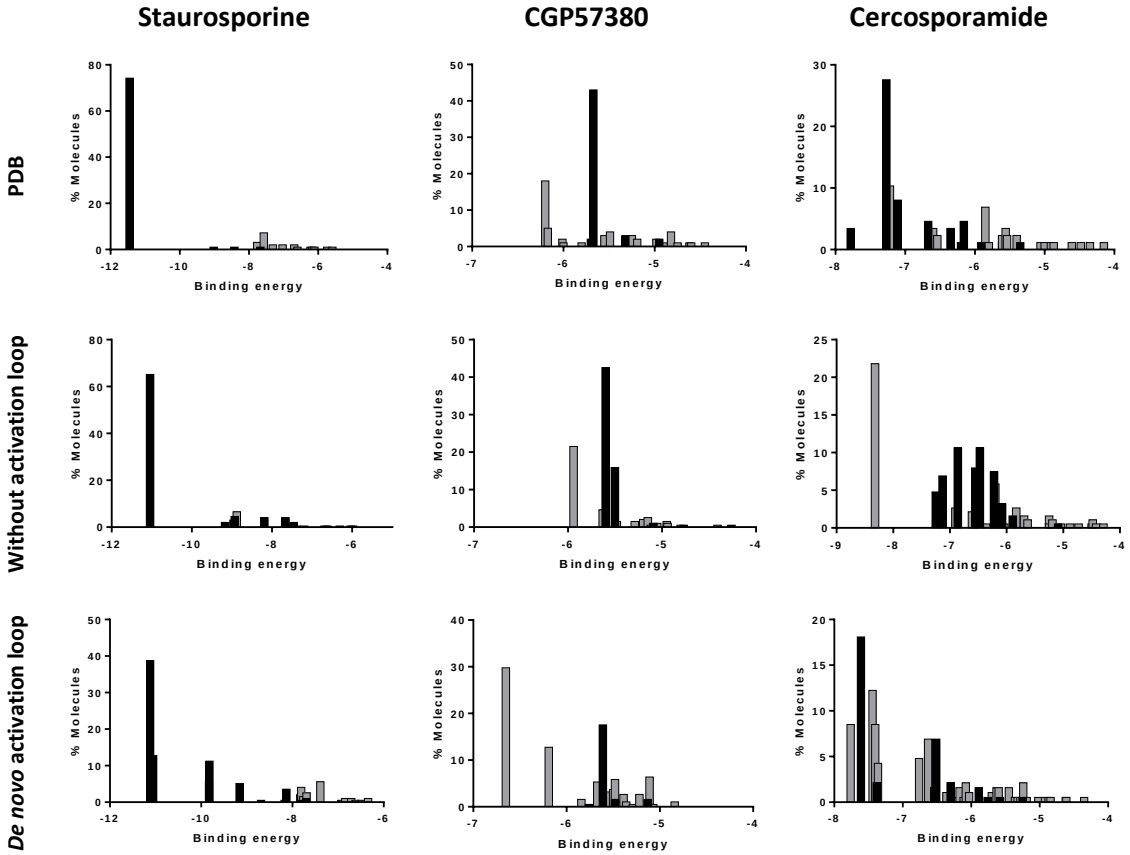

Figure 5.12. Cluster analysis from rigid docking. Molecules are divided in two groups depending on where they bind: the active site (black) or other parts of the protein, usually the α-helixes (grey).

Although staurosporine is preferentially bound to the ATP binding site, the spatial orientation of the most stable binding conformations predicted with the different models (with and without the activation loop) were slightly different (Figure 5.13). Structural differences could be appreciated when comparing the binding mechanism of two conformations of comparable score, obtaining two flipped conformations according to a symmetry axis.

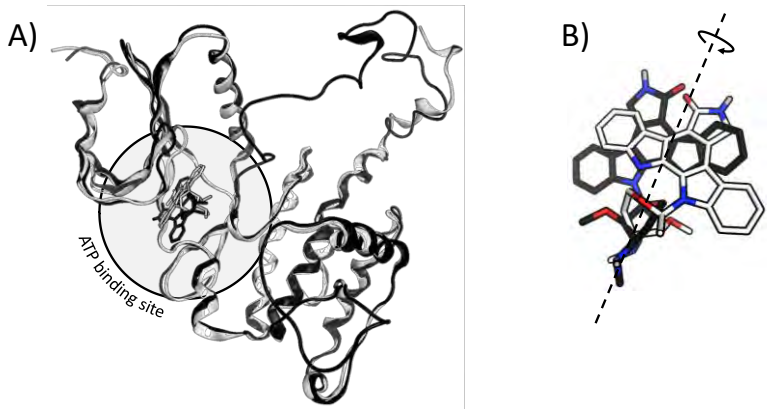

Figure 5.13. Comparison between the most stable staurosporine conformations predicted by docking when considering the MNK2 protein without activation loop (white) and containing a *de novo* modelled activation loop (black). (A) Position of the best ranked staurosporine conformations within the MNK2 protein, corresponding to the active site. (B) Comparison between the spatial orientations of both conformations obtained.[27]

According to these results, the activation loop may have a pivotal role in the recognition of the active site by ligands. However, rigid docking did not allow obtaining a correlation between the active site recognition and the scoring function value giving rise to unrealistic docking results. Therefore, it is considered of interest to repeat the study including protein flexibility.

Induced fit docking

The reference compounds were docked on the three MNK2 models with a blind docking with induced fit using MOE2014.09[15] generating 100 poses.

Induced fit docking revealed that the flexibility of the activation loop may contribute to guide ligands towards the active site. Interestingly, for each model, the reference compounds showed a similar behavior. The three ligands preferentially bound to the external part of the β-sheets in absence of the activation loop. However, when a small part of the loop was present (PDB model), more conformations were found in the helixes despite some conformations bound into the active site.

Finally, in the presence of the modelled loop a higher percentage of conformations ended up in the ATP binding site. Apparently, the modelled loop guides molecules to the Glycine rich loop and avoids binding to the C-helix. Moreover, the conformations with the best score were located in the ATP binding site while the conformations with a lower score were bound to helixes. Figure 5.14 shows the distribution of docking conformations obtained for each model.

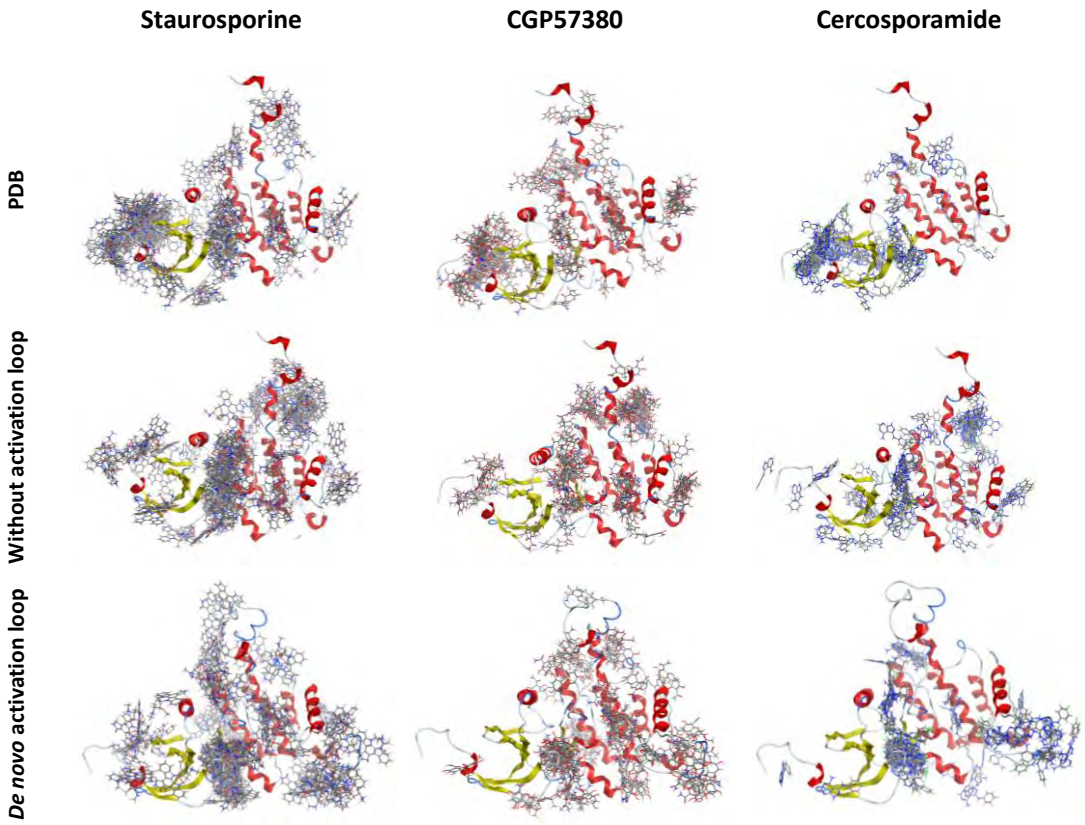

Figure 5.14. Graphical representation of the conformations obtained by induced fit docking.

Cluster analysis was used to quantify the number of molecules located in the active site in each model. As shown in Table 5.8, the model including the *de novo* modeled activation loop was the one that leads the higher number of high score conformations within the active site. The flexibility of the activation loop seems to be determinant in order to obtain these results.

Table 5.8. Percentage of molecules bound to the MNK2 ATP binding site.

	Staurosporine	**CGP57380**	**Cercosporamide**
PDB	28%	20%	12%
Without activation loop	18%	15%	11%
***De novo* activation loop**	33%	36%	22%

In order to make the visualization of these results easier, the three-dimensional coordinates of each MNK2 residue were projected into the H^2 hyperbolic plane. This procedure allows the representation of multidimensional points into a bidimensional space in which the distance between projected points increase exponentially with the radii by changing the metric definition (in this case, using Poincaré's disk model).[34] Residues were colored according to the protein region and their positions were compared with the location of staurosporine conformations (Figure 5.15).

As expected, results showed that a higher number of staurosporine conformations were located close to the DFD motive and the ATP binding site. It is a worth of attention the effect of the activation loop on the MNK2 projection, which modifies the conformation of the protein and induces a change into staurosporine distribution reducing binding affinity towards the β-sheets and the C-helix and concentrating conformations on the active site.

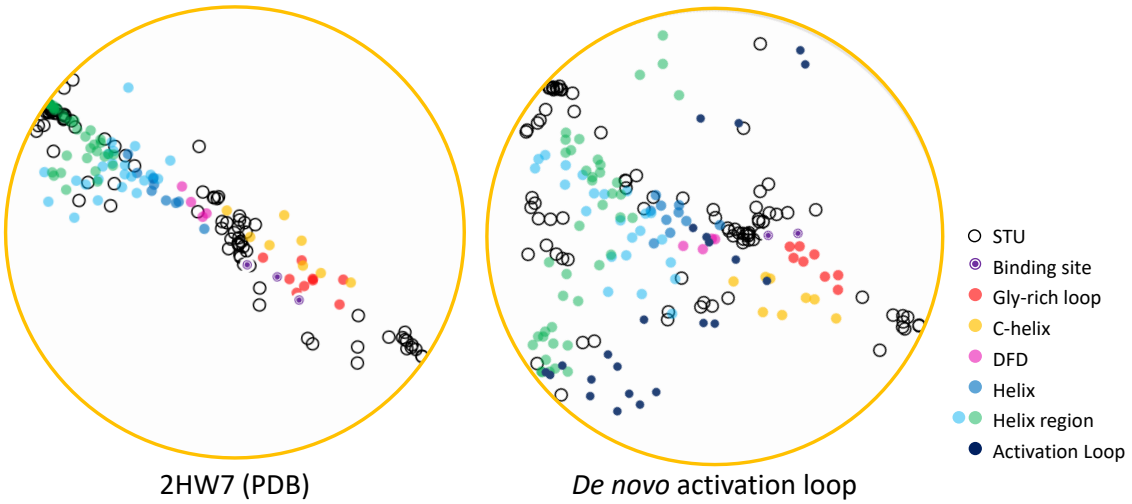

Figure 5.15. Hyperbolic projection of MNK2 residues resulting from flexible docking on PDB (2HW7) and the structure with the modelled loop.[27]

5.3.1.2. Conclusion

The effect of the activation loop on predicting the preferred binding site of MNK2 inhibitors has been evaluated by molecular docking.

These results were in disagreement with methodologies commonly reported in literature for designing new MNK2 inhibitors where most of research articles directly apply molecular docking on the DFG-mutated MNK2 structure available in the PDB (2HW7). This study suggests that these models may be over simplistic, and they could lead to unrealistic results.

The presence of the activation loop was shown to be essential to lead ligands towards the active site and receptor flexibility was required to obtain reliable results. Therefore, the modelling of the activation loop and including flexibility of the receptor are determinant for the correct description of the MNK2-ligand complex and should be considered when applying docking procedures in molecular design of new MNK2 inhibitors.

5.3.2. Study of MNK1. Structural models

The structure of MNK1 has not been studied in depth due to the lack of structural information available as only the crystal structure of the autoinhibited conformation (DFD-out) is published. It is therefore considered of interest to study the tridimensional structure of MNK1 and obtain models of their active and inactive conformations to increase the information available for SBDD strategies. Moreover, it is interesting to include the effect of the phosphorylation in the study.

5.3.2.1. Preparation of the models by molecular dynamics simulation.

With this in mind, four different models were created: the phosphorylated and unphosphorylated models of the active and inactive conformations of MNK1.

The models were created starting from the available crystal structures (Figure 5.16). On one hand, the inactive structures were created by modelling the missing fragments on the MNK1 DFD-out conformation crystal structure (PDB ID: 2HW6[24]). Using the loop modelling tool in MOE2014.09[15], the missing loops were modelled *de novo* obtaining the initial MNK1 inactive model (2hw6). The model was then manually phosphorylated on residues Thr209 and Thr214 generating the initial p-MNK1 inactive model (2hw6p).

On the other hand, the models of the active forms were based on the DFG-MNK2 mutant (PDB ID: 2HW7[24]) that presents an active conformation. First, the MNK2 active model was created. With this purpose, using the MNK2 PDB (PDB ID 2HW7) as a template, the mutation in the DFG motif was manually reversed (G228D) using MOE, recovering the typical DFD motif of the MNKs. Then, the missing fragments were modelled *de novo*. Finally, a 30 ns MD simulation was performed to obtain a stable conformation of this structure (2hw7).

The MNK1 active models were obtained by homology modelling using the active MNK2 model (2hw7). The sequence of amino acids of MNK1 was aligned with the sequence of MNK2 and the tridimensional structure was created based on the tertiary structure of MNK2 obtaining the active MNK1 structure (2hw6hm). Again, this model was manually phosphorylated on residues Thr209 and Thr214 generating the initial p-MNK1 active model (2hw6phm).

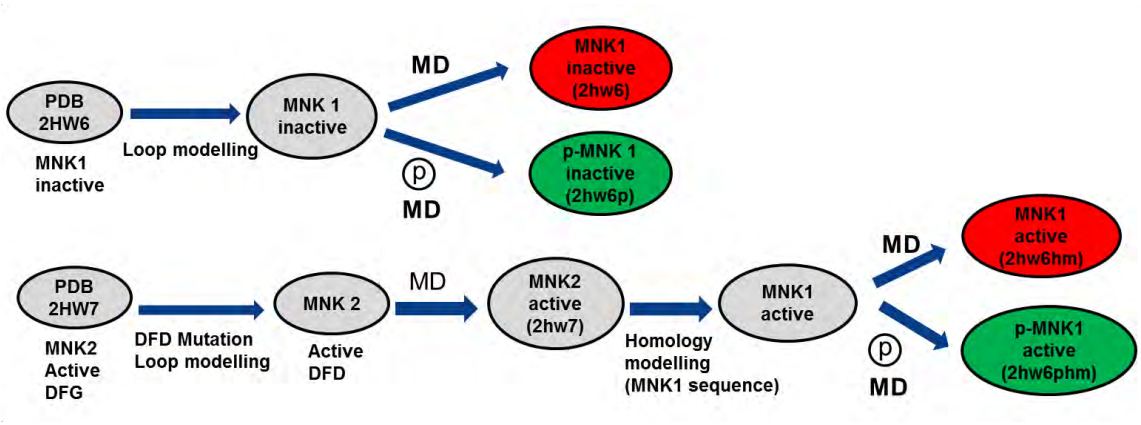

Figure 5.16. Summary of the preparation of the MNK1 models.

The four initial models were subjected to a MD simulation of at least 70 ns or until the RMSD plot did not indicate variations on the tertiary structure of the protein (Figure 5.17). MD simulation was performed with explicit solvent. The preparation of the protein structure was performed with MOE where the hydrogens were added and the partial charges were calculated. The protein was enclosed in a 12.0 Å water truncated octahedron box (TIP3PBOX) and the charges were neutralized with Na^+ or Cl^- conveniently. The simulation consisted on 8 different steps: (1) minimization of water molecules, (2) minimization of the protein, (3) equilibration of temperature (from 0 to 300K) with positional restrictions (only the modelled loop was considered. The rest of the protein was constrained with a force constant of 8 kcal/mol/A^2), (4) equilibration of pressure (to 1 bar) with restrictions (only considering the modelled loop), (5) MD simulation with restrictions (2 ns simulation of the loop), (6) equilibration of temperature (from 0 to 300K) without restrictions, (7) equilibration of pressure (to 1 bar) without restrictions and (8) MD simulation without restriction (70 ns or until RMSD was stable).

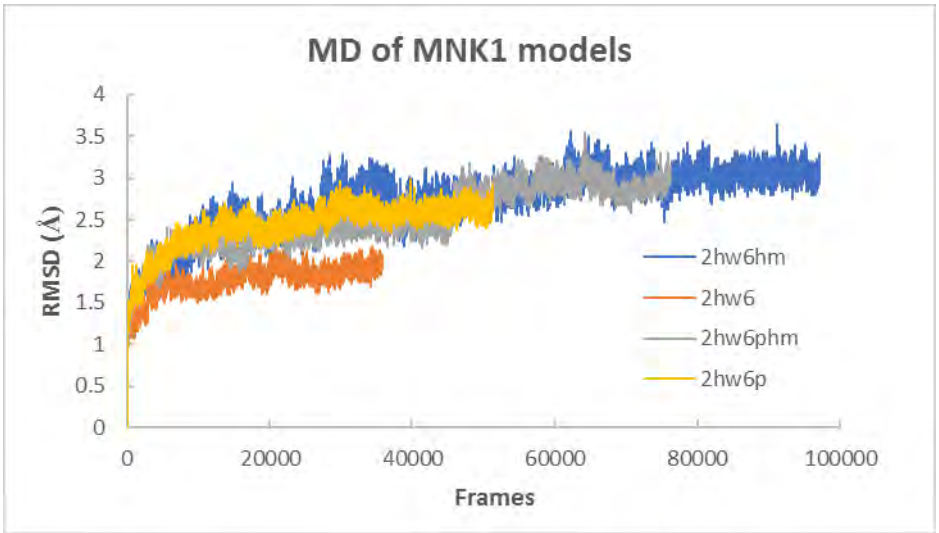

Figure 5.17. RMSD of the MD simulation (production step) for the MNK1 models. Each frame represents 2 ps of simulation. The RMSD is referred to the first frame and calculated with the alfa carbons of all residues except the loop (residues 197-222). (2hw6: inactive unphosphorylated model, 2hw6p: inactive phosphorylated model, 2hw6hm: active unphosphorylated model, 2hw6phm: active phosphorylated model).

The stable structures obtained with the MD simulations correspond to the closest energy minimum to the initial structure. For this reason, despite the obtained structures are stable conformations of the protein, it is possible that the exploration only reached a local minimum. In order to explore a higher number of stable conformations, an accelerated MD (aMD) simulation was performed (Figure 5.18).

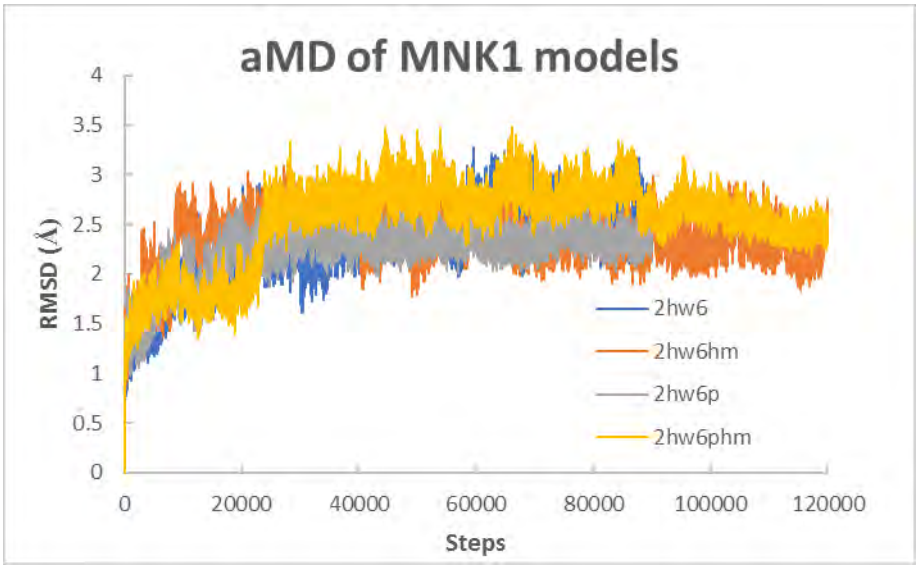

Figure 5.18. RMSD of the aMD simulation (production step) for the MNK1 models. The simulations were extended until the RMSD values were stable: the simulations inactive models (2hw6 and 2hw6p) were 90000 steps long while for the active models (2hw6hm and 2hw6phm) the simulations had to be extended 120000 steps to stabilize the RMSD. The RMSD is referred to the first frame and calculated with the alfa carbons of all residues except the loop (residues 197-222). (2hw6: inactive unphosphorylated model of MNK1, 2hw6p: inactive phosphorylated model of MNK1, 2hw6hm: active unphosphorylated model of MNK1, 2hw6phm: active phosphorylated model of MNK1).

In order to analyze the different conformations explored by the simulation, a cluster analysis was performed. The different conformations adopted by the protein during the simulation were grouped in clusters. The clusters were plotted *vs.* the simulation time to identify the most significant clusters (more populated and more stable along the simulation) (Figure 5.19).

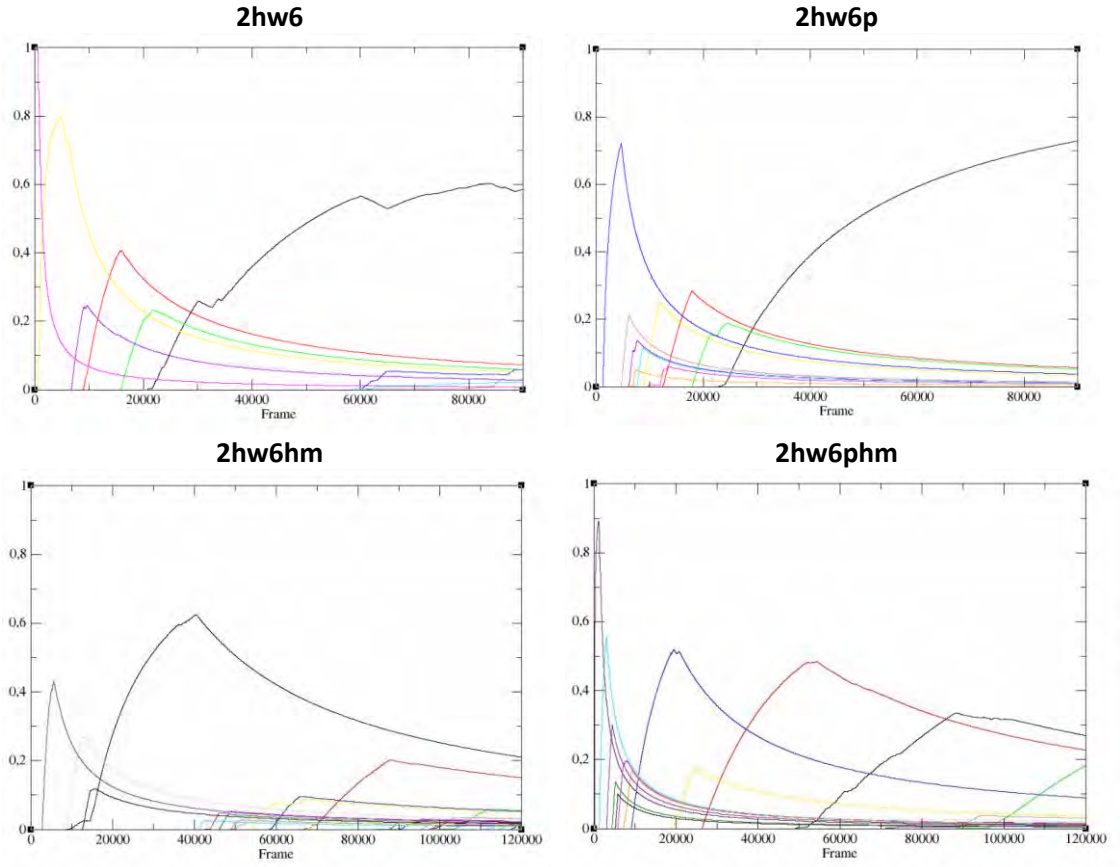

Figure 5.19. Cluster analysis of the aMD simulations. (2hw6: inactive unphosphorylated model of MNK1, 2hw6p: inactive phosphorylated model of MNK1, 2hw6hm: active unphosphorylated model of MNK1, 2hw6phm: active phosphorylated model of MNK1)

Comparing the different clusters in each model it was possible to study the flexibility of the different conformations of MNK1. In all the models, the biggest differences were observed in the loops but they were not considered as a conformation change due to the high flexibility of these fragments. The study was mainly focused on the structures around the ATP binding site.

The active phosphorylated model (2hw6phm) maintains the active conformation observed in the active MNK2 crystal structure (PDB ID 2HW7) with an open and exposed active site but a little bit smaller due to the shift of the β-sheets towards the activation loop. During the simulation the cavity of the active site was slightly modified due to the movement of the β-sheets.

Surprisingly, in the unphosphorylated active model (2hw6hm) the ATP cleft was much smaller and did not suffer any changes during the simulation. The main movement of this structure was observed in the regulatory α-helix at the beginning of the simulation. Despite being an active conformation (DFD-in), the shape of the ATP cleft does not allow the entrance of the ligands. These results would indicate that for MNK1, phosphorylation or the presence of the ligand (not tested) would be necessary to allow access to the active site.

The inactive phosphorylated model (2hw6p) presented a very high stability and the only differences between the clusters were found on the flexible loops. In the inactive forms (DFD-out), the activation loop is closed towards the β-sheets creating a smaller cavity. The direct access to the ATP cleft is hindered, and the entrance of ligands could only be achieved from below the activation loop.

Finally, the inactive unphosphorylated model (2hw6), the activation loop presented two very different conformations. The most common conformation was similar to the phosphorylated model (2hw6p) and did not block the lower part of the active site. However, in the less frequent conformations the activation loop was flipped towards the β-sheets closing even more the active site.

For each simulation, the most representative cluster was selected as the model to be used in the study of the binding mode of the different ligands (Figure 5.20).

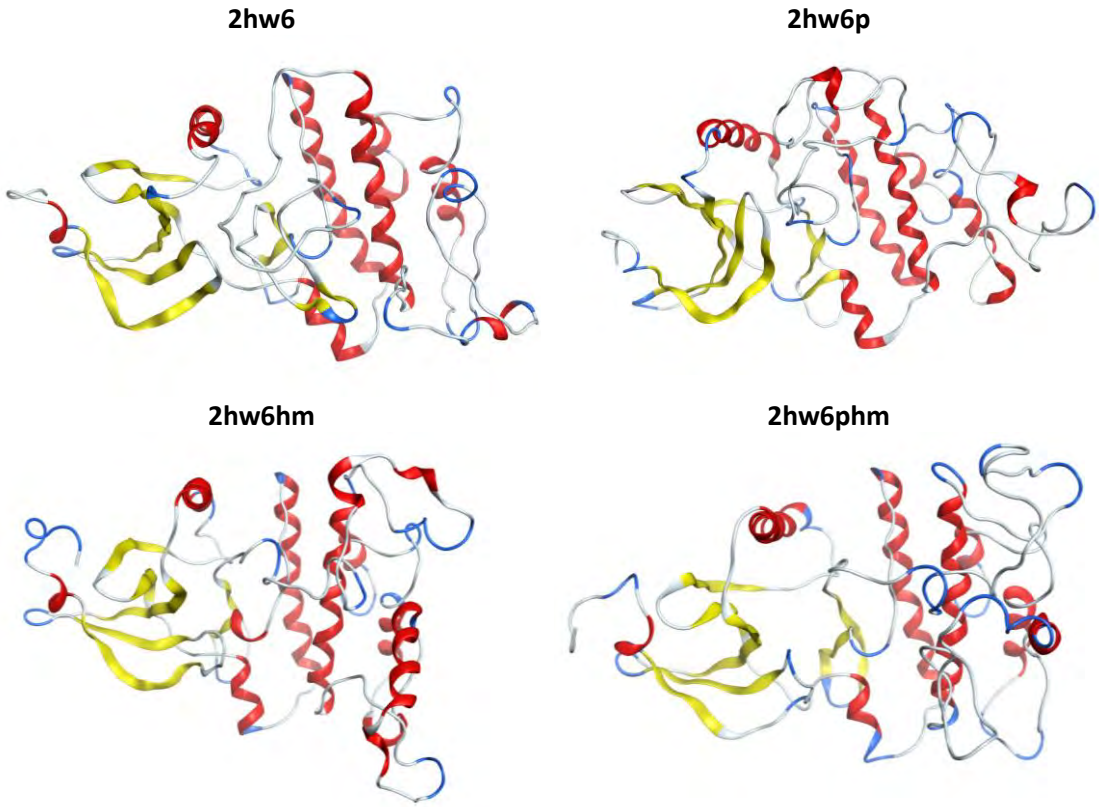

Figure 5.20. Principal clusters representing the most stable and frequent structures of each conformation. (2hw6: inactive unphosphorylated model of MNK1, 2hw6p: inactive phosphorylated model of MNK1, 2hw6hm: active unphosphorylated model of MNK1, 2hw6phm: active phosphorylated model of MNK1).

5.3.3. Study of the interaction mode of the ligands

During this project we were capable of identifying a small set of compounds with potential activity as MNK inhibitors. In particular, compound **EB1** showed excellent properties to become a very interesting hit. It is therefore of interest to elucidate its mechanism of action and describe the type of inhibitor that we have identified. Moreover, as all the active molecules presented a higher activity for MNK1 than for MNK2, the previously prepared models can be used to analyze the conformations affected by the inhibitor. To study the binding model of the compounds, the four models were used.

5.3.3.1. Identification of the binding site

The first cluster of each model was selected as the most representative structure of the different models (Figure 5.20) and was used to study the binding mode of the ligands. In order to identify the active site, the ligands were docked in the different models.

For each combination of receptor and ligand, a blind docking was performed with induced fit and generating 100 conformations using MOE2016.08.[35] The possible active sites were identified according to the number of poses. Thus, the areas with a higher number of poses were studied as possible binding sites.

The inactive models for MNK1 (i.e. 2hw6 and 2hw6p) presented similar results. The highest number of conformations were found in the ATP binding site under the activation loop that hiders the complete access to the cleft.

On the other hand, the active models presented very different possible binding sites. The unphosphorylated model (2hw6hm) presented a very small ATP binding site due to the movement of the β-sheets towards the activation loop. Therefore, the only possible sites were found on the superior part of the activation loop close to the regulatory α-helix and on the α-helix bundles.

The phosphorylated model (2hw6phm) presents an exposed ATP binding site were most of the conformations did bind. This site was found closer to the regulatory α-helix in comparison with the inactive models due to the flip of the DFD motif.

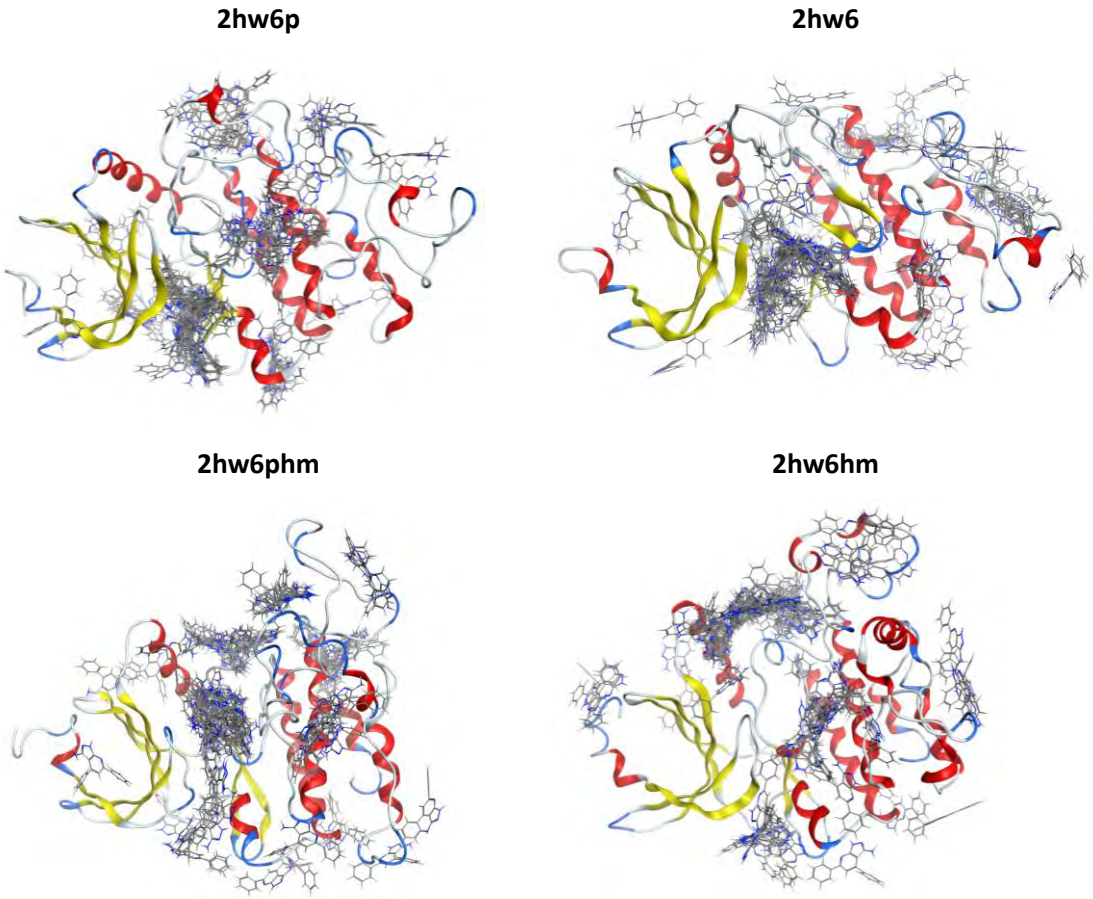

Figure 5.21. Binding site identification by blind docking of **EB1** in the four different models. Each model presents an area were more conformation bind which will be studied as a possible active site. (2hw6: inactive unphosphorylated model of MNK1, 2hw6p: inactive phosphorylated model of MNK1, 2hw6hm: active unphosphorylated model of MNK1, 2hw6phm: active phosphorylated model of MNK1).

The best ranked conformation of each docking was selected for the binding site study. Moreover, as sometimes the energetic criteria applied by the docking functions are not the best for the quantification of the interaction between the ligand and the receptor, the conformations were visually analyzed and two extra conformations (one for the 2hw6 model and one for the 2hw6hm) were included in the study.

Therefore, 6 ligand-protein complexes were further studied. In order to understand the stability of the interaction with time and to measure the binding energy, a MD simulation of the complexes was performed. The simulations were extended to 50 ns or to 90 ns if the RMSD was not stable after the first simulation (Table 5.9).

Table 5.9. Complex-ligand MD simulations. Summary of the results from the simulation of the complexes of the different models with **EB1**.The initial and the last conformations of the production step can be compared. The RMSD value calculated for the protein and the ligand indicates the stability of the complex. Each frame is 2 ns. (2hw6: inactive unphosphorylated model of MNK1, 2hw6p: inactive phosphorylated model of MNK1, 2hw6hm: active unphosphorylated model of MNK1, 2hw6phm: active phosphorylated model of MNK1).

Model	Initial conformation	Final conformation	RMSD
2hw6 (EB1 pose 1)		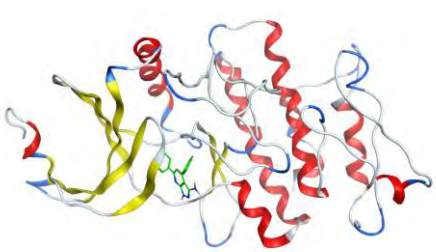	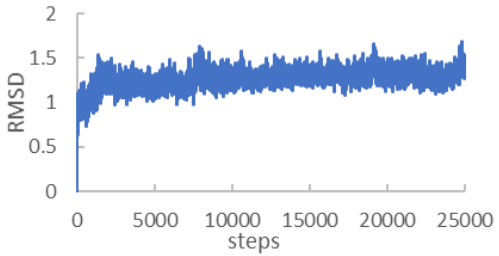
2hw6 (EB1 pose 2)		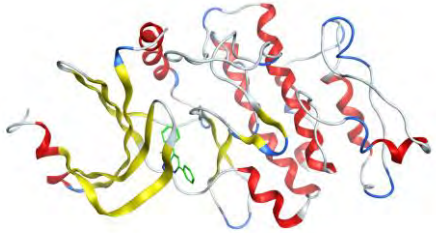	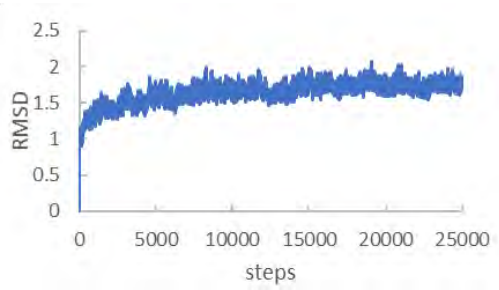
2hw6p	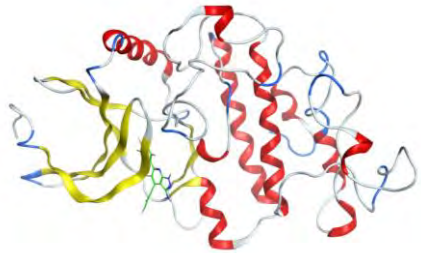	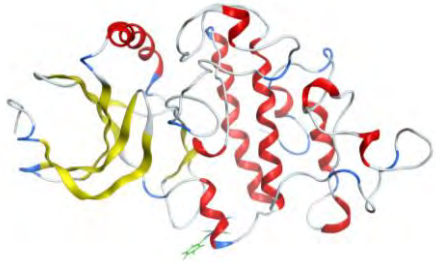	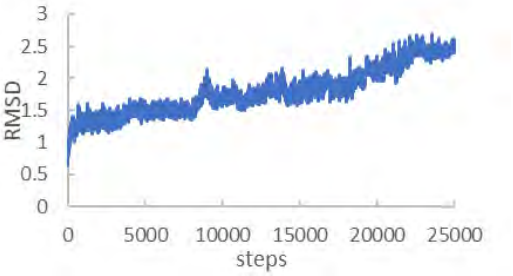

2hw6hm (EB1 pose 1)	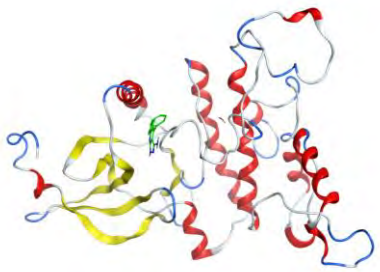		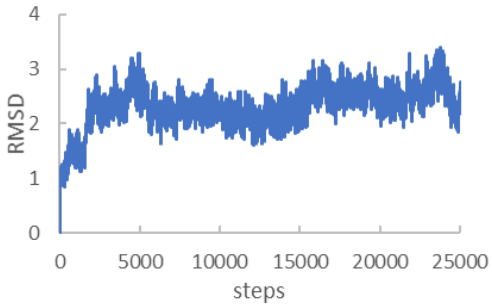
2hw6hm (EB1 pose 2)	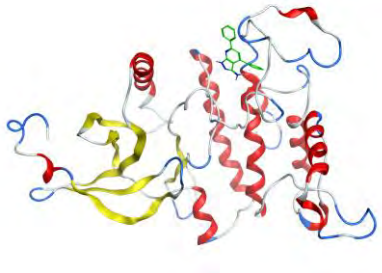	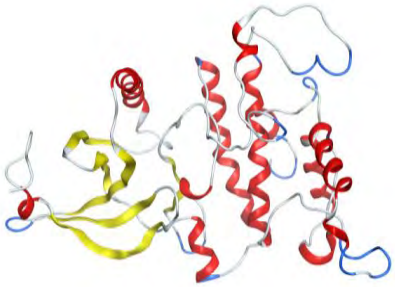	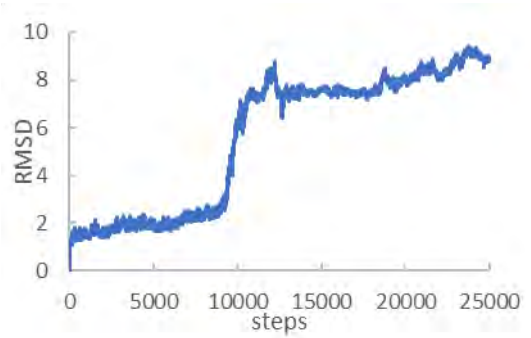
2hw6phm	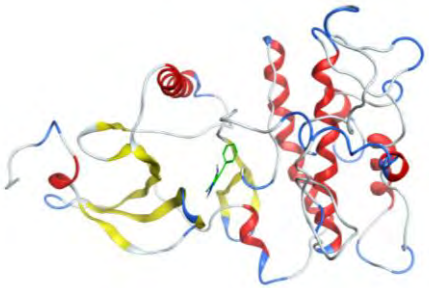	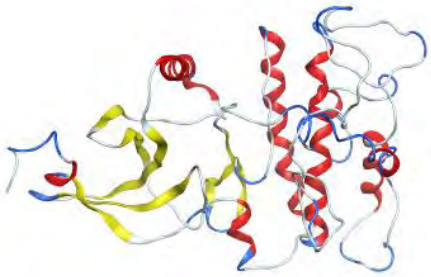	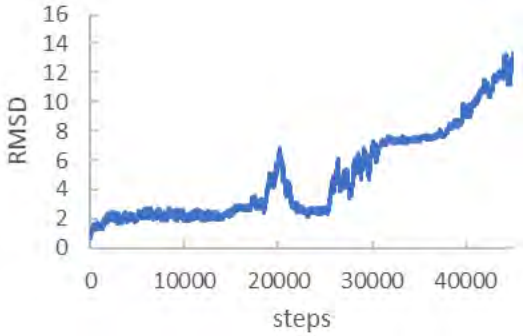

As shown in Table 5.9, in some cases, the ligand-protein complex was broken during the simulation indicating that the metastable interaction found in the docking study was not stable over time. With these results, 3 of the possible binding sites could be discarded. In the case of the active phosphorylated model (2hw6phm), the ligand did not remain in the ATP binding site and the **EB1** molecule left from the initial position after 40 ns of simulation. The molecule did then bind to the α-helix bundle for a while but then unbound the protein and was lost in the solvent.

A similar behavior was observed in the phosphorylated inactive model. The molecule abandoned the active site after approximately 40 ns of simulation and stuck to the α-helixes. A longer simulation would have shown that the complex was completely lost after some time.

Finally, in the case of the active unphosphorylated model two possible biding sites were studied. For the second complex, where the **EB1** molecule was located in a possible allosteric pocket on top of the α-helix bundles, the complex was completely lost after 20 ns of simulation demonstrating the low stability of such complex.

For the three complexes that were stable over time, a MM/PBSA calculation was performed on the last 5 ns of simulation to thermodynamically quantify the binding energy (Table 5.10). The second complex of the inactive unphosphorylated model (2hw6) showed a higher stability in comparison with the other two models indicating a preferential binding mode of **EB1** for the ATP binding site of the inactive form of MNK1.

Table 5.10. Energetic calculation of the stability of the complex of MNK1-EB1. (2hw6: inactive unphosphorylated model of MNK1, 2hw6hm: active unphosphorylated model of MNK1)

MODEL	ΔG (kcal/mol)
2hw6 (EB1 pose 1)	-21.87 ± 3.19
2hw6 (EB1 pose 2)	-27.12 ± 2.88
2hw6hm (EB1 pose 1)	-21.36 ± 2.86

5.3.3.2. Study of the binding mechanism of EB1 to MNK1

The previous studies did combine accelerated molecular dynamics to explore the maximum number of possible MNK1 conformations, cluster analysis to identify the most stable and common conformations, molecular docking to from the complexes with the ligand and molecular dynamics to analyze the stability of the interactions. The results indicate that **EB1** is a Type II inhibitor which binds to the ATP binding site of the inactive form of MNK1.

These Type II inhibitors were previously described by Kannan *et al.*[22] In order to validate the models and the possible mode of action, one representative molecule from the publication was docked in the inactive MNK1 model in the same conditions previously described. The docking results allowed identifying the same site as the binding site of the inactive conformation thus supporting the idea of a Type II inhibitor. Figure 5.22 shows an example conformation bound to the inactive MNK1.

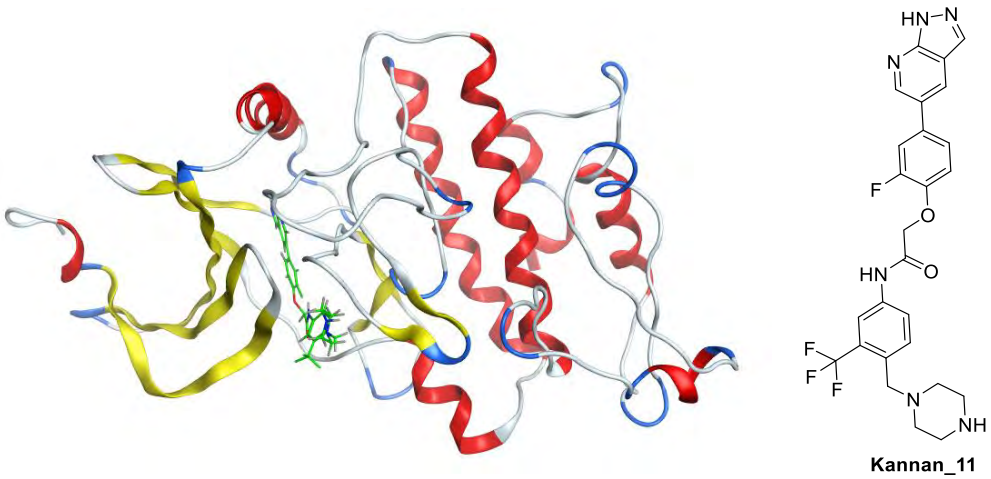

Figure 5.22. Molecular docking of compound **Kannan_11** in the MNK1 inactive unphosphorylated model (2hw6) fitting the ATP binding site

The MD simulation of the **EB1**-MNK1 complex was studied to understand the behavior of the ligand-protein interaction over time.

Analysis of the final complex demonstrates the importance of the unsubstituted 3-aminopyrazole. The study of the interactions between the ligand and the protein shows the formation of two hydrogen bonds between the 3-aminopyrazole moiety and the receptor (Glu128 and Gln128). Moreover, the pyrazole ring forms a hydrophobic interaction with Leu55.

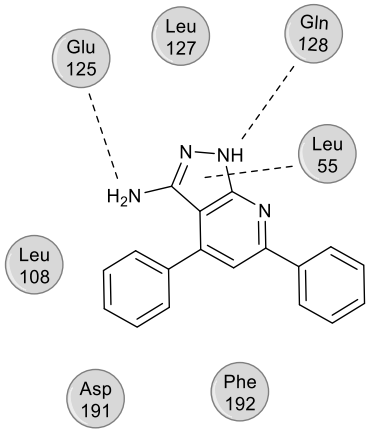

Figure 5.23. Interactions between **EB1** and MNK1.

The interaction with Glu125 was maintained during most part of the simulation indicating the essentiality of the amino group in the ligand. On the other hand, the interaction with Gln128 took around 35 ns to form but then has an essential role in the formation of the very stable final conformation (Figure 5.24). Moreover, the analysis of H-bonds formed between **EB1** and the protein showed two extra hydrogen bonds with Leu 127 and Leu106 that did stabilize the interaction over time.

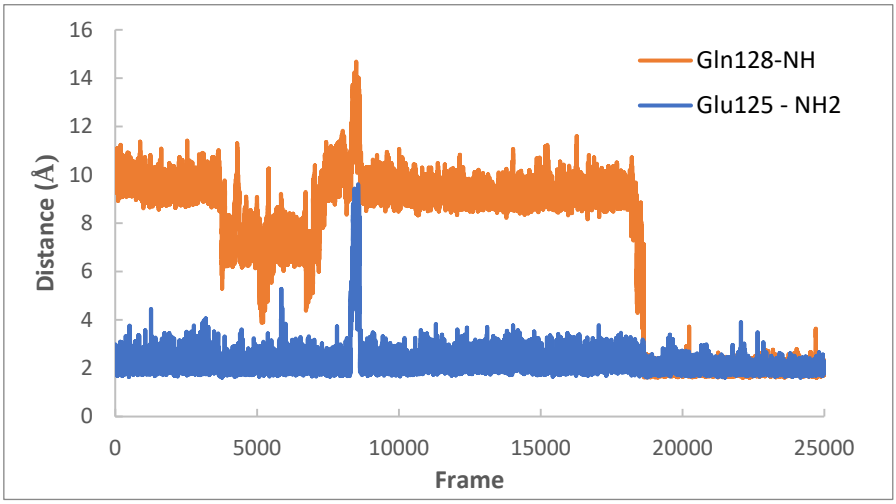

Figure 5.24. H-bond interactions between **EB1** and MNK1. Glu125-NH2 represents the distance between the O of the backbone carbonyl of Glu125 and the H of the NH_2 of **EB1**. Gln128 represents the distance between the O of the amide carbonyl of the side chain of Gln128 and the NH hydrogen of the pyrazole group.

When analyzing the progression of the H-bonds over time, a peak at around 16 ns was observed indicating a bigger distance between the residues and the ligand. At that point the molecule flipped towards the regulatory α-helix and the interactions with the residues were broken (Figure 5.25). However, this conformation was not stable, and the molecule moved back to the stable position 0.4 ns later.

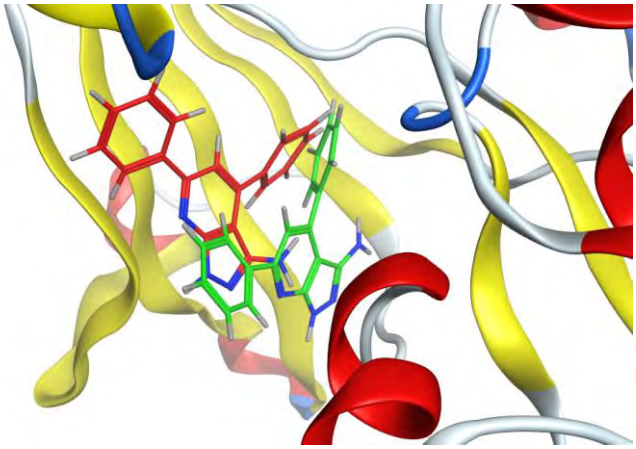

Figure 5.25. Flip observed in the molecule **EB1** during the simulation. For a short period of time (0.4 ns) the very stable conformation adapted by **EB1** in most of the simulation (green) rotates towards the α-helix (red).

In addition to the H-bonds that stabilized the interaction, **EB1** interacted with the phenylalanine residue (Phe192) of the DFD motif forming a π-π interaction between the phenyl ring of the residue and the phenyl rings of the 4,6-diphenyl substituted pyrazolo[3,4-*b*]pyridine scaffold, specifically the phenyl on position C6 of the pyridine ring (Figure 5.26). This interaction was maintained during all the simulation and seems to be the reason of the selectivity of this compound for the inactive form of MNK1. In the active forms of the protein, the ATP binding site presents a slightly different shape, but the compound should be capable of forming similar H-bonds. However, the active conformation has suffered the flip of the Phe192 residue to adopt the DFD-in active conformation. Therefore, this hydrophobic interaction with the Phe192 would not be possible. Targeting this inactive conformation and interaction with the DFD motif would prevent the activation of the protein and its activity.

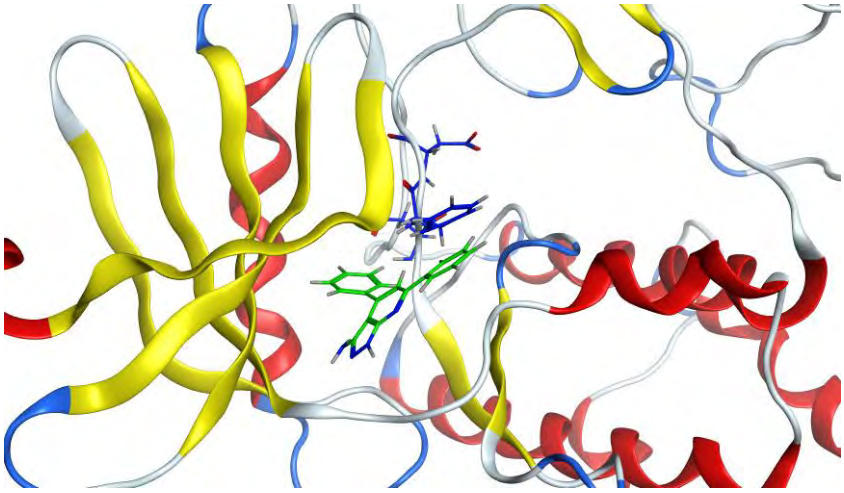

Figure 5.26. Interaction of **EB1** with the DFD motif of MNK1. The aromatic interaction between **EB1** (green) and the Phe192 residue of the DFD motif (blue) is essential for the stabilization of the inactive conformation of the protein. Despite the interaction is not completely vertical (is slightly diagonal towards the center of the ATP site) it is maintained during all the simulation. The two aromatic rings move simultaneously during the MD simulation maintaining this interaction.

The DFD motif is a unique feature of MNKs which induces the proteins to adopt a unusual stable inactive conformation which is not common for other kinases. Therefore, this interaction would provide the compound with selectivity against other kinases.

Finally, the second phenyl ring found in position C4 of the pyrazolo[3,4-*b*]pyridine scaffold, occupied the hydrophobic cleft in the most internal part of the pocket provably increasing the affinity and stability of the complex (Figure 5.27).

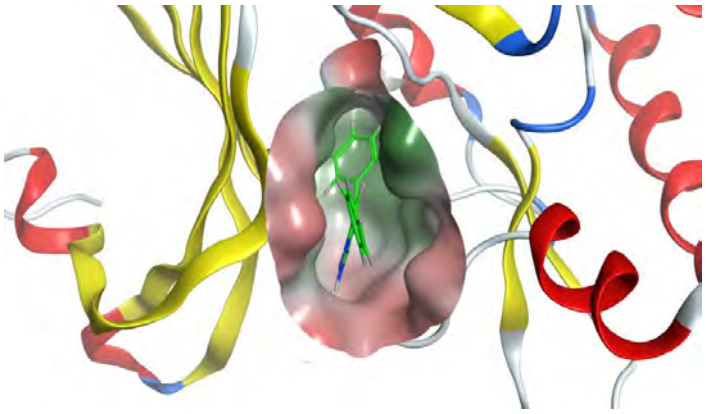

Figure 5.27. Surface representation of the ATP binding pocket showing the hydrophobic inner cavity occupied by the phenyl ring of EB1. Green = hydrophobic, white = neutral and red=hydrophilic.

The interaction mode was validated by studying the inactive molecule **139**{*3*,*3*,*2*} which did not show any activity on the preliminary tests. The compound was docked into the inactive unphosphorylated model (2hw6) and the complex was studied by MD simulation. The compound adopts a different orientation that **EB1** and this time the phenyl in position C6 occupied the hydrophobic cleft at the end of the binding site. In this case, it was not possible to form the stacking interaction between the Phe192 and the phenyl rings and only a weak hydrophobic interaction was formed between the α carbon of this residue and the pyrazole ring. The MM/PBSA calculation showed a lower stability of this complex (ΔG = -24.7 kcal/mol ± 3.1).

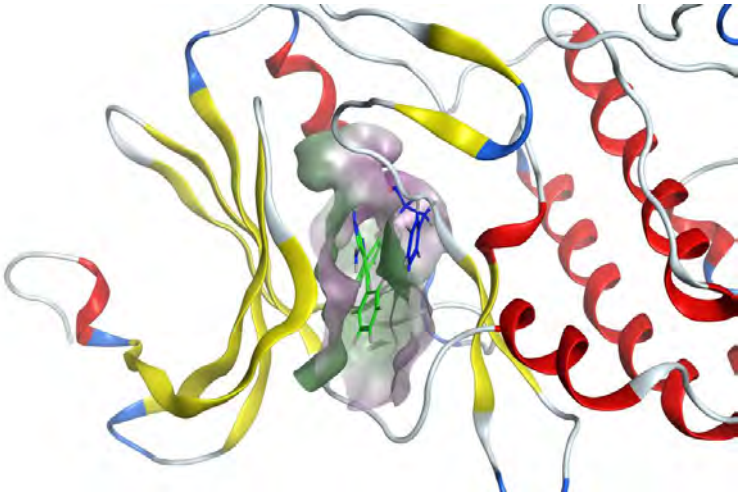

Figure 5.28. Compound **139**{*3*,*3*,*2*} in complex with inactive MNK1. The phenyl ring occupies the hydrophobic cleft providing the complex with some stability. However, no H-bonds are formed with the pyrazole ring which only shows a hydrophobic interaction with the backbone carbon of Phe192.

5.3.3.3. Conclusion

EB1 interacts with MNK1 as a Type II inhibitor which binds to the inactive conformation of the protein. The 4,6-diphenyl-pyrazolo[3,4-*b*]pyridine-3-amine scaffold plays a key role on the stabilization of the complex. The NH and NH_2 groups of the 3-amino pyrazole form very stable H-bonds with the residues of the active site (Glu125 and Gln128) while the pyrazolo[3,4-*b*]pyridine ring forms an hydrophobic interaction with Leu55.

The presence of the phenyl ring in position C6 is essential for the interaction with the inactive protein and the achievement of selectivity in front of other kinases. The Phe192 residue of the unique DFD motif of the MNKs interacts by π-π stacking with the phenyl ring of the compound, forming a selective and stable interaction that provides the compounds with its unique properties. Finally, the phenyl in position C4 occupies a mostly hydrophobic cavity at the end of the ATP cleft probably stabilizing the complex.

The elucidation of the binding mechanism of **EB1** provides an excellent opportunity for the hit to lead optimization process as the available information can be used in a structure-based optimization process.

Moreover, the fact that we have in hands a Type II inhibitor is very beneficial for the use of these compounds in the clinics. Up to know, no Type II MNK inhibitors have been studied *in vivo* and these results offer a novel opportunity to develop a new and effective drug with a different mechanism of action than the MNK inhibitors currently under study.

5.4. References

1. Lee, C., Huang, H. & Juan, H. Reviewing Ligand-Based Rational Drug Design: The Search for an ATP Synthase Inhibitor. *Int. J. Mol. Sci.* **12**, 5304–5318 (2011).

2. Wilson, G. L. & Lill, M. A. Integrating structure-based and ligand-based approaches for computational drug design. *Future Med. Chem.* **3,** 735–750 (2011).

3. Ojha, P. K., Mitra, I., Das, R. N. & Roy, K. Chemometrics and Intelligent Laboratory Systems Further exploring r 2 m metrics for validation of QSPR models. *Chemom. Intell. Lab. Syst.* **107,** 194–205 (2011).

4. Gaulton, A. *et al.* ChEMBL: a large-scale bioactivity database for drug discovery. *Nucleic Acids Res.* **40,** D1100–D1107 (2012).

5. Gaulton, A. *et al.* The ChEMBL database in 2017. *Nucleic Acids Res.* **45,** D945–D954 (2017).

6. Bento, A. P. *et al.* The ChEMBL bioactivity database: an update. *Nucleic Acids Res.* **42,** D1083–D1090 (2014).

7. Cabau, C. G. Design of novel Mnk1/2 dual inhibitors to avoid eIF4E phosphorylation in breast cancer. (IQS School of engineering, Universitat Ramon Llull, 2016).

8. Oyarzabal, J. *et al.* Discovery of Mitogen-Activated Protein Kinase-Interacting Kinase 1 Inhibitors by a Comprehensive Fragment-Oriented Virtual Screening Approach. *J. Med. Chem.* **53,** 6618–6628 (2010).

9. Diab, S. *et al.* Discovery of 5-(2-(phenylamino)pyrimidin-4-yl)thiazol-2(3H)-one derivatives as potent Mnk2 inhibitors: synthesis, SAR analysis and biological evaluation. *ChemMedChem* **9,** 962–972 (2014).

10. Kannan, S. *et al.* Probing the binding mechanism of Mnk inhibitors by docking and molecular dynamics simulations. *Biochemistry* **54,** 32–46 (2015).

11. Teo, T. *et al.* An integrated approach for discovery of highly potent and selective Mnk inhibitors: Screening, synthesis and SAR analysis. *Eur. J. Med. Chem.* **103,** 539–50 (2015).

12. Teo, T. *et al.* Pharmacologic Inhibition of MNKs in Acute Myeloid Leukemia. *Mol. Pharmacol.* **88,** 380–389 (2015).

13. Yu, M. *et al.* Discovery of 4-(dihydropyridinon-3-yl)amino-5-methylthieno[2,3-d]pyrimidine derivatives as potent Mnk inhibitors: synthesis, structure–activity relationship analysis and biological evaluation. *Eur. J. Med. Chem.* **95,** 116–126 (2015).

14. Cherian, J. *et al.* Structure-Activity Relationship Studies of Mitogen Activated Protein Kinase Interacting Kinase (MNK) 1 and 2 and BCR-ABL1 Inhibitors Targeting Chronic Myeloid Leukemic Cells. *J. Med. Chem.* **59,** 3063–3078 (2016).

15. Molecular Operating Environment (MOE), 2014.09. Chemical Computing Group ULC, 1010 Sherbooke St. West, Suite #910, Montreal, QC, Canada, H3A 2R7 (2014).

16. RapidMiner Studio. (2016).

17. Estrada Tejedor, R. Desenvolupament del programari ArIS (Artificial Intelligence Suite): implementació d'eines de cribratge virtual per a la química mèdica. (QS School of engineering, Universitat Ramon Llull, 2011).

18. Diab, S. *et al.* Unveiling new chemical scaffolds as Mnk inhibitors. *Future Med. Chem.* **8,** 271–285 (2016).

19. Reich, S. H. *et al.* Structure-based Design of Pyridone-Aminal eFT508 Targeting Dysregulated Translation by Selective Mitogen-activated Protein Kinase Interacting Kinases 1 and 2 (MNK1/2) Inhibition. *J. Med. Chem.* **61,** 3516–3540 (2018).

20. Han, W. *et al.* Discovery of a Selective and Potent Inhibitor of Mitogen-Activated Protein Kinase-Interacting Kinases 1 and 2 (MNK1/2) Utilizing Structure-Based Drug Design. *J. Med. Chem.* **59,** 3034–3045 (2016).

21. Zhan, Y. *et al.* MNK1/2 inhibition limits oncogenicity and metastasis of KIT-mutant melanoma. *J. Clin. Invest.* **127,** 4179–4192 (2017).

22. Kannan, S. *et al.* Small Molecules Targeting the Inactive Form of the Mnk1/2 Kinases. *ACS Omega* **2,** 7881–7891 (2017).

23. Basnet, S. K. C. *et al.* Identification of a Highly Conserved Allosteric Binding Site on Mnk1 and Mnk2. *Mol. Pharmacol.* **88,** 935–948 (2015).

24. Jauch, R. *et al.* Mitogen-activated protein kinases interacting kinases are autoinhibited by a reprogrammed activation segment. *EMBO J.* **25,** 4020–4032 (2006).

25. Jauch, R. *et al.* Crystal Structures of the Mnk2 Kinase Domain Reveal an Inhibitory Conformation and a Zinc Binding Site. *Structure* **13,** 1559–1568 (2005).

26. Matsui, Y. *et al.* A novel inhibitor stabilizes the inactive conformation of MAPK-interacting kinase 1. *Acta Crystallogr. Sect. F Struct. Biol. Commun.* **74,** 156–160 (2018).

27. Bou-Petit, E., Borrell, J. I., Ramon y Cajal, S. & Estrada-Tejedor, R. Structural implications of the DFD-in domain in computer-aided molecular design of MAP kinase interacting kinase 2 inhibitors . *Afinidad* **578,** 3–9 (2017).

28. Hou, J., Teo, T., Sykes, M. J. & Wang, S. Insights into the Importance of DFD-Motif and Insertion I1 in Stabilizing the DFD-Out Conformation of Mnk2 Kinase. *ACS Med. Chem. Lett.* **4,** 736–41 (2013).

29. Hou, J., Kam, F., Proud, C. G. & Wang, S. Targeting Mnks for Cancer Therapy. *Oncotarget* **3,** 118–131 (2012).

30. Cargnello, M. & Roux, P. P. Activation and Function of the MAPKs and Their Substrates, the MAPK-Activated Protein Kinases. *Microbiol. Mol. Biol. Rev.* **75,** 50–83 (2011).

31. Wu, H. *et al.* Discovery of a BTK/MNK dual inhibitor for lymphoma and leukemia. *Leukemia* **30,** 173–181 (2016).

32. Kumarasiri, M., Teo, T. & Wang, S. Dynamical insights of Mnk2 kinase activation by phosphorylation to facilitate inhibitor discovery. *Future Med. Chem.* **7,** 91–102 (2015).

33. Morris, G. M. *et al.* AutoDock4 and AutoDockTools4: Automated docking with selective receptor flexibility. *J. Comput. Chem.* **30,** 2785–2791 (2009).

34. Estrada, R., Nonell, S. & Teixidó, J. Changing the way of viewing QSAR methods: the application of hyperbolic projection in medicinal chemistry. *Rev. la Soc. Catalana Química* **11,** 61–67 (2012).

35. Molecular Operating Environment (MOE), 2016.08. Chemical Computing Group ULC, 1010 Sherbooke St. West, Suite #910, Montreal, QC, Canada, H3A 2R (2016).

CHAPTER 6

Experimental Part

6.1. Synthesis and compound characterization

6.1.1. Instrumentation

Nuclear Magnetic Resonance spectra (^{1}H-NMR and ^{13}C-NMR) were recorded in a Varian 400-MR spectrometer (^{1}H-NMR 400 MHz and ^{13}C-NMR 100.6 MHz), in the Organic Chemistry Department at IQS under the leadership of Dr. X. Batllori. Chemical shifts are reported in parts per million (ppm) on the δ scale and referenced to the residual signal of the solvent (DMSO-d_6: 2.5 ppm in ^{1}H-NMR and 39.52 ppm in ^{13}C-NMR, $CDCl_3$: 7.26 ppm in ^{1}H-NMR and 77.16 ppm in ^{13}C-NMR). Coupling constants (J) are reported in Hertz (Hz). Standard and peak multiplicities are designated as follows: s (singlet), d (doublet), dd (doublet of doublets), ddd (doublet of doublet of doublets), t (triplet), q (quartet), qn (quintet), m (multiplet), br (broad signal).

Infrared Spectra (IR) were recorded in a Nicolet iS10 FTIR spectrometer with Smart iTr (Thermo Scientific) by Mrs. N. Ruiz at the Organic and Pharmaceutical Chemistry department at IQS under the leadership of Dr. X. Batllori, using a potassium bromide (KBr) disc. Wave number values are reported in cm^{-1}. The notation used is: *st* (stretching), *b* (bending).

Organic elemental analysis (OEA) were obtained on a EuroEA 3000 Elemental Analyzer (EuroVector) by Mrs. N. Ruiz at the Organic and Pharmaceutical Chemistry department at IQS under the leadership of Dr. X. Batllori at the Organic and Pharmaceutical Chemistry Department at IQS.

Mass Spectrometry (MS) was conducted on an Agilent Technologies 5975 mass spectrometer operating in electron ionization (EI) mode at 70 eV and at 4kV accelerating potential.

High Resolution Mass Spectrometry (HRMS) was conducted on a micrOTOF (Bunker) high resolution mass spectrometer operating in APCI, ESI or EI mode at the Unidade de espectrometría de masas e proteomica (Universidade de Santiago de Compostela) under the leadership of Dr. Esteban Guitián.

The melting point (**MP**) was determined with a SMP3 melting point apparatus (Stuart Scientific).

Automatic flash chromatography was performed in an Combiflash®Rf (Teledyne Isco) with RediStep® silica gel columns or basic alumina columns.

Microwave irradiation experiments were carried out in an Initiator™ (Biotage) microwave apparatus, operating at a frequency of 2.45 GHz with continuous irradiation power from 0 to 400 W. Reactions were performed in 2.5, 5 and 20 mL glass tubes, sealed with aluminium/Teflon crimp tops, which can be exposed up to 250 °C and 20 bar internal pressure. Temperature was measured with an IR sensor on the outer surface of the process vial. After the irradiation period, the reaction vessel was cooled rapidly to 50 °C by air jet cooling.

X-ray crystallography was conducted by Dr. Cristina Puigjaner and her group at the Unitat de Difracció de RX. Centres Científics i Tecnològics de la Universitat de Barcelona (CCiTUB). The X-ray intensity data were measured on a D8 Venture system equipped with a multilayer monochromator and a Mo microfocus (λ = 0.71073 Å). The frames were integrated with the Bruker SAINT software package using a narrow-frame algorithm. The structure was solved and refined using the Bruker SHELXTL Software Package.

6.1.2. Synthesis of 3-arylacrylates and 2-arylacetates

Synthesis of methyl (E)-3-(4-methoxyphenyl) acrylate (60{*1,4*})

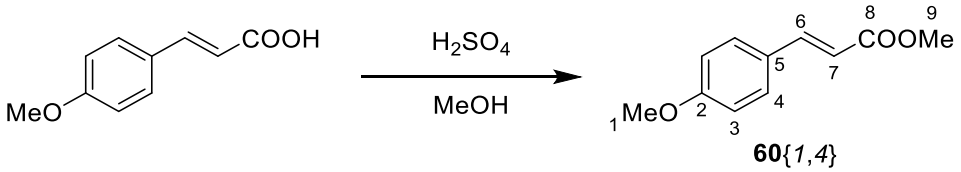

60{*1*,*4*}

2.55g (15.00 mmol) of (*E*)-3-(4-methoxyphenyl)acrylic acid were dissolved in a solution of 0.5 mL concentrated sulfuric acid in methanol (50 mL) and heated at reflux for 12h. 200 mL of water were added and the white solid was extracted with $CHCl_3$ (3x50 mL). The combined extracts were washed with 45 mL of a saturated sodium bicarbonate solution and dried with anhydrous $MgSO_4$. The solvent was removed under reduced pressure and to afford 2.54 g (13.21 mmol, 93%) of (*E*)-methyl-3-(4-methoxyphenyl)acrylate **60**{*1,4*} as white solid.

^{1}H-NMR (400 MHz, DMSO-d6) δ 7.70 – 7.65 (m, 2H, C4-H), 7.62 (d, J = 16.0 Hz, 1H, C6-H), 7.00 – 6.95 (m, 2H, C3-H), 6.49 (d, J = 16.0 Hz, 1H, C7-H), 3.80 (s, 3H, C1-H), 3.70 (s, 3H, C9-H).

Spectroscopic data are consistent with those previously described.[1]

Methyl 2-(3,4,5-trimethoxyphenyl)acetate

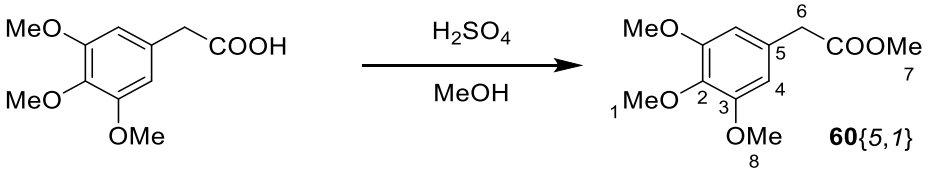

60{*5*,*1*}

1.31g (5.8 mmol) of 2-(3,4,5-trimethoxyphenyl)acetic acid were dissolved in a solution of 0.2 mL concentrated sulfuric acid in methanol (20 mL) and heated at reflux for 12h. 20 mL of water were added and the product was extracted with $CHCl_3$ (4x25 mL). The combined extracts were washed with 45 mL of a saturated sodium bicarbonate solution and dried with anhydrous $MgSO_4$. The solvent was removed under reduced pressure and to afford 1.4 g (5.8 mmol, quantitative yield) of methyl 2-(3,4,5-trimethoxyphenyl)acetate **60**{*5*,*1*} as colorless liquid.

^{1}H-NMR (400 MHz, $CDCl_3$): δ 6.50 (s, 2H, C4-H), 3.86 (s, 6H, C8-H_3), 3.83 (s, 3H, C1-H_3), 3.71 (s, 3H, C7-H_3), 3.56 (s, 2H, C6-H_2).

Spectroscopic data are consistent with those previously described.[2]

6.1.3. Synthesis of pyrazolo[3,4-*b*]pyridin-6-ones

6.1.3.1 Synthesis of 2-arylacrylates

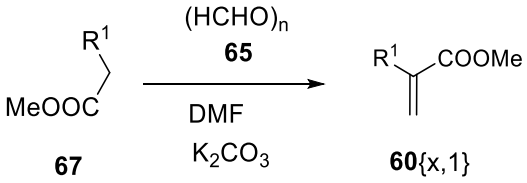

The corresponding methyl 2-arylacetate **67** (20.54 mmol) was dissolved in anhydrous DMF (90 mL). 0.80 g, 26.64 mmol of paraformaldehyde and 2.85 g, 20.62 mmol of potassium carbonate were added and the mixture was heated at 100 °C for 3 hours. The reaction mixture was quenched with water (80mL) and cooled down before extracting with diethyl ether (4 x 40 mL). The combined organic extracts were washed with a saturated solution of lithium chloride (3 x 50 mL) and dried with anhydrous $MgSO_4$. The solvent was removed under reduced pressure to afford the corresponding methyl 2-arylcrylate (**60**).

Methyl 2-phenylacrylate (60{*3,1*})

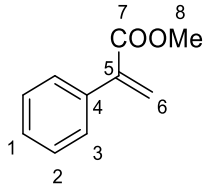

Starting from methyl 2-phenylacetate (**67**{*3,1*}). 62 % yield, colourless oil.

^{1}H-NMR (400 MHz, DMSO-d_6) δ 7.44 – 7.29 (m, 5H, C1-H, C2-H, C3-H), 6.25 (d, J = 0.8 Hz, 1H, C6-H), 6.02 (d, J = 0.8 Hz, 1H, C6-H), 3.77 – 3.74 (m, 3H, C8-H_3).

Spectroscopic data are consistent with those previously described.[3]

Methyl 2-(2,6-dichlorophenyl)acrylate (60{*7,1*})

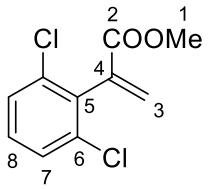

Starting from methyl 2-(2,6-dichlorophenyl)acetate (**67**{*7,1*}). 91 % yield, colourless oil.

^{1}H-NMR (400 MHz, $CDCl_3$): δ = 7.35 (d, *J* = 7.8 Hz, 2H, C7-H), 7.21 (m, 1H, C8-H), 6.79 (d, *J* = 0.9 Hz, 1H, C3-H), 5.83 (d, *J* = 0.9 Hz, 1H, C3-H), 3.77 (s, 3H, C1-H_3).

Spectroscopic data are consistent with those previously described.[4]

Methyl 2-(4-fluorophenyl)acrylate (60{6,1})

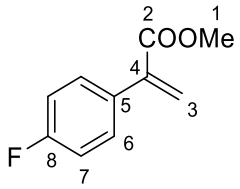

Starting from methyl 2-(4-fluorophenyl)acetate (**67**{*6*,*1*}). 84% yield, colourless oil.

^{1}H-NMR (400 MHz, $CDCl_3$): δ 7.39 (dd, J = 8.9, 5.4 Hz, 2H, C6-H), 7.04 (t, J = 8.8 Hz, 2H, C7-H), 6.36 (d, J = 1.1 Hz, 1H, C3-H), 5.87 (d, J = 1.1 Hz, 1H, C3-H), 3.82 (s, 3H, C1-H_3).

Spectroscopic data are consistent with those previously described.[2]

Methyl 2-(4-mehoxyphenyl)acrylate (60{*4*,*1*})

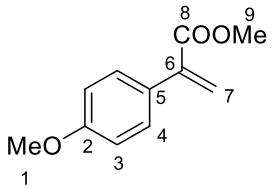

Starting from methyl 2-(4-mehoxyphenyl)acetate (**67**{*4*,*1*}). 33% yield, colourless oil.

The reaction is heated at 40 °C (instead of 100 °C) for 36h. The product was used without further purification.

^{1}H-NMR (400 MHz, DMSO-d_6): δ 7.36 (d, J = 8.9 Hz, 2H, C4-H), 6.93 (d, J = 9.0 Hz, 2H, C3-H), 6.13 (d, J = 1.0 Hz, 1H, C7-H), 5.94 (d, J = 1.0 Hz, 1H, C7-H), 3.77 (s, 3H, C1-H_3), 3.75 (s, 3H, C9-H_3).

Methyl 2-(3,4,5-trimethoxyphenyl)acrylate (60{*5*,*1*})

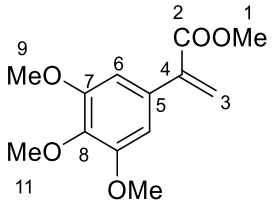

Starting from methyl 2-(3,4,5-trimethoxyphenyl)acetate (**67**{*5*,*1*}). 47% yield, colourless oil.

The reaction is heated at 40 °C (instead of 100 °C) for 72h.

^{1}H-NMR (400 MHz, $CDCl_3$): δ 6.65 (s, 2H, C6-H), 6.33 (d, *J* = 1.2 Hz, 1H, C3-H), 5.89 (d, *J* = 1.2 Hz, 1H, C3-H), 3.87 (s, 6H, C9-H_3), 3.86 (s, 3H, C10-H_3), 3.84 (s, 3H, C1-H_3).

Spectroscopic data are consistent with those previously described.[2]

Methyl 2-(2,4-dichlorophenyl)acrylate (60{*8*,*1*})

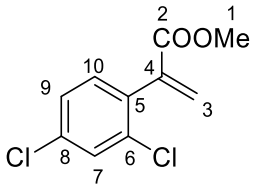

Starting from methyl 2-(4,6-dichlorophenyl)acetate (**67**{*8*,*1*}). 37 % yield, colourless oil.

^{1}H-NMR (400 MHz, $CDCl_3$): δ 7,41 (d, J = 2.0 Hz, 1H, C7-H), 7,26(dd, J = 8.4, 2.0 Hz, C9-H), 7,19 (d, J = 8.4 Hz, 1H, C10-H), 6,55 (d, J = 1.2 Hz, 1H, C3-H), 5,79 (d, J = 1.2 Hz, 1H, C3-H), 3,78(s, 3H, C1-H_3).

Spectroscopic data are consistent with those previously described.[2,5]

6.1.3.2 Synthesis of 2-methoxy-6-oxo-1,4,5,6-tetrahydropyridine-3-carbonitriles (62{*x*,*y*,*z*})

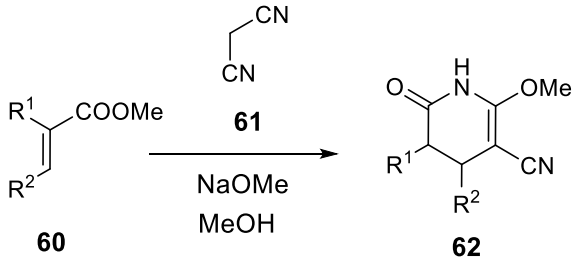

885 mg (13.4 mmol) of malononitrile (**61**) were added to a solution of 817 mg (15.1 mmol) of NaOMe in 20 mL of anhydrous methanol. 13.0 mmol of the corresponding acrylate (**60**) were added and the mixture was heated (see Table 6.1). The solvent was removed under reduced pressure and the residue was dissolved in the minimum amount of water. The solution was neutralized with HCl 2M. The solid was filtered, washed with water and dried *in vacuo* over P_2O_5 to afford the corresponding 2-methoxy-6-oxo-1,4,5,6-tetrahydropyridine-3-carbonitrile (**62**).

Alternatively, the reaction was performed under microwave irradiation at 85 ºC for 30 min.

Table 6.1. Reaction conditions for the preparation of **62**.

Product	Reaction conditions	Product	Reaction conditions
62{*2*,*1*}	5h, Reflux (100^{o}C)	**62**{*4*,*1*}	36h, 40^{o}C
62{*1*,*2*}	5h, Reflux (100^{o}C)	**62**{*5*,*1*}	MW, 30min, 85^{o}C
62{*3*,*1*}	3h, Reflux (100^{o}C)	**62**{*6*,*1*}	MW, 30min, 85^{o}C
62{*1*,*3*}	5h, Reflux (100^{o}C)	**62**{*7*,*1*}	5h, Reflux (100^{o}C)
62{*1*,*4*}	4.5h, Reflux (100^{o}C)	**62**{*8*,*1*}	4.5h, Reflux (100^{o}C)

2-methoxy-5-methyl-6-oxo-1,4,5,6-tetrahydropyridine-3-carbonitrile (62{*2,1*})

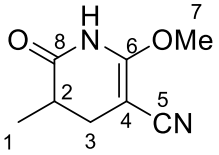

Starting from methyl methacrylate (**60**{*2,1*}). 46% yield, white solid

^{1}H-NMR (400 MHz, DMSO-d_6): δ (ppm) 10.46 (s, 1H, N1-H), 3.88 (s, J = 0.5 Hz, 3H, C7-H), 2.56-2.50 (m, 1H, C2-H), 2.38 (dd, J = 15.1, 6.7, 1H, C3-H), 2.17 (dd, J = 15.1, 12.2 Hz, 1H, C3-H), 1.05 (d, J = 6.8 Hz, 3H, C1-H).

^{13}C-NMR (100 MHz, DMSO-d_6): δ (ppm) 173.9 (C8), 160.2 (C6), 119.2 (C5), 63.2 (C4), 59.2 (C7), 34.6 (C2), 28.1 (C3), 14.7 (C1).

Spectroscopic data are consistent with previously described.[6]

2-methoxy-4-methyl-6-oxo-1,4,5,6-tetrahydropyridine-3-carbonitrile (62{*1,2*})

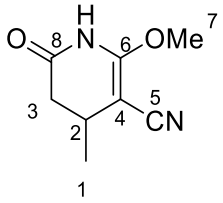

Starting from methyl but-2-enoate (**60**{*1,2*}). 34% yield, white solid

^{1}H-NMR (400 MHz, DMSO-d_6): δ 10.55 (s, 1H, NH), 3.88 (s, 3H, C7-H_3), 2.64 (dtd, *J* = 8.0, 6.8, 6.0 Hz, 1H, C2-H), 2.56 (dd, *J* = 16.0, 6.0 Hz, 1H, C3-H), 2.20 (dd, *J* = 16.0, 8.0 Hz, 1H, C3-H), 1.06 (d, *J* = 6.8 Hz, 3H, C1-H_3).

^{13}C-NMR (100 MHz, DMSO-d_6) δ 170.8 (C8), 160.1 (C6), 118.5 (C5), 70.3 (C4), 59.1 (C7), 38.4 (C2), 26.4 (C3), 19.3 (C1).

Spectroscopic data are consistent with previously described.[6]

2-methoxy-6-oxo-5-phenyl-1,4,5,6-tetrahydropyridine-3-carbonitrile (62{*3,1*})

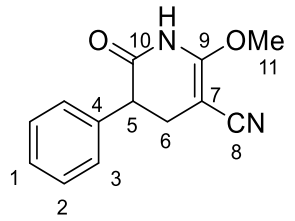

Starting from methyl 2-phenylacrylate (**60**{*3,1*}). 65% yield, yellowish solid

mp: 165-167 °C

^{1}H-NMR (400 MHz, DMSO-d_6): δ (ppm) 10.77 (s, 1H), 7.32 (m, 2H, C2-H), 7.26 (m, 1H, C1-H), 7.22 (m, 2H, C3-H), 3.92 (s, 3H, C11-H_3), 3.82 (dd, J = 6.8, 11.0 Hz, 1H, C5-H), 2.70 (dd, J = 15.3, 11.0 Hz, 1H, C6-H), 2.57 (dd, J = 15.4, 6.8 Hz, 1H, C6-H).

^{13}C-NMR (100 MHz, DMSO-d_6): δ (ppm) 171.8 (C10), 160.2 (C9), 138.2 (C4), 128.8, 128.8, 127.6 (C1), 119.0 (C8), 63.6 (C7), 59.5 (C11), 46.0 (C5), 28.4 (C6).

IR (KBr), vmax (cm^{-1}): 3427 (*st* N-H), 3226 (*st* Csp^2-H), 2204 (*st* C≡N), 1712, 1644 (*st* C=O).

MS (70 eV, EI): m/z (%) 228.1 (100%), 137.0 (29%), 110.1 (54%)

Spectroscopic data are consistent with those previously described.[7]

2-methoxy-6-oxo-4-phenyl-1,4,5,6-tetrahydropyridine-3-carbonitrile (62{*1,3*})

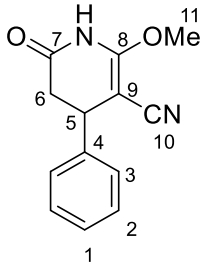

Starting from methyl cinnamate (**60**{*1,3*}). 78% yield, white solid

mp: 135-137 °C

^{1}H-NMR (400 MHz, DMSO-d_6): δ (ppm) 10.73 (s, 1H, N-H), 7.34 (m, 2H, C2-H), 7.27 (m, 1H, C1-H), 7.18-7.24 (m, 2H, C3-H), 3.94 (s, 3H, C11-H_3), 3.87 (dd, J = 7.0, 5.1 Hz, 1H, C5-H), 2.92 (dd, J = 16.2, 7.3 Hz, 1H, C6-H), 2.54 (dd, J = 16.2, 5.1 Hz, 1H, C6-H).

^{13}C-NMR (100 MHz, DMSO-d_6): δ (ppm) 170.2 (C7), 161.1 (C8), 141.5 (C4), 129.3 (C2), 127.8 (C1), 127.2 (C3), 118.8 (C10), 68.4 (C9), 59.3 (C11), 38.8 (C5), 37.1(C6).

IR (KBr), vmax (cm^{-1}): 3430 (*st* N-H), 3206 (*st* Csp^2-H), 2207 (*st* C≡N), 1697, 1641 (*st* C=O).

Elemental analysis: calculated for $C_{13}H_{12}N_2O_2$: C: 68.41%, H: 5.30%, N: 12.27%; Found: C: 68.37%, H: 5.25%, N: 12.23%.

2-methoxy-4-(4-methoxyphenyl)-6-oxo-1,4,5,6-tetrahydropyridine-3-carbonitrile (62{*1,4*})

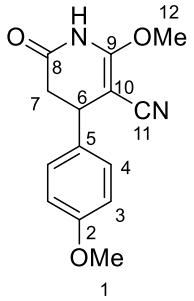

Starting from (*E*)-methyl-3-(4-methoxyphenyl)acrylate (**60**{*1,4*}). 77% yield, white solid

^{1}H-NMR (400 MHz, DMSO-d_6): δ (ppm) 10.69 (s, 1H, N1-H), 7.13 (m, 2H, C4-H), 6.89 (m, 2H, C3-H), 3.93 (s, 3H, C1-H), 3.81 (dd, J = 7.1, 5.3 Hz, 1H, C6-H), 3.71 (s, 3H, C12-H_3), 2.86 (m, 1H, C7-H), 2.50 (m, 1H, C7-H).

^{13}C-NMR (100 MHz, DMSO-d_6): δ (ppm) 170.2 (C8), 160.8 (C9), 158.9 (C2), 133.3 (C5), 128.3 (C4), 118.8 (C11), 114.6 (C3), 68.9 (C10), 59.3 (C1), 55.5 (C12), 39.0 (C7) 36.3 (C6).

IR (KBr) vmax (cm^{-1}): 3431 (*st* N-H), 3195 (*st* Csp^2-H), 2196 (*st* C≡N), 1691, 1626 (*st* C=O).

Elemental analysis: calculated for $C_{14}H_{14}N_2O_3$: C: 65.11%, H: 5.46%, N: 10.85%; Found: C: 65.03%, H: 5.24%, N: 11.11%.

2-methoxy-5-(4-methoxyphenyl)-6-oxo-1,4,5,6-tetrahydropyridine-3-carbonitrile (62{*4*,*1*})

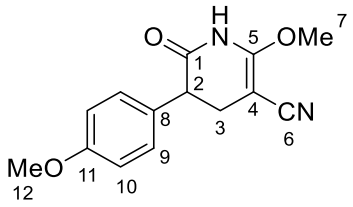

Starting from methyl 2-(4-methoxyphenyl)acrylate (**60**{*4*,*1*}). 33% yield, yellow-green solid.

mp: 177-180 °C

^{1}H-NMR (400 MHz, DMSO-d_6) δ 7.17 – 7.12 (m, 2H, C9-H), 6.93 – 6.87 (m, 2H, C10-H), 3.93 (s, 3H), 3.84 – 3.75 (m, 1H, C2-H), 3.74 (s, 3H), 2.67 (dd, *J* = 15.4, 10.6 Hz, 1H, C3-H), 2.57 (dd, *J* = 15.4, 6.8 Hz, 1H, C3-H).

^{13}C-NMR (100 MHz, DMSO-d_6) δ 171.7 (C1), 159.8, 158.4, 129.6, 129.4 (C9), 118.7 (C6), 113.9 (C10), 63.2, 59.0, 55.2, 44.8 (C2), 28.2 (C3).

IR (KBr), vmax (cm^{-1}): 3426(*st* N-H), 3205 (*st* Csp^2-H), 3109, 2956, 2198 (*st* C≡N), 1694 (*st* C=O), 1644, 1515, 1489, 1247, 1027

MS (70 eV, EI) m/z (%): 258.2 (19%), 148.1 (100%), 135.1 (24%), 120.1 (23%)

2-methoxy-6-oxo-5-(3,4,5-trimethoxyphenyl)-1,4,5,6-tetrahydropyridine-3-carbonitrile (62{*5*,*1*})

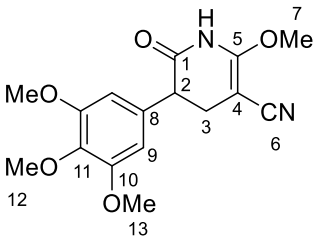

Starting from methyl 2-(3,4,5-trimethoxyphenyl)acrylate (**60**{*5*,*1*}). 47% yield, grey-purple solid.

mp: 182-185 °C

^{1}H-NMR (400 MHz, DMSO-d_6) δ 10.14 (s, 1H, NH), 6.57 (s, 2H, C9-H), 3.95 (s, 3H, C7-H_3), 3.75 (s, 6H, C13-H_3), 3.65 (s, 3H, C12-H_3), 3.81 – 3.75 (m, 1H, C2-H), 2.82 (dd, J = 15.3, 11.7 Hz, 1H, C3-H), 2.55 (dd, J = 15.4, 6.7 Hz, 1H, C3-H).

^{13}C-NMR (100 MHz, DMSO-d_6) δ 171.3 (C1), 159.8 (C5), 152.7 (C10), 136.6 (C11), 133.4 (C8), 118.5 (C4), 105.9 (C9), 63.3 (C6), 59.9 (C12), 59.0 (C7), 55.9 (C13), 45.8 (C3), 27.9 (C3).

IR (KBr), vmax (cm^{-1}): 3209(*st* N-H), 3111, 2984, 2196 (*st* C≡N), 1694 (*st* C=O), 1640, 1591, 1510, 1460, 1334, 1247, 1127, 1007

MS (70 eV, EI) m/z (%): 318.3 (69%), 209.0 (25%), 208.2 (95%), 194.2 (34%), 193.1 (100%), 165.1 (37%), 79.1 (31%).

5-(2,6-dichlorophenyl)-2-methoxy-6-oxo-1,4,5,6-tetrahydropyridine-3-carbonitrile (62{*7*,*1*})

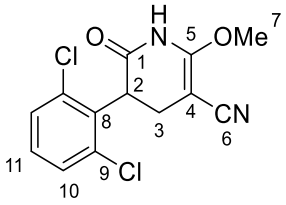

Starting from methyl 2-(2,6-dichlorophenyl)acrylate (**60**{*7*,*1*}). 91 % yield, white solid.

^{1}H-NMR (400 MHz, DMSO-d$_6$): δ 10.86 (s, 1H, NH), 7.56 – 7.46 (m, 2H, C10-H), 7.37 (m, 1H, C11-H), 4.69 (dd, J = 13.9, 8.4 Hz, 1H, C2-H), 3.97 (s, 3H, C7-H_3), 2.94 (dd, *J* = 15.1, 13.9 Hz, 1H, C3-H), 2.45 (dd, J = 15.2, 8.4 Hz, 1H, C3-H).

^{13}C-NMR (100 MHz, DMSO-d_6) δ 169.1 (C1), 159.6 (C5), 135.4 (C9), 134.7 (C9'), 133.8 (C8), 130.2 (C11), 129.7 (C10), 128.4 (C10'), 118.3 (C4), 62.6 (C6), 59.0 (C7), 42.8 (C4), 24.8 (C3).

Spectroscopic data are consistent with those previously described.[8]

5-(4-fluorophenyl)-2-methoxy-6-oxo-1,4,5,6-tetrahydropyridine-3-carbonitrile (62{*6,1*})

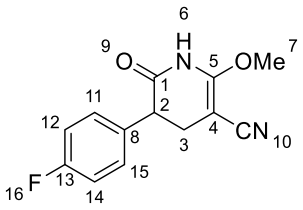

Starting from methyl 2-(4-fluorophenyl)acrylate (**60**{*6,1*}). 42 % yield, yellowish solid.

mp: 159-162 °C

^{1}H-NMR (400 MHz, DMSO-d_6) δ 10.79 (br s, 1H), 7.29 (m, 2H, C15-H), 7.17 (m, 2H, C14-H), 3.90 (dd, *J* =12.1 Hz, *J* =6.7 Hz, 1H), 2.74 (dd, *J* =15.3 Hz, *J* =12.0 Hz, 1H), 2.55 (dd, *J* =15.3 Hz, *J* =6.8 Hz, 1H).

^{13}C-NMR (100 MHz, DMSO-d_6) δ 171.3 (C1), 161.3 (d, J = 242.9 Hz, C13), 159.8 (C5), 133.9 (d, J = 3.1 Hz, C8), 130.5 (d, J = 8.1 Hz, C15), 118.5 (C4), 115.1 (d, J = 21.3 Hz, C14), 63.3 (C10), 58.9 (C7), 44.8 (C2), 27.9 (C3).

IR (KBr), vmax (cm^{-1}): 3407 (*st* N-H), 3227 (*st* Csp^2-H), 2955, 2200 (*st* C≡N), 1718 (*st* C=O), 1635, 1518, 1485, 1234, 1164, 836.

MS (70 eV, EI) m/z (%): 246.1 (21%), 241.1 (65%), 168 (60%), 139.1 (88%), 135.9 (100%), 133.1 (35%), 123.0 (37%), 122.1 (53%), 121.1 (73%), 109.0 (63%), 59.1 (41%), 44.1 (31%).

5-(2,4-dichlorophenyl)-2-methoxy-6-oxo-1,4,5,6-tetrahydropyridine-3-carbonitrile (62{*8,1*})

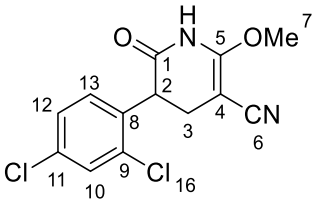

Starting from methyl 2-(2,4-dichlorophenyl)acrylate (**60**{*8,1*}). 84% yield, yellowish solid

^{1}H-NMR (400 MHz, DMSO-d_6) δ 10.91 (s, 1H, NH), 7.63 (d, J = 2.1 Hz, 1H, C10-H), 7.44 (dd, J = 8.4, 2.1 Hz, 1H, C12-H), 7.39 (d, J = 8.4 Hz, 1H, C13-H), 4.20 (dd, J = 13.7, 7.1 Hz, 1H, C2-H), 3.95 (s, 3H, C7-H$_3$), 2.84 (dd, J = 15.0, 13.7 Hz, 1H, C3-H), 2.45 (dd, J = 15.0, 7.1 Hz, 1H, C3-H).

^{13}C-NMR (100 MHz, DMSO-d_6) δ 169.8 (C1), 159.9 (C5), 134.5 (C9), 134.4 (C8), 132.7 (C11), 132.0 (C13), 128.8 (C10), 127.5 (C12), 118.3 (C6), 63.1 (C4), 58.9 (C7), 43.2 (C2), 26.4 (C3).

Spectroscopic data are consistent with those previously described.[5,9]

6.1.3.3 Synthesis of arylhydrazines

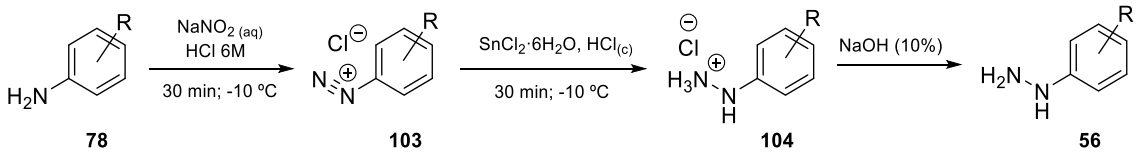

4.3 mmol of the corresponding aniline were diluted in 15 mL of 6M HCl. The solution was cooled to -10 °C. A solution of 0.37 g of sodium nitrite (5.3 mmol) in 1.5 mL of water was added dropwise with continuous stirring. After the addition, the reaction was stirred for an additional 30 min at -10 °C. Then, a solution of tin (II) chloride dihydrate (2.94 g, 13.0mmol) in concentrated HCl (5 mL) was added slowly. After 30 min of stirring at -10 °C, the precipitate was filtered obtaining the corresponding hydrazine hydrochloride (**104**). The hydrazine hydrochloride (**104**) was dissolved in water and the solution was neutralized with NaOH 6M. The product was extracted with diethyl ether (4 x 30 mL) and the combined organic layers were dried with anhydrous $MgSO_4$.The solvent was removed under reduced pressure to yield the corresponding arylhydrazine (**56**).

(4-fluorophenyl)hydrazine (56{*4*})

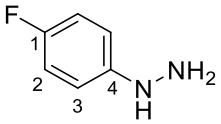

Starting from 4-fluoroaniline (**78**{*4*}). 50% yield. Orange liquid.

^{1}H-NMR (400 MHz, DMSO-d_6) δ 6.94 – 6.85 (m, 2H, C2-H), 6.76 – 6.70 (m, 2H, C3-H), 6.59 – 6.52 (s, 1H, NH), 3.91 (s, 2H, NH_2).

^{13}C-NMR (100 MHz, DMSO-d_6) δ 155.3 (d, *J* = 231.6 Hz, C1), 149.7 (d, *J* = 1.5 Hz, C4), 115.3 (d, *J* = 22.1 Hz, C2), 112.8 (d, *J* = 7.4 Hz, C3).

IR (KBr), vmax (cm^{-1}): 3335 (*st* N-H), 1506, 1219, 827.

(3,4-difluorophenyl)hydrazine hydrochloride (56{*5*})

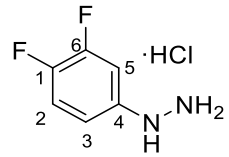

Starting from 3,4-difluoroaniline (**78**{*5*}). 77% yield. White solid.

^{1}H-NMR (400 MHz, DMSO-*d*$_6$) δ 10.07 (s, 3H, NH), 8.35 (s, 1H, NH_2), 7.34 (q, *J* = 9.5 Hz, 1H, C2-H), 7.02 (ddd, *J* = 12.8, 6.9, 2.7 Hz, 1H, C5-H), 6.75 (dd, *J* = 8.5, 3.9 Hz, 1H, C3-H).

^{13}C-NMR (100 MHz, DMSO-*d*$_6$) δ 149.9 (dd, *J* = 243.8, 13.6 Hz, C6), 144.5 (dd, *J* = 238.2, 12.6 Hz, C1), 144.0, 118.2 (d, *J* = 18.2 Hz), 110.9, 104.0 (d, *J* = 21.2 Hz).

IR (KBr), vmax (cm^{-1}): 3428 (*st* N-H), 3197, 2993, 2926, 2674, 1526, 1497, 858.

MS (70 eV, EI) m/z (%): 224.9 (22%), 144.1 (100%), 128.1 (49%), 101.1 (44%).

(4-chlorophenyl)hydrazine (56{*6*})

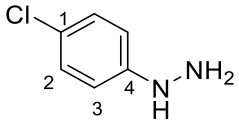

Starting from 4-chloroaniline (**78**{*6*}). 61% yield. Orange crystals.

^{1}H-NMR (400 MHz, DMSO-*d*$_6$) δ 7.10 – 7.04 (m, 2H, C2-H), 6.82 (s, 1H, NH), 6.76 – 6.71 (m, 2H, C3-H), 3.99 (s, 2H, NH_2)

^{13}C-NMR (100 MHz, DMSO-*d*$_6$) δ 151.4 (C4), 128.2 (C2), 119.5 (C1), 112.8 (C3).

(4-bromo-2-chlorophenyl)hydrazine (56{*7*})

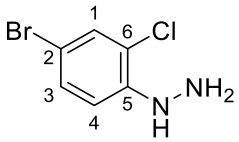

Starting from 4-bromo-2-chloroaniline (**78**{*7*}). 61% yield. Ochre solid.

^{1}H-NMR (400 MHz, DMSO-*d*$_6$) δ 7.35 (dd, *J* = 2.4, 1.1 Hz, 1H, C1-H), 7.31 – 7.26 (m, 1H, C3-H), 7.11 (dd, *J* = 8.8, 1.1 Hz, 1H, C4-H), 6.68 (s, 1H, NH), 4.15 (s, 2H, NH_2).

^{13}C-NMR (100 MHz, DMSO-*d*$_6$) δ 147.0 (C5), 130.3, 116.7, 114.1, 109.5, 106.2

IR (KBr), vmax (cm^{-1}): 3435 (st N-H), 3338, 3279 (*st* Csp^2-H), 1585, 1492, 1274, 1045, 863, 802.

Methyl 4-hydrazinylbenzoate (56{*8*})

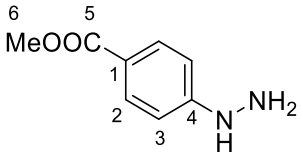

Starting from methyl 4-aminobenzoate (**78**{*8*}). 14% yield. Yellow solid.

^{1}H-NMR (400 MHz, DMSO-d_6) δ 7.73 – 7.66 (m, 2H, C2-H), 7.57 (s, 1H, NH), 6.82 – 6.73 (m, 2H, C3-H), 4.19 (s, 2H, NH_2), 3.73 (s, 3H, C6-H_3).

^{13}C-NMR (100 MHz, DMSO-d_6) δ 166.4 (C5), 156.1 (C4), 131.1 (C2), 130.7 (C1), 116.1 (C3), 112.6, 109.8, 51.2 (C6).

IR (KBr), vmax (cm^{-1}): 3295 (*st* N-H), 2210, 1897, 1602 (*st* C=O), 1515, 1177, 821.

4-hydrazinylbenzonitrile (56{*9*})

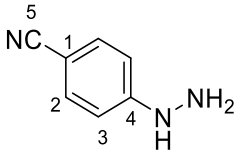

Starting from methyl 4-aminobenzonitrile (**78**{*9*}). 64% yield. Yellow crystals.

^{1}H-NMR (400 MHz, DMSO-d_6) δ 7.72 (s, 1H, NH), 7.48 – 7.38 (m, 1H, C2-H), 6.85 – 6.74 (m, 1H, C3-H), 4.29 – 4.16 (m, 1H, NH_2).

^{13}C-NMR (100 MHz, DMSO-d_6) δ 155.8 (C4), 134.2, 133.5, 122.5, 121.2, 111.0, 96.1.

IR (KBr), vmax (cm^{-1}): 3295 (*st* N-H), 2210 (*st* C≡N), 1897.30, 1602.40, 1515.45, 1177.21, 821.83.

6.1.3.4 Synthesis of 6-oxo-2-(2-arylhydrazono)piperidine-3-carbonitriles (76)

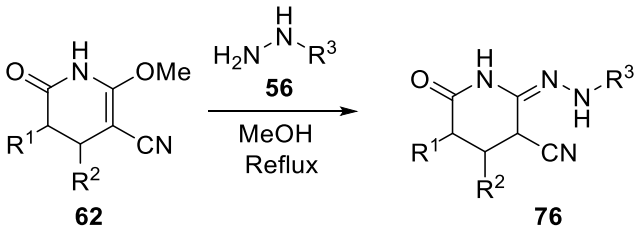

A mixture of 0.60 mmol of 2-methoxy-6-oxo-1,4,5,6-tetrahydropyridine-3-carbonitrile (**62**) and 1.20 mmol of arylhydrazine (**56**) in 4 mL of methanol was refluxed for 24 h. After cooling, the solvent was removed under reduced pressure and the crude was resuspended with the minimum amount of methanol. The solid was filtered, washed with cold methanol and dried *in vacuo* over P_2O_5 to yield the corresponding 6-oxo-2-(2-arylhydrazono)piperidine-3-carbonitriles (**76**)

2-(2-(4-cyanophenyl)hydrazono)-5-(2,6-dichlorophenyl)-6-oxopiperidine-3-carbonitrile (76{*7*,*1*,*9*})

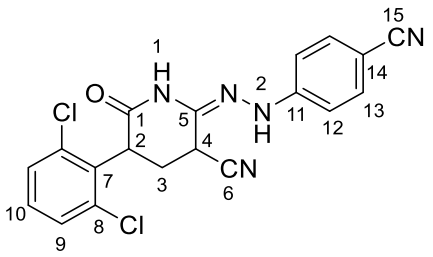

Starting from 5-(2,6-dichlorophenyl)-2-methoxy-6-oxo-1,4,5,6-tetrahydropyridine-3-carbonitrile (**62**{*7*,*1*}) and 4-hydrazinylbenzonitrile (**56**{*9*}). 35 % yield, pale yellow solid.

mp: > 280 °C

^{1}H-NMR (400 MHz, DMSO-d_6) δ 10.60 (br s, 1H, N1-H), 9.80 (s, 1H, N2-H), 7.65 (m, 2H, C13-H), 7.56 (m, 1H, C9-H), 7.49 (m, 1H, C9'-H), 7.39 (m, 1H, C10-H), 7.08 (m, 2H, C12-H), 4.81-4.76 (m, 2H, C2-H and C4-H), 2.55 (q, *J*=12.6 Hz, 1H, C3-H), 2.54-2.45 (m, 1H, C3-H)

^{13}C-NMR (100 MHz, DMSO-d_6) δ 168.4 (C1), 148.8 (C11), 135.6, 134.5, 134.1 (C7), 133.8 (C13), 131.1 (C5), 130.3 (C10), 129.7 (C9'), 128.6 (C9), 120.1 (C15), 117.2 (C6), 111.8 (C12), 99.6 (C14), 43.7, 30.5, 27.4 (C3).

IR (KBr), vmax (cm^{-1}): 3347 (*st* N-H), 3081 (*st* Csp^2-H), 2928 (*st* C-H), 2209 (*st* C≡N), 1687 (*st* C=N), 1604 (*st* C=O), 1526, 1437, 1390, 1249, 1170, 1129, 828.

Elemental analysis: calculated for $C_{19}H_{13}Cl_2N_5O$: C: 57.30 %, H: 3.29 %, N: 17.59 %, found: C: 57.20 %, H: 3.31 %, N: 17.21 %

MS (70 eV, EI) m/z (%): 247 (100%), 140 (13%).

5-(2,6-dichlorophenyl)-6-oxo-2-(2-phenylhydrazono)piperidine-3-carbonitrile (76{*7*,*1*,*3*})

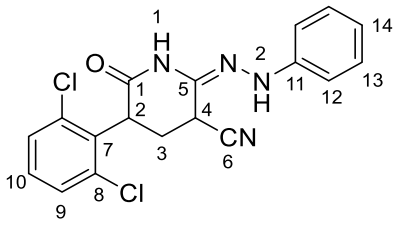

Starting from 5-(2,6-dichlorophenyl)-2-methoxy-6-oxo-1,4,5,6-tetrahydropyridine-3-carbonitrile (**62**{*7*,*1*}) and phenylhydrazine (**56**{*3*}). 37 % yield, white solid.

mp: 206-208 °C

^{1}H-NMR (400 MHz, DMSO-d_6) δ 10.49 (br s, 1H, N1-H), 9.15 (s, 1H, N2-H), 7.56 (m, 1H, C9'-H), 7.49 (m, 1H, C9-H), 7.39 (m, 1H, C10-H), 7.22 (m, 2H, C13-H), 7.00 (m, 2H,C12-H), 6.75 (m, 1H, C14-H), 4.79-4.72 (m, 2H, C2-H and C4-H), 2.58-2.42 (q, *J*=12.6 Hz, 1H, C3-H), 2.58-2.42 (m, 1H, C3-H)

^{13}C-NMR (100 MHz, DMSO-d_6) δ 168.2 (C1), 145.6 (C11), 135.5 (C8), 134.5 (C8'), 134.2 (C7), 130.2 (C10), 129.6 (C9), 129.1 (C13), 128.6 (C9'), 128.1 (C5), 118.8 (C14), 117.4 (C6), 111.7 (C12), 43.8 (C2), 30.4 (C4), 27.6 (C3).

IR (KBr), vmax (cm^{-1}): 3356 (*st* N-H), 3205, 3084 (*st* Csp^2-H), 2905 (*st* C-H), 2255 (*st* C≡N), 1690 (*st* C=N), 1604 (*st* C=O), 1498, 1435, 1382, 1243, 1133, 751, 694

Elemental analysis: calculated for $C_{18}H_{14}Cl_2N_4O$: C: 57.93%, H: 3.78%, N: 15.01%, found: C: 57.92%, H: 4.28%, N: 14.87%

MS (70 eV, EI) m/z (%): 374.0 (66%), 372.0 (100%), 337.1 (36%), 201 (27%), 186 (26%), 171 (34%), 92 (29%), 77 (54%).

Methyl 4-(2-(3-cyano-5-(2,6-dichlorophenyl)-6-oxopiperidin-2-ylidene)hydrazinyl)benzoate (76{*7*,*1*,*8*})

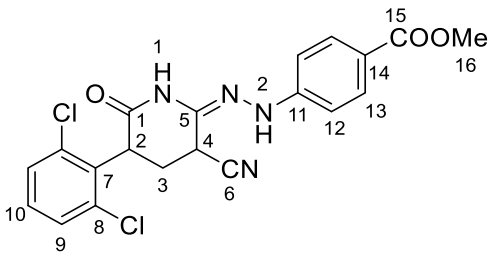

Starting from 5-(2,6-dichlorophenyl)-2-methoxy-6-oxo-1,4,5,6-tetrahydropyridine-3-carbonitrile (**62**{*7*,*1*}) and methyl 4-hydrazinylbenzoate (**56**{*8*}). 14 % yield, salmon solid.

mp: 214-234 °C

^{1}H-NMR (400 MHz, DMSO-d_6) δ 10.60 (br s, 1H, N1-H), 9.71 (s, 1H, N2-H), 7.84 (m, 2H, C13-H), 7.56 (m, 1H, C9'-H), 7.49 (m, 1H, C9-H), 7.39 (m, 1H, C10-H), 7.05 (m, 2H, C12-H), 4.81-4.76 (m, 2H, C2-H, C4-H), 3.78 (s, 3H, C16-H_3), 2.55 (q, *J*=12.5 Hz, 1H, C3-H), 2.54-2.44 (m, 1H, C3-H).

^{13}C-NMR (100 MHz, DMSO-d_6) δ 168.8 (C1), 166.5 (C15), 149.7 (C11), 136.0 (C8), 134.9 (C8'), 134.5 (C7), 131.5 (C13), 130.8, 130.7, 130.1 (C9'), 129.0 (C9), 119.8 (C14), 117.6 (C6), 111.4 (C12), 51.9 (C16), 44.2, 30.8, 27.9 (C3).

IR (KBr), vmax (cm^{-1}): 3347 (*st* N-H), 3208, 3079 (*st* Csp^2-H), 2901 (*st* C-H), 2257 (*st* C≡N), 1712 (*st* C=O), 1690 (*st* C=N), 1604 (*st* C=O), 1533, 1435 1380, 1240, 1114, 832, 768.

Elemental analysis: calculated for $C_{20}H_{16}Cl_2N_4O_3$: C: 55.70%, H: 3.74%, N: 12.99%, found: C: 55.71%, H: 3.39%, N: 12.80%

MS (70 eV, EI) m/z (%): 247 (100%), 140 (16%).

5-(2,6-dichlorophenyl)-2-(2-(3,4-difluorophenyl)hydrazono)-6-oxopiperidine-3-carbonitrile (76{*7*,*1*,*5*})

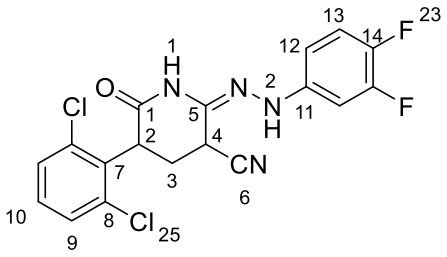

Starting from 5-(2,6-dichlorophenyl)-2-methoxy-6-oxo-1,4,5,6-tetrahydropyridine-3-carbonitrile (**62**{*7*,*1*}) and (3,4-difluorophenyl)hydrazine (**56**{*5*}). 14 % yield, beige solid.

mp: 215-220 °C

^{1}H-NMR (400 MHz, DMSO-d_6) δ 10.46 (br s, 1H, N1-H), 9.31 (s, 1H, N2-H), 7.56 (m, 1H, C9-H), 7.49 (m, 1H, C9'-H), 7.39 (m, 1H, C10-H), 7.28 (m, 1H), 6.92 (m, 1H), 6.71 (m, 1H), 4.79-4.73 (m, 2H, C2-H, C4-H), 2.57-2.43 (m, 2H, C3-H).

IR (KBr), vmax (cm^{-1}): 3357 (*st* N-H), 3197, 3081 (*st* Csp^2-H), 2915 (*st* C-H), 2255 (*st* C≡N), 1680 (*st* C=N), 1616 (*st* C=O), 1517, 1439, 1386, 1250, 1208, 1165, 844, 784.

Elemental analysis: calculated for $C_{18}H_{12}Cl_2F_2N_4O$: C: 52.83%, H: 2.96%, N: 13.69%, found: C: 52.65%, H: 3.35%, N: 13.78%.

MS (70 eV, EI) m/z (%): 410 (64%), 408 (100%), 373 (32%), 267 (29%), 237 (39%), 173 (56%), 171 (83%), 141 (38%), 128 (60%), 113 (81%), 101 (56%), 67 (24%).

2-(2-(4-cyanophenyl)hydrazono)-6-oxo-5-phenylpiperidine-3-carbonitrile (76{*7*,*1*,*9*})

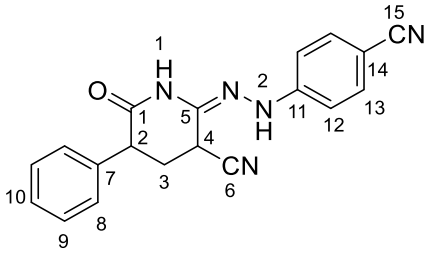

Starting from 2-methoxy-6-oxo-5-phenyl-1,4,5,6-tetrahydropyridine-3-carbonitrile (**62**{*3*,*1*}) and 4-hydrazinylbenzonitrile (**56**{*9*}). 43 % yield, salmon solid.

mp: 230-232 °C

^{1}H-NMR (400 MHz, DMSO-d_6) δ 10.51 (br s, 1H, N1-H or N1-H'), 10.37 (br s, 1H, N1-H or N1-H'), 9.82 (s, 1H, N2-H'), 9.78 (s, 1H, N2-H), 7.63 (m, 4H, C13-H and C13'-H), 7.38-7.26 (m, 10H, C8-H, C9-H, C8'-H, C9'-H), 7.06 (m, 4H, C12-H and C12'-H), 4.57 (dd, , *J* =12.8 Hz, *J* =4.2 Hz, 1H, C4-H), 4.28 (dd, *J* =6.2 Hz, *J* =4.8 Hz, 1H, C4'-H), 4.02-3.93 (m, 2H, C2'-H and C2-H), 2,62 (q, *J* =12.7 Hz, 1H, C3-H), 2.55-2.43 (m, 3H, C3-H and C3'-H)

^{13}C-NMR (100 MHz, DMSO-d_6) δ 170.4 (C1), 169.8 (C1'), 148.9 (C11), 148.7 (C11'), 138.4 (C7), 138.1 (C7'), 133.72 (C13 or C13'), 133.70 (C13 or C13'), 131.8 (C5), 130.7 (C5'), 128.9, 128.6, 128.5, 128.3, 127.3, 127.1, 120.1 (C15 or C15'), 120.0 (C15 or C15'), 118.4 (C6'), 117.7 (C6), 111.9 (C12'), 111.7 (C12), 99.6 (C14 or C14'), 99.3 (C14 or C14'), 47.1 (C2), 45.2 (C2'), 31.0 (C4), 30.8 (C3), 29.7 (C3'), 29.2 (C4').

IR (KBr), vmax (cm^{-1}): 3350 (*st* N-H), 3093 (*st* Csp^2-H), 2931 (*st* C-H), 2205 (*st* C≡N), 1693, 1604 (*st* C=O), 1530 (*st* Csp^2-Csp^2), 1245, 1171, 1131, 829, 759, 702

Elemental analysis: calculated for $C_{19}H_{15}N_5O$: C: 69.29%, H: 4.59%, N: 21.26%, found: C: 69.59%, H: 4.92%, N: 21.22%

MS (70 eV, EI) m/z (%): 176 (42%), 159 (100%), 145 (24%), 127 (22%), 109 (28%), 69 (26%), 57 (26%), 43.05 (61%).

2-(2-(4-cyanophenyl)hydrazono)-5-(4-methoxyphenyl)-6-oxopiperidine-3-carbonitrile (76{*4*,*1*,*9*})

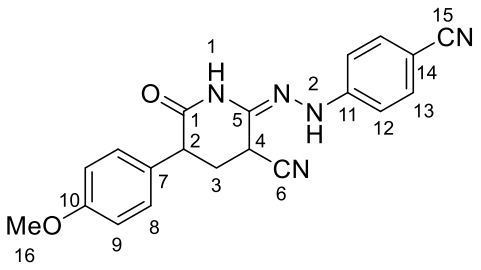

Starting from 2-methoxy-5-(4-methoxyphenyl)-6-oxo-1,4,5,6-tetrahydropyridine-3-carbonitrile (**62**{*4*,*1*}) and 4-hydrazinylbenzonitrile (**56**{*9*}). 14 % yield, salmon solid.

mp: 214-234 °C

^{1}H-NMR (400 MHz, DMSO-d_6) δ 10.48 (br s, 1H, N1-H or N1'-H), 10.33 (br s, 1H, N1-H or N1'-H), 9.81 (s, 1H, N2-H'), 9.77 (s, 1H, N2-H), 7.63 (m, 4H, C13-H and C13'-H), 7.23 (m, 2H, C8'-H), 7.18 (m, 2H, C8-H), 7.06 (m, 4H, C12-H and C12'-H), 6.92-6.88 (m, 4H, C9-H and C9'-H), 4.55 (dd, *J* =12.8 Hz, *J* =3.9 Hz, 1H, C4-H), 4.25 (dd, *J* =5.4 Hz, *J* =5.4 Hz, 1H, C4'-H), 3.96-3.86 (m, 2H, C2'-H and C2-H), 3.74 (s, 6H, C16-H), 2.52 (q, *J* =12.8 Hz, 1H, C3-H), 2.54-2.39 (m, 3H, C3-H and C3'-H)

^{13}C-NMR (100 MHz, DMSO-d_6) δ 170.6 (C1), 170.0 (C1'), 158.4 (C7 or C 7'), 158.3 (C7 or C 7'), 148.9 (C11), 148.7 (C11'), 133.7 (C13 or C13'),133.7 (C13 or C13'), 131.9 (C5), 130.8 (C5'), 130.4, 130.0, 129.9, 129.6, 120.1 (C15 or C15'), 120.0 (C15 or C15'), 118.4 (C6'), 117.7 (C6), 113.9 (C9 or C9'), 113.7 (C9 or C9'), 111.9 (C12'), 111.7 (C12), 99.5 (C14 or C14') 99.3 (C14 or C14'), 55.1 (C16 or C16'), 55.1 (C16 or C16'), 46.3 (C2), 44.4 (C2'), 31.0 (C4), 30.9 (C3), 29.8 (C3'), 29.2 (C4').

IR (KBr), vmax (cm^{-1}): 3348 (*st* N-H), 3095, (*st* Car-H), 2934 (*st* C-H), 2202 (*st* C≡N), 1693, 1603 (*st* C=O), 1514 (*st* Csp2-Car), 1243, 1131, 828.

Elemental analysis: calculated for $C_{20}H_{17}N_5O_2$: C: 66.84%, H: 4.77%, N: 19.49%, found: C: 66.43%, H: 4.75%, N: 19.44%

MS (70 eV, EI) m/z (%): 227.1 (28%), 148 (100%), 120 (21%).

2-(2-(4-cyanophenyl)hydrazono)-5-(4-fluorophenyl)-6-oxopiperidine-3-carbonitrile (76{*6*,*1*,*9*})

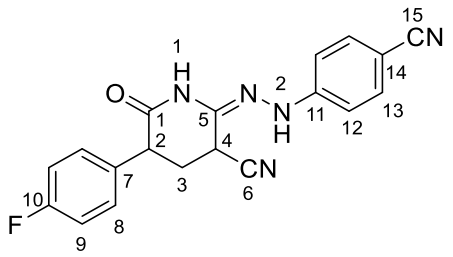

Starting from 5-(4-fluorophenyl)-2-methoxy-6-oxo-1,4,5,6-tetrahydropyridine-3-carbonitrile (**62**{*6*,*1*}) and 4-hydrazinylbenzonitrile (**56**{*9*}). 32 % yield, beige solid.

mp: 247-251 °C

^{1}H-NMR (400 MHz, DMSO-d_6) δ 10.42 (br s, 2H, N1-H), 9.81 (br s, 1H, N2-H), 9.78 (s, 1H, N2-H), 7.63 (m, 4H, C13-H and C13'-H), 7.38 (m, 2H, C8'-H), 7.32 (m, 2H, C8-H), 7.20-7.14 (m, 4H, C9-H and C9'-H), 7.06 (m, 4H, C12-H and C12'-H), 4.56 (dd, *J* = 12.8, 4.2 Hz, 1H, C4-H), 4.31 (dd, *J* = 5.9, 4.6 Hz, 1H, C4'H), 4.04 (dd, *J* = 9.8 Hz, *J* = 5.6 Hz, 1H, C2-H), 3.98 (dd, *J* = 12.7, 5.1 Hz, 1H, C2'-H), 2.63 (q, *J* = 12.7 Hz, 1H, C3-H), 2.59-2.42 (m, 3H, C3-H and C3'-H).

^{13}C-NMR (100 MHz, DMSO-d_6) δ 170.3 (C1), 169.8 (C1'), 162.6 (C7), 160.1 (C7'), 148.9 (C11), 148.6 (C11'), 134.5 (d, *J*=3.1 Hz, C8 or C8'), 134.3 (d, *J*=3.1 Hz, C8 or C8'), 133.7, 133.7, 131.8 (C5), 130.9, 130.8, 130.7, 130.7, 130.6, 120.1 (C15 or C15'), 120.0 (C15 or C15'), 118.4 (C6'), 117.7 (C6), 115.2 (d, *J*=21.5 Hz, C9 or C9'), 115.1 (d, *J*=21.3 Hz, C9 or C9'), 111.9 (C12'), 111.7 (C12), 99.6 (C14), 99.3 (C14'), 46.2 (C2), 44.3 (C2'), 31.0 (C4), 30.6 (C3), 29.5 (C3'), 9.4 (C4).

IR (KBr), vmax (cm^{-1}): 3350 (*st* N-H), 3092 (*st* Csp^2-H), 2930 (*st* C-H), 2204 (*st* C≡N), 1692 (*st* C=N), 1604 (*st* C=O), 1513 (*st* Csp^2-Csp^2), 1246, 1172, 1131, 827.

Elemental analysis: calculated for $C_{19}H_{14}FN_5O$: C: 65.70 %, H: 4.06%, N: 20.16%, found: C: 65.73%, H: 4.30%, N: 20.06%

MS (70 eV, EI) m/z (%): 247 (100%), 149 (25%), 119 (51%), 103 (30%), 83 (22%), 73 (33%), 57 (49%), 43 (63%).

4-methyl-6-oxo-2-(2-phenylhydrazono)piperidine-3-carbonitrile (76{*1,2,3*})

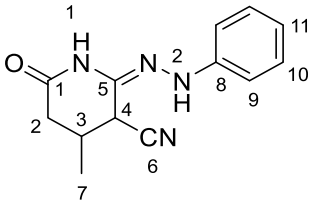

Starting from 2-methoxy-4-methyl-6-oxo-1,4,5,6-tetrahydropyridine-3-carbonitrile (**62**{*1*,*2*}) and phenylhydrazine (**56**{*3*}). 72 % yield, pale orange solid.

mp: 208-210 °C

^{1}H-NMR (400 MHz, DMSO-d_6) δ 10.17 (br s, 1H, N1-H), 9.04 (s, 1H, N2-H), 7.20 (m, 2H, C10-H), 7.97 (m, 2H, C9-H), 6.73 (m, 1H, C11-H), 4.05 (d, *J* = 10.9 Hz, 1H, C4-H), 2.58 (d, *J* = 12.9 Hz, 1H, C2-H), 2.40-2.29 (m, 2H, C2-H, C3-H), 1.14 (d, *J* = 6.1 Hz, 3H, C7-H).

^{13}C-NMR (100 MHz, DMSO-d_6) δ 168.8 (C1), 145.7 (C8), 129.0 (C10), 128.7 (C5), 118.7 (C11), 117.5 (C6), 111.7 (C9), 38.1 (C4), 37.6 (C2), 29.3 (C3), 18.6 (C7).

IR (KBr), vmax (cm^{-1}): 3341 (*st* N-H), 3204, 3074 (*st* Csp^2-H), 2982, 2931 (*st* C-H), 2252 (*st* C≡N), 1683 (*st* C=N), 1603 (*st* C=O), 1534, 1500, 1246, 1120, 1067, 749, 695.

Elemental analysis: calculated for $C_{13}H_{14}N_4O$: C: 64.45%, H: 5.82%, N: 23.13%, found: C: 64.32%, H: 5.87%, N: 23.09%

MS (70 eV, EI) m/z (%): 242.2 (100%), 92.1 (40%), 77.1 (31%), 69.1 (53%).

2-(2-(4-cyanophenyl)hydrazono)-6-oxo-4-phenylpiperidine-3-carbonitrile (76{*1,3,9*})

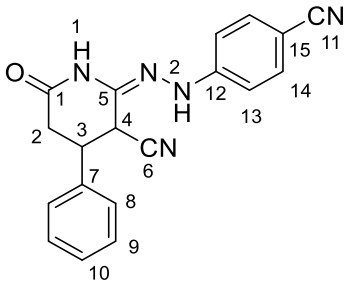

Starting from 2-methoxy-6-oxo-4-phenyl-1,4,5,6-tetrahydropyridine-3-carbonitrile (**62**{*1,3*}) and 4-hydrazinylbenzonitrile (**56**{*9*}). 37 % yield, coral solid.

mp: 116 °C

^{1}H-NMR (400 MHz, DMSO-d_6) δ 10.44 (br s, 1H, N1-H), 9.79 (s, 1H, N2-H), 7.64 (m, 2H, C14-H), 7.43-7.31 (m, 5H, C8-H, C9-H, C10-H), 7.05 (m, 2H, C13-H), 4.77 (d, *J* = 12.2 Hz, 1H, C4-H), 3.64 (td, *J* = 12.3, *J* = 4.5 Hz, 1H, C3-H), 2.90 (dd, *J* = 17.4, *J* = 12.4 Hz, 1H, C2-H), 2.67 (dd, *J* = 17.4, *J* = 4.5 Hz, 1H, C2-H).

^{13}C-NMR (100 MHz, DMSO-d_6) δ 168.7 (C1), 148.9 (C12), 139.6 (C7), 133.7 (C14), 131.6 (C5), 128.9, 127.9, 127.5, 120.1 (C11), 116.8 (C6), 111.8 (C13), 99.4 (C15), 39.8 (C3), 38.5 (C2), 37.4 (C4).

IR (KBr), vmax (cm^{-1}): 3339 (*st* N-H), 3206, 3085 (*st* Csp^2-H), 2917 (*st* C-H), 2219 (*st* C≡N), 1676 (*st* C=N), 1604 (*st* C=O), 1523, 1251, 1170, 1105, 833, 770, 694.

Elemental analysis: calculated for $C_{19}H_{15}N_5O$: C: 69.29%, H: 4.59%, N: 21.26%, found: C: 69.30%, H: 4.54%, N: 21.30%

MS (70 eV, EI) m/z (%): 252.1 (20%), 166.1 (76%), 129.1 (32%), 110.1 (40%), 97.0 (28%), 83.1 (34%), 73.0 (52%), 55.1 (71%), 43.1 (100%).

Synthesis of 6-oxo-4-phenyl-2-(2-phenylhydrazono)piperidine-3- carbonitrile 76{*1,3,3*}

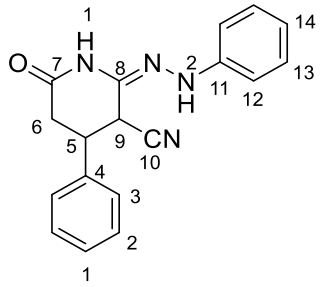

Starting from 2-methoxy-6-oxo-4-phenyl-1,4,5,6-tetrahydropyridine-3-carbonitrile (**62**{*1,3*}). 74% yield, white solid

^{1}H-NMR (400 MHz, DMSO-d_6) δ 10.32 (s, 1H, N1-H), 9.11 (s, 1H, N2-H), 7.40 (m, 4H, C2-H, C3-H), 7.32 (m, 1H, C1-H), 7.18 (dd, *J* = 8.5, 7.2 Hz, 2H, C13-H), 6.97 (m, 2H, C12-H), 6.71 (m, 1H, C14-H), 4.69 (d, *J* = 12.1 Hz, 1H, C9-H), 3.58 (td, *J* = 12.2, 4.5 Hz, 1H, C5-H), 2.86 (dd, *J* = 17.4, 12.3 Hz, 1H, C6-H), 2.63 (dd, *J* = 17.3, 4.6 Hz, 1H, C6-H).

^{13}C-NMR (100 MHz, DMSO-d_6) δ 169.0 (C7), 146.1 (C8), 140.2 (C10), 129.5 (C13), 129.3 (C3), 129.0, 128.2 (C1), 127.9 (C2), 119.2 (C14), 117.4, 112.2 (C12), 40.3 (C5), 39.0 (C6), 37.9 (C9).

IR (KBr), vmax (cm^{-1}): 3355 (*st* N-H), 3208 (*st* Csp^2-H), 2257 (*st* C≡N), 1682 (*st* C=O), 1536, 1501, 699 (*b* Csp2-H).

Elemental analysis: calculated for $C_{18}H_{16}N_4O$: C: 71.04%, H: 5.30%, N: 18.41%, found: C: 71.33%, H: 5.23%, N: 18.28%.

Methyl 4-(2-(3-cyano-4-(4-methoxyphenyl)-6-oxopiperidin-2-ylidene)hydrazinyl)benzoate (76{*1,4,8*})

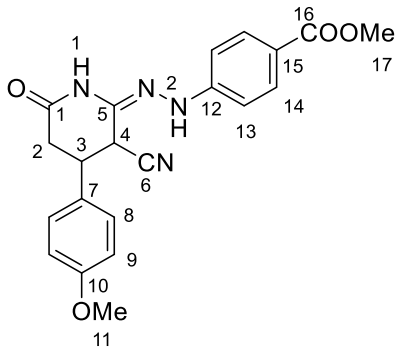

Starting from 2-methoxy-4-(4-methoxyphenyl)-6-oxo-1,4,5,6-tetrahydropyridine-3-carbonitrile (**62**{*1,4*}) and 4-hydrazinylbenzoate (**56**{*8*}). 47 % yield, pale orange solid.

mp: 199-209 °C

^{1}H-NMR (400 MHz, DMSO-d_6) δ 10.41 (br s, 1H, N1-H), 9.68 (s, 1H, N2-H), 7.82 (m, 2H, C14-H), 7.34 (m, 2H, C8-H), 7.02 (m, 2H,C13-H), 6.97 (m, 2H, C9-H), 4.68 (d, *J* = 12.1 Hz, 1H, C4-H), 3.77 (s, 3H, C17-H_3), 3.77 (s, 3H, C11-H_3), 3.57 (td, *J* = 12.2, *J* = 4.5 Hz, 1H, C3-H), 2.87 (dd, *J* = 17.3, *J* = 12.3 Hz, 1H, C2-H), 2.62 (dd, *J* = 17.3, *J* =.5 Hz, 1H, C2-H).

^{13}C-NMR (100 MHz, DMSO-d_6) δ 168.8 (C1), 166.1 (C16), 158.8 (C10), 149.4 (C12), 131.5 (C7), 131.1 (C14), 131.0 (C5), 128.7 (C8), 119.2 (C15), 116.9 (C6), 114.2 (C9), 111.0 (C13), 55.1 (C11), 51.5 (C17), 39.1 (C3), 38.7 (C2), 37.7 (C4).

IR (KBr), vmax (cm^{-1}): 3344 (*st* N-H), 3220, 3098 (*st* Csp^2-H), 2955 (*st* C-H), 2218 (*st* C≡N), 1708 (*st* C=O), 1689 (*st* C=N), 1602 (*st* C=O), 1535, 1514, 1253, 1167, 1100, 850, 831

MS (70 eV, EI) m/z (%): 393.1 (24%), 392.2 (100%), 391.2 (24%), 285.1 (54%), 242.1 (20%), 227.1 (33%), 161.0 (64%), 120.0 (25%), 77.1 (25%), 57.1 (25%), 43.1 (36%).

6-oxo-5-phenyl-2-(2-phenylhydrazono)piperidine-3-carbonitrile (76{*3*,*1*,*3*})

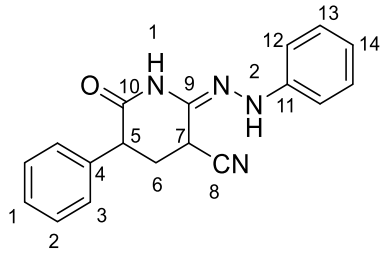

Starting from 2-methoxy-5-phenyl-6-oxo-1,4,5,6-tetrahydropyridine-3-carbonitrile (**62**{*3*,*1*}) and phenylhydrazine (**56**{*3*}). 26% yield, white solid.

^{1}H-NMR (400 MHz, DMSO-d_6): δ 10.25 (s, 1H, N1-H), 9.10 (s, 1H, N2-H), 7.31 (m, 2H, C2-H), 7.21 (m, 3H, C1-H, C3-H), 7.19 (m, 2H, C13-H), 6.97 (m, 2H, C12-H), 6.70-6.74 (m, 1H, C14-H), 4.50 (dd, J = 12.8, 4.2 Hz, 1H, C7-H), 3.91 (m, 1H, C5-H), 2.56 (q, J = 12.7 Hz, 1H, C6-H), 2.42 (ddd, J = 12.4, 5.3, 4.2 Hz, 1H, C6-H).

^{13}C-NMR (100 MHz, DMSO-d_6): δ 170.7 (C10), 146.2 (C9), 139.1, 129.5 (C13), 129.3 (C3), 129.2, 128.7 (C2), 127.5 (C1), 119.1 (C14), 118.3 (C8), 112.1 (C12), 47.5 (C5), 31.4 (C6) 31.4 (C7).

IR (KBr), νmax (cm^{-1}): 3349 (*st* N-H), 3204, 3073 (*st* Csp^2-H), 2254 (*st* C≡N), 1685 (*st* C=O), 1535, 701 (*b* Csp^2-H).

Elemental analysis: calculated for $C_{18}H_{16}N_4O$: C: 71.04%, H: 5.30%, N: 18.41%; Found: C: 71.17%, H: 5.31%, N: 18.26%.

4-(4-methoxyphenyl)-6-oxo-2-(2-phenylhydrazono)piperidine-3-carbonitrile (76{*1,4,3*})

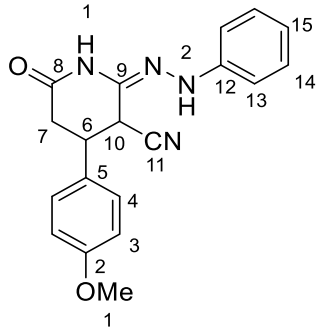

Starting from 2-methoxy-4-(4-methoxyphenyl)-6-oxo-1,4,5,6-tetrahydropyridine-3-carbonitrile (**62**{*1,4*}) and phenylhydrazine (**56**{*3*}). 70 % yield, white solid.

^{1}H-NMR (400 MHz, DMSO-d_6): δ 10.29 (s, 1H, N1-H), 9.09 (s, 1H, N2-H), 7.32 (d, J = 8.7 Hz, 2H, C4-H), 7.18 (dd, J = 8.5, 7.2 Hz, 2H, C14-H), 6.95 (m, 4H, C3-H, C13-H), 6.71 (m, 1H, C15-H), 4.61 (d, J = 12.0 Hz, 1H, C10-H), 3.74 (s, 3H, C1-H_3), 3.51 (td, J = 12.1, 4.5 Hz, 1H, C6-H), 2.83 (dd, J = 17.3, 12.3 Hz, 1H, C7-H), 2.59 (dd, J = 17.3, 4.5 Hz, 1H, C7-H).

^{13}C-NMR (100 MHz, DMSO-d_6): δ 169.2 (C8), 159.2 (C2), 146.1 (C9), 132.1, 129.5, 129.1, 129.0 (C4), 119.2 (C15), 117.5 (C11), 114.6, 112.2, 55.5 (C1), 39.6 (C6), 39.2 (C7), 38.2 (C10).

IR (KBr), vmax (cm^{-1}): 3343 (*st* N-H), 3214 (*st* Csp^2-H), 2255 (*st* C≡N), 1688 (*st* C=O), 1535, 1516, 1499, 691 (*b* Csp^2-H).

Elemental analysis: calculated for $C_{19}H_{18}N_4O_2$: C: 68.25%, H: 5.43%, N: 16.76%; Found: C: 68.25%, H: 5.39%, N: 16.72%.

5-methoxy-6-oxo-2-(2-phenylhydrazono)piperidine-3- carbonitrile (76{*2,1,3*})

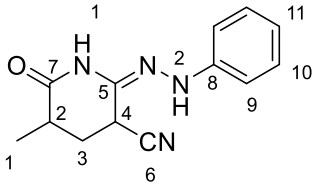

Starting from 2-methoxy-5-methyl-6-oxo-1,4,5,6-tetrahydropyridine-3-carbonitrile (**62**{*1,4*}) and phenylhydrazine (**56**{*3*}). 60 % yield, white solid.

^{1}H-NMR (400 MHz, DMSO-d_6): δ 10.04 (s, 1H, N1-H), 9.01 (s, 1H, N2-H), 7.17 (m, 2H, C9-H), 6.95 (m, 2H, C10-H), 6.68-6.70 (m, 1H, C11-H), 4.34 (dd, J = 13.0, 4.1 Hz, 1H, C4-H), 2.60 (ddd, J = 12.3, 7.1, 5.2 Hz, 1H, C3-H), 2.31 (ddd, J = 12.6, 5.2, 4.2 Hz, 1H, C2-H), 1.96 (q, J = 12.7 Hz, 1H, C3-H), 1.13 (d, J = 7.0 Hz, 3H, C1-H).

^{13}C-NMR (100 MHz, DMSO-d_6): δ 172.4 (C7), 146.2 (C6), 129.5, 129.5 (C9), 119.1 (C11), 118.6, 112.1 (C10), 35.6 (C3), 31.3 (C2), 31.1 (C4), 15.7 (C1).

IR (KBr), vmax (cm^{-1}): 3329, 3249 (*st* N-H), 3103 (*st* Csp^2-H) 2990-2874, 1697 (*st* C=O)

Elemental analysis: calculated for $C_{13}H_{14}N_4O$: C: 64.45%, H: 5.82%, N: 23.13%; Found: C: 64.72%, H: 5.90%, N: 23.18%.

6.1.3.5 Synthesis of 3-amino-2,4,5,7-tetrahydro-6*H*-pyrazolo[3,4-*b*]pyridin-6-ones

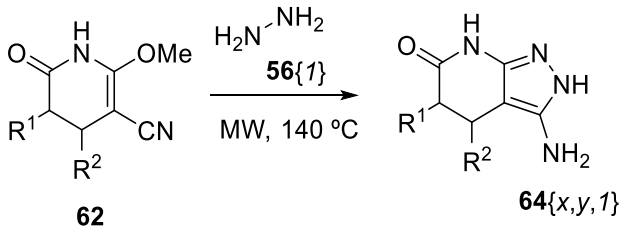

62 **64**{*x*,*y*,*1*}

A mixture of 0.60 mmol of 2-methoxy-6-oxo-1,4,5,6-tetrahydropyridine-3-carbonitrile (**62**) and 1.20 mmol of hydrazine monohydrate (**56**{*1*}) in 4 mL of methanol was heated under microwave irradiation at 140 °C for 30 minutes. The solvent was removed under reduced pressure, the residue was dissolved in the minimum amount of methanol and precipitated with ether. The solid was filtered, washed with ether and dried *in vacuo* over P_2O_5 to yield the corresponding 3-amino-2,4,5,7-tetrahydro-6H-pyrazolo[3,4-*b*]pyridin-6-ones (**64**{*x*,*y*,*1*}).

3-amino-5-methyl-2,4,5,7-tetrahydro-6*H*-pyrazolo[3,4-*b*]pyridin-6-one (64{*2*,*1*,*1*})

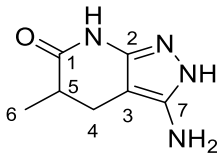

Starting from 2-methoxy-5-methyl-6-oxo-1,4,5,6-tetrahydropyridine-3-carbonitrile (**62**{*2*,*1*}).
36% yield, white solid.

mp: 246 °C

^{1}H-NMR (400 MHz, DMSO-d$_6$) δ 10.64 (s, 1H, N-H), 9.83 (s, 1H, N-H), 4.95 (s, 2H, N-H_2), δ 2.62 (dd, J = 14.8, 6.8 Hz, 1H, C4-H), 2.46-2.36 (m, 1H, C5-H), 2.12 (dd, J = 14.9, 9.6 Hz, 1H, C4-H*), 1.08 (d, J = 7.0 Hz, 3H, C6-H).

^{13}C-NMR (100 MHz, DMSO-d$_6$) δ 174.3 (C1), 148.7 (C7), 144.1 (C2), 82.9 (C3), 36.4 (C5), 23.8 (C4), 16.8 (C6).

IR (KBr) vmax (cm^{-1}): 3403 (*st* N-H), 3335 (*st* Csp^2-H), 3227, 2930, 1692 (st C=O), 1644, 1558, 1540, 1466, 1380, 1286, 798, 712.

MS (70 eV, EI): m/z (%): 166.1 (100%), 111.1 (40%), 110.1 (67%), 109.2 (29%), 68.1 (29%), 43.2 (32%).

HRMS (EI) m/z calculated for $C_7H_{10}N_4O$ $[M]^+$: 166.0859; found: 166.0855

3-amino-5-phenyl-2,4,5,7-tetrahydro-6*H*-pyrazolo[3,4-*b*]pyridin-6-one (64{*3*,*1*,*1*})

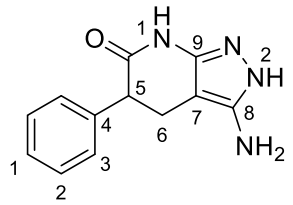

Starting from 2-methoxy-5-phenyl-6-oxo-1,4,5,6-tetrahydropyridine-3-carbonitrile (**62**{*3*,*1*}). 72% yield, white solid.

mp: > 250 °C

^{1}H-NMR (400 MHz, DMSO-d_6): δ 10.63 (s, 1H, N2-H), 10.11 (s, 1H, N1-H), 7.26 (m, 2H, C2-H), 7.20(m, 3H, C1-H, C3-H), 4.93 (s, 2H, NH_2), 3.68 (t, J=7.2 Hz, 1H, C5-H), 2.81 (dd, J = 15.1, 6.9 Hz, 1H, C6-H), 2.64 (dd, J = 15.1, 7.6 Hz, 1H, C6-H).

^{13}C-RMN (100 MHz, DMSO-d_6): δ 171.0 (C10), 148.2 (C9), 143.8 (C8), 141.0 (C4), 128.2 (C2), 128.1 (C3), 126.6 (C1), 81.9 (C7), 47.6 (C5), 24.1 (C6).

IR (KBr), vmax (cm^{-1}): 3348 (*st* N-H), 3230, 1656 (*st* C=O), 1619, 1561, 1381, 701 (*b* Csp^2-H).

MS (70 eV, EI) m/z (%): 228.1 (100%), 137.0 (29%), 110.1 (54%).

3-amino-5-(4-methoxyphenyl)-2,4,5,7-tetrahydro-6*H*-pyrazolo[3,4-*b*]pyridin-6-one (64{*4*,*1*,*1*})

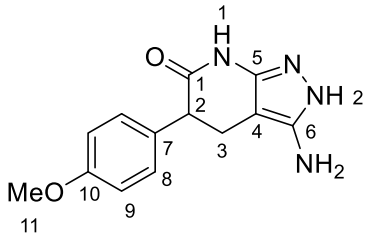

Starting from 2-methoxy-5-(4-methoxyphenyl)-6-oxo-1,4,5,6-tetrahydropyridine-3-carbonitrile (**62**{*4*,*1*}). 27% yield, white solid.

mp: > 250 °C

^{1}H-NMR (400 MHz, DMSO-d_6): δ 10.62 (s, 1H, NH), 10.06 (s, 1H, NH), 7.15 – 7.09 (m, 2H, C8-H), 6.86 – 6.80 (m, 2H, C9-H), 4.93 (s, 2H, NH_2), 3.71 (s, 3H, C11-H_3), 3.62 (t, J = 7.1 Hz, 1H, C2-H), 2.79 (dd, J = 15.0, 6.7 Hz, 1H, C3-H), 2.62 (dd, J = 14.9, 7.2 Hz, 1H, C3-H).

^{13}C-RMN (100 MHz, DMSO-d_6): δ 171.2 (C1), 157.9 (C10), 148.3, 143.6, 132.8 (C7), 129.0 (C8), 113.5 (C9), 81.9 (C4), 55.0 (C11), 46.7 (C2), 24.0 (C3).

IR (KBr), νmax (cm^{-1}): 3338 (*st* N-H), 3278 (*st* Csp^2-H), 1661 (*st* C=O), 1641, 1512 (*st* C=C), 1243 (*st* C-O), 830.

Elemental analysis: calculated for $C_{13}H_{14}N_4O_2$: C: 60.45%, H: 5.46%, N: 21.69%, Cl: O: 12.39%; found: C: 60.70%, H: 5.17%, N: 21.77%.

MS (70 eV, EI) m/z (%): 258.1 (100%), 257.1 (48%), 148.1 (24%), 110.1 (25%), 96.1 (24%), 69.1 (30%).

3-amino-5-(3,4,5-trimethoxyphenyl)-2,4,5,7-tetrahydro-6*H*-pyrazolo[3,4-*b*]pyridin-6-one (64{*5*,*1*,*1*})

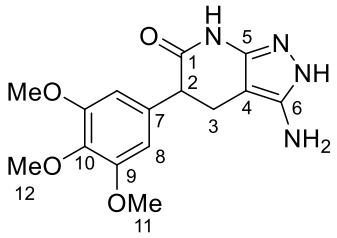

Starting from 2-methoxy-5-(3,4,5-trimethoxyphenyl)-6-oxo-1,4,5,6-tetrahydropyridine-3-carbonitrile (**62**{*5*,*1*}). 56% yield, red-brown solid.

mp: 208-213 °C

^{1}H-NMR (400 MHz, DMSO-*d*$_6$): δ 10.64 (s, 1H, NH), 10.08 (s, 1H, NH), 6.54 (s, 2H, C8-H), 4.96 (s, 2H, NH_2), 3.70 (s, 6H, C11-H_3), 3.63 (s, 3H, C12-H_3), 3.66 – 3.59 (m, 1H, C2-H), 2.79 (dd, J = 15.1, 6.8 Hz, 1H, C3-H), 2.69 (dd, J = 15.1, 8.2 Hz, 1H, C3-H).

^{13}C-RMN (100 MHz, DMSO-*d*$_6$): δ 170.9 (C1), 152.5 (C9), 148.7, 144.0, 136.4 (C7), 136.2, 105.7 (C8), 82.1 (C4), 59.9 (C12), 55.8 (C11), 47.8 (C2), 23.9 (C3).

IR (KBr) νmax (cm^{-1}): 3343 (*st* N-H), 2938, 1664 (*st* C=O), 1591 (*st* C=C), 1508, 1460, 1125 (*st* C-O)

MS (70 eV, EI) m/z (%): 252.1 (55%), 240.1 (58%), 208.1 (51%), 195.1 (100%), 193.1 (79%), 181.1 (99%), 98.1 (58%), 74.1 (53%), 59.0 (52%).

HRMS (APCI) m/z: calculated for $C_{15}H_{19}N_4O_4$ $[M+1]^+$: 319.1401, found: 319.1399.

3-amino-5-(4-fluorophenyl)-2,4,5,7-tetrahydro-6*H*-pyrazolo[3,4-*b*]pyridin-6-one (64{*6*,*1*,*1*})

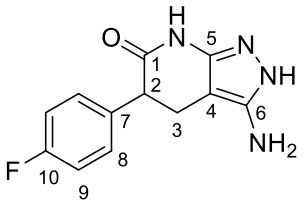

Starting from 2-methoxy-5-(4-fluoroyphenyl)-6-oxo-1,4,5,6-tetrahydropyridine-3-carbonitrile (**62**{*6*,*1*}). 39% yield, white solid.

mp: > 250 °C

^{1}H-NMR (400 MHz, DMSO-*d*$_6$): δ 10.65 (s, 1H, NH), 10.13 (s, 1H, NH), 7.30 – 7.21 (m, 2H, C8-H), 7.15 – 7.07 (m, 2H, C9-H), 3.73 (t, J = 7.6 Hz, 1H, C2-H), 2.81 (dd, J = 15.0, 6.8, 1H, C3-H), 2.68 - 2.58 (m, 1H, C3-H)).

^{13}C-RMN (100 MHz, DMSO-*d*$_6$): δ 170.8 (C1), 161.0 (d, J = 242.1 Hz, C10), 148.3, 143.6, 137.1 (d, J = 3.1 Hz, C7), 130.0 (d, J = 8.0 Hz, C8), 114.8 (d, J = 21.0 Hz, C9), 81.9 (C4), 46.8 (C2), 24.1 (C3).

IR (KBr), νmax (cm^{-1}): 3361 (*st* N-H), 3233, 1655 (*st* C=O), 1563 (*st* C=C), 1510, 1219 (*st* C-O), 838, 521.

MS (70 eV, EI) m/z (%): 246.1 (100%), 245.1 (23%), 137.0 (22%), 111 (20%), 110.0 (33%), 96.0 (23%), 43.1 (21%).

HRMS (APCI) m/z: calculated for $C_{12}H_{12}FN_4O$ $[M+1]^+$: 247.0990; found: 247.0988.

3-amino-5-(2,6-dichlorophenyl)-2,4,5,7-tetrahydro-6*H*-pyrazolo[3,4-*b*]pyridin-6-one (64{*7*,*1*,*1*})

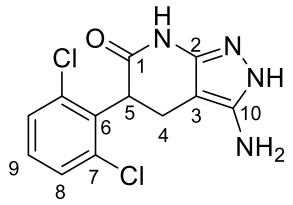

Starting from 2-methoxy-5-(2,6-dichlorophenyl)-6-oxo-1,4,5,6-tetrahydropyridine-3-carbonitrile (**62**{*7*,*1*}). Quantitative yield, white solid.

mp: 194 °C

^{1}H-NMR (400 MHz, DMSO-d_6) δ 10.72 (s, 1H, NH), 10.24 (s, 1H, NH), 7.53 – 7.49 (m, 1H, C8'-H), 7.49 – 7.45 (m, 1H, C8-H), 7.41 – 7.26 (m, 1H, C9-H), 5.01 (s, 2H, NH_2), 4.43 (dd, *J* = 11.8, 9.2 Hz, 1H, C5-H), 2.85 – 2.68 (m, 2H, C4-H).

^{13}C-NMR (100 MHz, DMSO-d_6) δ 168.3 (C1), 147.8 (C2), 143.8 (C10), 136.7 (C6), 134.9 (C7), 129.6 (C8), 129.3 (C9), 128.1 (C8'), 80.4 (C3), 44.2 (C5), 21.6 (C4).

IR (KBr), vmax (cm^{-1}): 3418.37 (*st* N-H), 1652.63 (*st* C=O), 1560.06, 1536.74, 1434.79, 1378.76, 775.37, 582.85.

MS (70 eV, EI) m/z (%): 296, 261 (100%), 137, 123, 110.

3-amino-5-(4,6-dichlorophenyl)-2,4,5,7-tetrahydro-6*H*-pyrazolo[3,4-*b*]pyridin-6-one (64{*8*,*1*,*1*})

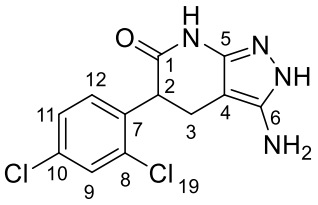

Starting from 2-methoxy-5-(2,6-dichlorophenyl)-6-oxo-1,4,5,6-tetrahydropyridine-3-carbonitrile (**62**{*8*,*1*}). 28% yield, white solid.

mp: > 250 °C

^{1}H-NMR (400 MHz, DMSO-d_6) δ 10.71 (s, 1H, NH), 10.29 (s, 1H, NH), 7.64 – 7.58 (m, 1H, C9-H), 7.42 – 7.33 (m, 2H, C11-H, C12-H), 4.99 (s, 2H, NH_2), 4.05 (dd, J = 10.9, 7.5 Hz, 1H, C2-H), 2.80 (dd, J = 14.4, 7.8 Hz, 1H, C3-H), 2.65 (dd, J = 14.8, 10.9 Hz, 1H, C3-H).

^{13}C-NMR (100 MHz, DMSO-d_6) δ 169.3 (C1), 148.1, 143.7, 137.5 (C8), 134.1 (C10), 132.0, 131.9, 128.8 (C9), 127.3, 81.4 (C4), 45.1 (C2), 23.1 (C3).

IR (KBr), vmax (cm^{-1}): 3464 (st N-H), 3359, 3213 (*st* Csp^2-H), 2925, 1664 (*st* C=O), 1641, 1559, 1532, 1474, 807.

Elemental analysis: calculated for $C_{12}H_{10}Cl_2N_4O$: C: 48.51%, H: 3.39%, N: 18.86%; found: C: 48.58%, H: 3.22%, N: 18.65%.

MS (70 eV, EI) m/z (%): 298.1 (40%), 296.1 (62%), 263.1 (33%), 261.1 (100%), 218.0 (33%), 174.0 (21%), 137.1 (43%), 123.0 (20%), 111.1 (41%), 110.1 (51%), 43.1 (26%).

3-amino-4-phenyl-2,4,5,7-tetrahydro-6*H*-pyrazolo[3,4-*b*]pyridin-6-one (64{*1*,*3*,*1*})

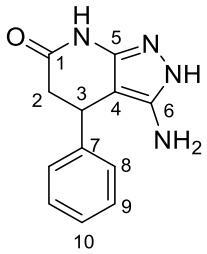

Starting from 2-methoxy-4-phenyl-6-oxo-1,4,5,6-tetrahydropyridine-3-carbonitrile (**62**{*1*,*3*}). 32% yield, white solid.

mp: > 250 °C

^{1}H-NMR (400 MHz, DMSO-d_6) δ 10.71 (s, 1H, NH), 10.04 (s, 1H, NH), 7.31 – 7.23 (m, 2H, C9), 7.20 – 7.13 (m, 3H, C8, C10), 4.80 (s, 2H, NH_2), 4.09 (dd, J = 7.3, 3.1 Hz, 1H, C3-H), 2.84 (dd, J = 15.8, 7.4 Hz, 1H, C2-H), 2.46 (dd, J = 15.6, 2.9 Hz, 1H, C2-H).

^{13}C-NMR (100 MHz, DMSO-d_6) δ 169.6 (C1), 148.3 (C7), 144.6, 143.8, 128.3 (C9), 126.7 (C8), 126.2 (C10), 85.7 (C4), 40.4 (C2), 32.7 (C3).

IR (KBr), vmax (cm^{-1}): 3403 (*st* N-H), 3320 (*st* Csp^2-H), 3150, 3085, 2921, 2797, 1641 (*st* C=O), 1559, 1539, 1362, 701.

MS (70 eV, EI) m/z (%): 228.1 (100%), 185.1 (39%), 151.1 (81%).

3-amino-4-methyl-2,4,5,7-tetrahydro-6*H*-pyrazolo[3,4-*b*]pyridin-6-one (64{*1,2,1*})

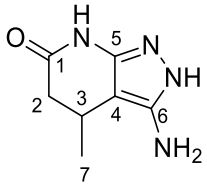

Starting from 2-methoxy-4-methyl-6-oxo-1,4,5,6-tetrahydropyridine-3-carbonitrile (**62**{*1,2*}). 89% yield, white solid.

mp: > 250 °C

^{1}H-NMR (400 MHz, DMSO-d_6): δ 10.56 (s, 1H, NH), 9.88 (s, 1H, NH), 4.87 (s, 2H, NH_2), 2.87 (dd, *J* = 6.8, 4.6 Hz, 1H, C3-H), 2.54 – 2.47 (dd, *J* = 15.7, 6.8 Hz, 1H, C2-H), 2.10 (dd, *J* = 15.7, 4.6 Hz, 1H, C2-H), 1.03 (d, *J* = 6.8 Hz, 3H, C7-H_3).

^{13}C-NMR (100 MHz, DMSO-d_6): δ 170.6 (C1), 148.2, 143.7, 88.5 (C4), 40.8 (C2), 22.9 (C3), 21.3 (C7).

IR (KBr) vmax (cm^{-1}): 3439 (*st* N-H), 3380 (*st* N-H), 1631, 1680 (*st* C=O).

MS (70 eV, EI) m/z (%): 166.2 (71%), 152.1 (23%), 151.1 (100%), 148.2 (25%), 136.1 (29%), 109.1 (20%), 95.1 (21%), 93.1 (22%), 81.1 (24%), 69.1 (25%), 68.1 (22%), 67.1 (27%), 66.1 (33%), 54.1 (21%), 53.1 (20%), 52.1 (28%), , 44.1 (20%), 43.1 (48%), 42.1 (41%), 41.1 (43%).

6.1.3.6 Synthesis of 3-amino-2,4,5,7-tetrahydro-6*H*-pyrazolo[3,4-*b*]pyridin-6-ones

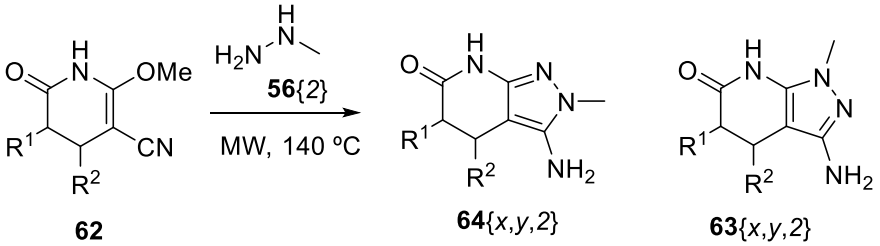

62 **64**{*x*,*y*,*2*} **63**{*x*,*y*,*2*}

A mixture of 0.60 mmol of 2-methoxy-6-oxo-1,4,5,6-tetrahydropyridine-3-carbonitrile (**62**) and 1.20 mmol of methylhydrazine (**56**{*2*}) in 4 mL of methanol was heated under microwave irradiation at 140 °C for 30 minutes. The solvent was removed under reduced pressure and the crude was purified by column chromatography (Al_2O_3 column. $CHCl_3$:MeOH gradient from 0% to 3% in 30 minutes) to yield to two separated isomers 2-methyl-3-amino-2,4,5,7-tetrahydro-6*H*-pyrazolo[3,4-*b*]pyridin-6-ones (**64**{*x*,*y*,*2*}) and 1-methyl-3-amino-2,4,5,7-tetrahydro-6*H*-pyrazolo[3,4-*b*]pyridin-6-ones (**63**{*x*,*y*,*2*}).

3-amino-2,5-dimethyl-2,4,5,7-tetrahydro-6*H*-pyrazolo[3,4-*b*]pyridin-6-one (64{*2*,*1*,*2*})

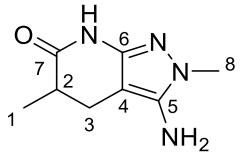

Starting from 2-methoxy-5-methyl-6-oxo-1,4,5,6-tetrahydropyridine-3-carbonitrile (**62**{*2*,*1*}).
56% yield, white solid.

mp: >250°C

^{1}H-NMR (400 MHz, DMSO-d_6) δ 9.87 (s, 1H, NH), 5.11 (s, 2H, NH_2), 3.35 (s, 3H, C8-H_3), 2.62 (dd, J = 14.7, 6.8 Hz, 1H, C3-H), 2.38 (dp, J = 10.0, 6.9 Hz, 1H, C2-H), 2.11 (dd, J = 14.7, 10.0 Hz, 1H, C3-H), 1.07 (d, J = 6.9 Hz, 3H, C1-H_3).

^{13}C-NMR (100 MHz, DMSO-d_6) δ 173.5 (C7), 147.0 (C6), 143.1 (C5) 83.0 (C4), 36.4 (C2), 34.2 (C8), 24.3 (C3), 16.8 (C1).

IR (KBr), vmax (cm^{-1}): 3384 (*st* N-H), 2964, 1651 (*st* C=O), 1557, 1539.

Elemental analysis: calculated for $C_8H_{12}N_4O$: C: 53.32%, H: 6.71%, N: 31.09%; found: C: 53.28%, H: 7.06%, N: 31.06%.

MS (70 eV, EI) m/z (%): 180.1 (100%), 179.15 (26%), 152.1 (22%), 151.1 (24%), 137.1 (26%), 125.1 (36%), 124.1 (62%).

3-amino-1,5-dimethyl-2,4,5,7-tetrahydro-6*H*-pyrazolo[3,4-*b*]pyridin-6-one (63{*2,1,2*})

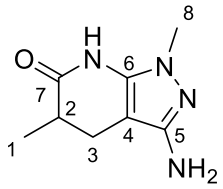

Starting from 2-methoxy-5-methyl-6-oxo-1,4,5,6-tetrahydropyridine-3-carbonitrile (**62**{*2,1*}). 20% yield, white solid.

mp: 219-222 °C

^{1}H-NMR (400 MHz, DMSO-d_6) δ 10.31 (s, 1H, NH), 4.43 (s, 2H, NH_2), 3.35 (s, 3H, C8-H_3), 2.61 (dd, J = 14.8, 7.1 Hz, 1H, C3-H), 2.45 (m, 1H, C2-H), 2.11 (dd, J=14.8, 10,7Hz, 1H, C3-H), 1.09 (d, J = 6.9 Hz, 3H, C1-H_3).

^{13}C-NMR (100 MHz, DMSO-d_6) δ 173.6 (C7), 150.7 (C6), 139.0 (C5) 85.2 (C4), 36.1 (C2), 34.2 (C8), 24.4 (C3), 16.5 (C1).

IR (KBr), vmax (cm^{-1}): 3399 (*st* N-H), 3013, 2973, 2936, 1667 (*st* C=O), 1515.

MS (70 eV, EI) m/z (%): 180.0 (100%), 179.0 (41%), 151.0 (34%), 123.0 (41%).

3-amino-2-methyl-4-phenyl-2,4,5,7-tetrahydro-6*H*-pyrazolo[3,4-*b*]pyridin-6-one (64{*1,3,2*})

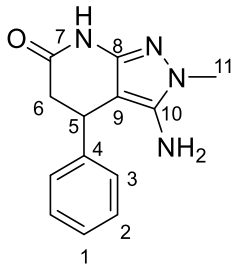

Starting from 2-methoxy-4-phenyl-6-oxo-1,4,5,6-tetrahydropyridine-3-carbonitrile (**62**{*3,1*}). 25% yield, white solid.

mp: 235-240 °C

^{1}H-NMR (400 MHz, DMSO-d_6) δ 10.08 (s, 1H, NH), 7.24 (m, 2H, C2-H), 7.16 (m, 1H, C1-H), 7.13 (m, 2H, C3-H), 5.06 (s, 2H, NH_2), 4.07 (dd, J = 7.4, 2.8 Hz, 1H, C5-H), 3.37 (s, 3H, C11-H_3), 2.84 (dd, J = 15.9, 7.4 Hz, 1H, C6-H), 2.44 (dd, J = 15.9, 2.8 Hz, 1H, C6-H).

^{13}C-NMR (100 MHz, DMSO-d_6) δ 167.0 (C7), 147.0 (C8), 145.0, 143.3, 128.9 (C2), 127.1 (C3), 126.7 (C1), 86.4 (C9), 40.8 (C6), 34.3 (C11), 33.3 (C5).

IR (KBr), vmax (cm^{-1}): 3348 (*st* N-H), 2927, 1669 (*st* C=O), 1562, 1536.

Elemental analysis: calculated for $C_{13}H_{14}N_4O$: C: 64.45%, H: 5.82%, N: 23.13%; found: C: 64.62%, H: 6.11%, N: 23.38%.

MS (70 eV, EI) m/z (%): 242.2 (99%), 199.1 (35%), 165.1 (100%).

3-amino-1-methyl-4-phenyl-2,4,5,7-tetrahydro-6*H*-pyrazolo[3,4-*b*]pyridin-6-one (63{*1*,*3*,*2*})

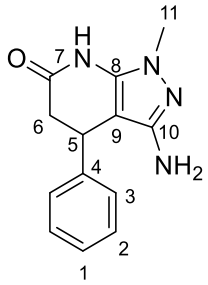

Starting from 2-methoxy-4-phenyl-6-oxo-1,4,5,6-tetrahydropyridine-3-carbonitrile (**62**{*3*,*1*}). 29% yield, white solid.

mp: 204-206 °C

^{1}H-NMR (400 MHz, DMSO-d_6) δ 10.53 (s, 1H, NH), 7.26 (m, 2H, C3-H), 7.17 (m, 1H, C1-H), 7.1 (m, 2H, C2-H), 4.31 (s, 2H, NH_2), 4.07 (dd, J = 7.5, 3.2 Hz, 1H, C5-H), 3.41 (s, 3H, C11-H_3), 2.91 (dd, J = 15.9, 7.6 Hz, 1H, C6-H), 2.53 – 2.49 (dd, J = 15.9, 3.1, 1H, C6-H).

^{13}C-NMR (100 MHz, DMSO-d_6) δ 170.2 (C7), 150.7 (C8), 144.4, 139.2, 128.9 (C3), 127.2 (C2), 126.8 (C1), 88.7 (C9), 40.6 (C6), 34.3 (C11), 33.4 (C5).

IR (KBr), vmax (cm^{-1}): 3438 (*st* N-H), 3178 (*st* Csp^2-H), 1674 (*st* C=O), 1514.

Elemental analysis: calculated for $C_{13}H_{14}N_4O$: C: 64.45%, H: 5.82%, N: 23.13%; found: C: 64.62%, H: 6.11%, N: 23.38%.

MS (70 eV, EI) m/z (%): 242.2 (100%), 241.2 (20%), 199.1 (55%), 165.1 (68%), 77.1 (23%), 57.2 (24%), 44.1 (65%), 43.1 (29%).

3-amino-4-(4-methoxyphenyl)-2-methyl-2,4,5,7-tetrahydro-6*H*-pyrazolo[3,4-*b*]pyridin-6-one (64{*1,4,2*})

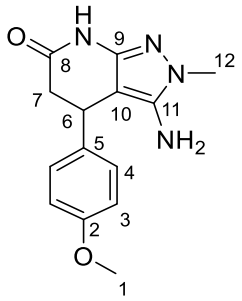

Starting from 2-methoxy-4-(4-methoxyphenyl)-6-oxo-1,4,5,6-tetrahydropyridine-3-carbonitrile (**62**{*4,1*}). 49% yield, white solid.

mp: 172 °C

^{1}H-NMR (400 MHz, DMSO-d_6): δ 10.03 (s, 1H, NH), 7.03 (m, 2H, C4-H), 6.81 (m, 2H, C3-H), 5.00 (s, 2H, NH_2), 4.00 (dd, J = 7.2, 3.1 Hz, 1H, C6-H), 3.68 (s, 3H, C1-H_3), 3.37 (s, 3H, C12-H_3), 2.79 (dd, J = 15.8, 7.3 Hz, 1H, C7-H), 2.40 (dd, J = 15.7, 3.1 Hz, 1H, C7-H).

^{13}C-NMR (100 MHz, DMSO-d_6): δ 170.0 (C8), 158.2 (C2), 146.9, 143.2, 136.8 (C5), 128.1 (C4), 114.2 (C3), 86.8 (C10), 55.5 (C1), 41.1 (C7), 34.3 (C12), 32.6 (C6).

IR (KBr) vmax (cm^{-1}): 3410-3380 (*st* N-H), 3106-2839 (*st* Csp^2-H), 1670 (*st* C=O), 1535, 1510.

Elemental analysis: calculated for $C_{14}H_{16}N_4O_2$: C: 61.75%, H: 5.92%, N: 20.58%; found: C: 61.64%, H: 6.14%, N: 20.46%

MS (70 eV, EI) m/z (%): 272.2 (51%), 192.1 (64%), 165.1 (36%), 161.1 (86%), 134.1 (21%), 133.1 (27%), 74.2 (100%), 73.2 (33%), 57.2 (21%), 57.2 (21%), 45.1 (100%), 44.2 (27%), 43.1 (74%), 42.1 (30%), 41.1 (51%).

3-amino-1-methyl-4-(4-methoxyphenyl)-2,4,5,7-tetrahydro-6*H*-pyrazolo[3,4-*b*]pyridin-6-one (63{*1*,*4*,*2*})

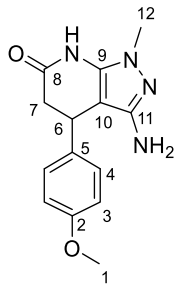

Starting from 2-methoxy-4-(4-methoxyphenyl)-6-oxo-1,4,5,6-tetrahydropyridine-3-carbonitrile (**62**{*4*,*1*}). 23% yield, white solid.

^{1}H-NMR (400 MHz, DMSO-d_6): δ 10.50 (s, 1H, NH), 7.09 (m, 2H, C4-H), 6.82 (m, 2H, C3-H), 4.26 (s, 2H, NH_2), 4.00 (dd, J = 7.4, 3.5 Hz, 1H, C6-H), 3.68 (s, 3H, C1-H_3), 3.41 (s, 3H, C12-H_3), 2.85 (dd, J = 15.8, 7.4 Hz, 1H, C7-H), 2.48 (dd, J = 15.8, 3.6 Hz, 1H, C7-H).

^{13}C-NMR (100 MHz, DMSO-d_6): δ 170.3 (C8), 158.3 (C2), 150.7 (C9), 139.2 (C11), 136.2 (C5), 128.2 (C4), 114.3 (C3), 89.1 (C10), 55.5 (C1), 40.9 (C7), 34.3 (C12), 32.7 (C6).

IR (KBr), vmax (cm^{-1}): 3435, 3297 (*st* N-H), 3177-2831(*st* Csp^2-H), 1666 (*st* C=O), 1513.

MS (70 eV, EI) m/z (%): 272.0 (100%), 271.0 (58%), 229.0 (81%), 165.0 (30%).

3-amino-4-methyl-2-methyl-2,4,5,7-tetrahydro-6*H*-pyrazolo[3,4-*b*]pyridin-6-one (64{*1*,*2*,*2*})

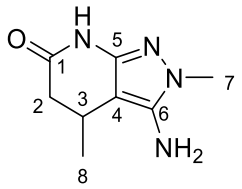

Starting from 2-methoxy-4-methyl-6-oxo-1,4,5,6-tetrahydropyridine-3-carbonitrile (**62**{*2*,*1*}). 56% yield, white solid.

mp: 247 °C

^{1}H-NMR (400 MHz, DMSO-*d*$_6$) δ 9.93 (s, 1H, NH), 5.12 (s, 2H, NH_2), 3.37 (s, 3H, C7-H_3), 2.88 (td, J = 6.8, 3.9 Hz, 1H, C3-H), 2.58 – 2.48 (m, 1H, C2-H), 2.10 (dd, J = 15.8, 3.9 Hz, 1H, C2-H), 1.02 (d, J = 6.8 Hz, 3H, C8-H_3).

^{13}C-NMR (100 MHz, DMSO-*d*$_6$) δ 169.9 (C1), 145.8 (C7), 142.4 (C6), 88.3(C4), 40.2 (C2), 33.7 (C7), 22.7 (C3), 21.0 (C8).

IR (KBr), vmax (cm^{-1}): 3388 (*st* N-H), 3207 (*st* N-H), 2971, 1667 (*st* C=O), 1555, 1538 (*st* C=C), 1365, 1344.

Elemental analysis: calculated for $C_8H_{12}N_4O$: C: 53.32%, H: 6.71%, N: 31.09%; found: C: 53.34%, H: 6.81%, N: 30.78%.

MS (70 eV, EI) m/z (%): 180.2 (36%), 165.2 (100%), 43.1 (16%).

3-amino-2-methyl-5-phenyl-2,4,5,7-tetrahydro-6*H*-pyrazolo[3,4-*b*]pyridin-6-one (64{*3*,*1*,*2*})

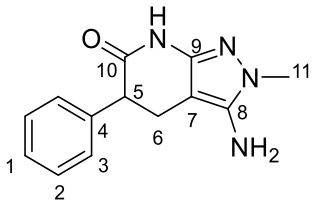

Starting from 2-methoxy-5-phenyl-6-oxo-1,4,5,6-tetrahydropyridine-3-carbonitrile (**62**{*3*,*1*}). 12% yield, white solid.

^{1}H-NMR (400 MHz, DMSO-d_6): δ 10.12 (s, 1H, NH), 7.26 (m, 2H, C2-H), 7.19 (m, 3H, C1-H, C3-H), 5.15 (s, 2H, NH_2), 3.67 (t, J = 7.2 Hz, 1H, C5-H), 3.36 (s, 3H, C11-H_3), 2.80 (dd, J = 15.1, 7.0 Hz, 1H, C6-H), 2.63 (dd, J = 15.1, 7.5 Hz, 1H, C6-H).

^{13}C-NMR (100 MHz, DMSO-d_6): δ 171.3 (C10), 146.9 (C9), 143.2 (C8), 141.4 (C4), 128.6 (C2), 128.5 (C3), 126.9 (C1), 82.5 (C7), 48.0 (C5), 34.3 (C11), 24.7 (C6).

IR (KBr) vmax (cm^{-1}): 3465, 3357 (*st* N-H), 2929, 2848, 1668 (*st* C=O), 1534.

MS (70 eV, EI) m/z (%): 242.0 (100%), 241.0 (73%), 213.0 (29%), 124.0 (25%).

3-amino-1-methyl-5-phenyl-2,4,5,7-tetrahydro-6*H*-pyrazolo[3,4-*b*]pyridin-6-one (63{*3*,*1*,*2*})

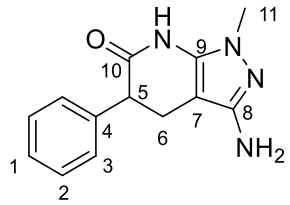

Starting from 2-methoxy-5-phenyl-6-oxo-1,4,5,6-tetrahydropyridine-3-carbonitrile (**62**{*3*,*1*}). 2% yield, white solid.

mp: > 250 °C

^{1}H-NMR (400 MHz, DMSO-d_6): δ 10.60 (s, 1H, NH), 7.28 (m, 2H, C2-H), 7.22 (m, 2H, C3-H), 7.20 (m, 1H, C1-H) 4.49 (s, 2H, NH_2), 3.75 (dd, J = 8.8, 7.2 Hz, 1H, C5-H), 3.39 (s, 3H, C11-H), 2.79 (dd, J = 15.3, 7.2 Hz, 1H, C6-H), 2.64 (dd, J = 15.3, 8.9 Hz, 1H, C6-H).

^{13}C-NMR (100 MHz, DMSO-d_6): δ 171.5 (C10), 150.8 (C9), 140.8 (C8), 138.9 (C4), 128.7 (C3), 128.6 (C2), 127.1 (C1), 85.2 (C7), 47.7 (C5), 34.3 (C11), 24.8 (C6).

IR (KBr) vmax (cm^{-1}): 3405, 3333 (*st* N-H), 3006 (*st* Csp^2-H), 2933, 1665 (*st* C=O), 1511.

MS (70 eV, EI) m/z (%): 242.0 (100%), 213.0 (38%), 124.0 (70%).

3-amino-5-(2,6-dichlorophenyl)-2-methyl-2,4,5,7-tetrahydro-6*H*-pyrazolo[3,4-*b*]pyridin-6-one (64{*7*,*1*,*2*})

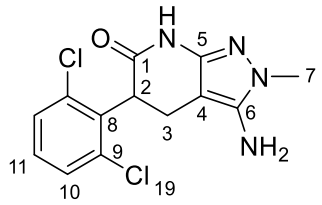

Starting from 2-methoxy-5-(2,6-dichlorophenyl)-6-oxo-1,4,5,6-tetrahydropyridine-3-carbonitrile (**62**{*7*,*1*}). 50% yield, white solid.

56% yield, white solid.

mp: >250°C

^{1}H-NMR (400 MHz, DMSO-d_6) δ 10.25 (s, 1H, NH), 7.53 – 7.45 (m, 2H, C10-H), 7.38 – 7.30 (m, 1H, C11-H), 5.23 (s, 2H, NH_2), 4.43 (dd, J = 11.9, 9.0 Hz, 1H, C2-H), 2.83 – 2.69 (m, 2H, C3-H_2).

^{13}C-NMR (100 MHz, DMSO-d_6) δ 168.2 (C1), 146.0, 143.0 (C6), 136.6 (C8), 134.9 (C9), 129.6 (C10'), 129.4 (C11), 128.1 (C10), 80.7 (C4), 44.1 (C2), 33.8 (C7), 21.9 (C3).

IR (KBr), vmax (cm^{-1}): 3414 (*st* N-H), 3320 (*st* Csp^2-H), 2927, 1662 (*st* C=O), 1536 (*st* C=C), 1331 (*st* C-O)

MS (70 eV, EI) m/z (%): 312.0 (50%), 311.0 (22%), 310.0 (78%), 277.0 (33%), 275.0 (100%), 151.0 (19%), 125.0 (50%), 124.0 (72%), 123.0 (31%).

6.1.3.7 Synthesis of 2-aryl-3-amino-2,4,5,7-tetrahydro-6*H*-pyrazolo[3,4-*b*]pyridin-6-ones

Protocol 1

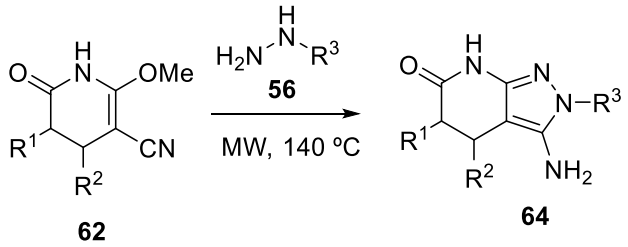

A mixture of 0.60 mmol of 2-methoxy-6-oxo-1,4,5,6-tetrahydropyridine-3-carbonitrile (**62**) and 1.20 mmol of arylhydrazine (**56**) in 4 mL of methanol was heated under microwave irradiation at 140 °C for 30 minutes. The solvent was removed under reduced pressure, the residue was dissolved in the minimum amount of methanol and if necessary precipitated with ether. The solid was filtered, washed with ether and dried *in vacuo* over P_2O_5 to yield the corresponding 3-amino-2,4,5,7-tetrahydro-6*H*-pyrazolo[3,4-*b*]pyridin-6-ones (**64**).

Protocol 2

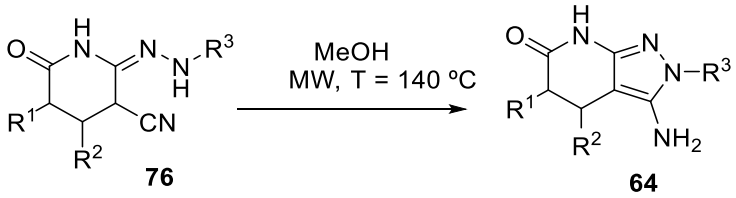

0.30 mmol of 6-oxo-2-(2-arylhydrazono)piperidine-3-carbonitrile (**76**) were dissolved in MeOH (3 mL) and heated at 140 °C for 30 minutes under microwave irradiation. The solvent was removed under reduced pressure and the residue was dissolved in the minimum amount of methanol and precipitated with ether. The solid was filtered, washed with ether and dried *in vacuo* over P_2O_5 to yield the corresponding 3-amino-2,4,5,7-tetrahydro-6*H*-pyrazolo[3,4-*b*]pyridin-6-ones (**64**).

3-amino-5-methyl-2-phenyl-2,4,5,7-tetrahydro-6*H*-pyrazolo[3,4-*b*]pyridin-6-one (64{*2,1,3*})

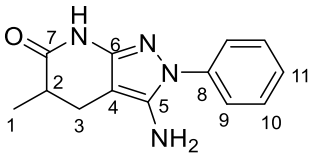

Starting from 2-methoxy-5-methyl-6-oxo-1,4,5,6-tetrahydropyridine-3-carbonitrile (**62**{*2,1*}) and phenylhydrazine (**56**{*3*}). 16% yield, white solid.

mp: > 250 °C

^{1}H-NMR (400 MHz, DMSO-d_6) δ 10.11 (s, 1H, NH), 7.51 (m, 2H, C9-H), 7.40 (m, 2H, C10-H), 7.20 (m, 1H, C11-H), 5.32 (s, 2H, NH_2), 2.75 (dd, J = 14.9, 6.8 Hz, 1H, C2-H), 2.48 (m, 1H, C3-H), 2.21 (dd, J = 15.0, 10.2 Hz, 1H, C3-H), 1.12 (d, J = 6.9 Hz, 3H, C1-H).

^{13}C-NMR (100 MHz, DMSO-d_6) δ 173.6 (C7), 149.5 (C6), 142.8 (C5), 140.1 (C8), 129.4 (C10), 125.5 (C11), 122.3 (C9), 85.8 (C4), 36.1 (C2), 24.1 (C3), 16.8 (C1).

IR (KBr), vmax (cm^{-1}): 3388 (*st* N-H), 3211 (*st* Csp^2-H) 2993 (*st* Csp^3-H), 1673, 1657 (*st* C=O), 1525, 1500.

MS (70 eV, EI) m/z (%): 241.1 (100%), 185.0 (30%).

HRMS (EI) m/z: calculated for $C_{13}H_{14}N_4O$ $[M+1]^+$: 242.1168; Found $[M+1]^+$: 242.1168

3-amino-2,5-diphenyl-2,4,5,7-tetrahydro-6*H*-pyrazolo[3,4-*b*]pyridin-6-one (64{*3,1,3*})

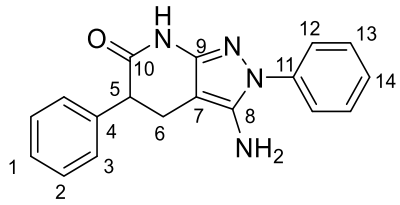

Starting from 2-methoxy-5-phenyl-6-oxo-1,4,5,6-tetrahydropyridine-3-carbonitrile (**62**{*3,1*}) and phenylhydrazine (**56**{*3*}). 56% yield, pale pink solid.

mp: > 250 °C

^{1}H-NMR (400 MHz, DMSO-d_6) δ 10.40 (s, 1H, NH), 7.53 (m, 2H, C12-H), 7.41 (m, 2H, C13-H), 7.27-7.30 (m, 2H, C3-H), 7.23 (m, 4H, C1-H, C2-H, C14-H), 5.38 (s, 2H, NH_2), 3.79 (t, J = 7.5 Hz, 1H, C5-H), 2.92 (dd, J = 15.3, 7.0 Hz, 1H, C6-H), 2.76 (dd, J = 15.3, 8.2 Hz, 1H, C6-H).

^{13}C-NMR (100 MHz, DMSO-d_6) δ 171.5 (C10), 149.4 (C9), 143.0 (C8), 141.1, 140.0, 129.5 (C13), 128.7 (C3), 128.6 (C2), 127.1, 125.6, 122.3 (C12), 85.4 (C7), 47.7 (C5), 24.6 (C6).

IR (KBr), vmax (cm^{-1}): 3404 (*st* N-H), 3330, 1664 (*st* C=O), 1642, 1522, 1500, 699.

Elemental analysis: calculated for $C_{18}H_{16}N_4O$: C: 71.04%, H: 5.30%, N: 18.41%; found: C: 71.11%, H: 5.28%, N: 18.20%.

MS (70 eV, EI) m/z (%): 305.15 (22%), 304.2 (100%), 227.1 (22%), 186.1 (23%).

3-amino-2-phenyl-5-(3,4,5-trimethoxyphenyl)-2,4,5,7-tetrahydro-6*H*-pyrazolo[3,4-*b*]pyridin-6-one (64{*5*,*1*,*3*})

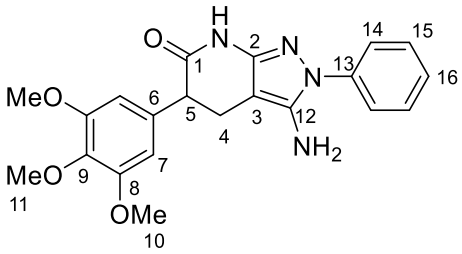

Starting from 2-methoxy-5-(3,4,5-trimethoxyphenyl)-6-oxo-1,4,5,6-tetrahydropyridine-3-carbonitrile (**62**{*5*,*1*}) and phenylhydrazine (**56**{*3*}). 22% yield, brownish solid.

mp: 148 °C

^{1}H-NMR (400 MHz, DMSO-d_6) δ 10.35 (s, 1H, NH), 7.54 – 7.49 (m, 2H, C14-H), 7.45 – 7.38 (m, 2H, C15-H), 7.24 – 7.18 (m, 1H, C16-H), 6.56 (s, 2H, C7-H), 5.39 (s, 2H, NH_2), 3.69 (s, 6H, C10-H_3), 3.63-3.61 (m, 1H, C5-H), 3.62 (s, 3H, C11-H_3), 2.89 (dd, *J* = 15.3, 6.9 Hz, 1H, C4-H), 2.80 (dd, *J* = 15.3, 8.4 Hz, 1H, C4-H).

^{13}C-NMR (100 MHz, DMSO-d_6) δ 171.1 (C1) 152.6 (C2), 149.0 (C8), 142.6 (C12), 139.6 (C13), 136.1 (C9), 133.8 (C6), 129.1 (C15), 125.2 (C16), 121.9 (C14), 105.7 (C7), 85.2 (C3), 60,0 (C11), 55.8 (C10), 47.5 (C5), 23.9 (C4).

IR (KBr), vmax (cm^{-1}): 3429 (*st* N-H), 2939, 2839, 2195, 2170, 1676 (*st* C=O), 1644, 1594, 1500, 1458, 1329, 1126, 1004, 767, 697, 617.

MS (70 eV, EI) m/z (%): 304.1 (24%), 208.1 (100%), 194.1 (43%), 193.1 (91%), 179.1 (36%).

HRMS (APCI) m/z: calculated for $C_{21}H_{23}N_4O_4$ $[M+1]^+$: 395.1714; Found $[M+1]^+$: 395.1713

3-amino-5-(2,6-dichlorophenyl)-2-phenyl-2,4,5,7-tetrahydro-6*H*-pyrazolo[3,4-*b*]pyridin-6-one (64{*7*,*1*,*3*})

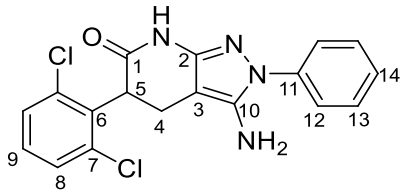

Starting from 2-methoxy-5-(2,6-dichlorophenyl)-6-oxo-1,4,5,6-tetrahydropyridine-3-carbonitrile (**62**{*7*,*1*}) and phenylhydrazine (**56**{*3*}). 60% yield, yellowish solid.

mp: >250°C

^{1}H-NMR (400 MHz, DMSO-d_6) δ 10.55 (s, 1H, NH), 7.57 – 7.54 (m, 2H, C12-H), 7.55 – 7.50 (m, 1H, C8-H), 7.51 – 7-47 (m, 1H, C8'-H), 7.48 – 7.42 (m, 2H, C13-H), 7.38 – 7.33 (m, 1H, C9-H), 7.28 – 7.23 (m, 1H, C14-H), 5.46 (s, 2H, NH_2), 4.54 (dd, *J* = 12.2, 8.7 Hz, 1H, C5-H), 2.94 (dd, *J* = 15.0, 8.8 Hz, 1H, C4-H), 2.82 (dd, *J* = 15.0, 12.3 Hz, 1H, C4-H).

^{13}C-NMR (100 MHz, DMSO-d_6) δ 168.5 (C1), 148.4 (C2), 142.7 (C10), 139.4 (C11), 136.4 (C6), 135.0 (C7), 129.6 (C8'), 129.5 (C9), 129.1 (C13), 128.2 (C8), 125.3 (C14), 122.1 (C12), 83.2 (C3), 43.8 (C5), 21.7 (C4).

IR (KBr), vmax (cm^{-1}): 3384 (*st* N-H), 3320, 3218 (*st* Csp^2-H), 2924, 2863, 1676 (*st* C=O), 1653, 1529, 1499, 1431, 1335, 1267 (*st* C-O), 1117, 891, 777, 684.

Elemental analysis: calculated for $C_{18}H_{14}Cl_2N_4O$: C: 57.93%, H: 3.78%, N: 15.01%; found: C: 57.85%, H: 3.66%, N: 15.00%.

MS (70 eV, EI) m/z (%): 374.1 (66%), 372.1 (100%), 337.1 (87%), 339.1 (29%), 247.0 (21%). 227.1 (32%), 187.1 (40%), 186.0 (66%), 172.0 (32%), 93.05 (29%), 77.05 (61%), 51.05 (21%).

3-amino-5-(4,6-dichlorophenyl)-2-phenyl-2,4,5,7-tetrahydro-6*H*-pyrazolo[3,4-*b*]pyridin-6-one (64{*8*,*1*,*3*})

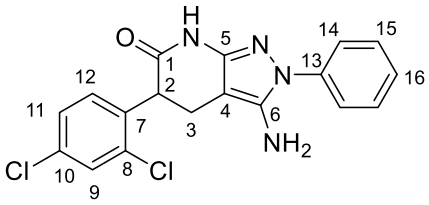

Starting from 2-methoxy-5-(4,6-dichlorophenyl)-6-oxo-1,4,5,6-tetrahydropyridine-3-carbonitrile (**62**{*8*,*1*}) and phenylhydrazine (**56**{*3*}). 33% yield, yellowish solid.

^{1}H-NMR (400 MHz, DMSO-d_6) δ 10.49 (s, 1H, NH), 7.60 – 7.58 (m, 1H), 7.51 – 7.47 (m, 2H), 7.47 – 7.41 (m, 2H), 7.40 – 7.38 (m, 2H), 7.28 – 7.23 (m, 1H), 5.37 (s, 2H, NH_2), 4.13 (dd, J = 11.3, 7.7 Hz, 1H, C2-H), 2.90 (dd, J = 15.0, 7.7 Hz, 1H, C3-H), 2.75 (dd, J = 15.0, 11.4 Hz, 1H, C3-H).

^{13}C-NMR (100 MHz, DMSO-d_6) δ 170.1 (C1), 149.0, 143.0, 139.6, 137.5, 134.7, 132.8, 132.7, 129.7, 129.4, 127.9, 126.2, 122.8, 84.7 (C4), 45.4 (C2), 23.4 (C3).

3-amino-2,4-diphenyl-2,4,5,7-tetrahydro-6*H*-pyrazolo[3,4-*b*]pyridin-6-one (64{*1*,*3*,*3*})

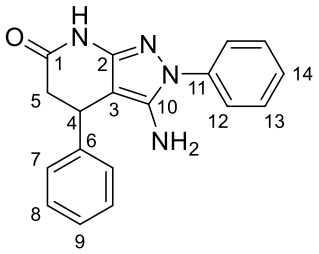

Starting from 2-methoxy-4-phenyl-6-oxo-1,4,5,6-tetrahydropyridine-3-carbonitrile (**62**{*1*,*3*}) and phenylhydrazine (**56**{*3*}). 42% yield, yellowish solid.

mp: 220-222 °C

^{1}H-NMR (400 MHz, DMSO-d_6) δ 10.34 (bs s, 1H, NH), 7.53-7.51 (m, 2H, C12-H), 7.43-7.39 (m, 2H, C13-H), 7.30-7.26 (m, 2H, C8-H), 7.22-7.17 (m, 4H, C7-H, C9-H, C14-H), 5.28 (bs s, 2H, NH_2), 4.22 (dd, *J* = 7.5, 2.7 Hz, 1H, C4-H), 2.95 (dd, *J* = 15.9, 7.4 Hz, 1H, C5-H), 2.50 (dd, *J* = 15.9, 2.7, 1H, C5-H).

^{13}C-NMR (100 MHz, DMSO-d_6) δ 170.2 (C7), 149.4 (C8), 144.7 (C10), 143.2, 139.9, 129.5 (C13), 128.9 (C2), 127.2 (C3), 126.8, 125.7, 122.5 (C12), 88.9 (C9), 40.6 (C6) 33.0 (C5).

IR (KBr), vmax (cm^{-1}): 3421 (*st* N-H), 3205 (*st* Csp^2-H), 1662 (*st* C=O), 1637, 1519, 1499, 695.

Elemental analysis: calculated for $C_{18}H_{16}N_4O$: C: 71.04%, H: 5.30%, N: 18.41%, found: C: 71.37%, H: 5.23%, N: 18.30%.

MS (70 eV, EI) m/z (%): 305.1 (30%), 304.1 (100%), 303.0 (40%), 227.0 (50%).

3-amino-4-methyl-2-phenyl-2,4,5,7-tetrahydro-6*H*-pyrazolo[3,4-*b*]pyridin-6-one (64{*1*,*2*,*3*})

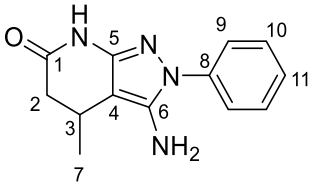

Starting from 4-methyl-6-oxo-2-(2-phenylhydrazono)piperidine-3-carbonitrile (**76**{*1*,*2*,*3*}). Quantitative yield, yellow solid.

mp: 82-86 °C

^{1}H-NMR (400 MHz, DMSO-d_6) δ 10.20 (br s, 1H, NH), 7.53 (m, 2H, C9-H), 7.43 (m, 2H, C10-H), 7.23 (m, 1H, C11-H), 5.34 (br s, 2H, NH_2), 3.03 (dd, *J* = 6.9, 3.3 Hz, 1H, C3-H), 2.65 (dd, *J* = 15.9, 6.9 Hz, 1H, C2-H), 2.19 (dd, *J* = 15.9, 3.2 Hz, 1H, C2-H), 1.08 (d, *J* = 6.8 Hz, 3H, C7-H_3).

^{13}C-NMR (100 MHz, DMSO-d_6) δ 170.2 (C1), 148.3, 142.2, 139.6 (C8), 129.0 (C10), 125.2 (C11), 122.1 (C9), 90.9 (C4), 39.8 (C2), 22.4 (C3), 21.0 (C7).

IR (KBr), vmax (cm^{-1}): 3328 - 3211 (*st* N-H), 3150 (*st* Csp^2-H), 2960 (*st* C-H), 1669, 1640, 1598 (*st* C=O), 1549, 1523, 1499 - 1457 (*st* Csp^2-Csp^2), 1358, 1306, 762, 697.

Elemental analysis: calculated for $C_{13}H_{14}N_4O$: C: 64.45%, H: 5.82%, N: 23.13%; found: C: 64.06%, H: 5.97%, N: 22.80%.

MS (70 eV, EI) m/z (%): 242.1 (45%), 227.1 (100%), 77.0 (23%).

3-amino-4-(4-methoxyphenyl)-2-phenyl-2,4,5,7-tetrahydro-6*H*-pyrazolo[3,4-*b*]pyridin-6-one (64{*1,4,3*})

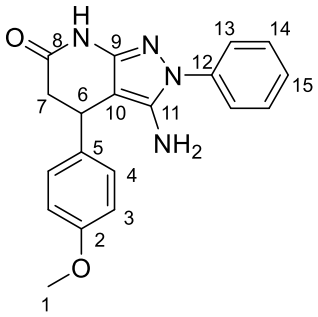

Starting from 4-(4-methoxyphenyl)-6-oxo-2-(2-phenylhydrazono)piperidine-3-carbonitrile (**76**{*1,4,3*})**.** 97% yield, white solid.

mp: 158-162 °C

^{1}H-NMR (400 MHz, DMSO-d_6) δ 10.32 (bs s, 1H, NH), 7.54-7.51 (m, 2H, C13-H), 7.43-7.39 (m, 2H, C14-H), 7.23-7.19 (m, 2H, C4-H), 7.12-7.10 (m, 2H, C3-H), 6.86-6.83 (m, 1H, C15-H), 5.23 (bs s, 2H, NH_2), 4.17 (dd, *J* = 7.2, 3.0 Hz, 1H, C6-H), 3.69 (s, 3H, C1-H_3), 2.90 (dd, *J* = 15.9, 7.3 Hz, 1H, C7-H), 2.48 (dd, *J* = 15.9, 3.0 Hz, 1H, C7-H).

^{13}C-NMR (100 MHz, DMSO-d_6) δ 170.3 (C8), 158.3 (C2), 149.4, 143.1, 139.9, 136.5, 129.5 (C14), 128.2 (C3), 125.7 (C4), 122.5 (C13), 114.3 (C15), 89.3 (C10), 55.5 (C1), 40.8 (C7), 32.3 (C6).

IR (KBr), vmax (cm^{-1}): 3434, 3326 (*st* N-H), 2965, 2836 (*st* Csp2-H), 1674, 1637 (*st* C=O), 1510, 1498, 699 (*b* Csp^2-H).

Elemental analysis: calculated for $C_{19}H_{18}N_4O_2$: C: 68.25%, H: 5.43%, N: 16.76%; found: C: 68.35%, H: 5.73%, N: 16.54%.

MS (70 eV, EI) m/z (%): 335.1 (21%), 334.1 (90%), 333.1 (28%), 227.0 (38%), 63.0 (100%).

Methyl 4-(3-amino-5-methyl-6-oxo-4,5,6,7-tetrahydro-2*H*-pyrazolo[3,4-*b*]pyridin-2-yl)benzoate (64{*2*,*1*,*8*})

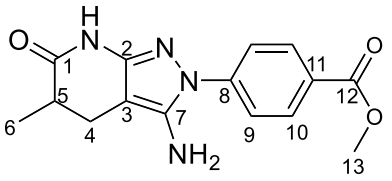

Starting from 2-methoxy-5-methyl-6-oxo-1,4,5,6-tetrahydropyridine-3-carbonitrile (**62**{*2*,*1*}) and methyl 4-hydrazinylbenzoate (**56**{*8*}). 24% yield, white solid.

mp: > 250 °C

^{1}H-NMR (400 MHz, DMSO-d_6) δ 10.23 (s, 1H, NH), 8.00 – 7.93 (m, 2H, C10-H), 7.75 – 7.67 (m, 2H, C9-H), 5.55 (s, 2H, NH_2), 3.83 (s, 3H, C13-H_3), 2.77 (dd, *J* = 15.1, 6.8 Hz, 1H, C4-H), 2.55 – 2.48 (1H, m, C5-H), 2.23 (1H, dd, *J* = 15.1, 10.2 Hz, C4-H), 1.12 (3H, d, *J* = 6.9 Hz, C6-H_3).

^{13}C-NMR (100 MHz, DMSO-d_6) δ 173.7 (C1), 166.2 (C12), 150.5 (C2), 144.2 (C8), 143.6 (C7), 130.7 (C10), 125.5 (C11), 120.8 (C9), 87.1 (C3), 52.5 (C13), 36.0 (C5), 24.0 (C4), 16.8 (C6).

IR (KBr), vmax (cm^{-1}): 3386.29 (*st* N-H), 3142.06 (*st* Csp^2-H), 2932.87, 2843.72, 1708.30 (*st* C=O), 1666.58 (*st* C=O), 1603.18, 1512.74, 1512.74, 1281.97 (*st* C-O), 1118.49, 770.74.

MS (70 eV, EI) m/z (%): 301.2 (21%), 300.2 (100%), 244.1 (22%), 120.1 (22%).

HRMS (APCI) m/z: calculated for $C_{15}H_{17}N_4O_3$ $[M+1]^+$: 301.1295; Found $[M+1]^+$: 301.1297

3-amino-5-(2,6-dichlorophenyl)-2-(4-fluorophenyl)-2,4,5,7-tetrahydro-6*H*-pyrazolo[3,4-*b*]pyridin-6-one (64{*7*,*1*,*4*})

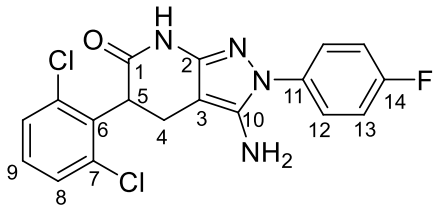

Starting from 2-methoxy-5-(2,6-dichlorophenyl)-6-oxo-1,4,5,6-tetrahydropyridine-3-carbonitrile (**62**{*7*,*1*}) and (4-fluorophenyl)hydrazine (**56**{*4*}). 23% yield, white solid.

mp: 235-240 °C

^{1}H-NMR (400 MHz, DMSO-d_6) δ 10.54 (s, 1H, NH) 7.58 – 7.53 (m, 2H, C12-H), 7.53 – 7.50 (m, 1H, C8'-H), 7.51 – 7.47 (m, 1H, C8-H), 7.42 – 7.31 (m, 1H, C9-H), 7.32 – 7.26 (m, 2H, C13-H), 5.46 (s, 2H, NH_2), 4.53 (dd, *J* = 12.2, 8.7 Hz, 1H, C5-H), 2.93 (dd, *J* = 15.0, 8.8 Hz, 1H, C4-H), 2.86 – 2.74 (dd, J=15.0, 12.2 Hz, 1H, C4-H).

^{13}C-NMR (100 MHz, DMSO-d_6) δ 168.5 (C1), 159.7 (d, *J* = 242.4 Hz) (C14), 148.4 (C2), 142.9 (C10), 136.4 (C6), 135.8 (d, *J* = 2.7 Hz) (C11), 135.0 (C7), 129.6 (C8), 129.5 (C9), 128.2 (C8'), 124.4 (d, *J* = 8.5 Hz) (C12), 115.8 (d, *J* = 22.7 Hz) (C13), 83.1 (C3), 43.8 (C5), 21.7 (C4).

IR (KBr), vmax (cm^{-1}): 3381, 3324 (*st* N-H), 3206 (*st* Csp^2-H), 2925, 2172, 1682 (*st* C=O), 1634, 1556, 1527, 1510, 1434, 1332, 1265 (*st* C-O), 1225, 839, 780, 607.

MS (70 eV, EI) m/z (%): 392.1 (66%), 391.1 (29%), 390.1 (100%), 357.1 (29%), 356.1 (20%), 355.1 (85%), 247.1 (24%), 245.1 (26%), 205.1 (37%), 204.0 (46%), 203.1 (26%), 190.0 (20%), 188.0 (36%), 186.0 (43%), 174.0 (31%), 137.1 (29%), 124.1 (26%), 123.1 (28%), 111.1 (34%), 110.1 (27%), 95.1 (46%), 75.0 (28%), 45.1 (24%), 44.1 (51%).

HRMS (APCI) m/z: calculated for $C_{18}H_{14}Cl_2FN_4O$ $[M+1]^+$: 391.0523; Found $[M+1]^+$: 391.0524

3-amino-5-(2,6-dichlorophenyl)-2-(3,4-difluorophenyl)-2,4,5,7-tetrahydro-6*H*-pyrazolo[3,4-*b*]pyridin-6-one (64{7,1,5})

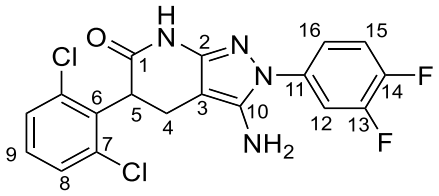

Starting from 2-methoxy-5-(2,6-dichlorophenyl)-6-oxo-1,4,5,6-tetrahydropyridine-3-carbonitrile (**62**{*7*,*1*}) and (3,4-difluorophenyl)hydrazine (**56**{*5*}). 38% yield, ocher solid.

mp: > 250 °C

^{1}H-NMR (400 MHz, DMSO-d_6) δ 10.59 (s, 1H, NH), 7.64 – 7.46 (m, 4H, C8-H, C12-H, C15-H), 7.45 – 7.31 (m, 2H, C9-H, C16-H), 5.58 (s, 2H, NH_2), 4.54 (dd, J = 12.2, 8.7 Hz, 1H, C5-H), 2.93 (dd, J = 15.0, 8.8 Hz, 1H, C4-H), 2.81 (dd, J = 15.1, 12.2 Hz, 1H, C4-H).

^{13}C-NMR (100 MHz, DMSO-d_6) δ 168.5 (C1), 148.9, 148.3, 147.9 (d, J = 13.6 Hz), 145.81 (d, J = 12.5 Hz), 143.1, 136.3, 134.9 (d, J = 10.1 Hz), 129.7 (C10), 129.5 (C9), 128.2 (C10'), 118.7 (dd, J = 6.6, 3.4 Hz, C16), 117.7 (d, J = 18.2 Hz), 111.5 (d, J = 20.3 Hz), 83.7 (C3), 43.7 (C5), 21.6 (C4).

IR (KBr), vmax (cm^{-1}): 3419 (*st* N-H), 3215, 1685 (*st* C=O), 1640, 1519 (*st* C=C), 1434, 1278 (*st* C-O), 782.

MS (70 eV, EI) m/z (%): 410.2 (55%), 409.3 (29%), 408.2 (85%), 375.2 (33%), 374.2 (25%), 373.1 (100%), 263.1 (32%), 223.1 (46%), 222.2 (62%), 221.3 (33%), 181.1 (22%), 155.1 (23%), 129.1 (22%), 113.1 (50%).

HRMS (APCI) m/z: calculated for $C_{18}H_{13}Cl_2F_2N_4O$ $[M+1]^+$: 409.0429; Found $[M+1]^+$: 409.0429

Methyl 4-(3-amino-5-(2,6-dichlorophenyl)-6-oxo-4,5,6,7-tetrahydro-2*H*-pyrazolo[3,4-*b*]pyridin-2-yl)benzoate (64{7,1,8})

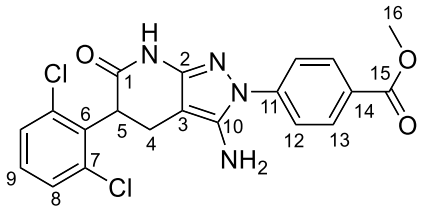

Starting from 2-methoxy-5-(2,6-dichlorophenyl)-6-oxo-1,4,5,6-tetrahydropyridine-3-carbonitrile (**62**{*7*,*1*}) and methyl 4-hydrazinylbenzoate (**56**{*8*}). 10% yield, white solid.

mp: > 250 °C

^{1}H-NMR (400 MHz, DMSO-d_6) δ 10.65 (s, 1H, NH), 8.11 – 7.93 (m, 2H, C13-H), 7.84 – 7.66 (m, 2H, C12-H), 7.62 – 7.45 (m, 2H, C8-H), 7.42 – 7.28 (m, 1H, C9-H), 5.68 (s, 2H, NH_2), 4.56 (dd, *J* = 12.1, 8.6 Hz, 1H, C5-H), 3.86 (s, 3H, C16-H_3), 2.96 (dd, *J* = 15.1, 8.6 Hz, 1H, C4-H), 2.82 (dd, *J* = 15.2, 12.1 Hz, 1H, C4-H).

^{13}C-NMR (100 MHz, DMSO-d_6) δ 169.0 (C1), 166.2 (C15), 149.8, 143.9 (C11), 143.9, 136.7 (C6), 135.4 (C7), 130.8 (C13), 130.1 (C8), 130.0 (C9), 128.7 (C8'), 125.8 (C14), 121.1 (C12), 84.9 (C3), 52.5 (C16), 44.1 (C5), 22.0 (C4).

IR (KBr), vmax (cm^{-1}): 3390 (*st* N-H), 3330, 2948, 1702 (*st* C=O), 1677 (*st* C=O), 1604 (*st* C=C), 1509, 1434, 1341, 1289 (*st*, C-O), 1114, 778, 706, 559.

MS (70 eV, EI) m/z (%): 433.1 (25%), 432.1 (86%), 431.1 (51%), 430.1 (100%), 397.1 (52%), 396.1 (39%), 395.1 (97%), 285.1 (40%), 245.1 (46%), 244.1 (57%).

4-(3-amino-5-(2,6-dichlorophenyl)-6-oxo-4,5,6,7-tetrahydro-2*H*-pyrazolo[3,4-*b*]pyridin-2-yl)benzonitrile (64{*7*,*1*,*9*})

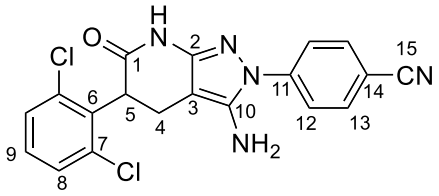

Starting from 2-(2-(4-cyanophenyl)hydrazono)-5-(2,6-dichlorophenyl)-6-oxopiperidine-3-carbonitrile (**76**{*7*,*1*,*9*}). Quantitative yield, white solid.

mp: > 250 °C

^{1}H-NMR (400 MHz, DMSO-d_6) δ 10.69 (s, 1H, NH), 7.94 – 7.85 (m, 2H, C13-H), 7.83 – 7.77 (m, 2H, C12-H), 7.56 – 7.48 (m, 2H, C8-H), 7.41 – 7.34 (m, 1H, C9-H), 5.72 (s, 2H, NH_2), 4.56 (dd, *J* = 12.2, 8.8 Hz, 1H, C5-H), 2.96 (dd, *J* = 15.2, 8.8 Hz, 1H, C4-H), 2.81 (dd, *J* = 15.2, 12.3 Hz, 1H, C4-H).

^{13}C-NMR (100 MHz, DMSO-d_6) δ 168.6 (C1) 149.7 (C2), 143.7 (C10), 143.3 (C11), 136.2 (C6), 135.0 (C7), 134.9 (C7'), 133.4 (C13), 129.7 (C8), 129.6 (C9), 128.2 (C8'), 121.2 (C12), 118.8 (C15), 106.5 (C14), 85.0 (C3), 43.6 (C5), 21.5 (C4).

IR (KBr), vmax (cm^{-1}): 3430 (*st* N-H), 3342, 3207 (*st* Csp^2-H), 2230, 1687 (*st* C=O), 1650, 1604, 1523 (*st* C=C), 1508, 1438, 1341, 1252 (*st* C-O), 1219, 1115, 781.

Elemental analysis: calculated for $C_{19}H_{13}Cl_2N_5O$: C: 57.03%, H: 3.29%, N: 17.59%; found: C: 57.15%, H: 3.39%, N: 17.49%.

MS (70 eV, EI) m/z (%): 399.2 (45%), 398.3 (49%), 397.2 (76%), 396.4 (32%), 364.2 (32%), 363.3 (40%), 362.2 (100%), 252.2 (21%), 212.2 (22%), 211.2 (57%), 210.3 (40%), 102.1 (32%), 101.8 (31%).

3-amino-5-(2,6-dichlorophenyl)-2-(pyridin-3-yl)-2,4,5,7-tetrahydro-6*H*-pyrazolo[3,4-*b*]pyridin-6-one (64{*7*,*1*,*10*})

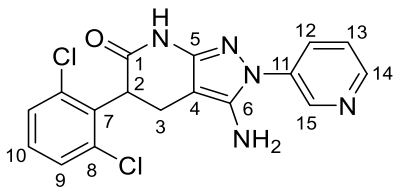

Starting from 2-methoxy-5-(2,6-dichlorophenyl)-6-oxo-1,4,5,6-tetrahydropyridine-3-carbonitrile (**62**{*7*,*1*}) and 3-hydrazinylpyridine (**56**{*10*}). 59% yield, white solid.

mp: > 250 °C

^{1}H-NMR (400 MHz, DMSO-d_6) δ 10.62 (s, 1H, NH), 8.83 – 8.78 (m, 1H, C15-H), 8.48 – 8.42 (m, 1H, C14-H), 7.98 – 7.91 (m, 1H, C12-H), 7.57 – 7.46 (m, 3H, C13-H, C9-H), 7.39 – 7.33 (m, 1H, C10-H), 5.62 (s, 2H, NH_2), 4.55 (dd, J = 12.2, 8.7 Hz, 1H, C2-H), 2.95 (dd, J = 15.1, 8.8 Hz, 1H, C3-H), 2.82 (dd, J = 15.1, 12.2 Hz, 1H, C3-H).

^{13}C-NMR (100 MHz, DMSO-d_6) δ 168.5 (C1), 149.3, 146.1, 143.3, 143.1, 136.3, 136.1, 135.0 (C8), 134.9 (C8'), 129.7, 129.5, 129.1, 128.2, 123.9, 83.9 (C4), 43.7 (C2), 21.60 (C3).

IR (KBr), vmax (cm^{-1}): 3421 (*st* N-H), 3344 (*st* N-H), 1663 (*st* C=O), 1524 (*st* C=C), 1444, 1352 (*st* C-O), 772 (*b* Csp^2-H).

MS (70 eV, EI) m/z (%): 375.1 (55%), 374.1 (31%), 373.1 (86%), 340.4 (32%), 339.3 (24%), 338.2 (100%), 336.2 (26%), 228.1 (23%), 188.1 (42%), 187.2 (49%), 186.3 (34%).

HRMS (APCI) m/z: calculated for $C_{17}H_{14}Cl_2N_5O$ $[M+1]^+$: 374.0570; found $[M+1]^+$: 374.0569

3-amino-2-(4-fluorophenyl)-5-(4-methoxyphenyl)-2,4,5,7-tetrahydro-6*H*-pyrazolo[3,4-*b*]pyridin-6-one (64{*4*,*1*,*4*})

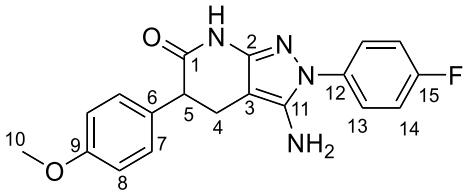

Starting from 2-methoxy-5-(4-methoxyphenyl)-6-oxo-1,4,5,6-tetrahydropyridine-3-carbonitrile (**62**{*4*,*1*}) and (4-fluorophenyl)hydrazine (**56**{*4*}). 37% yield, ochre solid.

mp: 162 °C

^{1}H-NMR (400 MHz, DMSO-d_6) δ 10.36 (s, 1H, NH), 7.60 – 7.50 (m, 2H, C13-H), 7.30 – 7.23 (m, 2H, C14-H), 7.19 – 7.13 (m, 2H, C7-H), 6.90 – 6.82 (m, 2H, C8-H), 5.39 (s, 2H, NH_2), 3.78 – 3.66 (m, 1H, C5-H), 3.72 (s, 3H, C10-H_3), 2.96 – 2.85 (m, 1H, C4-H), 2.79 – 2.70 (m, 1H, C4-H).

^{13}C-NMR (100 MHz, DMSO-d_6) δ 171.3 (C1), 159.5 (d, *J* = 242.2 Hz, C15), 158.0 (C9), 149.0 (C2), 142.7 (C11), 136.0 (d, *J* = 2.7 Hz, C12), 132.5 (C6), 129.1 (C7), 124.1 (d, *J* = 8.4 Hz, C13), 115.7 (d, *J* = 22.7 Hz, C14), 113.6 (C8), 85.0 (C3), 55.0 (C10), 46.4 (C5), 24.1 (C4).

IR (KBr), vmax (cm^{-1}): 3210 (*st* N-H), 2930, 1643 (*st* C=O), 1510, 1249 (*st* C-O), 838 (*b* Csp^2-H).

MS (70 eV, EI) m/z (%): 353.3 (19%), 352.9 (21%), 352.2 (100%), 351.8 (79%).

3-amino-2-(4-fluorophenyl)-5-(3,4,5-trimethoxyphenyl)-2,4,5,7-tetrahydro-6*H*-pyrazolo[3,4-*b*]pyridin-6-one (64{*5*,*1*,*4*})

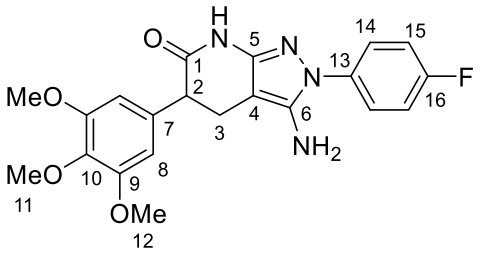

Starting from 2-methoxy-5-(3,4,5-trimethoxyphenyl)-6-oxo-1,4,5,6-tetrahydropyridine-3-carbonitrile (**62**{*5*,*1*}) and (4-fluorophenyl)hydrazine (**56**{*4*}). 37% yield, brownish solid.

mp: 140-143 °C

^{1}H-NMR (400 MHz, DMSO-d_6) δ 10.35 (s, 1H, NH), 7.56 – 7.48 (m, 2H, C14-H), 7.29 – 7.20 (m, 2H, C15-H), 6.55 (s, 2H, C8-H), 5.38 (s, 2H, NH_2), 3.69 (s, 6H, C12-H_3), 3.63 – 3.60 (m, 1H, C2-H), 3.61 (s, 3H, C11-H_3), 2.88 (dd, J = 15.2, 6.8 Hz, 1H, C3-H), 2.79 (dd, J = 15.3, 8.5 Hz, 1H, C3-H).

^{13}C-NMR (100 MHz, DMSO-d_6) δ 171.0 (C1), 159.6 (d, J = 254.1 Hz, C16), 152.6 (C9), 149.0, 142.7, 136.3 (C10), 136.1 (C13), 136.0 (C7) 124.2 (d, J = 8.5 Hz, C14), 115.7 (d, J = 22.6 Hz, C15), 105.7 (C8), 85.1 (C4), 60.0 (C11), 55.8 (C12), 47.5 (C2), 23.9 (C3).

IR (KBr), vmax (cm^{-1}): 3415 (*st* N-H), 1642 (*st* C=O), 1509, 1329, 1229, 1126, 841 (*b* Csp^2-H).

MS (70 eV, EI) m/z (%): 413.2 (24%), 412.2 (100%), 411.3 (21%), 335.1 (20%), 245.1 (47%), 205.1 (22%), 204.1 (24%), 193.1 (21%), 190.1 (20%), 168.1 (22%).

3-amino-2-(4-chlorophenyl)-5-(3,4,5-trimethoxyphenyl)-2,4,5,7-tetrahydro-6*H*-pyrazolo[3,4-*b*]pyridin-6-one (64{*5*,*1*,*6*})

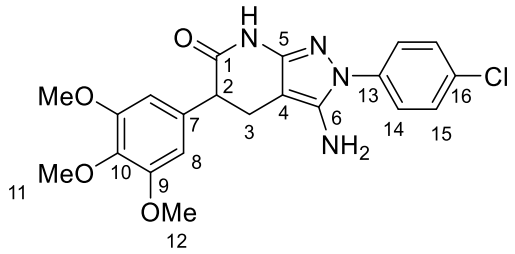

Starting from 2-methoxy-5-(3,4,5-trimethoxyphenyl)-6-oxo-1,4,5,6-tetrahydropyridine-3-carbonitrile (**62**{*5*,*1*}) and (4-chlorophenyl)hydrazine (**56**{*6*}). 37% yield, brownish solid.

mp: 130 °C

^{1}H-NMR (400 MHz, DMSO-d_6) δ 10.41 (s, 1H, NH), 7.57 (d, J = 8.9 Hz, 2H, C14-H), 7.48 (d, J = 9.0 Hz, 2H, C15-H), 6.58 (s, 2H, C8-H), 5.48 (s, 2H, NH_2), 3.71 (s, 6H, C12-H_3), 3.66 – 3.62 (m, 1H, C2-H), 3.64 (s, 3H, C11-H_3), 2.91 (dd, J = 15.3, 6.9 Hz, 1H, C3-H), 2.82 (dd, J = 15.3, 8.5 Hz, 1H, C3-H).

^{13}C-NMR (100 MHz, DMSO-d_6) δ 173.1, 171.1, 152.9, 152.6, 149.3, 142.8, 138.6, 136.0, 128.9, 123.3, 105.7, 85.7 (C4), 59.9, 55.8, 47.4 (C2), 23.8 (C3).

IR (KBr), vmax (cm^{-1}): 3341 (*st* N-H), 1680 (*st* C=O), 1644, 1952, 1492, 1328, 1241 (*st* C-O), 1127, 1008.

MS (70 eV, EI) m/z (%): 428.2 (47%), 427.4 (41%), 4262 (100%), 413.2 (35%), 412.3 (42%), 411.2 (85%), 325.1 (29%), 208.1 (24%), 197.6 (23%), 193.1 (35%), 181.1 (27%), 127.1 (27%), 111.0 (34%).

4-(3-amino-6-oxo-5-phenyl-4,5,6,7-tetrahydro-2*H*-pyrazolo[3,4-*b*]pyridin-2-yl)benzonitrile (64{*3*,*1*,*9*})

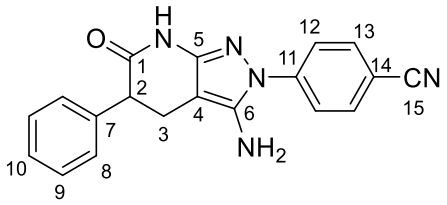

Starting from 2-(2-(4-cyanophenyl)hydrazono)-6-oxo-5-phenylpiperidine-3-carbonitrile (**76**{*3*,*1*,*9*}). Quantitative yield, white solid.

mp: >280 °C

^{1}H-NMR (400 MHz, DMSO-d_6) δ 10.57 (bs s, 1H, NH), 7.88 (m, 2H, C12-H), 7.80 (m, 2H, C13-H), 7.33-7.22 (m, 5H, C8-H, C9-H, C10-H), 5.67 (bs s, 2H, NH_2), 3.83 (t, *J* = 7.4 Hz, 1H, C2-H), 2.96 (dd, *J* = 15.4, 7.0 Hz, 1H, C3-H), 2.80 (dd, *J* = 15.4, 8.1 Hz, 1H, C3-H).

^{13}C-NMR (100 MHz, DMSO-d_6) δ 171.1 (C1), 150.3 (C5), 143.6, 143.4, 140.4 (C7), 133.3 (C12), 128.3, 128.1, 126.7, 120.9 (C13), 118.9 (C14), 106.2 (C15), 86.8 (C4), 47.1 (C2), 23.9 (C3).

IR (KBr), vmax (cm^{-1}): 3381, 3321 (*st* N-H), 3159 (*st* Csp^2-H), 2956 (*st* C-H), 2228 (*st* C≡N), 1668, 1649, 1602 (*st* C=O), 1554, 1508 (*st* Csp^2-Csp^2), 1430, 1373, 1348, 1333, 846, 794, 761, 705.

Elemental analysis: calculated for $C_{19}H_{15}N_5O$: C: 69.29%, H: 4.59%, N: 21.26%; found: C: 68.99%, H: 4.97%, N: 20.99%.

MS (70 eV, EI) m/z (%): 329.1 (100%), 252.0 (31%), 211.1 (23%), 118.0 (20%), 102.0 (22%).

4-(3-amino-5-(4-methoxyphenyl)-6-oxo-4,5,6,7-tetrahydro-2*H*-pyrazolo[3,4-*b*]pyridin-2-yl)benzonitrile (64{*4*,*1*,*9*})

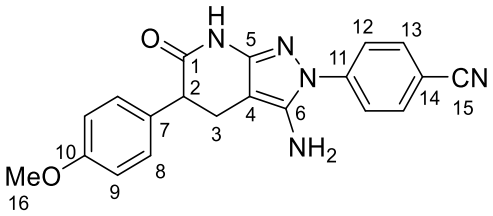

Starting from 2-(2-(4-cyanophenyl)hydrazono)-5-(4-methoxyphenyl)-6-oxopiperidine-3-carbonitrile (**76**{*4*,*1*,*9*}). Quantitative yield, white solid.

mp: 278-282 °C

^{1}H-NMR (400 MHz, DMSO-d_6) δ 10.51 (bs s, 1H, NH), 7.87 (m, 2H, C12-H), 7.79 (m, 2H, C13-H), 7.15 (m, 2H, C8-H), 6.86 (m, 2H, C9-H), 5.65 (bs s, 2H, NH_2), 3.75 (t, *J* = 7.2 Hz, 1H,C2-H), 2.92 (dd, *J* = 15.4, 6.8 Hz, 1H, C3-H), 2.77 (dd, *J* = 15.4, 7.6 Hz, 1H, C3-H).

^{13}C-NMR (100 MHz, DMSO-d_6) δ 171.6 (C1), 158.2 (C10), 150.4 (C5), 143.7, 143.5 (C6), 133.5 (C12), 132.3 (C7), 129.2 (C8), 121.1 (C13), 119.1 (C14), 113.8 (C9), 106.4 (C15), 87.0 (C4), 55.2 (C16), 46.3 (C2), 23.9 (C3).

IR (KBr), vmax (cm^{-1}): 3382, 3282 (*st* N-H), 3100 (*st* Csp^2-H), 2938, 2839 (*st* C-H), 2220 (*st* C≡N), 1683, 1649, 1603 (*st* C=O), 1555, 1514 (*st* Csp^2-Csp^2), 1241, 1180, 837.

Elemental analysis: calculated for $C_{20}H_{17}N_5O_2$: C: 66.84%, H: 4.77%, N: 19.49%; found: C: 66.91%, H: 4.74%, N: 19.53%.

MS (70 eV, EI) m/z (%): 166.0(21%), 149.0 (38%), 129.1 (21%), 111.1 (23%), 97.1 (33%), 95.1 (20%), 85.1 (30%), 84.1 (23%), 83.1 (41%), 81.1 (24%), 73.1 (50%), 71.1 (49%), 70.1 (24%), 69.1 (55%), 67.1 (22%), 60.0 (50%), 57.1 (79%), 56.1 (28%), 55.1 (78%), 45.1 (30%), 44.1 (26%), 43.1 (100%), 42.1 (22%), 41.1 (77%).

4-(3-amino-5-(4-fluorophenyl)-6-oxo-4,5,6,7-tetrahydro-2*H*-pyrazolo[3,4-*b*]pyridin-2-yl)benzonitrile (64{*7,1,9*})

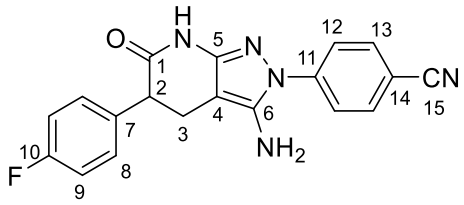

Starting from 2-(2-(4-cyanophenyl)hydrazono)-5-(4-fluorophenyl)-6-oxopiperidine-3-carbonitrile (**76**{*6,1,9*}). Quantitative yield, white solid.

mp: >280 °C

^{1}H-NMR (400 MHz, DMSO-d_6) δ 10.58 (bs s, 1H, NH), 7.88 (m, 2H, C12-H), 7.80 (m, 2H, C13-H), 7.30 (m, 2H, C8-H), 7.14 (m, 2H, C9-H), 5.68 (bs s, 2H, NH_2), 3.87 (dd, *J* = 8.8, 6.9 Hz, 1H, C2-H), 2.95 (dd, *J* = 15.3, 7.0 Hz, 1H, C3-H), 2.78 (dd, *J* = 15.4, 8.9 Hz, 1H, C3-H).

^{13}C-NMR (100 MHz, DMSO-d_6) δ 171.0 (C1), 161.1 (d, *J* = 242.4 Hz, C10), 150.3 (C5), 143.5, 143.4, 136.5 (d, *J* = 3.0 Hz, C7), 133.4 (C12), 130.1 (d, *J* = 7.9 Hz, C8), 121.0 (C13), 118.9 (C14), 115.0 (d, *J* = 21.1 Hz, C9), 106.3 (C15), 86.9 (C4), 46.3 (C2), 24.0 (C3).

IR (KBr), vmax (cm^{-1}): 3389, 3324 (*st* N-H), 3165 (*st* Csp^2-H), 2953 (*st* C-H), 2229 (*st* C≡N), 1670, 1649, 1602 (*st* C=O), 1553, 1508 (*st* Csp^2-Csp^2), 1430, 1372, 1345, 1333, 1226 (*st* C-O), 843.

Elemental analysis: calculated for $C_{19}H_{14}FN_5O$: C: 65.70%, H: 4.06%, N: 20.16%; found: C: 65.63%, H: 4.30%, N: 20.09%.

MS (70 eV, EI) m/z (%): 348.1 (22%), 347.1 (100%), 346.1 (30%), 252.1 (25%), 102.0 (22%).

Methyl 4-(3-amino-4-(4-methoxyphenyl)-6-oxo-4,5,6,7-tetrahydro-2*H*-pyrazolo[3,4-*b*]pyridin-2-yl)benzoate (64{*1,4,8*})

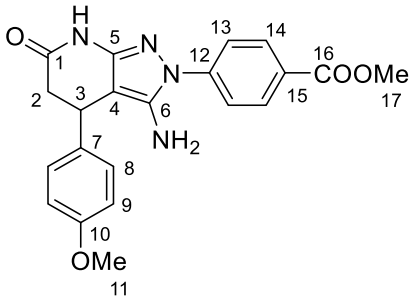

Starting from methyl 4-(2-(3-cyano-4-(4-methoxyphenyl)-6-oxopiperidin-2-ylidene)hydrazinyl)benzoate (**76**{*1,4,8*}). Quantitative yield, pale pink solid.

mp: 109-113 °C

^{1}H-NMR (400 MHz, DMSO-d_6) δ 10.44 (bs s, 1H, NH), 8.00 (m, 2H, C14-H), 7.75 (m, 2H, C13-H), 7.12 (m, 2H, C8-H), 6.87 (m, 2H, C9-H), 5.50 (bs s, 2H, NH_2), 4.21 (dd, *J* = 7.2, 2.8 Hz, 1H, C3-H), 3.85 (s, 3H, C17-H), 3.71 (s, 3H, C11-H_3), 2.94 (dd, *J* = 15.9, 7.2 Hz, 1H, C2-H), 2.54-2.50 (dd, 1H, C2-H).

^{13}C-NMR (100 MHz, DMSO-d_6) δ 169.9 (C1), 165.8 (C16), 157.9 (C10), 149.9 (C5), 143.6, 143.4, 135.8 (C7), 130.3 (C14), 127.7 (C8), 125.3 (C15), 120.6 (C13), 113.9 (C9), 90.1 (C4), 55.1 (C11), 52.1 (C17), 40.2 (C2), 31.7 (C3).

IR (KBr), vmax (cm^{-1}): 3412 (*st* N-H), 3150 (*st* Csp^2), 2951, 2836, 1719, 1680 (*st* C=O), 1638, 1605, 1550 (*st* C=C), 1511, 1435, 1343, 1280 (*st* C-O), 1251, 832.

Elemental analysis: calculated for $C_{21}H_{20}N_4O_4$: C: 64.28%, H: 5.14%, N: 14.28%; found: C: 64.41%, H: 5.22%, N: 14.17%.

MS (70 eV, EI) m/z (%): 170.0 (100%), 141.1 (55%), 105.0 (20%), 77.0 (42%), 51.1 (29%).

4-(3-amino-6-oxo-4-phenyl-4,5,6,7-tetrahydro-2*H*-pyrazolo[3,4-*b*]pyridin-2-yl)benzonitrile (64{*1*,*3*,*9*})

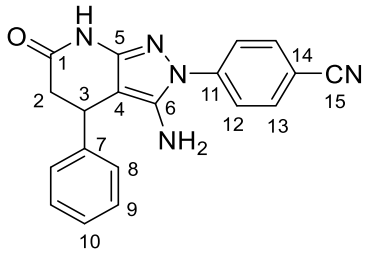

Starting from 2-(2-(4-cyanophenyl)hydrazono)-6-oxo-4-phenylpiperidine-3-carbonitrile (**76**{*1*,*3*,*9*}). Quantitative yield, brown-orange solid.

mp: 138-140 °C

^{1}H-NMR (400 MHz, DMSO-d_6) δ 10.51 (bs s, 1H, NH), 7.88 (m, 2H, C12-H), 7.81 (m, 2H, C13-H), 7.33-7.29 (m, 2H, C9-H), 7.21 (m, 3H, C8-H and C10-H), 5.61 (bs s, 2H, NH_2), 4.28 (dd, *J* = 7.4, 2.5 Hz, 1H, C3-H), 3.00 (dd, *J* = 16.0, 7.4 Hz, 1H, C2-H), 2.55 (dd, *J* = 16.1, 2.6 Hz, 1H, C2-H).

^{13}C-NMR (100 MHz, DMSO-d_6) δ 169.8 (C1), 150.3 (C5), 143.9, 143.7, 143.3 (C11), 133.3 (C12), 128.5 (C9), 126.7, 126.5, 121.1 (C13), 118.8 (C14), 106.5 (C15), 90.1 (C4), 39.9 (C2), 32.4 (C3).

IR (KBr), vmax (cm^{-1}): 3410 (*st* N-H), 3197 (*st* Csp^2-H), 2226, 1679 (*st* C=O), 1639, 1603, 1550 (*st* C=C), 1508, 1340, 844, 743, 702.

MS (70 eV, EI) m/z (%): 329.1 (23%), 252.1 (24%), 173.1 (42%), 117.0 (32%), 103.0 (40%), 90.0 (24%), 77.0 (23%), 58.1 (31%), 43.1 (100%).

6.1.3.8 Synthesis of 3-amino-7-methyl-2,4,5,7-tetrahydro-6*H*-pyrazolo[3,4-*b*]pyridin-6-ones

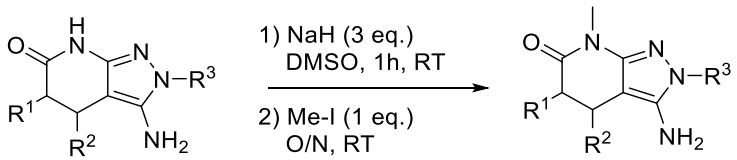

64 **102**

0.30 mmols of the corresponding 3-amino-pyrazolo[3,4-*b*]pyridine-6-one (**64**) were dissolved in 4 mL of anhydrous DMSO. 0.6 mmols of NaH were added and the mixture wass stirred for 1.5h under argon atmosphere at room temperature. Then, 0.30 mmols of MeI were added and the mixture was stirred at room temperature overnight.

Water was added to force precipitation of the product. The solid corresponding to the 3-amino-7-methyl-pyrazolo[3,4-*b*]pyridine-6-one (**102**) was filtered and dried *in vacuo* over P_2O_5

3-amino-7-methyl-2,5-diphenyl-2,4,5,7-tetrahydro-6*H*-pyrazolo[3,4-*b*]pyridin-6-one (102{*3,1,3*})

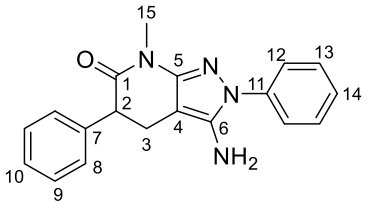

Starting from 3-amino-2,5-diphenyl-2,4,5,7-tetrahydro-6*H*-pyrazolo[3,4-*b*]pyridin-6-one (**76**{*3,1,3*}). 83% yield, light brown solid.

mp: > 250 °C

^{1}H-NMR (400 MHz, DMSO-d_6) δ 7.61 – 7.55 (m, 2H, C12-H), 7.49 – 7.42 (m, 2H, C13-H), 7.35 – 7.27 (m, 2H, C9-H), 7.27 – 7.21 (m, 4H, C8-H, C10-H, C14-H), 5.44 (s, 2H, NH_2), 3.93 (t, J = 7.4 Hz, 1H, C2-H), 3.21 (s, 3H, C15-H_3), 2.95 (dd, J = 15.3, 6.9 Hz, 1H, C3-H), 2.80 (dd, J = 15.3, 8.0 Hz, 1H, C3-H).

^{13}C-NMR (100 MHz, DMSO-d_6) δ 169.7 (C1), 150.2 (C5), 143.2 (C6), 140.7 (C7), 139.5 (C11), 129.1 (C13), 128.2 (C9), 128.1 (C8), 126.7 (C7), 125.4 (C14), 122.2 (C12), 85.0 (C4), 47.6 (C2), 27.8 (C15), 23.6 (C3).

IR (KBr), vmax (cm^{-1}): 3374 (st N-H), 3296, 3206, 1651 (st C=O), 1635, 1525, 1499, 1348, 697.

MS (70 eV, EI) m/z (%): 319.3 (33%), 318.3 (100%), 317.8 (80%), 226.2 (20%).

HRMS (APCI) m/z: calculated for $C_{19}H_{19}N_4O$ $[M+1]^+$: 319.1553; Found $[M+1]^+$: 319.1555

3-amino-5-(2,6-dichlorophenyl)-7-methyl-2-phenyl-2,4,5,7-tetrahydro-6*H*-pyrazolo[3,4-*b*]pyridin-6-one (102{*7,1,3*})

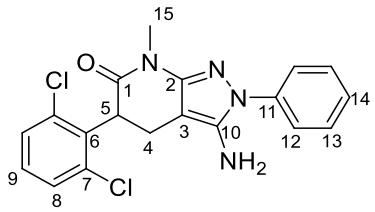

Starting from 3-amino-5-(2,6-dichlorophenyl)-2-phenyl-2,4,5,7-tetrahydro-6*H*-pyrazolo[3,4-*b*]pyridin-6-one (**76**{*7,1,3*}). 55% yield, purple solid.

mp: > 250 °C

^{1}H-NMR (400 MHz, DMSO-d_6) δ 7.60 – 7.56 (m, 2H, C12-H), 7.56 – 7.52 (m, 1H, C8-H), 7.52 – 7.49 (m, 1H, C8'-H), 7.49 – 7.45 (m, 2H, C13-H), 7.39 – 7.34 (m, 1H, C9-H), 7.31 – 7.26 (m, 1H, C14-H), 5.49 (s, 2H, NH_2), 4.70 – 4.60 (dd, *J* = 12.4, 8.8 Hz, 1H, C5-H), 3.21 (s, 3H, C15-H_3), 2.95 (dd, *J* = 15.0, 8.8 Hz, 1H, C4-H), 2.83 (dd, *J* = 15.0, 12.4 Hz, 1H, C4-H).

^{13}C-NMR (100 MHz, DMSO-d_6) δ 167.3 (C1), 149.6 (C2), 143.4 (C10), 139.3 (C11), 136.6 (C6), 134.8 (C7), 129.7 (C8'), 129.5 (C9), 129.1 (C13), 128.2 (C8), 125.6 (C14), 122.4 (C12), 83.2 (C3), 44.1 (C5), 27.6 (C15), 21.2 (C4).

IR (KBr), vmax (cm^{-1}): 3397 (*st* N-H), 3307, 3196 (*st* Csp^2-H), 1636.28 (*st* C=O), 1619.32, 1594.50, 1557.5, 1525.95, 1492.67, 1431.57, 1348.50, 792.47.

MS (70 eV, EI) m/z (%): 386.1 (62%), 375.0 (29%), 363.1 (39%), 351.1 (100%), 338.1 (38%), 199.0 (21%), 170.0 (22%), 93.0 (32%), 77.0 (76%).

HRMS (EI) m/z: calculated for $C_{19}H_{16}Cl_2N_4O$ $[M+1]^+$: 386.0701; Found $[M+1]^+$: 386.0701

3-amino-5-(2,6-dichlorophenyl)-2,7-dimethyl-2,4,5,7-tetrahydro-6*H*-pyrazolo[3,4-*b*]pyridin-6-one (102{*7*,*1*,*2*})

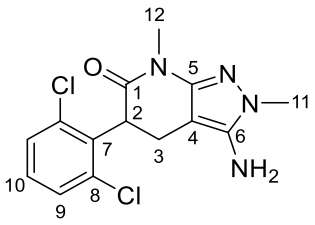

Starting from 3-amino-5-(2,6-dichlorophenyl)-2-methyl-2,4,5,7-tetrahydro-6*H*-pyrazolo[3,4-*b*]pyridin-6-one (**76**{*7*,*1*,*3*}). 12% yield, red-brown solid.

mp: 215-218 °C

^{1}H-NMR (400 MHz, DMSO-d_6) δ 7.53 – 7.50 (m, 1H, C9-H), 7.49 – 7.45 (m, 1H, C9'-H), 7.39 – 7.30 (m, 1H, C10-H), 5.30 (s, 2H, NH_2), 4.53 (dd, J = 12.2, 9.0 Hz, 1H, C2-H), 3.45 (s, 3H, C11-H_3), 3.13 (s, 3H, C12-H_3), 2.77 (dd, J = 12.0, 9.7 Hz, 2H, C3-H_2).

^{13}C-NMR (100 MHz, DMSO-d_6) δ 167.0 (C1), 147.2 (C6), 143.7 (C5), 136.8 (C7), 134.9 (C8), 129.6 (C9'), 129.4 (C10), 127.9 (C9), 80.8 (C4), 44.4 (C2), 34.0 (C11), 27.5 (C12), 21.4 (C3).

IR (KBr), vmax (cm^{-1}): 3430 (*st* N-H), 2927, 1619 (*st* C=O), 1533, 1434, 1340, 757.

MS (70 eV, EI) m/z (%): 326.1 (33%), 325.3 (29%), 324.1 (53%), 291.2 (28%), 290.3 (29%), 289.2 (100%), 138.3 (25%), 137.2 (20%).

6.1.3.9 Synthesis of 3-amino-2,7-dihydro-6*H*-pyrazolo[3,4-*b*]pyridin-6-ones

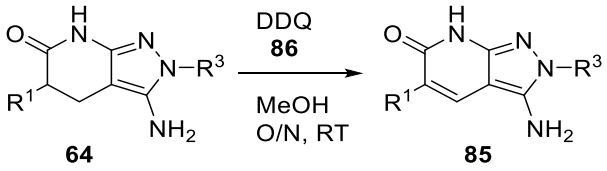

0.16 mmol of the corresponding 3-amino-2,4,5,7-tetrahydro-6*H*-pyrazolo[3,4-*b*]pyridin-6-one (**64**) and 0.32 mmol of DDQ were suspended in 4 mL of MeOH and stirred overnight at room temperature. The solid was filtered and washed with cold MeOH. The solid was dried *in vacuo* over P_2O_5 to afford the corresponding 3-amino-2,7-dihydro-6*H*-pyrazolo[3,4-*b*]pyridin-6-one (**85**)

3-amino-2,5-diphenyl-2,7-dihydro-6*H*-pyrazolo[3,4-*b*]pyridin-6-one (85{*3,1,3*})

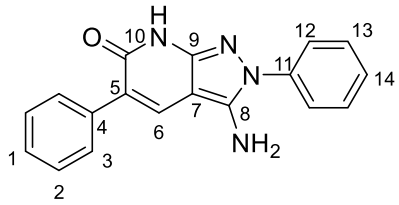

Starting from 3-amino-2,5-diphenyl-2,4,5,7-tetrahydro-6*H*-pyrazolo[3,4-*b*]pyridin-6-one **64**{*3*,*1*,*3*}. 71% yield. Brownish solid

mp: 238-242 °C

^{1}H-NMR (400 MHz, DMSO-d_6) δ 11.40 (s, 1H, NH), 8.02 (s, 1H, C6-H), 7.60 (m, 5H, C12-H, C13-H, C14-H), 7.36 (m, 5H, C1-H, C2-H, C3-H), 6.58 (s, 2H, NH_2).

^{13}C-NMR (100 MHz, DMSO-d_6) δ 163.3 (C10), 149.1 (C9), 143.4 (C8), 138.8 (C11), 138.4 (C5), 132.4 (C6), 129.8 (C4), 128.8 (C13), 128.2 (C3), 127.3 (C2), 126.9 (C1), 123.7 (C14), 122.0 (C12), 93.5 (C7).

IR (KBr), vmax (cm^{-1}) 3422 (*st* N-H), 2921 (*st* Csp^2-H), 1638 (*st* C=O), 1595, 1565, 702 (*b* Csp^2-H).

MS (70 eV, EI) m/z (%) 303.1 (23%), 302.1 (100%), 77.0 (24%).

3-amino-5-(2,6-dichlorophenyl)-2-phenyl-2,7-dihydro-6*H*-pyrazolo[3,4-*b*]pyridin-6-one (85{*7*,*1*,*3*})

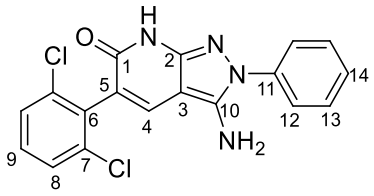

Starting from 3-amino-5-(2,6-dichlorophenyl)-2-phenyl-2,4,5,7-tetrahydro-6*H*-pyrazolo[3,4-*b*]pyridin-6-one **64**{*7*,*1*,*3*}. 55% yield. white solid

mp: > 250 °C

^{1}H-NMR (400 MHz, DMSO-d_6) δ 11.50 (s, 1H, NH), 7.72 (s, 1H, C4-H), 7.63 – 7.58 (m, 2H, C12-H), 7.57 – 7.53 (m, 2H, C8-H), 7.55 – 7.49 (m, 2H, C13-H), 7.42 – 7.38 (m, 1H, C9-H), 7.40 – 7.35 (m, 1H, C14-H), 6.60 (s, 2H, NH_2).

^{13}C-NMR (100 MHz, DMSO-d_6) δ 161.5 (C1), 149.2 (C2), 143.0 (C10), 138.5 (C5), 136.1 (C6), 135.6 (C11), 133.8 (C4), 129.8 (C9), 129.3 (C8), 127.9 (C13), 126.8 (C14), 123.4 (C12), 118.7 (C7), 92.1 (C3).

IR (KBr), vmax (cm^{-1}): 3381 (*st* N-H), 3191 (*st* Csp^2-H), 1616 (*st* C=O), 1554, 1429, 1313, 818, 794, 769.

Elemental analysis: calculated for $C_{18}H_{12}Cl_2N_4O$: C: 58.24%, H: 3.26%, N: 15.09%; found: C: 58.37%, H: 3.23%, N: 15.03%.

MS (70 eV, EI) m/z (%): 372.2 (28%), 337.2 (53%), 336.3 (33%), 335.2 (100%).

3-amino-5-(2,6-dichlorophenyl)-2-phenyl-2,7-dihydro-6*H*-pyrazolo[3,4-*b*]pyridin-6-one (85{*7,1,2*})

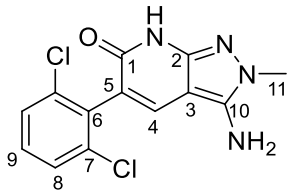

Starting from 3-amino-5-(2,6-dichlorophenyl)-2-phenyl-2,4,5,7-tetrahydro-6*H*-pyrazolo[3,4-*b*]pyridin-6-one **64**{*7,1,2*}. 22% yield. white solid

mp: > 250 °C

^{1}H-NMR (400 MHz, DMSO-d_6) δ 11.31 (s, 1H, NH), 7.55 (s, 1H, C4-H), 7.52 – 7.48 (m, 2H, C8-H), 7.40 – 7.31 (m, 1H, C9-H), 6.37 (s, 2H, NH_2), 3.54 (s, 3H, C11-H_3).

^{13}C-NMR (100 MHz, DMSO-d_6) δ 161.4 (C1), 147.7, 143.3, 136.4, 135.7, 133.7, 129.7, 127.9, 117.5, 91.3 (C3), 34.2 (C11).

IR (KBr), vmax (cm^{-1}): 3449, 3324 (*st* N-H), 3203, 3080, 2932, 1632 (*st* C=O), 1577, 1528, 795.

MS (70 eV, EI) m/z (%): 275.1 (44%), 274.3 (27%), 273.2 (100%)

3-amino-5-(2,6-dichlorophenyl)-7-methyl-2-phenyl-2,7-dihydro-6*H*-pyrazolo[3,4-*b*]pyridin-6-one (102{*7,1,3*})

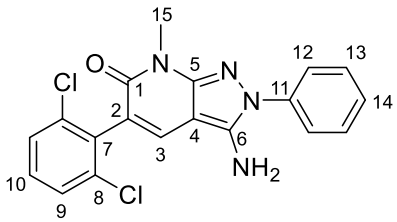

Starting from 3-amino-5-(2,6-dichlorophenyl)-7-methyl-2-phenyl-2,4,5,7-tetrahydro-6*H*-pyrazolo[3,4-*b*]pyridin-6-one **101**{*7,1,3*}. The mixture was stirred for 72h. 16% yield. Purple solid.

mp: > 250 °C

^{1}H-NMR (400 MHz, DMSO-d_6) δ 7.75 (s, 1H, C3-H), 7.65 – 7.61 (m, 2H), 7.59 – 7.52 (m, 4H), 7.44 – 7.37 (m, 2H), 6.68 (s, 2H, NH_2), 3.40 (s, 3H, C15-H_3).

^{13}C-NMR (100 MHz, DMSO-d_6) 168.8 (C1), 161.8, 150.0, 143.9, 138.3, 135.6, 132.8, 129.9, 129.4, 127.9, 123.8, 120.3, 117.9, 91.6 (C4), 27.8 (C15).

IR (KBr), vmax (cm^{-1}): 3414, 3299 (*st* N-H), 3177, 1619, 1533, 1491, 794, 774 (*b* Csp^2-H).

MS (70 eV, EI) m/z (%): 386.2 (32%), 385.5 (22%), 351.2 (68%), 350.5 (51%), 349.2 (100%), 77 (36%).

6.1.4. Alternative synthesis *via* an 6-oxo-2-(1-phenylhydrazinyl)-1,4,5,6-tetrahydropyridine-3-carbonitrile intermediate

6.1.4.1 Synthesis of 5-methyl-6-oxo-2-(phenylamino)-1,4,5,6-tetrahydropyridine-3-carbonitrile (79)

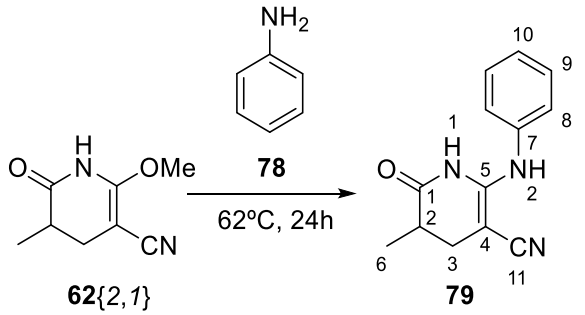

A mixture of 2-methoxy-5-methyl-6-oxo-1,4,5,6-tetrahydropyridine-3-carbonitrile (**62**{*2,1*}) (1.75 g, 10.5 mmol) and aniline **78** (9.8 g, 105.2 mmol) was heated at 65 °C for 24 h. Diethyl ether (40 mL) was added and the solid was filtered, washed with diethyl ether and dried *in vacuo* to afford 5-methyl-6-oxo-2-(phenylamino)-1,4,5,6-tetrahydropyridine-3-carbonitrile (**79**). 69% yield peach solid.

mp: 187-195 °C

^{1}H-NMR (400 MHz, DMSO-d_6) δ 9.93 (br s, 1H, N1-H), 8.58 (br s, 1H, N2-H), 7.25 (m, 2H, C9-H), 6.96-6.90 (m, 3H, C8-H and C9-H), 2.67-2.57 (m, 1H, C2-H), 2.43 (dd, *J* = 15.1, 6.3 Hz, 1H, C3-H), 2.24 (dd, *J* = 15.1, 12.0 Hz, 1H, C3-H), 1.12 (d, *J* = 6.8 Hz, 3H, C6-H_3).

^{13}C-NMR (100 MHz, DMSO-d_6) δ 173.5 (C1), 148.4 (C5), 140.8 (C7), 128.9 (C9), 121.4 (C10), 120.0 (C11), 118.6 (C8), 65.1 (C4), 35.1 (C2), 28.3 (C3), 14.3 (C6).

IR (KBr), vmax (cm^{-1}): 3274 (*st* N-H), 3048 (*st* Csp^2-H), 2975 (*st* C-H), 2831, 2176 (*st* C≡N), 1692 (*st* C=C), 1634 (*st* C=O), 1598 (*st* Csp^2-Csp^2), 1428, 1367, 1350, 1257, 1230, 693.

Elemental analysis: calculated for $C_{13}H_{13}N_3O$: C: 68.61%, H: 5.70%, N: 18.2 %; found: C: 68.70%, H: 5.77%, N: 18.49%.

MS (70 eV, EI) m/z (%): 227.2 (100%), 212.2 (28%), 170.1 (67%), 119.1 (20%), 93.2 (27%), 77.2 (27%).

6.1.4.2 Synthesis of 5-methyl-3-nitroso-6-oxo-2-(phenylimino)piperidine-3-carbonitrile (82)

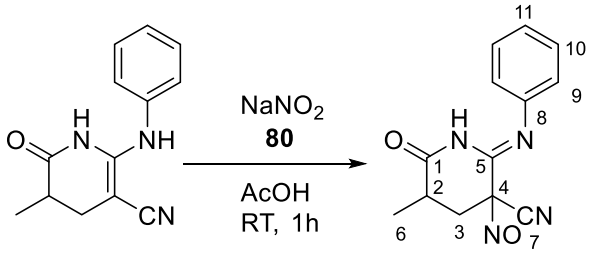

5-methyl-6-oxo-2-(phenylamino)-1,4,5,6-tetrahydropyridine-3-carbonitrile (**79**) (48 mg, 0.21 mmol) was dispersed in acetic acid (0.5 mL). Then, sodium nitrite (24 mg, 0.35 mmol) and acetic acid (1 ml) were added into the solution. The mixture was stirred at room temperature for 1 hour. After the addition of water (10 mL), the solid was filtered, washed with water and dried *in vacuo* over P_2O_5 at room temperature to afford the final nitrosated product **82**. 57% yield, salmon solid.

^{1}H-NMR (400 MHz, DMSO-d_6) δ 10.66 (br s, 1H, NH), 10.57 (br s, 1H, NH'), 7.40-7.32 (m, 4H, C10-H, C10-H'), 7.17-7.11 (m, 2H, C11-H, C11-H'), 6.88 (m, 4H, C9-H. C9-H'), 3.22-3.14 (m, 3H, C3-H, C3-H', C3-H'*), 3.03 (t, *J* = 12.9 Hz, 1H, C3-H*), 2.91-2.81 (m, 1H, C2-H), 2.71-2.61 (m, 1H, C2-H'), 1.26 (d, *J* = 6.8 Hz, 3H, C6-H_3), 1.17 (d, *J* = 6.8 Hz, 3H, C6-H_3').

^{13}C-NMR (100 MHz, DMSO-d_6) δ 171.6 and 171.6 (C1 or C1'), 145.6 and 145.2 (C8 or C8'), 142.8 (C5 and C5'), 129.8 and 129.7 (C11 or C11'), 125.2 and 125.1 (C12 and C12'), 121.0 and 120.6 (C10 or C10'), 113.7 (C7'), 113.1 (C7), 87.5 (C4'), 86.8 (C4), 35.6 (C3'), 35.0 (C3), 33.6 (C2), 31.7 (C2'), 15.0 and 14.9 (C6 or C6').

IR (KBr), vmax (cm^{-1}): 3427 (*st* N-H), 3216, 3083 (*st* Csp^2-H), 2940 (*st* C-H), 1719, 1680 (C=O), 1576 (*st* Csp^2-Csp^2), *st* C=O), 1488, 1257, 1236, 1207, 793, 771, 697.

MS (70 eV, EI) m/z (%): 226.1 (61%), 77.1 (33%), 69.1 (100%).

6.1.4.3 Synthesis of *N*-(3-cyano-5-methyl-6-oxo-1,4,5,6-tetrahydropyridin-2-yl)-*N*-phenylnitrous amide (81)

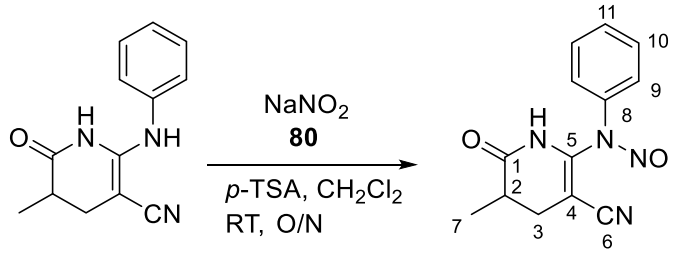

79 **81**

1.00 g (4.20 mmol) of 5-methyl-6-oxo-2-(phenylamino)-1,4,5,6-tetrahydropyridine-3-carbonitrile (**79**) was added to a round bottomed flask together with *p*-toluenesulfonic acid monohydrate (0.80 g, 4.40 mmol), sodium nitrite (0.29 g, 4.40 mmol) and dichloromethane (7 mL). The mixture was stirred overnight at room temperature. The crude was filtered and washed with dichloromethane. The filtrate was dried with anhydrous $MgSO_4$ and the solvent was removed carefully under reduced pressure at room temperature to afford the final product **81**. 82% yield, brown solid.

^{1}H-NMR (400 MHz, $CDCl_3$) δ 8.19 and 8.17 (br s, 1 H, NH, NH'), 7.86-7.81 (m, 2H, C11-H, C11-H'), 7.60-7.46 (m, 4H, C9-H, C9-H', C10-H, C10-H'), 3.20-3.12 (m, 0.3H, C2-H'), 3.11-3.01 (m, 0.8H, C2-H), 2.80-2.74 (m, 1H, C3-H, C3-H'), 2.64 (dd, *J* = 14.2, 12.9 Hz, 0.8, C3-H), 2.44 (dd, *J* = 13.8, 4.8 Hz, 0.5H, C3-H'), 1.47 (d, *J* = 6.9 Hz, 1.2H, C7-H'), 1.40 (d, *J* = 6.9 Hz, 2.6H, C7-H).

^{13}C-NMR (100 MHz, $CDCl_3$) δ 173.0 (C1), 172.7 (C1'), 163.0, 162.6, 150.4 and 150.4 (C8 or C8'), 133.6 and 133.2 (C9 or C9'), 129.5 and 129.4 (C10 or C10'), 123.8 and 123.7 (C11 or C11'), 114.3, 113.7, 76.2, 74.7, 37.0 (C3), 35.8 (C3'), 34.2 (C2'), 32.3 (C2), 15.1 and 15.0 (C7 or C7').

IR (KBr), vmax (cm^{-1}): 3192 (*st* N-H), 3102 (*st* Csp^2-H), 2940 (*st* C-H), 2874, 2196 (*st* C≡N), 1713, 1600-1503-1452 (*st* Csp^2-Csp^2), 1380, 1213, 1021, 767, 688.

MS (70 eV, EI) m/z (%): 105.1 (35%), 78.1 (50%), 77.1 (100%), 63.1 (30%), 56.1 (46%).

6.1.5. Alternative synthesis: Synthesis of 3-amino-1,5-diphenyl-1,7-dihydro-6*H*-pyrazolo[3,4-*b*]pyridin-6-one

Synthesis of 3-amino-5-phenyl-2,7-dihydro-6*H*-pyrazolo[3,4-*b*]pyridin-6-one (84{*3,1,1*}).

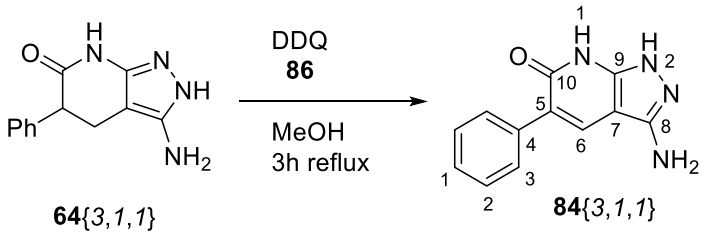

64{*3,1,1*} **84**{*3,1,1*}

50 mg (0.22 mmol) of 3-amino-5-phenyl-2,4,5,7-tetrahydro-*6H*-pyrazolo[3,4,*b*]pyridin-6-one (**64**{*3,1,1*}) and 74.59 mg (0.33 mmol) of 2,3-dichloro-5,6-dicyano-1,4-benzoquinone (DDQ) (**86**) were dissolved in 4 mL of methanol. The mixture was refluxed at 100 °C for 3 h. Then, the solvent was removed under reduced pressure and the black residue was stirred in the minimum volume of ethyl acetate. The solid was filtered and dried *in vacuo* over P_2O_5, yielding 40.7 mg (0.18 mmol, 82%) of 3-amino-5-phenyl-2,7-dihydro-6*H*-pyrazolo[3,4-*b*]pyridin-6-one (**84**{*3,1,1*}), as a brown solid.

mp: > 250 °C

^{1}H-NMR (400 MHz, DMSO-d_6) δ 11.26 (s, 1H, N1-H), 7.90 (s, 1H, C6-H), 7.57 – 7.54 (m, 2H, C3-H), 7.50 (br, 1H, NH), 7.36 – 7.32 (m, 2H, C2-H), 7.22 – 7.24 (m, 1H, C1-H), 6.06 (s, 2H, NH_2).

^{13}C-NMR (100 MHz, DMSO-d_6) δ 163.1 (C10), 148.2 (C9), 145.8 (C8), 138.8 (C4), 132.8 (C6), 128.6 (C3), 128.2 (C2), 126.6 (C1), 120.8 (C5), 92.8 (C7).

IR (KBr), vmax (cm^{-1}): 3342 (*st* N-H), 3194 (*st* Csp^2-H), 1639 (*st* C=O), 1455, 698 (*b* Csp^2-H).

MS (70 eV, EI) m/z (%): 226.1 (18%), 183.1 (18%), 43.1 (100%).

HRMS (EI): calculated for $C_{12}H_{10}N_4O$ [M+]: 226.09; found: 227.09.

Synthesis of 3-amino-1,5-diphenyl-1,7-dihydro-6*H*-pyrazolo[3,4-*b*]pyridin-6-one (84{*3,1,3*}).

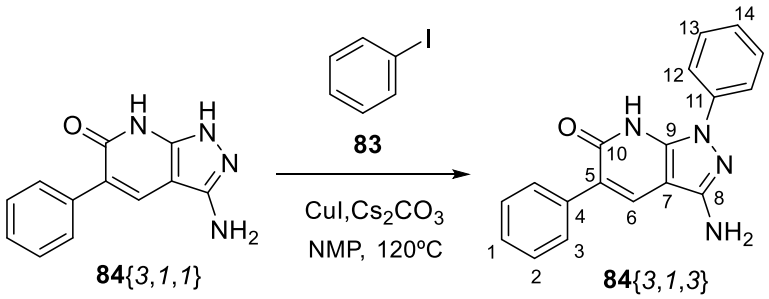

57 mg (0.25 mmol) of 3-amino-5-phenyl-2,7-dihydro-6*H*-pyrazolo[3,4-*b*]pyridin-6-one ((**84**{*3,1,1*}), 4.8 mg (0.03 mmol) of CuI and 81.5 mg (0.25 mmol) of Cs_2CO_3 were added to an oven dried Schlenk flask and flushed with argon. 0.04 mL (0.75 mmol) of iodobenzene (**83**) and 0.75 mL of NMP were added to the tube reaction using a syringe and the tube was coated with a screw cap. The tube was placed in a preheated oil bath and the reaction mixture was stirred at 120 °C for 24 hours. The mixture was left to cool to room temperature and filtered through a Celite pad washing with DMF. The solvent was removed under reduced pressure and the crude was purified by column chromatography (Silica column. Cy:AcOEt gradient 0% to 100% in 5 minutes and then isocratic at 100% AcOEt for 10 minutes). 15.5 mg (0.05 mmol, 20%) of 3-amino-1,5-diphenyl-1,7-dihydro-6*H*-pyrazolo[3,4-*b*]pyridin-6-one (**84**{*3,1,3*}) were obtained as a brown solid.

mp: 233-236 °C

^{1}H-NMR (400 MHz, DMSO-d_6) δ 11.48 (s, 1H, NH), 8.24 (d, J= 6.49 Hz, 2H, C12-H), 8.18 (s, 1H, C6-H), 7.59 (d, J= 7.22 Hz, 2H, C3-H), 7.44 (m, 4H, C2-H, C13-H), 7.33 (t, J= 7.71 Hz, 1H, C1-H), 7.13 (t, J= 6.49 Hz, 1H, C14-H), 5.98 (s, 2H, NH_2).

^{13}C-NMR (100 MHz, DMSO-d_6) δ 161.1 (C10), 149.6 (C9), 147.9 (C8), 140.0 (C11), 137.6 (C4), 132.7 (C6), 129.0 (C3), 128.8 (C2), 128.1 (C13), 126.8 (C1), 123.2 (C14), 118.3 (C12), 116.7 (C5), 104.4 (C7).

IR (KBr), vmax (cm^{-1}): 3426 (*st* N-H), 3304 (*st* Csp^2-H), 1632, 1590 (*st* C=O), 1501, 695 (*b* Csp^2-H).

MS (70 eV, EI) m/z (%): 303.2 (26%), 302.2 (100%), 301.9 (65%), 77.0 (31%).

Synthesis of 3-(dimethylamino)-7-methyl-1,5-diphenyl-1,7-dihydro-6*H*-pyrazolo[3,4-*b*]pyridin-6-one (88{*3,1,3*}).

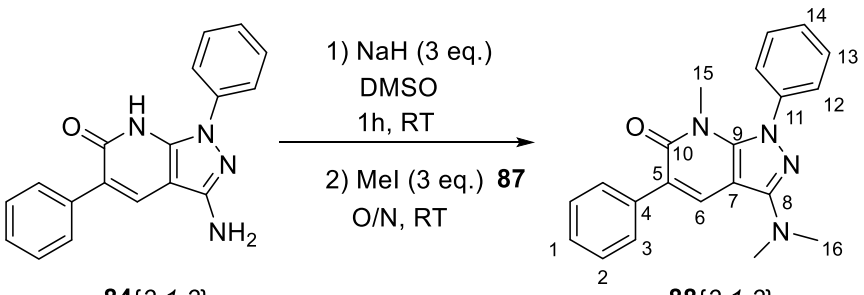

20 mg (0.07 mmol) of 3-amino-1,5-diphenyl-1,7-dihydro-6*H*-pyrazolo[3,4-*b*]pyridin-6-one (**84**{*3*,*1*,*3*}) were dissolved in 2 mL of DMSO. 13.3 mg (0.20 mmol) of NaH were added and the mixture was stirred at room temperature and under Argon atmosphere, for 1h. 12.5 µL (0.20 mmol) of MeI were added and to the mixture was stirred at room temperature overnight under Argon atmosphere. Water was added to facilitate precipitation and the product was filtered and dried *in vacuo* over P_2O_5, obtaining 10.8 mg (0.03 mmol, 45%) of 3-(dimethylamino)-7-methyl-1,5-diphenyl-1,7-dihydro-6*H*-pyrazolo[3,4-*b*]pyridin-6-one (**88**{*3*,*1*,*3*}).

^{1}H-NMR (400 MHz, DMSO-d_6) δ 8.31 (dd, J= 8.79, 1.16 Hz, 2H, C12-H), 8.22 (s, 1H, C6-H), 7.59 (d, J= 6.99 Hz, 2H, C3-H), 7.48 (m, 4H, C2-H, C13-H), 7.36 (t, J= 7.41 Hz, 1H, C1-H), 7.19 (t, J= 7.19 Hz, 1H, C14-H), 4.03 (s, 3H, C15-H_3), 3.15 (s, 6H, C16-H_3).

6.1.6. Alternative synthesis: Synthesis of 1,5-diphenyl-1,7-dihydro-6*H*-pyrazolo[3,4-*b*]pyridin-6-one (98).

Synthesis of 5-amino-1-phenyl-*1H*-pyrazole-4-carbonitrile (90).

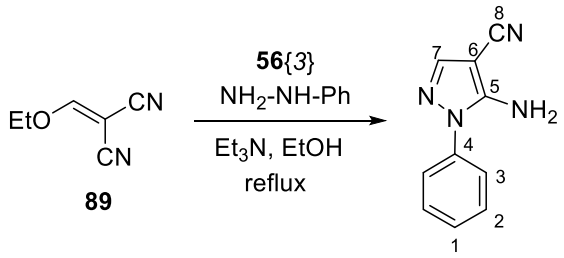

3 g (24.56 mmol) of 2-(ethoxymethylene)malononitrile (**89**) and 3 mL (24.56 mmol) of triethylamine were added to a solution of 2.5 g (23.33 mmol) of phenylhydrazine (**56**{*3*}) in 24 mL of absolute ethanol. The mixture was stirred at room temperature for 10 min, and then refluxed at 75 °C for 1.5 h. Once the reaction had reached room temperature, the solvent was removed under reduced pressure. The crude was suspended in water and extracted with AcOEt. The combined organic layers were washed with brine, dried with anhydrous $MgSO_4$ and concentrated under reduced pressure. The remaining residue was stirred in cyclohexane and the solid was filtered and dried *in vacuo* over P_2O_5. 2.7 g (14.66 mmol, 60%) of 5-amino-1-phenyl-*1H*-pyrazole-4-carbonitrile (**90**) were obtained as a brown-red solid.

mp: 122-126 °C

^{1}H-NMR (400 MHz, DMSO-d_6) δ 7.79 (s, 1H, C7-H), 7.51 (m, 4H, C2-H, C3-H), 7.43 (m, 1H, C1-H), 6.68 (s, 2H, NH_2).

^{13}C-NMR (100 MHz, DMSO-d_6) δ 151.5 (C5), 141.7 (C7), 137.5 (C4), 129.4 (C3), 128.0 (C1), 124.3 (C2), 114.9 (C8), 73.7 (C6).

IR (KBr), vmax (cm^{-1}): 3325 (*st* N-H), 3323 (*st* Csp^2-H), 2224 (*st* C≡N), 1562, 1537, 694 (*b* Csp^2-H).

MS (70 eV, EI) m/z (%): 184.1 (100%), 183.2 (35%), 121.1 (21%), 93.1 (34%), 77.1 (45%), 66.1 (31%), 65.1 (21 %), 51.1 (28%), 44.1 (28%), 43.1 (29%), 41.1 (20%)

Synthesis of 5-amino-1-phenyl-*1H*-pyrazolo-4-carbaldehyde (92).

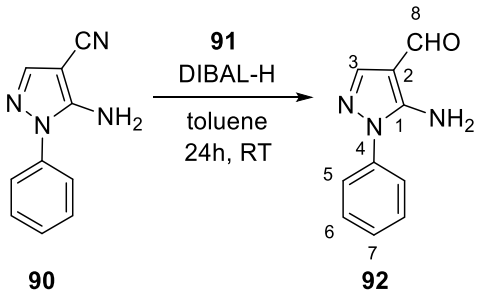

90 **92**

300 mg (1.62 mmol) of 5-amino-1-phenyl-*1H*-pyrazole-4-carbonitrile (**90**) were dissolved in 1.2 mL of toluene. Then, 0.6 mL (3.24 mmol) of DIBAL-H (**91**) were slowly added and the mixture was stirred for 1h at room temperature. Then, a second equivalent (3.24 mmol) of DIBAL-H was added to the solution and the mixture was stirred for 24h. The reaction was quenched with water and the product was extracted with diethyl ether. The organic layers were washed with brine, dried with anhydrous $MgSO_4$, filtered and concentrated under reduced pressure. The residue was purified by column chromatography (silica column, Cy:AcOEt 1:1) to yield 231 mg (1.24 mmol, 77%) of 5-amino-1-phenyl-*1H*-pyrazolo-4-carbaldehyde (**92**) as a brown solid.

mp: 100 °C

^{1}H-NMR (400 MHz, DMSO-d_6) δ 9.64 (s, 1H, C8-H), 7.78 (s, 1H, C3-H), 7.48 – 7.52 (m, 4H, C5-H, C6-H), 7.44 – 7.42 (m, 1H, C7-H), 6.68 (s, 2H, NH_2).

^{13}C-NMR (100 MHz, DMSO-d_6) δ 151.5 (C1), 141.7 (C3), 137.6 (C4), 129.5 (C5), 127.8 (C7), 124.1 (C6), 114.7 (C8), 106.9 (C2).

IR (KBr), vmax (cm^{-1}): 3424 (st N-H), 3315 (st Car-H), 1649, 1610 (st CHO), 1546, 1498 (δ NH), 694 (b Csp2-H).

MS (70 eV, EI) m/z (%): 187.1 (100%), 186.2 (36%), 143.1 (20%), 77.1 (31%).

Synthesis of ethyl 6-oxo-1-phenyl-6,7-dihydro-1*H*-pyrazolo[3,4-*b*]pyridine-5-carboxylate (94).

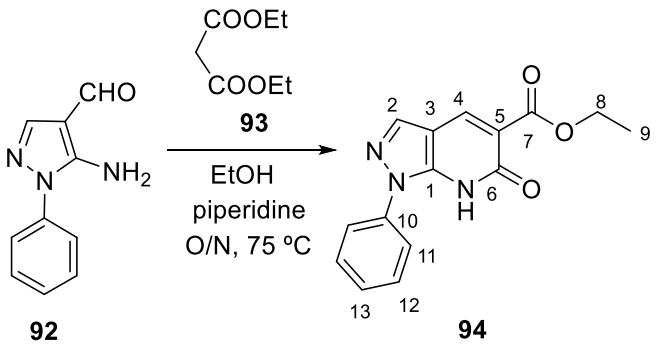

80 mg (0.43 mmol) of 5-amino-1-phenyl-*1H*-pyrazolo-4-carbaldehyde (**92**) were dissolved in 1.2 mL of EtOH. The solution was treated with 0.1 mL (0.86 mmol) of diethyl malonate (**93**) and 0.04 mL (0.43 mmol) of piperidine and heated at 75 °C in an oil bath overnight. The reaction mixture was concentrated under reduced pressure and the brown residue was treated with 200 mL of a 1:1 solution of AcOEt:Cy. The precipitate was filtered, washed with cyclohexane and dried *in vacuo* over P_2O_5, affording 70.8 mg (25 mmol, 58%) of ethyl 6-oxo-1-phenyl-6,7-dihydro-1*H*-pyrazolo[3,4-*b*]pyridine-5-carboxylate (**94**), as beige solid.

mp: 152 °C

^{1}H-NMR (400 MHz, DMSO-d_6) δ 11.9 (s, 1H, NH), 8.53 (s, 1H, C2-H), 8.22 (s, 1H, C4-H), 8.19 (m, 2H, C11-H), 7.50 (t, J= 7.39 Hz, 2H, C12-H), 7.29 (t, J= 7.47 Hz, 1H, C13-H), 4.29 (q, J= 14.21, 7.10 Hz, 2H, C8-H_2), 1.32 (t, J= 7.11 Hz, 3H, C9-H_3).

^{13}C-NMR (100 MHz, DMSO-d_6) δ 166.9 (C7), 165.1 (C6), 150.7 (C10), 139.2 (C1, C5), 136.1 (C4), 135.8 (C2), 128.9 (C12), 125.6 (C13) 120.5 (C11), 109.4 (C3), 60.7 (C8), 14.3 (C9).

IR (KBr), vmax (cm^{-1}): 3429 (*st* N-H), 3096 (*st* Csp^2-H), 1675 (*st* C=O), 1418, 814 (*b* Csp^2-H).

Elemental analysis: calculated for $C_{15}H_{13}N_3O_3$: C: 63.60%, H: 4.63%, N: 14.83%; found: C: 63.50%, H: 4.45%, N: 15.01%.

MS (70 eV, EI) m/z (%): 284.2 (25%), 283.2 (96%), 238.1 (38%), 237.1 (100%), 210.1 (26%), 209.1 (43%), 154.1 (21%), 77.1 (35%).

Synthesis of ethyl 7-methyl-6-oxo-1-phenyl-6,7-dihydro-1*H*-pyrazolo[3,4-*b*]pyridine-5-carboxylate (100).

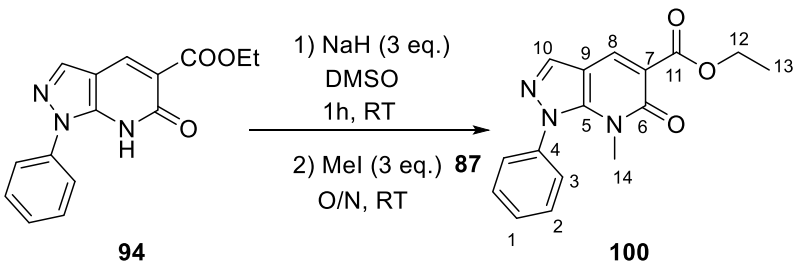

30 mg (0.11 mmol) of ethyl 6-oxo-1-phenyl-6,7-dihydro-1*H*-pyrazolo[3,4-*b*]pyridine-5-carboxylate (**94**) were dissolved in 3 mL of DMSO. 7.92 mg (0.33 mmol) of NaH were added to the solution and the mixture was stirred at room temperature for 1h under Argon atmosphere. Then, 21 µL (0.33 mmol) of MeI were added to the mixture and stirred at room temperature overnight under Argon atmosphere. The product was precipitated with water, filtered and dried *in vacuo* over P_2O_5, yielding 21 mg (0.07 mmol, 64%) of ethyl 7-methyl-6-oxo-1-phenyl-6,7-dihydro-1*H*-pyrazolo[3,4-*b*]pyridine-5-carboxylate (**100**) as a white solid.

mp: 88-90 °C

^{1}H-NMR (400 MHz, DMSO-d_6) δ 8.74 (s, 1H, C10-H), 8.42 (s, 1H, C8-H), 8.26 (m, 2H, C3-H), 7.59 (t, J= 8.61 Hz, 2H, C2-H), 7.37 (t, J= 8.78 Hz, 1H, C1-H), 4.31 (q, J= 14.21, 7.11 Hz, 2H, C12-H_2), 4.07 (s, 3H, C14-H_3), 1.33 (t, J= 7.11 Hz, 3H, C13-H_3).

^{13}C-NMR (100 MHz, DMSO-d_6) δ 164.6 (C11), 162.3 (C6), 148.8 (C4), 139.3 (C5), 137.0 (C8), 136.7 (C10), 129.8 (C2), 126.5 (C1) 120.5 (C3), 112.0 (C9), 111.3 (C7), 61.1 (C14), 54.9 (C12), 14.6 (C13).

IR (KBr), vmax (cm^{-1}): 3433 (*st* N-H), 2978 (*st* Csp^2-H), 1621, 1598 (*st* C=O), 1413, 793 (*b* Csp^2-H).

Elemental analysis: calculated for $C_{16}H_{15}N_3O_3$: C: 64.64%, H: 5.09%, N: 14.13%; found: C: 64.21%, H: 5.05%, N: 14.09%.

MS (70 eV, EI) m/z (%): 298.2 (27%), 297.2 (100%), 253.1 (21%), 252.1 (90%), 250.1 (26%), 223.1 (23%), 195.1 (21%), 77.1 (49%).

Synthesis of 5-bromo-1-phenyl-1,7-dihydro-6*H*-pyrazolo[3,4-*b*]pyridin-6-one (96)

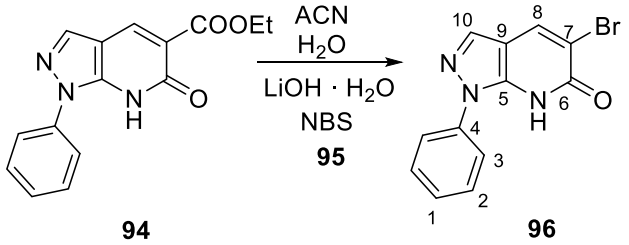

94 **96**

100 mg (0.35 mmol) of ethyl 1-phenyl-6-oxo-6,7-diydro-*1H*-pyrazolo-[3,4,*b*]pyridine-5-carboxylate (**94**) was dissolved in 1 mL of ACN and 1 mL of water at room temperature. 37.5 mg (0.89 mmol) of lithium hydroxide monohydrate were added and the suspension was heated at 90 °C for 1h. The reaction was cooled to 35 °C, treated with 62.3 mg (0.35 mmol) of *N*-bromosuccinimide (NBS) and stirred for 1h at room temperature. Then, an additional portion (0.35 mmol) of *N*-bromosuccinimide was added and the mixture was stirred for an one extra hour at room temperature. The reaction mixture was neutralized with a saturated solution of $NaHCO_3$ and extracted with AcOEt. The combined organic layers were washed with water and brine, dried over anhydrous $MgSO_4$ and concentrated under reduced pressure. The remaining residue was suspended in water, filtered and dried *in vacuo* over P_2O_5 to afford 72.6 mg (0.25 mmol, 71%) of 5-bromo-1-phenyl-1,7-dihydro-6*H*-pyrazolo[3,4-*b*]pyridin-6-one (**96**).

mp: 220-224 °C

^{1}H-NMR (400 MHz, DMSO-d_6) δ 12.52 (s, 1H, NH), 8.49 (s, 1H, C10-H), 8.16 (m, 3H, C8-H, C3-H), 7.55 (t, J= 7.59 Hz, 2H, C2-H), 7.34 (t, J= 7.42 Hz, 1H, C1-H).

^{13}C-NMR (100 MHz, DMSO-d_6) δ 159.3 (C6), 146.9 (C9), 138.9 (C4), 135.8 (C8), 134.2 (C10), 129.1 (C2), 126.1 (C1), 120.8 (C3) 112.5 (C5), 101.8 (C7).

IR (KBr), vmax (cm^{-1}): 3432 (*st* N-H), 3059 (*st* Csp^2-H), 1638 (*st* C=O), 1592, 1566, 778 (*b* Csp^2-H).

MS (70 eV, EI) m/z (%): 291.1 (97%), 289.1 (100%), 84.1 (26%), 77.1 (61%), 51.1 (25%).

Synthesis of 1,5-diphenyl-1,7-dihydro-6*H*-pyrazolo[3,4-*b*]pyridin-6-one (98).

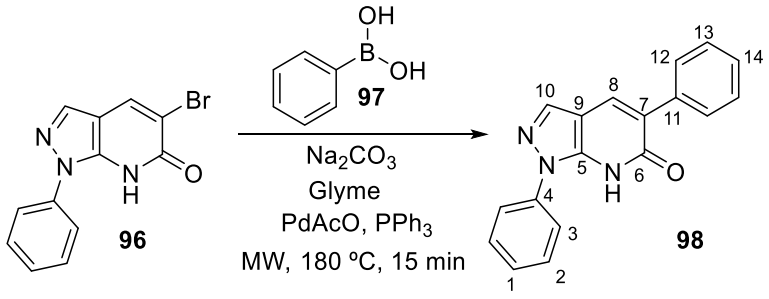

25 mg (0.09 mmol) of 5-bromo-1-phenyl-1,7-dihydro-6*H*-pyrazolo[3,4-*b*]pyridin-6-one (**96**), 33 mg (0.27 mmol) of phenylboronic acid (**97**), 29 mg (0.27 mmol) of Na_2CO_3 and 1 mL of glyme were placed in a microwave vial containing a stirring bar. Then, 1 mg (0.004 mmol) of palladium acetate and 2.5 mg (0.008 mmol) of triphenylphosphine were added. The vial was sealed and heated under microwave irradiation at 180 °C for 15 min. The solvent was eliminated under reduced pressure and the residue was extracted into CH_2Cl_2. The organic layers were washed with water, dried over anhydrous $MgSO_4$ and concentrated under reduce pressure. The residue was purified by column chromatography (Silica column, DCM:MeOH gradient 0% to 1% in 40 minutes) to yield 10.5 mg (0.04 mmol, 42%) of 1,5-diphenyl-1,7-dihydro-6*H*-pyrazolo[3,4-*b*]pyridin-6-one (**98**) as a white solid.

mp: 201-203 °C

^{1}H-NMR (400 MHz, DMSO-d_6) δ 11.81 (s, 1H, NH), 8.28 – 8.24 (m, 2H, C3-H), 8.24 (s, 1H, C10-H), 8.17 (s, 1H, C8-H), 7.64 – 7.58 (m, 2H, C12-H), 7.59 – 7.53 (m, 2H, C2-H), 7.48 – 7.41 (m, 2H, C13-H), 7.39 – 7.30 (m, 2H, C1-H, C14-H).

^{13}C-NMR (100 MHz, DMSO-d_6) δ 161.2 (C6), 147.4 (C5), 139.2 (C4), 137.2 (C11), 135.1 (C10), 132.8 (C8), 129.2 (C12), 129.1 (C2), 128.1 (C13), 127.1 (C14), 125.8 (C1), 120.5 (C3), 120.1 (C7), 111.8 (C9).

IR (KBr), vmax (cm^{-1}): 3435 (*st* N-H), 3052 (*st* Csp^2-H), 1633, 1616 (*st* C=O), 1501, 694 (*b* Csp^2-H).

MS (70 eV, EI) m/z (%): 288.2 (22%), 286.2 (28%), 187.2 (100%).

HRMS (TOF) m/z (%): calculated for $C_{12}H_{16}N_3O$, $[M]^+$: 287,110; found: 288.110.

Synthesis of 7-methyl-1,5-diphenyl-1,7-dihydro-6*H*-pyrazolo[3,4-*b*]pyridin-6-one (101)

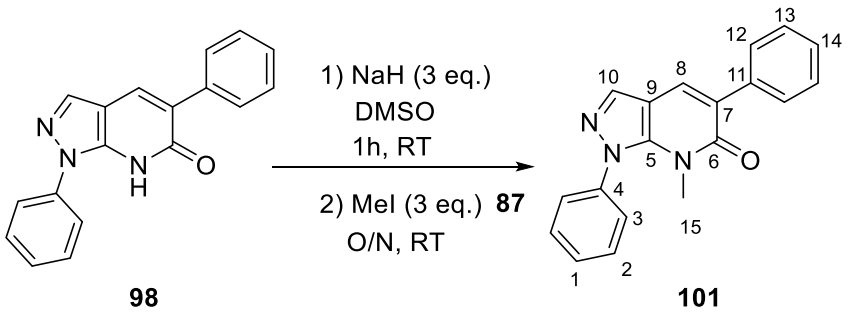

30 mg (0.11 mmol) of 1,5-diphenyl-1,7-dihydro-6*H*-pyrazolo[3,4-*b*]pyridin-6-one (**98**) were dissolved in 3 mL of DMSO. 5 mg (0.21 mmol) of NaH were added to the solution and the mixture was stirred at room temperature for 1.5h under Argon atmosphere. Then, 7.5 µL (0.11 mmol) of MeI were added and the mixture was stirred at room temperature overnight under Argon atmosphere. The product was precipitated with water, filtered and dried *in vacuo* over P_2O_5, yielding 24.0 mg (0.08 mmol, 72%) of 7-methyl-1,5-diphenyl-1,7-dihydro-6*H*-pyrazolo[3,4-*b*]pyridin-6-one (**101**) as a white solid.

^{1}H-NMR (400 MHz, DMSO-d_6) δ 8.36 – 8.31 (m, 2H, C3-H), 8.31 (s, 1H, C10), 8.20 (s, 1H, C8), 7.62 – 7.55 (m, 4H, C2-H, C12-H), 7.48 – 7.43 (m, 2H, C13-H), 7.41 – 7.31 (m, 2H, C1-H, C14-H), 4.03 (s, 3H, C15-H_3)

^{13}C-NMR (100 MHz, DMSO-d_6) δ 160.8 (C6), 147.1 (C5), 139.2 (C4), 136.6 (C11), 135.1 (C10), 132.8 (C8), 129.3 (C12), 129.2 (C2), 128.2 (C13), 127.4 (C14), 125.7 (C1), 120.8 (C7), 119.9 (C3), 112.3 , 54.1 (C15).

IR (KBr), vmax (cm^{-1}): 3430 (*st* N-H), 3058 (*st* Csp^2-H), 2946, 1617 (*st* C=O), 1597, 1501 (*st* Csp^2-Csp^2), 1407, 1304, 756 (*b* Csp^2-H).

Elemental analysis: calculated for $C_{19}H_{15}N_3O$: C: 75.73%, H: 5.02%, N: 13.94%; found: C: 75.90%, H: 5.12%, N: 13.99%.

MS (70 eV, EI) m/z (%): 302.0 (22%), 301.1 (100%), 300.1 (39%), 77.0 (32%), 51.0 (16%)

6.1.7. Synthesis of *N*-acyl substituted 3-amino-1,4,5,7-tetrahydro-6*H*-pyrazolo[3,4-*b*]pyridin-6-ones

6.1.7.1 Synthesis of 1-acyl 3-amino-1,4,5,7-tetrahydro-6*H*-pyrazolo[3,4-*b*]pyridin-6-ones

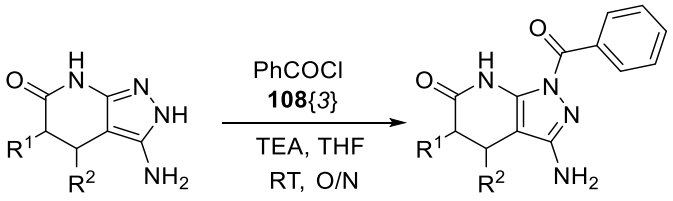

64 **109**

0.219 mmol of the corresponding 3-amino-2,4,5,7-tetrahydro-6*H*-pyrazolo[3,4-*b*]pyridin-6-one (**64**), 31 µL (0.219 mmol) of benzoyl chloride (**108**{*3*}) and 31 µL (0.219 mmol) of TEA were dissolved in 10 mL of THF. The mixture was stirred at room temperature overnight. The solid was filtered, and the filtrate was evaporated under reduced pressure. The residue was suspended in MeOH, the solid was filtered and the filtrate was evaporated under reduced pressure. If necessary the crude was purified by column chromatography (silica column, DCM:MeOH gradient from 0% to 5% of MeOH in 60 min) to afford the corresponding 3-amino-1-benzoyl-1,4,5,7-tetrahydro-6*H*-pyrazolo[3,4-*b*]pyridin-6-one (**109**).

3-amino-1-benzoyl-4-methyl-1,4,5,7-tetrahydro-6*H*-pyrazolo[3,4-*b*]pyridin-6-one (109{*1,2,3*})

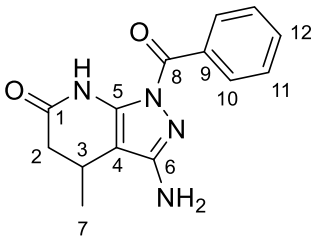

Starting from 3-amino-4-methyl-1,4,5,7-tetrahydro-6*H*-pyrazolo[3,4-*b*]pyridin-6-one (**64**{*1,2*}). 69%, yellowish solid.

mp: 73-77 °C

^{1}H-NMR (400 MHz, DMSO-d_6) δ 9.58 (s, 1H, NH), 8.09 – 7.86 (m, 2H, C10-H), 7.61 – 7.52 (m, 1H, C12-H), 7.50 – 7.42 (m, 2H, C11-H), 5.70 (s, 2H, NH_2), 2.97 (dd, *J* = 7.4, 2.6 Hz, 1H, C3-H), 2.85 (dd, *J* = 16.2, 7.4 Hz, 1H, C2-H), 2.35 – 2.27 (dd, *J* = 16.2, 2.6 Hz, 1H, C2-H), 1.06 (d, *J* = 6.9 Hz, 3H, C7-H_3).

^{13}C-NMR (100 MHz, DMSO-d_6) δ 169.5 (C1), 167.3 (C8), 155.2, 141.3, 133.2 (C9), 132.4 (C12), 130.7 (C10), 128.2 (C11), 98.0 (C4), 39.2 (C2), 22.4 (C3), 20.3 (C7).

IR (KBr), vmax (cm^{-1}): 3342 (*st* N-H), 2923 (*st* Csp^2-H), 1667, 1595 (*st* C=O), 1533, 1500, 708(*b* Csp^2-H).

MS (70 eV, EI) m/z (%): 270.2 (33%), 105.2 (100%).

3-amino-1-benzoyl-4-phenyl-1,4,5,7-tetrahydro-6*H*-pyrazolo[3,4-*b*]pyridin-6-one (109{*1*,*3*,*3*})

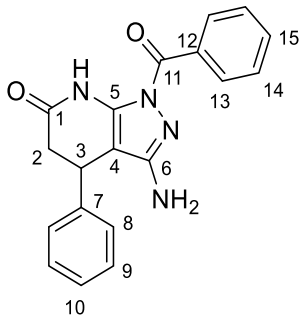

Starting from 3-amino-4-phenyl-1,4,5,7-tetrahydro-6*H*-pyrazolo[3,4-*b*]pyridin-6-one (**64**{*1*,*3*}). 58%, white solid.

mp: 192-196 °C

^{1}H-NMR (400 MHz, DMSO-d_6) δ 9.80 (s, 1H, NH), 8.03 – 7.92 (m, 2H, C13-H), 7.65 – 7.55 (m, 1H, C15-H), 7.52 – 7.46 (m, 2H), 7.37 – 7.27 (m, 2H), 7.24-7.20 (m, 2H, C8-H), 7.21 – 7.19 (m, 1H, C10-H), 5.62 (s, 2H, NH_2), 4.20 (dd, *J* = 7.9, 2.2 Hz, 1H, C3-H), 3.19 (dd, *J* = 16.3, 8.0 Hz, 1H, C2-H), 2.62 (dd, *J* = 16.3, 2.3 Hz, 1H, C2-H).

^{13}C-NMR (100 MHz, DMSO-d_6) δ 169.2 (C1), 167.3 (C11), 155.3, 142.8, 142.4 (C7), 133.2 (C12), 132.5 (C15), 130.8 (C13), 129.1, 128.2, 127.3 (C10), 127.2 (C8), 95.9 (C4), 39.8 (C2), 32.4 (C3).

IR (KBr), vmax (cm^{-1}): 3463 (*st* N-H), 3309 (*st* Csp^2-H), 1669 (*st* C=O), 1509, 698 (*b* Csp^2-H).

MS (70 eV, EI) m/z (%): 332.3 (49%), 105.2 (100%), 104.7 (26%).

3-amino-5-methyl-1-picolinoyl-1,4,5,7-tetrahydro-6*H*-pyrazolo[3,4-*b*]pyridin-6-one (109{*2*,*1*,*2*})

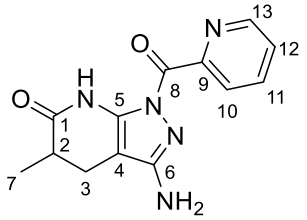

Starting from 3-amino-5-methyl-1,4,5,7-tetrahydro-6*H*-pyrazolo[3,4-*b*]pyridin-6-one (**64**{*2*,*1*}) and using picolinoyl chloride **108**{*4*} instead of benzoyl chloride. 64% yield, yellowish solid

^{1}H-NMR (400 MHz, DMSO-d_6) δ 9.82 (s, 1H, NH), 8.69 (m, 1H), 8.06 – 8.00 (m, 1H), 8.00 – 7.94 (m, 1H), 7.65 – 7.57 (m, 1H), 4.89 (s, 2H, NH_2), 2.69 – 2.59 (m, 2H, C2-H, C3-H), 2.12 (dd, *J* = 14.7, 10.1 Hz, 1H, C3-H), 1.09 (d, *J* = 6.9 Hz, 3H, C6-H_3).

3-amino-1-benzoyl-5-phenyl-1,4,5,7-tetrahydro-6*H*-pyrazolo[3,4-*b*]pyridin-6-one (109{*3*,*1*,*3*})

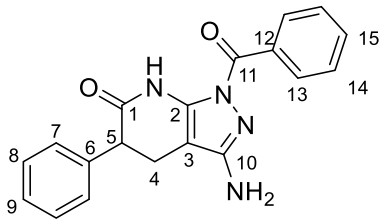

Starting from 3-amino-5-phenyl-1,4,5,7-tetrahydro-6*H*-pyrazolo[3,4-*b*]pyridin-6-one (**64**{*3*,*1*}). 15% yield, yellowish solid.

^{1}H-NMR (400 MHz, DMSO-d_6) δ 10.64 (s, 1H, NH), 7.93 – 7.82 (m, 2H, C13-H), 7.60 – 7.55 (m, 1H, C15-H), 7.52 – 7.46 (m, 2H, C14-H), 7.35 – 7.30 (m, 2H, C8-H), 7.27 – 7.22 (m, 3H, C7-H, C9-H), 6.78 (s, 2H, NH_2), 3.85 (t, J = 7.3 Hz, 1H, C5-H), 2.94 (dd, J = 15.6, 7.0 Hz, 1H, C4-H), 2.80 (dd, J = 15.6, 7.8 Hz, 1H, C4-H).

^{13}C-NMR (100 MHz, DMSO-d_6) δ 171.4 (C1), 169.2 (C11), 152.6 (C10), 146.9 (C2), 140.1 (C6), 133.8 (C12), 131.6 (C15), 129.9 (C13), 128.3 (C8), 128.0 (C7), 127.7 (C14), 126.8 (C9), 84.1 (C3), 46.7 (C5), 23.1 (C4).

IR (KBr), vmax (cm^{-1}): 3447 (*st* N-H), 3307, 2925, 1671 (*st* C=O), 1598 (*st* C=C), 1503, 1383, 1351, 1330, 1229 (*st* C-O), 696.

6.1.7.2 Syntesis of picolinoyl chloride 108{*4*}

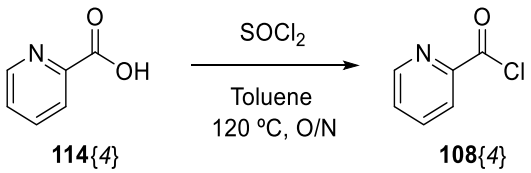

114{*4*} **108**{*4*}

200 mg (1.6 mmol) of piconylic acid (**114**{*4*}) and 0.58 mL (8 mmol) of $SOCl_2$ were added into a 10 mL round bottomed flask with 4 mL of toluene. The solution was refluxed overnight at 120 °C. The solvent was removed under reduced pressure to afford 135 mg (59%) of picolinoyl chloride (**108**{*4*}) as a black-purple solid.

^{1}H-NMR (400 MHz, DMSO-d_6) δ 8.75 – 8.72 (m, 1H), 8.12 – 8.04 (m, 2H), 7.73 – 7.68 (m, 1H). Spectroscopic data are consistent with those previously described.[10]

6.1.7.3 Synthesis of *N*-(1-benzoyl-6-oxo-4,5,6,7-tetrahydro-1*H*-pyrazolo[3,4-*b*]pyridin-3-yl)benzamides

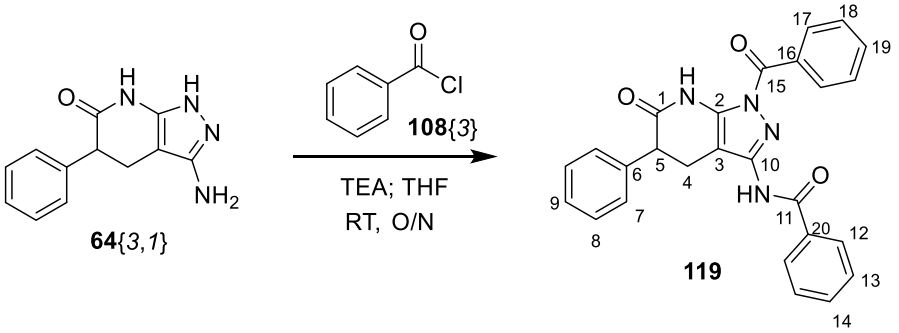

50 mg (0.219 mmol) of 3-amino-5-phenyl-1,4,5,7-tetrahydro-6*H*-pyrazolo[3,4-*b*]pyridin-6-one (**64**{*3,1*}), 31 µL (0.219 mmol) of benzoyl chloride **108**{*4*} and 31 µL (0.219 mmol) of TEA were dissolved in 10 mL of THF. The mixture was stirred at room temperature overnight. The solid was removed by filtration and the filtrate was evaporated under reduced pressure. The residue was suspended in MeOH and filtered to remove the salts. The solvent was removed under reduced pressure and the crude was purified by column chromatography (silica column, DCM:MeOH gradient from 0% to 5% of MeOH in 60 min) to afford 54 mg (56%) of N-(1-benzoyl-6-oxo-5-phenyl-4,5,6,7-tetrahydro-1*H*-pyrazolo[3,4-*b*]pyridin-3-yl)benzamide (**119**) as a yellowish solid.

^{1}H-NMR (400 MHz, DMSO-d_6) δ 10.94 (s, 1H, NH), 10.24 (s, 1H,NH), 8.06 – 8.02 (m, 2H, C17-H), 7.98 – 7.95 (m, 2H, C12-H), 7.71 – 7.66 (m, 1H, C19-H), 7.61 – 7.54 (m, 3H, C18-H and C14-H), 7.51 – 7.45 (m, 2H, C13-H), 7.36 – 7.31 (m, 4H, C7-H and C8-H), 7.30 – 7.25 (m, 1H, C9-H), 4.07 – 4.00 (m, 1H, C5-H), 3.00 (dd, J = 9.0, 6.2 Hz, 2H, C4-H_2).

^{13}C-NMR (100 MHz, DMSO-d_6) δ 170.1 (C1), 167.2 (C15), 165.7 (C11), 147.6 (C10), 141.9 (C2), 139.3 (C6), 132.9 (C19), 132.9 (C20), 132.2 (C14), 131.7 (C16), 130.8 (C17), 128.5 (C7*), 128.4 (C16), 128.3 (C8*), 128.1 (C18), 128.1 (C12), 126.9 (C9), 97.9 (C3), 46.4 (C5), 26.2 (C4).

IR (KBr), vmax (cm^{-1}): 3378 (*st* N-H), 3272 (*st* Csp^2-H), 3029, 1680 (*st* C=O), 1547, 1497, 1345, 1213 (*st* C-O), 1180, 874, 699.

6.1.7.4 Synthesis of *N*-(1-benzoyl-5-methyl-6-oxo-4,5,6,7-tetrahydro-1*H*-pyrazolo[3,4-*b*]pyridin-3-yl)benzamide (121)

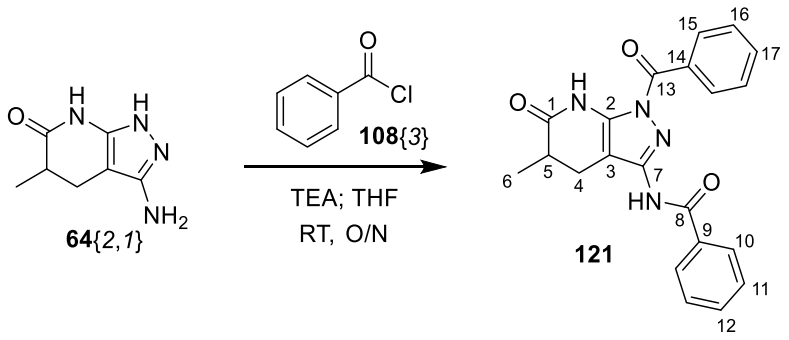

50 mg (0.3 mmol) of 3-amino-5-phenyl-1,4,5,7-tetrahydro-6*H*-pyrazolo[3,4-*b*]pyridin-6-one (**64**{*2,1*}), 41 µL (0.3 mmol) of benzoyl chloride **108**{*4*} and 42 µL (0.3 mmol) of TEA were dissolved in 10 mL of THF. The mixture was stirred at room temperature overnight. The solid was removed by filtration and the filtrate was evaporated under reduced pressure. The residue was suspended in MeOH and filtered to remove the salts. The solvent was removed under reduced pressure and the crude was purified by column chromatography (silica column, DCM:MeOH gradient from 0% to 5% of MeOH in 60 min) to afford 21 mg (19%) of *N*-(1-benzoyl-5-methyl-6-oxo-4,5,6,7-tetrahydro-1*H*-pyrazolo[3,4-*b*]pyridin-3-yl)benzamide (**121**) as a white solid.

^{1}H-NMR (400 MHz, DMSO-d_6) δ 10.91 (s, 1H, NH), 9.93 (s, 1H, NH), 8.04 – 7.97 (m, 4H), 7.70 – 7.64 (m, 1H), 7.63 – 7.58 (m, 1H), 7.57 – 7.48 (m, 4H), 2.83 (dd, J = 15.8, 7.2 Hz, 1H, C4-H), 2.71 (dt, J = 11.5, 7.0 Hz, 1H, C5-H), 2.48 – 2.42 (m, 1H, C4-H), 1.18 (d, J = 6.8 Hz, 3H, C6-H).

^{13}C-NMR (100 MHz, DMSO-d_6) δ 172.2 (C1), 167.2 (C13), 165.7 (C8), 147.7 (C7), 141.9 (C2), 132.9, 132.8, 132.2, 131.8, 130.7, 128.4, 128.1, 97.9 (C3), 34.8 (C5), 25.5 (C4), 15.6 (C6).

IR (KBr), vmax (cm^{-1}): 3387 (*st* N-H), 2932, 1679 (*st* C=O), 1548 (*st* C=C), 1507, 1344, 1291 (*st* C-O), 873, 710.

6.1.7.5 Synthesis of *N*-(5-methyl-6-oxo-4,5,6,7-tetrahydro-1*H*-pyrazolo[3,4-*b*] pyridin-3-yl)benzamide (122)

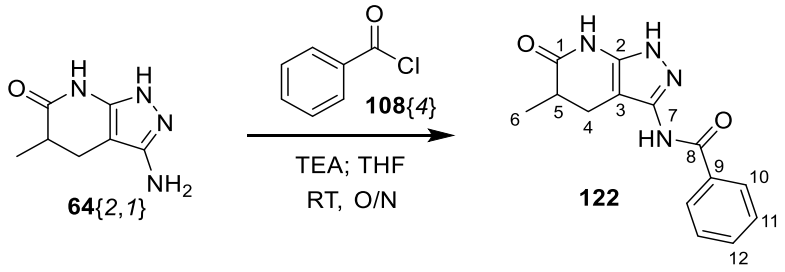

50 mg (0.3 mmol) of 3-amino-5-phenyl-1,4,5,7-tetrahydro-6*H*-pyrazolo[3,4-*b*]pyridin-6-one (**64**{*2*,*1*}), 41 µL (0.3 mmol) of benzoyl chloride **108**{*4*} and 42 µL (0.3 mmol) of TEA were dissolved in 10 mL of THF. The mixture was stirred at room temperature overnight. The solid was removed by filtration and the filtrate was evaporated under reduced pressure. The residue was suspended in MeOH and filtered to remove the salts. The solvent was removed under reduced pressure and the crude was purified by column chromatography (silica column, DCM:MeOH gradient from 0% to 5% of MeOH in 60 min) to afford 14 mg (17%) of N-(5-methyl-6-oxo-4,5,6,7-tetrahydro-1*H*-pyrazolo[3,4-*b*]pyridin-3-yl)benzamide (**122**) as a white solid.

^{1}H-NMR (400 MHz, DMSO-*d*$_6$) δ 11.90 (s, 1H, NH), 10.54 (s, 1H, NH), 10.16 (s, 1H, NH), 7.96 (d, J = 7.6 Hz, 2H, C10-H), 7.61 (d, J = 7.3 Hz, 1H, C12-H), 7.55 (d, J = 7.6 Hz, 2H, C11-H), 2.88 – 2.77 (m, 1H, C4-H), 2.47 (s, 1H, C5-H), 2.35 – 2.31 (m, 1H, C4-H), 1.13 (d, J = 6.9 Hz, 3H, C6-H$_3$).

^{13}C-NMR (100 MHz, DMSO-*d*$_6$) δ 173.0 (C1), 165.1 (C8), 147.5 (C7), 133.3 (C9), 132.1 (C12), 128.5 (C11), 127.8 (C10), 92.2 (C3), 35.6 (C5), 24.4 (C4), 16.2 (C6).

IR (KBr), vmax (cm^{-1}): 3243 (*st* N-H), 2930, 1661 (*st* C=O), 1514, 1283 (*st* C-O), 709.

6.1.7.6 Synthesis of 2-acyl 3-amino-1,4,5,7-tetrahydro-6*H*-pyrazolo[3,4-*b*]pyridin-6-ones (110)

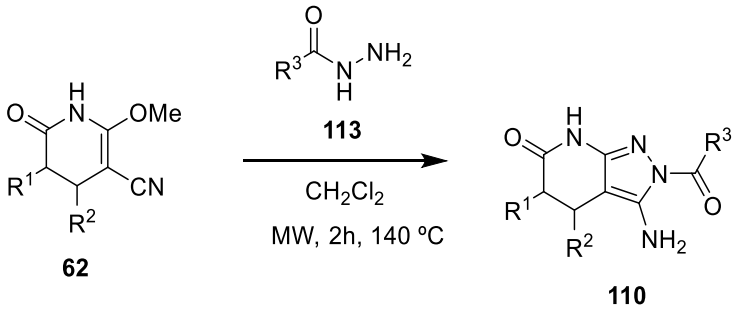

0.26 mmol of the corresponding 2-methoxy-6-oxo-1,4,5,6-tetrahydropyridine-3-carbonitrile (**62**) and 0.51 mmol of hydrazide (**113**) were suspended in 4 mL of CH_2Cl_2 in a 5 mL microwave vial. The mixture was heated under microwave irradiation for 2 h at 140 °C. The solution was washed with H_2O (3 x 5mL) and the organic layer was dried with $MgSO_4$. The solvent was removed under reduced pressure to afford the corresponding 3-amino-2-acyl-2,4,5,7-tetrahydro-6*H*-pyrazolo[3,4-*b*]pyridin-6-one (**110**)

3-amino-2-benzoyl-4-methyl-2,4,5,7-tetrahydro-6*H*-pyrazolo[3,4-*b*]pyridin-6-one (110{*1,2,3*})

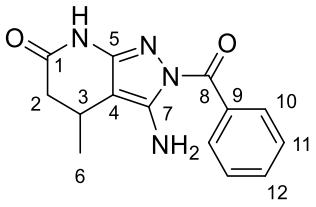

Starting from 2-methoxy-4-phenyl-6-oxo-1,4,5,6-tetrahydropyridine-3-carbonitrile (**62**{*1,2*}) and benzhydrazide (**113**{*3*}). 42% yield, white solid.

mp: 75-80 °C

^{1}H-NMR (400 MHz, DMSO-d_6) δ 10.44 (s, 1H, NH), 7.94 – 7.77 (m, 2H, C10-H), 7.61 – 7.52 (m, 1H, C12-H), 7.51 – 7.44 (m, 2H, C10-H), 6.77 (s, 2H, NH_2), 3.10 – 3.00 (m, 1H, C3-H), 2.67 (dd, J = 16.0, 6.9 Hz, 1H, C2-H), 2.21 (dd, J = 16.0, 3.1 Hz, 1H, C2-H), 1.08-1.04 (m, 3H, C6-H_3).

^{13}C-NMR (100 MHz, DMSO-d_6) δ 170.9 (C1), 169.9 (C8), 152.4, 147.1, 134.3 (C9), 131.9 (C12), 130.2 (C10), 128.2 (C11), 90.2 (C4), 39.6 (C2), 22.1 (C3), 20.7 (C6).

IR (KBr), vmax (cm^{-1}): 3447 (*st* N-H), 3336 (*st* Csp^2-H), 1669, 1595 (*st* C=O), 1546, 1500, 706(*b* Csp^2-H).

MS (70 eV, EI) m/z (%): 270.15 (41%), 105.10 (100%), 77.1(31%).

HRMS (TOF) m/z (%): calculated for $C_{14}H_{15}N_4O_2$, $[M+1]^+$: 271,1190; found $[M+1]^+$: 271.1190.

3-amino-2-benzoyl-4-phenyl-2,4,5,7-tetrahydro-6*H*-pyrazolo[3,4-*b*]pyridin-6-one (110{*1*,*3*,*3*})

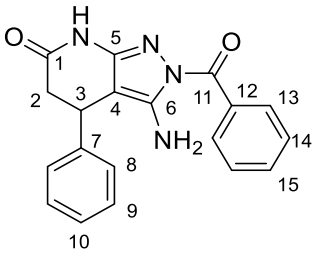

Starting from 2-methoxy-4-phenyl-6-oxo-1,4,5,6-tetrahydropyridine-3-carbonitrile (**62**{*1*,*3*}) and benzhydrazide (**113**{*3*}). 58% yield, white solid.

mp: 200-204 °C

^{1}H-NMR (400 MHz, DMSO-d_6) δ 10.59 (s, 1H, NH), 7.94 – 7.81 (m, 2H), 7.61 – 7.55 (m, 1H, C15-H), 7.52 – 7.46 (m, 2H), 7.35 – 7.29 (m, 2H), 7.24 (t, *J* = 1.4 Hz, 1H, C10-H), 7.23 – 7.18 (m, 2H, C8-H), 6.76 (s, 2H, NH_2), 4.29 (dd, *J* = 7.4, 2.4 Hz, 1H, C3-H), 3.01 (dd, *J* = 16.1,7.4 Hz, 1H, C2-H),2.55 (ddd, *J* = 16.0,2.4, 0.7 Hz,1H, C2-H).

^{13}C-NMR (100 MHz, DMSO-d_6) δ 170.1 (C1), 169.4 (C11), 152.5, 147.2, 143.3 (C7), 133.8, 131.6 (C15), 129.9, 128.6, 127.7, 126.6 (C10), 126.6 (C8), 87.3 (C4), 39.6 (C2), 31.8 (C3).

IR (KBr), vmax (cm^{-1}): 3480 (*st* N-H), 3357 (*st* Csp^2-H), 1670, 1598 (*st* C=O), 1536, 1490, 704(*b* Csp^2-H).

MS (70 eV, EI) m/z (%): 283.2 (30%), 237.1 (33%), 208.2 (34%), 151.1 (65%), 105.1 (69%), 84.2 (33%), 77.1 (71%), 69.1 (49%), 67.1 (33%), 57.1 (60%), 56.2 (51%), 55.1 (70%), 44.1 (39%), 43.1 (100%), 42.2 (50%), 41.2 (86%).

HRMS (TOF) m/z (%): calculated for $C_{19}H_{17}N_4O_2$, $[M+1]^+$: 333.1345; found $[M+1]^+$: 333.1345.

3-amino-2-benzoyl-5-methyl-2,4,5,7-tetrahydro-6*H*-pyrazolo[3,4-*b*]pyridin-6-one (110{*2*,*1*,*3*})

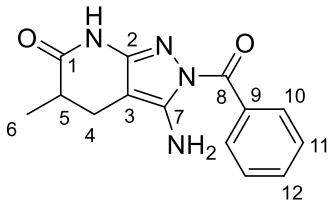

Starting from 2-methoxy-5-methyl-6-oxo-1,4,5,6-tetrahydropyridine-3-carbonitrile (**62**{*2*,*1*}) and benzhydrazide (**113**{*3*}). 32% yield, white solid.

mp: 198-201 °C

^{1}H-NMR (400 MHz, DMSO-d_6) δ 10.50 (s, 1H, NH), 7.96 – 7.91 (m, 2H, C11-H), 7.87 – 7.81 (m, 1H, C12-H), 7.64 – 7.46 (m, 2H, C10-H), 6.74 (s, 2H, NH_2), 2.80 – 2.70 (m, 1H, C4-H), 2.60 – 2.51 (m, 1H, C5-H), 2.24 (dd, J = 15.3, 10.0 Hz, 1H, C4-H), 1.13 (d, J = 6.9 Hz, 3H, C6-H_3).

^{13}C-NMR (100 MHz, DMSO-d_6) δ 173.6 (C1), 169.2 (C8), 165.7 (C9), 152.7 (C7), 146.8 (C2), 131.8 (C12), 129.8 (C10), 127.4 (C11), 84.4 (C3), 35.2 (C5), 22.8 (C4), 16.3 (C6).

IR (KBr) vmax (cm^{-1}): 3443 (*st* N-H), 3358, 1667 (*st* C=O), 1602 (*st* C=O), 1549, 1510, 1446, 1349.

MS (70 eV, EI) m/z (%): 232.2 (22%), 105.1 (100%).

2-acetyl-3-amino-5-methyl-2,4,5,7-tetrahydro-6*H*-pyrazolo[3,4-*b*]pyridin-6-one (110{*2*,*1*,*2*})

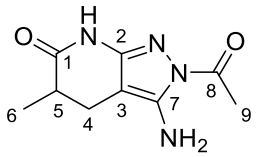

Starting from 2-methoxy-5-methyl-6-oxo-1,4,5,6-tetrahydropyridine-3-carbonitrile (**62**{*2*,*1*}) and acethydrazide (**113**{*2*}). 40% yield, yellowish solid.

mp: 162-165 °C

^{1}H-NMR (400 MHz, DMSO-d_6) δ 10.39 (s, 1H, NH), 6.60 (s, 2H, NH_2), 2.71 (dd, J = 15.2, 6.8 Hz, 1H, C4-H), 2.50 (dq, J = 3.2, 1.6 Hz, 1H, C5-H), 2.40 (s, 3H, C9-H_3), 2.22 – 2.14 (m, 1H, C4-H), 1.12 (dd, J = 6.7, 2.2 Hz, 3H, C6-H_3).

^{13}C-NMR (100 MHz, DMSO-d_6) δ 173.7 (C1), 172.2 (C8), 152.0 (C7), 145.7 (C2), 84.0 (C3), 35.3 (C5), 23.1 (C9), 22.7 (C4), 16.3 (C6).

IR (KBr) vmax (cm^{-1}): 3442 (*st* N-H), 3341, 3297, 3237 (*st* Csp^2-H), 2934, 2216, 1709, 1674 (*st* C=O, 1653 (*st* C=O), 1599, 1502, 1381, 1365, 1340, 1227 (*st* C-O).

MS (70 eV, EI) m/z (%): 208.1 (27%), 166.1 (100%), 112.1 (46%), 111.1 (65%).

2-acetyl-3-amino-4-methyl-2,4,5,7-tetrahydro-6*H*-pyrazolo[3,4-*b*]pyridin-6-one (110{*1*,*2*,*2*})

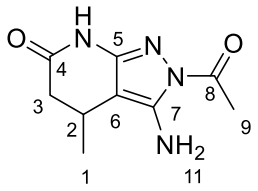

Starting from 2-methoxy-4-methyl-6-oxo-1,4,5,6-tetrahydropyridine-3-carbonitrile (**62**{*1*,*2*}) and acethydrazide (**113**{*2*}). 40% yield, white solid.

mp: 174-178 °C

^{1}H-NMR (400 MHz, DMSO-d_6) δ 10.46 (s, 1H, NH), 6.63 (s, 2H, NH_2), 2.98 (dd, *J* = 6.9, 3.5 Hz, 1H, C2-H), 2.63 (dd, *J* = 16.0, 6.9 Hz, 1H, C3-H), 2.40 (s, 3H, C9-H_3), 2.18 (ddd, *J* = 16.0, 3.1, 0.6 Hz, 1H, C3-H), 1.03 (d, *J* = 6.9 Hz, 3H, C1-H_3).

^{13}C-NMR (100 MHz, DMSO-d_6) δ 172.4 (C4), 170.5 (C8), 151.3, 145.5, 89.4 (C6), 39.2 (C3), 23.1 (C9), 21.7 (C2), 20.2 (C1).

IR (KBr), vmax (cm^{-1}): 3474(*st* N-H), 3370(*st* Csp_2-H), 1689, 1670 (*st* C=O), 1596, 1486.

MS (70 eV, EI) m/z (%): 166.2 (26%), 151.1 (98%), 67.1 (22%), 55.1 (20%), 44.1 (95%), 43.1 (100%), 42.1 (28%), 41.2 (49%).

HRMS (TOF) m/z (%): calculated for $C_9H_{15}N_4O_2$, $[M+1]^+$: 209.1033; found $[M+1]^+$: 209.1033.

2-acetyl-3-amino-4-(4-methoxyphenyl)-2,4,5,7-tetrahydro-6*H*-pyrazolo[3,4-*b*]pyridin-6-one (110{*1,4,3*})

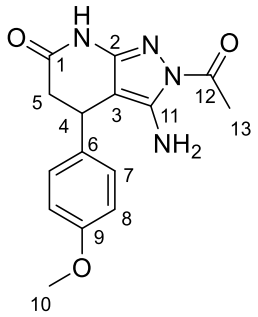

Starting from 2-methoxy-4-(4-methoxyphenyl)-6-oxo-1,4,5,6-tetrahydropyridine-3-carbonitrile (**62**{*1,4*}) and acethydrazide (**113**{*2*}). 39% yield, brownish solid.

mp: 105-107 °C

^{1}H-NMR (400 MHz, DMSO-d_6): δ 10.58 (s, 1H, NH), 7.09 – 7.04 (m, 2H, C7-H), 6.89 – 6.83 (m, 2H, C8-H), 6.56 (s, 2H, NH_2), 4.14 (dd, J = 7.2, 2.7 Hz, 1H, C4-H), 3.70 (s, 3H, C10-H_3), 2.91 (dd, J = 16.0, 7.2 Hz, 1H, C5-H), 25.3-2.45 (m, 1H, C5-H), 2.44 (s, 3H, C13-H_3).

^{13}C-NMR (100 MHz, DMSO-d_6): δ 172.4 (C1), 170.2 (C12), 157.9 (C9), 151.8 (C11), 145.9 (C2), 135.1 (C6), 127.6 (C7), 113.9 (C8), 87.4 (C3), 55.1 (C10), 39.7 (C5), 31.0 (C4), 23.1 (C13).

IR (KBr) vmax (cm^{-1}): 3450 (*st* N-H), 3358, 1689 (*st* C=O), 1646 (*st* C=O), 1512, 1384, 1335, 1250 (*st* C-O).

MS (70 eV, EI) m/z (%): 300.2 (23%), 258.2 (90%), 243.2 (24%), 227.2 (34%), 215.2 (100%), 172.1 (23%), 161.1 (41%), 151.1 (43%).

6.1.7.7 Synthesis of ^{13}C labelled 3-amino-2-benzoyl-4-methyl-2,4,5,7-tetrahydro-6*H*-pyrazolo[3,4-*b*]pyridin-6-one (118)

Synthesis of benzhydrazide (113)

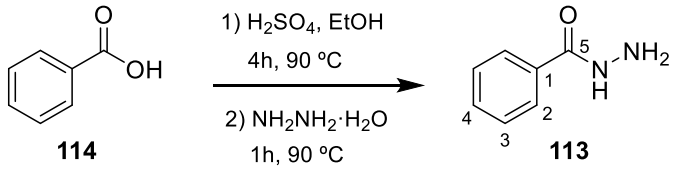

114 **113**

200 mg (1.6 mmol) of benzoic acid (**114**) were dissolved in 3 mL of EtOH and 0.3 mL (0.006 mmol) of H_2SO_4 were added into the solution. The mixture was heated for 4h at 90 °C. Then, the solution was neutralized by adding solid $NaHCO_3$, and filtered to remove the salts. 310 µL (6.4 mmol) of hydrazine monohydrate **56**{*1*} were added into the solution and refluxed for 1h at 90 °C. The solvent was removed under reduced pressure to afford 123 mg (56%) of benzohydrazide (**113**) as a white solid.

^{1}H-NMR (400 MHz, DMSO-d_6) δ 9.75 (s, 1H, NH_2), 7.84 – 7.78 (m, 2H, C2-H), 7.54 – 7.48 (m, 1H, C4-H), 7.47 – 7.41 (m, 2H, C3-H), 4.45 (s, 2H, NH_2).

Spectroscopic data are consistent with those previously described.[10]

Synthesis of ^{13}C benzhydrazide (117)

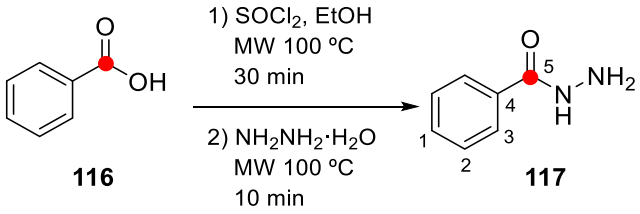

150 mg (1.2 mmol) of (**116**) and 48 µL (0.66 mmol) of $SOCl_2$ were added into a 5 mL microwave vial with 4 mL of EtOH. The mixture was heated under microwave irradiation for 30 min at 100 °C. The solvent was removed under reduced pressure to eliminate the excess of $SOCl_2$. The crude was dissolved with 4 mL of EtOH and 480 µL (9.9 mmol) of hydrazine monohydrate **6** were added into the solution. The mixture was heated under microwave irradiation for 10 min at 100 °C and the solvent was removed under reduced pressure. The crude was resuspended in diethyl ether and the pure ^{13}C-benzhydrazide (**117**) was filtered as white crystals in 57% yield (97 mg).

^{1}H-NMR (400 MHz, DMSO-*d_6*) δ 9.75 (s, 1H, NH), 7.84 – 7.78 (m, 2H, C3-H), 7.54 – 7.48 (m, 1H, C1-H), 7.47 – 7.41 (m, 2H, C2-H), 4.45 (s, 2H, NH_2).

Spectroscopic data are consistent with those previously described[10].

Synthesis of ^{13}C labelled 3-amino-2-benzoyl-4-methyl-2,4,5,7-tetrahydro-6*H*-pyrazolo[3,4-*b*]pyridin-6-one (118)

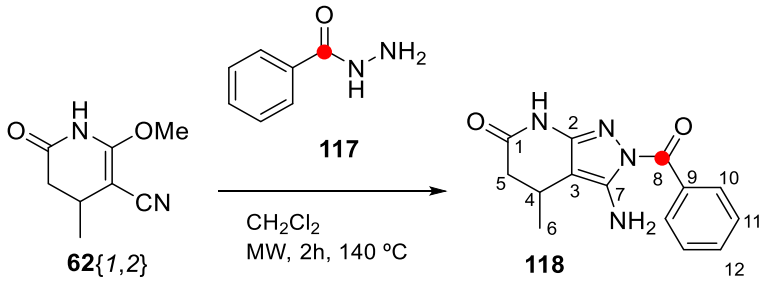

44 mg (0.26 mmol) of 2-methoxy-4-methyl-6-oxo-1,4,5,6-tetrahydropyridine-3-carbonitrile (**62**{*1*,*2*}) and 70 mg (0.51 mmol) of ^{13}C-benzhydrazide (**117**) were suspended in 4 mL of CH_2Cl_2 in a 5 mL microwave vial. The mixture was heated under microwave irradiation for 2 h at 140 °C. The crude was purified by column chromatography (silica column, Cy:AcOEt gradient 0-50% in 10 minutes and then isocratic 50:50 for 30 minutes) to afford 14 mg (19%) of 3-amino-2-benzoyl-4-methyl-2,4,5,7-tetrahydro-6*H*-pyrazolo[3,4-*b*]pyridin-6-one (**118**) as a yellowish solid.

^{1}H-NMR (400 MHz, DMSO-d_6) δ 10.44 (s, 1H, NH), 7.89 – 7.82 (m, 2H, C10-H), 7.55 (d, J = 7.3 Hz, 1H, C12-H), 7.48 (d, J = 7.6 Hz, 2H, C10-H), 6.77 (s, 2H, NH_2), 3.10 – 3.02 (m, 1H, C4-H), 2.67 (dd, J = 16.0, 6.9 Hz, 1H, C5-H), 2.21 (dd, J = 16.0, 3.1 Hz, 1H, C5-H), 1.08 (d, J = 6.8 Hz, 3H, C6-H_3).
^{13}C-NMR (100 MHz, DMSO-d_6) δ 170.5 (C1), 169.4 (C8), 152.0 (d, J = 6.1 Hz, C7), 146.6 (d, J = 1.9 Hz, C2), 133.9 (d, J = 68.6 Hz, C9), 131.5 (C12), 129.8 (d, J = 2.3 Hz, C10), 127.7 (d, J = 4.5 Hz, C11), 89.8 (C3), 39.2 (C5), 21.7 (C4), 20.2 (C6).

6.1.8. Synthesis of pyrazolo[3,4-*b*]pyridin-3-amines

6.1.8.1 Synthesis of 6-chloro-5-(2,6-dichlorophenyl)-2-phenyl-2*H*-pyrazolo[3,4-*b*]pyridin-3-amine (123)

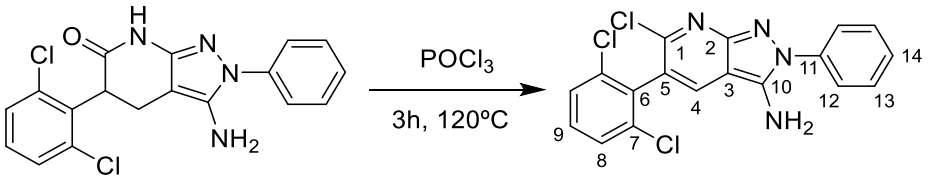

64{*7*,*1*,*3*} **123**

50 mg (0.1 mmol) of 3-amino-5-(2, 6-dichlorophenyl)-2-phenyl-2,4,5,7-tetrahydro-6*H*-pyrazolo [3,4-*b*]pyridine-6-one (**64**{*7*,*1*,*3*}) were suspended in 3 mL of $POCl_3$. The mixture was refluxed for 3h at 120 °C. The $POCl_3$ was removed under reduced pressure, the crude was resuspended in water and neutralized with $NaHCO_3$. The solid was filtered and purified by column chromatography (alumina column, Cy:AcOEt gradient 0% to 60% in 30 minutes) to give 13 mg (10%) of 6-chloro-5-(2,6-dichlorophenyl)-2-phenyl-2*H*-pyrazolo[3,4-*b*]pyridin-3-amine as a yellowish solid.

mp: > 250 °C

^{1}H-NMR (400 MHz, DMSO-d_6) δ 8.16 (s, 1H, C4-H), 7.73 – 7.69 (m, 2H, C13-H), 7.67 – 7.59 (m, 4H, C8-H, C12-H), 7.55 – 7.48 (m, 2H, C9-H, C14-H), 6.95 (s, 2H, NH_2).

^{13}C-NMR (100 MHz, DMSO-d_6) δ 155.8 (C2), 151.3 (C10), 142.9 (C1), 138.5 (C4), 136.5 (C6), 135.8, 135.6, 131.5, 129.9 (C12), 128.7 (C8), 128.7, 125.1 (C13), 120.0, 101.1 (C3).

IR (KBr), vmax (cm^{-1}): 3383 (*st* N-H), 3304, 1628, 1598, 1545, 1428, 1285, 1107, 963, 774, 760.

MS (70 eV, EI) m/z (%): 392.1 (32%), 391.1 (28%), 390.1 (94%), 389.2 (46%), 388.1 (100%), 304.2 (35%), 93.1 (20%), 92.1 (26%), 77.1 (77%), 51.1 (31%)**.**

6.1.8.2 Synthesis of *N*-(5-(2,6-dichlorophenyl)-6-oxo-2-phenyl-4,5,6,7-tetrahydro-2*H*-pyrazolo[3,4-*b*]pyridin-3-yl)-*N*,*N*-dimethylformimidamide (126)

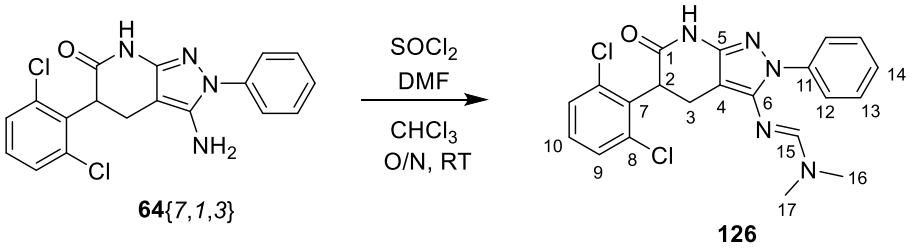

64{*7*,*1*,*3*}

126

200 mg (0.53 mmol) of 3-amino-5-(2,6-dichlorophenyl)-2-phenyl-2,4,5,7-tetrahydro-6*H*-pyrazolo[3,4-*b*]pyridine-6-one (**64**{*7*,*1*,*3*}), 67.7 µL of DMF and 0.31 mL of $SOCl_2$ were suspended in 3 mL of $CHCl_3$ and the mixture was stirred overnight at room temperature. The solvent was removed under reduced pressure. The crude was dissolved in water and neutralized with $NaHCO_3$. The solid was filtered to yield 46.5 mg (21%) of *N*-(5-(2,6-dichlorophenyl)-6-oxo-2-phenyl-4,5,6,7-tetrahydro-2*H*-pyrazolo[3,4-*b*]pyridin-3-yl)-*N*,*N*-dimethylformimidamide (**126**) as a yellow solid.

mp: > 250 °C

^{1}H-NMR (400 MHz, DMSO-d_6) δ 10.65 (s, 1H, NH), 7.92 (s, 1H, C15-H), 7.82 – 7.77 (m, 2H, C12-H), 7.53-7.50 (m, 2H, C9-H), 7.41 – 7.33 (m, 3H, C13-H, C10-H), 7.19 – 7.14 (m, 1H, C14-H), 4.55 (dd, J = 12.2, 8.6 Hz, 1H, C2-H), 3.22 (dd, J = 15.3, 12.2 Hz, 1H, C3-H), 2.99 (s, 3H, C16-H_3), 2.91 (s, 4H, C17-H_3, C3-H).

^{13}C-NMR (100 MHz, DMSO-d_6) δ 168.8 (C1), 155.8 (C15), 148.6 (C5), 146.6 (C6) , 140.7 (C11), 136.6 (C7), 135.7 (C8), 135.5 (C7'), 130.0 (C9), 129.9 (C10), 128.8 (C13), 128.6 (C9'), 124.9 (C14), 122.2 (C12), 87.5 (C4), 44.5 (C2), 40.1 (C16), 34.3 (C17), 23.2 (C3).

IR (KBr), vmax (cm^{-1}): 3414 (*st* N-H), 3163, 1677 (*st* C=O), 1537, 1498, 1434, 1230, 771, 757.

MS (70 eV, EI) m/z (%): 429.1 (67%), 428.2 (29%), 427.1 (100%), 392.2 (31%), 320.0 (21%), 242.1 (21%), 186.0 (31%), 77.1 (41%), 71.1 (20%), 69.1 (21%), 57.1 (36%), 44.1 (26%), 43.1 (44%), 42.1 (40%), 41.1 (23%).

HRMS (ESI) m/z: calculated for $C_{21}H_{19}Cl_2N_5O$ $[M+1]^+$: 428.3170; Found $[M+1]^+$: 428.1039

6.1.8.3 Synthesis of 5,6-dichloro-2,4-diphenyl-2*H*-pyrazolo[3,4-*b*]pyridin-3-amine (127)

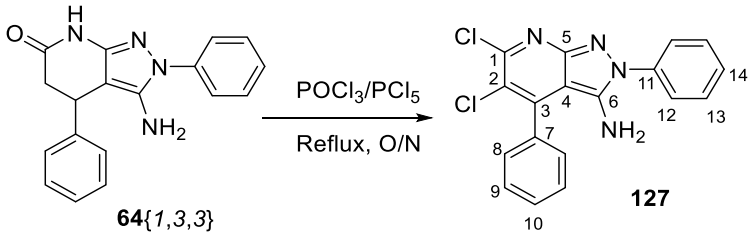

100 mg (0.33 mmol) of 3-amino-4-phenyl-2-phenyl-2,4,5,7-tetrahydro-6*H*-pyrazolo[3,4-*b*] pyridine-6-one (**64**{*1,3,3*}) and 341 mg (1.64 mmol) of PCl_5 were dissolved in 2.5 mL of $POCl_3$ and the mixture was refluxed for 18h. The mixture was poured into ice and the precipitate was filtered and washed with water. The solid was then resuspended in water and the suspension was neutralized with $NaHCO_3$. The solid was filtered and dried *in vacuo* over P_2O_5 to yield 5,6-dichloro-2,4-diphenyl-2*H*-pyrazolo[3,4-*b*]pyridin-3-amine (**127**) in 72% yield

mp: 130-133 °C

^{1}H-NMR (400 MHz, DMSO-d_6) δ 7.67 – 7.56 (m, 7H), 7.55 – 7.48 (m, 3H), 5.02 (s, 2H, NH_2).

^{13}C-NMR (100 MHz, DMSO-d_6) δ 153.4 (C5), 149.8, 146.0, 140.8, 137.6, 133.3, 129.7, 129.6, 129.1, 128.7, 128.3, 124.9, 115.2, 100.1 (C4).

IR (KBr), vmax (cm^{-1}): 3428 (*st* N-H), 1615 (*st* C=C), 1597, 1224, 1136, 747 (*b* sp^2 C-H).

MS (70 eV, EI) m/z (%): 356.1 (65%), 355.1 (38%), 354.1 (100%), 353.1 (28%), 227.1 (21%), 148.0 (52%), 77.1 (35%).

HRMS (ESI) m/z: calculated for $C_{18}H_{13}Cl_2N_4$ $[M+1]^+$: 355.0512; Found $[M+1]^+$: 355.0513

6.1.8.4 Synthesis of ethyl 1-phenyl-6-(((trifluoromethyl)sulfonyl)oxy)-1*H*-pyrazolo[3,4-*b*]pyridine-5-carboxylate (132)

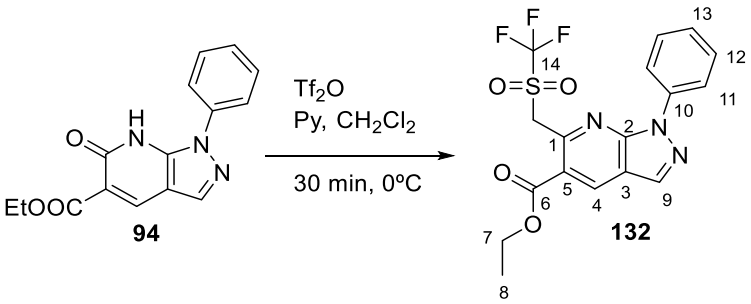

100 mg (0.35 mmol) of ethyl 6-oxo-1-phenyl-6,7-dihydro-1*H*-pyrazolo[3,4-*b*]pyridine-5-carboxylate (**94**), 119 µL (0.7 mmol) of triflic anhydride and 56 µL (0.7 mmol) of pyridine were dissolved in 5 mL CH_2Cl_2 and stirred for 30 minutes at 0 °C. The solvent was removed under reduced pressure and the crude was suspended in water. The solid was filtered and dried *in vacuo* at room temperature over P_2O_5 to yield 133 mg (91% yield) of ethyl 1-phenyl-6-(((trifluoromethyl)sulfonyl)oxy)-1*H*-pyrazolo[3,4-*b*]pyridine-5-carboxylate (**132**) as a yellow solid

mp: 130 °C

^{1}H-NMR (400 MHz, DMSO-d_6) δ 9.24 (s, 1H, C4-H), 8.75 (s, 1H, C9-H), 8.14 – 8.04 (m, 2H, C11-H), 7.65 - 7.59 (m, 2H, C12-H), 7.52 – 7.42 (m, 1H, C13-H), 4.42 (q, *J* = 7.1 Hz, 2H, C7-H_2), 1.38 (t, *J* = 7.1 Hz, 3H, C8-H_3).

^{13}C-NMR (100 MHz, DMSO-d_6) δ 162.1 (C6), 151.5 (C1), 146.6 (C2), 139.8 (C4), 137.7 (C10), 137.1 (C9), 129.4 (C12), 127.3 (C13), 120.8 (C11), 117.3, 112.5, 109.5, 62.1 (C7), 13.9 (C8).

IR (KBr), vmax (cm^{-1}): 3431 (*st* N-H), 1726 (*st* C=O), 1620, 1597 (*st* C=C), 1425, 1228 (*st* C-O), 1208, 1138, 898, 762, 599.

Elemental analysis: calculated for $C_{16}H_{12}F_3N_3O_5S$: C: 46.27%, H: 2.91%, N: 10.12%, S: 7.72%; found: C: 46.29%, H: 2.85%, N: 9.97%, S: 7.69%.

MS (70 eV, EI) m/z (%): 415.1 (100%), 237.1 (23%), 236.1 (83%), 77.1 (32%).

6.1.8.5 Synthesis of ethyl 6-(4-methylpiperazin-1-yl)-1-phenyl-1*H*-pyrazolo[3,4-*b*]pyridine-5-carboxylate (134)

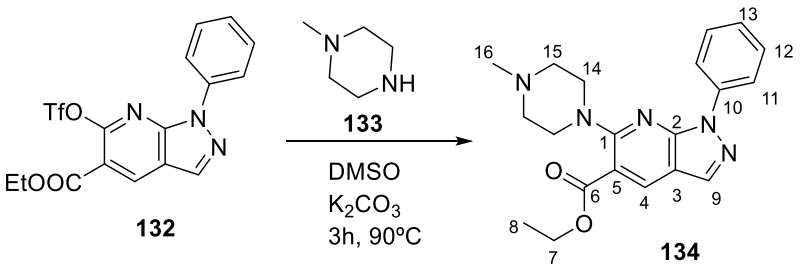

0.5 mmol (50 µL) of 1-methylpiperazine (**133**) were dissolved in 5 mL of DMSO. 50 mg (0.12 mmol) of ethyl 1-phenyl-6-(((trifluoromethyl)sulfonyl)oxy)-1*H*-pyrazolo[3,4-*b*]pyridine-5-carboxylate (**132**) and 65.8 mg (1.15 mmol) of K_2CO_3 were added and the mixture was heated at 90 °C for 3h. After cooling, 5 mL of water were added and the product was extracted with AcOEt (3 x 10 mL) and washed with brine (2 x 10 mL). The organic phase was dried with anhydrous $MgSO_4$ and the solvent was removed under reduced pressure to yield 33 mg (71% yield) of ethyl 6-(4-methylpiperazin-1-yl)-1-phenyl-1*H*-pyrazolo[3,4-*b*]pyridine-5-carboxylate (**134**)

^{1}H-NMR (400 MHz, DMSO-d_6) δ 8.48 (s, 1H, C4-H), 8.26 (s, 1H, C9-H), 8.26 – 8.22 (m, 2H, C11-H), 7.58 – 7.51 (m, 2H, C12-H), 7.34 – 7.27 (m, 1H, C13-H), 4.31 (q, J = 7.1 Hz, 2H, C7-H_2), 3.45 – 3.40 (m, 4H, C14-H_2), 2.48 – 2.41 (m, 4H, C15-H_2), 2.21 (s, 3H, C16-H_3), 1.33 (t, J = 7.1 Hz, 3H, C8-H_3).

^{13}C-NMR (100 MHz, DMSO-d_6) δ 166.8 (C6), 158.1 (C1), 149.2 (C2), 139.1 (C10), 136.2 (C4), 136.0 (C9), 129.2 (C12), 125.6 (C13), 119.8 (C11), 111.8, 110.0, 61.0 (C7), 54.2 (C15), 48.9 (C14), 45.7 (C16), 14.1 (C8).

IR (KBr), vmax (cm^{-1}): 2977 (*st* C-H), 2935, 2843, 2796, 1715 (*st* C=O), 1615, 1596 (*st* sp^2-sp^2), 1559, 1494, 1441, 1413, 1250 (*st* C-O), 1170, 1101 (*st* C-N), 1006, 980, 755, 691.

MS (70 eV, EI) m/z (%): 308.2 (46%), 295.2 (21%), 283.2 (83%), 282.3 (38%), 249.1 (100%), 238.1 (20%), 237.1 (79%), 209.1 (24%), 77.1 (29%), 71.2 (20%), 57.2 (29%), 43.1 (29%).

6.1.8.6 Synthesis of 2-methoxynicotinonitriles (135)

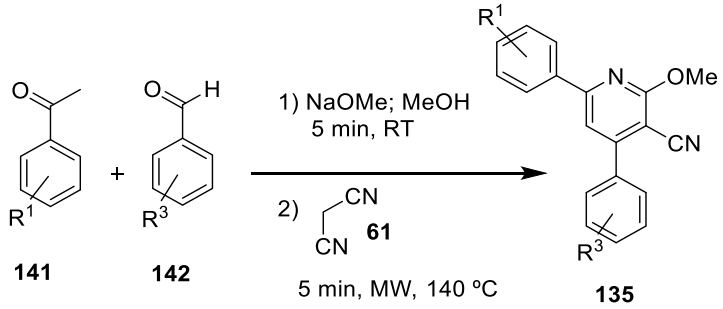

101 mg (1.87 mmol) of NaOMe were dissolved in 5 mL of MeOH in a microwave vial. 1.7 mmol of phenylketone (**141**) and 1.7 mmol of phenylaldehide (**142**) were added and the mixture was stirred for 5 min at room temperature. Then, 1.7 mmol of malononitrile (**61**) were added and the reaction was heated under microwave irradiation for 5 min at 140 °C. The solvent was removed under reduced pressure. The solid obtained was resuspended in MeOH and filtered to afford the corresponding 2-methoxynicotinonitrile (**135**).

2-methoxy-4,6-bis(4-methoxyphenyl)nicotinonitrile (135{*4,4*})

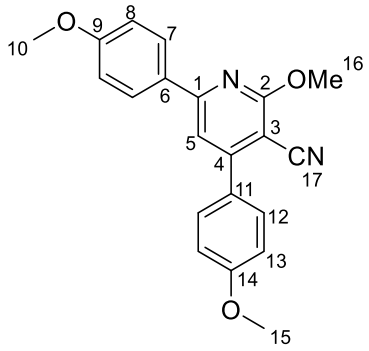

Starting from 1-(3-methoxyphenyl)ethan-1-one (**141**{*4*}) and 4-methoxybenzaldehyde (**142**{*4*}). 20% yield, yellowish solid.

mp: 184-186 °C

^{1}H-NMR (400 MHz, DMSO-d_6) δ 8.28 – 8.19 (m, 2H, C7-H), 7.76 – 7.68 (m, 3H, C12-H and C5-H), 7.17 – 7.11 (m, 2H, C13-H), 7.10 – 7.04 (m, 2H, C8-H), 4.12 (s, 3H, C16-H_3), 3.85 (s, 6H, C10-H_3, C15-H_3).

^{13}C-NMR (100 MHz, DMSO-d_6) δ 164.4 (C2), 161.4 (C9), 160.7 (C14), 156.9 (C1), 155.7 (C6), 130.2 (C12), 129.1 (C7), 128.0 (C11), 115.8 (C17), 114.3 (C8, C13), 112.5 (C5), 109.5 (C4), 90.7 (C3), 55.4 (C10), 55.4 (C15), 54.3 (C16).

IR (KBr), vmax (cm^{-1}): 2217 (*st* C≡N), 1610, 1586, 1548, 1513 (*st* C=C), 1450, 1364, 1258 (*st* C-O), 1238, 1182, 1029, 820.

Elemental analysis: calculated for $C_{21}H_{18}N_2O_3$: C: 72.82%, H: 5.24%, N: 8.09%; found: C: 72.94%, H: 5.40%, N: 8.11%.

MS (70 eV, EI) m/z (%): 347.1 (22%), 346.15 (100%), 345.3 (51%).

4,6-bis(4-(dimethylamino)phenyl)-2-methoxynicotinonitrile (135{*7*,*7*})

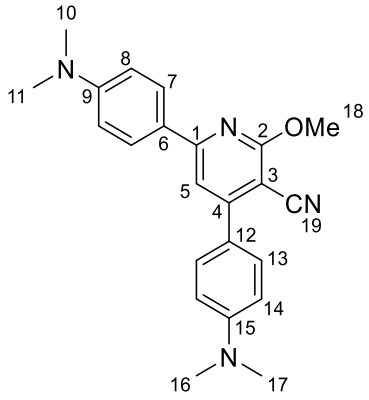

Starting from 1-(4-(dimethylamino)phenyl)ethan-1-one (**141**{*7*}) and 4-(dimethylamino)-benzaldehyde (**142**{*7*}). 26% yield, yellowish solid.

mp: > 250 °C

^{1}H-NMR (400 MHz, DMSO-*d*$_6$) δ 8.14 – 8.08 (m, 2H, C7-H), 7.66 – 7.59 (m, 2H, C13-H), 7.55 (s, 1H, C5-H), 6.88 – 6.83 (m, 2H, C14-H), 6.82 – 6.78 (m, 2H, C8-H), 4.09 (s, 3H, C18-H$_3$), 3.01 (s, 6H), 3.00 (s, 6H).

^{13}C-NMR (100 MHz, DMSO-*d*$_6$) δ 164.6 (C2), 157.2, 155.6, 151.8, 151.3, 129.5 (C13), 128.6 (C7), 123.8, 122.8, 116.6, 111.7 (C14), 111.6 (C8), 110.7 (C5), 88.2 (C3), 54.0 (C18), 39.5, 39.1.

IR (KBr), vmax (cm^{-1}): 3425, 2893, 2214 (*st* C≡N), 1610, 1577 (*st* Csp^2=Csp^2), 1519, 1440, 1360, 1185, 1168, 1139, 816.

MS (70 eV, EI) m/z (%): 372.3 (100%), 372.1 (34%), 371.9 (32%), 371.8 (46%), 185.1 (28%).

HRMS (APCI) m/z: calculated for $C_{23}H_{25}N_4O$ [M+1]$^+$: 373.2023; found [M+1]$^+$: 373.2023

4-(4-(dimethylamino)phenyl)-2-methoxy-6-(2-methoxyphenyl)nicotinonitrile (135{*6*,*7*})

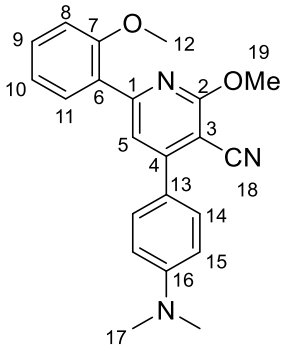

Starting from 1-(2-methoxyphenyl)ethan-1-one (**141**{*6*}) and 4-(dimethylamino)benzaldehyde (**142**{*7*}). 30% yield, brownish solid.

mp: 155-159 °C

^{1}H-NMR (400 MHz, DMSO-*d*$_6$) δ 7.99 – 7.94 (m, 1H), 7.72 (s, 1H, C5-H), 7.62 – 7.56 (m, 2H, C14-H), 7.51 – 7.46 (m, 1H), 7.22 – 7.18 (m, 1H), 7.15 – 7.09 (m, 1H), 6.88 – 6.85 (m, 2H, C15-H), 4.07 (s, 3H), 3.88 (s, 3H), 3.01 (s, 6H, C17-H_3).

^{13}C-NMR (100 MHz, DMSO-*d*$_6$) 164.3, 157.4, 155.4, 155.1, 151.4, 131.5, 130.8, 129.4, 126.3, 122.4, 120.8, 117.5, 116.1, 112.3, 111.9, 101.1, 90.1, 55.8, 54.3

MS (70 eV, EI) m/z (%): 359.4 (24%), 359.2 (32%), 315.2 (20%), 283.2 (29%), 135.1 (39%), 134.2 (100%).

2-methoxy-4-(4-methoxyphenyl)-6-phenylnicotinonitrile (135{*3*,*4*})

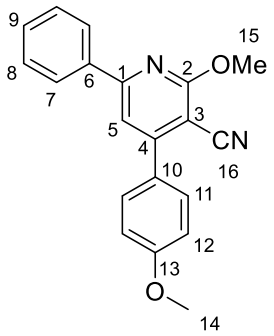

Starting from acetophenone (**141**{*3*}) and 4-methoxybenzaldehyde (**142**{*4*}). 33% yield, yellowish solid.

mp: 181-183 °C

^{1}H-NMR (400 MHz, DMSO-d_6) δ 8.30 – 8.24 (m, 2H, C7-H), 7.80 (s, 1H, C5-H), 7.78 – 7.72 (m, 2H, C12-H), 7.58 – 7.51 (m, 3H, C8-H, C9-H), 7.18 – 7.11 (m, 2H, C11-H), 4.15 (s, 3H, C15-H_3), 3.86 (s, 3H, C14-H_3).

^{13}C-NMR (100 MHz, DMSO-d_6) δ 164.4 (C2), 160.8 (C15), 157.1 (C1), 155.9 (C4), 136.8 (C6), 130.6, 130.2 (C10), 128.9, 127.9, 127.4 (C7), 115.7, 114.3 (C11), 113.5 (C5), 91.8 (C3), 55.4 (C14), 54.5 (C15).

IR (KBr) vmax (cm^{-1}): 3432, 2999, 2221 (*st* C≡N), 1593 (st Csp^2=Csp^2), 1548, 1518, 1456, 1360, 1246 (*st* C-O), 1189, 1144, 1023, 836, 770, 691.

MS (70 eV, EI) m/z (%): 317.1 (31%), 316.1 (100%), 315.3 (70%), 301.1 (22%).

HRMS (APCI) m/z: calculated for $C_{20}H_{17}N_2O_2$ $[M+1]^+$: 317.1285; Found $[M+1]^+$: 317.1281

4-(4-(dimethylamino) phenyl)-2-methoxy-6-(4-methoxyphenyl) nicotinonitrile (135{*4,7*})

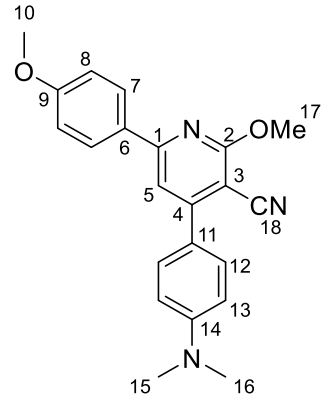

16{*2,3*}

Starting from 1-(4-methoxyphenyl) ethan-1-one (**141**{*4*}) and 4-(dimethylamino)benzaldehyde (**142**{*7*}). 20% yield, yellowish solid.

mp: 215-218 °C

^{1}H-NMR (400 MHz, DMSO-*d*$_6$) δ 8.25 – 8.19 (m, 2H, C7-H), 7.69 – 7.62 (m, 3H, C12-H and C5-H), 7.13 – 7.03 (m, 2H, C8-H), 6.89 – 6.82 (m, 2H, C13-H), 4.11 (s, 3H, C17-H_3), 3.84 (s, 3H, C10-H_3), 3.01 (s, 6H, C15-H_3 and C16-H_3).

^{13}C-NMR (100 MHz, DMSO-*d*$_6$) δ 164.6 (C2), 161.2 (C9), 156.5 (C14), 156.0 (C1), 151.4 (C6), 129.6 (C11), 129.3 (C12), 129.0 (C7), 122.4 (C18), 116.3 (C4), 114.2 (C8), 111.9 (C5), 111.7 (C13), 89.7 (C3), 55.4 (C10), 54.2 (C17), 39.8 (C15 and C16).

IR (KBr) vmax (cm^{-1}): 3450, 2946, 2214 (*st* C≡N), 1617, 1586, 1561 (*st* Csp^2-Csp^2), 1536, 1447, 1415, 1363, 1244 (*st* C-O), 1024, 817.

MS (70 eV, EI) m/z (%): 359.2 (100%), 358.9 (41%).

HRMS (APCI) m/z: calculated for $C_{22}H_{22}N_3O_2$ $[M+1]^+$: 360.1707; Found $[M+1]^+$: 360.1705

2-methoxy-6-(4-methoxyphenyl)-4-(p-tolyl)nicotinonitrile (135{*4*,*5*})

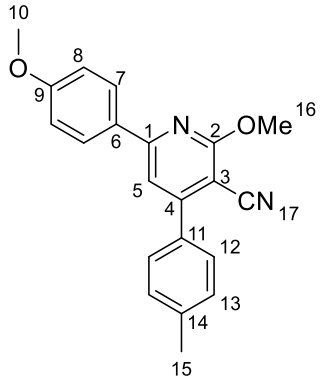

Starting from 1-(4-methoxyphenyl)ethan-1-one (**141**{*4*}) and 4-methylbenzaldehyde (**142**{*5*}). 33% yield, yellowish solid.

mp: 189-191 °C

^{1}H-NMR (400 MHz, DMSO-d_6) δ 8.27 – 8.22 (m, 2H, C7-H), 7.71 (s, 1H, C5-H), 7.67 – 7.62 (m, 2H, C12-H), 7.42 – 7.37 (m, 2H, C13-H), 7.10 – 7.06 (m, 2H, C8-H), 4.13 (s, 3H, C16-H_3), 3.84 (s, 3H, C10-H_3), 2.41 (s, 3H, C15-H_3).

^{13}C-NMR (100 MHz, DMSO-d_6) δ 164.3 (C2), 161.4 (C9), 157.0 (C1), 156.1 (C6), 139.9 (C), 133.1 (C11), 129.4 (C13), 129.2 (C7), 129.1 (C12), 128.5 (C12), 115.7 (C17), 114.3 (C8), 112.6 (C5), 91.0 (C3), 55.4 (C16), 54.4 (C10), 20.9 (C15).

IR (KBr), vmax (cm^{-1}): 3433, 2951, 2225 (*st* C≡N), 1582, 1546 (St Csp^2-Csp^2), 1512, 1451, 1364, 1241 (*st* C-O), 1172, 1024, 834.

MS (70 eV, EI) m/z (%): 330.1 (100%), 329.9 (32%), 329.5 (43%), 305.1 (41%), 304.3 (45%), 135.1 (51%).

HRMS (APCI) m/z: calculated for $C_{21}H_{19}N_2O_2$ $[M+1]^+$: 331.1441; Found $[M+1]^+$: 331.1440

4-(4-(dimethylamino)phenyl)-2-methoxy-6-(3-methoxyphenyl)nicotinonitrile (135{*5*,*7*})

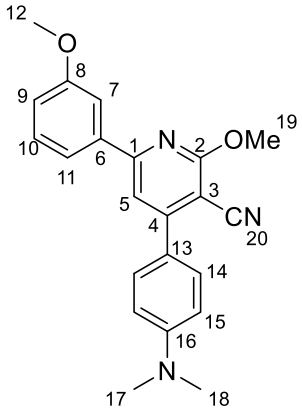

16{*4*,3}

Starting from 1-(3-methoxyphenyl)ethan-1-one (**141**{*5*}) and 4-(dimethylamino)benzaldehyde (**142**{*7*}). 18% yield, yellow solid.

mp: 162-164 °C

^{1}H-NMR (400 MHz, DMSO-d_6) δ 7.84 – 7.80 (m, 1H, C11-H), 7.77 – 7.75 (m, 1H, C7-H), 7.73 (s, 1H, C5-H), 7.70 – 7.65 (m, 2H, C14-H), 7.47-7.43 (m, 1H, C10-H), 7.11 – 7.06 (m, 1H, C9-H), 6.88 – 6.83 (m, 2H, C15-H), 4.11 (s, 3H, C19-H_3), 3.85 (s, 3H, C12-H_3), 3.01 (s, 6H, C17-H_3, C18-H_3).

^{13}C-NMR (100 MHz, DMSO-d_6) δ 164.6 (C2), 159.7 (C8), 156.4 (C1), 156.3 (C4), 151.5 (C16), 138.4 (C6), 129.9 (C10), 129.7 (20), 122.2 (C13), 119.7 (C11), 116.2, 116.0 (C9), 113.1 (C5), 112.7 (C7), 111.8 (15), 90.8 (C3), 55.3 (C19), 54.3 (C12), 39.8 (C17, C18).

IR (KBr), vmax (cm^{-1}): 3427, 2947, 2219 (*st* C≡N), 1611, 1580 (*st* Csp^2-Csp^2), 1525, 1454, 1359, 1289 (*st* C-O), 1143, 819.

MS (70 eV, EI) m/z (%): 360.2 (21%), 359.2 (88%), 283.2 (30%), 381.2 (26%), 148.1 (23%), 135.1 (29%), 134.1 (100%).

HRMS (APCI) m/z: calculated for $C_{22}H_{22}N_3O_2$ $[M+1]^+$: 360.1707; Found $[M+1]^+$: 360.1706

4-(4-fluorophenyl)-2-methoxy-6-(3-methoxyphenyl)nicotinonitrile (135{*5*,*6*})

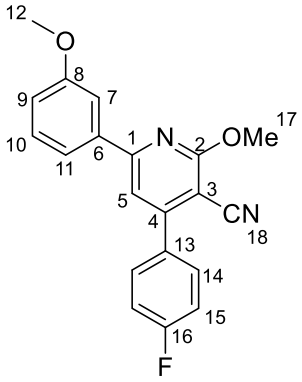

Starting from 1-(3-methoxyphenyl)ethan-1-one (**141**{*5*}) and 4-fluorobenzaldehyde (**142**{*6*}). 25% yield, white solid.

mp: 157-159 °C

^{1}H-NMR (400 MHz, DMSO-d_6) δ 7.91 – 7.74 (m, 5H), 7.52 – 7.40 (m, 3H), 7.18 – 7.07 (m, 1H, C5-H), 4.15 (s, 3H, C17-H_3), 3.85 (s, 3H, C12-H_3).

^{13}C-NMR (100 MHz, DMSO-d_6) δ 164.1, 163.2 (d, J = 248.0 Hz), 159.7, 157.1, 155.3, 138.1, 131.2 (d, J = 8.8 Hz), 130.0, 119.9, 116.3, 115.8 (d, J = 21.8 Hz), 115.3, 114.0, 112.7, 92.5, 55.3, 54.5.

IR (KBr), vmax (cm^{-1}): 3419, 2950, 2223 (*st* C≡N), 1582, 1551, 1513, 1456, 1361, 1286 (*st* C-O), 1233, 1142, 834.

MS (70 eV, EI) m/z (%): 334.2 (58%), 333.2 (65%), 308.1 (23%), 258.1 (55%), 136.2 (21%), 135.2 (100%), 135.0 (23%), 109.0 (23%), 107.0 (38%).

HRMS (APCI) m/z: calculated for $C_{20}H_{16}FN_2O_2$ $[M+1]^+$: 335.1190; Found $[M+1]^+$: 335.1192

2-methoxy-6-(3-methoxyphenyl)-4-phenylnicotinonitrile (135{*5*,*3*})

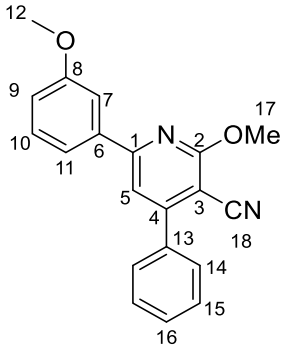

Starting from 1-(3-methoxyphenyl)ethan-1-one (**141**{*5*}) and benzaldehyde (**142**{*3*}). 20% yield, white solid.

mp: 153-155 °C

^{1}H-NMR (400 MHz, DMSO-d_6) δ 7.88 – 7.86 (m, 1H, C7-H), 7.85 (s, 1H, C5-H), 7.80 – 7.78 (m, 1H, C11-H), 7.77 – 7.73 (m, 2H, C14-H), 7.61 – 7.57 (m, 3H, C15-H, C16-H), 7.46 (t, J = 8.0 Hz, 1H, C10-H), 7.13 – 7.08 (m, 1H, C9-H), 4.15 (s, 3H, C17-H_3), 3.85 (s, 3H, C12-H_3).

^{13}C-NMR (100 MHz, DMSO-d_6) δ 164.2 (C2), 159.7 (C8), 157.1 (C1), 156.4, 138.1 (C6), 135.8, 130.0, 130.0 (C10), 128.8, 128.7, 119.9 (C7), 116.4 (C9), 115.3, 114.0 (C5), 112.7 (C11), 92.4 (C3), 55.3 (C12), 54.5 (C17).

IR (KBr), vmax (cm^{-1}): 3420, 2948, 2221 (*st* C≡N), 1549, 1453, 1362, 1290 (*st* C-O), 1250, 1050, 1015, 767.

MS (70 eV, EI) m/z (%): 316.1 (77%), 315.1 (100%), 291.1 (24%), 290.2 (31%), 240.1 (24%), 135.1 (49%).

HRMS (APCI) m/z: calculated for $C_{20}H_{17}N_2O_2$ $[M+1]^+$: 317.1285; Found $[M+1]^+$: 317.1282

2-methoxy-6-(3-methoxyphenyl)-4-(4-methoxyphenyl)nicotinonitrile (135{*5*,*4*})

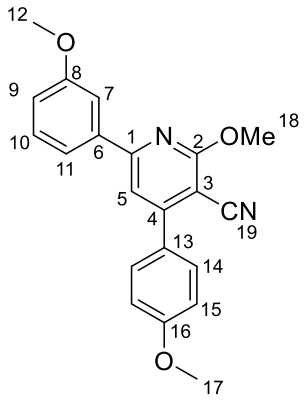

Starting from 1-(3-methoxyphenyl)ethan-1-one (**141**{*5*}) and 4-methoxybenzaldehyde (**142**{*4*}). 20% yield, yellowish solid.

mp: 138-140 °C

^{1}H-NMR (400 MHz, DMSO-d_6) δ 7.87 – 7.83 (m, 1H, C7-H), 7.81 (s, 1H, C5-H), 7.80 – 7.78 (m, 1H, C11-H), 7.77 – 7.73 (m, 2H, C14-H), 7.48-7.44 (m, 1H, C10-H), 7.17 – 7.13 (m, 2H, C15-H), 7.13 – 7.09 (m, 1H, C9-H), 4.14 (s, 3H, C18-H_3), 3.85 (d, J = 1.0 Hz, 6H, C12-H_3, C17-H_3).

^{13}C-NMR (100 MHz, DMSO-d_6) δ 164.3 (C2), 160.8 (C16), 159.7 (C8), 156.8 (C1), 155.9 (C4), 138.2 (C6), 130.3 (C14), 130.0 (C10), 127.8 (C13), 119.8 (C7), 116.2 (C9), 115.6 (C19), 114.3 (C15), 113.7 (C5), 112.7 (C11), 91.9 (C3), 55.4 (C17*), 55.3 (C12*), 54.4 (C18).

IR (KBr), vmax (cm^{-1}): 3421, 2951, 2223 (*st* C≡N), 1577, 1548, 1515, 1356, 1251 (*st* C-O), 1143, 1037, 826.

MS (70 eV, EI) m/z (%): 346.2 (100%), 315.2 (29%), 345.3 (30%), 345.2 (89%), 316.1 (34%).

HRMS (APCI) m/z: calculated for $C_{21}H_{19}N_2O_3$ $[M+1]^+$: 347.1390; Found $[M+1]^+$: 347.1393

2-methoxy-6-(2-methoxyphenyl)-4-(4-methoxyphenyl)nicotinonitrile (135{*6,4*})

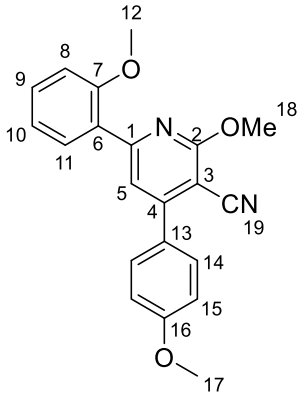

Starting from 1-(2-methoxyphenyl)ethan-1-one (**141**{*6*}) and 4-methoxybenzaldehyde (**142**{*4*}). 65% yield, yellowish solid.

mp: 131-133 °C

^{1}H-NMR (400 MHz, DMSO-d_6) δ 8.01 – 7.94 (m, 1H, C11-H), 7.74 (s, 1H, C5-H), 7.70 – 7.65 (m, 2H, C14-H), 7.54 – 7.46 (m, 1H, C9-H), 7.24 – 7.19 (m, 1H, C8-H), 7.17 – 7.11 (m, 3H, C15-H and C10-H), 4.09 (s, 3H, C18-H_3), 3.87 (s, 3H, C12-H_3), 3.85 (s, 3H, C17-H_3).

^{13}C-NMR (100 MHz, DMSO-d_6) δ 164.1 (C2), 160.7 (C16), 157.4 (C7), 155.9 (C1), 154.8 (C4), 131.6 (C9), 130.9 (C11), 130.0 (C14), 128.1 (C6), 126.1 (C13), 120.8 (C10), 117.9 (C5), 115.6 (C19), 114.4 (C15), 112.3 (C8), 91.2 (C3), 55.8 (C12), 55.4 (C17), 54.4 (C18).

IR (KBr), vmax (cm^{-1}): 3429, 2948, 2220 (*st* C≡N), 1586, 1514, 1456, 1363, 1254 (*st* C-O), 1141, 1018, 834, 759.

MS (70 eV, EI) m/z (%): 346.1 (27%), 270.2 (30%), 135.1 (100%), 121.1 (62%).

HRMS (APCI) m/z: calculated for $C_{21}H_{19}N_2O_3$ $[M+1]^+$: 347.1390; Found $[M+1]^+$: 347.1387

2-methoxy-6-(2-methoxyphenyl)-4-(p-tolyl)nicotinonitrile (135{*6*,*5*})

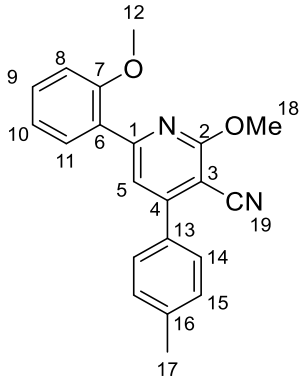

Starting from 1-(2-methoxyphenyl)ethan-1-one (**141**{*6*}) and 4-methylbenzaldehyde (**142**{*5*}). 88% yield, yellowish solid.

mp: 157-159 °C

^{1}H-NMR (400 MHz, DMSO-d_6) δ 8.01 – 7.97 (m, 1H, C11-H), 7.74 (s, 1H, C5-H), 7.62 – 7.56 (m, 2H, C14-H), 7.53 – 7.46 (m, 1H, C9-H), 7.41 – 7.37 (m, 2H, C15-H), 7.23 – 7.19 (m, 1H, C10-H), 7.16 – 7.10 (m, 1H, C8-H), 4.10 (s, 3H, C18-H_3), 3.87 (s, 3H, C12-H_3), 2.40 (s, 3H, C17-H_3).

^{13}C-NMR (100 MHz, DMSO-d_6) δ 164.0 (C2), 157.4 (C7), 156.0 (C1), 155.2 (C4), 139.9 (C16), 133.1 (C13), 131.7 (C9), 130.9 (C11), 129.5 (C15), 128.3 (C14), 126.0 (C6), 120.8 (C10), 118.1 (C5), 115.5 (C19), 112.3 (C8), 91.5 (C3), 55.8 (C12), 54.5 (C18), 20.9 (C17).

IR (KBr), vmax (cm^{-1}): 3430, 2946, 2221 (*st* C≡N), 1588, 1547(*st* Csp^2-Csp^2), 1456, 1363, 1243 (*st* C-O), 1142, 1013, 764.

MS (70 eV, EI) m/z (%): 330.2 (99%), 314.9 (25%), 305.2 (71%), 304.4 (40%), 299.2 (28%), 297.2 (34%), 296.9 (21%), 274.1 (30%), 272.1 (26%), 254.1 (30%), 244.1 (22%), 239.1 (26%), 200.1 (43%), 135.0 (100%), 128.0 (21%), 118.1 (20%), 115.1 (29%), 105.00 (22%).

4-(4-fluorophenyl)-2-methoxy-6-phenylnicotinonitrile (135{*3*,*6*})

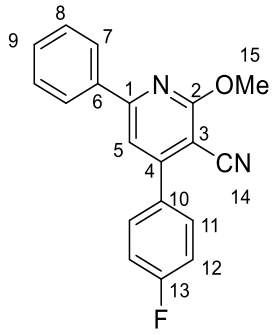

Starting from acetophenone (**141**{*3*}) and 4-fluorobenzaldehyde (**142**{*6*}). 62% yield, yellowish solid.

mp: 165-169 °C

^{1}H-NMR (400 MHz, DMSO-d_6) δ 8.31 – 8.25 (m, 2H), 7.87 – 7.81 (m, 3H), 7.56 – 7.53 (m, 2H), 7.49 – 7.42 (m, 2H), 4.16 (s, 3H, C15-H_3).

^{13}C-NMR (100 MHz, DMSO-d_6) δ 164.3, 163.2 (d, J = 248.0 Hz), 157.3, 155.3, 136.6, 132.2 (d, J = 3.1 Hz), 131.1 (d, J = 8.8 Hz), 130.7, 128.9, 127.5, 115.9 (d, J = 21.9 Hz), 115.3, 113.8, 92.3, 54.6.

IR (KBr) vmax (cm^{-1}): 3430, 3083 (*st* Csp^2-H), 2992, 2950, 2224 (*st* C≡N), 1550, 1514, 1454, 1433, 1368, 836, 766, 681.

MS (70 eV, EI) m/z (%): 304.2 (82%), 303.2 (100%), 276.1 (22%), 275.2 (20%), 273.2 (26%).

HRMS (APCI) m/z: calculated for $C_{19}H_{14}FN_2O$ $[M+1]^+$: 305.1085; Found $[M+1]^+$: 305.1081

6.1.8.7 Synthesis of 2-bromonicotinonitriles

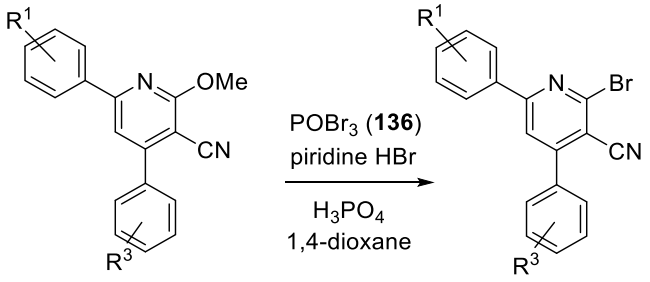

135 **137**

0.6 mmol of the corresponding 2-methoxy-nicotinonitrile (**135**) were dissolved in 4 mL 1,4-dioxane together with $POBr_3$ (1.34 mmol), pyridinium HBr (0.015 mmol) and H_3PO_4 (0.026 mmol). The mixture was refluxed for 18 h under argon atmosphere and then quenched with cold water. The mixture was neutralized with NaOH (6M) and the precipitate was filtered and washed with cold water. The solid was dried *in vacuo* over P_2O_5 to yield the corresponding 2-bromonicotinonitrile (**137**).

2-bromo-4,6-diphenylnicotinonitrile (137{*3*,*3*})

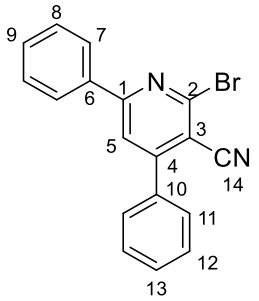

Starting from 2-methoxy-4,6-diphenylnicotinonitrile (**135**{*3*,*3*}). 84% yield, white solid.

mp: 123-125 °C

^{1}H-NMR (400 MHz, DMSO-d_6) δ 8.26 (s, 1H, C5-H), 8.24 (m, 2H, C7-H), 7.80 (m, 2H, C11-H), 7.62 (m, 3H) and 7.57 (m, 3H).

^{13}C-NMR (100 MHz, DMSO-d_6) δ 159.3 (C1), 156.2 (C4), 144.4 (C2), 135.5, 135.3, 131.3, 130.5, 129.1, 128.9, 127.7, 119.7 (C5), 116.5 (C14) and 109.7 (C3).

IR (KBr) vmax (cm^{-1}): 3432, 3029 (*st* Csp^2-H), 2225 (*st* C≡N), 1649, 1575 (*st* Csp^2-Csp^2), 1517, 1493, 1419, 1373, 772, 747, 702, 686.

Elemental analysis: calculated for $C_{18}H_{11}BrN_2$: C: 64.50%, H: 3.31%, N: 8.36%; found: C: 64.83%, H: 3.58%, N: 8.31%.

MS (70 eV, EI) m/z (%): 336.1 (96%), 335.1 (68 %), 334.1 (100%), 333.1 (52%), 286.2 (36%), 285.2 (46%), 255.1 (69%), 254.1 (20%), 253.1 (31%), 228.1 (26%), 227.1 (55%), 100.1 (20%), 77.1 (43%), 51.0 (22%).

2-bromo-4,6-bis(4-methoxyphenyl)nicotinonitrile (137{*4,4*})

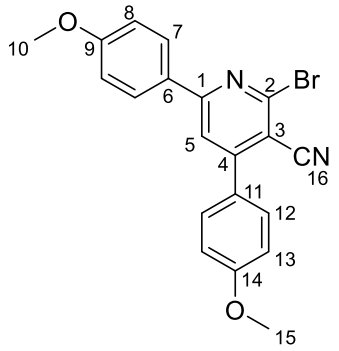

Starting from 2-methoxy-4,6-bis(4-methoxyphenyl)nicotinonitrile (**135**{*4,4*}). 92% yield, white solid.

mp: 221-223 °C

^{1}H-NMR (400 MHz, DMSO-d_6) δ 8.24 – 8.19 (m, 2H, C7-H), 8.13 (s, 1H, C5-H), 7.78 – 7.72 (m, 2H, C12-H), 7.17 – 7.13 (m, 2H, C13-H), 7.12 – 7.07 (m, 2H, C8-H), 3.86 (s, 3H, C15-H_3), 3.85 (s, 3H, C10-H_3).

^{13}C-NMR (100 MHz, DMSO-d_6) δ 161.9 (C9), 161.0 (C14), 158.8 (C1), 155.6 (C4), 142.8 (C2), 130.5 (C12), 129.5 (C7), 127.9 (C6), 127.4 (C11), 120.2 (C3), 118.4 (C5), 116.9 (C16), 114.5 (C8), 114.3 (C13), 55.5 (C10, C15).

IR (KBr), vmax (cm^{-1}): 3431, 2975, 2221 (*st* C≡N), 1608, 1518 (*st* Csp^2-Csp^2), 1262 (*st* C-O), 1188, 1167, 1028, 827.

MS (70 eV, EI) m/z (%): 394.1 (100%), 371.2 (20%), 369.2 (20%), 316.2 (32%), 315.2 (38%).

HRMS (APCI) m/z: calculated for $C_{20}H_{16}BrN_2O_2$ $[M+1]^+$: 395.0390; Found $[M+1]^+$: 395.0387

2-bromo-4-(4-methoxyphenyl)-6-phenylnicotinonitrile (137{*3,4*})

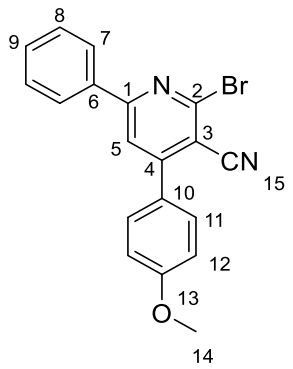

Starting from 2-methoxy-4-(4-methoxyphenyl)-6-phenylnicotinonitrile (**135**{*3,4*}). 82% yield, grey solid.

mp: 214-216 °C

^{1}H-NMR (400 MHz, DMSO-d_6) δ 8.24 – 8.18 (m, 3H, C5-H, C7-H), 7.80 – 7.73 (m, 2H, C11-H), 7.57 – 7.53 (m, 3H C8-H, C9-H), 7.18 – 7.12 (m, 2H, C12-H), 3.85 (s, 3H, C14-H_3).

^{13}C-NMR (100 MHz, DMSO-d_6) δ 161.1 (C13), 159.1 (C1), 155.8 (C4), 144.5 (C2), 135.5 (C6), 131.2 (C9*), 130.6 (C13), 129.1 (C8*), 127.6 (C7), 127.3 (C10), 119.5 (C5), 116.8 (C15), 114.3 (C12), 109.2 (C3), 55.5 (C14).

IR (KBr), vmax (cm^{-1}): 3411, 2924, 2835, 2221 (*st* C≡N), 1608, 1582 (*st* Csp^2-Csp^2), 1508, 1266, 1257 (*st* C-O), 1185, 1053, 830, 686.

MS (70 eV, EI) m/z (%): 364.1 (57%), 315.2 (20%), 242.1 (33%), 240.1 (36%), 239.3 (55%), 223.1 (50%), 214.1 (23%), 121.0 (100%), 108.9 (21%), 107.2 (25%), 105.2 (48%).

HRMS (APCI) m/z: calculated for $C_{19}H_{14}BrN_2O$ $[M+1]^+$: 365.0284; Found $[M+1]^+$: 365.0282

2-bromo-6-(4-methoxyphenyl)-4-(p-tolyl)nicotinonitrile (137{*4*,*5*})

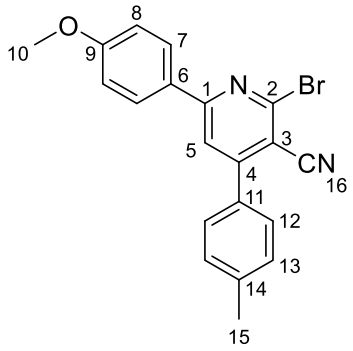

Starting from 2-methoxy-6-(4-methoxyphenyl)-4-(p-tolyl)nicotinonitrile (**135**{*4*,*5*}). 83% yield, orange solid.

mp: 207-209 °C

^{1}H-NMR (400 MHz, DMSO-d_6) δ 8.24 – 8.17 (m, 2H, C7-H), 8.13 (s, 1H, C5-H), 7.70 – 7.65 (m, 2H, C12-H), 7.43 – 7.39 (m, 2H, C13-H), 7.13 – 7.07 (m, 2H, C8-H), 3.85 (s, 3H, C10-H_3), 2.42 (s, 3H, C15-H_3).

^{13}C-NMR (100 MHz, DMSO-d_6) δ 161.9 (C9), 159.0 (C1), 155.9 (C4), 144.3 (C2), 140.3 (C14), 132.5 (C11), 129.5 (C13), 129.4 (C7), 128.7 (C12), 127.8 (C6), 118.5 (C5), 116.7 (C16), 114.5 (C8), 108.3 (C3), 55.5 (C10), 20.9 (C15).

IR (KBr), vmax (cm^{-1}): 3419, 2918, 2223 (*st* C≡N), 1581 (*st* Csp^2-Csp^2), 1518, 1499, 1375, 1251 (*st* C-O), 1168, 1028, 818.

Elemental analysis: calculated for $C_{20}H_{15}BrN_2O$: C: 63.34%, H: 3.99%, N: 7.39%; found: C: 63.75%, H: 3.99%, N: 7.39%.

MS (70 eV, EI) m/z (%): 378.1 (29%), 355.1 (40%), 353.1 (41%), 253.2 (79%), 237.2 (36%), 139.1 (20%), 137.1 (20%), 135.1 (100%), 107.1 (27%).

2-bromo-4-(4-fluorophenyl)-6-(3-methoxyphenyl) nicotinonitrile (137{*5*,*6*})

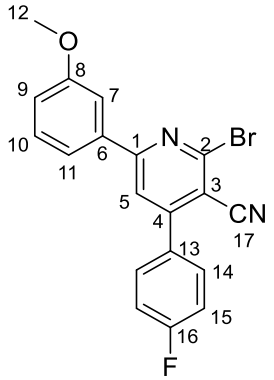

Starting from 4-(4-fluorophenyl)-2-methoxy-6-(3-methoxyphenyl)nicotinonitrile (**135**{*5*,*6*}). 67% yield, brownish solid.

mp: 191-195°C

^{1}H-NMR (400 MHz, DMSO-d_6) δ 8.29 (s, 1H, C5-H), 7.90 – 7.84 (m, 2H), 7.84 – 7.81 (m, 1H), 7.77 – 7.73 (m, 1H), 7.51 – 7.43 (m, 3H), 7.17 – 7.12 (m, 1H), 3.86 (s, 3H, C12-H_3).

^{13}C-NMR (100 MHz, DMSO-d_6) δ 163.4 (d, J = 248.3 Hz), 159.8, 159.1, 155.5, 144.2, 136.9, 131.7 (d, J = 3.1 Hz), 131.5 (d, J = 8.8 Hz), 130.3, 120.1, 120.1, 117.2, 116.5, 115.9 (d, J = 22.0 Hz), 112.7, 109.9, 55.5.

IR (KBr), vmax (cm^{-1}): 3428, 2941, 2225 (*st* C≡N), 1576 (*st* Csp^2-Csp^2), 1507, 1373, 1270 (*st* C-O), 1224, 1054, 1040, 844.

Elemental analysis: calculated for $C_{19}H_{12}BrFN_2O$: C: 59.55%, H: 3.16%, N: 7.31%; found: C: 58.92%, H: 3.12%, N: 6.94%.

MS (70 eV, EI) m/z (%): 382.2 (91%), 381.1 (82%), 358.2 (37%), 356.1 (35%), 258.1 (38%), 257.1 (79%), 135.2 (100%), 109.2 (51%), 107.2 (48%).

2-bromo-6-(3-methoxyphenyl)-4-phenylnicotinonitrile (137{*5,3*})

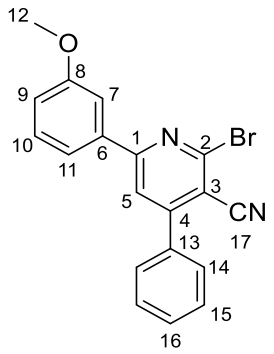

Starting from 2-methoxy-6-(3-methoxyphenyl)-4-phenylnicotinonitrile (**135**{*5,3*}). 68% yield, brownish solid.

mp: 184-186 °C

^{1}H-NMR (400 MHz, DMSO-d_6) δ 8.29 (s, 1H, C5-H), 7.85-7.82 (m, 1H, C11-H), 7.80 – 7.77 (m, 2H, C14-H), 7.76 – 7.74 (m, 1H, C7-H), 7.64 – 7.59 (m, 3H C15-H, C16-H), 7.50-7.45 (m, 1H, C10-H), 7.17 – 7.12 (m, 1H, C9-H), 3.86 (s, 3H, C12-H_3).

^{13}C-NMR (100 MHz, DMSO-d_6) δ 159.8 (C8), 159.0 (C1), 156.2 (C4), 144.2 (C2), 136.9 (C6), 135.3 (C13), 130.4, 130.2 (C10), 128.9, 128.8, 120.1 (C11), 120.0 (C5), 117.2 (C9), 116.5 (C17), 112.6 (C7), 109.8 (C3), 55.4 (C12).

IR (KBr), vmax (cm^{-1}): 3421, 2936, 2226 (*st* C≡N), 1573 (*st* Csp^2-Csp^2), 1515, 1495, 1272 (*st* C-O), 1226, 1041, 792, 698.

MS (70 eV, EI) m/z (%): 364.2 (99%), 363.2 (79%), 151.1 (39%), 109.1 (53%), 107.1 (31%).

HRMS (APCI) m/z: calculated for $C_{19}H_{14}BrN_2O$ $[M+1]^+$: 365.0284; Found $[M+1]^+$: 365.0284

2-bromo-6-(3-methoxyphenyl)-4-(4-methoxyphenyl) nicotinonitrile (137{*5,4*})

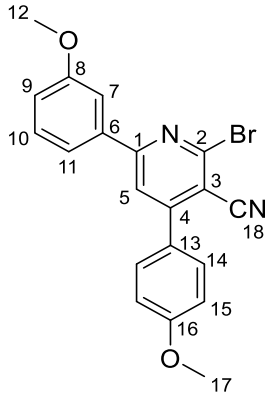

Starting from 2-methoxy-6-(3-methoxyphenyl)-4-(4-methoxyphenyl)nicotinonitrile (**135**{*5,4*}). 90% yield, grey solid.

mp: 219-221 °C

^{1}H-NMR (400 MHz, DMSO-d_6) δ 8.23 (s, 1H, C5-H), 7.83 – 7.76 (m, 3H, C14-H and C11-H), 7.75 – 7.72 (m, 1H, C7-H), 7.50-7.46 (m, 1H, C10-H), 7.19 – 7.10 (m, 3H C15-H and C9-H), 3.86 (s, 3H, C12-H_3), 3.86 (s, 3H, C17-H_3).

^{13}C-NMR (100 MHz, DMSO-d_6) δ 161.1 (C16), 159.8 (C8), 158.9 (C1), 155.9 (C4), 144.4 (C2), 137.0 (C6), 130.6 (C14), 130.2 (C10), 127.3 (C13), 120.1 (C11), 119.7 (C5), 117.1 (C9), 116.8 (C18), 114.3 (C15), 112.6 (C7), 109.3 (C3), 55.5 (C12*), 55.4 (C17*).

IR (KBr), vmax (cm^{-1}): 3427, 2937, 2220 (*st* C≡N), 1604, 1571 (*st* Csp^2-Csp^2), 1509, 1374, 1257, 1228 (*st* C-O), 1180, 1025, 836.

Elemental analysis: calculated for $C_{20}H_{15}BrN_2O_2$: C: 60.78%, H: 3.83%, N: 7.09%; found: C: 60.47%, H: 4.04%, N: 7.08%.

MS (70 eV, EI) m/z (%): 395.3 (21%), 153.0 (21%), 152.1 (24%), 139.1 (24%), 137.0 (24%), 135.1 (34%), 121.1 (52%), 109.0 (84%), 107.1 (100%).

2-bromo-6-(2-methoxyphenyl)-4-(4-methoxyphenyl) nicotinonitrile (137{*6,4*})

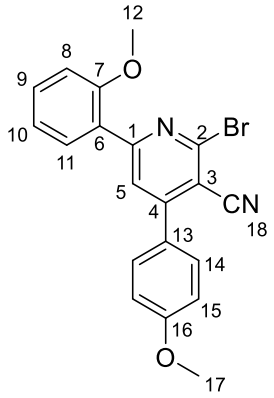

Starting from 2-methoxy-6-(2-methoxyphenyl)-4-(4-methoxyphenyl)nicotinonitrile (**135**{*6,4*}). 75% yield, white solid.

mp: 197-198 °C

^{1}H-NMR (400 MHz, DMSO-d_6) δ 8.10 (s, 1H, C5-H), 7.87-7.83 (m, 1H, C11-H), 7.73 – 7.69 (m, 2H, C14-H), 7.55-7.52 (m, 1H, C9-H), 7.25-7.21 (m, 1H, C8-H), 7.19 – 7.13 (m, 3H, C15-H and C10-H), 3.87 (s, 3H, C12-H_3), 3.86 (s, 3H, C17-H_3).

^{13}C-NMR (100 MHz, DMSO-d_6) δ 161.0 (C16), 158.0 (C7), 157.4 (C1), 154.6 (C6), 143.9 (C4), 132.4 (C9), 130.9 (C11), 130.3 (C14), 127.4 (C13), 124.9 (C18), 123.7 (C5), 120.9 (C10), 116.7 (C2), 114.5 (C15), 112.4 (C8), 108.6 (C3), 55.9 (C12), 55.4 (C17).

IR (KBr), vmax (cm^{-1}): 3432, 3005 (*st* Csp^2-H), 2932, 2836, 2224 (st C≡N), 1608, 1582 (st Csp^2-Csp^2), 1563, 1503, 1489, 1259 (*st* C-O), 1244, 1181, 1022, 826, 749, 608.

MS (70 eV, EI) m/z (%): 394.1 (23%), 315.2 (29%), 270.1 (22%), 268.2 (46%), 254.1 (21%), 253.1 (84%), 145.0 (52%), 139.0 (39%), 137.0 (38%), 135.1 (100%), 121.1 (99%), 109.0 (46%), 107.0 (55%).

2-bromo-6-(2-methoxyphenyl)-4-(p-tolyl)nicotinonitrile (137{*6,5*})

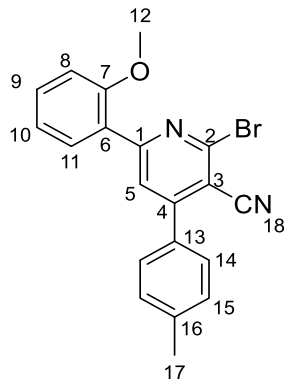

Starting from 2-methoxy-6-(2-methoxyphenyl)-4-(p-tolyl)nicotinonitrile (**135**{*6,5*}). 65% yield, brownish solid.

mp: 198-200 °C

^{1}H-NMR (400 MHz, DMSO-d_6) δ 8.11 (s, 1H, C5-H), 7.88 – 7.83 (m, 1H, C11-H), 7.65 – 7.59 (m, 2H, C14-H), 7.57 – 7.51 (m, 1H, C9-H), 7.43 – 7.39 (m, 2H, C15-H), 7.26 – 7.21 (m, 1H, C8-H), 7.18 – 7.12 (m, 1H, C10-H), 3.87 (s, 3H, C12-H_3), 2.41 (s, 3H, C17-H_3).

^{13}C-NMR (100 MHz, DMSO-d_6) δ 158.2 (C6), 157.5 (C7), 155.0 (C4), 143.8 (C1), 140.4 (C16), 132.5 (C13), 132.4 (C9), 131.00 (C11), 129.6 (C15), 128.6 (C14), 124.8 (C18), 123.8 (C5), 120.9 (C10), 116.6 (C2), 112.4 (C8), 108.9 (C3), 55.9 (C12), 20.9 (C17).

IR (KBr) vmax (cm^{-1}): 3431, 3011 (st Csp^2-H), 2947, 2838, 2225 (*st* C≡N), 1579 (*st* Csp^2-Csp^2), 1489, 1242 (*st* C-O), 1023, 816, 743.

Elemental analysis: calculated for $C_{20}H_{15}BrN_2O$: C: 63.34%, H: 3.99%, N: 7.39%; found: C: 63.26%, H: 4.03%, N: 7.12%.

MS (70 eV, EI) m/z (%): 378.1 (20%), 253.1 (53%), 237.1 (22%), 161.0 (34%), 135.0 (100%), 108.0 (30%), 105.1 (28%).

2-bromo-4-(4-fluorophenyl)-6-phenylnicotinonitrile (137{*3*,*6*})

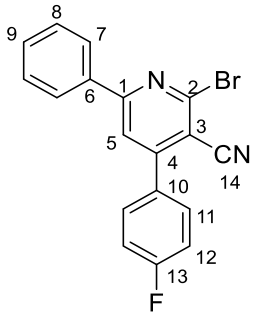

Starting from 4-(4-fluorophenyl)-2-methoxy-6-phenylnicotinonitrile (**135**{*3*,*6*}). 85% yield, brownish solid.

mp: 184-187 °C

^{1}H-NMR (400 MHz, DMSO-d_6) δ 8.26 (s, 1H, C5-H), 8.25 – 8.21 (m, 2H, C7-H), 7.91 – 7.83 (m, 2H), 7.60 – 7.54 (m, 3H), 7.50 – 7.44 (m, 2H, C12-H).

^{13}C-NMR (100 MHz, DMSO-d_6) δ 163.4 (d, J = 248.6 Hz), 159.3, 155.1, 144.3, 135.4, 131.7 (d, J = 3.0 Hz), 131.5 (d, J = 8.9 Hz), 131.3, 129.1, 127.7, 119.8, 116.5, 115.9 (d, J = 22.0 Hz), 109.8.

IR (KBr) vmax (cm^{-1}): 3425, 3068 (*st* Csp^2-H), 2224 (*st* C≡N), 1576 (*st* Csp^2-Csp^2), 1508, 1493, 1370, 1244, 1220, 1164, 839.

MS (70 eV, EI) m/z (%): 352.0 (100%), 351.2 (47%), 273.1 (50%), 245.1 (40%), 227.1 (65%), 109.0 (77%), 107.0 (58%), 105.0 (58%).

HRMS (APCI) m/z: calculated for $C_{18}H_{11}BrFN_2$ $[M+1]^+$: 353.0084; Found $[M+1]^+$: 353.0082

2-bromo-nicotinonitrile (137{*1,1*})

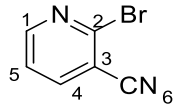

Starting from 2-methoxy-nicotinonitrile (**135**{*1,1*}). 50% yield, white crystals

mp: 170-172 °C

^{1}H-NMR (400 MHz, DMSO-d_6) 8.68 (dd, J = 4.9, 2.0 Hz, 1H, C4-H), 8.42 (dd, J = 7.8, 2.0 Hz, 1H, C1-H), 7.69 (dd, J = 7.7, 4.9 Hz, 1H, C5-H).

^{13}C-NMR (100 MHz, DMSO-d_6) 153.8 (C4), 143.9 (C1), 142.8 (C2), 123.5 (C5), 116.2 (C6), 113.1 (C3).

IR (KBr) vmax (cm^{-1}): 3433, 3060 (*st* Csp^2-H), 2924, 2239 (*st* C≡N), 1629, 1573 (*st* Csp^2-Csp^2), 1547, 1441, 1400, 1066, 810, 760, 729, 658.

Elemental analysis: calculated for $C_6H_3N_2Br$: C: 39.38%, H: 1.65%, N: 15.31%; found: C: 39.21%, H: 1.71%, N: 15.53%.

MS (70 eV, EI) m/z (%): 184.0 (90%), 182.0 (92%), 103.1 (100%), 76.1 (67%), 75.1 (26%).

6.1.8.8 Synthesis of pyrazolo[3,4-*b*]pyridine-3-amine

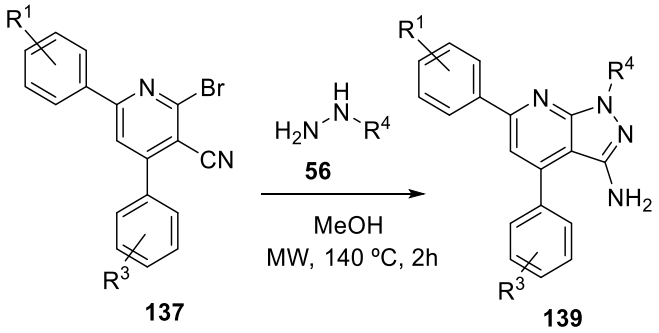

0.18 mmol of the corresponding 2-bromonicotinonitrile (**137**) and 0.36 mmols of hydrazine (**56**) were dissolved in 3 mL of methanol and sealed in a 5 mL microwave vial. The mixture was heated under microwave irradiation for 2 hours at 140 °C and cooled rapidly. The solvent was removed under reduced pressure and the crude was resuspended in methanol. The solid was filtered, washed with methanol and dried *in vacuo* over P_2O_5 to yield the corresponding pyrazolo[3,4-*b*]pyridine-3-amine (**139**)**.**

4,6-diphenyl-1*H*-pyrazolo[3,4-*b*]pyridin-3-amine (139{*3*,*3*,*1*})

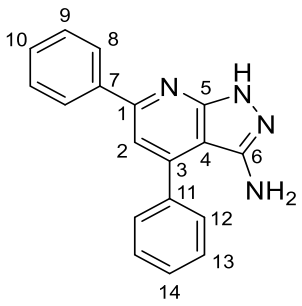

Starting from 2-bromo-4,6-diphenylnicotinonitrile (**157**{*3*,*3*}) and hydrazine monohydrate (**56**{*1*}). Purification by column chromatography (silica column, Cy:AcOEt gradient 0% to 20% in 10 minutes, 20% isocratic for 5 minutes and 20% to 100% in 15 minutes). 71% yield, yellow solid.

mp 219-220 °C

^{1}H-NMR (400 MHz, DMSO-d_6) δ 12.37 (s, 1H, NH), 8.21 – 8.15 (m, 2H), 7.73 – 7.67 (m, 2H), 7.63 – 7.47 (m, 6H), 7.48 (s, 1H, C2-H), 4.56 (s, 2H, NH_2).

^{13}C-NMR (100 MHz, DMSO-d_6) δ 155.5, 153.3, 147.2, 145.4, 138.9, 137.2, 129.2, 128.9, 128.8, 128.8, 128.7, 127.2, 112.4 (C2), 102.0 (C4).

IR (KBr), vmax (cm^{-1}): 3423 (*st* N-H), 3297, 3193, 1737, 1623, 1591 (*st* Csp^2-Csp^2), 1567, 1525, 1401, 1354, 1292, 702.

Elemental analysis: calculated for $C_{18}H_{14}N_4$: C: 75.50%, H: 4.90%, N: 19.60%; found: C: 75.43%, H: 4.90%, N: 19.56%.

MS (70 eV, EI) m/z (%): 287.1 (21%), 286.1 (100%), 285.1 (38%).

4,6-bis(4-methoxyphenyl)-1*H*-pyrazolo[3,4-*b*]pyridin-3-amine (139{*4,4,1*})

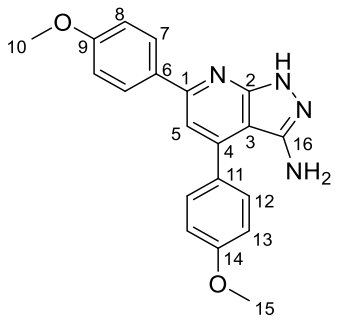

Starting from 2-bromo-4,6-bis(4-methoxyphenyl)nicotinonitrile (**137**{*4,4*}) and hydrazine monohydrate (**56**{*1*}). 65% yield, yellow solid.

mp: 228-230 °C

^{1}H-NMR (400 MHz, DMSO-d_6) δ 12.23 (s, 1H, NH), 8.19 – 8.02 (m, 2H, C7-H), 7.71 – 7.56 (m, 2H, C12-H), 7.38 (s, 1H, C5-H), 7.16 – 7.11 (m, 2H, C13-H), 7.07 – 7.02 (m, 2H, C8-H), 4.56 (s, 2H, NH_2), 3.85 (s, 3H, C15-H_3), 3.82 (s, 3H, C10-H_3).

^{13}C-NMR (100 MHz, DMSO-d_6) δ 160.3 (C9), 159.8 (C14), 155.2 (C1), 153.4 (C2), 147.2 (C16), 145.0 (C4), 131.4 (C6), 130.1 (C12), 129.5 (C11), 128.5 (C7), 114.3 (C13), 114.1 (C8), 111.6 (C5), 101.6 (C3), 55.3 (C10*), 55.2 (C15*).

IR(KBr) vmax (cm^{-1}): 3348 (*st* N-H), 3173, 1589, 1516 (*st* Csp^2-Csp^2), 1498, 1399, 1242 (*st* C-O), 1182, 1170, 1027, 821.

MS (70 eV, EI) m/z (%): 346.1 (100%), 345.2 (21%).

HRMS (APCI) m/z: calculated for $C_{20}H_{19}N_4O_2$ $[M+1]^+$: 347.1503; Found $[M+1]^+$: 347.1499

4-(4-fluorophenyl)-6-(3-methoxyphenyl)-1*H*-pyrazolo[3,4-*b*] pyridin-3-amine (139{*5*,*6*,*1*})

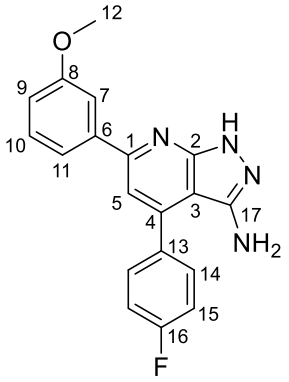

Starting from 2-bromo-4-(4-fluorophenyl)-6-(3-methoxyphenyl)nicotinonitrile (**137**{*5*,*6*}) and hydrazine monohydrate (**56**{*1*}). 50% yield, yellow solid.

mp: 194-195 °C

^{1}H-NMR (400 MHz, DMSO-d_6) δ 12.39 (s, 1H, NH), 7.80 – 7.69 (m, 4H), 7.49 (s, 1H, C5-H), 7.45 – 7.36 (m, 3H), 7.05-7.01 (m, 1H), 4.60 (s, 2H, NH_2), 3.85 (s, 3H, C12-H_3).

^{13}C-NMR (100 MHz, DMSO-d_6) δ 162.6 (d, J = 245.8 Hz), 159.6, 155.2, 153.2, 147.2, 144.3, 140.4, 133.4 (d, J = 3.1 Hz), 131.1 (d, J = 8.4 Hz), 129.8, 119.6, 115.6 (d, J = 21.6 Hz), 115.2, 112.6, 112.2, 102.1, 55.2.

IR (KBr), vmax (cm^{-1}): 3443 (*st* N-H), 3298, 3187, 2940, 2835, 1602, 1578 (*st* Csp^2-Csp^2), 1514, 1486, 1304, 1262 (*st* C-O), 1222, 1158, 1041, 836, 786.

MS (70 eV, EI) m/z (%): 334.2 (100%), 333.2 (47%).

HRMS (APCI) m/z: calculated for $C_{19}H_{16}FN_4O$ $[M+1]^+$: 335.1303; Found $[M+1]^+$: 335.1298

6-(4-methoxyphenyl)-4-(p-tolyl)-1*H*-pyrazolo[3,4-*b*]pyridin-3-amine (139{*4*,*5*,*1*})

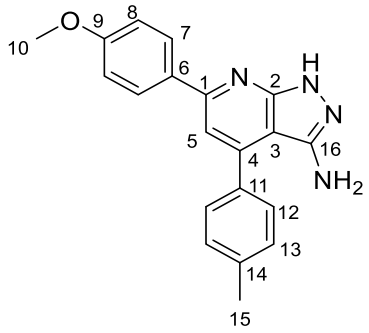

18{*2*,*4*,*1*}

Starting from 2-bromo-6-(4-methoxyphenyl)-4-(p-tolyl)nicotinonitrile (**137**{*4*,*5*}) and hydrazine monohydrate (**56**{*1*}). 47% yield, yellow solid.

mp: 203-207 °C

^{1}H-NMR (400 MHz, DMSO-d_6) δ 12.25 (s, 1H, NH), 8.17 – 8.10 (m, 2H, C7-H), 7.61 – 7.53 (m, 2H, C12-H), 7.42 – 7.37 (m, 3H, C5-H, C13-H), 7.08 – 7.02 (m, 2H, C8-H), 4.53 (s, 2H, NH_2), 3.82 (s, 3H, C10-H_3), 2.42 (s, 3H, C15-H_3).

^{13}C-NMR (100 MHz, DMSO-d_6) δ 160.3 (C9), 155.2 (C11), 153.3 (C2), 147.1 (C16), 145.2 (C4), 138.4 (C14), 134.4 (C6), 131.4 (C1), 129.4 (C13), 128.6 (C12), 128.5 (C7), 114.1 (C8), 111.6 (C5), 101.5 (C3), 55.3 (C10), 20.9 (C15).

IR (KBr), vmax (cm^{-1}): 3196 (*st* N-H), 2931, 2835, 1590 (*st* Csp^2-Csp^2), 1516, 1354, 1296, 1241 (*st* C-O), 1176, 1032, 821.

MS (70 eV, EI) m/z (%): 330.2 (100%), 329.2 (24%).

HRMS (APCI) m/z: calculated for $C_{20}H_{19}N_4O$ $[M+1]^+$: 331.1553; Found $[M+1]^+$: 331.1554

4-(4-methoxyphenyl)-6-phenyl-1*H*-pyrazolo[3,4-*b*]pyridin-3-amine (139{*3,4,1*})

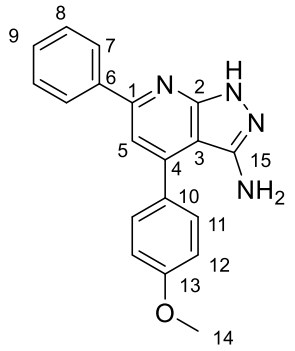

Starting from 2-bromo-4-(4-methoxyphenyl)-6-phenylnicotinonitrile (**137**{*3,4*}) and hydrazine monohydrate (**56**{*1*}). 64% yield, brownish solid.

mp: 196-198 °C

^{1}H-NMR (400 MHz, DMSO-d_6) δ 12.32 (s, 1H, NH), 8.19 – 8.12 (m, 2H C7-H), 7.69 – 7.64 (m, 2H, C11-H), 7.55 – 7.42 (m, 4H, C5-H, C9-H, C8-H), 7.18 – 7.13 (m, 2H, C12-H), 4.60 (s, 2H, NH_2), 3.85 (s, 3H, C14-H_3).

^{13}C-NMR (100 MHz, DMSO-d_6) δ 159.9 (C13), 155.4 (C1), 153.4 (C2), 147.2 (C15), 145.2 (C4), 139.0 (C6), 130.2 (C11), 129.3 (C10), 129.1 (C8), 128.7 (C9*), 127.1 (C7), 114.3 (C12), 112.2 (C5), 102.0 (C3), 55.3 (C14).

IR (KBr), vmax (cm^{-1}): 3299 (*st* N-H), 3198, 1607, 1591, 1567 (*st* Csp^2-Csp^2), 1515, 1295, 1245 (*st* C-O), 1179, 1026, 836.

MS (70 eV, EI) m/z (%): 316.2 (100%), 315.2 (30%).

HRMS (APCI) m/z: calculated for $C_{19}H_{17}N_4O$ $[M+1]^+$: 317.1397; Found $[M+1]^+$: 317.1393

6-(3-methoxyphenyl)-4-phenyl-1*H*-pyrazolo[3,4-*b*]pyridin-3-amine (139{*5*,*3*,*1*})

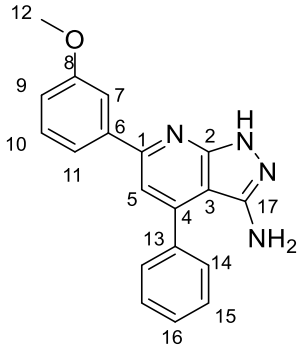

Starting from 2-bromo-6-(3-methoxyphenyl)-4-phenylnicotinonitrile (**137**{*5*,*3*}) and hydrazine monohydrate (**56**{*1*}). Purification by column chromatography (silica column, Cy:AcOEt gradient 0% to 40% in 20 minutes and then isocratic at 40% for 30 minutes). 60% yield, yellow solid.

mp: > 250 °C

^{1}H-NMR (400 MHz, DMSO-d_6) δ 12.38 (s, 1H, NH), 7.78 – 7.73 (m, 1H, C11-H), 7.73 – 7.67 (m, 3H C7-H, C14-H), 7.63 – 7.53 (m, 3H C15-H, C16-H), 7.49 (s, 1H, C5-H), 7.42-7.40 (m, 1H, C10-H), 7.07 – 7.00 (m, 1H, C9-H), 4.56 (s, 2H, NH_2), 3.85 (s, 3H, C12-H_3).

^{13}C-NMR (100 MHz, DMSO-d_6) δ 159.6 (C8), 155.3 (C1), 153.2 (C2), 147.1 (C17), 145.3, 140.4 (C6), 137.1 (C13), 129.8 (C10), 128.9, 128.8 (C14), 128.8 (C4), 119.6 (C11), 115.2 (C9), 112.5 (C7), 112.1 (C5), 102.1 (C3), 55.2 (C12).

IR (KBr), vmax (cm^{-1}): 3146 (*st* N-H), 2925, 2852, 1600, 1581 (*st* Csp^2-Csp^2), 1488, 1401, 1263 (*st* C-O), 1217, 1037, 791, 765.

Elemental analysis: calculated for $C_{20}H_{18}N_4O$: C: 72.71%, H: 5.49%, N: 16.96%; found: C: 72.71%, H: 5.46%, N: 16.63%.

MS (70 eV, EI) m/z (%): 316.1 (100%), 315.2 (41%), 302.1 (38%), 301.1 (36%).

6-(3-methoxyphenyl)-4-(4-methoxyphenyl)-1*H*-pyrazolo[3,4-*b*]pyridin-3-amine (139{*5,4,1*})

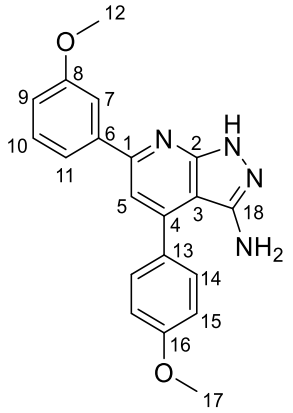

Starting from 2-bromo-6-(3-methoxyphenyl)-4-phenylnicotinonitrile (**137**{*5,4*}) and hydrazine monohydrate (**56**{*1*}). 48% yield, yellowish solid.

mp: 191-193 °C

^{1}H-NMR (400 MHz, DMSO-d_6) δ 12.32 (s, 1H, NH), 7.76 – 7.72 (m, 1H, C11-H), 7.71 – 7.69 (m, 1H, C7-H), 7.68 – 7.63 (m, 2H, C14-H), 7.45 – 7.38 (m, 2H, C5-H and C10-H), 7.17 – 7.12 (m, 2H, C15-H), 7.05 – 7.01 (m, 1H, C9-H), 4.60 (s, 2H, NH_2), 3.85 (s, 3H, C17-H_3*), 3.85 (s, 3H, C1-H_3*).

^{13}C-NMR (100 MHz, DMSO-d_6) δ 159.9 (C16), 159.6 (C8), 155.2 (C1), 153.3 (C2), 147.2 (C18), 145.2 (C4), 140.5 (C6), 130.2 (C14), 129.8 (C10), 129.3 (C13), 119.6 (C11), 115.1 (C9), 114.3 (C15), 112.3 (C7), 112.1 (C5), 102.2 (C3), 55.3 (C12*), 55.2 (C17*).

IR (KBr), vmax (cm^{-1}): 3423 (*st* N-H), 3289, 3196, 2949, 1592 (*st* Csp^2-Csp^2), 1514, 1402, 1256 (*st* C-O), 1177, 1035, 838.

Elemental analysis: calculated for $C_{20}H_{18}N_4O_2$: C: 69.35%, H: 5.24%, N: 16.17%; found: C: 69.40%, H: 5.44%, N: 15.70%.

MS (70 eV, EI) m/z (%): 346.2 (100%), 345.2 (39%).

6-(2-methoxyphenyl)-4-(4-methoxyphenyl)-1*H*-pyrazolo[3,4-*b*]pyridin-3-amine (139{*6*,*4*,*1*})

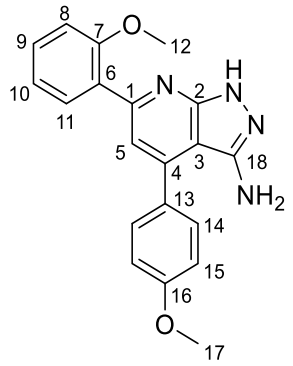

Starting from 2-bromo-6-(2-methoxyphenyl)-4-(4-methoxyphenyl)nicotinonitrile (**137**{*6*,*4*}) and hydrazine monohydrate (**56**{*1*}). Purification by column chromatography (silica column, Cy:AcOEt gradient 0% to 70% for 25 minutes, then isocratic at 70% for 45 minutes). 55% yield, yellowish solid.

mp: 236-238 °C

^{1}H-NMR (400 MHz, DMSO-d_6) δ 12.26 (s, 1H, NH), 7.74 – 7.68 (m, 1H, C11-H), 7.62 – 7.56 (m, 2H, C14-H), 7.45 – 7.40 (m, 1H, C10-H), 7.30 (s, 1H, C5-H), 7.19 – 7.12 (m, 3H, C15-H and C9-H), 7.11 – 7.05 (m, 1H, C8-H), 4.58 (s, 2H NH_2), 3.85 (s, 3H, C17-H_3), 3.82 (s, 3H, C12-H_3).

^{13}C-NMR (100 MHz, DMSO-d_6) δ 159.8 (C16), 156.9 (C7), 154.9 (C1), 153.2 (C2), 147.1 (C18), 143.6 (C4), 130.9 (C11), 130.1 (C10), 130.0 (C15), 129.5 (C13), 128.9 (C6), 120.6 (C8), 116.5 (C5), 114.3 (C15), 112.0 (C9), 101.3 (C3), 55.6 (C12), 55.3 (C17).

IR (KBr), vmax (cm^{-1}): 3305 (*st* N-H), 3202, 2925, 1606, 1583 (*st* Csp^2-Csp^2), 1510, 1295, 1252 (*st* C-O), 1024, 834, 755.

Elemental analysis: calculated for $C_{20}H_{18}N_4O_2$: C: 69.35%, H: 5.24%, N: 16.17%; found: C: 69.60%, H: 5.66%, N: 16.57%.

MS (70 eV, EI) m/z (%): 346.1 (100%), 345.1 (57%), 317.0 (26%), 316.2 (46%), 315.1 (30%), 263.2 (45%), 241.1 (40%).

4-(4-fluorophenyl)-6-phenyl-1*H*-pyrazolo[3,4-*b*]pyridin-3-amine (139{*3*,*6*,*1*})

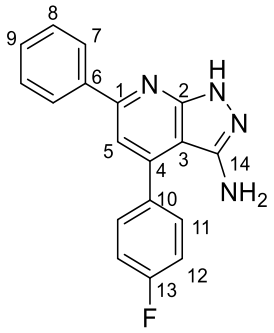

Starting from 2-bromo-4-(4-fluorophenyl)-6-phenylnicotinonitrile (**137**{*3*,*6*}) and hydrazine monohydrate (**56**{*1*}). 48% yield, yellowish solid.

mp: 194-199 °C

^{1}H-NMR (400 MHz, DMSO-d_6) δ 12.38 (s, 1H, NH), 8.20 – 8.16 (m, 2H), 7.79 – 7.73 (m, 2H), 7.54 – 7.45 (m, 4H), 7.44 – 7.38 (m, 2H), 4.61 (s, 2H, NH_2).

^{13}C-NMR (100 MHz, DMSO-d_6) δ 162.6 (d, J = 245.7 Hz), 155.5, 153.3, 147.2, 144.3, 138.9, 133.5 (d, J = 3.2 Hz), 131.1 (d, J = 8.4 Hz), 129.2, 128.7, 127.2, 115.7 (d, J = 21.6 Hz), 112.5, 102.0.

IR (KBr), vmax (cm^{-1}): 3196, 1600, 1575, 1513, 1414, 1352, 1293, 1226, 1158, 838, 757.

MS (70 eV, EI) m/z (%): 304.2 (100%), 303.2 (38%).

HRMS (APCI) m/z: calculated for $C_{18}H_{14}FN_4$ $[M+1]^+$: 305.1197; Found $[M+1]^+$: 305.1197

6-(2-methoxyphenyl)-4-(p-tolyl)-1*H*-pyrazolo[3,4-*b*]pyridin-3-amine (139{*6*,*5*,*1*})

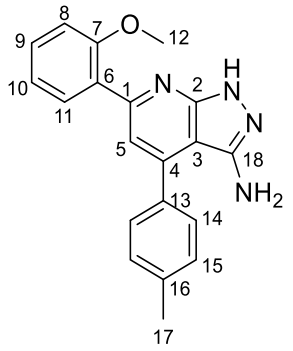

Starting from 2-bromo-6-(2-methoxyphenyl)-4-(p-tolyl)nicotinonitrile (**137**{*6*,*5*}) and hydrazine monohydrate (**56**{*1*}). Purification by column chromatography (Cy/AcOEt gradient 0% to 70% in 40 minutes), 60% yield, yellowish solid.

mp: 219-220 °C

^{1}H-NMR (400 MHz, DMSO-d_6) δ 12.29 (s, 1H, NH), 7.74 – 7.70 (m, 1H, C11-H), 7.55 – 7.52 (m, 2H, C14-H), 7.46 – 7.41 (m, 1H, C10-H), 7.41 – 7.36 (m, 2H, C15-H), 7.32 (s, 1H, C5-H), 7.18 – 7.13 (m, 1H, C9-H), 7.11 – 7.05 (m, 1H, C8-H), 4.55 (s, 2H, NH_2), 3.81 (s, 3H, C12-H_3), 2.41 (s, 3H, C17-H_3).

^{13}C-NMR (100 MHz, DMSO-d_6) δ 156.9 (C7), 154.9 (C1), 153.2 (C2), 147.1 (C18), 143.8 (C4), 138.3 (C16), 134.4 (C13), 130.9 (C11), 130.2 (C10), 129.5 (C15), 128.8 (C6), 128.6 (C14), 120.6 (C8), 116.5 (C5), 112.0 (C9), 101.3 (C3), 55.6 (C12), 20.9 (C17).

IR (KBr), vmax (cm^{-1}): 3301 (st N-H), 3198, 2922, 1583 (*st* Csp^2-Csp^2), 1563, 1463, 1351, 1296, 1243 (*st* C-O), 1116, 1022, 821, 757.

MS (70 eV, EI) m/z (%): 330.2 (100%), 329.3 (28%), 329.1 (26%), 225.1 (36%).

HRMS (APCI) m/z: calculated for $_{C20}H_{19}N_4O$ $[M+1]^+$: 331.1553; Found $[M+1]^+$: 331.1552

4,6-bis(4-methoxyphenyl)-1-methyl-1*H*-pyrazolo[3,4-*b*] pyridin-3-amine (139{*4,4,2*})

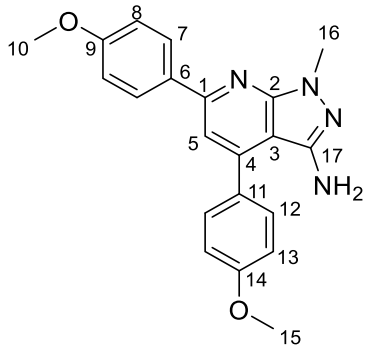

Starting from 2-bromo-4,6-bis(4-methoxyphenyl)nicotinonitrile (**137**{*4,4*}) and methylhydrazine (**56**{*2*}). 81% yield, yellowish solid.

mp: 192-195 °C

^{1}H-NMR (400 MHz, DMSO-d_6) δ 8.23 – 8.16 (m, 2H, C7-H), 7.68 – 7.60 (m, 2H, C12-H), 7.39 (s, 1H, C5-H), 7.17 – 7.12 (m, 2H, C13-H), 7.10 – 7.03 (m, 2H, C8-H), 4.65 (s, 2H, NH_2), 3.87 (s, 3H, C16-H_3), 3.85 (s, 3H, C15-H_3), 3.83 (s, 3H, C10-H_3).

^{13}C-NMR (100 MHz, DMSO-d_6) δ 160.4 (9), 159.9 (C14), 155.1 (C1), 151.4 (C2), 146.3 (C17), 145.3 (C4), 131.2 (C6), 130.1 (C12), 129.3 (C11), 128.6 (C7), 114.3 (C13), 114.1 (C8), 111.3 (C5), 101.8 (C3), 55.3 (C10*), 55.3 (C15*), 32.7 (C16).

IR (KBr), vmax (cm^{-1}): 3414 (*st* N-H), 3199, 1606, 1583 (*st* Csp^2-Csp^2), 1562, 1513, 1417, 1251 (*st* C-O), 1238, 1180, 1028, 826.

Elemental analysis: calculated for $C_{21}H_{20}N_4O_2$: C: 69.98%, H: 5.59%, N: 15.55%; found: C: 69.53%, H: 5.67%, N: 15.83%.

MS (70 eV, EI) m/z (%): 360.2 (100%).

4-(4-methoxyphenyl)-1-methyl-6-phenyl-1*H*-pyrazolo[3,4-*b*] pyridin-3-amine (139{*3,4,2*})

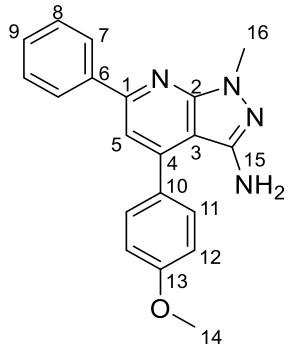

Starting from 2-bromo-4-(4-methoxyphenyl)-6-phenylnicotinonitrile (**137**{*3,4*}) and methylhydrazine (**56**{*2*}). 75% yield, yellowish solid.

mp: 192-194 °C

^{1}H-NMR (400 MHz, DMSO-d_6) δ 8.25 – 8.20 (m, 2H, C7-H), 7.68 – 7.63 (m, 2H, C11-H), 7.55 – 7.46 (m, 3H, C9-H and C8-H), 7.45 (s, 1H, C5-H), 7.16 – 7.12 (m, 2H, C12-H), 4.69 (s, 2H, NH_2), 3.89 (s, 3H, C16-H_3), 3.85 (s, 3H, C14-H_3).

^{13}C-NMR (100 MHz, DMSO-d_6) δ 159.9 (C13), 155.3 (C1), 151.4 (C2), 146.3 (C15), 145.5 (C4), 138.8 (C6), 130.2 (C11), 129.3 (C10), 129.1 (C8*), 128.7 (C9*), 127.2 (C7), 114.3 (C12), 111.9 (C5), 102.3 (C3), 55.3 (C16), 32.7 (C16).

IR (KBr), vmax (cm^{-1}): 3433 (*st* N-H), 3291, 3186, 1610, 1581 (*st* Csp^2-Csp^2), 1567, 1515, 1248 (*st* C-O), 1177, 1032, 837, 774, 690.

Elemental analysis: calculated for $C_{20}H_{18}N_4O$: C: 72.71%, H: 5.49%, N: 16.96%; found: C: 72.72%, H: 5.43%, N: 16.66%.

MS (70 eV, EI) m/z (%): 330.2 (100%), 329.2 (36%).

1-methyl-4,6-diphenyl-1*H*-pyrazolo[3,4-*b*]pyridin-3-amine (139{*3*,*3*,*2*})

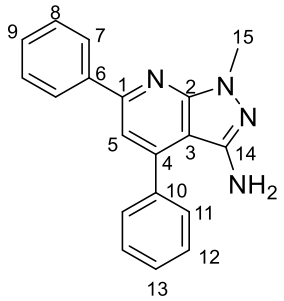

Starting from 2-bromo-4,6-diphenylnicotinonitrile (**137**{*3*,*3*}) and methylhydrazine (**56**{*2*}). 57% yield, yellow solid.

mp: 176-177 °C

^{1}H-NMR (400 MHz, DMSO-d_6) δ 8.27 – 8.21 (m, 2H), 7.72 – 7.67 (m, 2H), 7.62 – 7.44 (m, 6H), 7.49 (s, 1H, C5-H), 4.66 (s, 2H, NH_2), 3.90 (s, 3H, C15-H_3).

^{13}C-NMR (100 MHz, DMSO-d_6) δ 155.4, 151.3, 146.2, 145.7, 138.7, 137.0, 129.4, 129.0, 128.9, 128.7, 128.7, 127.2, 112.1, 102.2, 32.7 (C15).

IR (KBr), vmax (cm^{-1}): 3425 (*st* N-H), 3292, 3196, 3055 (*st* Csp^2-H), 2924, 1622, 1582 (*st* Csp^2-Csp^2), 1566, 1531, 1409, 1355, 765.

Elemental analysis: calculated for $C_{20}H_{18}N_4O$: C: 72.71%, H: 5.49%, N: 16.96%; found: C: 72.72%, H: 5.43%, N: 16.66%.

MS (70 eV, EI) m/z (%): 336.0 (40%), 335.0 (27%), 334.0 (41%), 333.0 (20%), 301.2 (22%), 300.2 (100%), 299.2 (38%), 255.2 (33%), 227.1 (22%).

1-methyl-*1H*-pyrazolo[3,4-*b*]pyridin-3-amine (139{*1,1,2*})

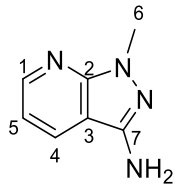

Starting from 2-bromonicotinonitrile (**137**{*1,1*}) and methylhydrazine (**56**{*2*}). 43% yield, yellow solid.

mp: 115-116°C

^{1}H-NMR (400 MHz, DMSO-d_6) δ 8.36 (dd, J = 4.5, 1.6 Hz, 1H, C1-H), 8.10 (dd, J = 7.9, 1.6 Hz, 1H, C4-H), 6.95 (dd, J = 7.9, 4.6 Hz, 1H, C5-H), 5.66 (s, 2H, NH_2), 3.75 (s, 3H, C6-H_3).

^{13}C-NMR (100 MHz, DMSO-d_6) δ 150.5 (C2), 148.6 (C1), 147.2 (C7), 129.9 (C4), 113.6 (C5), 106.5 (C3), 32.5 (C6).

IR (KBr), vmax (cm^{-1}): 3374 (*st* N-H), 3338, 3199, 3059 (*st* Csp^2-H), 2926, 1638, 1605, 1579 (*st* Csp^2-Csp^2), 1547, 1498, 1422, 1378, 1271, 764.

Elemental analysis: calculated for $C_7H_8N_4$: C: 56.74%, H: 5.40%, N: 37.80%; found: C: 56.93%, H: 5.30%, N: 37.40%.

MS (70 eV, EI) m/z (%): 148.2 (100%), 147.9 (60%), 78.1 (31%), 52.1 (22%), 51.1 (25%)

1*H*-pyrazolo[3,4-*b*]pyridin-3-amine (139{*1,1,2*})

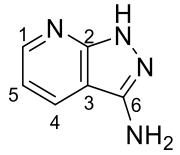

Starting from 2-bromo-nicotinonitrile (**137**{*1,1*}) and hydrazine monohydrate (**56**{*1*}). 57% yield, orange solid.

mp: 162-164 °C

^{1}H-NMR (400 MHz, DMSO-d_6) δ 11.90 (s, 1H, NH), 8.33 (dd, J = 4.6, 1.6 Hz, 1H, C1-H), 8.11 (dd, J = 7.9, 1.6 Hz, 1H, C4-H), 6.94 (dd, J = 7.9, 4.5 Hz, 1H, C5-H), 5.55 (s, 2H, NH_2).

^{13}C-NMR (100 MHz, DMSO-d_6) δ 152.4 (C2), 148.5 (C1), 148.1 (C6), 129.6 (C4), 113.8 (C5), 106.2 (C3).

IR (KBr), vmax (cm^{-1}): 3339 (*st* N-H), 3243, 3163, 3045 (*st* Csp^2-H), 2974, 2581, 1630, 1609, 1595 (*st* Csp^2-Csp^2), 1541, 1495, 1416, 1298, 1104, 759, 733.

MS (70 eV, EI) m/z (%): 134.0 (100%), 105.0 (22%), 79.0 (50%), 52.1 (26%).

1-phenyl-*1H*-pyrazolo[3,4-*b*]pyridin-3-amine (139{*1,1,3*})

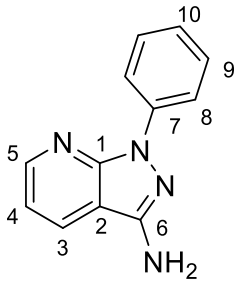

Starting from 2-bromo-nicotinonitrile (**137**{*1,1*}) and phenyl hydrazine (**56**{*3*}). 3% yield, orange solid. Temperature was increased to 180 °C. Purification by column chromatography (Alumina column, Cy:AcOEt gradient 0-20% for 15 min and isocratic at 20% for 10 min).

mp: 170-172 °C

^{1}H-NMR (400 MHz, DMSO-d_6) δ 8.54 (dd, J = 4.6, 1.7 Hz, 1H, C5-H), 8.29 (dd, J = 7.9, 1.7 Hz, 1H, C3-H), 8.28 – 8.24 (m, 2H, C8-H), 7.50 – 7.41 (m, 2H, C9-H), 7.18 (dd, J = 7.9, 4.6 Hz, 1H, C4-H), 7.16 – 7.11 (m, 1H, C10-H), 6.20 (s, 2H, NH_2).

^{13}C-NMR (100 MHz, DMSO-d_6) δ 150.1 (C1), 149.3 (C5), 149.1 (C6), 140.0 (C7), 130.5 (C3), 128.9 (C9), 123.2 (C10), 118.2 (C8), 115.7 (C4), 109.8 (C2).

2-phenyl-*2H*-pyrazolo[3,4-*b*]pyridin-3-amine (140{*1,1,3*})

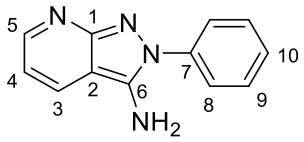

Starting from 2-bromo-nicotinonitrile (**137**{*1,1*}) and phenyl hydrazine (**56**{*3*}). 9% yield, dark orange solid. Temperature was increased to 180 °C. Purification by column chromatography (Alumina column, Cy:AcOEt gradient 0-20% for 15 min and isocratic at 20% for 10 min).

mp: 170-175 °C

^{1}H-NMR (400 MHz, DMSO-d_6) δ 8.43 (dd, J = 4.2, 1.8 Hz, 1H, C5-H), 8.18 (dd, J = 8.2, 1.8 Hz, 1H, C3-H), 7.74 – 7.67 (m, 2H, C8-H), 7.61 – 7.55 (m, 2H, C9-H), 7.50 – 7.43 (m, 1H, C10-H), 6.73 (dd, J = 8.2, 4.2 Hz, 1H, C4-H), 6.61 (s, 2H, NH_2).

^{13}C-NMR (100 MHz, DMSO-d_6) δ 157.0, 152.5 (C5), 141.0, 138.7 (C7), 131.1 (C3), 129.4 (C9), 127.7 (C10), 124.4 (C8), 112.6 (C4), 101.5 (C2).

2,4,6-triphenyl-*2H*-pyrazolo[3,4-*b*]pyridin-3-amine (140{*3,3,3*})

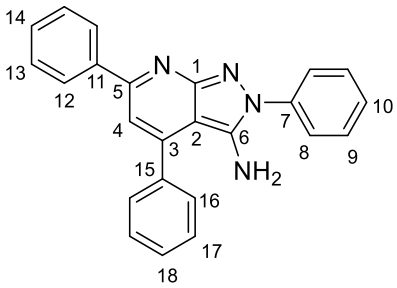

Starting from 2-bromo-nicotinonitrile (**137**{*3,3*}) and phenyl hydrazine (**56**{*3*}). 19% yield, yellow solid. Temperature was increased to 180 °C. Purification by column chromatography (Alumina column, Cy:AcOEt gradient 0% to 20% in 40 min).

mp: 190-193 °C

^{1}H-NMR (400 MHz, DMSO-d_6) δ 8.25 – 8.16 (m, 2H, C12-H), 7.77 – 7.69 (m, 4H), 7.66 – 7.45 (m, 9H), 7.34 (s, 1H, C4-H), 5.31 (s, 2H, NH_2).

^{13}C-NMR (100 MHz, DMSO-d_6) δ 158.0, 157.1, 153.8, 147.1, 143.9, 140.1, 138.9, 138.2, 136.7, 129.5, 129.1, 128.7, 128.4, 127.4 (C12), 124.9, 123.5, 111.9 (C4), 98.4 (C2).

1,4,6-triphenyl-*1H*-pyrazolo[3,4-*b*]pyridin-3-amine (139{*3*,*3*,*3*})

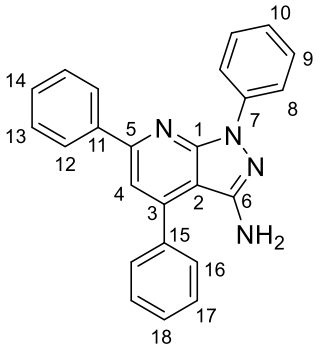

Starting from 2-bromo-nicotinonitrile (**137**{*3*,*3*}) and phenyl hydrazine (**56**{*3*}). 17% yield, yellow solid. Temperature was increased to 180°C. Purification by column chromatography (Alumina column with a Cy:AcOEt gradient 0-20% for 40 min).

mp: 193-195 °C

^{1}H-NMR (400 MHz, DMSO-d_6) δ 8.40 – 8.37 (m, 2H, C8-H), 8.31 – 8.26 (m, 2H, C12-H), 7.75 – 7.71 (m, 2H), 7.68 (s, 1H, C4-H), 7.66 – 7.46 (m, 8H), 7.24 – 7.19 (m, 1H), 5.04 (s, 2H, NH_2).

^{13}C-NMR (100 MHz, DMSO-d_6) δ 156.1 (C5), 150.8, 148.1, 146.3, 139.8, 138.4, 136.5, 129.7, 129.2, 129.0, 128.9, 128.8, 127.4 (C12), 123.9, 119.0 (C8), 113.9 (C4), 105.2 (C2).

IR (KBr), vmax (cm^{-1}): 3459 (*st* N-H), 3302, 3195, 3054 (*st* Csp^2-H), 2923, 2852, 1632, 1597 (*st* Csp^2-Csp^2), 1562, 1535 1501, 1417, 1354, 756, 689.

MS (70 eV, EI) m/z (%): 363.2 (32%), 362.2 (99%), 336.0 (98%), 335.2 (92%), 334.1 (100%), 333.3 (81%), 255.1 (78%), 253.2 (44%), 228.1 (32%), 227.1 (68%), 77.1 (92%), 57.1 (50%), 51.1 (55%), 43.1 (37%).

6.2. Determination of the biological activity

6.2.1. MNK1 and MNK2 enzymatic *in vitro* assay

6.2.1.1 Measure of the residual activity

Determination of the effect of the compounds on the kinase activity of MNKs (and other kinases) *in vitro* was performed with a radiometric protein kinase assay (^{33}PanQinase® Activity Assay) at ProQinase® (www.proqinase.com). Protein kinases used at Proqinase® were purchased from Life Technologies (Invitrogen Corporation).

The compounds were provided as solids and were dissolved to 1 x 10^{-3}M stock solutions in 100% DMSO (100x stock). The 10x stock solution was prepared by dissolving 10 µl of the 100x stock in 90 µl of water resulting in a 1 x 10^{-4} M/10 % DMSO solution.

The final working concentration was 1 x 10^{-5} M, resulting in a final concentration of 1% DMSO. All compounds were tested in singlicate.

Protein Kinase Assay

A radiometric protein kinase assay (^{33}PanQinase® Activity Assay) was used for measuring the kinase activity of the two protein kinases MNK1 and MNK2 (Figure 6.1). All kinase assays were performed in 96-well FlashPlatesTM from PerkinElmer (Boston, MA, USA) in a 50 µl reaction volume. The reaction cocktail was pipetted in 4 steps in the following order: (1) 20 µl of assay buffer, (2) 5 µl of ATP solution (in H_2O), (3) 5 µl of test compound (in 10% DMSO), (4) 20 µl enzyme/substrate mix.

The assay for all protein kinases contained 70 mM HEPES-NaOH pH 7.5, 3 mM $MgCl_2$, 3 mM $MnCl_2$, 3 µM Na-orthovanadate, 1.2 mM DTT, 50 µg/ml PEG_{20000}, ATP (variable amounts, corresponding to the apparent ATP-K_m of the respective kinase, 1 µM for MNK1 and 0.3 µM for MNK2), [γ-^{33}P]-ATP (approx. 1.2 x 10^6 cpm per well), protein kinase (variable amounts depending on the stock) and substrate (S6 peptide, 2 µg/50ul).

The reaction cocktails were incubated at 30 °C for 60 minutes. The reaction was stopped with 50 µl of 2 % (v/v) H_3PO_4 and the plates were aspirated and washed two times with 200 µl 0.9 % (w/v) NaCl. Incorporation of ^{33}Pi was determined with a microplate scintillation counter (Microbeta, Wallac).

All assays were performed with a Beckman Coulter/SAGIAN™ Core System.

Evaluation of Raw Data

The residual activity (in %) for each well of a particular plate was calculated by using the following formula:

Res. Activity (%) = 100 x [(cpm of compound – low control) / (high control – low control)]

Cpm of compound corresponds to the counts per minute measured for the mix containing the compound. "low control" reflects unspecific binding of radioactivity to the plate in the absence of a protein kinase but in the presence of the substrate. "high control" is full activity in the absence of any inhibitor. The difference between high and low control was taken as 100 % activity.

Quality Controls

As a parameter for assay quality, the Z´-factor[11] for the low and high controls of each assay plate (n = 8) was used. ProQinase®´s criterion for repetition of an assay plate is a Z´-factor below 0.4.[12]

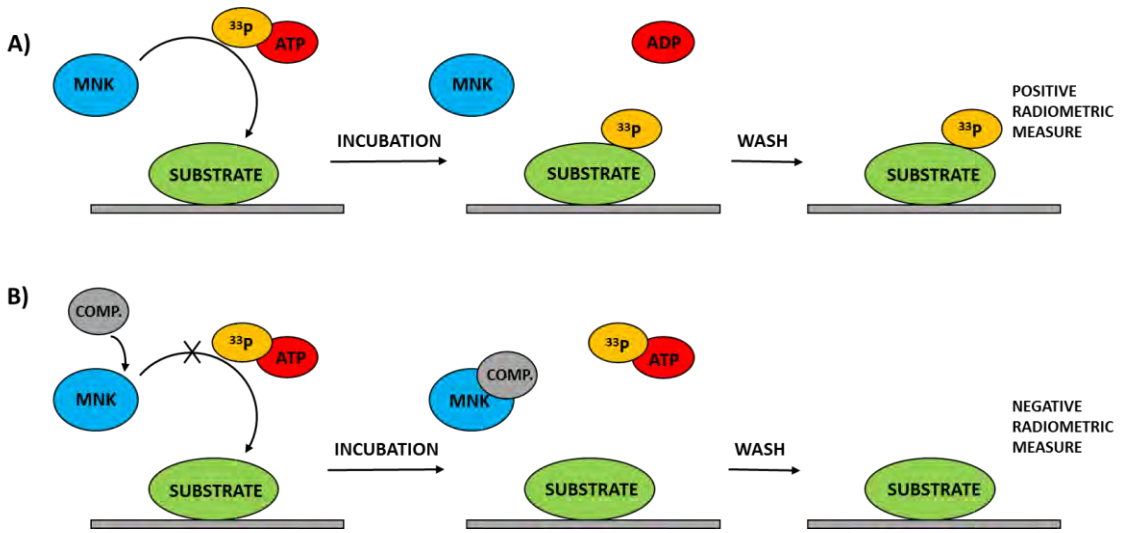

Figure 6.1. Schematic representation of the radiometric kinase assay. A) Without an inhibitor, the recombinant kinase is capable of phosphorylating the substrate with the radiolabeled phosphate and, after washing, a radiometric signal is measured. B) In the presence of an inhibitor, the kinase is inhibited and the substrate is not phosphorylated showing no radiometric signal.

6.2.1.2 Determination of the IC_{50}

The IC_{50} profile of the compounds was determined using the previously described radiometric protein kinase assay (^{33}PanQinase® Activity Assay). IC_{50} values were measured by testing 10 concentrations of the compounds in the range from $5 \cdot 10^{-5}$ M to $1.5 \cdot 10^{-9}$ M.

6.2.1.3 Determination of the kinome

The kinase inhibition profile of one compound was determined by measuring residual activity values at 0.1 and 1 µM for 320 wild-type protein kinases. The residual activity of each kinase is determined with the radiometric protein kinase assay described above (^{33}PanQinase® Activity Assay).

6.2.2. Cellular *in vitro* assays

6.2.3. Cell lines

In this project several cell lines were used. Despite the project was mainly focused on breast cancer, other cell lines were used to study sensitivity and cell line dependency of MNK inhibitors.

- MDA-MB-231: Human breast carcinoma triple negative (ER-, PR-, HER2-) cell line (American Type Culture Collection (ATCC); number CRM-HTB-26).
- MDA-MB-468: Human breast carcinoma triple negative (ER-, PR-, HER2-) cell line (ATCC; number HTB-132).
- MCF7: human breast carcinoma ER+, PR+, HER2- cell line (ATCC; number CRM-HTB-22).
- MCF10A: Epithelial breast cell line (ATCC, number CRL-10317). Immortalized, non-tumorigenic cells.
- BT-549: Human breast ductal carcinoma (ATCC, number HTB-122)
- HeLa: Cervix adenocarcinoma (ATCC, number CCL-2)
- A375M: Metastatic melanoma (RRID: CVCL_B222)
- MV4-11: Acute myeloid leukemia. Homozygous for the FLT3 mutation (ATCC number CRL-9591)
- HL-60: Acute myeloid leukemia. Wildtype for the FLT3 mutation (ATCC number CCL-240)
- MOLM-14: Acute myeloid leukemia. Heterozygous for the FLT3 mutation (RRID:CVCL_7916).

Breast cancer cell lines were purchased from the American Type Culture Collection (ATCC) and authenticated by DNA profiling using short tandem repeat (STR) (GenePrint® 10 System, Promega) at Genomics Core Facility of the Instituto de Investigaciones Biomédicas Alberto Sols (CSIC-UAM). Leukemia cells were kindly provided by Dr. Marta Crespo from Vall d´Hebron Institute of Oncology (VHIO). Melanoma cell lines were kindly provided by Dr. Sonia del Rincon (Department of Oncology, McGill University).

6.2.4. Cell culture

MDA-MB-231, MDA-MB-468, MCF7, BT-549, A375M and HeLa cells were grown in DMEM medium (Dulbecco's modified Eagle's medium: 4.5 g/l D-glucose; 580 mg/l L-Glutamine (Gibco)) supplemented with 10% heat-inactivated fetal bovine serum (FBS) (Life Technologies), 100 U/ml penicillin and 100 µg/ml streptomycin (Life Technologies).
MCF10A cells were grown in DMEM/F-12 medium (Dulbecco's Modified Eagle Medium: 3.125 g/L D-Glucosa, 365 mg/L L-Glutamine, Nutrient Mixture F-12 (Gibco)) supplemented with 10% FBS, 100 U/ml penicillin, 100 µg/ml streptomycin, 1% L-Glutamine (Cambrex), 10 ng/ml choleric toxin (Sigma-Aldrich), 0.005 mg/ml insulin (Sigma), 100 ng/ml hydrocortisone (Sigma) and 20ng/ml EGF (Epidermal growth factor, Sigma).
MV4-11 cells were grown in IMDM medium (Iscove's Modified Dulbecco's Medium, Gibco) supplemented with 10% FBS, 1% L-glutamine, 100 U/ml penicillin and 100 µg/ml streptomycin.
HL-60 and MOLM-14 cells were grown in RPMI-1640 medium (Sigma) supplemented with 10% FBS, 1% L-glutamine, 100 U/ml penicillin and 100 µg/ml streptomycin.

Cell culture was performed in sterile conditions using a vertical laminar flux cabinet (Bio II, Telstar, Life Science solutions). Cells were maintained at 37 °C in 5% CO_2 humidified incubator (AutoFlow UN-5510 incubator, Nuaire).
For cell expansion, passage of cells was made when cultures reached 70-80% of confluence. Culture medium was aspirated, cells were washed with 1x PBS (phosphate buffered saline, Sigma), trypsinized and seeded in a new plate to the optimal dilution. For trypsinization, 1 mL of TrypLE (rProtease and 0.457 g/L EDTA, (Gibco)) was added to each 10 cm plate and the plates were incubated at 37 °C for 5 minutes or until cells detached from the plate. Subsequently, cells were suspended in 3 mL of medium with FBS and centrifuged for 5 minutes at 200 g. Supernatant was discarded and the pellet was re-suspended in fresh media.

For long term storage, cells were maintained in FBS with 10% DMSO at in liquid nitrogen. In order to create the cell stock, cells were trypsinized, suspended in medium and centrifuged for 5 minutes at 200 g. Medium was then aspired and the pellet was suspended in FBS with 10% DMSO, divided into cryogenic tubes and frozen at -80 °C.
For defrosting of cells, tubes were thawed at 37 °C, diluted in medium and centrifuged for 5 minutes at 200 g. Cell pellet was then suspended in media and transferred to a plate.

Cells were counted using the Neubauer method or a Countess™ II Automated Cell Counter (Invitrogen). Cells were trypsinized, centrifuged for 5 minutes at 200 g and resuspended in media. 20 µL of cell suspension were mixed with 20 µL of Trypan Blue (0.4%, Invitrogen) and 10 µL mixture were introduced in the chamber in order to count the number of live cells.

6.2.5. Cell proliferation

Proliferation curves were performed at 24h, 48, and 72h.

Cells were seeded in a 96 well plates (4000 cells/well, 3 replicates for each condition, one plate per time-point). After 24h, a plate was fixed as time 0 and the other were treated. The different treatments were prepared in the corresponding media from a 200x stock of the drug in DMSO (Table 6.2). The final DMSO concentration was maintained at 0.5%. Controls were included: 0.5% DMSO as negative control, CGP57380 40 µM or ETF508 100 nM as positive control. The plates were incubated for 24h, 48, or 72h.

After the corresponding time, the media was removed, the cells were fixed with PFA (para-formaldehyde solution 4% in PBS) for 30 minutes and washed twice with PBS. 100 µL of a crystal violet solution (0.5% in water) were added to each well and the plates were shaked for 15 minutes. The crystal violet solution was removed, and the plates were washed with water and let to dry. The crystal violet was dissolved in 200 µL of 15% AcOH and the optical density of the solution was measured at 595 nm (Epoch Microplate Spectrophotometer, BioTek). The results are analyzed using GraphPad Prism 6.

Table 6.2. Final concentrations and stock concentrations used for the treatments in the proliferation assays.

Final concentration (µM)	Stock concentration (mM)
0.312	0.063
0.625	0.125
1.25	0.25
2.5	0.5
5	1
10	2
20	4
40	8

6.2.6. Biological activity of compounds determined by eIF4E phosphorylation

The biological activity of the compounds was studied by western blot analysis of eIF4E phosphorylation, a known substrate of the MNK kinases. Selective inhibition of MNKs was furthermore determined by analysis of the activity state (phosphorylation) of signaling proteins up-stream of the MNK kinases.

Cell treatment

Cells were seed in 6 cm plates and incubated overnight at 37°C, 5% CO_2. The number of seeded cells depended on the treatment time: 700000 cells for 24h, 500000 cells for 48h and 300000 cells for 72h. Cells were treated with 3 mL of the compound solution in media. Treatments were prepared from a 200x stock in DMSO. The final DMSO concentration was maintained at 0.5%. Controls were included: DMSO 0.5% as negative control and CGP57380 40 µM as positive control.

Protein extraction

Cell medium was aspirated and the cells were washed twice with PBS 1x. Then, cells were lysed with 60 µL of lysis buffer (50 mM Tris, 200 mM NaCl, 5 mM EDTA, 0.1% Triton 100x, pH 7.5 with protease inhibitors (EDTA-free Protease Inhibitor Cocktail Set III, Calbiochem) and phosphatase inhibitors (Phosphatase Inhibitor Cocktail Set II, Calbiochem)). Cell were scraped, and the lysate was collected in an Eppendorf and mixed every 5 minutes for 30 minutes. Lysate was then centrifuged for 20 minutes at 4 °C and at 15000 g. The supernatant was recollected in a clean Eppendorf and the pellet was discarded. This process was performed maintaining cells and extracts at 4 °C.

Protein quantification

In a 96 well plate, 1 µL of the protein suspension was diluted in 200 µL of 1x Bio-Rad Protein Assay (BioRad, diluted in distilled water from 5x stock) and the absorbance was measured at 595 nm. Protein concentration was obtained through interpolation in a BSA (Bovine Serum Albumin, Sigma-Aldrich) calibration curve ranging from 0 µg/mL to 2 µg/mL.

Western blot

Samples were diluted to a common concentration with lysis buffer and charge buffer 1x (Laemmli 5x: 15 mL destiled water; 2.5 mL Tris-HCl 1 M pH 6.8; 10 mL glycerol, 8mL SDS 10%, 2 mL b-mercaptoetanol; 500 µl bromofenol blue 0.5% in water). Proteins were then denaturalized at 95 °C for 5 minutes.

Proteins were separated depending on their molecular weight in a poly acrylamide gel. Gels were composed by two different parts: The stacking gel, with a lower acrylamide concentration (5%) and slightly acidic pH (pH 6.8) is porous and concentrates the sample to form thin bands. The resolving gel is basic (pH 8.8) and contains a higher concentration of acrylamide forming narrower pores. It allows separation of the proteins depending on their molecular weight as smaller proteins travel more rapidly than larger proteins. In this case, 12% acrylamide gel was used to correctly separate all the proteins of interest.

Table 6.3. Composition of a western blot gels

12% Resolving Gel (10 mL gel)	
Component	**Volume/mL**
water	3.3
30% acrylamide mix	4.0
1.5M Tris (pH 8.8)	2.5
10 % SDS	0.1
10% ammonium persulfate	0.1
TEMED	0.004

5% Stacking gel (4 mL gel)	
Component	**Volume/mL**
water	2.7
30% acrylamide mix	0.67
1.0 M Tris (pH 6.8)	0.5
10 % SDS	0.04
10% ammonium persulfate	0.04
TEMED	0.004

For each sample, around 20 µg of protein were loaded in each well. A *Precision Plus Protein Standards dual color* (Bio-Rad) marker was used to identify the weights. Electrophoresis was performed in running buffer (0.1 % SDS, 25 mM Tris and 190 mM glycine) at 80V until the sample has reached the resolving gel and then increased to 120 V.

Proteins were then electrophoretically transferred onto a Polyvinylidene fluoride (PDVF) membrane applying 0.4 A for 90 minutes. The gel was maintained in transfer buffer (25 mM tris, 190 mM glycine and 20% methanol) and in ice.

Membranes were then blocked in 5% BSA in TTBS (Tris-HCl 50 mM pH 7.4; NaCl 150 mM and 0.1% de Tween-20) for 30 min in order to prevent non-specifically binding of antibodies.

Protein detection was performed using antibodies labelled with horseradish peroxidase (HRP). Membranes were incubated overnight in the primary antibody in 5% BSA in TTBS at 4 °C, washed three times for 10 min with TTBS to remove unbound antibody and incubated with the secondary antibody (Goat Anti-Rabbit IgG HRP Labelled, ThermoScientific, 1:10000) in 5% BSA for an hour.

Actin was used as loading control and membranes were incubated for an hour in the antibody in 5% TBST. As it is already conjugated with HRP, no secondary antibody was needed.
After washing with TTBS (three times, 10 min), proteins were revealed in a dark room using chemiluminesence emission ECL (Amersham Pharma-Biotech).

Table 6.4. Antibodies used for western blot analysis

Primary antibody	Molecular weight (kDa)	Commercial brand
p-4E-BP1 (Thr37/46)	15 to 20	Cell Signalling (9459)
4E-BP1	15 to 20	Cell Signalling (9452)
p-eIF4E (ser 209)	25	Novus (81898)
eIF4E	25	Cell signaling (9742)
p-ERK1/2 (p-p44/42) (Thr202/Tyr204)	42, 44	Cell Signalling (9101)
ERK1/2 (p44/42)	42, 44	Cell Signalling (9102)
p-MNK1 (Thr197/202)	50	Cell signaling (2111)
MNK1	50	Cell Signalling (2195)

6.2.7. Synergy with doxorubicin

In order to test the synergistic effects of the combination of **EB1** with doxorubicin, the IC_{50} of doxorubicin was calculated alone and in combination with the MNK inhibitor.

Cells were seeded in 96 well plates (3000 cells/well) and let to attach overnight. The treatments were added (Table 6.5) and the plates were incubated for 48h. Then, the media was removed and the cells were fixed with PFA (paraformaldehyde solution 4% in PBS) for 30 minutes and washed with PBS. 100 µL of a crystal violet solution (0.5% in water) were added to each well and the plates were shaked for 15 minutes. The crystal violet solution was removed, and the plates were washed with water and let to dry. The crystal violet was dissolved in 200 µL of 15% AcOH and the optical density of the mixture was measured at 595 nm (Epoch Microplate Spectrophotometer, BioTek). The results are analyzed using GraphPad Prism 6 and excel.

Table 6.5. Combinations for the synergy assays. Different concentrations of doxorubicin are prepared to in combination with the different co-treatment compounds (DMSO as control or the MNK inhibitors under study **EB1** and **eFT508**)

Co-treatment	Doxorubicin (nM)								
DMSO (0.5%)	0	3	10	30	100	300	1000	3000	10000
EB1 (5 µM)	0	3	10	30	100	300	1000	3000	10000
eFT508 (100 nM)	0	3	10	30	100	300	1000	3000	10000

6.2.8. Cell migration assay

Cells were seeded in 24 well plates (500000 cells/well) to form a monolayer and, once attached, were treated overnight with mitomycin C (2 µg/mL, Santa Cruz Biotechnology). Then, a wound was made in the monolayer with a 100 µL pipette tip and the wells were washed with PBS. The medium was replaced by the treatment and the cells were incubated in normal conditions. Pictures of the wounds were taken at 0, 8 and 24 hours and the wound closure was measured using ImageJ software.

6.2.9. Cell invasion assay

65 µL of a 1.5 mg/mL solution of Matrigel Matrix (Corning 356231), dissolved in serum free medium, was added to the bottom of each insert (PET membrane of 0.3 cm^2 of surface with 8 µm pores, (Sarstedt)) placed in a 24 well plate and incubated at 37 °C for 4h or until solidified. Cells were trypsinized and suspended in serum free media or a treatment solution in serum free media (500000 cells/mL). 100 µL of the suspension (50000 cells) were placed in the inserts on top of the Matrigel. The well was filled with 500 µL of treatment in culture medium (with FBS). Plates were incubated at 37 °C in 5% CO_2 for 24h.

The media and the Matrigel were aspirated and the wells were washed with PBS. Cells were fixed with PFA (4% solution in water, 200 µL inside the insert and 500 µL inside the well) for 15 minutes and then washed twice with PBS.

The cells were stained with a 5 mg/mL solution of Hoechst in PBS (200 µL inside the insert and 500 µL inside the well) for 15 minutes in the darkness. The inserts were washed with a cotton swab and with PBS.

Pictures of the inserts were taken using blue fluorescence (4 pictures per insert, 4.2x, Olympus FSX100) and the number of cells was measured using ImageJ software.

6.2.10. Clonal cell growth assay.

Cells were seeded in six-well plates (300 cells/well) and let to attach. The treatment was added (1 mL) and the cells were incubated for 7 days at 37 °C and 5% CO_2. Treatment was changed every 48h. The supernatant was discarded and the cells were gently washed with 1 mL of PBS. For clonal cell growth quantification, cells were fixed with PFA and stained with crystal violet. The crystal violet was solubilized in 800 µL of 15% acetic acid and the optical density of the solution (200 µL) was measured at 595 nm.

6.2.11. Cell cycle analysis

The effect of **EB1** on the cell cycle of MDA-MB-231 cells was analyzed by staining with propidium iodide and analyzing the DNA content by Flow Cytometry.

10^6 of cells were seeded in 10 cm plates and treated with a solution of the compounds or controls for 72h hours. Then the cells were fixed: Cells were trypsinized, washed twice with PBS and finally resuspended in 0.3 mL of PBS. Then 0.7 mL of ice-cold absolute EtOH was added while mixing by vortex. The mixtures were maintained on ice for 2h.

For the propidium iodide staining, the suspension was pelleted and the supernatant was discarded. The pellet was washed twice with PBS and suspended in the working solution (RNAse A (300 µg/mL, Sigma), sodium citrate (1.14 mM) and Propidium iodide (15 µg/mL, Sigma)). The suspension was incubated at 4 °C overnight and analyzed on a FACS Fortessa instrument integrated with FACSDiva (BD Biosciences).

6.3. Computational methods

6.3.1. QSAR and QSPR models

Database preparation

All databases needed were created using Molecular Operating Environment (MOE 2014.09)[13] on a 2.30 GHz Intel® Core™ i7-3610QM processor with 8 GB RAM.

To create the databases of published molecules, the structures were manually drawn using the software and saved in a database together with their activity values. This databases include the information available in literature and in the ChEMBL database[14–16] and the published articles. For the first models, the molecules published by Oyzarzabal *et al.*[17], Diab *et al.*[18], Kannan *et al.*[19], Teo *et al.*[20,21], Yu *et al.*[22] and Cherian *et al.*[23] were used. For the modification of the models the molecules from Diab *et al.*[24], Reich *et al.*[25], Han *et al.*[26] and Zhan *et al.*[27] were included. For the creation of the models, the molecules from the ChEMBL database were curated selecting only those entries with a percentage of inhibition between 0-50% tested at 1 µM against MNK1 and MNK2 or a residual activity higher than 50%. Moreover, the molecules having non numerical values, such as IC_{50}>10 µM or Ki>10, were removed. The databases used for the models are found on the *Database.pdf* file.

To prepare the databases for candidate selection, a combinatorial library was used. Different databases were created by manually drawing the scaffolds or the different substituents (one database for each substitution point). The substitution points were indicated in the scaffolds as A1, A2, A3… while the attachment points from the substituents were labelled as A0. The scaffolds and the substituents were combined to create a final database of candidates using the combinational library tool in MOE.

Molecules were prepared using the MMFF94x forcefield: hydrogen atoms were added when necessary, the partial charges were calculated and the molecules were minimized using a RMS Gradient of 0.001 $kcal \cdot mol^{-1} \cdot Å^{-2}$. For energy minimization, MOE combines the Steepest Descent (SD) with the Conjugate Gradient (CG) searching algorithms.

The 2D and i3D (internal 3D) descriptors offered by MOE2014.09 (344 descriptors) were calculated to create the models.

Descriptors selection

RapidMiner Studio[28] was used on a 2.30 GHz Intel® Core™ i7-3610QM processor with 8 GB RAM to select a small number of representative descriptors (Table 6.7). First, the correlation between the activity of the molecules and each descriptor was calculated (using the Correlation Matrix operator) and the descriptors with a higher correlation were selected. For each model, a threshold value was applied and the descriptors with a lower correlation with the activity were discarded (Table 6.6). Then, the correlation between each pair of descriptors was calculated and avoided by eliminating one of the two correlated descriptors of each pair (Remove Correlated Attributes operator, filter relation: greater equals, attribute order: random, use absolute correlation). Again, for each model, a maximum correlation value was defined (Table 6.6). Finally, those descriptors with the same value in most of the compounds were eliminated (Remove Useless Attributes operator, numerical minimum deviation 0.0, nominal useless above 0.8, nominal useless below 0.0).

Table 6.6. Parameters used for the selection of descriptors.

MODEL	Correlation with activity	Correlation between descriptors
QSPR initial MNK1	0.3	0.8
QSPR initial MNK2	0.4	0.85
QSAR MNK1	0.3	0.75
QSAR MNK2	0.3	0.8
QSPR modified MNK1	0.04	0.8
QSPR modified MNK2	0.14	0.8

Table 6.7. Selected descriptors for the QSPR and QSAR models.

MODEL	Selected descriptors
QSPR initial MNK1 model	a_base, b_double, PEOE_VSA_FPOS, SlogP_VSA3, SlogP_VSA4, PM3_dipole, vsurf_HB1.
QSPR initial MNK2 model	PC-, PEOE_VSA_POS, ASA_P, FCASA+, PM3_dipole, vsurf_HB1, vsurf_W3.
QSAR MNK1 model	BCUT_PEOE_1, b_1rotR, KierA3, Q_RPC+, SlogP_VSA6, E_tor, vsurf_IW8.
QSAR MNK2 model	a_acc, GCUT_PEOE_1, PEOE_VSA-1, E_strain, PM3_IP.
QSPR modified MNK1 model	b_double, h_pKb, GCUT_PEOE_0, logP(o/w), PEOE_VSA_FNEG, PEOE_VSA_POS, Q_VSA_FNEG, SlogP_VSA3, SMR_VSA2, vsurf_A, vsurf_CW2, vsurf_HB1, vsurf_IW6.
QSPR modified MNK2 model	a_nN, h_ema, PEOE_VSA_POS, Q_RPC-, vsurf_HB1, vsurf_HB5

QSPR classificatory model

The activity of the molecules was classified as active (1) or inactive (0) according to the criteria defined in Table 6.8.

The models were created using RapidMiner Studio[28] on a 2.30 GHz Intel® Core™ i7-3610QM processor with 8 GB RAM. The data was divided into two groups (Split Data operator), the training set (80%) and the test set (20%), using a stratified sampling. Then, the model was generated on the training set using a neural network (Neural Net operator), and it was afterwards applied to the test set. The quality of the model was evaluated taking into account the accuracy, the class recall and the class precision (Performance (Classification) operator) of the prediction. (Figure 6.2)

The final parameters of each model are found in Table 6.9. The parameters of the Neural Network were optimized for each model varying the number of neurons, the learning rate and the training cycles (Annex 5).

Table 6.8: Criteria to classify the molecules as active or inactive inhibitors depending on their activity values and tests.

	IC_{50} / µM	Ki	Residual Activity %	Inhibition %
ACTIVE (1)	<10	<10	<50	>50
INACTIVE (0)	≥10	≥10	≥50	≤50

Table 6.9. Optimized parameters for the QSPR models

MODEL	Model parameters
QSPR initial MNK1 model	7-6-4-2 artificial neural network with 0.05 learning rate and 15000 training cycles
QSPR initial MNK2 model	7-7-4-2 artificial neural network with 0.04 learning rate and 15000 training cycles)
QSPR modified MNK1 model	13-7-4-1 artificial neural network with 0.04 learning rate and 15000 training cycles
QSPR modified MNK2 model	6-7-4-1 artificial neural network with 0.04 learning rate and 15000 training cycles

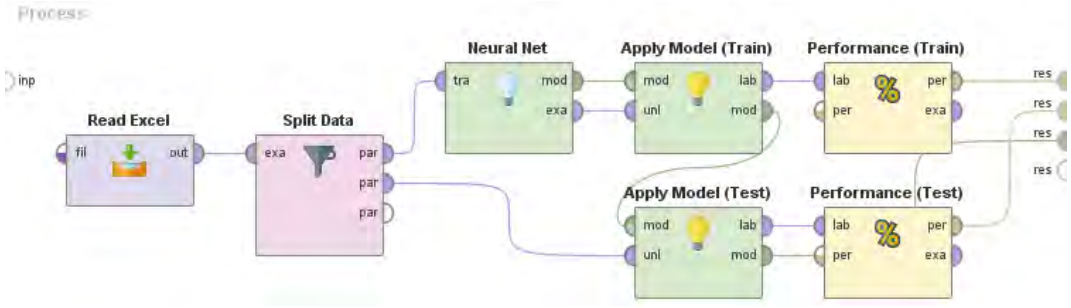

Figure 6.2 Scheme of the model generation using RapidMiner.

In order to predict the activity of new molecules, the models were saved (Write Model Operator) and then applied to a new database containing the candidates with the corresponding descriptors. The descriptors were calculated using MOE2014.09 and saved in an excel file which is read (Read Excel Operator) and applied to the model (Apply Model Operator). The results with the prediction of the activity of the candidates were written on a second excel file.

In the case of the "voting" strategy used in the last modification of the models, a breakpoint was introduced in the cross-validation operator and after each validation the model was saved obtaining a total of 5 models.

To predict the activity of the candidates, the 5 generated models were applied in parallel obtaining 5 different predictions (Figure 6.3). The 5 excel files were then manually analyzed to combine the different predictions and define which molecules were considered as active depending on the number of positive predictions. For the candidate selection, active molecules were selected when classified as active in at least 3 models.

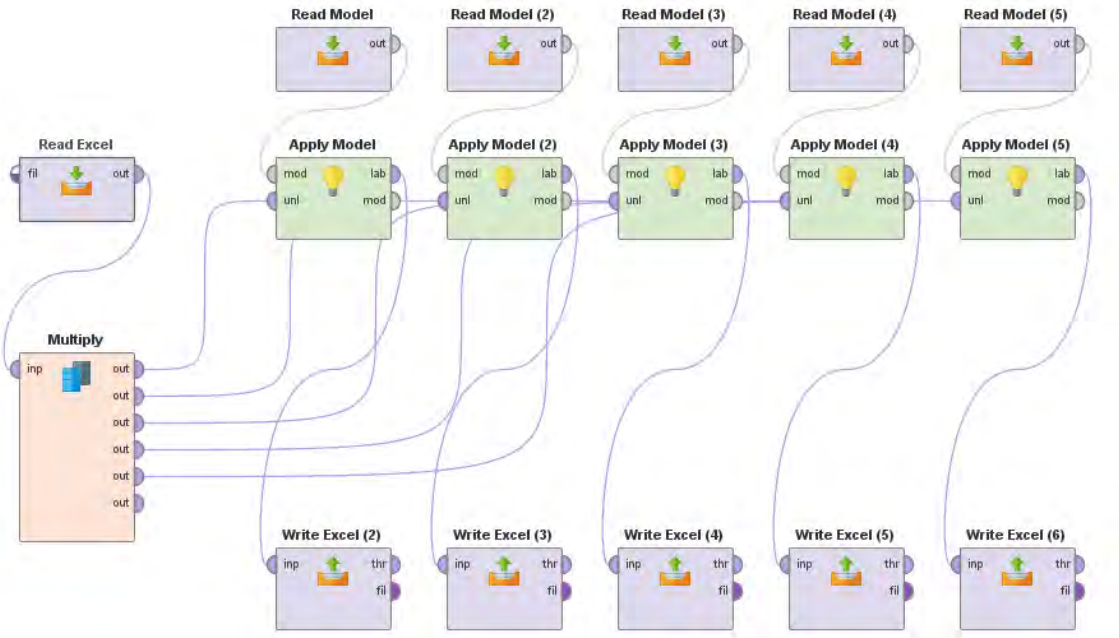

Figure 6.3. Application of the "voting" models using RapidMiner. The 5 models generated with the cross-validation are applied to the same file containing the candidates and their descriptors. For each model, the activity of the candidates is predicted and saved in an excel file

QSAR Predictive model

QSAR models were created using ArIS[29] on a 3.00GHz Intel® Core™ i5-7500 processor with 8 GB RAM. To build a QSAR predictive model using ArIS it is necessary to introduce the topology of the neural net, this being the number of inputs (corresponding to the number of descriptors), the number of hidden layers and the neurons in each layer. Then, it is necessary to define the number of iterations and the learning rate. The parameters of the final models are found in Table 6.10.The optimization of the parameters and the inputs to run the software are found in Annex 5.

For the creation of the models, a multilayer perceptron scheme was used defining the backpropagation batch as the learning algorithm. The split-sample validation and the leave-one-out cross-validation were used for model validation.[30]

In order to make the final model available for virtual screening of large databases, the model was implemented in MOE2014.09 using the SVL programing language.

Table 6.10. Optimized parameters for the QSPR models

MODEL	Model parameters
MNK1 QSAR model	7-6-4-1 artificial neural network with 0.0001 learning rate and 30000 iterations
MNK2 QSAR model	5-5-3-1 artificial neural network with 0.001 learning rate and 30000 iterations

6.3.2. Structure based drug design strategies

6.3.2.1 Preparation of the models for the study of the importance of the activation loop

Structure preparation

Structure of the MNK2 D228G mutant in the active conformation (PDB ID: 2HW7[31]) was downloaded from the PDB and prepared by using MOE2014.09[13]. Hydrogen atoms were added, minimized and protonation states were assigned, and crystallographic waters were removed.

This structure was used as reference to generate two additional structural models: (1) a model without the activation loop, obtained by manually removing the residues of the DFD-motif (D226-G228) included in 2HW7 and (2) a second model of the wildtype MNK2 protein including the activation loop in the active conformation. To generate the latest model, residue G228 was de-mutated to recover the wildtype sequence. The tertiary structure of the activation loop (involving L229-C251 residues) was predicted *de novo* by applying the loop modeler module available in MOE2014.09. All calculations were conducted using the Amber12 forcefield.

Modelling of the loop by molecular dynamics

The best loop candidate was selected and energy minimized by molecular dynamics (MD) simulations to obtain the final model. AMBER software [32] was used on a 3.5 GHz x 8 Intel Seon® CPU E3-1270 V3 with 32 GB. Amber ff13 forcefield was used for the parameters of standard amino acids. The system was subjected to a first minimization including a 5000-step minimization of TIP3P water molecules followed by a 20000-step energy minimization of the entire system. The system was then heated to 300 K in 200 ps using the Langevin thermostat restraining the backbone atoms except the loop atoms using an 8 $kcal \cdot mol^{-1} \cdot Å^{-2}$ force constant. Pressure equilibration (1 atm) was performed for 1000 ps maintaining the restraints previously described. The SHAKE algorithm[33] was used throughout to restrain the bonds involving hydrogens and the Particle Mesh Ewald[34] method for long range electrostatic, while the short range interactions had a 10Å cutoff radius. The production phase was extended to 20 ns defining a 2 fs time-step.

Molecular docking

Rigid docking was performed using AutoDock 4 and AutoDock Tools[35] on a 1.80 GHz Intel® Core™ i5-3337U processor with 4 GB RAM. A 126x126x126 Å grid was defined to perform a blind docking. Lamarckian Genetic Algorithms (GA) were used as docking search method, fixing the number of GA runs to 200, defining a population size of 500 and a maximum number of 2500000 evaluations. The evaluation of the results was performed by performing a cluster analysis using the same software.

MOE2014.09 software was applied to include a flexible receptor into docking procedure (i.e. induced fit protocol). Docking poses were generated using the triangle matcher placement method (2000 poses) and scored using London ΔG scoring function and GBVI/WSA ΔG for rescoring (100 poses).

6.3.2.2 Preparation of the MNK1 models

The three dimensional structure of the active models was obtained by homology modelling using the active MNK2 model (with the activation loop) previously described. The sequence of MNK1 and the MNK2 model were aligned and the tridimensional structure was created based on the tertiary structure of the MNK2 model obtaining the active MNK1 structure (2hw6hm). Using MOE2014.09, the phosphorylated model was prepared by manually phosphorylating the residues Thr209 and Thr214 to create the initial p-MNK1 active model (2hw6phm).

The inactive unphosphorylated model (referred as 2hw6 in the text) was created using the available crystal structure (PDB ID: 2HW6[31]). The tertiary structure of the missing fragments was predicted *de novo* by applying the loop modeler module available in MOE2014.09. The best loop candidate was energy minimized by molecular dynamics (MD) simulations, using AMBER software [32], by applying the same protocol previously described for MNK2. In this case, the short range interactions were set at 8 Å cutoff radius. The production was extended to 2 ns defining a 2 fs time-step. Amber ff13 forcefield was used for the parameters of standard amino acids.
Finally, the inactive phosphorylated model (2hw6p) was prepared by manually phosphorylating residues Thr209 and Thr214 of the inactive model.

The four models were then submitted to a MD simulation using the same conditions previously described but with no restrictions. Amber ff13 forcefield was used for the parameters of standard amino acids. The parameters described by Homeyer *et al.* were used for phosphorylated amino acids.[36] The production stage was extended to at least 70 ns defining a 2 fs time-step (until RMSD was stable). These simulations were performed using the resources from the BSC-RES (throughout BCV-2015-2-0001, BCV-2015-3-0009 and BCV-2016-3-0016 granted projects)

Finally, an accelerated MD (aMD) simulation was performed to explore a higher number of stable conformations. The parameters used in each for the aMD simulation were calculated from the corresponding MD simulation and are summarized in Table 6.11. The simulations were extended until the RMSD values were stable: simulations inactive models (2hw6 and 2hw6p) were 90000 steps long while for the active models (2hw6hm and 2hw6phm) the simulations had to be extended 120000 steps to stabilize the RMSD. Simulations were performed in a 4.20 GHz x 8 Intel® Core™ i7-7700K processor with 16 GB RAM and a GeForce GTX 1050 Ti/PCIe/SSE2 graphic card.

Table 6.11. Parameters for the aMD simulation obtained from the MD simulation. (2hw6: inactive unphosphorylated model of MNK1, 2hw6p: inactive phosphorylated model of MNK1, 2hw6hm: active unphosphorylated model of MNK1, 2hw6phm: active phosphorylated model of MNK1)

Parameter	2hw6	2hw6p	2hw6hm	2hw6phm	input flag
E(tot)	-205630.7	-206406.9	-150665.2	-147028	EthreshP
alpha(tot)	14664.6	14655.2	10772.2	10465	alphaP
E(dih)	383.8	300.23	344	343.2	EthreshD
alpha(dih)	209.3	209.3	210	206	alphaD

Cluster analysis was performed with CPPTRAJ[37] (Annex 5). For each simulation, the most populated and stable cluster was selected as the representative structure of each state of the protein.

6.3.2.3 Study of the interaction mode of the ligands

Complex preparation

For each of the four models, the most plausible active site was identified by performing a blind docking of different ligands using MOE 2016.08[38] on a 2.6 GHz Intel®Core™ i7-6700HQ with 8 GB RAM. Docking poses were generated using the triangle matcher placement method (1000 poses) with the induce fit protocol and scored using London ΔG scoring function and GBVI/WSA ΔG for rescoring (100 poses). The most populated cluster was defined as the active site. For each model, a conformation of the ligand found in the identified active site was selected to study the interaction with the protein.

MD simulation

A 50 ns MD simulation was performed for each ligand-protein complex. The system was subjected to a first minimization including a 5000-step minimization of TIP3P water molecules followed by a 20000-step energy minimization of the entire system. Then, the system was heated to 300 K in 200 ps using the Langevin thermostat. Pressure equilibration (1 atm) was performed for 1000 ps. The SHAKE algorithm[33] was used throughout to restrain the bonds involving hydrogens and the Particle Mesh Ewald[34] method for long range electrostatic, while the short range interactions had a 8 Å cutoff radius. The production phase was extended to 50 ns defining a 2 fs time-step. Amber ff13 forcefield was used for the parameters of standard amino acids. The parameters described by Homeyer *et al.* were used for phosphorylated residues.[36] Simulations were performed in a 4.20 GHz x 8 Intel® Core™ i7-7700K processor with 16 GB RAM and a GeForce GTX 1050 Ti/PCIe/SSE2 graphic card.

Characterization of the interaction

The binding free energy of the complexes was calculated using the Molecular Mechanics Poison-Boltzmann Surface Area (MM-BPSA) methodology available in AMBER 14.[32] For each complex, 2500 conformations were extracted from the last 5 ns of the MD simulations. The interaction energy and solvation free energy for complex, receptor, and ligand were calculated to estimate of the binding free energy.

The study of the hydrogen bond pattern was performed using CPPTRAJ.[37] Hydrogen bonds were determined using simple geometric criteria such as the donor to acceptor heavy atom distance.

Ligand-protein interactions were visualized with MOE2016.08.[38]

6.3.3. Quantum mechanics calculations

All electronic structure calculations were carried out using the Gaussian 09 Rev. E.01[39]. An hybrid non-local density functional theory (DFT), particularly Becke's gradient-corrected exchange-correlation density functional B3LYP with the 6-31++G(d,p) basis set was used for the geometry optimization and the calculation of frequencies. All calculations were performed on a 3.00GHz Intel® Core™ i5-7500 processor with 8 GB RAM.

6.4. References

1. Peterson, J. R., Russell, M. E. & Surjasasmita, I. B. Synthesis and experimental ionization energies of certain (E)-3-arylpropenoic acids and their methyl esters. *J. Chem. Eng. Data* **33,** 534–537 (1988).

2. Camarasa, M. Tesi Doctoral. Disseny, Síntesi i Activitat Biològica de Sistemes Pirido[2,3-d] pirimidínics com a Inhibidors del Virus de l'Hepatitis C. (IQS School of Engineering, Universitat Ramon Llull, 2014).

3. Clarke, M. L. & Roff, G. J. Highly Regioselective Rhodium-Catalysed Hydroformylation of Unsaturated Esters: The First Practical Method for Quaternary Selective Carbonylation. *Chem. Eur. J.* **12,** 7978–7986 (2006).

4. Berzosa, X., Bellatriu, X., Teixidó, J. & Borrell, J. I. An Unusual Michael Addition of 3,3-Dimethoxypropanenitrile to 2-Aryl Acrylates: A Convenient Route to 4-Unsubstituted 5,6-Dihydropyrido[2,3- d]pyrimidines. *J. Org. Chem.* **75,** 487–490 (2010).

5. Matarín, J. Design and synthesis of heterocyclic compounds with activity against pancreatic cancer. *Master Thesis* (IQS School of Engineering, Universitat Ramon Llull, 2017).

6. J. Victory, P. & Garriga, M. Cyclization of Dinitriles by Hydrogen Halides. 2. Hydrogen Chloride and Hydrogen Iodine. *Heterocycles* **23,** 2853 (1985).

7. Bou-Petit, E. Study of new antitumor therapeutic applications: Design, synthesis and validation of inhibitors of eIF4E phosphorylation. (IQS School of Engineering, Universitat Ramon Llull, 2014).

8. Galve Murillo, I. Síntesis de pirido[2,3-d]pirimidin-7(8H)-onas 2-arilamino sustituidas y derivados. (IQS School of Engineering, Universitat Ramon Llull, 2013).

9. Massip, V. Síntesi de sistemes pirido[2,3-d]pirimidin-7(8H)-ones com a inhibidors potencials de VEGFR2 (IQS School of Engineering, Universitat Ramon Llull, 2017).

10. Klingele, M. H. & Brooker, S. FromN-Substituted Thioamides to Symmetrical and Unsymmetrical 3,4,5-Trisubstituted 4H-1,2,4-Triazoles: Synthesis and Characterisation of New Chelating Ligands. *European J. Org. Chem.* 3422–3434 (2004).

11. Zhang, J.-H., Chung, T. & Oldenbrug, K. A Simple Statistical Parameter for Use in Evaluation and Validation of High Throughput Screening Assays. *J. Biomol. Screen.* **4,** 67–73 (1999).

12. Iversen, P. W., Eastwood, B. J., Sittampalam, G. S. & Cox, K. L. A Comparison of Assay Performance Measures in Screening Assays: Signal Window, Z' Factor, and Assay Variability Ratio. *J. Biomol. Screen.* **11,** 247–252 (2006).

13. Molecular Operating Environment (MOE), 2014.09. Chemical Computing Group ULC, 1010 Sherbooke St. West, Suite #910, Montreal, QC, Canada, H3A 2R7 (2014).

14. Gaulton, A. *et al.* ChEMBL: a large-scale bioactivity database for drug discovery. *Nucleic Acids Res.* **40,** D1100–D1107 (2012).

15. Gaulton, A. *et al.* The ChEMBL database in 2017. *Nucleic Acids Res.* **45,** D945–D954 (2017).

16. Bento, A. P. *et al.* The ChEMBL bioactivity database: an update. *Nucleic Acids Res.* **42,** D1083–D1090 (2014).

17. Oyarzabal, J. *et al.* Discovery of Mitogen-Activated Protein Kinase-Interacting Kinase 1 Inhibitors by a Comprehensive Fragment-Oriented Virtual Screening Approach. *J. Med. Chem.* **53,** 6618–6628 (2010).

18. Diab, S. *et al.* Discovery of 5-(2-(phenylamino)pyrimidin-4-yl)thiazol-2(3H)-one derivatives as potent Mnk2 inhibitors: synthesis, SAR analysis and biological evaluation. *ChemMedChem* **9,** 962–972 (2014).

19. Kannan, S. *et al.* Probing the binding mechanism of Mnk inhibitors by docking and molecular dynamics simulations. *Biochemistry* **54,** 32–46 (2015).

20. Teo, T. *et al.* An integrated approach for discovery of highly potent and selective Mnk inhibitors: Screening, synthesis and SAR analysis. *Eur. J. Med. Chem.* **103,** 539–50 (2015).

21. Teo, T. *et al.* Pharmacologic Inhibition of MNKs in Acute Myeloid Leukemia. *Mol. Pharmacol.* **88,** 380–389 (2015).

22. Yu, M. *et al.* Discovery of 4-(dihydropyridinon-3-yl)amino-5-methylthieno[2,3-d]pyrimidine derivatives as potent Mnk inhibitors: synthesis, structure–activity relationship analysis and biological evaluation. *Eur. J. Med. Chem.* **95,** 116–126 (2015).

23. Cherian, J. *et al.* Structure-Activity Relationship Studies of Mitogen Activated Protein Kinase Interacting Kinase (MNK) 1 and 2 and BCR-ABL1 Inhibitors Targeting Chronic Myeloid Leukemic Cells. *J. Med. Chem.* **59,** 3063–3078 (2016).

24. Diab, S. *et al.* Unveiling new chemical scaffolds as Mnk inhibitors. *Future Med. Chem.* **8,** 271–285 (2016).

25. Reich, S. H. *et al.* Structure-based Design of Pyridone-Aminal eFT508 Targeting Dysregulated Translation by Selective Mitogen-activated Protein Kinase Interacting Kinases 1 and 2 (MNK1/2) Inhibition. *J. Med. Chem.* **61,** 3516–3540 (2018).

26. Han, W. *et al.* Discovery of a Selective and Potent Inhibitor of Mitogen-Activated Protein Kinase-Interacting Kinases 1 and 2 (MNK1/2) Utilizing Structure-Based Drug Design. *J. Med. Chem.* **59,** 3034–3045 (2016).

27. Zhan, Y. *et al.* MNK1/2 inhibition limits oncogenicity and metastasis of KIT-mutant melanoma. *J. Clin. Invest.* **127,** 4179–4192 (2017).

28. RapidMiner Studio. (2016).

29. Estrada Tejedor, R. Implementació d'algorismes genètics en el programari Pralins per a la selecció de quimioteques. (IQS School of Engineering, Universitat Ramon Llull, 2006).

30. Estrada Tejedor, R. Desenvolupament del programari ArIS (Artificial Intelligence Suite): implementació d'eines de cribratge virtual per a la química mèdica. (IQS School of Engineering, Universitat Ramon Llull, 2011).

31. Jauch, R. *et al.* Mitogen-activated protein kinases interacting kinases are autoinhibited by a reprogrammed activation segment. *EMBO J.* **25,** 4020–4032 (2006).

32. Case, D. A. *et al.* AMBER 14. University of California, San Francisco (2014).

33. Ryckaert, J., Ciccotti, G. & Berendsen, H. Numerical integration of the cartesian equations of motion of a system with constraints: molecular dynamics of n-alkanes. *J. Comput. Phys.* **23,** 327–341 (1977).

34. Darden, T., York, D. & Pedersen, L. Particle mesh Ewald: An N ·log(N) method for Ewald sums in large systems. *J. Chem. Phys.* **98,** 10089–10092 (1993).

35. Morris, G. M. *et al.* AutoDock4 and AutoDockTools4: Automated docking with selective receptor flexibility. *J. Comput. Chem.* **30,** 2785–2791 (2009).

36. Homeyer, N., Horn, A. H. C., Lanig, H. & Sticht, H. AMBER force-field parameters for phosphorylated amino acids in different protonation states: phosphoserine, phosphothreonine, phosphotyrosine, and phosphohistidine. *J. Mol. Model.* **12,** 281–289 (2006).

37. Roe, D. R. & Cheatham, T. E. PTRAJ and CPPTRAJ: Software for Processing and Analysis of Molecular Dynamics Trajectory Data. *J. Chem. Theory Comput.* **9,** 3084–3095 (2013).

38. Molecular Operating Environment (MOE), 2016.08. Chemical Computing Group ULC, 1010 Sherbooke St. West, Suite #910, Montreal, QC, Canada, H3A 2R7 (2016).

39. Frisch, M. J. *et al.* Gaussian (G09). Wallingford CT (2009).

CHAPTER 7

General discussion

7.1. General discussion and future directions

Identification of suitable scaffolds for the development of MNK inhibitors

A big effort is being done on the development of new, more potent and effective strategies for cancer treatment. Among those, the pharmacological inhibition of MNK1/2 to reduce eIF4E phosphorylation has been proposed as a new effective and non-toxic strategy.[1] Consequently, different research groups have focused on identifying new chemical scaffolds to inhibit MNK kinase activity as a first step in the development of new cancer therapies.[2,3]

When starting with the project, only few inhibitors had been described and despite their activity towards MNK kinases, this compounds did not show a significant selectivity for MNKs.[1] Among these compounds, **CGP57380** was considered as the most interesting product and was widely used to study the function of the MNK/eIF4E axis. However, the lack of selectivity and low efficacy (micromolar range) of **CGP57380** asked for the development of new inhibitors with a potential use in the clinics.[4] Based on the described activity towards MNKs, **CGP57380** was used as reference molecule for the development of new MNK inhibitors as putative drug candidates.

Since the pyrazolo[3,4-*b*]pyridine-6-one scaffold, which has been intensively studied by the Grup de Química Farmacèutica (GQF) from the IQS[5], presented some similarities with **CGP57380**, we started the development of novel MNK inhibitors based on this scaffold. Initially, two sets of compounds were prepared and general methodologies to synthesize these compounds with the desired combination of substituents were optimized. At that point, a general exploration of the possible chemical space was necessary, as no information was available to rationally select the candidates. Unfortunately, none of the first set of compounds showed a significant inhibition of MNKs.

By that time, some articles containing structures with inhibitory activities for MNKs had been published.[6–11] Data from the previously synthetized compounds and the new compounds described in the literature were used to create a classificatory QSPR and a predictive QSAR model for the selection of the next candidates. To the best of our knowledge, there are no reports in the literature where a ligand-based strategy has been used for the development of MNK inhibitors. Taken the published data on MNK inhibitors into consideration, this strategy was expected to be a fast and efficient methodology for the selection of new candidates. Unfortunately, none of the tested molecules was active, demonstrating that the initial model was not capable of predicting the activity of the scaffolds under study.

As the generation of accurate models largely relies on precise experimental data, the increasing amount on published data helped to improve the model.[2,12–14] The preparation of models for candidate selection is an iterative process which requires the continuous introduction of new and actualized data. The final model obtained in this project presents a solid predicting capacity and can be therefore used in the selection of future candidates derived from this project.

The main difference between the compounds presented in this work and the compounds that had been published was the presence of the lactam group, which was expected to increase the interactions between the inhibitor and the protein by providing an extra H-bond donor and acceptor. However, the effect on compound solubility and the possible dimerization of the compounds was a concern.

Consequently, we decided to substitute the pyridone moiety of pyrazolo[3,4-*b*]pyridin-6-ones by a pyridine ring and use pyrazolo[3,4-*b*]pyridines as scaffolds. The study of a small family of these compounds allowed the identification of an initial hit (compound **139**{*3*,*3*,*1*} or **EB1**). SAR analysis revealed that the presence of phenyl rings in positions C4 and C6 of the pyridine moiety was essential for the activity. Moreover, it was also necessary to maintain the amino-pyrazole ring unsubstituted. With this information in mind, a new methodology for the preparation of pyrazolo[3,4-*b*]pyridines was developed which combines the recently described one-pot methodology from Amer *et al*.[15] with the experience and knowledge of the GQF of IQS. In that way, we prepared a family of 4,6-aryl-substituted pyrazolo[3,4-*b*]pyridines with representative substituents in different positions of the phenyl rings that were biologically evaluated.

Despite it was not possible to identify a molecule with a higher activity than **EB1**, SAR analysis of the results allowed the identification of combinations of positions and functional groups that should permit the modulation of the activity to design selective or dual inhibitors. Although, it was not possible to apply such knowledge during this project, this information can provide new opportunities to increase the activity of such molecules and develop potent inhibitors.

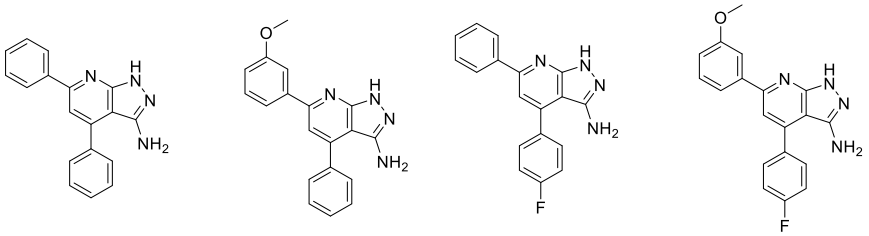

139{*3*,*3*,*1*}
EB1

139{*5*,*3*,*1*}
EB2

139{*3*,*6*,*1*}
EB3

139{*5*,*6*,*1*}
EB4

Figure 7.1. Structure of 4,6-diphenyl-pyrazolo[3,4-b]pyridin-3-amines studied in this project

Three compounds (**EB2**, **EB3** and **EB4**) were selected and studied together with the initial compound (**EB1**). These molecules selectively inhibited MNKs with no effect on cell growth. These features have been defined as characteristic of MNK inhibitors and are also described for the two main compounds that have recently entered in clinical trials.[12,16]

For all the studied compounds, no alteration was observed on other pathway-related proteins indicating that inhibition of eIF4E phosphorylation was caused only by the effect of the compounds on the MNKs. Moreover, the kinome analysis performed for **EB1** indicated that the compound affected only 16 out of 320 tested kinases. The results of the kinome are remarkable for an initial hit, especially when taking into consideration the small size of the molecule. Moreover, most of the identified off-targets have been crystalized and their structures are available in the PDB database.[17–19] This information will be crucial for the further improvement of the molecule as the main interactions between the "off-target" kinases and the inhibitor can be identified with structure-based strategies. Eliminating those interactions and potentiating the interactions of interest will surely further improve the efficacy and selectivity of the newly designed and synthesized compounds towards MNKs.

Although the 3-amino-pyrazolo[3,4-*b*]pyridine scaffold has been described in certain applications, there are no reports of the use of such structures as MNK inhibitors. Furthermore, some published MNK inhibitors contain a pyrazolo[3,4-*b*]pyridine moiety in their structure but the activity of the pyrazolo[3,4-*b*]pyridine core itself has not been considered as the active moiety of this compounds.[20,21] Altogether, the simplicity and small size of the compounds makes it perfect hit and suitable for future compound optimization.

The structure of MNK2 and its activation mechanism has been widely studied in the last years.[22] However, there are no equivalent studies with MNK1 provably due to the lack of information of the active forms. During this project, we have developed *in silico* models for both the active and inactive forms of MNK1 and we have considered the effect of phosphorylation. With these models, the binding mode of **EB1** was studied and the compound was proposed to be a Type II inhibitor that binds to the inactive form of MNK1. Contrary to other studies, where only a single model has been applied to define the inhibitor type[21], our strategy takes into account four possible states of the protein (active/inactive, phosphorylated and unphosphorylated). The binding mode of the inhibitor has been finally defined according the best fitting model. While this computational based prediction will need experimental support in the future, the chosen strategy can be considered to provide more reliable results.

The identification of a small molecule capable of interacting as a Type II inhibitors is promising. Up to know, the only two molecules that have reached clinical trials are ATP-competitive Type I inhibitors.[12,16] The identification of potent Type II inhibitors would provide new treatment opportunities alternative to the actual inhibitors and opens a new line of investigation on the field.

In addition to the studies of the binding mode, these models can be used for SAR studies and simplify compound selection with a structure-based optimization procedure. This strategy would be equivalent to those already applied by several authors on the development of MNK2 inhibitors.[7,12,23,24]

Finally, **EB1** was shown to sensitize triple negative breast cancer cells to chemotherapy. MNK inhibitors are being designed as non-cytotoxic sensitizers for current treatments, especially for chemotherapy. The use of MNK inhibitors as sensitizing agents is also described for both MNK inhibitors that are currently in clinical trial stages (**EFT508** and **BAY1143269**).[12,16] While this indicates that the use of this type of compounds can be potentially implicated in the clinics, it is also remarkable that, besides **EB1**, none of these inhibitors has been described for the use in triple negative breast cancer, neither *in vitro* nor *in vivo*. Future comparative analysis between the different inhibitors will help to figure out, if this is due to the fact that only **EB1** is a Type II inhibitor. Furthermore, pre-clinical *in vivo* studies will be required to test the potential application of **EB1** as sensitizing agent for the treatment of TNBC. In this respect, the study for the treatment of orthotopic models of TNBC has been designed and will consist of a combined treatment of a MNK inhibitor and chemotherapy after tumor resection – a scenario more similar to the potential application of such treatment in the clinics.

Combination of research areas on the drug development process

This project has effectively combined three different areas for the development of new inhibitors. The computational studies have provided methods for candidate selection and identification of binding modes. Then, the compounds have been synthesized, a process that usually requires the optimization of the methodologies and the conscious study of spectroscopic data to ensure the structure of the molecules. And finally, the biological testing of the candidates has been performed at both at protein and at *in vitro* level in different cell lines.

The combination of the three different areas in the same project is considered a necessary strategy as the combined knowledge is the key for obtaining positive and useful results.

In this project, the design of novel MNK inhibitors has also taken in consideration the available bibliographic information and the know-how of the involved groups. This project has been developed at a time when the development of inhibitors of eIF4E phosphorylation is booming and at every different step, the evolution of the project has included the most recent publications and advances in the field. Despite the efforts of scientist and companies, this field is still under study and no drugs have reached the market yet demonstrating that the development of potent and selective MNK inhibitors is still a challenge.

7.2. References

1. Hou, J., Kam, F., Proud, C. G. & Wang, S. Targeting Mnks for Cancer Therapy. *Oncotarget* **3,** 118–131 (2012).

2. Diab, S. *et al.* Unveiling new chemical scaffolds as Mnk inhibitors. *Future Med. Chem.* **8,** 271–285 (2016).

3. Dreas, A. *et al.* Mitogen-activated Protein Kinase (MAPK) Interacting Kinases 1 and 2 (MNK1 and MNK2) as Targets for Cancer Therapy: Recent Progress in the Development of MNK Inhibitors. *Curr. Med. Chem.* **24,** 3025–3053 (2017).

4. Wheater, M. J., Johnson, P. W. & Blaydes, J. P. The role of MNK proteins and eIF4E phosphorylation in breast cancer cell proliferation and survival. *Cancer Biol. Ther.* **10,** 728–735 (2010).

5. Falcó, J. L. *et al.* Design, synthesis and biological activity of acyl substituted 3-amino-5-methyl-1,4,5,7-tetrahydropyrazolo[3,4-b]pyridin-6-ones as potential hypnotic drugs. *Eur. J. Med. Chem.* **40,** 1179–1187 (2005).

6. Oyarzabal, J. *et al.* Discovery of Mitogen-Activated Protein Kinase-Interacting Kinase 1 Inhibitors by a Comprehensive Fragment-Oriented Virtual Screening Approach. *J. Med. Chem.* **53,** 6618–6628 (2010).

7. Diab, S. *et al.* Discovery of 5-(2-(phenylamino)pyrimidin-4-yl)thiazol-2(3H)-one derivatives as potent Mnk2 inhibitors: synthesis, SAR analysis and biological evaluation. *ChemMedChem* **9,** 962–972 (2014).

8. Kannan, S. *et al.* Probing the binding mechanism of Mnk inhibitors by docking and molecular dynamics simulations. *Biochemistry* **54,** 32–46 (2015).

9. Teo, T. *et al.* An integrated approach for discovery of highly potent and selective Mnk inhibitors: Screening, synthesis and SAR analysis. *Eur. J. Med. Chem.* **103,** 539–550 (2015).

10. Yu, M. *et al.* Discovery of 4-(dihydropyridinon-3-yl)amino-5-methylthieno[2,3-d]pyrimidine derivatives as potent Mnk inhibitors: synthesis, structure–activity relationship analysis and biological evaluation. *Eur. J. Med. Chem.* **95,** 116–126 (2015).

11. Cherian, J. *et al.* Structure-Activity Relationship Studies of Mitogen Activated Protein Kinase Interacting Kinase (MNK) 1 and 2 and BCR-ABL1 Inhibitors Targeting Chronic Myeloid Leukemic Cells. *J. Med. Chem.* **59,** 3063–3078 (2016).

12. Reich, S. H. *et al.* Structure-based Design of Pyridone-Aminal eFT508 Targeting Dysregulated Translation by Selective Mitogen-activated Protein Kinase Interacting Kinases 1 and 2 (MNK1/2) Inhibition. *J. Med. Chem.* **61,** 3516–3540 (2018).

13. Han, W. *et al.* Discovery of a Selective and Potent Inhibitor of Mitogen-Activated Protein Kinase-Interacting Kinases 1 and 2 (MNK1/2) Utilizing Structure-Based Drug Design. *J. Med. Chem.* **59,** 3034–3045 (2016).

14. Hu, K., Zhang, J., Yu, M. & Xiong, C. Inhibition of Mnk-eIF4E pathway sensitizes the efficacy to chemotherapy in anaplastic thyroid cancer. *Futur. Oncol.* **13,** 489–498 (2017).

15. Amer, A. A. & Abdelhamid, A. A. Microwave-Assisted, One-Pot Multicomponent Synthesis of Some New Cyanopyridines. *J. Heterocycl. Chem.* **54,** 3126–3132 (2017).

16. Santag, S. *et al.* BAY 1143269, a novel MNK1 inhibitor, targets oncogenic protein expression and shows potent anti-tumor activity. *Cancer Lett.* **390,** 21–29 (2017).

17. Campbell, J. C. *et al.* Structural Basis of Cyclic Nucleotide Selectivity in cGMP-dependent Protein Kinase II. *J. Biol. Chem.* **291,** 5623–5633 (2016).

18. Kikani, C. K. *et al.* Structural Bases of PAS Domain-regulated Kinase (PASK) Activation in the Absence of Activation Loop Phosphorylation. *J. Biol. Chem.* **285,** 41034–41043 (2010).

19. Overman, R. C., Debreczeni, J. E., Truman, C. M., McAlister, M. S. & Attwood, T. K. Completing the structural family portrait of the human EphB tyrosine kinase domains. *Protein Sci.* **23,** 627–638 (2014).

20. Klar, U. *et al.* Substituted pyrazolo-pyridinamines. WO 2015/004024 A1 (2015).

21. Kannan, S. *et al.* Small Molecules Targeting the Inactive Form of the Mnk1/2 Kinases. *ACS Omega* **2,** 7881–7891 (2017).

22. Hou, J., Teo, T., Sykes, M. J. & Wang, S. Insights into the Importance of DFD-Motif and Insertion I1 in Stabilizing the DFD-Out Conformation of Mnk2 Kinase. *ACS Med. Chem. Lett.* **4,** 736–41 (2013).

23. Jin, X. *et al.* Design, synthesis and activity of Mnk1 and Mnk2 selective inhibitors containing thieno[2,3-d]pyrimidine scaffold. *Eur. J. Med. Chem.* 735–751 (2019).

24. Teo, T. *et al.* An integrated approach for discovery of highly potent and selective Mnk inhibitors: Screening, synthesis and SAR analysis. *Eur. J. Med. Chem.* **103,** 539–550 (2015).

CHAPTER 8

Conclusions

Conclusions

1. The cyclization 2-methoxy-6-oxo-1,4,5,6-tetrahydropyridin-3-carbonitriles (**62**) with hydrazines (**56**) has been studied in depth to elucidate the reaction mechanism and the possible formation of the N1 and N2 substituted isomers. The reaction with arylhydrazines only affords N2-aryl substituted compounds while the reaction with methylhydrazine yields a mixture of both isomers proving that the reaction is directed by the relative nucleophilicity of the nitrogen atoms of the hydrazine. The reaction occurs *via* the formation of an open intermediate 2-hydrazono-6-oxo-piperidine-3-carbonitrile (**76**) which then cyclizes to the corresponding 3-amino-pyrazolo[3,4-*b*]pyridin-6-one (**63**/**64**). The high energetic barriers on the cyclization with phenylhydrazine (~42 Kcal/mol) allow the isolation of such intermediate.

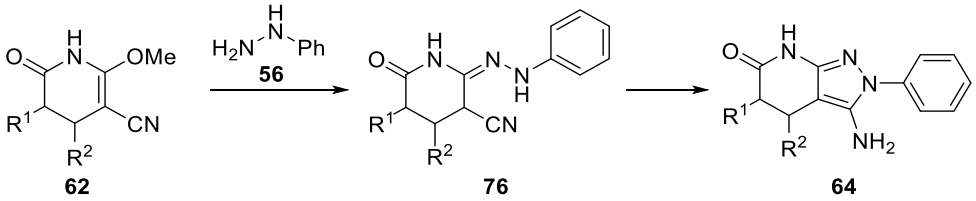

2. The synthesis of the N1-aryl substituted 3-amino-pyrazolo[3,4-*b*]pyridin-6-ones (**84**) has been achieved using Ullman catalytic conditions to introduce the phenyl ring in the N1 position of the dehydrogenated 3-amino-5-phenyl-2,7-dihydro-6*H*-pyrazolo[3,4-*b*]pyridin-6-one (**85**{*3,1,1*}) despite in low yields. An alternative "reverse" synthesis based on the construction of the pyridone ring from a preformed pyrazole ring only led to the 1,5-diphenyl-1,7-dihydro-6*H*-pyrazolo[3,4-*b*]pyridin-6-one (**98**).

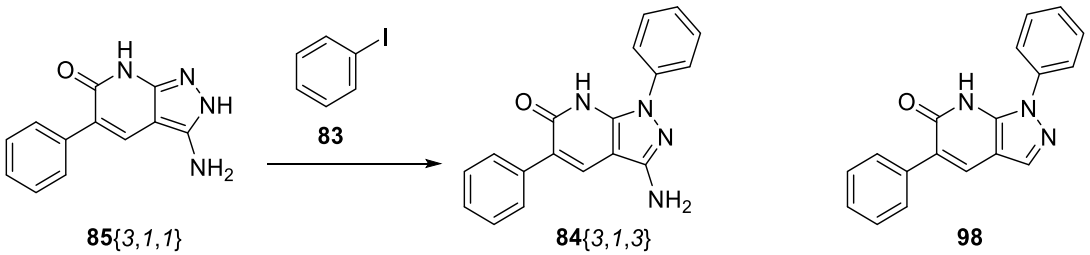

3. The acylation reaction of 3-amino-pyrazolo[3,4-*b*]pyridin-6-ones follows a kinetic *vs.* thermodynamic reaction control were the N1-acyl substituted product (**109**) is the kinetic isomer, obtained at low temperatures, and the N2-acyl substituted product (**110**) is the thermodynamic isomer, obtained at high temperatures. The thermodynamic isomer was also obtained by the cyclization of 2-methoxy-6-oxo-1,4,5,6-tetrahydropyridin-3-carbonitriles (**62**) with hydrazides (**113**). The final assignment of the structures was performed by labelling the molecule with ^{13}C.

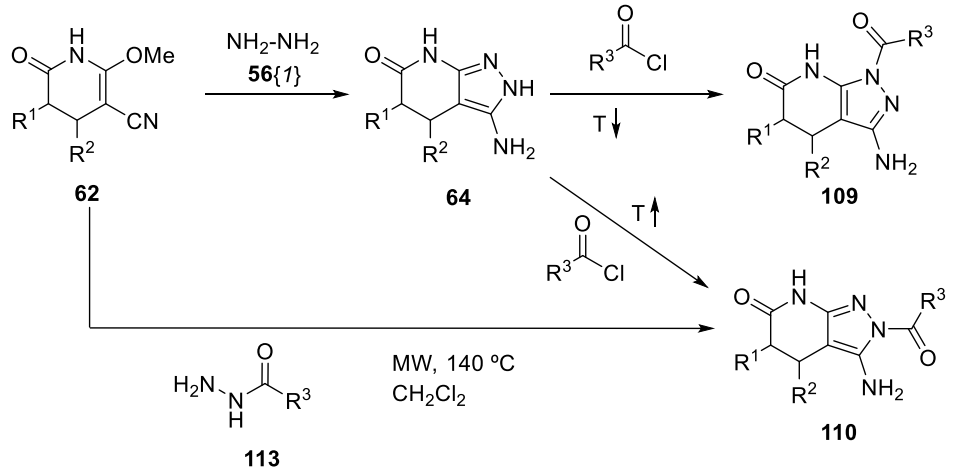

4. The library of pyrazolo[3,4-*b*]pyridin-6-ones obtained has been evaluated as MNK inhibitors. Unfortunately, these compounds do not inhibit the phosphorylation of eIF4E and, consequently, the pyrazolo[3,4-*b*]pyridin-6-one scaffold has been discarded for the development of MNK inhibitors.

5. A general methodology for the preparation of pyrazolo[3,4-*b*]pyridin-3-amine derivatives (**54**), consisting in the cyclization of 2-bromonicotinonitriles (**137**) with hydrazines (**56**) has been developed. It was not possible to obtain such compounds from the corresponding 3-amino-pyrazolo[3,4-*b*]pyridin-6-ones (**64**).

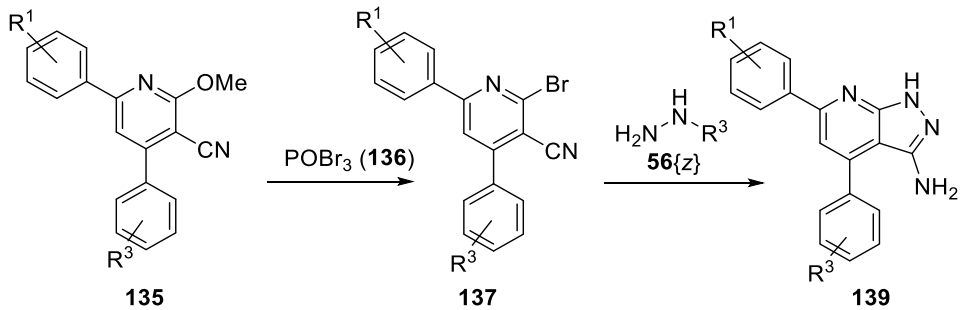

6. The library of pyrazolo[3,4-*b*]pyridin-3-amines has been evaluated as MNK inhibitors. 10 compounds reduced the residual activity of MNK1/2 and the levels of p-eIF4E in TNBC cells (MDA-MB-231). The presence of two aryl rings at positions C4 and C6 of the pyridine ring and the absence of substituents in the pyrazole are essential for the activity.

7. Compounds **EB1-4** have been characterized *in vitro*. These compounds present a higher potency for MNK1 with an enzymatic IC_{50} in the low micromolar range. The compounds completely inhibit eIF4E phosphorylation between 2.5 and 5 µM with minimal cytotoxicity. The effect on eIF4E phosphorylation is caused by a selective inhibition of MNK1/2 as no other pathway related proteins are affected by the compounds. Moreover, these compounds are not cell line selective.

8. **EB1** was combined with doxorubicin in MDA-MB-231 cells. The co-treatment with **EB1** clearly increased the sensitivity of MDA-MB-231 cells to doxorubicin improving the efficacy of the drug in inhibiting cell growth.

9. Structural models of the active/inactive and phosphorylated/unphosphorylated forms of MNK1 have been developed to study the interaction mechanism of the compounds. **EB1** is a Type II inhibitor that binds to the inactive form of MNK1 and stabilizes this conformation by interacting with the Phe192 from the DFD motif.

10. A structural model of the active form of MNK2 has been developed. Considering receptor flexibility and including the activation loop in the model are determinant for the correct description of the MNK2-ligand complex when applying SBDD strategies.

11. Ligand-based approaches have been applied developing a classificatory QSPR model and a predictive QSAR model. The predictive ability of the model is characterized by a very low rate of false positive results and can be therefore used to improve the enrichment of chemical libraries.